Viscoplasticité et endommagement des roches en application à la modélisation du comportement à long terme des ouvrages souterrains

Frederic Pellet

Université Joseph Fourier – Grenoble I

Mémoire de Diplôme d'Habilitation à Diriger des Recherches

Viscoplasticité et endommagement des roches en application à la modélisation du comportement à long terme des ouvrages souterrains

---

Frédéric Pellet

Docteur ès Sciences Techniques

Maître de conférences (Associate Professor)

Laboratoire Sols Solides Structures (3S)

Ecole Polytechnique de l'Université de Grenoble I

Présenté le 15 juin 2004 devant le jury composé de :

Prof. Jacky Mazars	Institut National Polytechnique de Grenoble	Président
Prof. Giovanni Barla	Politecnico di Torino	Rapporteur
Prof. Herbert Einstein	Massachusetts Institute of Technology	Rapporteur
Prof. Jack-Pierre Piguet	Ecole Supérieure des Mines de Nancy	Rapporteur
Prof. Pierre Bérest	Ecole Polytechnique	Examinateur
Prof. Peter Egger	Ecole Polytechnique Fédérale de Lausanne	Examinateur

Avant Propos

Le présent mémoire de synthèse est le résultat de sept années de recherche consacrées à l'étude du comportement à long terme des ouvrages souterrains. Ce travail est le fruit d'une collaboration étroite établie dans le cadre de relations contractuelles avec l'Institut de Radioprotection et de Sûreté Nucléaire principalement, mais aussi avec d'importants organismes privés et publics. Ce programme de recherche s'est orienté sur la problématique des ouvrages souterrains de stockage de déchets radioactifs en formation géologique profonde. Il a donné lieu à la réalisation de cinq thèses de doctorat que j'ai eu le plaisir de diriger ou de co-diriger (deux sont actuellement en voie d'achèvement). Par ailleurs des collaborations scientifiques ont été établies, au niveau international, notamment avec le Massachusetts Institute of Technology (MIT), l'Ecole Polytechnique Fédérale de Lausanne (EPFL), l'Université de Tsinghua (Chine), et l'International Institute of Earthquake Engineering and Seismology (Iran).

Ingénieur civil de formation, j'ai effectué une grande partie de mes études supérieures à l'étranger. Ces longs séjours en Suisse, au Canada puis aux Etats-Unis, m'ont imprégné des cultures scientifiques germanique et anglo-saxonne. De ce métissage, ma démarche scientifique s'est progressivement forgée pour me conduire vers le développement d'outils théoriques applicables à la résolution de problèmes pratiques.

On oppose en effet souvent, dans le monde académique, recherche fondamentale et recherche appliquée ou encore approche théorique et approche expérimentale. Cela n'a pas, à mon sens, grande signification car la résolution de problèmes liés à l'ingénierie nécessite obligatoirement de parcourir le continuum de la recherche scientifique en respectant un juste équilibre entre développements théoriques, expérimentations en laboratoire et observations in situ. Dans ma conception ce continuum de la recherche en géomécanique doit être parcouru dans un sens précis et son point de départ doit impérativement être l'observation in situ du problème posé. Dans un premier temps, il s'agit donc de décrire les phénomènes. Puis, vient le temps du formalisme théorique et de l'expérimentation en laboratoire pour enfin revenir sur le terrain en appliquant et en confrontant les résultats obtenus à la réalité, souvent par le biais de modélisations numériques. Dans ce contexte, je pense qu'il est capital de ne pas perdre de vue que la modélisation d'un phénomène n'est qu'une idéalisation, par essence simplificatrice, d'un ensemble de phénomènes complexes qu'il est nécessaire de hiérarchiser afin de ne pas se perdre dans le n^{ième} ordre de certains, au détriment du 1er ordre d'autres plus importants.

La géomécanique et la mécanique des roches en particulier demeurent une science incroyablement passionnante car la nature extrêmement diverse des roches et la variété de leurs conditions de gisement nécessitent pour leur étude une approche pluridisciplinaire, associant toutes les branches des géosiences (géochimie, géologie, géomécanique, etc). L'interaction entre formations géologiques et ouvrages de génie civil met en jeu des phénomènes se produisant sur une échelle très étendue, allant de la microstructure de la roche à l'échelle macroscopique de l'ouvrage. Dans ce contexte, les grands enjeux de société actuels, tels que les risques naturels ou anthropiques, lancent un défi permanent aux scientifiques et aux ingénieurs. Nul doute que dans le futur de substantiels progrès seront accomplis grâce à cette approche pluridisciplinaire et contemporaine.

Dans ce mémoire, j'ai délibérément pris le parti, à une exception près, de ne pas exposer mes travaux scientifiques antérieurs à ma venue au laboratoire 3S. Ainsi, ni ma thèse de doctorat, réalisée à l'Ecole Polytechnique Fédérale de Lausanne dans le domaine du renforcement des massifs rocheux, ni les études effectuées lors de mon passage dans des sociétés d'ingénierie, ne seront présentées. Le lecteur intéressé trouvera néanmoins, les références relatives à ces sujets dans mon curriculum vitae, en fin de fascicule ainsi que la publication synthétisant mon travail de doctorat à l'annexe IV.

Dans ce qui suit, j'exposerai ma contribution scientifique à l'étude du comportement à long terme des ouvrages souterrains. Bien que de nombreux secteurs de l'activité économique soient concernés, comme la gestion de l'espace souterrain dans les grands centres urbains, les projets de grandes infrastructures souterraines de transport (liaisons ferroviaires transalpines) ou encore la fermeture d'exploitations souterraines dans les bassins miniers, je m'attacherai à fournir des éléments de réponse à l'une des grandes questions actuelles, à savoir le stockage de déchets radioactifs en souterrain.

Grenoble, mars 2004

Abstract

Viscoplasticity and rock damage applied to modelling of the long-term behaviour of underground structures

The construction of civil works and in particular the excavation of underground cavities produces strain, which in most cases develops partly instantaneously and partly in a delayed manner. Consequently, rock damage and possible failure rarely occur instantaneously, but rather after a few hours or even years after the stress state has been modified as a result of building the structure. The first part of this report will therefore be devoted to experimental results, with a view to characterising the damageable viscoplastic behaviour of rocks. These involve mainly monotonic and cyclic creep, relaxation and quasi-static loading tests carried out in the laboratory and supplemented by observations of changes in rock microstructure. The second part describes a constitutive model designed to reproduce the observed phenomena, taking into account in particular volume variations associated with viscoplastic strain and anisotropic damage. The last part describes the numerical simulation of underground structure excavations, based on real, carefully instrumented cases. Particular emphasis is given to ways of simulating time-dependent changes in the damaged zone around underground storage cavities. To conclude, a number of prospective experimental and theoretical developments will be outlined.

Keywords : Viscoplasticity, creep and relaxation, damage, anisotropy, dilatancy, constitutive model for rocks, numerical modelling of time dependent behaviour, underground structures, radioactive waste disposal, excavated damage zone (EDZ).

Sommaire

1 Introduction 9

2 Observations en laboratoire du comportement viscoplastique endommageable des roches 13

2.1 Caractérisation de l'endommagement d'un grès anisotrope à partir d'essais de chargement cyclique 13

2.2 Propriétés viscoplastiques des roches sédimentaires 16

2.2.1 Essais de compression monotone et quasi-statique 16
2.2.2 Essais de fluage statique et de fluage oligocyclique 17
2.2.3 Essai de relaxation 19

2.3 Endommagement des discontinuités rocheuses sous sollicitations cycliques 19

2.4 Conclusion 21

3 Une loi de comportement viscoplastique endommageable pour les roches 23

3.1 Loi viscoplastique avec déformation volumique irréversible 23

3.2 Loi d'endommagement anisotrope induit 25

3.3 Couplage viscoplasticité et endommagement 27

3.4 Conclusion 28

4 Application à la modélisation numérique d'ouvrages souterrains 31

4.1 Modélisation du comportement viscoplastique d'ouvrages existants 31

4.2 Modélisation du comportement viscoplastique endommageable d'un puits circulaire et d'un tunnel 33

4.3 Modélisation viscoplastique avec dilatance et endommagement anisotrope de galeries circulaires 36

4.4 Conclusion 36

5 Conclusions générales et perspectives 39

6 Bibliographie 41

6.1 Références de l'auteur jointes en annexe 41

6.2 Rapports scientifiques 42

6.3 Références des thèses dirigées et co-dirigées par l'auteur 42

6.4 Quelques références générales 43

Annexe I : Publications relatives aux programmes expérimentaux 45

Annexe II : Publication relative aux développements théoriques 127

Annexe III : Publications relatives à la modélisation numérique d'ouvrages 177

Annexe IV : Publication de synthèse de ma thèse de Doctorat 225

Activités de recherche et d'enseignement 253

1 Introduction

La réalisation d'ouvrages de génie civil et particulièrement l'excavation d'ouvrages souterrains occasionnent des déformations qui, dans la grande majorité des cas, se développent pour une partie instantanément et pour une autre, de manière différée, c'est à dire évoluant au cours du temps. La rupture éventuelle survient par conséquent que rarement instantanément mais bien souvent de manière différée, c'est à dire quelques heures voir plusieurs années après la modification de l'état de contraintes consécutive à la réalisation de l'ouvrage.

Ce phénomène de rupture différée a été observé lors du creusement de nombreux ouvrages souterrains, notamment ceux des traversées alpines, comme le tunnel du Mont-Blanc, où des ruptures par écaillage en parois se sont produites plusieurs jours après le passage du front de taille. Dans les roches dures telles que les granits et les basaltes, ce type de rupture se manifeste généralement brutalement par décompressions violentes. Ces ruptures sont souvent par ailleurs précédées par une activité acoustique intense comme celle qui fut enregistrée plusieurs mois après la réalisation d'une galerie du laboratoire souterrain d'Energie Atomique du Canada creusée dans le granit du lac de Bonnet. Dans les roches tendres par contre, les convergences observées s'accompagnent de grandes déformations. On parle alors de "squeezing rock" ou de roches poussantes comme celles rencontrées dans le tunnel du Fréjus. Par ailleurs, des catastrophes telles que celle du tunnel de Vierzy (1972) où un train de voyageurs est entré en collision avec le matériau effondré de la voûte d'un tunnel témoignent de la dangerosité du phénomène.

Très tôt, les ingénieurs praticiens de la mécanique des roches se sont préoccupés de ce phénomène de rupture différée en tentant de le prendre en compte lors de la conception des cavités souterraines. Ainsi Lauffer (1958) puis Bieniaswski (1976) ont établi des abaques qui bien qu'étant de nature semi-empirique permettent de corréler le temps de tenue d'une excavation souterraine non soutenue avec la qualité du terrain, traduite dans ce cas précis, par le coefficient RMR (Rock Mass Rating). Cette intéressante approche pragmatique nécessite cependant d'être, dans la mesure du possible, rattachée à des fondements scientifiques.

D'un point de vue théorique, si l'on examine de plus près ce qui se produit au pourtour d'une cavité souterraine, on constate que l'excavation conduit à une redistribution des contraintes qui va générer des déformations. L'évolution de ces déformations s'accompagne du développement d'un anneau de terrain endommagé qui, si le déviateur des contraintes en paroi est suffisamment élevé, peut conduire à la plastification complète voire éventuellement à la rupture progressive de la cavité. Tout le problème réside alors dans la détermination du soutènement à mettre en place pour prévenir la rupture par effondrement de la cavité. Cette

approche, connue sous l'expression de Nouvelle Méthode Autrichienne pour ce qui concerne la phase de réalisation de l'ouvrage, peut être calculée en phase de conception par la méthode dite de " convergence-confinement ". Cette méthode s'avère souvent suffisante en génie civil, car l'ingénieur concepteur cherche à déterminer le chargement maximum que devra supporter le système de soutènement, sans se soucier de l'état d'endommagement de la roche. Accessoirement, il est amené à connaître l'extension de la zone perturbée de façon à dimensionner correctement le soutènement, comme dans le cas d'ancrages par exemple.

Dans le cas des ouvrages de stockage d'hydrocarbures, de gaz naturel ou encore de déchets radioactifs, le problème est de nature différente. Les concepteurs ne peuvent pas se contenter de vérifier simplement que la stabilité de la cavité souterraine est assurée. Ils souhaitent de surcroît, connaître avec précision l'état d'endommagement de la roche environnant la cavité. En effet, si la roche est fortement endommagée, sa porosité et donc sa perméabilité seront accrues et son rôle de confinement sera amoindri, autorisant ainsi des pertes et des fuites pouvant contaminer l'environnement et la biosphère. Aussi, pour ce type d'ouvrages, la détermination de l'extension de cette zone endommagée ou perturbée, souvent dénommée EDZ, pour " Excavated Damaged or Disturbed Zone ", est d'une importance capitale. De plus, dans le cas de stockage de déchets radioactifs à Haute Activité et à Vie Longue (HAVL), la connaissance de l'évolution de cette zone endommagée dans le temps sur des périodes de plusieurs millénaires est primordiale. Cette question est largement ouverte et la communauté scientifique en débat régulièrement. Parmi les récentes conférences consacrées à la question, citons le Cluster de la Commission Européenne (novembre 2003) ou encore le workshop EDZ, tenu à Toronto en 2002 dans le cadre du North American Rock Mechanics Symposium.

Un autre secteur dans lequel la prise en compte des déformations et de la rupture différée est capitale concerne les mines abandonnées. En effet il n'est pas rare, dans les anciens bassins miniers, d'observer de grandes zones de subsidence provoquées par la rupture en fluage tertiaire de piliers de mines. Les dégâts corporels et matériels occasionnés en surface, notamment sur le bâti peuvent être importants. La gestion de la période post-exploitation appelée "après mines" fait l'objet actuellement d'importants programmes de recherche visant à estimer les principales conséquences de l'ennoyage de ces anciennes galeries en association avec le vieillissement des géomatériaux.

En conséquence, la modélisation à long terme du comportement des ouvrages souterrains nécessite de prendre en compte le temps dans la formulation des lois constitutives utilisées pour la description du comportement mécanique des roches. Cela conduit fort logiquement à des lois de type viscoplastique intégrant par ailleurs l'évolution temporelle de l'endommagement. Pour être validées, ces lois doivent d'abord être confrontées à des résultats d'investigations expérimentales, réalisées en laboratoire dans des conditions contrôlées, puis ensuite, être évaluées par la simulation numérique d'ouvrages existants ayant fait l'objet de programmes d'auscultation précis et complets. Ce point est particulièrement délicat car en effet peu de données quantitatives concernant des ouvrages ayant atteint la rupture de manière différée sont à ce jour disponibles.

Par ailleurs, la compréhension des phénomènes de déformations et de rupture différées nécessite de réaliser des observations de l'évolution de l'endommagement à l'échelle de la microstructure de la roche. En effet, l'origine des déformations observées à l'échelle macroscopique (celle de l'ouvrage) réside dans la présence de défauts de la structure atomique à l'échelle micro voire nano-scopique (comme les dislocations). De plus, les interactions entre phase minérale solide et particules fluides engendrent, dans le cas des roches argileuses, des

forces atomiques, d'attraction ou de répulsion, de nature électrochimique responsables des déformations différées, comme celles liées au gonflement observé dans certains tunnels.

Dans ce mémoire, mon propos sera limité au comportement viscoplastique des roches et à l'évolution de l'endommagement mécanique qui lui est associé, sans inclure les effets hydrauliques et thermiques ni leurs couplages respectifs. De même, les phénomènes de sorption, de désaturation ou encore de vieillissement des matériaux consécutifs à leur transformation physico-chimique ne seront pas abordés.

Je commencerai par présenter au **chapitre 2**, les résultats d'études expérimentales (incluant des observations microstructurales) réalisées en laboratoire et destinées à caractériser le comportement viscoplastique endommageable des roches. Puis, le développement d'une loi constitutive destinée à reproduire les phénomènes observés de rupture différée sera exposé au **chapitre 3**. Enfin dans le **chapitre 4**, je présenterai la modélisation numérique d'ouvrages souterrains ainsi que la simulation du creusement d'un ouvrage réel, soigneusement instrumenté.

Conformément aux directives de l'Université Joseph Fourier, ce mémoire a été rédigé dans l'esprit d'un résumé retraçant les lignes directrices de mon travail de recherche. Pour obtenir le détail de chaque partie, le lecteur pourra se reporter aux publications jointes en annexe. Cependant quelques illustrations représentatives et quelques équations fondamentales ont été incluses dans le texte principal afin d'en faciliter la lecture.

2 Observations en laboratoire du comportement viscoplastique endommageable des roches

Les géomatériaux et particulièrement les roches constituant les couches géologiques profondes présentent un comportement mécanique complexe gouverné à la fois par leur composition minéralogique et par leurs conditions de formation ou de transformation (cas des roches métamorphiques). Bien que toutes les roches puissent, en fonction de la profondeur à laquelle elles se situent, de l'échelle de temps considérée et de la température auxquelles elles sont soumises, présenter un comportement visqueux, nous nous concentrerons dans ce qui suit sur les roches sédimentaires formées par diagenèse. La plupart de ces roches présentent, à des degrés divers, une anisotropie de structure. Par ailleurs, leurs propriétés de viscosité sont marquées et cela d'autant plus que la fraction de minéraux argileux qu'elles contiennent est importante et que leur teneur en eau est élevée.

Dans ce qui suit, je présenterai les principaux résultats de programmes expérimentaux que nous avons réalisés au laboratoire 3S. L'étude de l'endommagement différé des roches est abordée à partir d'essais de compression cyclique, d'essais de compression monotone quasi-statique (réalisés à différentes vitesses de chargement), d'essais de fluage et d'essais de relaxation. Tous visent à caractériser le développement des déformations et de l'endommagement en mettant en évidence leurs évolutions dans le temps. Enfin, une dernière partie est consacrée à l'endommagement des discontinuités rocheuses sous sollicitations cycliques.

Les publications relatives à ce chapitre sont rassemblées à l'annexe I.

2.1 Caractérisation de l'endommagement d'un grès anisotrope à partir d'essais de chargement cyclique

L'objectif de ce programme de recherche était de caractériser l'apparition et le développement de l'endommagement dans une roche anisotrope. Les résultats ont fait l'objet de la publication [1] de l'annexe I et de la thèse de Nicolas Gatelier (2001) [17].

Il est peut être utile à ce stade de rappeler que l'endommagement est défini comme une perte progressive de résistance correspondant à la dégradation de la cohésion du matériau. Ce processus se développe avant le pic de résistance matérialisant la rupture. Physiquement, à

l'échelle micro structurale, il correspond à l'initiation de la croissance des micro-fissures préexistantes jusqu'à leur coalescence complète, stade ultime de la rupture. Au début, cette propagation est stable pour, à partir d'une certaine vitesse, devenir instable. L'endommagement se développe dans un premier temps de manière diffuse pour progressivement conduire à la rupture localisée. Le développement de l'endommagement est souvent considéré comme isotrope ce qui à l'évidence constitue une simplification. En effet, sous faible contrainte moyenne, les micro-fissures mécaniquement induites apparaissent en mode d'extension (mode I). La fissuration est donc orientée et se développe suivant la direction de la contrainte principale majeure suite à l'ouverture des fissures qui s'opère dans la direction perpendiculaire, c'est à dire celle de la contrainte mineure. Le développement de l'endommagement induit donc une anisotropie qui va se superposer à l'anisotropie de structure initiale du matériau. Cette anisotropie induite est une conséquence de l'évolution de l'endommagement qui engendre une dilatance globale de la roche et qui conduit à la rupture différée.

Si l'endommagement pouvait être considéré isotrope, une seule variable scalaire suffirait à le décrire. Dans ce cas la variation de volume pourrait lui être associée. Par contre, dans le cas d'un endommagement anisotrope, il est nécessaire d'avoir recours à une ou plusieurs variables de nature tensorielle. Aussi, partant de l'évidence que la variation de volume ne peut seule caractériser l'endommagement anisotrope, nous avons élaboré un protocole d'essais destinés à déterminer l'évolution des déformations dans toutes les directions de l'espace. Pour ce faire, nous avons conçu un programme expérimental constitué d'essais de chargement cyclique à faible fréquence réalisés en compression dans et hors axes d'orthotropie. Certains essais ont été réalisés en conditions triaxiales avec pression de confinement. Le matériau testé est un grès des Vosges présentant une symétrie axiale de type orthotropie de révolution. La porosité moyenne est de 23 %. L'anisotropie structurale initiale laisse apparaître un rapport de module d'élasticité variant de 20 % suivant la direction concernée et un rapport de résistance de 50 % environ.

Les mesures des déformations irréversibles stabilisées dans les directions principales des contraintes, à la fin de chaque groupe de cycles, ont permis de mettre en évidence le développement progressif de l'endommagement. Ces déformations atteignent des valeurs plus importantes pour des essais conduits hors-axes d'orthotropie, lorsque les plans d'anisotropie sont peu inclinés. Cette observation confirme l'influence de l'anisotropie de structure initiale sur le développement de la micro fissuration, même si l'application d'une pression de confinement tend à l'estomper. De plus, à l'intérieur d'un pas de chargement, les premiers cycles se montrent les plus endommageants. Cette constatation est en parfait accord avec les variations de modules directionnels observées. Par ailleurs la variation de la déformation volumique irréversible montre, dans tous les cas, une première phase contractante qui est suivie par une phase de dilatance. Au cours du cyclage, à l'intérieur d'un pas de chargement, le point de contractance a tendance à se déplacer pour progressivement passer en dilatance (Figure 2.1). Une procédure d'identification des composantes du tenseur d'endommagement a ainsi pu être aussi proposée.

Grâce à l'analyse micro-structurale de l'endommagement faite au microscope à balayage électronique sur des lames minces, nous avons pu mettre en évidence que deux modes de déformation et de rupture sont en compétition : d'une part, la compaction qui s'opère dans la direction du chargement et qui se traduit par une augmentation du module axial liée à l'écrouissage positif du matériau et d'autre part, le développement de la micro-fissuration qui conduit à une diminution drastique des modules transversaux révélant ainsi une perte progressive de rigidité (Figure 2.2). A l'échelle macroscopique, l'endommagement peut donc être caractérisé soit par la variation de propriétés mécaniques apparentes, comme les modules

d'élasticité directionnels ou encore par l'évolution des déformations irréversibles en fonction du nombre de cycles.

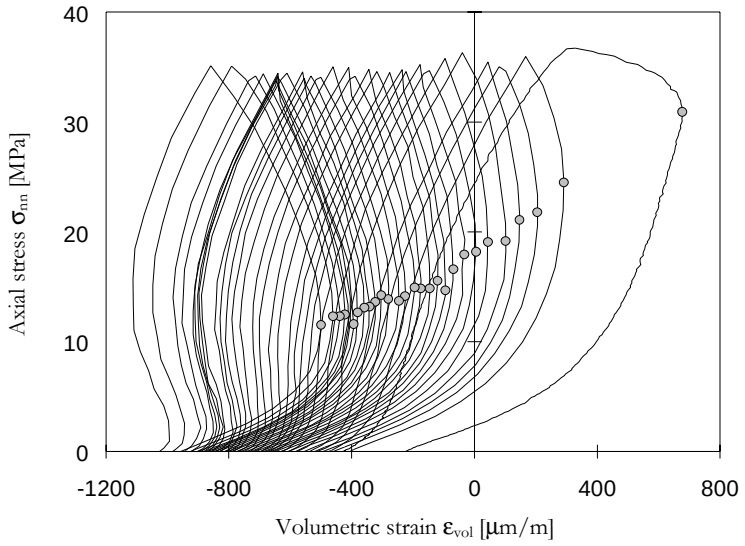

Figure 2.1 : Evolution de la déformation volumique, ε_{vol}, en fonction de la contrainte axiale, σ_{nn}, pour un essai en compression simple cyclique - étape de chargement menant à la rupture - d'après Gatelier et al. [1]. Remarquons le passage progressif du point de contraction maximum en dilatance.

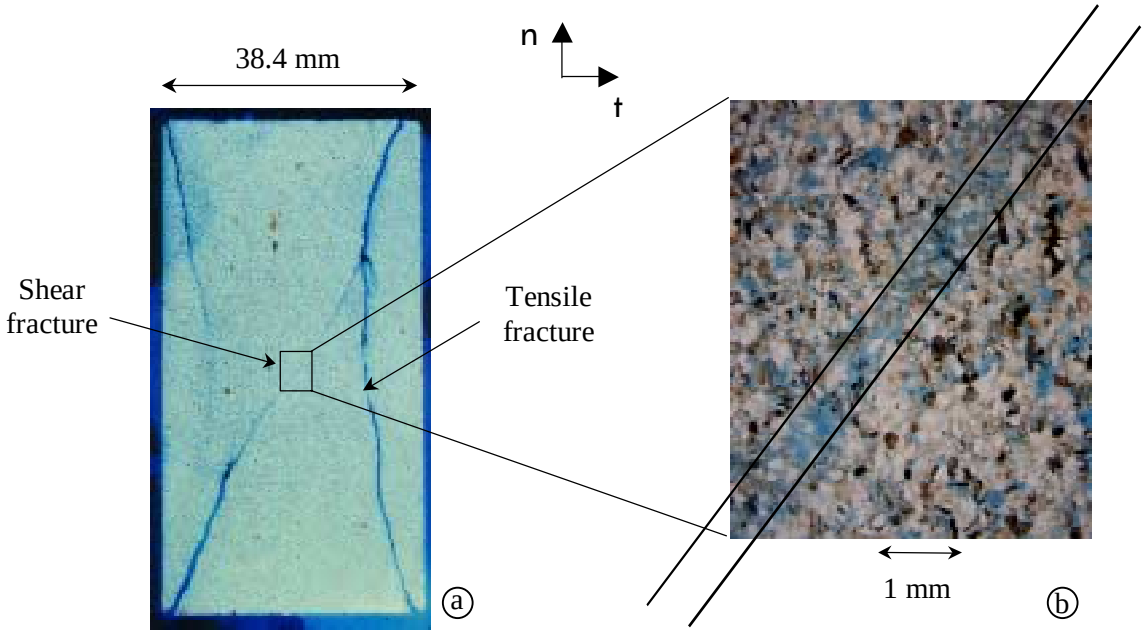

Figure 2.2 : Image réalisée au Microscope à Balayage Electronique sur un échantillon de grès, testé en compression simple, d'après Gatelier et al. [1]. On observe, un double mode de rupture en extension et en cisaillement après compaction.

En conclusion, par cette étude nous avons mis en évidence expérimentalement l'apparition et le développement de l'endommagement anisotrope en définissant les variables susceptibles de décrire son évolution. En fonction de l'orientation des plans d'anisotropie structurale par rapport à la direction du chargement, l'endommagement apparaît plus ou moins précocement, c'est à dire pour un niveau de contrainte plus faible. Une des conséquences de cette observation est que pour un ouvrage souterrain creusé dans un massif anisotrope le lieu d'apparition de l'endommagement dépendra de l'orientation des strates (i.e. plans d'anisotropie). Par exemple, pour une cavité circulaire dans un massif soumis à un état de contraintes initial isotrope, si les strates sont horizontales le lieu d'apparition de l'endommagement sera la clé de voûte alors qu'à l'inverse si ces strates sont verticales, ce sera en piédroit. Cette conclusion peut s'avérer utile pour la conception d'un éventuel système de soutènement.

2.2 Propriétés viscoplastiques des roches sédimentaires

L'étude présentée dans le paragraphe précédent était centrée sur le développement et l'évolution de l'endommagement. Dans ce qui suit, nous nous concentrons sur l'influence du temps sur le comportement mécanique des roches en nous appuyant sur des résultats d'essais de compression monotone réalisés à plusieurs vitesses de chargement, sur des essais de fluage et sur des essais de relaxation. Les résultats des différentes campagnes d'essais ont fait l'objet des publications [2], [3], [4] de l'annexe I et de la thèse d'Eric Boidy (2002) [18].

Cette campagne d'essais a porté essentiellement sur quatre roches : le grès des Vosges présenté précédemment, l'argilite de l'Est de la France constituant la couche hôte du futur laboratoire souterrain pour l'étude du stockage de déchets radioactifs de l'Andra, l'argilite du tunnel de Tournemire et la marne du Mont d'Or, prélevée dans un tunnel ferroviaire situé dans le Jura à la frontière Franco-Suisse.

2.2.1 Essais de compression monotone et quasi-statique

Nous savons que lorsqu'un échantillon de roche est soumis à un chargement monotone, sa réponse mécanique dépend de la vitesse de sollicitation. Globalement, plus la vitesse de sollicitation est élevée, plus la raideur et la résistance à la rupture sont importantes. Si par contre, on réalise plusieurs essais à vitesse de chargement décroissante, il est possible de mettre en évidence une limite en deçà de laquelle plus aucune variation n'est observée. On parle alors d'essai de chargement quasi-statique et la courbe obtenue, appelée courbe limite, indique que tous les effets visqueux se sont développés en temps réel. En d'autres termes, si à partir d'un point de la courbe, on maintient la contrainte ou la déformation constante, on observera respectivement ni déformation de fluage, ni relaxation de la contrainte. A l'échelle de la microstructure du matériau cela indique que les dislocations atomiques ont été libres de migrer et qu'il n'y a plus d'écrouissage liés au blocage de ces défauts.

Nous avons réalisé des essais en compression à partir d'un bâti de chargement que nous avons modifié pour appliquer des vitesses de déformation très lentes (inférieures à $10^{-9}.s^{-1}$ pour des échantillons de 80 mm de hauteur). L'influence de la vitesse de chargement sur la réponse d'un grès et de l'argilite de l'Est a été mise en évidence avec plusieurs vitesses de chargement variant dans un rapport allant de 1 à 10^4. Outre la variation sur les déformations axiales et

transversales, on constate une influence sur l'apparition de la dilatance. Pour une roche poreuse comme le grès, la dilatance est précoce lorsque la vitesse de chargement est faible. Par contre, pour une roche peu poreuse comme l'argilite de l'Est, la dilatance se manifeste tardivement et semble moins sensible à la vitesse de chargement. Lorsque la vitesse augmente, dans un rapport de 5.10^5, on voit nettement un raidissement du matériau traduisant un écrouissage. L'effet d'un ralentissement du chargement est quant à lui plus difficile à mettre en évidence car il se superpose à un effet inverse, le radoucissement du matériau.

D'un point de vue géotechnique, cette vitesse de chargement peut être corrélée à la vitesse d'avancement du creusement d'un tunnel. On peut en conclure, toutes choses étant égales par ailleurs, que plus la vitesse est élevée moins les déformations instantanées seront importantes mais qu'il faudra s'attendre à des convergences différées plus élevées.

2.2.2 Essais de fluage statique et de fluage oligocyclique

Nous avons vu que suite à l'application d'un déviateur de contraintes, des déformations inélastiques se développent en fonction du temps. Si le déviateur des contraintes appliqué n'est pas trop élevé, ces déformations vont s'amortir et se stabiliser tandis qu'à l'inverse si le déviateur est important on observera à partir d'un certain point, une accélération des déformations qui conduit à la rupture du matériau.

Classiquement, la courbe déformation en fonction du temps d'un essai de fluage réalisé en compression laisse apparaître trois phases : une phase de fluage primaire au cours de laquelle les phénomènes visqueux et d'écrouissage se manifestent, comme en témoigne la diminution de la vitesse de déformation. Une phase de fluage secondaire pendant laquelle seule la viscosité est active et qui se développe à vitesse de déformation constante. Puis enfin, une phase de fluage tertiaire correspondant à l'endommagement du matériau au cours de laquelle les vitesses de déformation augmentent pour conduire progressivement à la rupture. A l'échelle de la micro structure, on distingue le fluage-dislocation et le fluage-diffusion. En fait, le raidissement observé lors de la phase de fluage primaire correspond à l'écrouissage du matériau qui est dû à l'augmentation de la densité des dislocations qui s'enchevêtrent et se bloquent les unes les autres.

Le développement de trois bâtis de fluage, conçus pour réaliser des essais de longue durée dans un environnement contrôlé en température, est venu compléter le dispositif expérimental destiné à caractériser finement la viscosité des roches étudiées. Les essais de fluage que nous avons réalisés montrent que, très tôt, une dilatance du matériau est observée ce qui suggèrerait que l'endommagement s'initie bien avant la phase de fluage tertiaire ou que la déformation viscoplastique, contrairement à ce qui est communément admis, ne s'opère pas à volume constant (Figure 2.3). Des analyses faites au microscope électronique sur des lames minces réalisées à partir des échantillons rompues ont confirmé ces observations.

Par ailleurs, la prévision à très long terme (plusieurs milliers d'années) du comportement des cavités souterraines de stockage conduit à envisager des processus permettant d'accélérer les déformations visqueuses par des processus mécaniques, thermiques ou électrochimiques. Parmi les processus mécaniques, nous avons tenté de mettre en œuvre des essais de fluage cyclique et oligocyclique (Figure 2.4). Nous avons ainsi réalisé une série d'essais, qui jusqu'à ce jour n'a pas fourni d'indications claires et définitives, même si une très légère accélération des déformations a pu être mise en évidence. L'influence de la restauration lors de la décharge a aussi été testée.

Pour l'application de ces conclusions au comportement des ouvrages souterrains, il faut indiquer que les conditions d'un essai de fluage correspondent à ce qui se passerait à la paroi d'un tunnel non soutenu. Nous verrons par la suite ce qu'il en est des ouvrages soutenus.

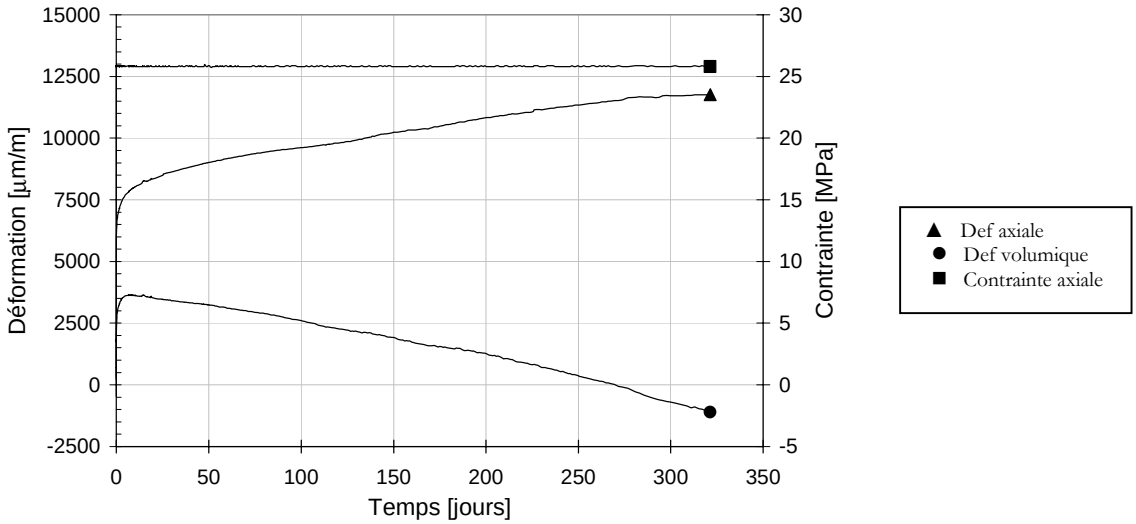

Figure 2.3 : Déformation axiale et déformation volumique en fonction du temps pour un essai de fluage sur l'argilite de l'Est, d'après Fabre et Pellet [3]. Notons l'apparition précoce de la variation de volume (dilatance).

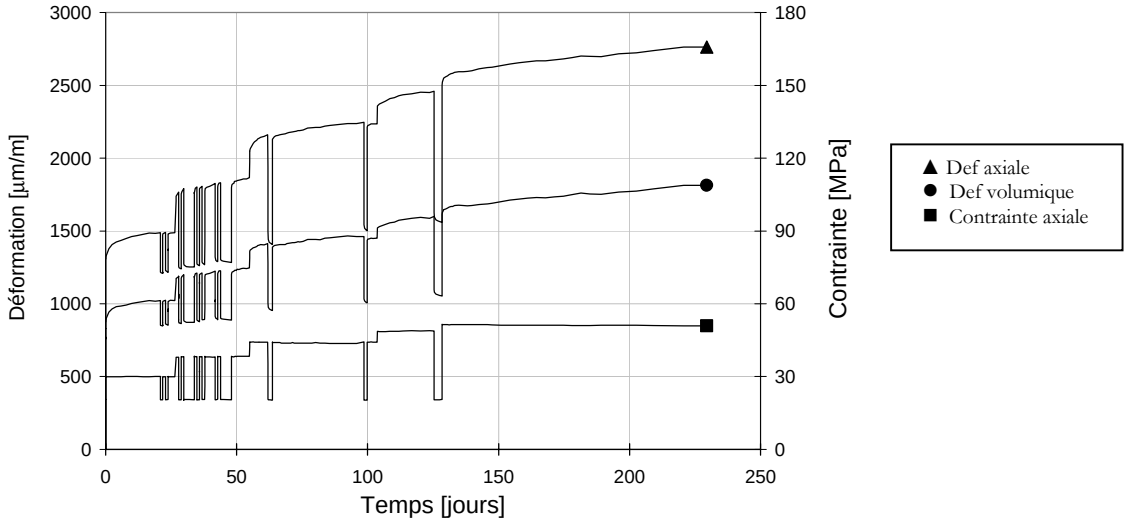

Figure 2.4 : Déformation axiale et déformation volumique en fonction du temps pour un essai de fluage cyclique sur l'argilite du Mont d'Or, d'après Pellet et Fabre [4].

2.2.3 Essai de relaxation

La relaxation des contraintes constitue une autre manifestation de la viscosité. Nous avons montré sur des essais ayant duré une quarantaine de jours que la chute de contrainte peut être substantielle, de l'ordre de 25 %. Evidemment, cette chute dépend de la valeur du déviateur appliqué, mais dans tous les cas, la stabilisation des contraintes s'opère plus rapidement que celle des déformations de fluage. Cela nous a conduit à préférer ce type d'essais pour ajuster les paramètres de loi de comportement qui dépendent du temps caractéristique de relaxation. La variation de volume au cours des paliers de relaxation a aussi été mise en évidence confirmant ainsi les observations faites sur les essais de fluage.

Ces observations sont utiles pour le cas des tunnels et galeries soutenues par un revêtement rigide. En effet, dans le cas idéalisé d'un revêtement plaqué parfaitement au terrain et dont les propriétés mécaniques ne se dégradent pas dans le temps, on observera alors une relaxation des contraintes dans le terrain qui conduira donc à une diminution des contraintes exercées sur le revêtement. Précisons toutefois, que cette analyse ne tient pas compte de l'endommagement et de son évolution, ni de la possible cicatrisation de la roche.

2.3 Endommagement des discontinuités rocheuses sous sollicitations cycliques

Le dernier point abordé dans ce chapitre consacré à l'expérimentation en laboratoire est en relation avec le comportement des discontinuités rocheuses. Dans le cadre d'une collaboration avec l'International Institute of Earthquake Engineering and Sismology de Téhéran, nous avons étudié les dégradations que subissent les ouvrages souterrains réalisés dans des zones sismiquement active. Il s'agissait principalement de quantifier l'action répétée de séismes de faible magnitude. Les principaux résultats de ces campagnes d'essais ont fait l'objet des publications [5] et [6] de l'annexe I.

Une série d'essais triaxiaux cycliques a été réalisée sur des échantillons cylindriques pourvus d'une discontinuité artificielle à indentation régulière. Les résultats ont montré que la dégradation des propriétés mécaniques de la discontinuité dépend de la vitesse de chargement, du nombre de cycles, de la fréquence et de l'amplitude du chargement. Sur la base de ces résultats, des relations empiriques ont été établies permettant d'estimer la perte de résistance consécutive à l'endommagement en fonction des paramètres précités. Ce type de relations empiriques pourrait être introduit dans des modèles de comportement de joint rocheux tels que ceux utilisés dans la méthode des éléments distincts.

Une autre série d'essais a été réalisée en cisaillement direct avec des amplitudes de déplacements plus grandes. Dans cette série, les déplacements étant parfaitement contrôlés dans les trois directions de l'espace, la variation de l'angle de dilatance a pu être mise en évidence en cours du cyclage et donc être corrélée à l'endommagement (Figure 2.5 et 2.6).

Les principaux enseignements tirés de ces essais indiquent que, pour un tunnel ou une galerie recoupant une faille ou plus simplement pour un ouvrage souterrain creusé dans un massif rocheux diaclasé, l'action répétée de séismes de faible magnitude peut provoquer une dégradation des propriétés mécaniques plus importante que celle d'un seul et unique séisme de magnitude supérieure. L'endommagement cumulé des discontinuités peut conduire à terme à l'effondrement de la galerie.

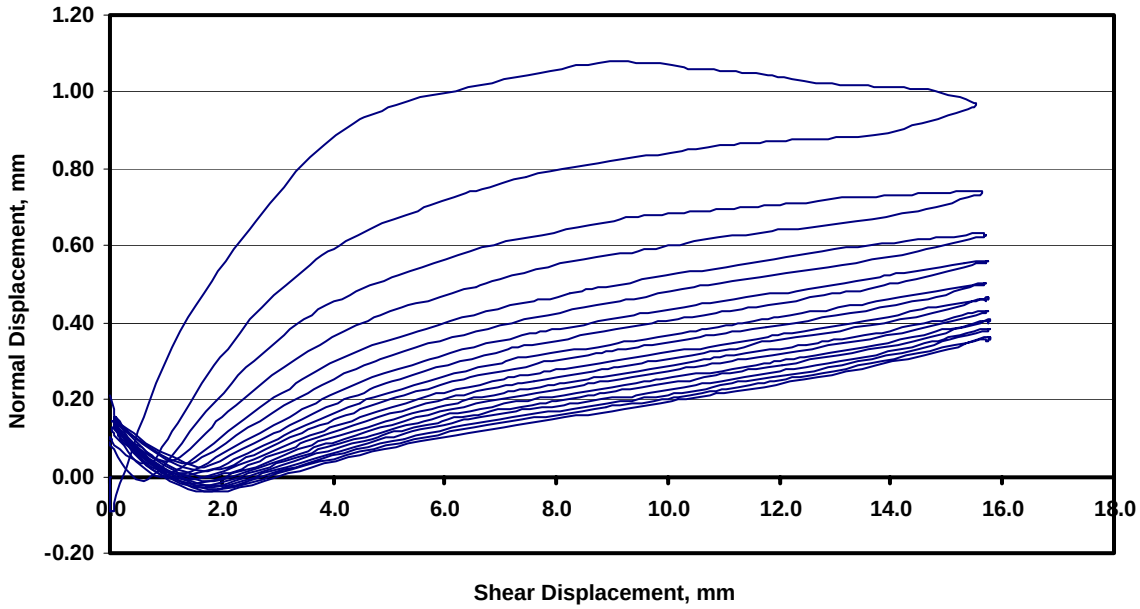

Figure 2.5 : Evolution du déplacement normal en fonction du déplacement de cisaillement lors d'un essai de cisaillement cyclique, d'après Jafari et al. [6]. L'angle de dilatance décroît progressivement traduisant l'endommagement de la discontinuité.

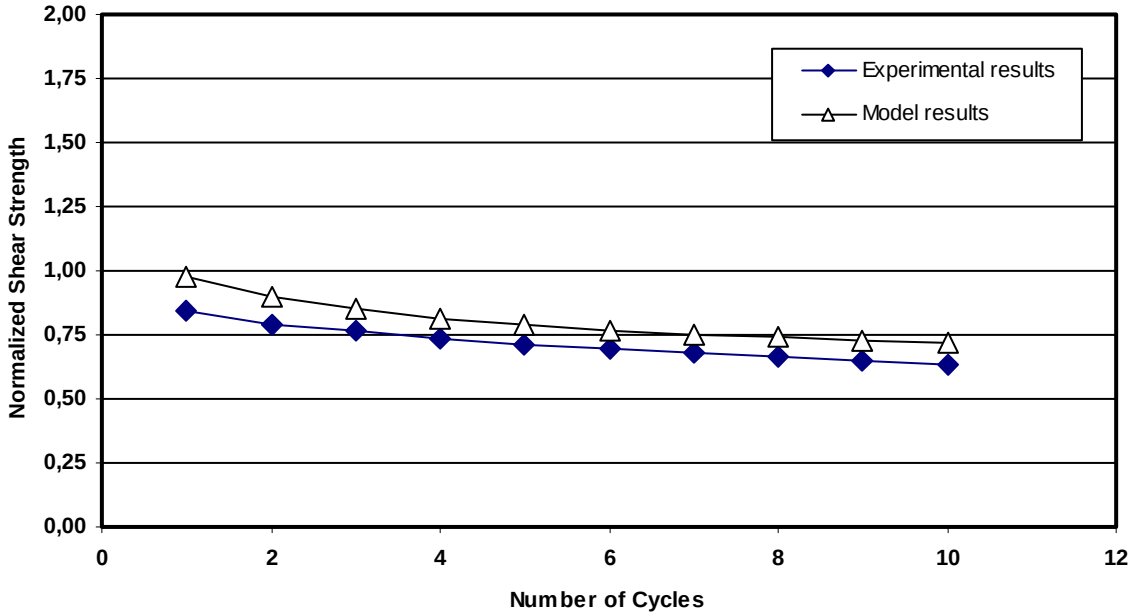

Figure 2.6 : Evolution de la résistance au cisaillement en fonction du nombre de cycle, lors d'un essai de cisaillement cyclique, d'après Jafari et al. [6]. Comparaison des valeurs expérimentales et du modèle semi-empirique.

2.4 Conclusion

Les résultats expérimentaux présentés dans ce chapitre ont permis de mettre en évidence les propriétés visqueuses de certaines roches ainsi que de caractériser l'évolution de leur endommagement dans le temps. La principale contribution à la compréhension de ces phénomènes porte sur les deux points suivants : premièrement, la mise en évidence de l'apparition au cours du temps d'une augmentation de volume (dilatance) associée au développement des déformations viscoplastiques; deuxièmement, la mise en évidence d'une anisotropie de l'endommagement qui peut être décrite soit par l'évolution des modules directionnels, soit par les déformations irréversibles cumulées mesurées dans les directions principales. Pour le comportement viscoplastique, un des points fondamentaux est constitué par la détermination de la courbe de réponse limite de la roche représentant le seuil en deçà duquel aucune manifestation du temps n'est perceptible.

En conséquence, dans la perspective de la modélisation numérique du comportement à long terme d'ouvrages souterrains, il convient d'utiliser une loi constitutive prenant en compte la variation de volume viscoplastique ainsi qu'une variable d'endommagement de nature tensorielle.

3 Une loi de comportement viscoplastique endommageable pour les roches

Nous avons vu que les observations expérimentales faites en laboratoire ou sur des ouvrages auscultés montrent la nécessité d'associer comportement différé et rupture progressive. Pour modéliser ce type de comportement, il est donc nécessaire d'avoir recours à des lois constitutives viscoplastiques associées à des modèles d'endommagement.

Concernant le comportement mécanique différé traduit par les déformations viscoplastiques, il n'existe à vrai dire que peu de lois constitutives adaptées aux roches. En effet, les nombreuses lois de fluage établies notamment pour le sel gemme ne sont pas généralisables car le temps intervient explicitement. Pour satisfaire le principe d'objectivité, une loi de comportement doit en effet être formulée en vitesse.

La théorie de l'endommagement quant à elle, repose sur le concept de la contrainte effective proposé par Kachanov [28]. Couplée à une loi constitutive de type viscoplastique, cette théorie rend possible la traduction des phénomènes de rupture progressive et différée, caractérisée par la phase de fluage tertiaire. Cependant, la plupart des lois constitutives existantes ne permettent pas de mettre en évidence les déformations volumiques irréversibles différées associées au développement de l'endommagement, ni l'anisotropie de l'endommagement observée lors d'essais de laboratoire.

Dans ce qui suit, nous résumons les améliorations apportées à une loi viscoplastique endommageable. La totalité des développements théoriques ainsi que les procédures d'identification des paramètres et leurs significations physiques sont décrites dans la référence[7] de l'annexe II et dans la thèse d'Attila Hajdu (2003), [19]. Les performances du modèle y sont aussi comparées aux résultats d'essais de laboratoire.

3.1 Loi viscoplastique avec déformation volumique irréversible

Les lois viscoplastiques couramment mises en œuvre pour décrire le comportement différé des géomatériaux dérivent pour la plupart de lois à potentiel développées pour les métaux. Pour mettre en évidence la variation de volume d'abord contractante puis dilatante, lorsque s'initie et se développe l'endommagement, nous sommes partis de la loi de Lemaitre [29]. Cette loi dérive d'un potentiel viscoplastique et repose sur le principe de la surcontrainte proposées par Perzyna [34]. L'approche classique en élasto-viscoplasticité consiste alors à

définir une surface de charge dans l'espace des contraintes à l'intérieur de laquelle les états de contrainte atteints occasionnent des déformations entièrement réversibles. Ici, les états de contraintes à l'extérieur de la surface de charge sont autorisés et le temps de relaxation nécessaire pour revenir sur la surface dépend de la loi d'écoulement. En d'autres termes, cela revient à considérer la plasticité comme un cas particulier de la viscoplasticité.

Dans un premier temps, nous nous sommes limités à la modélisation des phénomènes visqueux en ignorant l'endommagement différé mais en prenant en compte la déformation volumique. Sans reprendre l'ensemble des développements théoriques, il peut être utile de rappeler les étapes essentielles ainsi que les principales équations.

Rappelons en premier lieu, que le cadre de la thermodynamique des processus viscoplastiques étant basé sur le concept des surfaces équipotentielles, la loi viscoplastique est entièrement définie par le potentiel de dissipation. Ce dernier permet de calculer directement le taux de déformation viscoplastique en appliquant la règle de normalité. Dans sa version originale, la loi de Lemaitre fait appel à la surface de charge de von Mises qui est mal adaptée aux géomatériaux puisqu'elle ne permet pas de traduire de déformation volumique inélastique. Nous avons repris la démarche proposée par Lemaitre, mais en introduisant une surface de charge dépendante non seulement du second invariant du déviateur des contraintes mais aussi du premier invariant des contraintes. Nous avons donc gardé la forme fonction puissance du potentiel de dissipation proposée par Lemaitre en remplaçant le critère de von Mises par un critère de type Drucker-Prager. L'expression de la surface de charge $f(J_2;I_1)$ qui désigne la fonction de la surface équipotentielle s'écrit :

$$f(J_2;I_1) = \sigma_{eq} + \alpha\sigma_m - k \qquad [1]$$

Où : σ_m est la contrainte moyenne et σ_{eq} est la contrainte équivalente de von Mises

Le paramètre α qui multiplie la contrainte moyenne permet de caractériser la déformation volumique différée. Il est lié à l'angle de dilatance différé, ψ. Le coefficient k permet de définir le seuil de viscoplasticité dans le cas où l'on souhaiterait prendre en compte un domaine d'élasticité. Ce seuil de viscoplasticité se révèle en pratique souvent très faible ce qui mathématiquement revient à supposer que k = 0. Le potentiel de dissipation viscoplastique peut donc s'écrire :

$$\Omega^{vp} = \frac{K}{N+1}\left\langle \frac{\sigma_{eq} + \alpha\sigma_m}{K} \right\rangle^{N+1} p^{-N/M} \qquad [2]$$

Où : K,M et N sont les paramètres du modèle et p, la déformation viscoplastique cumulée.

Le taux de déformation viscoplastique se déduit alors du potentiel de dissipation simplement par application de la règle de normalité; soit :

$$\dot{\boldsymbol{\varepsilon}}^{\mathbf{vp}} = \left\langle \frac{\sigma_{eq} + \alpha\sigma_m}{Kp^{1/M}} \right\rangle^N \left(\frac{3}{2}\frac{\mathbf{S}}{\sigma_{eq}} + \frac{\alpha\mathbf{I}}{3} \right) \qquad [3]$$

Où : **I** et **S** sont respectivement le tenseur identité et le déviateur des contraintes.

En considérant un écrouissage isotrope du matériau et en supposant qu'il n'y a pas de processus de restauration, la valeur de la variable est toujours croissante. La déformation viscoplastique cumulée, p, peut être alors utilisée comme indicateur de l'état d'écrouissage du matériau. Elle se calcule par :

$$\dot{p} = \sqrt{\frac{2}{3}\dot{\boldsymbol{\varepsilon}}^{\mathbf{vp}} : \dot{\boldsymbol{\varepsilon}}^{\mathbf{vp}}} \qquad [4]$$

Finalement, le taux de déformation viscoplastique peut être mis sous la forme suivante :

$$\dot{\boldsymbol{\varepsilon}}^{\mathbf{vp}} = \dot{p}\left(\frac{2}{9}\alpha^2 + 1 \right)^{-1/2} \left(\frac{3}{2}\frac{\mathbf{S}}{\sigma_{eq}} + \frac{\alpha\mathbf{I}}{3} \right) \qquad [5]$$

Le modèle de Lemaitre a donc été enrichi d'un paramètre supplémentaire α que l'on appellera paramètre de dilatance. Pour des valeurs positives de l'angle α, le comportement différé est contractant tandis que des valeurs négatives génèrent une dilatance. En fixant $\alpha = 0$ les déformations volumiques viscoplastiques disparaissent et l'on retrouve le modèle d'origine de Lemaitre.

Remarquons que d'un point de vue thermomécanique, cette loi n'est pas standard au sens strict puisque le paramètre, p, intervient dans le potentiel de dissipation. C'est une caractéristique des lois d'écrouissage-viscosité multiplicatives qui nécessite l'introduction d'une condition supplémentaire, en plus de la règle de normalité généralisée, afin d'assurer la condition de Clausius-Duhem.

3.2 Loi d'endommagement anisotrope induit

Nous avons ensuite proposé une description appropriée des mécanismes d'endommagement qui conduisent progressivement à la rupture différée en introduisant une variable d'endommagement de nature tensorielle afin de prendre en compte l'anisotropie induite.

En effet, la loi viscoplastique de Lemaitre classiquement couplée à un endommagement isotrope décrit par une variable d'endommagement scalaire, D, ne peut pas traduire l'anisotropie de l'endommagement observée in situ. Plusieurs auteurs ont montré que les propriétés géométriques d'un état d'endommagement donné peuvent être correctement décrites par un tenseur symétrique d'ordre deux. La limitation principale de cette approche est que, dans le cas le plus général, l'endommagement décrit présente une symétrie orthotrope où les axes d'orthotropie s'identifient avec les directions principales du tenseur d'endommagement. Toutefois, cette limitation n'est pas pénalisante pour la modélisation de la plupart des géomatériaux et nous avons retenu un tenseur symétrique d'ordre deux, **D**, pour traduire l'anisotropie de l'endommagement.

La description de l'endommagement du matériau repose sur le concept de la contrainte effective. On trouve dans la littérature diverses suggestions pour la formulation d'un tenseur de contrainte effective symétrique liée à un tenseur d'endommagement du second ordre. Nous avons opté pour une expression provenant du principe d'équivalence en énergie. Elle présente l'avantage, contrairement à une formulation basée sur le principe d'équivalence en déformation, d'assurer automatiquement la symétrie du tenseur des contraintes effectives.

L'évolution de l'endommagement au cours du temps dépend aussi de l'état de la contrainte appliquée et de l'état actuel d'endommagement du matériau. Il est possible de les représenter par une contrainte motrice fictive, $\hat{\boldsymbol{\sigma}}$, qui apparaît dans l'équation de l'évolution de l'endommagement à la place de la contrainte appliquée réellement et de la variable d'endommagement. Pour traduire le degré d'anisotropie de l'endommagement, un paramètre, β, a été introduit. $\beta = 1$ correspond à une évolution isotrope tandis que $\beta = 0$ modélise une évolution anisotrope où l'endommagement ne se développe que dans la direction perpendiculaire à la contrainte motrice. Evidemment, β peut prendre n'importe quelle valeur réelle intermédiaire (Figure 3.1).

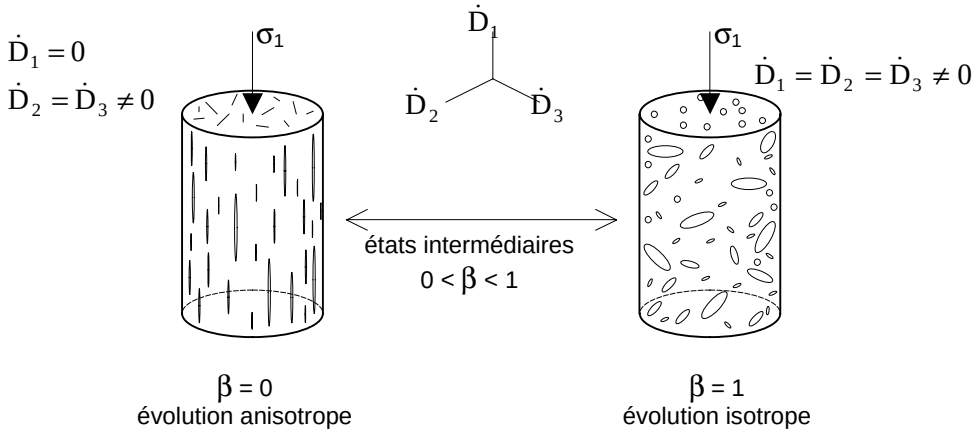

Figure 3.1 : Schéma illustrant la signification du paramètre d'anisotropie, β

On peut montrer que la forme du tenseur de structure implique que les vecteurs propres du tenseur taux d'endommagement ont la même orientation que ceux du tenseur de la contrainte motrice. La rupture du matériau intervient lorsque la valeur propre majeure de **D** atteint une valeur critique $D_{crit.} = 1$. Pour une sollicitation uniaxiale, avec une évolution isotrope $(\beta = 1)$ on retrouve exactement l'expression classique de Kachanov et Rabotnov pour décrire l'évolution de l'endommagement en fluage tertiaire.

Remarquons également que les effets unilatéraux liés à la fermeture et ainsi à la désactivation des micro-fissures n'ont pas été pris en compte. En absence de sollicitations cycliques, nous avons jugé inutile d'intégrer des conditions de désactivation dans le modèle. Finalement, l'endommagement est toujours croissant ou constant, autrement dit la "cicatrisation" du matériau n'est pas autorisée par le modèle.

3.3 Couplage viscoplasticité et endommagement

Disposant d'un modèle d'endommagement anisotrope et d'une loi viscoplastique capable de traduire une variation de volume différée, nous avons associé les deux pour bâtir un modèle viscoplastique endommageable.

Le couplage de la loi viscoplastique avec déformation volumique irréversible et de la loi d'endommagement anisotrope permet de traduire que la réponse en contraintes et en déformations du matériau dépend non seulement des mécanismes visqueux mais aussi, simultanément, de l'endommagement. Les calculs couplés permettent d'obtenir à tout moment les états de contraintes, de déformations et d'endommagement dans les problèmes évolutifs. Afin de décrire le comportement d'un matériau viscoplastique écrouissable et endommageable, on applique simplement le principe d'équivalence en remplaçant la contrainte $\boldsymbol{\sigma}$ par la contrainte effective $\tilde{\boldsymbol{\sigma}}$.

Cette modification concerne toutes les déformations. L'hypothèse de partition des déformations divise la déformation totale en une partie élastique et en une partie inélastique. La cohérence dans la formulation exige le remplacement de la contrainte par la contrainte effective dans les relations contrainte-déformation élastiques et viscoplastiques. Ainsi le comportement élastique isotrope est décrit par la loi de Hooke couplée :

$$\dot{\boldsymbol{\varepsilon}}^{e} = \frac{1+\nu}{E}\tilde{\tilde{\boldsymbol{\sigma}}} - \frac{\nu}{E}\mathrm{tr}(\tilde{\tilde{\boldsymbol{\sigma}}})\cdot\mathbf{I} \qquad [6]$$

Le paramètre α, défini précédemment, traduit la dilatance. Ce paramètre reste également indépendant et n'est pas influencé par l'endommagement, c'est-à-dire que les effets de l'endommagement se superposent aux effets de la viscosité. Cette séparation permet de simuler des comportements volumiques plus complexes (par exemple, dans un premier temps contractant ensuite dilatant).

Le tenseur de vitesse de déformations viscoplastiques s'exprime alors par :

$$\dot{\boldsymbol{\varepsilon}}^{\mathbf{vp}} = \left\langle \frac{\tilde{\sigma}_{eq} + \alpha\tilde{\sigma}_m}{Kp^{1/M}} \right\rangle^N \left(\frac{3}{2}\frac{\tilde{\tilde{\mathbf{S}}}}{\tilde{\sigma}_{eq}} + \frac{\alpha(\mathbf{I}-\mathbf{D})^{-1}}{3} \right) \qquad [7]$$

avec la notation :

$$\tilde{\tilde{\mathbf{S}}} \equiv (\mathbf{I}-\mathbf{D})^{-1/2} \cdot \tilde{\mathbf{S}} \cdot (\mathbf{I}-\mathbf{D})^{-1/2} \qquad [8]$$

L'état d'écrouissage du matériau, caractérisé toujours par la déformation viscoplastique cumulée, se calcule par :

$$\dot{p} = \sqrt{\frac{2}{3}} \left\langle \frac{\tilde{\sigma}_{eq} + \alpha\tilde{\sigma}_m}{Kp^{1/M}} \right\rangle^N \left\| \left(\frac{3}{2}\frac{\tilde{\tilde{\mathbf{S}}}}{\tilde{\sigma}_{eq}} + \frac{\alpha(\mathbf{I}-\mathbf{D})^{-1}}{3} \right) \right\| \qquad [9]$$

où le signe $\| \ \|$ désigne la norme euclidienne. Ce qui permet de mettre la loi constitutive sous la forme finale suivante :

$$\dot{\boldsymbol{\varepsilon}}^{\mathbf{vp}} = \sqrt{\frac{3}{2}}\dot{p} \frac{\left(\frac{3}{2}\frac{\tilde{\tilde{\mathbf{S}}}}{\tilde{\sigma}_{eq}} + \frac{\alpha(\mathbf{I}-\mathbf{D})^{-1}}{3} \right)}{\left\| \left(\frac{3}{2}\frac{\tilde{\tilde{\mathbf{S}}}}{\tilde{\sigma}_{eq}} + \frac{\alpha(\mathbf{I}-\mathbf{D})^{-1}}{3} \right) \right\|} \qquad [10]$$

3.4 Conclusion

Le modèle exposé ci-dessus permet de décrire le comportement viscoplastique endommageable des roches en tenant compte de la dilatance viscoplastique et de l'anisotropie de l'endommagement. Sa confrontation à des résultats d'essais de fluage de relaxation et d'essais quasi-statiques (Figure 3.2) montre que l'on peut raisonnablement reproduire les comportements observés. Bien sûr la détermination des huit paramètres du modèle nécessite de suivre une procédure d'identification à partir d'un nombre d'essais suffisant.

Ce modèle, qui sera implémenté dans un code de calcul éléments finis, a été appliqué au cas simple d'une cavité circulaire creusée dans un massif soumis à un champ de contraintes isotrope. Les résultats seront exposés au chapitre suivant

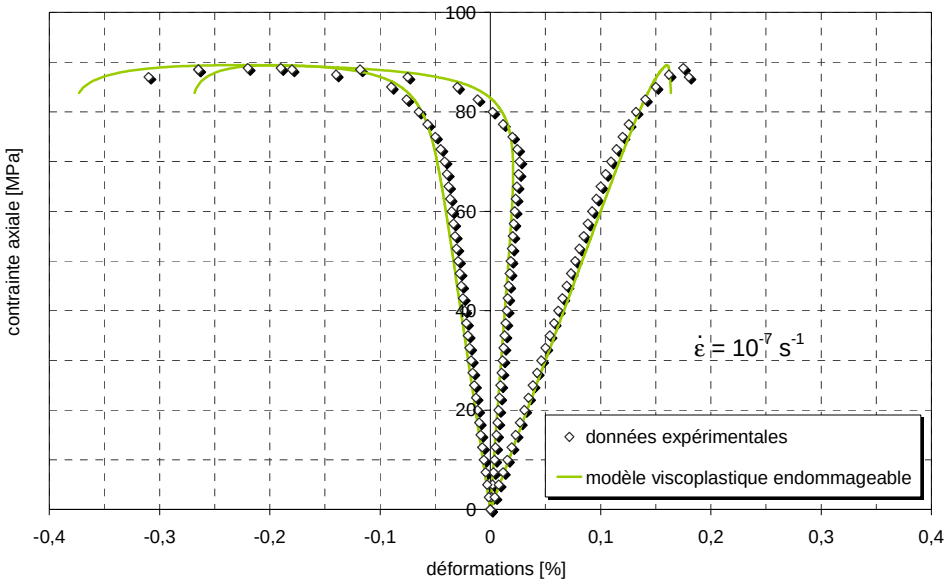

E = 60000 MPa ; ν = 0.4 ; N = 10 ; M = 75 ; K = 2100 MPa.s ; α = 0.5 ; r = 10 ; q = 0 ; A = 165 MPa.s ; β = 0.15

Figure 3.2 : Essai de compression quasi-statique réalisé sur une anhydrite. Comparaison entre valeurs expérimentales et prédiction du modèle, d'après Pellet et al. [7]. Les paramètres ont été ajustés par optimisation pour montrer l'aptitude du modèle à reproduire les phénomènes observés.

4 Application à la modélisation numérique d'ouvrages souterrains

La finalité de tout modèle constitutif étant d'être opérationnel dans un contexte industriel, il est nécessaire de pouvoir le valider en confrontant ses performances, dans un premier temps avec des essais de laboratoire réalisés dans des conditions contrôlées et dans un second temps avec des mesures faites sur des ouvrages réels soigneusement auscultés. Ce point est plus délicat pour plusieurs raisons. En premier lieu, parce que les exemples d'ouvrages en vraie grandeur, soigneusement instrumentés, réalisés dans des terrains homogènes de caractéristiques connues sont rares et deuxièmement parce qu'il est indispensable de prendre en compte les effets d'échelle, spatiale et temporelle, encore mal connus.

Avant de présenter les applications numériques relatives au comportement viscoplastique endommageable des roches, il m'a semblé utile de joindre en annexe III, deux références concernant la modélisation numérique tridimensionnelle (3D). La première [8] montre l'influence des forces d'écoulement hydrauliques sur la stabilité du front de taille d'un micro-tunnel réalisé à Lausanne sur le site de l'EPFL. Dans ce cas le calcul 3D s'impose, car l'effet voûte favorable à la stabilité ne pourrait pas être pris en compte en deux dimensions. La seconde publication [9] traite du franchissement d'accidents géologiques par un tunnel. Ici aussi, la prise en compte de la troisième dimension permet de tenir compte de l'effet bénéfique du report des contraintes par effet voûte sur les zones compétentes du massif.

Dans ce qui suit, nous présentons les résultats de simulations numériques du comportement viscoplastique endommageable pour les ouvrages souterrains. Le détail peut être trouvé dans les publications [10], [11], [12], [13] de l'annexe III , dans les rapports [15] et [16] et dans les thèses d'Eric Boidy (2002), [18] et d'Attila Hajdu (2003), [19].

4.1 Modélisation du comportement viscoplastique d'ouvrages existants

Nous avons, dans cette perspective, accompli l'analyse du comportement d'un ouvrage instrumenté et ausculté sur une période d'environ dix années. Il s'agit de la galerie de reconnaissance du tunnel autoroutier du Mont-Terri réalisé en Suisse [10].

La modélisation numérique a été réalisée avec le code Flac 2D dans lequel la loi de Lemaitre a été implémentée. Les contraintes in situ étant approximativement isotropes, nous

avons pu mener les calculs en conditions axisymétriques sans faire une hypothèse trop restrictive. Les résultats de calcul montrent que l'on peut raisonnablement mettre en évidence les phénomènes différés. Les ordres de grandeur des convergences à la paroi (Figure 4.1), des contraintes dans le terrain et au contact du revêtement ou encore des efforts dans le revêtement sont raisonnables. Par ailleurs, le phasage, l'influence de la vitesse d'avancement et de l'arrêt du front sur les convergences ont pu être simulés. Bien sûr, les paramètres de la loi viscoplastique déduits de résultats d'essais de laboratoire, n'ont pu être introduits sans correction, tenant compte de l'effet d'échelle et de la dispersion liée à l'hétérogénéité des terrains. Soulignons aussi que pour l'utilisation d'un code explicite tel que Flac, une attention particulière doit être portée à la détermination du pas de temps critique [11]. En effet, le temps physique et le temps numérique se superposant, la stabilité numérique ne peut être assurée que si le pas de temps respecte un critère de pas de temps critique.

Une autre simulation réalisée sur un ancien tunnel ferroviaire [12] a montré que la relaxation des contraintes peut se produire dans le terrain. Pour ce type d'ouvrage, une des difficultés est de modéliser un revêtement en pierres de taille appareillées par des éléments adéquats.

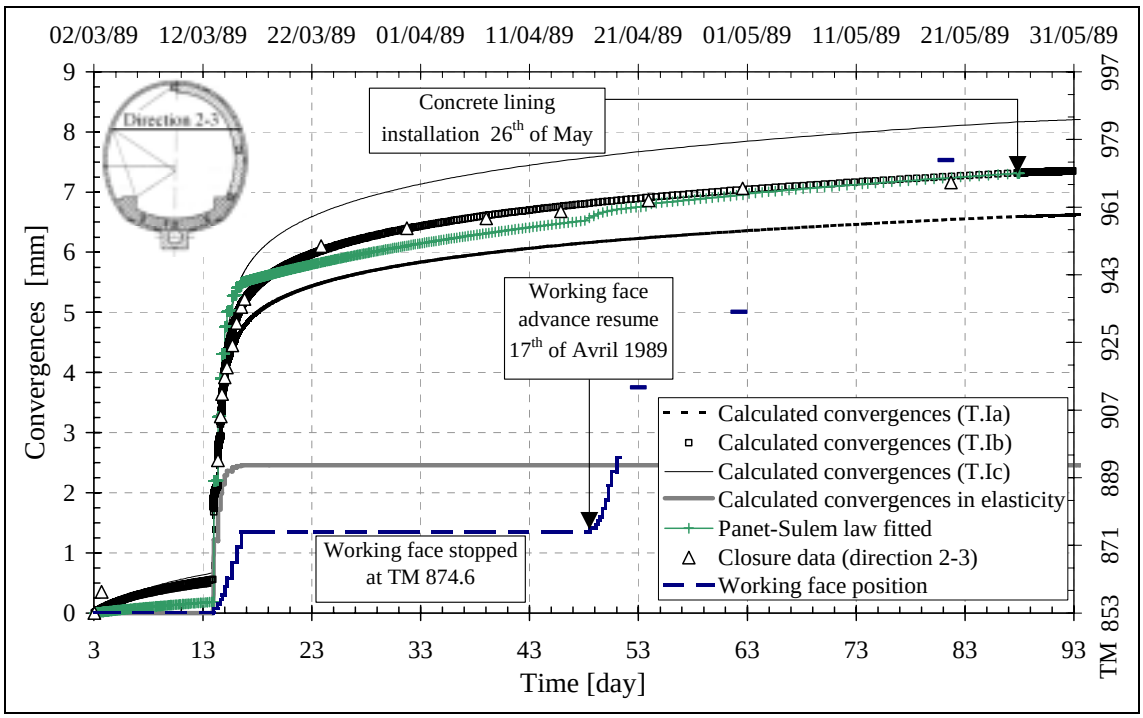

Figure 4.1 : Convergence de la paroi de la galerie du Mont Terri. Comparaison entre valeurs mesurées et valeurs calculées avec le modèle viscoplastique de Lemaitre, d'après Boidy et al. [10].

4.2 Modélisation du comportement viscoplastique endommageable d'un puits circulaire et d'un tunnel

Il s'agit ici principalement de mettre en évidence l'accélération des déplacements à la paroi de l'excavation consécutive à la rupture en fluage tertiaire ainsi que l'évolution de la progression dans le terrain de la zone endommagée. Cela requiert, comme nous l'avons vu, l'utilisation de loi de comportement viscoplastique endommageable. Pour y parvenir, nous avons utilisé le code de calcul par éléments finis Cast3M avec la loi viscoplastique endommageable de Lemaitre, [13] .

Nous avons donc simulé le creusement d'un puits vertical. Les résultats des calculs montrent, pour le jeu de paramètres choisi, que la rupture peut survenir longtemps après l'excavation, 180 jours dans le cas étudié. De plus, dans le cas d'un puits non soutenu, la zone endommagée progresse plus rapidement. On observe alors, en paroi, une chute de la contrainte orthoradiale consécutive à l'endommagement et à la rupture de la roche.

D'autres calculs, ont montré que pour un puits dont les parois sont soutenues par un revêtement rigide, la progression de la zone endommagée dans le terrain est fortement limitée. Par ailleurs, si le revêtement conserve ses propriétés mécaniques au cours du temps, la relaxation des contraintes dans le terrain peut même conduire à une régression de la zone endommagée. Evidemment cela supposerait que la roche ait la capacité de se cicatriser ce qui expérimentalement a été démontré pour le sel gemme mais pas pour les argilites.

Nous avons par ailleurs simulé le comportement d'un ancien tunnel ferroviaire existant, le tunnel de Tournemire, qui aujourd'hui sert de laboratoire à l'Institut de Radioprotection et de Sûreté Nucléaire. Dans ce tunnel, deux galeries, creusées perpendiculairement à l'axe du tunnel, ont permis d'observer que la zone endommagée s'était développée en piédroit, sur une distance à la paroi de l'ouvrage variant entre 1 et 3 mètres. Quelques illustrations des premiers résultats de calcul, présentées aux Figures 4.2, 4.3 et 4.4, montrent que l'on peut raisonnablement reproduire numériquement la progression de la zone endommagée et ce sur une période de 150 ans correspondant à l'âge de l'ouvrage [15].

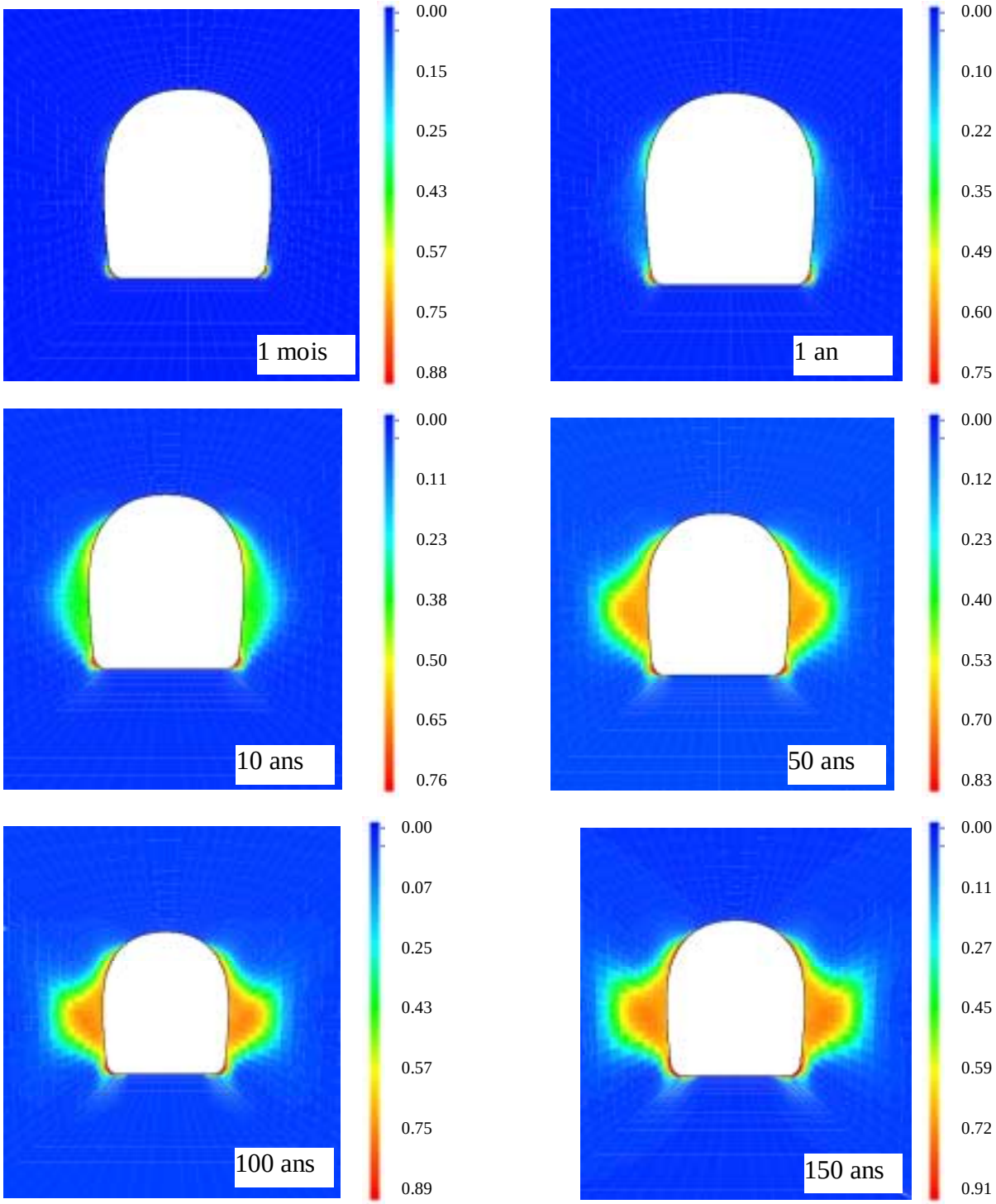

Figure 4.2 : Evolution de l'endommagement autour du tunnel soutenu en fonction du temps : l'échelle représente le paramètre d'endommagement D (Loi viscoplastique endommageable de Lemaitre, état de contrainte initial anisotrope, σ_v = 5.0 MPa, σ_h = 2.0 MPa).

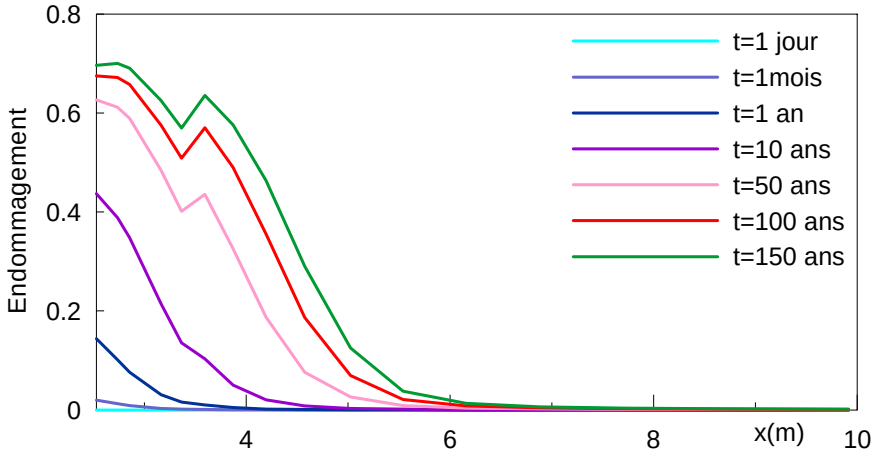

Figure 4.3 : Evolution de l'endommagement le long sur une ligne horizontale à mi-hauteur du tunnel au cours du temps. L'endommagement augmente et se propage vers l'intérieur du massif.

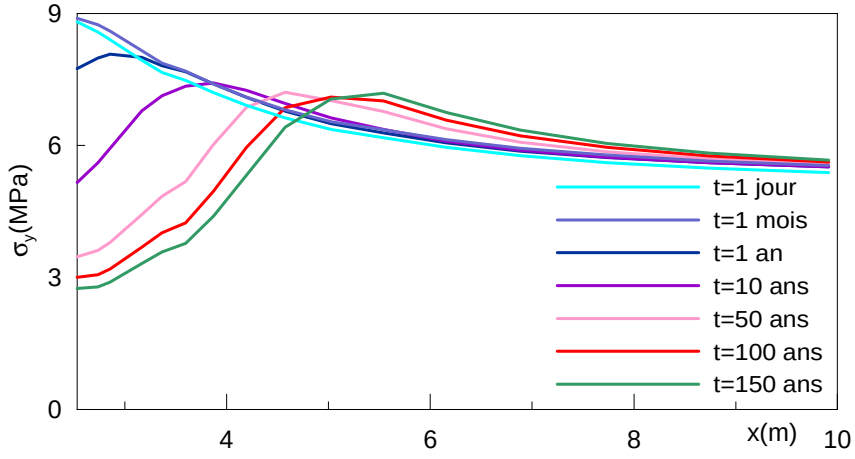

Figure 4.4 : Evolution de la contrainte orthoradiale sur une ligne horizontale à mi-hauteur du tunnel au cours du temps. Le point de contrainte maximale se déplace vers l'intérieur du massif. L'endommagement commence à se développer en un point lorsque la contrainte atteint son maximum. A proximité de la paroi, la contrainte orthoradiale diminue au cours du temps alors que pour x>6m, elle augmente.

4.3 Modélisation viscoplastique avec dilatance et endommagement anisotrope de galeries circulaires

Les calculs présentés dans le paragraphe précédent ne permettent pas de mettre en évidence la variation de volume de la zone endommagée. Le modèle viscoplastique endommageable avec dilatance et anisotropie, présenté au chapitre 3 est appliqué ici au cas d'une galerie circulaire.

Pour des conditions initiales en contraintes isotropes, la loi peut être exprimée analytiquement. Les résultats du calcul, extraits de la thèse de Attila Hajdu [19], sont présentés aux Figures 4.5, 4.6, 4.7 et 4.8. Ils montrent l'évolution de la variable d'endommagement en fonction du temps pour des points situés à différentes distances de la paroi. L'évolution de la déformation volumique en ces points indique qu'après une contractance, la dilatance se développe pour atteindre environ 0.5 %. Pour ce cas, la zone sujette à la dilatance s'étend sur 1.5 fois le rayon.

Ces informations sont précieuses pour les ouvrages de stockage pour lesquels, l'augmentation de la perméabilité des terrains est directement liée à cette augmentation de volume. Evidemment, compte tenu de l'anisotropie de l'endommagement, la perméabilité du massif sera, elle aussi, anisotrope ce qui dans le cas particulier serait probablement plutôt favorable.

4.4 Conclusion

En conclusion de ce chapitre, les résultats des modélisations numériques montrent que l'on peut raisonnablement reproduire à l'aide d'un modèle viscoplastique endommageable le comportement différé à long terme d'ouvrages souterrains. La difficulté réside toujours dans la possibilité de déterminer des propriétés mécaniques de la roche réalistes et fiables à l'échelle de l'ouvrage.

Les modélisations confirment bien qu'en ouvrages souterrains, on peut se trouver dans deux situations extrêmes. Si les parois du tunnel sont non revêtues, on aura à faire à des déformations de fluage alors qu'à l'inverse, si les parois du tunnel sont soutenues par un revêtement infiniment rigide, les déformations des parois seront nulles et l'on observera de la relaxation des contraintes. Dans la réalité, on se trouve souvent dans une situation intermédiaire, où dans un premier temps, les parois étant non revêtues, on observe des déformations différées de fluage qui, lorsque le revêtement est posé, sont ralenties et stoppées plus ou moins rapidement en fonction de la raideur de ce dernier.

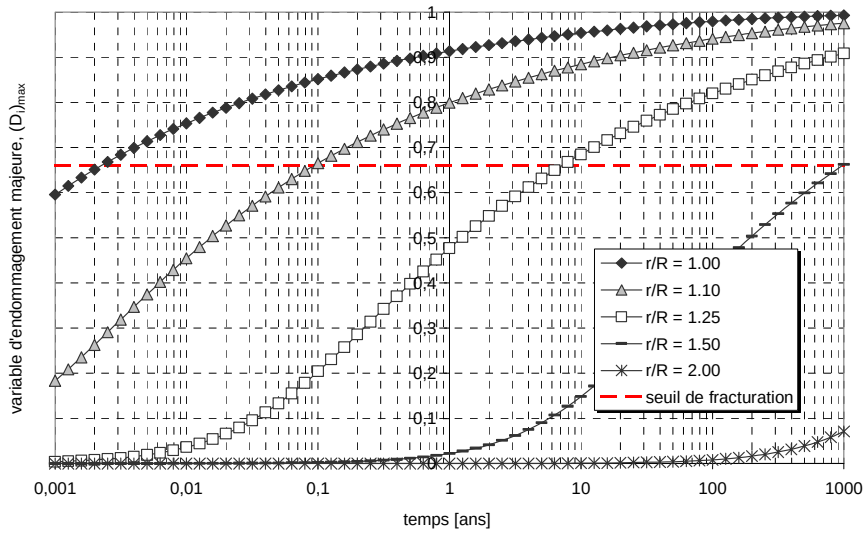

Figure 4.5 : Evolution de l'endommagement principal majeur en fonction du temps en différents points du massif au voisinage d'une cavité circulaire selon l'axe vertical de la cavité (θ = 90°) sous un état de contrainte initial anisotrope (K_0 = 1.5), simulation semi-analytique à l'aide du modèle avec prise en compte de la déformation volumique couplée à un endommagement anisotrope, d'après Hajdu [19].

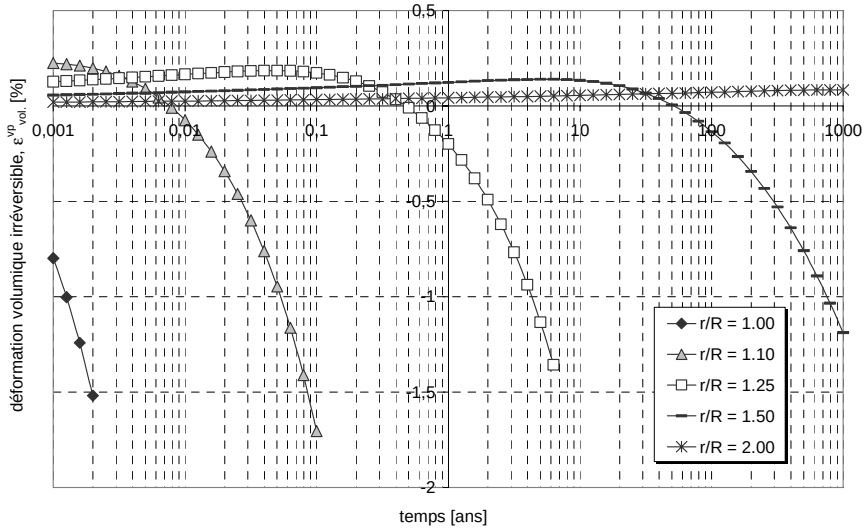

Figure 4.6 : Evolution de la déformation volumique en fonction du temps en différents points du massif au voisinage d'une cavité circulaire selon l'axe vertical de la cavité (θ = 90°) sous un état de contrainte initial anisotrope (K_0 = 1.5), simulation semi-analytique à l'aide du modèle avec prise en compte de la déformation volumique couplée à un endommagement anisotrope, d'après Hajdu [19].

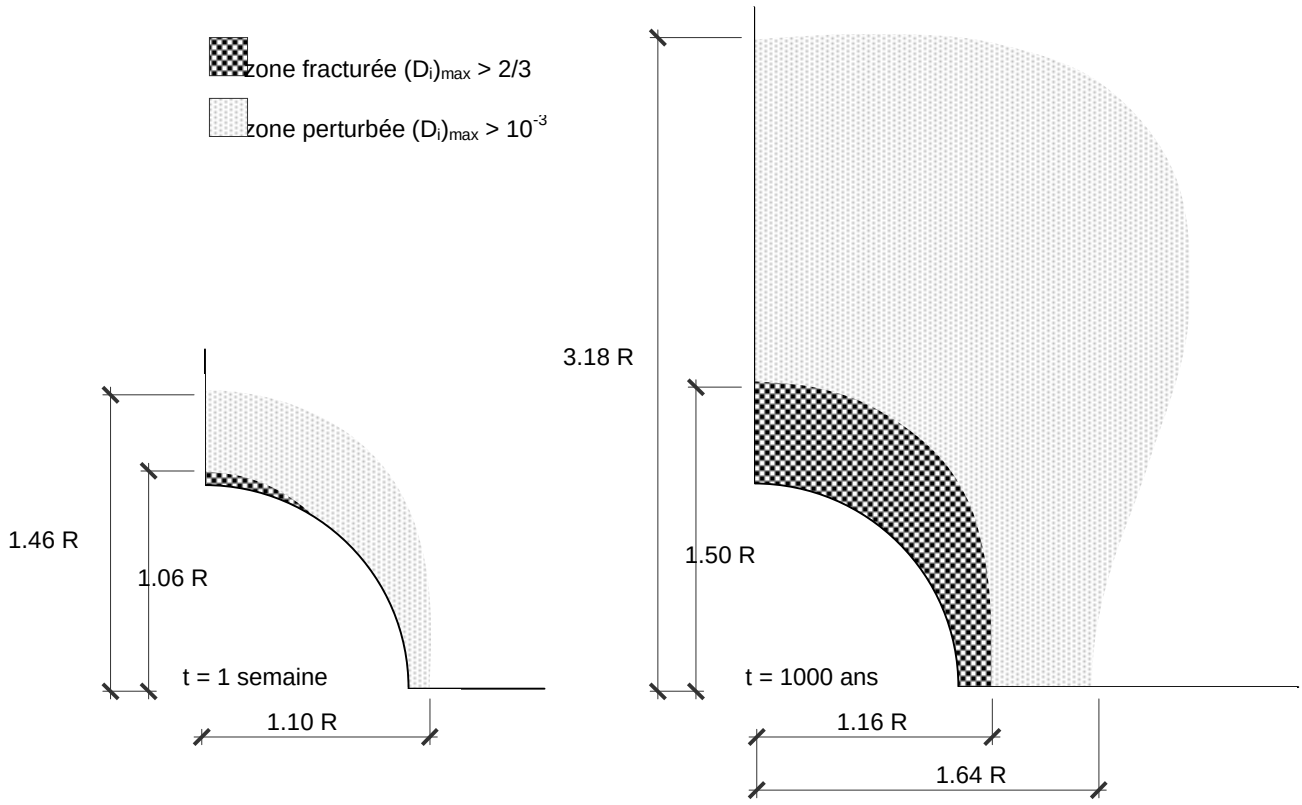

Figure 4.7 : Etendue des zones perturbées et fracturées dans le massif au voisinage d'une cavité circulaire à 1 semaine (à gauche) et à 1000 ans (à droite) sous un état de contrainte initial anisotrope (K_0 = 1.5), simulation semi-analytique à l'aide du modèle avec prise en compte de la déformation volumique couplée à un endommagement anisotrope, d'après Hajdu [19].

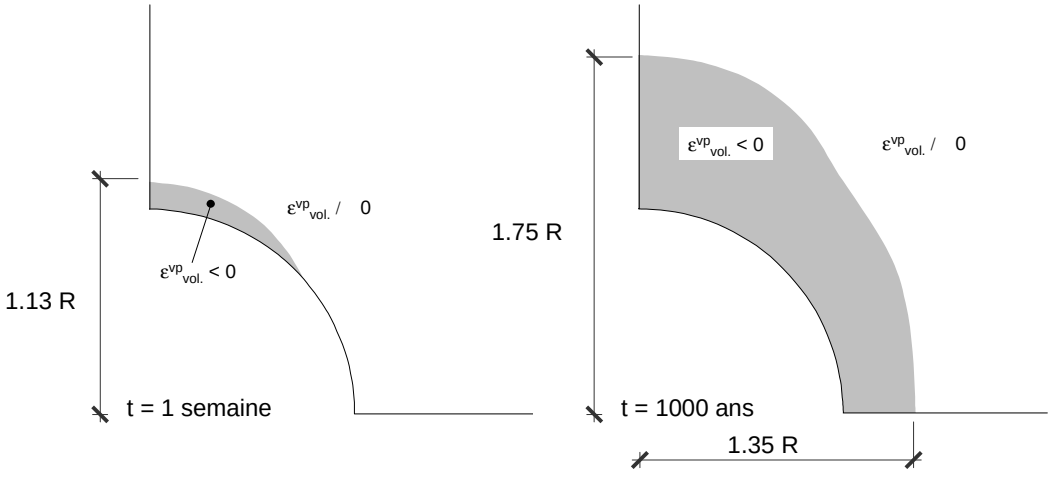

Figure 4.8 : Etendue des zones de dilatance dans le massif au voisinage d'une cavité circulaire à 1 semaine (à gauche) et à 1000 ans (à droite) sous un état de contrainte initial anisotrope (K_0 = 1.5), simulation semi-analytique à l'aide du modèle avec prise en compte de la déformation volumique couplée à un endommagement anisotrope, d'après Hajdu [19].

5 Conclusions générales et perspectives

Tout au long de ce mémoire, nous avons vu que le comportement viscoplastique endommageable des roches est d'une importance capitale dans la perspective de modéliser le comportement différé à long terme des ouvrages souterrains. Ce point est essentiel pour la conception des installations de stockage de déchets radioactifs pour lesquels des prédictions à très long terme, sur des périodes de plusieurs millénaires, sont requises. Dans la hiérarchie des phénomènes régissant le comportement des géomatériaux, ceux qui dépendent du temps figurent au premier rang. Malheureusement ils restent encore trop souvent ignorés dans les modélisations. L'approche d'un tel problème nécessite donc de mener de front des études expérimentales, théoriques et numériques appliquées à des cas concrets.

Les principaux faits et apports des expérimentations en laboratoire présentées dans ce mémoire résident dans la mise en évidence, d'une part de la variation de volume viscoplastique, et d'autre part de l'anisotropie de l'endommagement. L'association de ces deux types de comportement, étudiée à partir d'essais de fluage, de relaxation et de chargement quasi-statique, conduit à la rupture différée identifiée par un temps à la rupture. Nous avons aussi montré que l'anisotropie peut être caractérisée à partir d'essais de chargement cycliques en mesurant les déformations irréversibles dans les directions principales du chargement. Par ailleurs, l'analyse micro structurale des échantillons testés, nous a permis de caractériser l'initiation et l'évolution de la propagation de la fissuration. La thèse de G. Fabre [20], actuellement en cours, devrait nous fournir des informations quantitatives sur la localisation de la rupture (inter ou intra granulaire ? dans quels cristaux ?) et sur la capacité d'auto cicatrisation des argilites, qui reste encore à démontrer expérimentalement.

Il reste cependant encore beaucoup à faire, dans le domaine expérimental notamment, pour tenter d'accélérer les phénomènes différés. Personnellement je vois deux possibilités. La première pourrait se faire par des processus d'activation thermique, mais cela nécessiterait des températures élevées atteignant au minimum le tiers de la température de fusion de la roche. La deuxième, applicable aux roches saturées ou partiellement saturées, consisterait à accélérer la désaturation par électro-osmose. Enfin, l'accélération des déformations viscoplastiques par essais de fluage cyclique mérite d'être poursuivie.

D'un point de vue théorique, le développement d'un modèle constitutif, prenant en compte à la fois la déformation volumique viscoplastique et le développement d'un endommagement anisotrope, constitue une avancée. Ce modèle prototype a montré son aptitude à décrire les essais réalisés en laboratoire et son application, à un cas simple de cavité

circulaire, a permis de mettre en évidence l'évolution dans le temps de la zone endommagée (EDZ) ainsi que les zones entrées en dilatance. Ce modèle pourra être amélioré notamment en y introduisant une surface de charge plus sophistiquée que celle de Drucker Prager, permettant aussi de prendre en compte la cicatrisation de la roche et l'anisotropie du fluage. Enfin rappelons, qu'à terme, les couplages thermo-hydro-chimio-mécaniques et particulièrement les phénomènes électrochimiques de sorption, devront être pris en compte.

Concernant la modélisation numérique des ouvrages, le point crucial est, répétons le, lié à la représentativité des valeurs des paramètres introduits dans les modèles. Les effets d'échelle nécessitent encore d'être mieux appréhendés, et dans cette perspective, des procédures d'optimisation à partir d'algorithmes mathématiques d'analyse inverse, pratiquées sur des ouvrages instrumentés, devraient se révéler bénéfiques. Par ailleurs, le manque évident de données expérimentales devrait être partiellement comblé par les résultats d'auscultation des ouvrages du laboratoire souterrain de l'Andra qui constitueront une base de données précieuse. Nous souhaitons pouvoir accéder à ces mesures faites in situ et ainsi réaliser les simulations a posteriori du comportement des ouvrages (puits et galeries). La confrontation avec les calculs 3D déjà réalisés et les mesures in situ devrait nous permettre de poursuivre la validation de nos modèles constitutifs. Les points que nous suivrons en priorité pour le comportement différé, concerneront l'évolution des convergences des galeries en fonction du temps, la mesure de la propagation de l'endommagement dans la roche, l'interaction entre les soutènements et la roche ainsi que le vieillissement des matériaux.

D'autre part, les installations de stockage à grande échelle peuvent nécessiter pour leur modélisation une approche par homogénéisation car en effet, la discrétisation de chaque partie d'ouvrage (alvéole, chambre de manutention, etc) devient pénalisante. Nous avons entrepris des recherches dans cette direction (thèse de N.P. Zokimila, [21]) qui devraient déboucher prochainement. Cette recherche a pour but de quantifier l'impact à grande échelle des ouvrages sur la couche géologique d'accueil. D'un point de vue mécanique, l'approche par homogénéisation se fait à plusieurs niveaux. L'homogénéisation de la géométrie des ouvrages, qui peut être assimilée à une structure périodique, et l'homogénéisation des caractéristiques mécaniques, élastiques, plastiques et visqueuses. Pour ce point, l'étude est centrée sur le passage micro-macro et sur les effets d'échelle dimensionnels et temporels. Les conclusions de ce travail pourraient si les résultats sont satisfaisants être étendues ultérieurement à d'autres questions comme celle de l'après mines.

La résolution de la problématique du stockage de déchets nécessitera à n'en pas douter encore de longs efforts dans un cadre interdisciplinaire associant géochimistes, géologues, géomécaniciens et ingénieurs du génie civil. La fédération des actions de recherche des organismes nationaux sous l'égide d'institutions internationales, telles que la Commission Européenne, l'Agence pour l'Energie Nucléaire de l'Organisation de Coopération et de Développement Economiques ou encore de l'Agence Internationale de l'Energie Atomique des Nations Unies, devrait y contribuer fortement.

6 Bibliographie

6.1 Références de l'auteur jointes en annexe

1 - N. Gatelier, F. Pellet & B. Loret (2002), Mechanical damage of an anisotropic rock under cyclic triaxial tests, International Journal of Rock Mechanics and Mining Sciences, Pergamon Press, vol 39, n° 3, pp 335-354.

2 - E. Boidy & F. Pellet (2000), Identification of mechanical parameters for modeling time-dependent behavior of shale, Workshop Andra, Paris – France, pp 11-22.

3 - G. Fabre & F. Pellet (2002), Identification des caractéristiques visqueuses d'une roche argileuse, Proceedings of the International Symposium on Identification and Determination of Soil and Rock Parameters for Geotechnical Design, PARAM, Paris - France, pp 33-40.

4 - F. Pellet & G. Fabre (2003), Comportement mécanique de roches argileuses lors d'essais de fluage de longue durée, Colloque du GdR Forpro - CNRS, La Grande Motte – France.

5 - M.K. Jafari, F. Pellet, M. Boulon & K. Amini Hosseini (2004), Experimental study of mechanical behaviour of rock joints under cyclic loading, Rock Mechanics and Rock Engineering, Springer Verlag, Ed. G. Barla, vol 37, n° 1, pp 3-23.

6 - M. K Jafari , K Amini Hosseini, F. Pellet, M. Boulon & O. Buzzi (2003), Evaluation of shear strength of rock joints subjected to cyclic loading, Soil Dynamics and Earthquake Engineering, Elsevier Science, vol 23, n° 7, pp 619-630.

7 - F. Pellet, A. Hajdu, F. Deleruyelle & F. Besnus, A viscoplastic constitutive model including anisotropic damage for the time dependent mechanical behaviour of rock, to be submitted.

8 - F. Pellet, F. Descoeudres & P. Egger (1993), The effect of water seepage forces on the face stability of an experimental micro tunnel, Canadian Geotechnical Journal, vol. 30, n° 2, pp 363 - 369.

9 - F. Pellet & O. Benoit (1999), Modélisation numérique 3D du comportement d'ouvrages souterrains lors de la traversée d'accidents géologiques, Proceedings of the 9th International Congress on Rock Mechanics, Paris - France, pp 213-218.

10 - E. Boidy, A. Bouvard & F. Pellet (2002), Back analysis of time-dependent behavior of a monitored tunnel, International Journal of Tunneling and Underground Space Technology, Elsevier Science, vol 17, n° 4, pp 415-424.

11 - E. Boidy, F. Pellet & M. Boulon (2001), Numerical modeling of deep tunnels including time-dependent behavior, Proceedings of the 10th International Conference on Computer Methods and Advances in Geomechanics - IACMAG, Tucson, Arizona - US, pp 1663-1668.

12 - N.P. Zokimila, E. Flavigny, F. Pellet & A. Billon (2003), Modélisation numérique du comportement à court et à long terme d'un tunnel ferroviaire, Conférence régionale africaine de Mécanique des Sols, Casablanca, Maroc, pp 233-239.

13 - F. Pellet, A Hajdu, M. Boulon, F. Deleruyelle & F. Besnus (2002), Numerical modeling of underground structures taking into account the visco-plastic behavior and rock damage, Proceedings of the International Conference on Numerical Models in Geomechanics - NUMOG VIII, Roma - Italy, pp 399-404.

14 - F. Pellet & P. Egger (1996), Analytical model for the mechanical behavior of bolted rock joints subjected to shearing, Rock Mechanics and Rock Engineering, Springer Verlag, Ed. H.H Einstein & K. Kovari, vol. 29, no 2, pp 73-97.

6.2 Rapports scientifiques

15 - Etude de la rupture différée autour des cavités souterraines : Application au tunnel de Tournemire, rapport préliminaire IRSN (2004).

16 - Comportement viscoplastique avec dilatance et endommagement anisotrope : Application du modèle au cas d'une cavité circulaire**,** rapport IRSN (2004).

6.3 Références des thèses dirigées et co-dirigées par l'auteur

17 - Nicolas Gatelier, Etude expérimentale et numérique de l'endommagement des roches anisotropes, thèse de doctorat présentée à l'Université Joseph Fourier en janvier 2001.

18 - Eric Boidy, Modélisation numérique du comportement différé des cavités souterraines, thèse de doctorat financée en convention CIFRE par Coyne et Bellier, présentée à l'Université Joseph Fourier en avril 2002.

19 - Attila Hajdu, Comportement viscoplastique endommageable des roches et application aux grandes cavités souterraines de stockage, thèse de doctorat financée par l'Institut de Radioprotection et de Sûreté Nucléaire (IRSN), présentée à l'Université Joseph Fourier en décembre 2003.

20 - Géraldine Fabre, Analyse micro-mécanique de l'endommagement viscoplastique des roches anisotropes, soutenance prévue en octobre 2004.

21 - Pierre Zokimila, Modélisation numérique par homogénéisation du comportement des ouvrages de stockage à grande échelle, soutenance prévue en octobre 2004.

6.4 Quelques références générales

22 - D. Allirot, J.-P. Boehler & A Sawczuk., Irreversible strains of an anisotropic rock under hydrostatic pressure. Int. J. Rock Mech. Min. Sci. & Geomech. Abstr., 31, pp.77-83, 1977.

23 - P. Berest, Viscoplasticité en mécanique des roches, Manuel de rhéologie des géomatériaux, Presses de l'ENPC, sous la direction de F. Darve, pp. 235-257, 1987.

24 - Z. T. Bieniawski, Mechanism of brittle fracture of rock :Part III – Fracture in tension and under long-term loading, Int. J. Rock Mech. Min. Sci. & Geomech. Abstr. Vol. 4, pp. 425-430, 1967.

25 - Z. T. Bieniawski, Rock mass classifications in rock engineering, Proc. of Symp. In exploration for rock engineering, Vol 1, pp 97 – 106, 1976.

26 - J.-P. Cordebois & F. Sidoroff, Endommagement anisotrope en élasticité et plasticité, Journal de Mécanique Théorique et Appliquée, n° spécial, pp. 45-59, 1982.

27 - N. D. Cristescu & U. Hunsche, Time effects in rock mechanics, John Wiley & Sons, New York, 1997.

28 - M. Kachanov, Effective elastic properties of cracked solid : critical review of some basic concepts, ASME Appl. Mech. Rev., Vol. 45, n°8, pp. 304-335, 1959.

29 - J. Lemaitre & J.-L. Chaboche, Mécanique des matériaux solides, 2ème édition, Dunod, 1996

30 - H. Lauffer, Gebirgsklassifiezierung für den Stollenbau, Geologie und Bauwesen, vol 24, Number 1, pp. 46-51, 1958.

31 - P. Lunardi, Application de la mécanique des roches aux tunnels autoroutiers, exemples du tunnel du Fréjus et du Gran Sasso, Revue Française de Géotechnique, no 12, pp. 5-43, 1980.

32 - D. E. Munson & P. R. Dawson, Proc. 1st Conf. on the Mechanical Behavior of Salt, Trans. Tech. Publications, Clausthal, pp. 717-737, 1984.

33 - M. Panet, Quelques problèmes de mécanique des roches posés par le tunnel du Mont Blanc, Bulletin des Laboratoires des Ponts et Chaussées, Vol. 42, pp. 115-145, 1969.

34 - P. Perzyna, Fundamental problems in viscoplasticity, Adv. Appl. Mech, Vol. 9, pp. 247-377, 1966.

35 - R.P. Young, Interpreting the amount and orientation of microcracks in the excavation disturbed zone using velocity, modulus and crack density values, International EDZ workshop, Ed. Atomic Energy of Canada Limited, 2002.

Annexe I : Publications relatives aux programmes expérimentaux

1 - N. Gatelier, F. Pellet & B. Loret (2002), Mechanical damage of an anisotropic rock under cyclic triaxial tests, International Journal of Rock Mechanics and Mining Sciences, Pergamon Press, vol 39, n° 3, pp 335-354.

2 - E. Boidy & F. Pellet (2000), Identification of mechanical parameters for modeling time-dependent behavior of shale, Workshop Andra, Paris – France, pp 11-22.

3 - G. Fabre & F. Pellet (2002), Identification des caractéristiques visqueuses d'une roche argileuse, Proceedings of the International Symposium on Identification and Determination of Soil and Rock Parameters for Geotechnical Design, PARAM, Paris - France, pp 33-40.

4 - F. Pellet & G. Fabre (2003), Comportement mécanique de roches argileuses lors d'essais de fluage de longue durée, Colloque du GdR Forpro - CNRS, La Grande Motte – France.

5 - M.K. Jafari, F. Pellet, M. Boulon & K. Amini Hosseini (2004), Experimental study of mechanical behaviour of rock joints under cyclic loading, Rock Mechanics and Rock Engineering, Springer Verlag, Ed. G. Barla, vol 37, n° 1, pp 3-23.

6 - M. K Jafari , K Amini Hosseini, F. Pellet, M. Boulon & O. Buzzi (2003), Evaluation of shear strength of rock joints subjected to cyclic loading, Soil Dynamics and Earthquake Engineering, Elsevier Science, vol 23, n° 7, pp 619-630.

PERGAMON

International Journal of Rock Mechanics & Mining Sciences 39 (2002) 335–354

International Journal of
Rock Mechanics
and Mining Sciences

www.elsevier.com/locate/ijrmms

Mechanical damage of an anisotropic porous rock in cyclic triaxial tests

N. Gatelier[1], F. Pellet*, B. Loret

Laboratoire Sols, Solides, Structures, BP 53 X, 38041 Grenoble, France

Accepted 27 March 2002

Abstract

This paper presents an extensive laboratory investigation of the mechanical properties of a porous sandstone which exhibits transversely isotropic behaviour. Particular attention has been paid to the influence of the structural anisotropy on the progressive development of pre-peak damage. Uniaxial and triaxial cyclic tests were performed for several orientations of the isotropy planes with respect to the principal stress directions in order to quantify the irreversible strains and the changes of oriented moduli with the cumulative damage. Two main mechanisms are involved throughout the loading process: compaction and microcracking. Compaction is active at all stress levels. In the uniaxial tests, both mechanisms are shown to be strongly influenced by the inclination of loading with respect to the isotropy planes. However, with increased confining pressures, the influence of anisotropy is significantly reduced. © 2002 Published by Elsevier Science Ltd.

Keywords: Sandstone; Transverse isotropy; Oriented moduli; Damage; Cyclic loading tests; Irreversible strains

1. Introduction

During the past few years, considerable efforts have been made to study mechanical damage of rocks. Damage is the destruction of certain bonds in the microstructure of a material subjected to loading. From a macroscopic point of view, it can be measured by its consequences on the effective properties of the material. In general, the damaging process leads to drastic changes in both the mechanical and hydraulic properties.

For practical and economic reasons, rock damage is highly detrimental in many engineering structures such as boreholes and underground caverns designed for storage of gas or oil. Estimating the extent of the disturbed zone surrounding the cavern is of the utmost importance in determining the increase of rock permeability in order to prevent leakage of gas.

Due to their mode of formation, or to deformations they have undergone, most rocks exhibit anisotropic properties to some degree. Although many studies have described the pattern and failure modes under compressive loading of isotropic rocks as well as rocks with a strong structural anisotropy, principally of metamorphic nature, data on sedimentary rocks are scarce. For these rocks, the influence of fabric on damage and its mechanical effects are not well understood. Experimental study reported here aims at assessing the interactions between initial anisotropic mechanical properties of the initially intact rock and the development of damage in such a rock.

In Section 2, previous observations concerning rock damage are reported. The physical properties of the rock tested, the specific instrumentation of the specimens and the experimental programme are described in Section 3. Section 4 presents qualitative observations on the stress–strain behaviour of the rock. The initial elastic properties and the development of damage are investigated in Section 5.

2. Overview of previous studies

2.1. Rock deformation process

Rocks are heterogeneous media containing crystals as well as defects such as pores, cracks and grain

*Corresponding author. Tel.: +33-4-76-82-70-23; fax: +33-4-76-82-70-43.

E-mail address: frederic.pellet@hmg.inpg.fr (F. Pellet).

[1] Now at Geostock Consulting Engineers, 92563 Rueil, Malmaison, France.

1365-1609/02/$ - see front matter © 2002 Published by Elsevier Science Ltd.
PII: S1365-1609(02)00029-1

boundaries at the microscale. As mentioned by Kemeny and Cook [1], cracks may grow through several mechanisms such as pore crushing, sliding along pre-existing cracks, elastic mismatch between grains, dislocation movement and hertzian contact. Microdiscontinuities play an important role. They may induce local tensile stresses, even if the external applied load is compressive, and thus lead to the initiation and propagation of microcracks in opening mode. During the loading process, interaction and coalescence of the microdefects lead to strain localisation and finally to rock failure [2].

Since the fundamental works of Bieniawski [3] and Brace et al. [4], it is commonly accepted that brittle rock deformation can be split into stages characterised by changes in the stress–strain response. In particular, dilatant volumetric strain is the consequence of the growth of microcracks with a preferred orientation parallel to the maximum principal compressive stress. As mentioned by Wong [5] and Wu et al. [6], this phenomenon results in stress-induced anisotropic rock properties.

2.2. Mechanical behaviour of rock subjected to cyclic loading

The progressively deteriorating properties of damaged rock can be highlighted by performing cyclic loading tests [7]. Two types of cyclic tests represented in Fig. 1 are distinguished, i.e. type 1—where the loading is cycled between two prescribed limits and type 2—where the loading is increased from one cycle to the next. Most of the published data concerning type 1 tests aim at producing S–N curves, that relate the peak stress, S, to the number of cycles at failure N [8–11]. The results provided by Scholz and Koczynski [9] and Costin and Holcomb [12] have shown that cycling decreases rock strength, possibly by a combination of cyclic fatigue and stress corrosion.

For a prescribed stress higher than a certain threshold, damage increases rapidly in the first few cycles, then stabilises and increases again in the last few cycles.

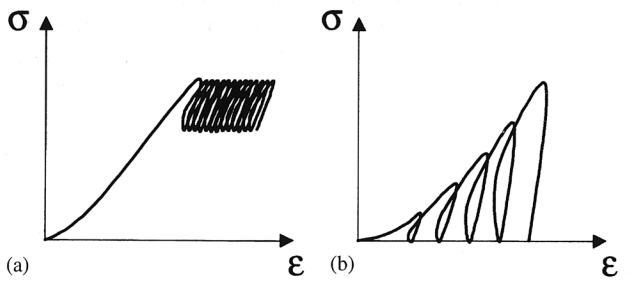

Fig. 1. Schematic axial strain—axial stress curve for cyclic tests: (a) cyclic loading between two prescribed limits (type 1 test), (b) increasing load from one cycle to the next (type 2 test).

Damage is reflected by an irreversible dilatant volumetric strain observed after complete unloading. In contrast, for a prescribed axial stress lower than this threshold, damage stabilises without additional irreversible dilatant volumetric strain. Then the response of the rock becomes independent of the cycles [12]. This behaviour has been encountered in a wide variety of rocks deformed in the brittle regime.

Mineral composition and fabric have a key effect on damage mechanisms. Using type 1 tests on granite and marble, Saint-Leu and Sirieys [13] have shown that the volumetric response of these rocks under cyclic loading may differ depending on rock composition. For instance, the axial stress level where the volumetric strain rate changes sign decreases significantly for granite whereas it is almost constant for marble.

More recently, Martin and Chandler [14] performed type 2 tests on Lac du Bonnet granite at prescribed increments of lateral deformation. The damage parameter, ω_{vol}, was defined as the cumulated irreversible volumetric strain. They found that the stress level where the volumetric strain rate changes sign, called *crack damage stress* σ_{cd}, decreases significantly as ω_{vol} increases. In the post-peak region of the stress–strain curve, σ_{cd} reaches a threshold. In this approach, cohesion and friction components are related in such a way to crack damage stress that the failure process involves simultaneous mobilisation of friction and loss of cohesion. Similar results were obtained by Su et al. [15] on another granite. By performing hydrostatic loading–unloading tests, they showed that the stress-induced anisotropy changes with the damage parameter ω_{vol}. Eberhardt et al. [16] performed the same kind of tests, focusing on the pre-peak region of the stress–strain curve. In addition to the parameter ω_{vol}, damage has been defined in terms of the cumulated irreversible axial and lateral strains, named respectively ω_{ax} and ω_{lat}. One damage type is related to the closure of transversal cracks whereas a second damage type is due to the opening and growth of axial cracks.

2.3. Influence of anisotropy on mechanical damage

The structural anisotropy of rocks plays an important role in both deformation and damage processes. For example, Ewy and Cook [17,18] noticed the strongly preferred orientation of failure on thick-walled cylinders of Berea sandstone submitted to increasing external pressure.

However, most studies concerning the anisotropic mechanical behaviour of rocks have focused on elastic deformability and failure strength. These studies have been performed on sedimentary or metamorphic rocks with a strong planar anisotropy due to cleavage, bedding or schistosity as well as on granitic rocks with oriented microcracks. It has been shown that anisotropy

of the mechanical and physical properties of the materials are well correlated with their fabric arrangement [19–25].

In studying progressive microcrack development on Lac du Bonnet granite by ultrasonic measurements, Chow et al. [26] noticed the influence of pre-existing anisotropy on the damage process. Tests were conducted in uniaxial cyclic loading conditions between zero and peak stress which did not exceed the crack damage stress (type 1). However, these measurements did not permit to establish any reliable correlation between the stress–strain behaviour of the rock and its initial anisotropy.

In fact, for anisotropic rocks, few studies have been devoted to the influence of structural symmetries on overall rock behaviour [27–30]. Therefore, the development of non-linear constitutive equations is hampered by this lack of results. Nevertheless, Allirot et al. [31] showed in a spectacular way the influence of initial anisotropy on the mechanical behaviour of a soft stratified rock subjected to hydrostatic loading. They found the occurrence of irreversible strains with a deviatoric component for cylindrical samples with inclined strata, even for a purely hydrostatic stress state. Lérau et al. [28] showed that the onset of dilatancy of a transversely isotropic slate subjected to deviatoric stress occurs only for orientations of the major principal compression inside a cone of revolution coaxial to the axis of symmetry with half apex angle of about 45°. For principal directions outside this cone, the rock breaks without significant dilatancy.

The strength variations as well as the failure modes are affected by the structural anisotropy of rock [27,28,30,32–35]. They depend on the directional properties of the material with respect to the loading. For rocks with a strong planar anisotropy the main failure modes in most cases are as follows:

- for unconfined conditions, failure occurs by splitting along (respectively across) the bedding plane in the event of loading subparallel (respectively perpendicular) to the bedding plane; for intermediate orientations failure occurs by shearing along the bedding plane,
- for moderate confining pressure, failure occurs either by structural shearing in the case of highly inclined bedding planes or by non-structural shearing for parallel, perpendicular and slightly inclined bedding planes,
- for high confining pressure, failure occurs by kink bands in samples compressed parallel to the bedding plane and by cataclastic flow for other directions.

Moreover, the steepest line of both the shear failure plane and the bedding plane lie on the same plane. This result has been observed in a wide variety of transversely isotropic materials and theoretically confirmed by Millien [36].

3. Experimental programme

The objective of the experiments is to improve the knowledge on pre-peak damage of a porous sedimentary rock subjected to cyclic loading. Damage is quantified by both the effective elastic rock properties and the development of irreversible strains assuming the rock specimens can be idealised as a continuum with homogeneously embedded microdefects. In the strain-softening part of the stress–strain curve, these measurements are not representative of the sample deformation since the assumption of a continuous medium is questionable due to the occurrence of a fault plane at the macroscale.

In addition to high rock homogeneity, great care has been taken in the choice of the samples to obtain a representative set of results.

3.1. Rock tested and sample instrumentation

The rock is Adamswiller sandstone from the Vosges region located in the eastern part of France. Its modal composition is: quartz 44%, feldspar K 38%, mica 12%, and chlorite 6% [36]. The directional arrangement of the mica minerals parallel to the strata is a reason of a structural anisotropy of the rock, which is considered to be transversely isotropic at macroscopic scale. Average material properties are listed in Table 1. Initial rock anisotropy is confirmed by ultrasonic measurements performed on dry samples—P-wave velocity parallel to the strata is 15% higher than perpendicular to the strata.

Samples of Adamswiller sandstone were drilled out from blocks in seven different directions, oriented at $\theta = 0°$, 15°, 30°, 45°, 60°, 75° and 90° with respect to the structural symmetry axis v_3 (Fig. 2). Each sample was prepared according to the ISRM standards [37] from 38.8 mm diameter cores with a length to diameter ratio equal to 2:1.

Strains were measured with strain gauges glued to the samples. The number and arrangement of the gauges depend on the orientation θ. Let us consider a triaxial test on a transversely isotropic material as shown in Fig. 2. Theoretical analysis leads to the following strain tensor expressed in the principal axes (s, t, n) of the stress

Table 1
Average material properties for Adamswiller sandstone

Porosity (%)	Density (g/cm^3)	Grain size (mm)	*P*-wave velocity (m/s)	
			Parallel to strata	Perpendicular to strata
22.9	2.07	0.10	2340	2030

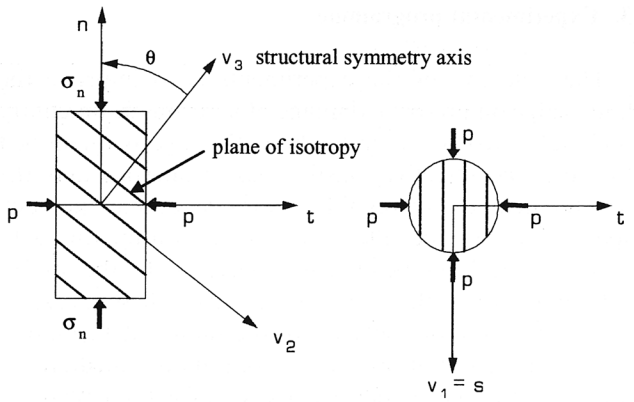

Fig. 2. Triaxial tests on a transversely isotropic material.

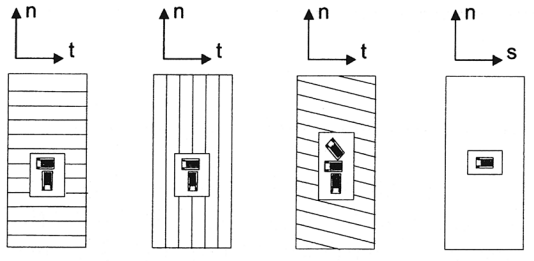

Fig. 3. Strain gauges arrangement as a function of orientation θ.

tensor [38]:

$$[\varepsilon] = \begin{bmatrix} \varepsilon_{ss} & 0 & 0 \\ 0 & \varepsilon_{tt} & \varepsilon_{tn} \\ 0 & \varepsilon_{nt} & \varepsilon_{nn} \end{bmatrix}_{(s,t,n)}, \quad (1)$$

where ε_{nn} is the axial strain, ε_{tt} the out-of-plane transversal strain, ε_{ss} the in-plane transversal strain and $\varepsilon_{nt} = \varepsilon_{tn}$ the shear strain.

Tests are called "in axis" when the structural symmetry axis, v_3, matches with one of the principal directions of the stress ($\theta = 0°$ or 90°). Then the principal directions of the strain and stress are identical ($\varepsilon_{nt} = 0$). Therefore, in order to determine all the components of the strain, samples are instrumented as follows:

- for $\theta = 0°$, one axial and one lateral gauge in two planes (t,n) diametrically opposite measure respectively the components ε_{nn} and $\varepsilon_{tt} = \varepsilon_{ss}$ (Fig. 3a),
- for $\theta = 90°$, one axial and one lateral gauge in two planes (t,n) diametrically opposite measure respectively the components ε_{nn} and ε_{tt} (Fig. 3b) and one lateral gauge in two planes (s,n) diametrically opposite measures the component ε_{ss} (Fig. 3d).

For "off-axis" tests ($\theta \neq 0°$ and 90°), the principal directions of the stress and strain are not coaxial. Components ε_{nn}, ε_{tt} and ε_{nt} are therefore determined by two sets of three gauges mounted in a rosette in the (t,n) planes (Fig. 3c). Strain ε_{ss} is measured by one lateral gauge in two planes (s,n) diametrically opposed (Fig. 3d).

3.2. Testing apparatus and procedure

Tests are conducted with a servo-hydraulic press with four stiff columns constructed by Schenck. Force is measured using a 1.0 MN capacity load cell with 0.02% precision. The confining pressure is generated and controlled by a pressure generating system (SBEL) with a maximum output pressure of 140 MPa. The triaxial cell is equipped with three linear variable differential transformers (LVDT) installed every 120° between two pistons of the cell to check the absence of a bending moment. A 100 MPa capacity pressure transducer measures the confining pressure. Data are acquired by a microcomputer supplied with a 16 bit resolution data acquisition board and 100 kHz sampling rate.

A specific cyclic loading path was followed in order to measure the progressive development of rock damage. It combines type 1 and type 2 tests as defined in Section 2.2. Loading–unloading cycles were performed from zero differential stress (axial stress σ_{nn} minus confining pressure p) to a prescribed axial strain, also termed *fatigue axial strain*, until the irreversible axial strain measured at complete unloading stabilises. It is assumed that stabilisation is reached if the increments of the irreversible axial strain between two consecutive cycles do not exceed 1 or 2 μm/m over ten cycles (Fig. 4). A set of cycles for a given fatigue axial strain will be referred to in the following as a loading step, denoted N. Fatigue axial strain values were imposed at levels of $N \times 620$ μm/m ($N = 1, 2, 3$, etc.) with an accuracy of $\pm 3\%$.

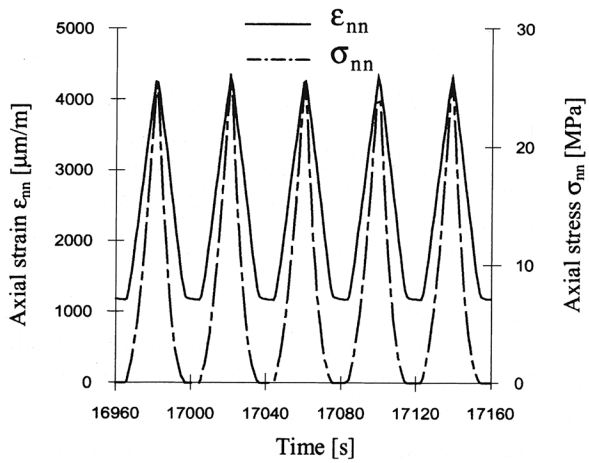

Fig. 4. Axial strain (continuous line) and axial stress (discontinuous line) as a function of time, detail of the loading step $N = 7$ ($\varepsilon_{nn} = 4300$ μm/m) for uniaxial test ($p = 0$ MPa) and inclination $\theta = 0°$.

Table 2
Experimental programme. p: confining pressure, θ: inclination of strata, f: frequency, $\dot{\varepsilon}_{nn}$: axial strain rate

Test number	p (MPa)	θ (deg)	f (Hz)	$\dot{\varepsilon}_{nn}$ (μm/m/s)[a]
EC0-0	0	0	0.025	$31 \times N$
EC0-15	0	15	0.025	$31 \times N$
EC0-30	0	30	0.025	$31 \times N$
EC0-45	0	45	0.025	$31 \times N$
EC0-60	0	60	0.025	$31 \times N$
EC0-75	0	75	0.025	$31 \times N$
EC0-90	0	90	0.025	$31 \times N$
EC25-0	25	0	0.200	$200 \times N$
EC25-30	25	30	0.200	$200 \times N$
EC25-60	25	60	0.200	$200 \times N$
EC25-90	25	90	0.200	$200 \times N$
EC50-0	50	0	0.200	$2002 \times N$
EC50-30	50	30	0.200	$200 \times N$
EC50-60	50	60	0.200	$200 \times N$
EC50-90	50	90	0.200	$200 \times N$

[a] N is the loading step.

Loading–unloading cycles were carried out using axial displacement rate control with a frequency of 0.025 Hz for uniaxial tests and 0.200 Hz for triaxial tests. Uniaxial tests were performed on samples with normal to the strata, v_3, oriented at $\theta = 0°$, 15°, 30°, 45°, 60°, 75° and 90°. Triaxial tests were performed with a confining pressure, p, equal to 25 and 50 MPa on samples with orientations $\theta = 0°$, 30°, 60° and 90°. Data were recorded every second for the uniaxial tests and every 0.1 s for the triaxial tests. The uniaxial tests took about 5–8 h depending on the orientation θ. In the triaxial tests, the number of axial strain increments until failure is larger.

Each test is identified by the notation ECX–Y, where X is the value of the confining pressure in MPa and Y the value of the orientation θ in degrees. Table 2 summarises the experimental programme.

4. Description of the results

An extensive testing progamme has already been run by Millien [36] for the rock under study revealing its mechanical anisotropy and showing the great reproducibility of the tests. The mean standard deviation of the rock strength for three to six uniaxial and triaxial tests performed in the same conditions is ±2.8%.

The general trends of the experimental results are now outlined on typical stress–strain curves. A complete set of curves is given in [39]. A quantitative discussion will be presented in Section 5.

4.1. Uniaxial tests

In Figs. 5–7, typical stress–strain curves for in-axis and off-axis unconfined tests are shown for orientations $\theta = 0°$, 45° and 90° respectively. For the sake of clarity, only the first loading and ten last cycles corresponding to the stabilisation of irreversible axial strain are plotted. Ten, eight and seven loading steps were performed respectively for the above three inclinations in order to reach failure. For the last loading step, leading to rock failure, only the first loading has been plotted because in the subsequent cycles non-homogeneous behaviour was observed in macroscale. Figs. 5–7 display the characteristic behaviour of sedimentary porous rocks, namely non-linearity of the stress–strain relationships, hysteresis in unloading-reloading cycles and irreversible strain upon complete unloading.

For $\theta \neq 0°$, the rock anisotropy is reflected in the difference between the in-plane ε_{ss} and the out-of-plane

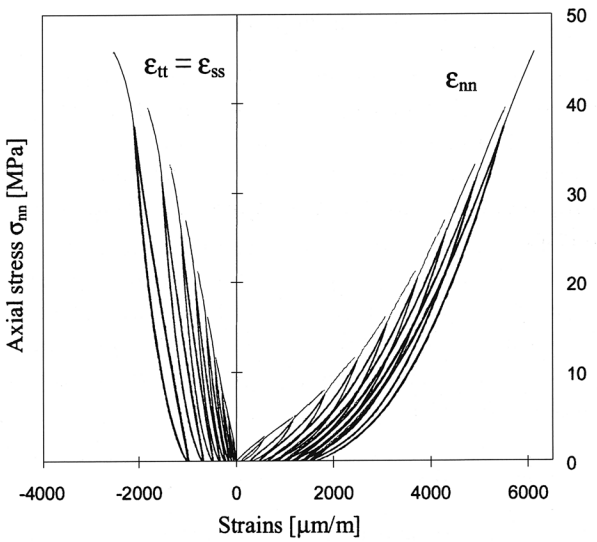

Fig. 5. Axial stress σ_{nn} as a function of strains for uniaxial test EC0-0 ($p = 0$ MPa, $\theta = 0°$).

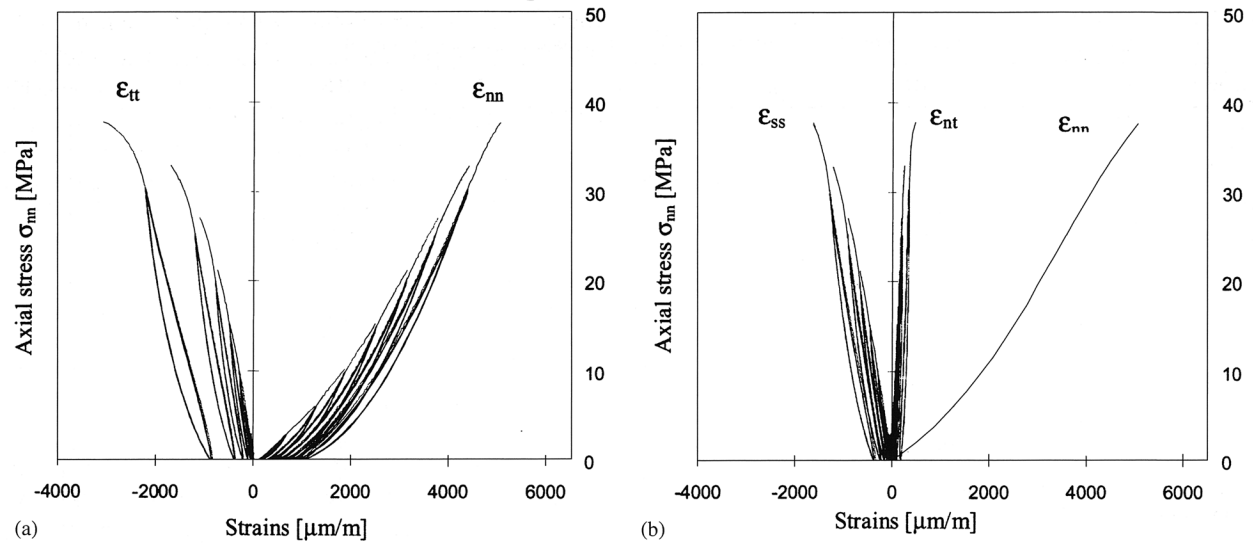

Fig. 6. Axial stress σ_{nn} as a function of strains for uniaxial test EC0-45 ($p = 0$ MPa, $\theta = 45°$): (a) axial strain ε_{nn} and out-of-plane transversal strain ε_{tt}, (b) in-plane transversal strain ε_{ss}, shear strain ε_{nt} and envelope of axial strain.

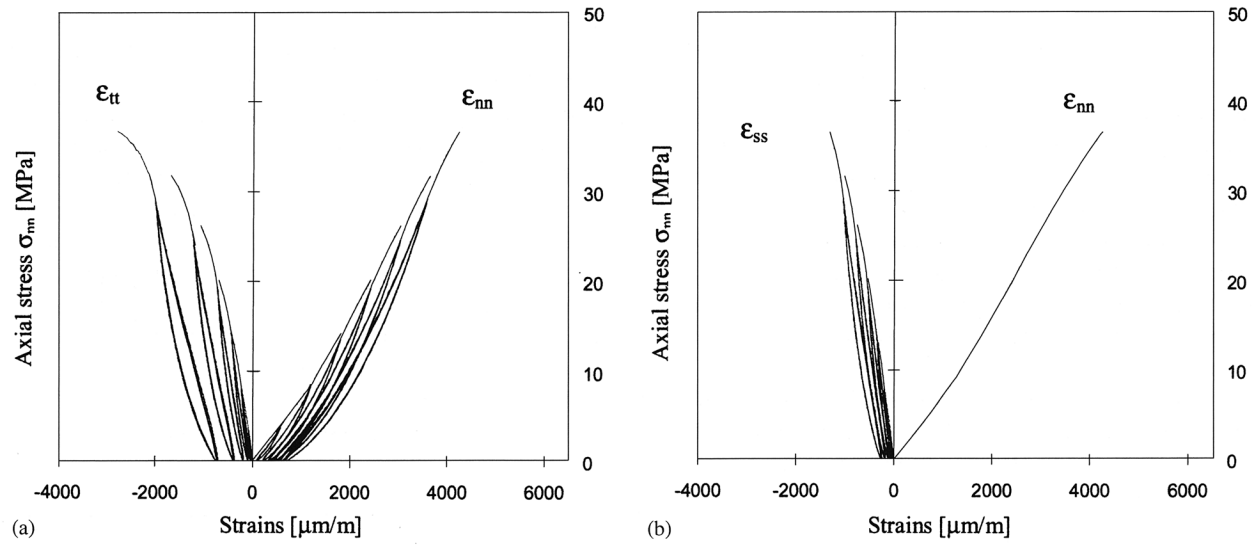

Fig. 7. Axial stress σ_{nn} as a function of strains for uniaxial test EC0-90 ($p = 0$ MPa, $\theta = 90°$): (a) axial strain ε_{nn} and out-of-plane transversal strain ε_{tt}, (b) in-plane transversal strain ε_{ss} and envelope of axial strain.

ε_{tt} transversal strains (Figs. 6 and 7) and in the off-axis tests, by the presence of a perceptible shear strain ε_{nt} showing the non-coincidence of the principal directions of the stress and strain (Fig. 6b). Moreover, as shown in Fig. 8, the initial axial stiffness of the sandstone is smaller when loading is perpendicular to the strata than when it is parallel.

4.2. Triaxial tests

Rock pressure sensitivity is shown in Fig. 9, where the envelope of the differential stress–strain curves for tests EC0-60, EC25-60 and EC50-60 has been plotted. The volumetric strain is the sum of axial and transversal strains

$$\varepsilon_{\mathrm{vol}} = \varepsilon_{nn} + \varepsilon_{ss} + \varepsilon_{tt}. \tag{2}$$

As expected, the crack closure phase observed on the axial stress-axial strain curve in uniaxial tests is significantly reduced when confining pressure is applied. The dilatancy is also reduced and even vanishes for $p = 50$ MPa. In fact, the total contracting response of the rock indicates a transition from quasi-brittle to ductile behaviour. The decrease in peak stress in Fig. 9c for the two last loading steps is not a softening response but the consequence of the loading history. This could

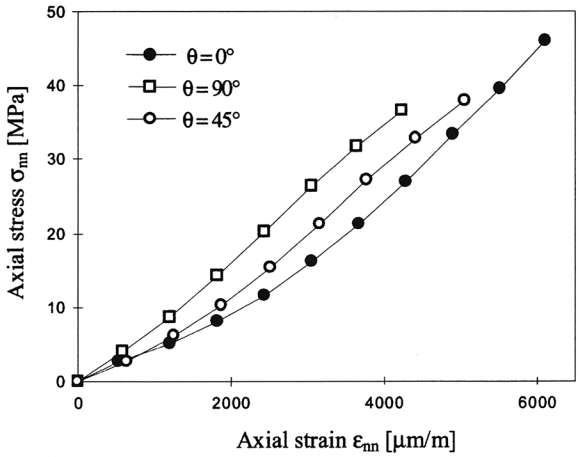

Fig. 8. Envelope of axial stress-axial strain curves for uniaxial tests and inclinations $\theta = 0°$, 45° and 90°.

therefore be termed *cyclic softening*. In fact, monotonic loading after the cyclic loading sequence showed that the rock can sustain higher stress than the maximum value reached during the cycling.

The difference between the in-plane and out-of-plane transversal strains decrease with increasing confining pressure. Also, the shear strain becomes negligible. As a general trend, the effect of structural anisotropy on the mechanical properties decreases with increasing confinement.

5. Analysis and discussion of the test results

The above qualitative observations are now analysed in detail. First, the initial elastic parameters of the transversely isotropic rock are quantified and their

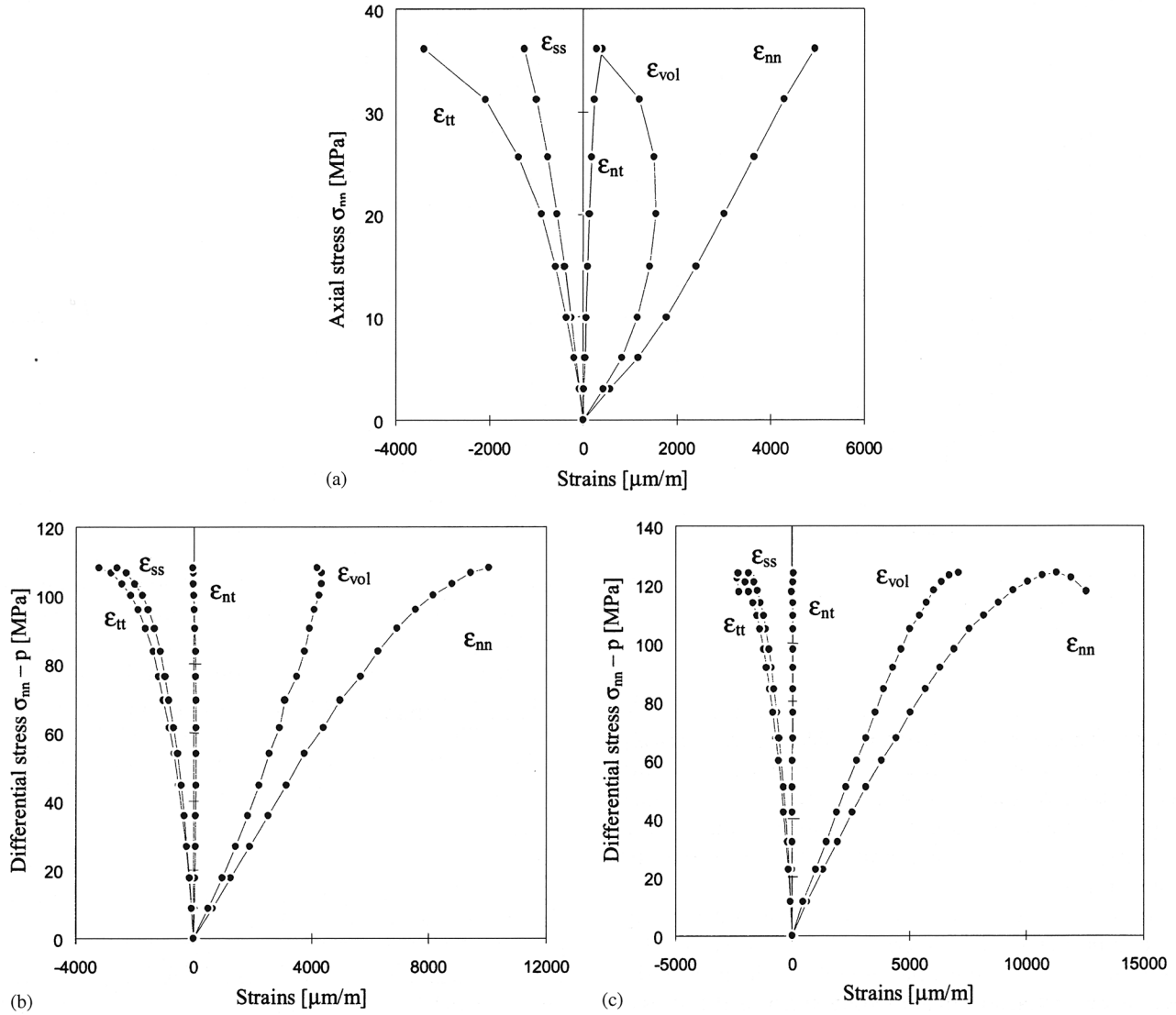

Fig. 9. Envelope of axial stress–strain curves, influence of confinement for $\theta = 60°$: (a) uniaxial test EC0-60 ($p = 0$ MPa), (b) triaxial test EC25-60 ($p = 25$ MPa), (c) triaxial test EC50-60 ($p = 50$ MPa).

pressure dependence is investigated. The influence of structural anisotropy on the progressive development of damage is then studied by measuring the oriented moduli and irreversible strains for different loading orientations with respect to the axis of structural symmetry.

5.1. Initial elastic properties

For a transversely isotropic rock which is stress-free in an undistorted state, the elastic stress–strain relations are given by the generalised Hooke's law

$$[\varepsilon] = C[\sigma], \tag{3}$$

where C is the compliance matrix.

In any privileged orthonormal frame (v_1, v_2, v_3) where v_3 is normal to the strata, (3) takes the form

$$\begin{bmatrix} \varepsilon_{11} \\ \varepsilon_{22} \\ \varepsilon_{33} \\ \varepsilon_{23} \\ \varepsilon_{13} \\ \varepsilon_{12} \end{bmatrix} = \begin{pmatrix} \frac{1}{E_1} & -\frac{\nu_1}{E_1} & -\frac{\nu_3}{E_3} & 0 & 0 & 0 \\ -\frac{\nu_1}{E_1} & \frac{1}{E_1} & -\frac{\nu_3}{E_3} & 0 & 0 & 0 \\ -\frac{\nu_3}{E_3} & -\frac{\nu_3}{E_3} & \frac{1}{E_3} & 0 & 0 & 0 \\ 0 & 0 & 0 & \frac{1}{2G} & 0 & 0 \\ 0 & 0 & 0 & 0 & \frac{1}{2G} & 0 \\ 0 & 0 & 0 & 0 & 0 & \frac{1+\nu_1}{E_1} \end{pmatrix} \times \begin{bmatrix} \sigma_{11} \\ \sigma_{22} \\ \sigma_{33} \\ \sigma_{23} \\ \sigma_{13} \\ \sigma_{12} \end{bmatrix}, \tag{4}$$

where E_1 and E_3 are Young's moduli, respectively parallel and normal to the strata, ν_1 and ν_3 are the lateral expansion coefficients parallel to the strata under compressive loading, respectively parallel and normal to the strata, and G is the shear modulus for planes parallel to the strata.

For a given confining pressure, five independent elastic parameters are determined by measuring for each θ the oriented tangential moduli, as defined by the slope of the initial linear unloading stage of the stress–strain curves. Indeed, by a transformation of the co-ordinate system, the oriented moduli are linked to five elastic parameters and to θ in the following way:

$$\begin{aligned} \frac{1}{E_{nn}} &= \frac{1}{E_1}\sin^4\theta + \frac{1}{E_3}\cos^4\theta \\ &\quad + \left(\frac{1}{G} - 2\frac{\nu_3}{E_3}\right)\sin^2\theta\cos^2\theta \\ \frac{1}{E_{tt}} &= \left(\frac{1}{E_1} + \frac{1}{E_3} - \frac{1}{G}\right)\sin^2\theta\cos^2\theta \\ &\quad - \frac{\nu_3}{E_3}(\sin^4\theta + \cos^4\theta) \\ \frac{1}{E_{ss}} &= -\frac{\nu_1}{E_1}\sin^2\theta - \frac{\nu_3}{E_3}\cos^2\theta \\ \frac{1}{E_{nt}} &= \left[\frac{1}{E_3}\cos^2\theta - \frac{1}{E_1}\sin^2\theta + \left(\frac{\nu_3}{E_3} - \frac{1}{2G}\right)\right. \\ &\quad \left.\times(\cos^2\theta - \sin^2\theta)\right]\sin\theta\cos\theta, \end{aligned} \tag{5}$$

where E_{nn}, E_{tt}, E_{ss} and E_{nt} are respectively the slopes of the initial linear portions of unloading stage of the variation of ε_{nn}, ε_{tt}, ε_{ss} and ε_{nt} as a function of the differential stress $\sigma_{nn} - p$.

The oriented moduli E_{nn}, E_{tt} and E_{ss} were measured for each orientation θ over the first loading–unloading cycle of the first loading step ($N = 1$). In practice , the modulus E_{nt} is difficult to measure accurately and has been removed from Eq. (5). The over-determined set of equations is solved by a least-square method in order to compute the five elastic parameters.

The results are presented in Table 3. The dots in Fig. 10 give the estimated values of axial modulus as a function of θ on the basis of experimental data from uniaxial tests. As already reported in the literature for other sedimentary rocks, the material is stiffer when the loading is parallel to the strata. The continuous line gives the back-prediction (Eq. (5a)) obtained using the values of the elastic parameters for $p = 0$ MPa (in Table 3).

Most rock materials exhibit stress-dependent elastic parameters. As shown in Table 3, Young's moduli E_1, E_3 and shear modulus G increase significantly with the confining pressure, whereas Poisson's ratios are less affected. The increase levels off at high confinement (Fig. 11). This phenomenon may be linked to crack closure under the effect of the hydrostatic stress.

The difference between two Poisson's ratios is smaller than the relative experimental errors ($\pm 8\%$). Therefore,

Table 3
Initial elastic parameters as a function of confining pressure calculated by a least-square minimisation process

p (MPa)	E_1 (GPa)	E_3 (GPa)	G (GPa)	ν_1	ν_3
0	11.0	8.7	4.1	0.155	0.140
25	25.9	24.0	10.5	0.172	0.185
50	28.5	27.6	11.8	0.178	0.194

the influence of structural anisotropy on Poisson's ratios can be neglected.

The degree of anisotropy of the elastic properties can be characterised by two parameters:

$$e_1 = 1 - \frac{E_3}{E_1}, \quad e_2 = 1 - 2G\frac{1+\nu_1}{E_1}. \tag{6}$$

Both of them decrease rapidly with the increasing confining pressure (Fig. 12). Hence, the influence of the structural anisotropy on the elastic parameters cannot be neglected in unconfined conditions (e_1 is as high as 20%) whereas for high confinement—of the order of the uniaxial compressive strength—the initial elastic properties can be considered as isotropic.

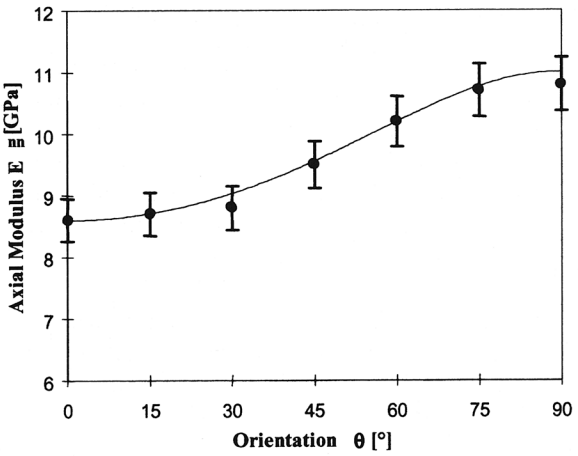

Fig. 10. Experimental variation of axial modulus E_{nn} (filled circles) as a function of orientation θ for uniaxial tests. The continuous line is the analytical back-prediction.

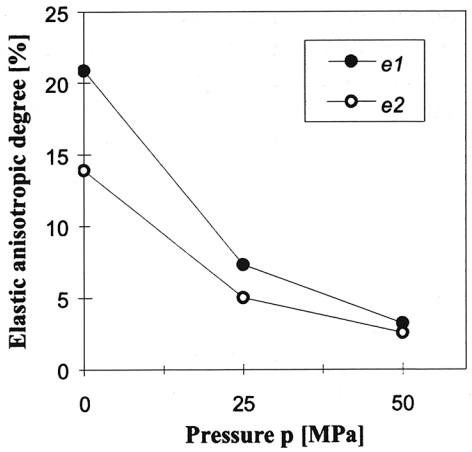

Fig. 12. Variation in the two degrees of elastic anisotropy as a function of confining pressure.

5.2. Development of anisotropic damage

Damage is generally defined by all microstructural changes in the material such as pore collapse, crack propagation, grain compaction, etc. From a macroscopic point of view, damage can be quantified by changes in mechanical properties. For example, in crystalline rocks, crack propagation, which is known to be the dominant damage mechanism, results in degradation of elastic stiffness, dilatant inelastic volumetric strain and loss of cohesion. In porous materials like sandstone, in addition to crack propagation, pore collapse plays an important role [40,41]. As will be shown below, both damage mechanisms are influenced by the initial anisotropy of Adamswiller sandstone.

The mechanisms can be correlated with the changes in oriented moduli during the loading history. For this purpose, these moduli were measured over the first cycle of each loading step. Fig. 13 shows the curves for the loading step $N = 7$ (i.e. a fatigue axial strain of 4300 μm/m)

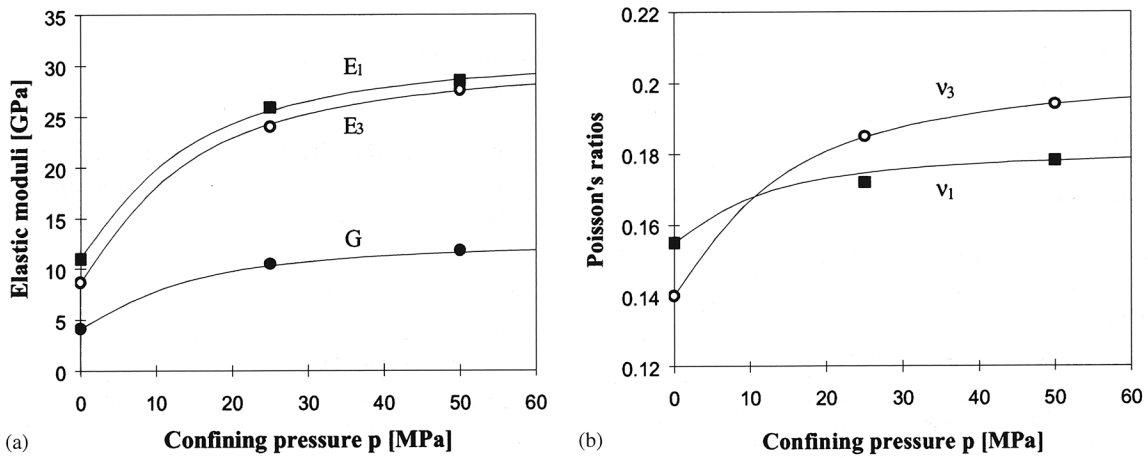

Fig. 11. Variation in elastic parameters as a function of confining pressure: (a) Young's moduli E_1, E_3 and shear modulus G, (b) Poisson's ratios ν_1 and ν_3.

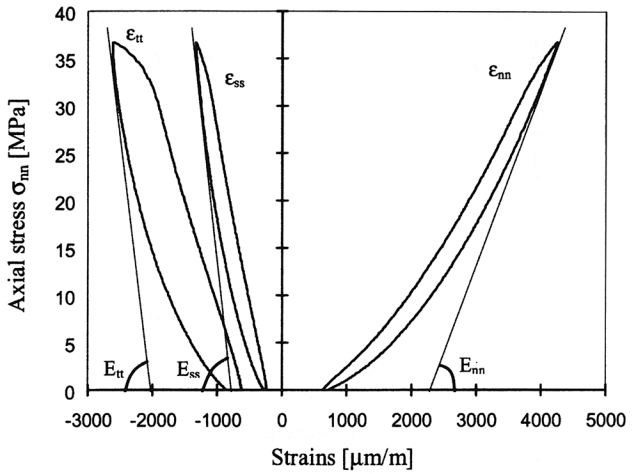

Fig. 13. Axial stress–strain curves for test EC0-90 (first loading-unloading cycle for $N = 7$, i.e. a fatigue axial strain of 4400 μm/m) and parameter definition.

for test EC0-90. The results were normalised with respect to the moduli measured during the first loading step, used to calculate the initial elastic constants.

Distinct variation of the moduli was not detected inside a loading step [42]. On the other hand, high sensitivity of the moduli to fatigue axial strain was observed in both uniaxial and triaxial tests.

The changes in normalised oriented moduli as a function of prescribed axial strain show an increase of rock anisotropy, especially under unconfined conditions (Fig. 14). In test EC0-90, both transversal moduli decrease, whereas axial modulus increases. Hence, two damage mechanisms occur simultaneously: compaction, which results in structural reinforcement parallel to the loading direction, and axial microcracking marked by the degradation of transversal stiffnesses. Moreover, the influence of structural anisotropy on microcracking is demonstrated by the sharper decrease of the out-of-plane transversal modulus E_{tt} than the decrease of the in-plane modulus E_{ss}. In the triaxial test EC50-90, the compaction mechanism is no longer active (Fig. 14b), because a limit state of compaction has been reached during the hydrostatic loading. Correlatively, cracks are generated perpendicularly to the axial stress and the axial modulus decreases as the fatigue axial strain increases.

A possible micromechanism for the appearance of these cracks normal to the loading has been recently described by Lajtai [43]. He assumes that intergranular material can be crushed inside normal grain boundaries due to high compressive stress concentrations, such that a load-normal crack forms on unloading as a result of elastic rebound.

There is a very similar decreasing tendency of the in-plane and the out-of-plane transversal moduli (Fig. 14b). This result confirms the decreasing influence of initial structural anisotropy on mechanical behaviour with increasing confinement.

The compaction rate for uniaxial compression tests is higher for samples with strata that are steeply inclined with respect to the loading direction (Fig. 15). Thus, the compaction mechanism is anisotropic.

5.3. Irreversible strains

The change in irreversible strain ε^{irr} as a function of the number of loading cycles is presented in Fig. 16 for uniaxial tests and inclinations $\theta = 0°$, 30°, 60° and 90°. Rock anisotropy is here reflected by a difference between the in-plane $(\varepsilon_{ss})^{irr}$ and the out-of-plane $(\varepsilon_{tt})^{irr}$ irreversible transversal strains for $\theta \neq 0°$ and the presence of an irreversible shear strain $(\varepsilon_{nt})^{irr}$ for off-axis tests.

The difference between $(\varepsilon_{ss})^{irr}$ and $(\varepsilon_{tt})^{irr}$ in unconfined conditions increases as θ varies from 15° to 90°. Hence, crack propagation is enhanced by the presence of the

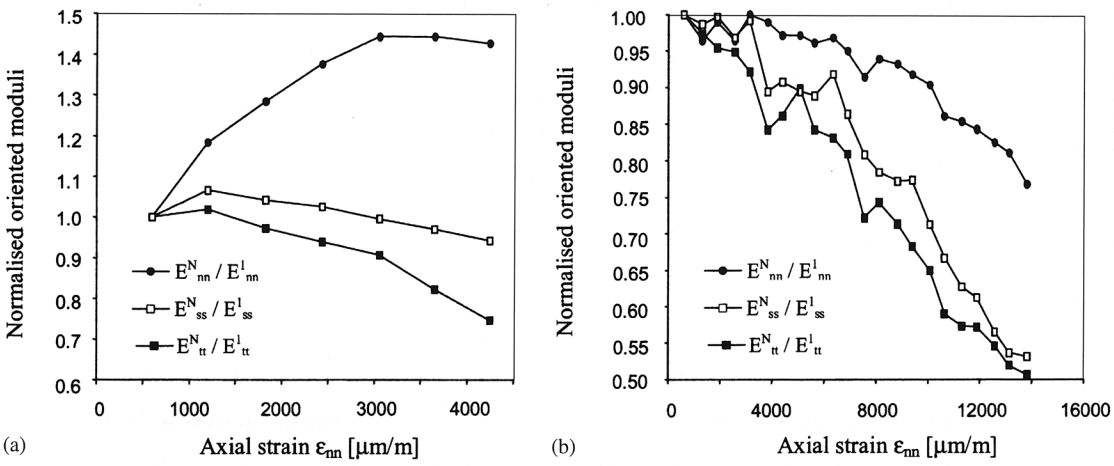

Fig. 14. Normalised oriented moduli as a function of fatigue axial strain for $\theta = 90°$ and (a) $p = 0$ MPa, (b) $p = 50$ MPa.

strata. In the triaxial tests, the difference between $(\varepsilon_{ss})^{irr}$ and $(\varepsilon_{tt})^{irr}$ diminishes and $(\varepsilon_{nt})^{irr}$ vanishes for $p = 50$ MPa (Fig. 17).

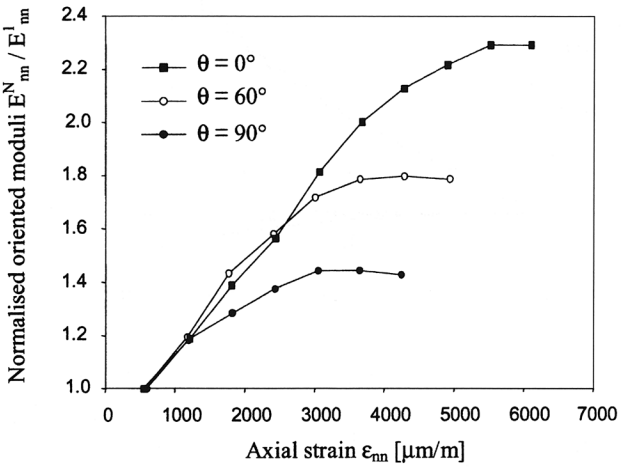

Fig. 15. Normalised axial moduli as a function of fatigue axial strain for uniaxial compression tests (EC0-0, EC0-60, EC0-90).

Within a given loading step, the first loading–unloading cycle is the most damaging (Fig. 18). This observation is consistent with the variation in the oriented moduli. This behaviour is similar to the well-known Kaiser effect noticed in a wide range of materials; once rock has been loaded to a certain stress level, it will not produce any acoustic emission upon reloading until the previous maximum stress level has been exceeded.

The change in incremental irreversible volumetric strain which is the result of one loading-unloading cycle as a function of the number of cycles for the entire loading history (except for the loading step leading to sample failure), shows competition between compaction and microcracking. Compaction mechanism is revealed in Fig. 19 by positive incremental irreversible volumetric strain measured over the first cycle for loading steps $N = 1$, 2, 3 and 4. The regular decreasing tendency of this value suggests that microcracking occurs very soon. It should be noted that, for loading step $N = 5$ (i.e. a fatigue axial strain of 3100 μm/m), rock is deformed

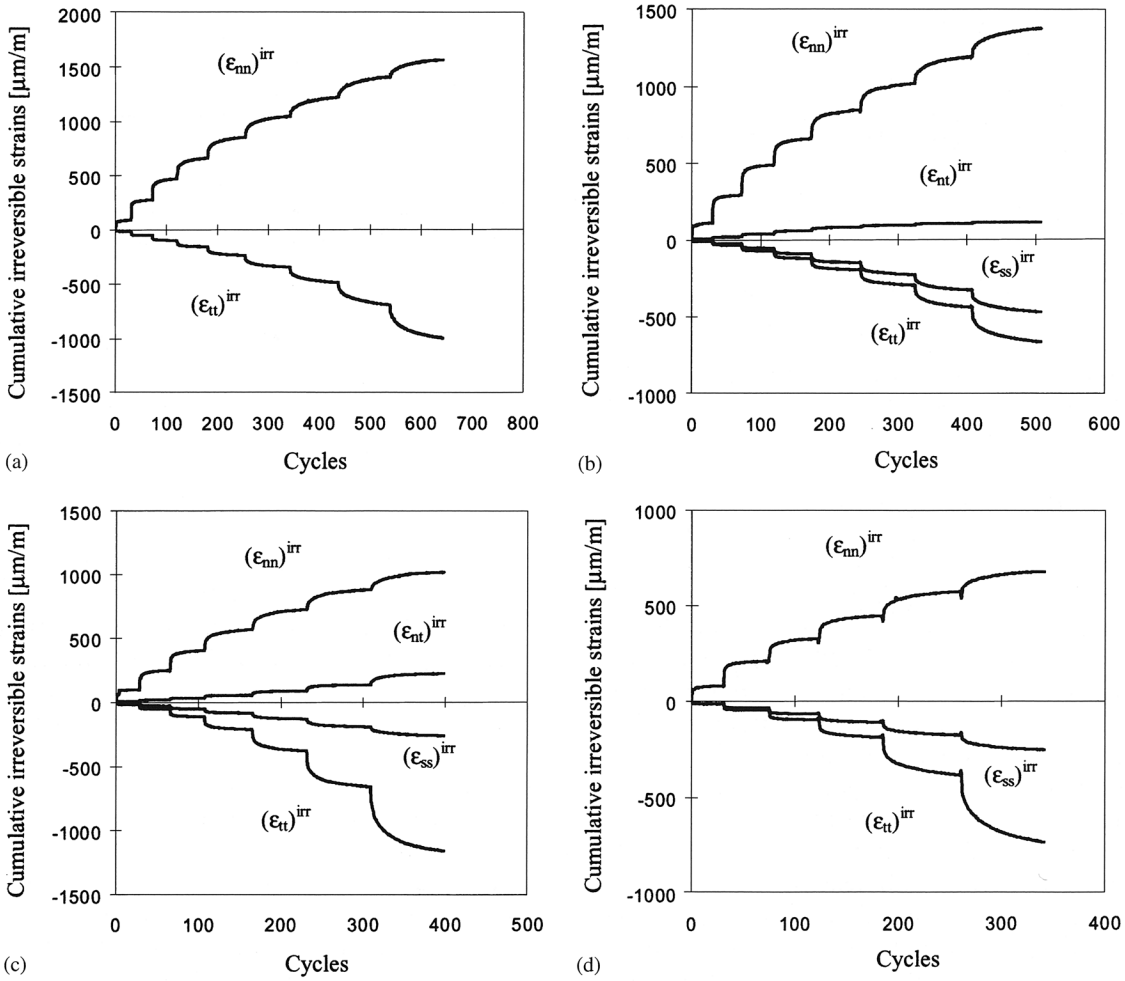

Fig. 16. Irreversible strains as a function of cycles for uniaxial tests ($p = 0$ MPa): (a) EC0-0 ($\theta = 0°$), (b) EC0-30 ($\theta = 30°$), EC0-60 ($\theta = 60°$), EC0-90 ($\theta = 90°$).

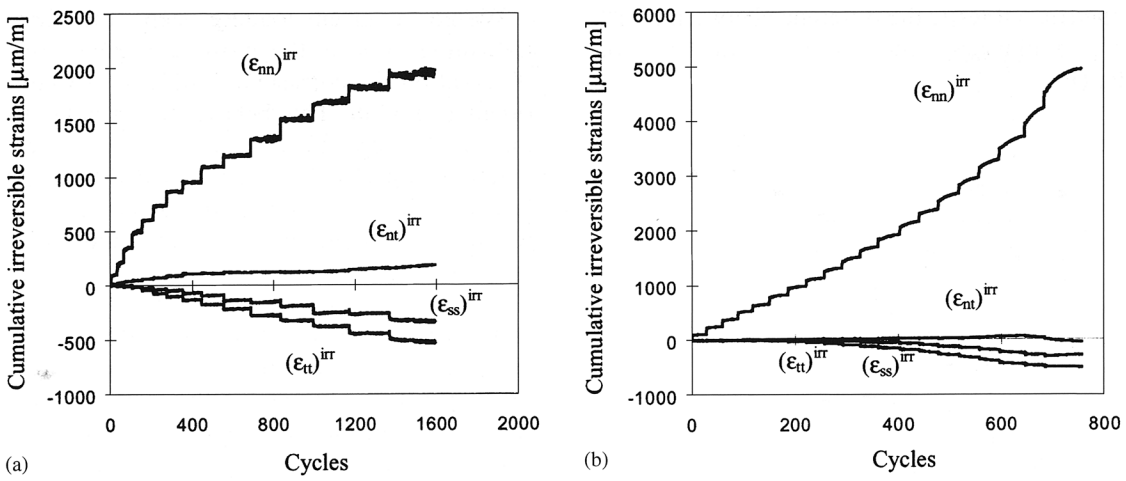

Fig. 17. Irreversible strains as a function of cycles for triaxial tests $\theta = 60°$: (a) EC25-60 ($p = 25$ MPa), (b) EC50-60 ($p = 50$ MPa).

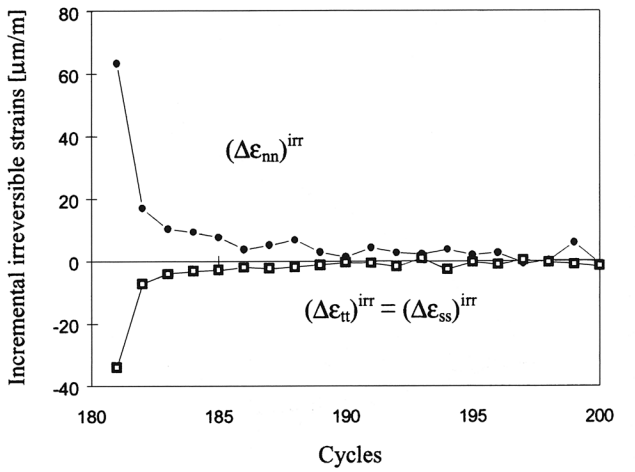

Fig. 18. Incremental irreversible strains as a function of cycles for test EC0-0 ($p = 0$ MPa, $\theta = 0°$) for the first 20 cycles of loading step $N = 5$.

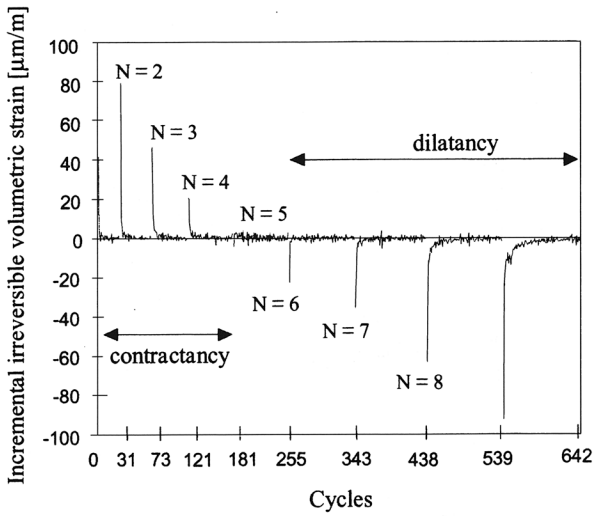

Fig. 19. Incremental irreversible volumetric strain as a function of cycles for the entire loading history of test EC0-0 ($p = 0$ MPa, $\theta = 0°$).

without any irreversible volumetric strain variation. Negative irreversible volumetric strain measured for subsequent loading steps suggests that axial microcracking becomes the dominant inelastic mechanism.

The change in cumulated irreversible strains at the end of each loading step as a function of fatigue axial strain is presented in Fig. 20 for all inclinations tested in the uniaxial tests. The irreversible axial strain (Fig. 20a) is quasi-linear with a decreasing ratio when θ increases. Hence, the compaction rate is higher when the isotropy plane is steeply inclined with respect to the axial loading. Irreversible transversal out-of-plane strain (Fig. 20c) and in-plane strain (Fig. 20d) tend to develop faster and faster. The former is more sensitive to the initial rock anisotropy: for a given fatigue axial strain, higher values are noted for $\theta = 60°$, 75° and 90°. This result confirms the enhancement of axial microcracking due to dominant direction of grain arrangement.

For all inclinations, irreversible volumetric strain is initially contractant then dilatant (Fig. 20b). As a result of the inelastic mechanisms anisotropy, both the maximum contractancy and the axial strain at the reversal point have a tendency to decrease when θ increases.

In triaxial tests with a confining pressure of 25 and 50 MPa, the influence of the initial anisotropy on irreversible strain was not detected by our measurements. The effect of confining pressure is shown in Fig. 21. The dilatant part of the irreversible volumetric strain is significantly reduced for $p = 25$ MPa, whereas it vanishes for $p = 50$ MPa. The increasing contractant rate measured in the last loading steps for $p = 50$ MPa may be the result of pore collapse.

The effect of confining pressure on the irreversible strains is displayed in Fig. 22. Irreversible axial strain is

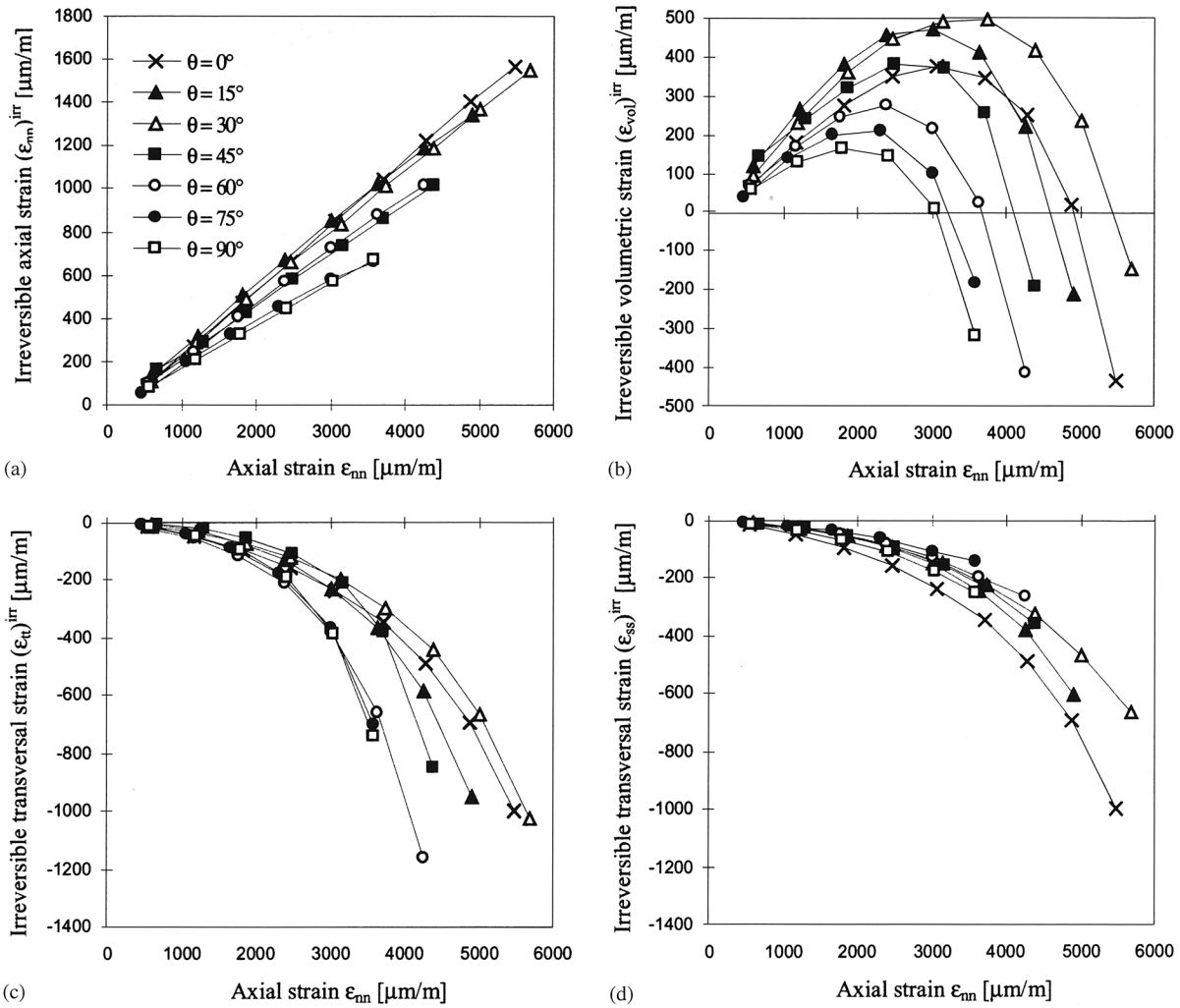

Fig. 20. Irreversible strains at the end of each loading step as a function of fatigue axial strain ε_{nn} for uniaxial tests: (a) irreversible axial strain $(\varepsilon_{nn})^{irr}$, (b) irreversible volumetric strain $(\varepsilon_{vol})^{irr}$, (c) irreversible out-of-plane transversal strain $(\varepsilon_{tt})^{irr}$ and (d) irreversible in-plane transversal strain $(\varepsilon_{ss})^{irr}$.

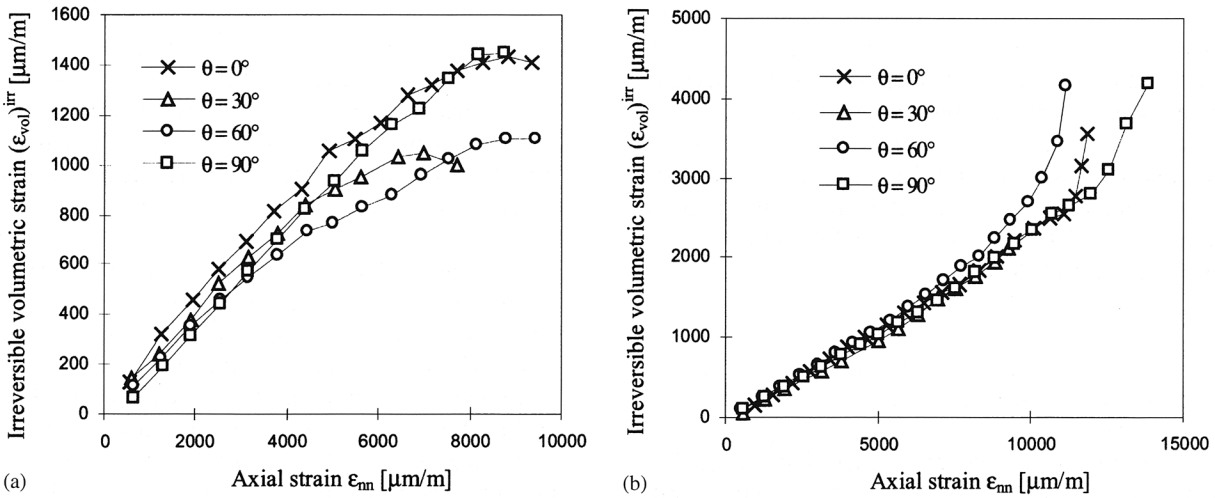

Fig. 21. Irreversible volumetric strain $(\varepsilon_{vol})^{irr}$ at the end of each loading step as a function of fatigue axial strain ε_{nn} for triaxial tests: (a) $p = 25$ MPa, (b) $p = 50$ MPa.

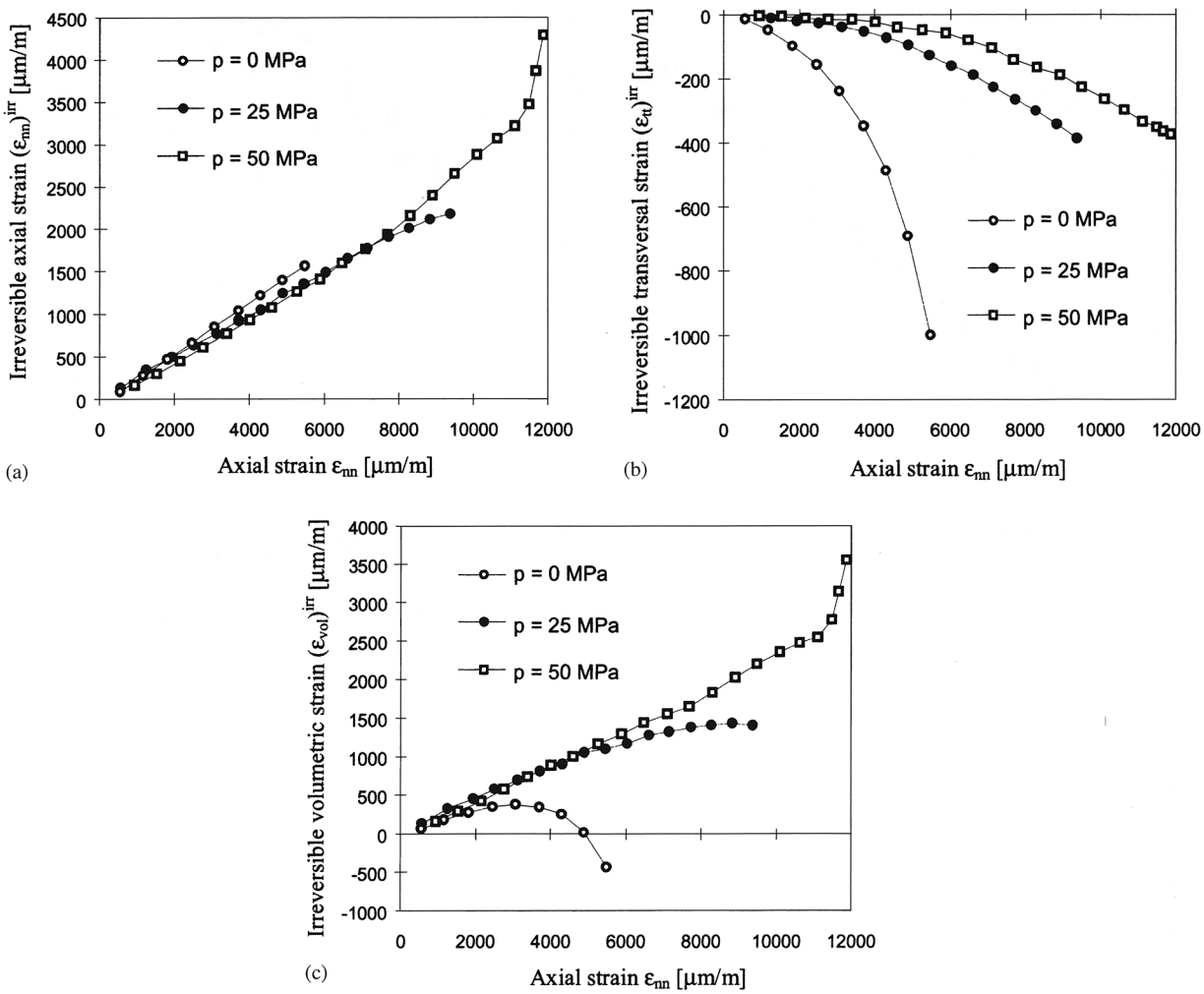

Fig. 22. Irreversible strains as a function of fatigue axial strain ε_{nn} for inclination $\theta = 0°$ and a confining pressure $p = 0$, 25 and 50 MPa: (a) irreversible axial strain $(\varepsilon_{nn})^{irr}$, (b) irreversible transversal strain $(\varepsilon_{tt})^{irr}$, (c) irreversible volumetric strain $(\varepsilon_{vol})^{irr}$.

almost insensitive to the confining pressure (Fig. 22a) whereas the transversal strain significantly decreases (Fig. 22b). Thus, confining pressure inhibits crack propagation. As a consequence, the contribution of the irreversible axial strain to the irreversible volumetric strain increases with increasing confining pressure (Fig. 22c).

The change from a dilatant to a contractant behaviour at low pressure and at high pressure respectively characterises the transition from a brittle regime to cataclastic flow.

5.4. Characteristic stress-thresholds

Following Bieniawski [3] and others [14,16,41], it is customary to define typical stress thresholds which reflect crack growth. Five characteristic quantities are introduced (Fig. 23), namely:

- the crack closure stress σ_{cc}, which is determined at the onset of linearity of the axial strain–stress curves,
- the crack initiation stress σ_{ci-tt} (respectively σ_{ci-ss}) at the onset of non-linearity of the transversal out-of-plane strain ε_{tt} (respectively ε_{ss}),
- the crack damage stress σ_{cd}, where the volume rate changes sign,
- the failure strength σ_f at the peak of the axial strain–stress curve.

The characteristic stress thresholds were measured on the envelope of strain–stress curves for all tests performed under unconfined conditions (Fig. 24). All thresholds have a tendency to decrease with increasing θ. The ratio σ_{cc}/σ_f decreases from 0.48 at $\theta = 0°$ to 0.35 at $\theta = 90°$. This result must be related to the influence of the initial rock anisotropy on the compaction mechanism. The ratio σ_{cd}/σ_f is independent of the inclination θ; it has a mean value of 0.65 with a standard deviation of ± 0.05.

However, it was found that the crack damage stress σ_{cd} is dependent on the stress history. As shown in Fig. 25, σ_{cd} increases from one loading step to the next. Correlatively, the maximum contractancy decreases significantly whereas the initial rock compressibility is unaffected by the cycling (the irreversible volumetric strain has been removed for comparison). The mean ratio σ_{cd}/σ_f for the loading step before failure and for the loading step leading to the failure are respectively 0.76 and 0.85 with a standard deviation of ± 0.05.

As it was stated by Martin and Chandler [14] with regard to granitic rocks, a substantial decrease in crack damage stress during cycling may be noted for the loading step leading to failure (Fig. 26). This phenomenon has been interpreted by these authors as a loss of cohesion. However, it should be borne in mind that measurements carried out during this cycling process

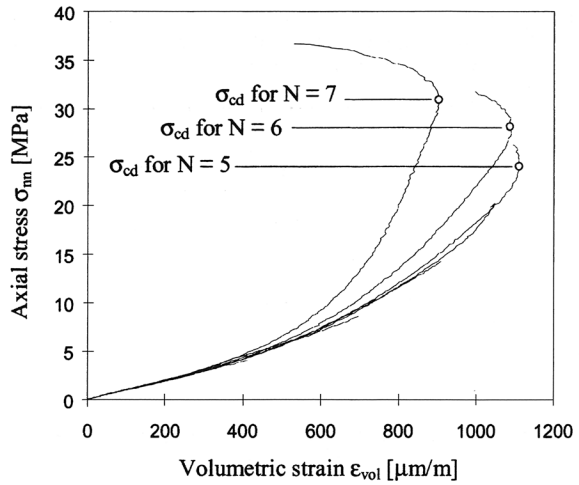

Fig. 25. Axial stress σ_{nn} as a function of volumetric strain ε_{vol}: first loading of each loading step for test EC0-90 ($p = 0$ MPa, $\theta = 90°$). Irreversible volumetric strain has been removed for comparison.

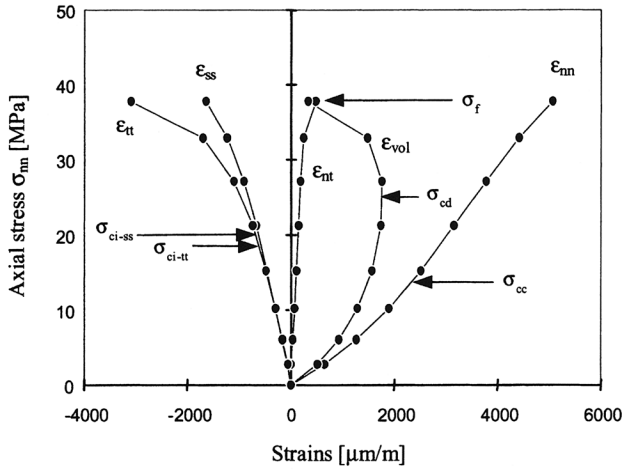

Fig. 23. Stress–strain diagram: envelope of cyclic loading for uniaxial test EC0-45 ($p = 0$ MPa, $\theta = 45°$) and characteristic stress thresholds.

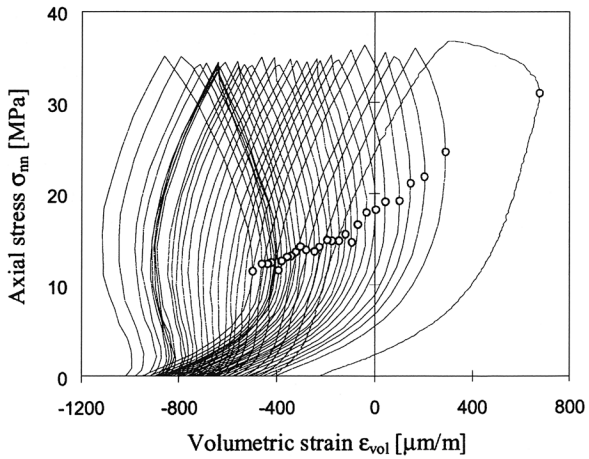

Fig. 26. Axial stress σ_{nn} as a function of volumetric strain ε_{vol} for loading step $N = 7$ leading to failure of the sample EC0-90 ($p = 0$ MPa, $\theta = 90°$).

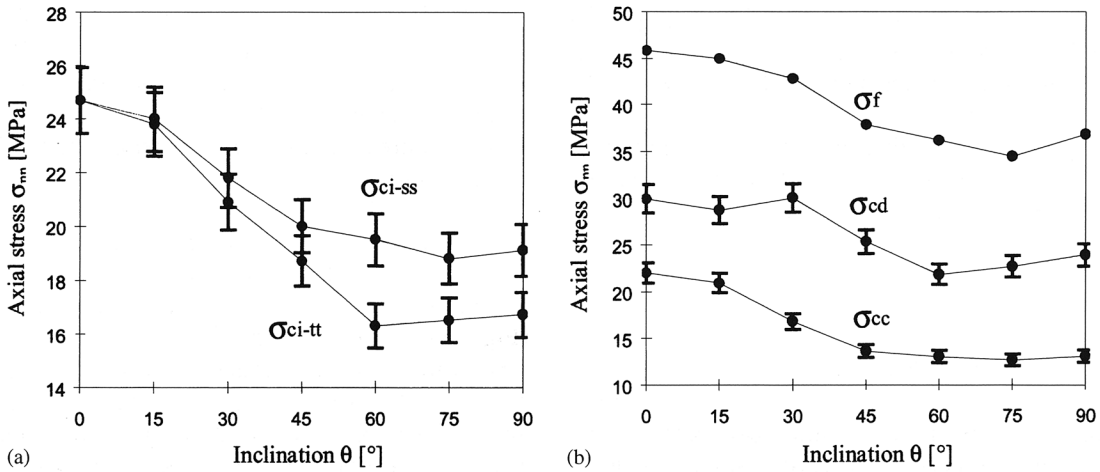

Fig. 24. Characteristic stress thresholds as a function of inclination θ for uniaxial tests: (a) in-plane crack initiation stress σ_{ci-ss}, out-of-plane crack initiation stress σ_{ci-tt}, (b) crack closure stress σ_{cc}, crack damage stress σ_{cd} and uniaxial compressive strength σ_f.

Table 4
Characteristic stress thresholds for uniaxial and triaxial tests (unit: MPa)

	$p = 0$ MPa					$p = 25$ MPa		$p = 50$ MPa
θ (deg)	σ_{cc}	σ_{ci-tt}	σ_{ci-ss}	σ_{cd}	σ_f	$\sigma_{cd} - p$	$\sigma_f - p$	$\sigma_f - p$
0	22.0	24.7	24.7	29.9	45.8	101.5	113.1	139.8
15	20.9	23.8	24.0	28.7	44.9	—	—	—
30	16.8	20.9	21.8	30.0	42.8	100.2	111.5	136.1
45	13.6	18.7	20.0	25.3	37.8	—	—	—
60	13.0	16.3	19.5	21.8	36.1	103.4	108.0	133.2
75	12.6	16.5	18.8	22.6	34.4	—	—	—
90	13.0	16.7	19.1	23.8	36.7	103.2	108.2	132.2

may not be representative of homogeneous behaviour, as strains may become localised.

In the triaxial tests with a confining pressure of 25 MPa, the differential crack damage stress, $\sigma_{cd} - p$, and the strength, $\sigma_f - p$, are insensitive to the initial rock anisotropy. Moreover, the volumetric strain reversal occurs later on the stress–strain diagram due to the inhibiting effect of pressure on the axial cracking process. The mean ratio $(\sigma_{cd} - p)/(\sigma_f - p)$ measured on the envelope of the cycles is 0.93 with a standard deviation of ± 0.03.

Values of characteristic stress thresholds for uniaxial and triaxial tests are summarised in Table 4. A degree of anisotropy of the characteristic stress thresholds has been defined as

$$e = \frac{2}{\pi} \sum_{\theta=0}^{\pi/2} \frac{|\sigma(\theta) - \bar{\sigma}|}{\bar{\sigma}} \Delta\theta, \tag{7}$$

where $\bar{\sigma} = \text{mean}_\theta\{\sigma(\theta)\}$ is the mean value of the characteristic stress and $\Delta\theta = \pi/12$.

In order to illustrate Eq. (7), the variation in uniaxial compressive strength, σ_f, as a function of θ is plotted in Fig. 27; the degree of anisotropy e represents the ratio between hatched and grey areas.

The degrees of anisotropy e_{cc}, e_{cd}, e_f respectively for σ_{cc}, σ_{cd}, and $\sigma_f - p$ are presented in Table 5 for uniaxial and triaxial tests. In the uniaxial tests, the degree of anisotropy decreases as loading proceeds ($e_{cc} > e_{cd} > e_f$). Indeed, the initial anisotropy is progressively cancelled whereas new symmetries are acquired by the material due to stress-induced anisotropy. In the triaxial tests, both e_{cd} and e_f are insensitive to the initial rock anisotropy.

5.5. Microstructural observations

Since the fundamental theoretical analyses of Walsh [44–46] regarding the influence of cracks in a homogeneous linearly elastic mass, it has been commonly accepted that the presence of defects can account for non-linear rock deformability, provided that friction is assumed to act along defect interfaces. Therefore, in order to investigate the micromechanics of damage, some thin sections cut in the n–t plane were taken from failed samples impregnated under vacuum with an epoxy resin coloured blue.

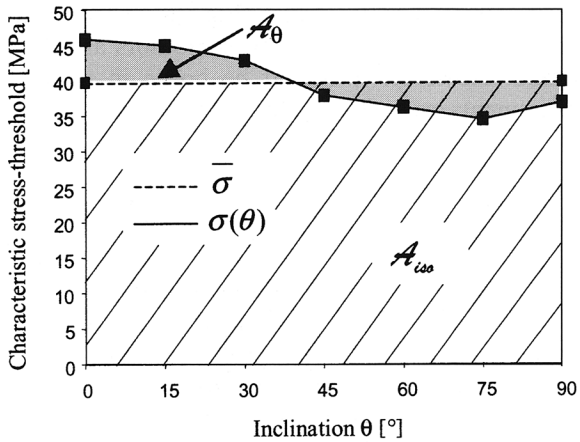

Fig. 27. Variation in uniaxial compressive strength σ_f as a function of inclination θ. $\bar{\sigma}$ is the mean value of σ_f over θ. The degree of anisotropy is defined as $e = A_\theta/A_{iso}$ with A_θ the grey area and A_{iso} the hatched area.

Table 5
Degree of anisotropy for characteristic stress thresholds

	$p = 0$ MPa	$p = 25$ MPa	$p = 50$ MPa
e_{cc} (%)	24.5	0	0
e_{cd} (%)	13.5	0.8	0
e_f (%)	11.9	2.5	2.6

In the uniaxial tests, the failure occurs by brittle faulting. A representative fracture pattern is shown in Fig. 28 for test EC0-90 ($p = 0$ MPa, $\theta = 90°$). Two main fractures cross the entire axial section of the sample (Fig. 28a): a tensile fracture initiated at the sample edges, and a shear fracture in the middle third with an average inclination of 30° to the loading direction, which links the tensile fractures. The details of the incipient shear fracture shows that it involves significant contribution from intergranular cracking and relative movement among grains (Fig. 28b). It is in accordance

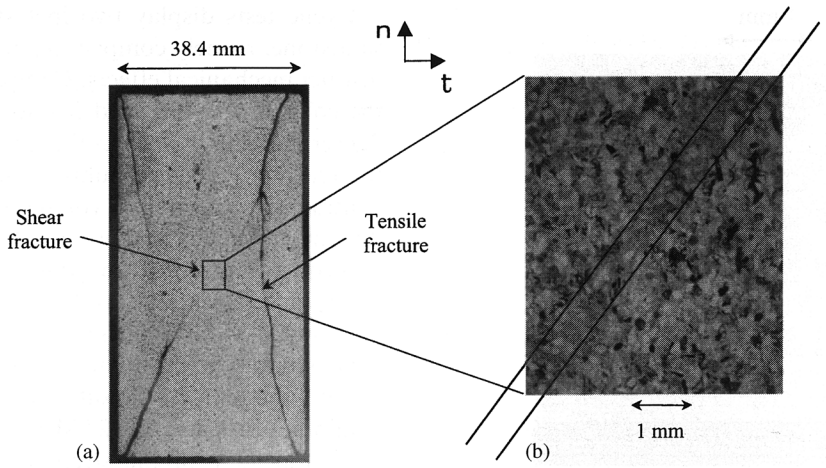

Fig. 28. Thin section of the sample EC0-90 ($p = 0$ MPa, $\theta = 90°$) in the n–t plane: (a) fracture patterns over the entire section, (b) detail of incipient shear fracture.

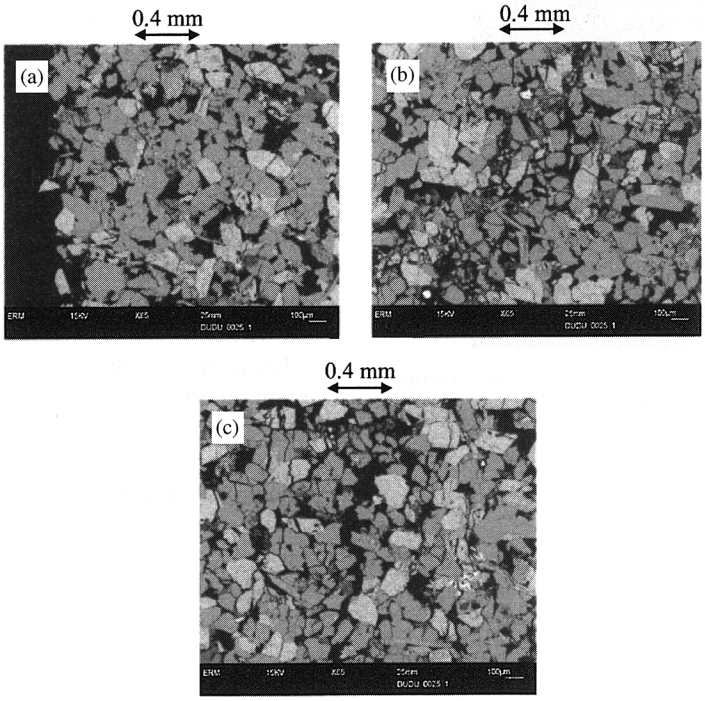

Fig. 29. SEM micrographs of the failed sample EC0-0 ($p = 0$ MPa, $\theta = 0°$): (a) clear edge of a tensile fracture, (b) well-developed shear fracture showing intense grain crushing inside the band, (c) intergranular cracks and axial transgranular crack at grain contacts. σ_{nn} direction is vertical.

with previous observations made on Berea sandstone [47], having an initial porosity close to the porosity of Adamswiller sandstone.

Tensile fractures primarily occurred along grain boundary cracks with clear edges (Fig. 29a), whereas shear fracture involves intense grain crushing, which is extended to a width of two to three grains [48] (Fig. 29b). Damage observed outside the shear band is mainly due to intergranular cracking and to a less extent, to intragranular cracking radiating at grain contacts with a preferred orientation subparallel to σ_{nn} (Fig. 29c). Some instances of kinking and exfoliation of mica grains have also been observed.

Under a confining pressure of 50 MPa, failure is ductile. Damage is characterised by clusters of intense intragranular cracking distributed in a diffuse manner inside the thin section (Fig. 30a). Stress-induced cracking seems relatively isotropic, which is consistent with the macroscopic measurements. Besides the brittle behaviour of the constitutive grains, the ductile

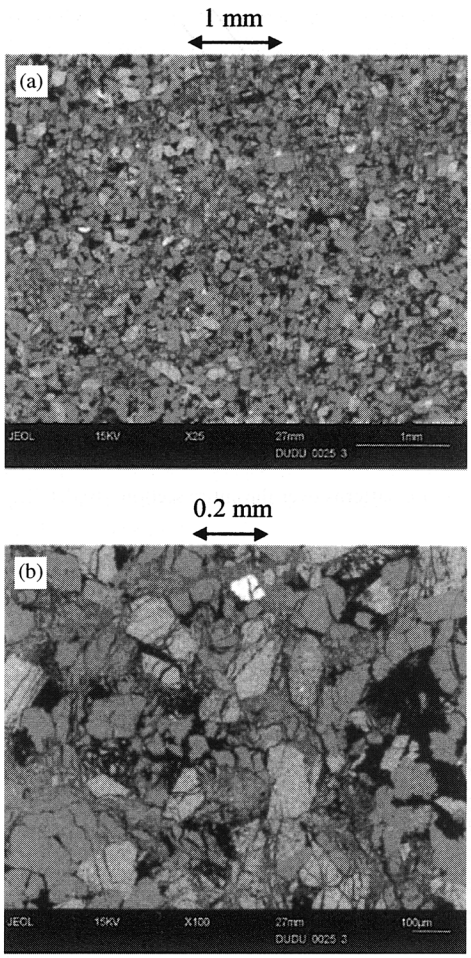

Fig. 30. Damage inside samples tested in triaxial condition: (a) diffuse clustering of damage for sample EC50-30 ($p = 50$ MPa, $\theta = 30°$), (b) brittle and ductile damage inside a crushed zone for sample EC50-0 ($p = 50$ MPa, $\theta = 0°$).

behaviour of the clay minerals contributes to the damage (Fig. 30b).

6. Summary and conclusions

The influence of structural anisotropy on the mechanical behaviour of a sandstone has been investigated by cyclic compression tests under different confining pressures and loading orientations.

The five elastic constants of the transverse isotropic rock in its quasi-virgin state (before straining) were determined by measuring the oriented moduli over the first loading–unloading cycle. These measurements were carried out under unconfined and confined conditions. Elastic behaviour is highly sensitive to confining pressure. In particular, the deviation from isotropic elasticity diminishes with the increase in confining pressure.

Cyclic tests display two inelastic mechanisms in the sandstone, namely compaction and microcracking, with distinct mechanical effects. Compaction, which is due to the collapse of pores and readjustment of grains into a denser packing pattern in the direction of axial stress, is the reason of axial modulus increase and occurrence of contractant irreversible volumetric strain. In contrast, dilatancy, which is due to intergranular cracks and subsequent movement of grains, produces a decrease in the transverse moduli and the appearance of dilatant irreversible volumetric strain. It was shown that the axial stress where volumetric strain rate changes sign under unconfined conditions and in tests with a confining pressure of 25 MPa occurs respectively at 65% and 93% of the strength value. However, these values seem to be stress-path dependent.

Both mechanisms are influenced by the initial anisotropy due to the depositional nature of the rock, especially under unconfined conditions. Indeed, compaction is maximum (respectively minimum) under deviatoric loading when the isotropy plane is perpendicular (respectively parallel) to the loading. The isotropy plane acts as a plane of weakness for the microcracking process. Complex structural symmetries can result from the superimposition of initial and induced anisotropies.

Stereological measurements on oriented thin sections of deformed samples are still needed, in order to correlate mechanically produced anisotropy with the distribution of microcracks, their density and morphology.

These results may be of importance to predict the extent of the damaged zone surrounding underground excavations, especially for cavities designed for oil or gas storage. In such cases, damage leads to a change of porosity, which may cause fluid leakage and ground contamination. For example, let us considered a circular cavity excavated in a rock mass in which there exists an isotropic initial state of stress. It was shown that for Vosges sandstone, the elastic moduli do not exhibit a great variation so that the orthoradial stress may be considered as constant around the excavation. However, the crack damage stress, σ_{cd}, which governs damage initiation, is clearly lower when the compressive stress acts parallel to the bedding planes than when it acts perpendicular.

As a result if excavation is carried out in a horizontally bedded rock, damage will occur first at the roof. On the other hand, if strata are inclined vertically, rock damage occurs along the sides. Of course if the initial state of stress is not isotropic, the locus of appearance of damage will depend on both the ratio of initial stress anisotropy and on the ratio of damage anisotropy threshold. These remarks confirm the necessity to install support systems in a proper place in order to limit the extent of the damage zone around underground cavities.

Acknowledgements

We would like to dedicate this paper to the memory of late Professor Jean-Paul Boehler, who has initiated this research.

We are grateful to Professor Patrick Dudoignon from Université de Poitiers, France, for the scanning electron microscopy.

References

[1] Kemeny JM, Cook NGW. Micromechanics of deformation in rocks. In: Shah SP, editor. Toughening mechanisms in quasi-brittle materials. Dordrecht: Kluwer Academic Publishers, 1991. p. 155–88.

[2] Wong T-F. Micromechanics of faulting in Westerly granite. Int J Rock Mech Min Sci Geomech Abstr 1982;19:49–64.

[3] Bieniawski ZT. Mechanism of brittle rock fracture. Part I: theory of the fracture process. Int J Rock Mech Min Sci Geomech Abstr 1967;4(4):395–406.

[4] Brace WF, Paulding BW, Scholz CH. Dilatancy in the fracture of crystalline rocks. J Geophys Res 1966;71(16):3939–54.

[5] Wong T-F. Development of stress-induced anisotropy and localized deformation in brittle rock. In: Boehler J-P, editor. Plastic behavior of anisotropic solids. Editions du CNRS, 1981. p. 321–39.

[6] Wu XY, Baud P, Wong T-F. Micromechanics of compressive failure and spatial evolution of anisotropic damage in Darley Dale sandstone. Int J Rock Mech Min Sci Geomech Abstr 2000;37:143–60.

[7] Martin CD. The effect of cohesion loss and stress path on brittle rock strength. Can Geotech J 1997;34:698–725.

[8] Attewell PB, Farmer IW. Fatigue behavior of rock. Int J Rock Mech Min Sci Geomech Abstr 1973;10:1–9.

[9] Scholz CH, Koczynski TA. Dilatancy anisotropy and the response of rock to large cyclic loads. J Geophys Res 1979;84(B10):5525–34.

[10] Zhenyu T, Haihong M. An experimental study and analysis of the behaviour of rock under cyclic loading. Int J Rock Mech Min Sci Geomech Abstr 1990;27(1):51–6.

[11] Ray SK, Sarkar M, Singh TN. Effect of cyclic loading and strain rate on the mechanical behaviour of sandstone. Int J Rock Mech Min Sci Geomech Abstr 1999;36:543–9.

[12] Costin LS, Holcomb DJ. Time-dependent failure of rock under cyclic loading. Tectonophysics 1981;79:279–96.

[13] Saint-Leu C, Sirieys P. La fatigue des roches. C R Symp Soc Internat Méc Roches, Nancy 1971, Rapport II-18 (in French).

[14] Martin CD, Chandler NA. The progressive fracture of Lac du Bonnet granite. Int J Rock Mech Min Sci Geomech Abstr 1994;31(6):643–59.

[15] Su K, Ghoreychi M, Chanchole S. Experimental study of damage in granite. Géotechnique 2000;50(3):235–41.

[16] Eberhardt E, Stead D, Stimpson B. Quantifying progressive pre-peak brittle fracture damage in rock during uniaxial compression. Int J Rock Mech Min Sci Geomech Abstr 1999;36:361–80.

[17] Ewy RT, Cook NGW. Deformation and fracture around cylindrical openings in rocks- part I. Observations and analysis of deformations. Int J Rock Mech Min Sci Geomech Abstr 1990;27(5):387–407.

[18] Ewy RT, Cook NGW. Deformation and fracture around cylindrical openings in rocks- part II. Initiation, growth and interaction of fractures. Int J Rock Mech Min Sci Geomech Abstr 1990;27(5):409–27.

[19] Peres Rodrigues F. Anisotropy of granites: modulus of elasticity and ultimate strength ellipsoids, joint systems, slopes attitude and their correlations. Proceedings of the First Congress ISRM, vol. 1. Lisbon, 1966. p. 721–31.

[20] Peres Rodrigues F, Aires-Barros L. Anisotropy of endogenetic rocks: correlation between micropetrographic index, ultimate strength and modulus of elasticity ellipsoids. Proceedings of the Second Congress ISRM, vol. 1. Belgrade, 1970. p. 161–4.

[21] Douglass PM, Voight B. Anisotropy of granites: a reflection of microscopic fabric. Géotechnique 1969;19(3):376–98.

[22] Chen Y, Nishiyama T, Kusuda H, Kita H, Sato T. Correlation between microcrack distribution patterns and granitic rock splitting planes. Int J Rock Mech Min Sci Geomech Abstr 1999;36:535–41.

[23] Gottschalk RR, Kronenberg K, Russel JE, Handin J. Mechanical anisotropy of gneiss: failure criterion and textural sources of directional behavior. J Geophys Res 1990;95(B13):21613–34.

[24] Blümel M, Brosch F-J, Fasching A. Investigations on fabrics and related mechanical properties of a highly anisotropic gneiss. Proceedings of the Ninth Congress ISRM, vol. 2. Paris, 1999. p. 1001–5.

[25] Homand F, Morel E, Henry J-P, Cuxac P, Hammade E. Characterization of the moduli of elasticity of an anisotropic rock using dynamic and static methods. Int J Rock Mech Min Sci Geomech Abstr 1993;30(5):527–35.

[26] Chow TM, Meglis IL, Young RP. Progressive microcrack development in tests on Lac du Bonnet granite-II ultrasonic tomographic imaging. Int J Rock Mech Min Sci Geomech Abstr 1995;32(8):751–61.

[27] Allirot D, Boehler J-P. Evolution of mechanical properties of a stratified rock under confining pressure. Proceedings of the Fourth Congress ISRM, vol. 1. Montreux, 1979. p. 15–22 (in French).

[28] Lérau J, Saint-Leu C, Sirieys P. Anisotropy of dilatancy of slates. Rock Mech 1981;13(3):185–96 (in French).

[29] Smith MB, Cheatham JB. An anisotropic compacting yield condition applied to porous limestone. Int J Rock Mech Min Sci Geomech Abstr 1980;17:159–65.

[30] Niandou H, Shao JF, Henry J-P, Fourmaintraux D. Laboratory investigation of the mechanical behaviour of Tournemire shale. Int J Rock Mech Min Sci Geomech Abstr 1997;34(1):3–16.

[31] Allirot D, Boehler J-P, Sawczuk A. Irreversible deformations of an anisotropic rock under hydrostatic pressure. Int J Rock Mech Min Sci Geomech Abstr 1977;14:77–83.

[32] Donath FA. Experimental study of shear failure in anisotropic rocks. Bull Geol Soc Am 1961;72:985–90.

[33] Hoek E. Fracture of anisotropic rock. J S Afr Inst Min Metall 1964;64(10):501–17.

[34] McLamore R, Gray KE. The mechanical behavior of anisotropic sedimentary rocks. J Eng Ind Trans ASME 1967;89:62–73.

[35] Saint-Leu C, Lérau J, Sirieys P. Mécanismes de rupture des schistes de Lacaune (Tarn): influence de la pression isotrope. Bull Minéral 1978;101:437–41 (in French).

[36] Millien A. Comportement anisotrope du grès des Vosges: élasto-plasticité, localisation, rupture. Thèse de Doctorat en Sciences, Université Joseph Fourier, Grenoble, 1993 (in French).

[37] ISRM. Suggested methods for determining the strength of rock material in triaxial compression: revised version. Int J Rock Mech Min Sci Geomech Abstr 1983;20(6):285–9.

[38] Boehler J-P. In: Boehler J-P, editor. Applications of tensor functions in solid mechanics. Berlin: Springer, 1987 [Chapters 1–7].

[39] Gatelier N. Etude expérimentale et théorique de l'endommagement des roches anisotropes. Thèse de Doctorat en Sciences, Université Joseph Fourier, Grenoble, 2001 (in French).

[40] Bessinger BA, Cook NGW. Laboratory comparison of rock properties controlling geologic compression-driven extensile fracturing. In: Aubertin M, Hassani F, Mitri H, editors. Proceedings of the Second North Am Rock Mech Symp. Montreal, 1996. p. 1137–44.
[41] Stead D, Eberhardt E, Szczepanik Z. Acoustic emission studies on stress-induced damage in sandstone. Proceedings of the Ninth Congress ISRM, vol. 1. Paris, 1999. p. 681–5.
[42] Pellet F, Gatelier N, Loret B. Experimental study of damage of an anisotropic rock using cyclic compression tests. Proc Eurock 2000 Symp, Aachen, 2000. p. 687–92.
[43] Lajtai EZ. Microscopic fracture processes in a granite. Rock Mech Rock Eng 1998;31(4):237–50.
[44] Walsh JB. The effet of cracks in rocks on Poisson's ratio. J Geophys Res 1965;70:5249–57.
[45] Walsh JB. The effect of cracks on the compressibility of rock. J Geophys Res 1965;70:381–9.
[46] Walsh JB. The effect of cracks on the uniaxial elastic compression of rocks. J Geophys Res 1965;70:399–411.
[47] Menéndez B, Zhu W, Wong T-F. Micromechanics of brittle faulting and cataclastic flow in Berea sandstone. J Struct Geol 1996;18:1–16.
[48] Bésuelle P, Desrues J, Raynaud S. Experimental characterisation of the localisation phenomenon inside a Vosges sandstone in a triaxial cell. Int J Rock Mech Min Sci Geomech Abstr 2000;37(8):1223–37.

Hydromechanical and Thermohydromechanical Behaviour of Deep Argillaceous Rock, Hoteit, Su, Tijani & Shao (eds)

Identification of mechanical parameters for modelling time-dependent behaviour of shales

Eric Boidy
Coyne et Bellier, Consulting Engineers, Gennevilliers, France

Frederic Pellet
Laboratory 3S, University Joseph Fourier, Grenoble, France

Abstract: Time-dependent behaviour of geomaterials, for instance creep, is of a great importance for the design of deep underground structures such as those for waste disposal. For example, in order to ensure structural safety for several centuries, a good prediction of deformations and damage is needed. For this purpose, a new visco-plastic law has been implemented in a two-dimensional explicit finite-difference program. This law, known as Lemaitre's creep model is based on the use of internal state variables attached to specific phenomena, including isotropic hardening. This approach relies on theoretical analysis and experience. On one hand, for such a long-term computation, a special analysis of the time step is required to define a suitable discretisation of the study time period, in order to ensure numerical stability. On the other hand, the mechanical concepts are illustrated by results obtained on shale samples subjected to different loading conditions, including constant strain rate tests and relaxation or constant strain tests. An application to deep tunnel modelling is then presented.

1. Introduction

The mechanical time-dependent behaviour of shales or argillaceous rocks has been investigated over the last decade and numerous research works have also been promoted by programs on radioactive waste disposal in such materials. The behaviour of shales, like many other geomaterials, for example rock salt (Fokker 1998), or hard rock (Malan 1999) is characterised by delayed straining when subjected to sustained loading.
The design of underground structures, excavated in such rate-sensitive materials, requires the determination of a time-dependent constitutive law capable of predicting long-term behaviour. The law implemented in the finite-difference program FLAC Version 3.4, corresponds to the model proposed by Lemaitre (1996). This study analyses the stability of the explicit numerical solution which requires specific time-step conditions. The approach relates the modelling of relaxation tests to deep circular tunnel simulation in order to define a suitable time step discretisation. But first of all, time-dependent behaviour of shales must be defined and several laboratory tests are possible. Complementary to classical creep tests, relaxation tests provide additional information for describing phenomena occurring around an excavation. The identification of time-dependent mechanical parameters are thus presented in this paper.

2. Experimental investigation

Shale mechanical behaviour is rapidly dominated by inelastic deformation processes, also known as visco-plastic flows. The elastic limit is low and behaviour very sensitive to strain rate. Under uniaxial conditions, constant strain rate tests give a ductile response. In this regime, inelastic straining is relatively isovolumetric and may also involve dislocation propagation leading to material hardening. This approach is based on the formulation of internal state variables often used for describing the ductile inelastic flow of metals (Lemaitre 1996) or geomaterials (Tatsuoka et al. 1998).
For this material, hardening and recovery phenomena, defined by Fokker 1998, probably take place simultaneously at the microstructural level. Recovery phenomenon counteract the hardening effect and also cause a step-by-step return to the virgin-state microstructure. Long-term stability is also reached and can be represented by a limit loading curve (Figure 1) obtained by long-term relaxation or creep tests (CFMR 2000) or by quasi-static tests (for very low constant strain rate $\dot{\varepsilon}_s$). On this limit curve, the equilibrium between strain hardening and recovery is always reached.
For this study, five laboratory tests were performed under uniaxial loading and undrained conditions. The samples subjected were not saturated, even during loading. The saturation index was found between 68% and 88%. Thus time-dependent phenomena can not be related to consolidation. No water flow was observed.

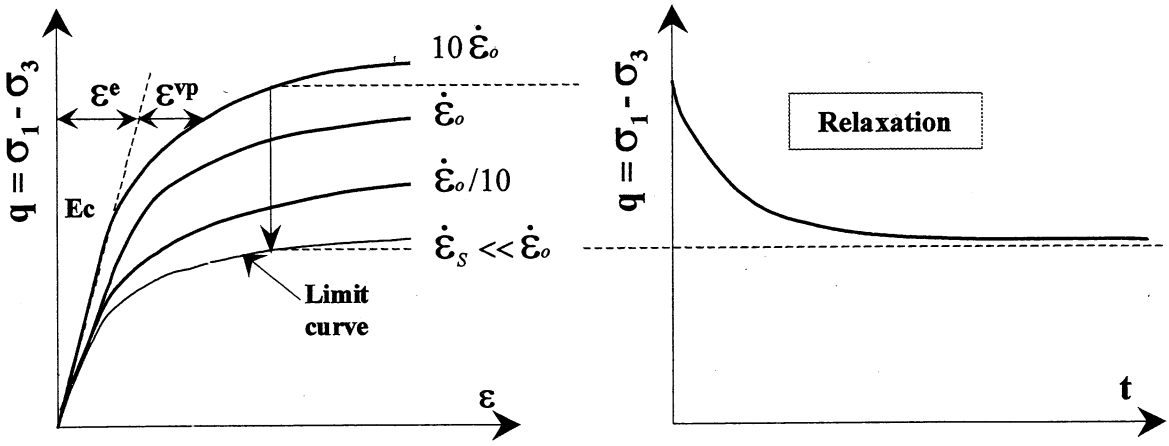

Figure 1. Theoretical influence of strain hardening and recovery phenomena on stress flow.

In order to analyse the time-dependent phenomena, the main controlled loading variables are:

- the strain rate, as in constant strain rate tests or relaxation tests (for which the axial strain rate is nil),
- the deviatoric stress, as in creep tests (in which case, the applied stress is constant).

2.1. Observations on constant strain rate tests

For this experimental study, constant strain rate tests were carried out under a very wide range of deformation rates, from 10^{-9} to 10^{-3} s^{-1}. Five tests were performed under loading, relaxation, unloading, and reloading conditions. Theses tests indicated that shale has a great tendency to strain-harden. It was found that the stress-strain curve is non-linear and depends on the strain rate. For instance, in such a test, the flow stress increases substantially when the strain rate rises suddenly (Figure 2). On the other hand, a reduction in strain rate leads to a decrease in flow stress (Figure 3). This is less obvious because the hardening modulus, which is the slope of the stress-strain curve, decreases naturally with increasing strain. Partial unloading creates an elastic response due to material hardening but after reloading no increase in its yield strength, reached between 36 and 37 MPa, was noticed.

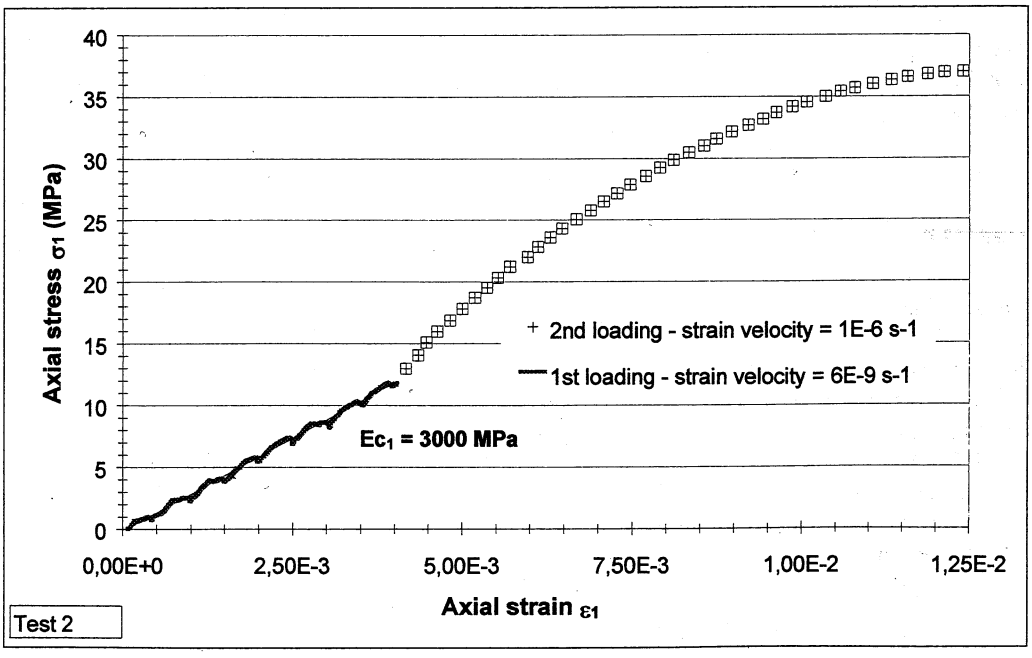

Figure 2. Influence of an increase in strain rate on the stress flow

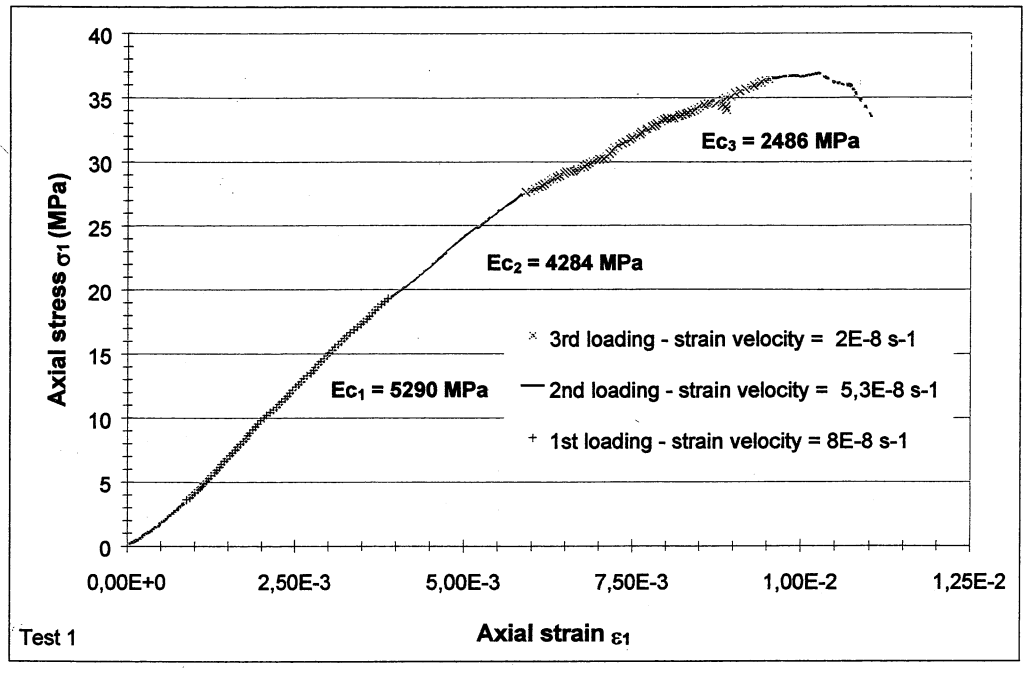

Figure 3. Influence of three successive decreases in strain rate on the stress flow

2.2. Analysis of relaxation tests

Before each relaxation test, the previous loading was performed at a constant strain velocity of about 10^{-6} s^{-1}, as presented in Figure 6. Two initial different stress levels were also fixed (50% and 75% of unconfined compressive strength). Three relaxation tests were then carried out for maximum one month until relative stabilisation of the stress response was achieved. Relaxation can be regarded as the conversion of initial elastic strain to inelastic strain when the stress progressively decreases, as will be explained in the following paragraph.

Although transient phases were detected during the relaxation tests, a tendency towards steady-state behaviour was also apparent over a period of two weeks. The test results exhibit daily oscillations due to temperature influences. Relaxation curves can also be represented by a succession of marks found in the same temperature conditions. At the end of the two relaxation tests No.5 (Figure 4), an irreversible increase in room temperature induces a spurious additional relaxation in axial stress.

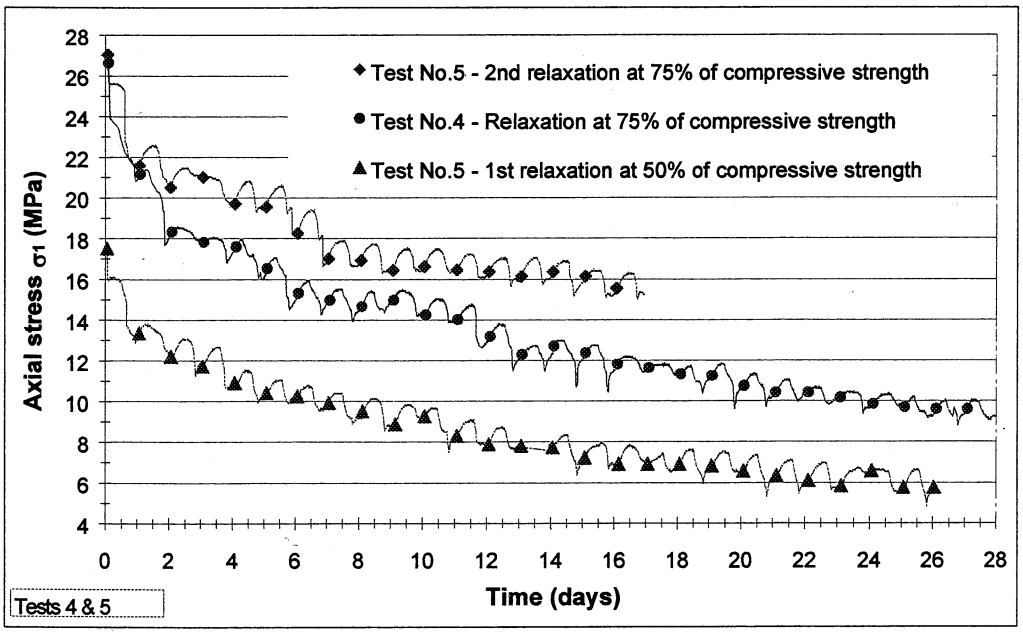

Figure 4. Relaxation tests No.4 & 5 at 50% and 75% of compressive strength

3. Modelling of time-dependent phenomena

In this paragraph, the authors present an approach for formulating the constitutive equations of Lemaitre's visco-plastic model developed for the fully ductile regime. This model does not include a damage component. All the attention is focused on how a simple model can be used to describe time-dependent phenomena under a variety of load paths. The choice of long-term parameters is also discussed here.
Engineering calculations, such as those performed for radioactive waste disposal, require time-dependent inelastic model. The most frequently used models are based on a deviatoric stress power law equation, know as Norton's creep law (Norton 1929) which is of the following type:

$$\dot{\varepsilon}^{vp} = A.q^n \tag{1}$$

where:

- $\dot{\varepsilon}^{vp}$ is the steady-state deviatoric strain rate,
- q is the deviatoric stress,
- A and n are experimental parameters.

A is the viscosity constant which depends on temperature but this analysis focuses only on the time-dependent behaviour at room temperature (18 – 23°C). Compared to the following model, the Norton's simple formulation does not take into account strain-hardening phenomena.

3.1. Constitutive equation of Lemaitre's model

This law is based on the overstress visco-plasticity theory formulated by Perzyna's (1966) for rate-sensitive plastic materials. It gives incremental constitutive equations for the transient creep phase. The basic assumption is that the strain rate tensor can be divided into an instantaneous reversible (elastic) part and an irreversible (inelastic) part:

$$\dot{\boldsymbol{\varepsilon}}_{ij} = \dot{\boldsymbol{\varepsilon}}^{e}_{ij} + \dot{\boldsymbol{\varepsilon}}^{vp}_{ij} \tag{2}$$

where irreversible strain rate combines viscous and plastic effects and is given by the following relationship:

$$\dot{\boldsymbol{\varepsilon}}^{vp}_{ij} = \gamma\langle\Phi(F)\rangle\frac{\partial G}{\partial \boldsymbol{\sigma}_{ij}} \tag{3}$$

with:

- γ the viscosity coefficient of the material,
- G the visco-plastic potential,
- F the static yield function and Φ the flow rule, controlled by the brackets defined by Macauly: $\langle\Phi(F)\rangle = \frac{1}{2}[\Phi(F) + |\Phi(F)|]$, where $|\Phi(F)|$ is the classical absolute value.

The function F includes the overstress concept through the classical plastic function f and the strain hardening parameter κ, which depends only on the updated accumulated visco-plastic strains (second invariant of the stress tensor). The assumption of isotropic hardening is also involved. This function F has the following form:

$$F(\boldsymbol{\sigma}_{ij}, \boldsymbol{\varepsilon}^{vp}_{kl}) = \frac{f(\boldsymbol{\sigma}_{ij}, \boldsymbol{\varepsilon}^{vp}_{kl})}{\kappa(\varepsilon^{vp})} - 1 \tag{4}$$

with the internal state variable corresponding to strain-hardening:

$$\varepsilon^{vp} = \int_0^t \left(\frac{2}{3}\dot{\boldsymbol{\varepsilon}}^{vp}_{ij} \otimes \dot{\boldsymbol{\varepsilon}}^{vp}_{ij}\right)^{\frac{1}{2}} d\tau \tag{5}$$

Practically, all these expressions are simplified by considering two other assumptions. First, the constitutive law can be defined as associated, for which f corresponds to G and can be linked directly to the second invariant of the stress tensor q by assuming a Von Mises plastic criterion:

$$f = G = q \tag{6}$$

This assumption takes into account the fact that visco-plastic deformations develop without any volume changes, this having been verified experimentally for sandstones (Pellet et al.) and recently for shales although this needs to be confirmed. On the other hand, in order to produce a practical and representative tool, power laws for the flow rule Φ and for the strain hardening parameter κ have been introduced similar to those proposed by Lemaitre. The relationships are summarised below by equations (7a) and (7b).

$$\Phi(F) = (F+1)^n, \qquad \kappa(\varepsilon^{vp}) = (\varepsilon^{vp})^{-m/n} \tag{7a, b}$$

Thus, the irreversible strain rate which combines viscous and plastic effects is given by the following relation :

$$\dot{\varepsilon}_{ij}^{vp} = \frac{3}{2} A.q^{n-1}.\left(\varepsilon^{vp}\right)^{m} \mathbf{s}_{ij} \tag{8}$$

where $\mathbf{s}_{ij}$ is the deviatoric part of the stress tensor and q the second invariant of the stress tensor. This law needs the identification of the three following parameters:

- A, the viscosity coefficient of the material ($A > 0$),
- n, the stress exponent ($n \geq 1$),
- m^*, the strain hardening exponent ($m^* = -m/n \geq 0$) verifying the following restriction : $m^* \leq 1-1/n$.

In order to match the results of relaxation tests, a strain rate threshold can be introduced into the model. This improvement induces steady-state behaviour as soon as the visco-plastic strain rate goes below a specific threshold detected in the laboratory. This law has been developed and implemented in the two-dimensional explicit finite-difference program (FLAC 3.4) using the Fish language. The time stepping is also subjected to stability conditions, analysed and discussed in the following paragraph.

3.2. Study of critical time stepping

For such a long-term explicit prediction, a specific analysis of the time step is necessary in order to define the critical discretisation of the study time period. Given that the system is required always to be in mechanical equilibrium, the time-dependent stress increment must not be large compared to the strain-dependent stress increment (Billaux et al., 1993); otherwise, out-of-balance forces can rapidly become large, and inertial effects (which are theoretically absent) may affect the solution. Cormeau (1975) has given the expression of the critical time step for such an explicit mode of resolution in the general case. The stability limit, in the case of Lemaitre's visco-plastic law, becomes:

$$\Delta t_{crit} = \frac{4(1+\nu)}{3E\alpha\beta a.q^{\beta-1}.t^{\alpha-1}} \tag{9}$$

where E is Young's modulus; ν is Poisson's ratio; α and β are exponents; a represents an other viscosity parameter. These three constants are a function of the previous parameters m, n and A. They verify the three next relationships listed in equation (10).

$$\alpha = \frac{1}{1-m};\ \beta = \alpha.n = \frac{n}{1-m};\ a = \left(\frac{1}{\alpha}A\right)^{\alpha} \tag{10}$$

According to Cormeau, the critical time step gives the maximum time increment to ensure the stability of the explicit calculation. However, in order to obtain a good accuracy of the solution, a suitable time step must be defined. A safety factor (S.F.) applicable to Cormeau's critical time step will also be determined in §5.1.

4. Identification of the parameter values for Lemaitre's visco-plastic model

In this section, the procedure followed to obtain the material constants is briefly described. This method is based on several constant strain rate tests and relaxation tests.

4.1. Identification of the ratio m*

The linear part of the stress-strain curves using the axial and radial measurements gives the elastic constants Ec, the loading modulus (secant modulus at the beginning of compression) and ν, Poisson's ratio.

The visco-plastic part of the deformations can be calculated on the basis of the strain partition (Figure 3) by introducing the predetermined loading strain modulus. By expressing the deviator stress function (axial stress here) of the visco-plastic deformations, it is also possible to obtain an accurate determination of the value of the ratio m* which gives the concavity of the curve in the (σ_1, ε_1) diagram. The expression (11) was then represented in the ($\ln(\sigma_1)$-$\ln(\varepsilon^{vp})$) diagram (Figure 5) where the ratio m* represents the slope of the curves.

$$\sigma_1 = \frac{1}{A^{1/n}}\left(\dot{\varepsilon}_1 - \frac{\dot{\sigma}_1}{Ec}\right)^{1/n}\left(\varepsilon^{vp}\right)^{-m/n} \qquad \text{with:} \quad \varepsilon^{vp} = \varepsilon_1 - \frac{\sigma_1}{Ec} \tag{11}$$

m* was found to be around 0.2. The linearity is well verified in a strain section, between the elastic limit and the highly damaged zone (Figure 5). In the same diagram, the intercept of the y-axis gives the viscosity parameter A which depends on n. Thus, the parameters m and A are defined in relation to n. Two degrees of freedom are fixed and it thus suffices to determine the value of n in order to identify a single set of parameters.

By reproducing this analysis on several constant strain rate tests at various strain velocities, this ratio m* can be adjusted, with relatively small natural dispersions. It is clearly apparent that it is fairly constant but tends to increase

with strain rate. Moreover, a modification of strain rate during the compression test (test No.1) or an intermediate relaxation test (test No.4) does not affect this ratio. There is much more dispersion on parameter A because also depending on the degree of damage. The result of the identification is summarised in Table 1.

Table 1. Summary of the parameters Ec and (-m/n) for constant strain rate tests

Test references	Strain rate(s^{-1})	Loading strain modulus (MPa)	Ratio (-m/n)
No.1 (Load No. 2)	5.3×10^{-8}	4285	0.204
No.1 (Load No. 3)	2.1×10^{-8}	2485	0.193
No.2 (Load No. 2)	1.05×10^{-6}	6250	0.222
No.3 (Load No. 2)	4.7×10^{-3}	8750	0.288
No.4 (Load No. 1)	9.85×10^{-7}	3620	0.196
No.4 (Reload)	1.05×10^{-6}	5200	0.192
No.5 (Reload)	9.2×10^{-7}	8330	0.192

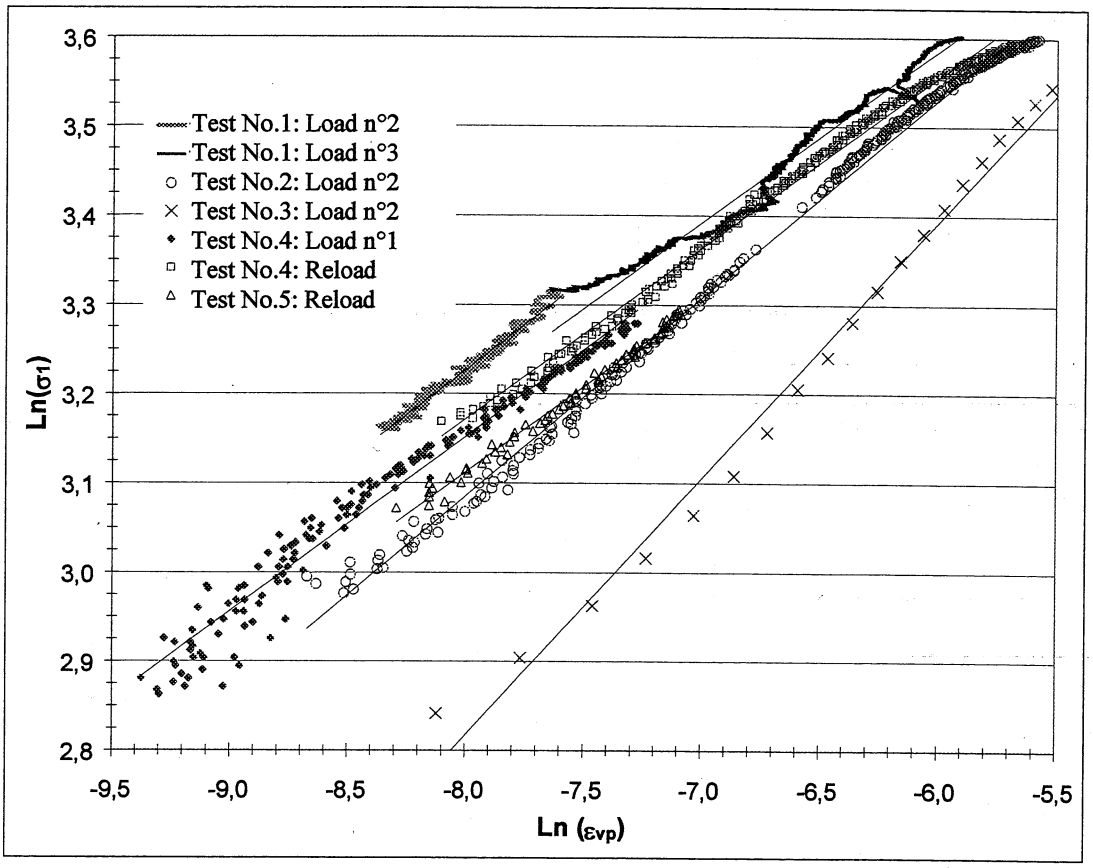

Figure 5. Results for five constant strain rate tests

4.2. Parametric study for long-term tendency simulation

In order to fix a set of parameters, relaxation tests provide a complementary information in addition to the two degrees of freedom linking m and A to n. Moreover, relaxation tests seem to highlight a threshold parameter (steady-state relaxation). In this context, it is possible to make a parametric study of n by keeping the relations giving m and A, and determined before. To be complete, the identification of the parameter n requires the knowledge of a "relaxation modulus" assumed here to be equal to Ec obtained beforehand on constant strain rate tests.

Test No.4 is presented below (Figure 6) and the two successive constant strain rate tests give a ratio m* equal to 0.19 (Table 1).

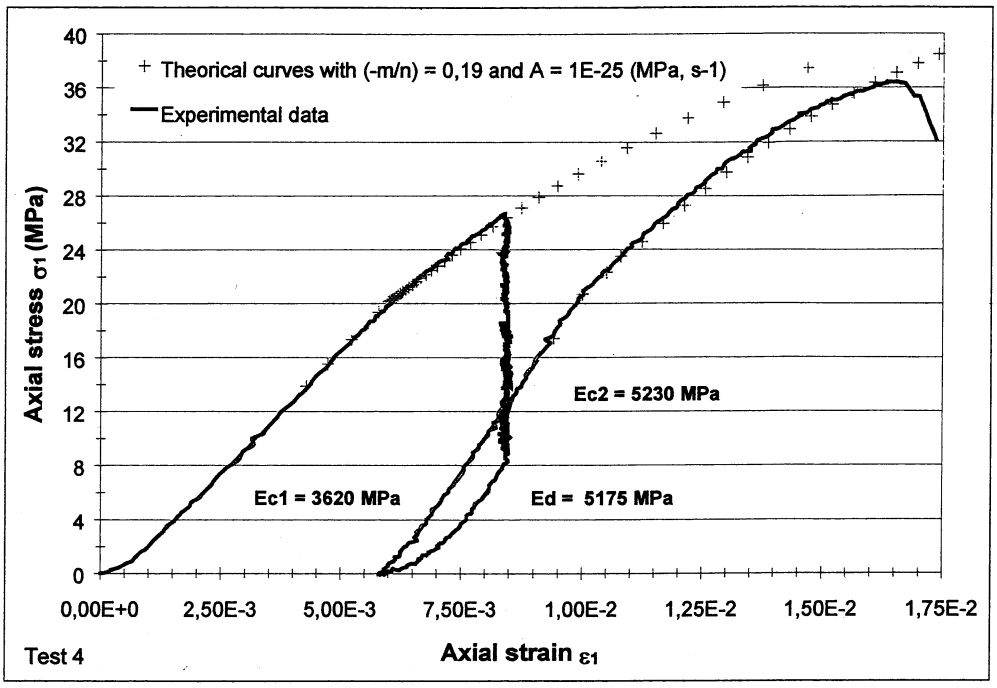

Figure 6. Measured and calculated response of a shale sample subjected to constant strain rate test and relaxation test

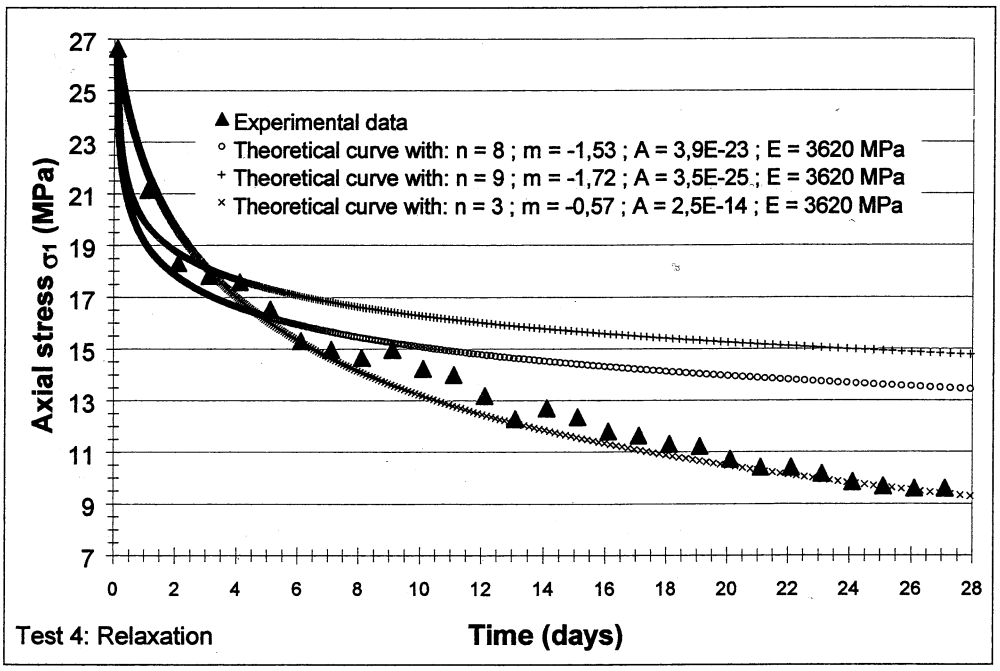

Figure 7a. Measured and parametric study results of a shale sample subjected to a relaxation test
Modelling without any stress rate threshold

Without any stress threshold (Figure 7a), a very low value for the parameter m must be considered. But, in this case, long-term behaviour becomes thus very pessimistic because strain-hardening is quite negligible. However, for such an interpretation, it is necessary to know whether a relaxation limit really exists or not (limit curve, Figure 3).
To match the parametric study on experimental data of the three relaxation tests, it was necessary to take into account the steady-state tendency. A stress rate threshold (Figure 7b) was also introduced in the model. It was found to be around 3.9×10^{-6} MPa s^{-1} and corresponds to a secondary strain rate equal to 10^{-9} s^{-1} (calculated with the loading strain rate modulus). This latter value is really very low and to give an order of magnitude, it would be necessary to carry out a creep test under a deviator of 27 MPa for 4 months in order to detect such a low strain rate. This simple calculation shows the great advantage of the relaxation tests which enable the time of observation to be compressed by considering

the loading strain modulus. This result is all the more interesting in as much that, for the theoretical simulation, the unrecoverable strain (visco-plastic), calculated analytically, is about 5.5 x 10^{-3} after 25 days, and experimentally after unloading it was measured at 5.8 x 10^{-3}. In this case, it was as if two phenomena were superimposed. The unrecoverable strain part related to Lemaitre's law (primary phase) is around 3.3 x 10^{-3} and the part due to the steady-state phase is 2.2 x 10^{-3}. These considerations were also verified for test No.5 but after strain hardening, the second relaxation exhibits no steady-state phase.

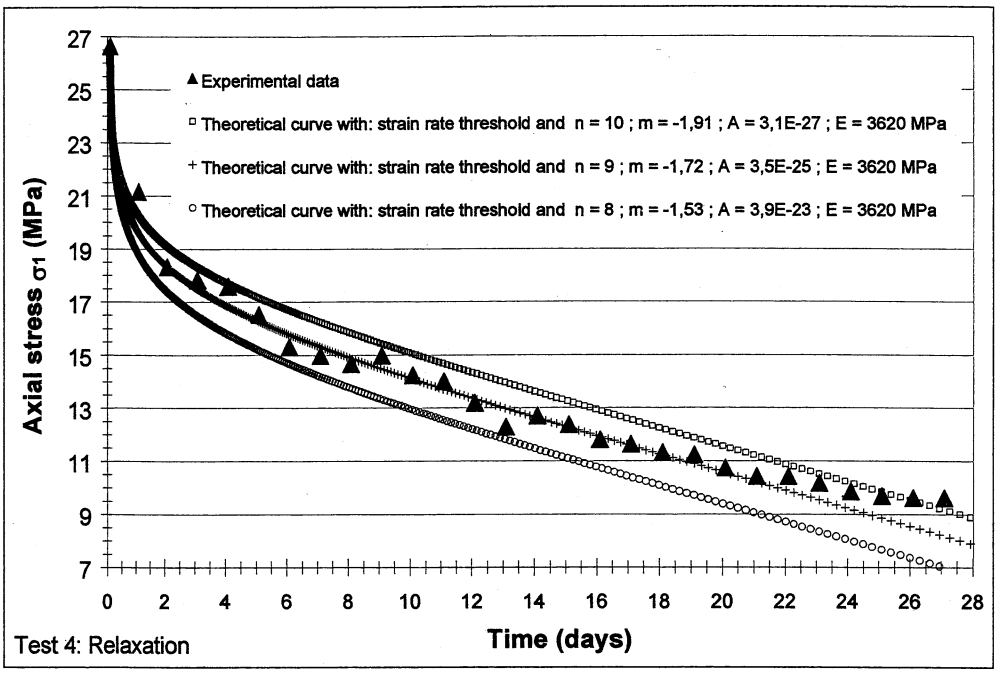

Figure 7b. Measured and parametric study results of a shale sample subjected to a relaxation test
Modelling with a stress rate threshold of around 3.9 x 10^{-6} MPa s^{-1}

Table 2. Summary of inelastic parameters

Test references	n	m	A (MPa, s^{-1})	Strain rate threshold (s^{-1})	Parameter (-m/n)
Test No.1 – 1B	9	-1.8	3 x 10^{-27}	-	0.20
Test No.2 – 2C	9 to 11	-2.0 to -2.5	10^{-25} to 10^{-30}	-	0.22
Test No.3 – 2A	?	?	?	-	0.29
Test No.4 – 2B	9	-1.7	3.5 x 10^{-25}	1 x 10^{-9}	0.19
Test No.5 – 1C	9	-1.7	3.5 x 10^{-25}	6 x 10^{-10}	0.19

These initial tests have highlighted the time-dependent behaviour of shales from the East site through their sensitivity to strain loading rate and their relaxation potential. Under certain conditions, the relaxation tests demonstrated the existence of a steady-state phase in their time-dependent behaviour, and this still needs to be properly defined both by undertaking new tests and by thin-film analysis by scanning electron microscopy (SEM). In addition, it would seem possible to develop Lemaitre's law by the introduction of different strain rate and stress thresholds which need to be define more precisely.

5. Validation of the FLAC model and application to deep tunnel modelling

For proper evaluation of the effect of the time step, a theoretical reference must be verified with numerical results before underground modelling. The relaxation test was chosen (after a constant strain rate loading) to avoid the disturbance due to initial conditions. Indeed, the sample represented by an axisymmetric mesh is simply jammed between the plates of the frame after loading (test No.4 was loaded at constant strain rate 9.85 x 10^{-7} s^{-1}, until 26 MPa of axial compressive strength was obtained).

The long-term mechanical characteristics for this relaxation modelling are as follows:

$$\begin{cases} E = 3620 \text{ MPa} \\ \nu = 0.3 \\ n = 9.25 \\ m = -1.77 \\ A = 10^{-25} \text{ (MPa, s}^{-1}\text{)} \end{cases}$$

with a minimum threshold of steady-state creep motion close to 10^{-9} s^{-1}.

5.1. Definition of a suitable time step

Various initial time steps were tested in order to study how rapidly the initial disturbance is calmed. For this calculation, a suitable time step value would be around 0.1 s. Close to 10 s, it leads to a considerable imbalance (Figure 8a), but not necessarily irreversible in the long term (Figure 8b) because this also depends on the geometrical time progression, defined by the expression:

$$\Delta t_{n+1}\left[t + \Delta t_n(t)\right] = p\Delta t_n(t) \tag{12}$$

where p is the geometrical pace of this progression.

According to Cormeau, the initial critical time step would be around 30 s and thus 300 times greater than the suitable value. The safety factor (S.F.) to apply to Cormeau's critical time step can also be determined. This approach fits in with the observations made by Detournay (1998) who recommends practically taking a safety factor between 100 to 1000 on the estimate of the critical time step proposed by Itasca (quite similar as Cormeau's formulation). In the long term, it is the geometrical pace p which has the greatest influence on the stability of the solution. Regardless of the value of the initial time step, computation stability is obtained with some reversible oscillations around the analytical solution for a pace equal to p = 1.001 (Figures 8a, b). On the other hand, for an unsuitable geometrical pace, instability conditions may occur or at least conditions with an unacceptable accuracy for the solution. But even if there is a substantial margin of error for a time period tested, the entire stability is not necessarily called into question in the long term.

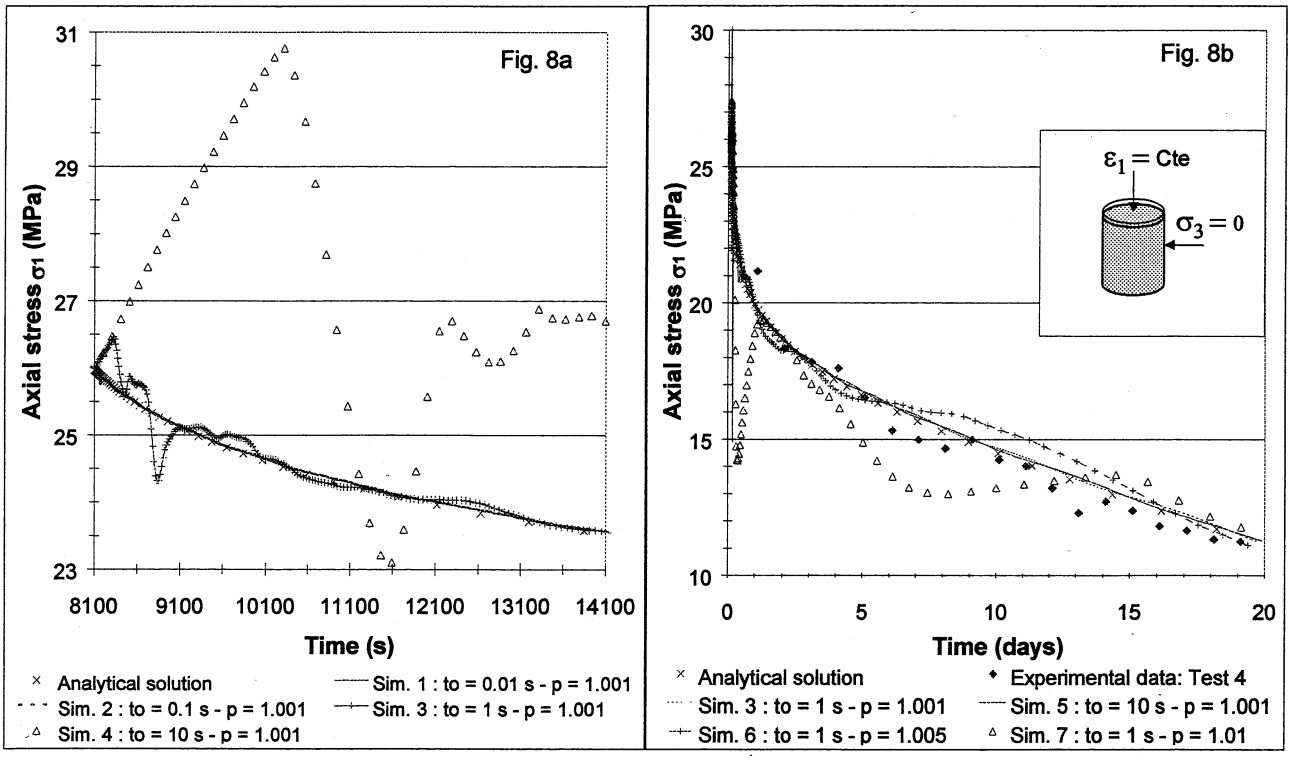

Figure 8: Influence of the initial time step on the numerical stability for relaxation test – a: Zoom at short term, b: Long term behavior compared to experimental data (test No. 4)

Through these different numerical responses, the safety factor can be given on the critical time step defined by Cormeau, compatible with good accuracy. The value of this factor reaches 500 to 1000. In this case, the suitable solution considered here (with to = 0.1 s and p = 1.001) induces a safety factor of around 750 (Figures 9a, b).

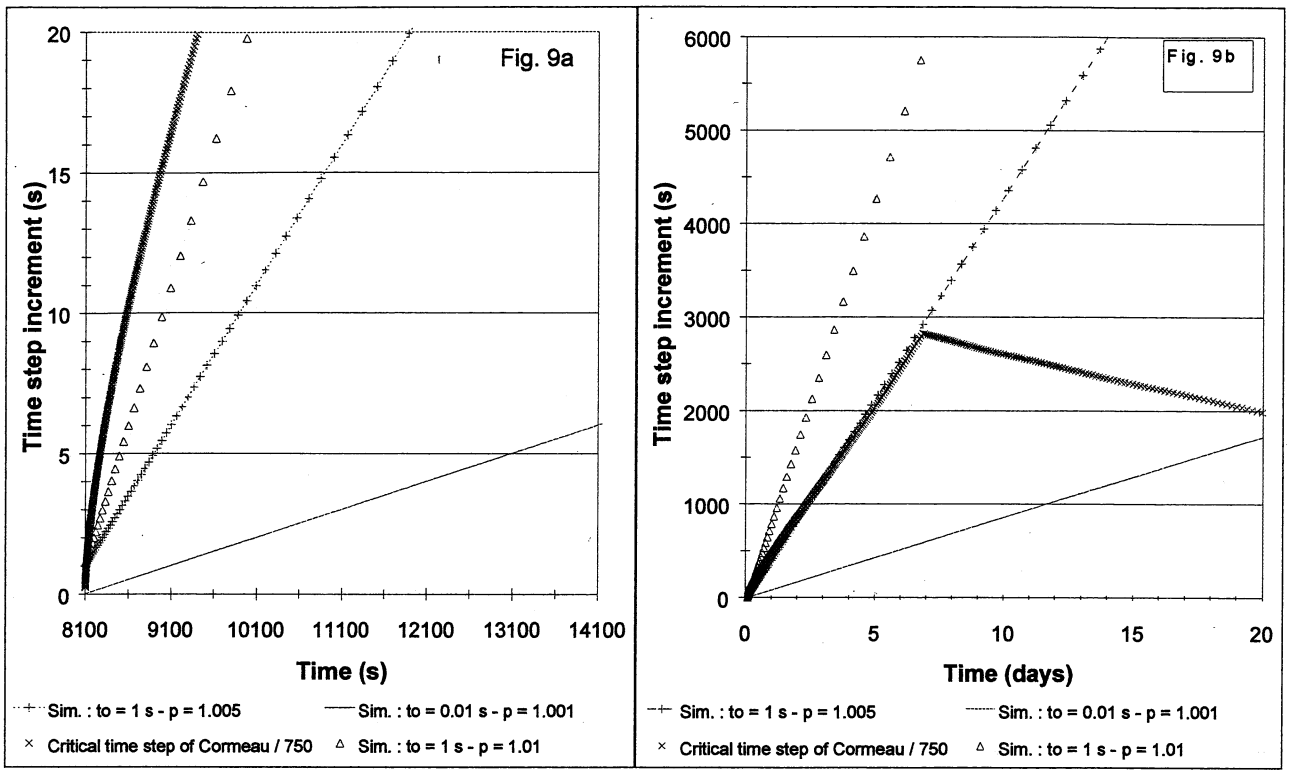

Figure 9: Definition of a suitable time progression
– a: Zoom at the beginning of the relaxation simulation, b: Long term variation

5.2. Implications for deep circular tunnelling

Practically, for an engineering calculation, it is advisable to choose a suitable time step progression in order to satisfy requirements of accuracy and computation time. For example, the design of a complex underground structure such as a deep excavation or tunnel can require up to 48 hours of computation time for behaviour extrapolation over data for several centuries. To illustrate this aim, an example is proposed whereby the behaviour of the tunnel wall around a deep circular tunnel is displayed. Stress isotropy is assumed here with $\sigma_v = \sigma_h = 12$ MPa, and time-dependent phenomena start after a decompression related to the excavation and considered to be elastic. Figure 10 shows the 2D-mesh and the initial conditions of the model.

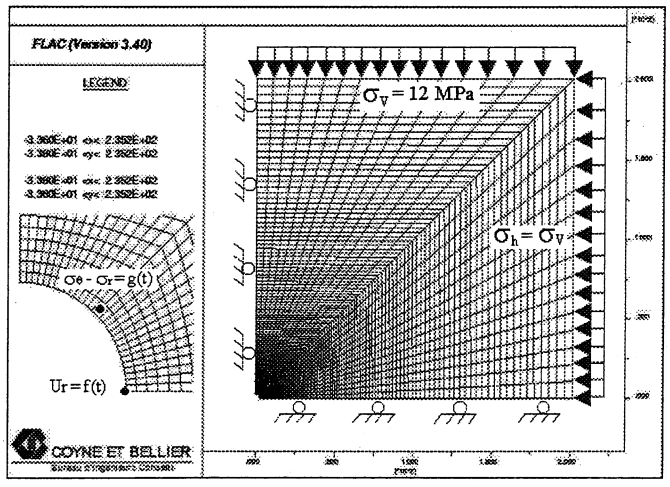

Figure 10. FLAC zone geometry and model boundary conditions

The parameters of Lemaitre's law used here are the same as for relaxation test modelling but no strain rate threshold was introduced. The aim of this calculation was to qualify time-dependent displacements and relaxation of the tunnel wall over a period of two hundred years.

The initial time step was thus fixed at 10 s in order to give good accuracy as early as one month after the start. Then, the important result demonstrated by Nguyen-Minh and Pouya (1992), concerning the existence of a steady stress state, can be used for a long-term prediction like this. Considering a safety factor S.F = 750 on the critical time step defined by Cormeau (and previously justified on relaxation test modelling), it is also possible to succeed rapidly in determining a suitable geometrical progress for a specific duration of the envisaged study (200 years in this case). By introducing this safety factor, the geometric pace p was found to be around 1.0005.

For this example, the reduced deviator near the tunnel wall, $q / 2\sigma_0 = (\sigma_\theta - \sigma_r)_t / (\sigma_\theta - \sigma_r)_{to}$ (Figures 11a, b), and the radial strain at the tunnel wall, Ur / r (Figures 12a, b) can also be indexed as a function of time. The different numerical tests show that the solution is stable with an acceptable accuracy as soon as the pace p is lower than 1.001. For a higher value of the pace p, there is a real risk of overvaluation of galleries' closure.

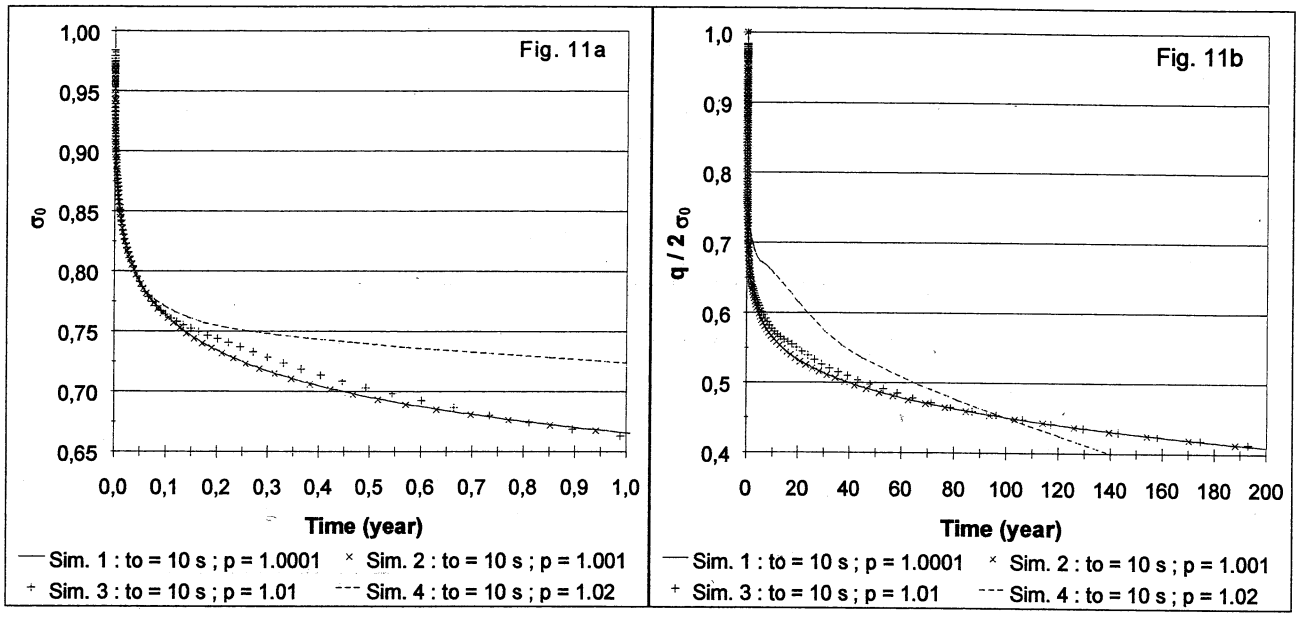

Figure 11: Deviator variations at the tunnel wall – a: At short term, b: At long term

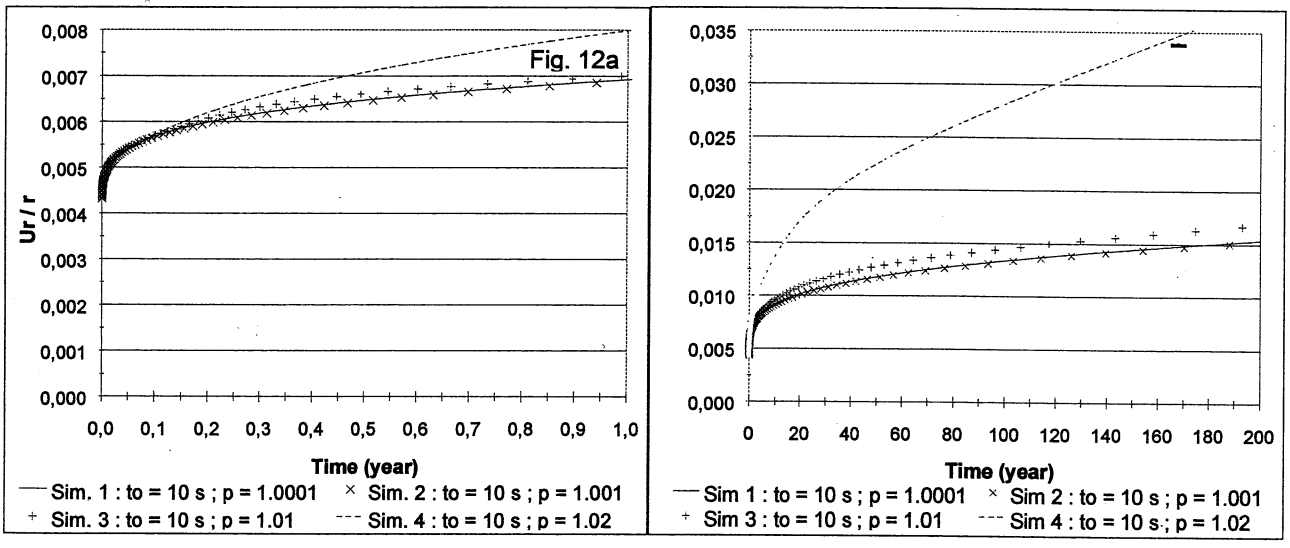

Figure 12: Gallery's closure variations – a: At short term, b: At long term

The modelling requires ¼ hour CPU time for a pace p = 1.02, but it rises to more than 2 days with p = 1.0001. Thus with a suitable geometrical progression (p = 1.001), the saving on CPU time is considerable, about 90% in relation to the smaller progression tested. It is also possible to optimise this computation in 4 hours according to an unbalanced forces analysis (Boidy et al.). On the other hand, the behaviour of the tunnel wall is related to creep and relaxation phenomena. This justify to take into account relaxation tests in the identification of time-dependent parameters.

6. Conclusions

For a long term prediction of gallery's closure (several centuries), the determination of time-dependent parameters based only on middle term creep tests performed during one to three months is not enough accurate. To overcome this problem, relaxation tests are necessary in order to detect more rapidly some possible steady-state behaviour and define a potential stress rate threshold. In addition, relaxation of stress seems to vanish after one month and a long-term stability may perhaps be reached. In order to quantify inelastic parameters of Lemaitre's creep law, the ratio (-m/n) can be easily established with a small dispersion from the constant strain rate tests. The parameters A and n can thus be linked by a simple relation. Then, relaxation tests performed on the same sample allow one to choose a representative value of the parameter n for a long-term prediction.

The study of the time-dependent behaviour of geomaterials, requires a specific analysis of the time step progression and a justification of the choice of a suitable one. In this respect, special attention was given to Lemaitre's visco-plastic law which was implemented in the explicit finite-difference program FLAC 3.4. The theoretical critical time step defined by Cormeau can also constitute a reference on which a safety factor of around 100 to 1000 must be applied in order to define a suitable time step progression.

This study should lead to a better prediction of time-dependent behaviour of soft rock, like shales. In the future, it is planned to compare this approach with a micro-structural analysis in order to qualify the mechanism of time-dependent deformation (slide and dislocation) and to define more precisely certain general constitutive laws, which could be used for such time-dependent modelling. On the other hand, it is hoped to validate this approach with in-situ measurements to extrapolate this behaviour over a very long period of time.

7. References

Fokker P. A. 1998. The micro-mechanics of creep in rocksalt. In: Proc. of the 4th Conf. on the Mechanical Behaviour of Salt, M. Aubertin and H. Reginald Hardy, Jr. (eds.), Trans Tech Publications: 49-61.

Malan, D.F. 1999. Time-dependent Behaviour of deep level tabular excavations in hard rock. Rock Mech. Rock Engng. 32: 123-155.

Lemaitre J., & Chaboche, J.L. 1996. Mecanique des materiaux solides: Dunod.

Tatsuoka F., Santucci de Magistris F., Hayano K., Momoya Y., Koseki J. 1998. Some new aspects of time effects on the stress-strain behaviour of stiff geomaterials. Keynote Lecture for the 2nd Int. Conf. On Hard Soils and Soft Rocks, Napoli, 69 pp.

CFMR. 2000. Manuel de Mecanique des Roches. Tome 1: Fondements. Presses de l'Ecole des Mines de Paris: 78-80.

Norton F. H. 1929. Creep of Steel at High Temperatures. New York: McGraw-Hill Book Company.

Perzyna, P. 1966. Fundamental Problems in Viscoplasticity. In Academic Press (ed.), Advances in Applied Mechanics 9: 243-377.

Pellet F., Sahli M., Boidy E., Boulon M. October 2000. (to be published). Modelling of time-dependent behaviour of sandstones for deep underground openings. Proc. Int. Conf. on Engng. and Tech. Science (ICETS 2000), Beijing, China.

Billaux, D. & Cundall, P. 1993. Modelling of Geomaterials using the Lagrangian Element method [In French]. Revue Francaise de Geotechnique 63: 9-21.

Cormeau, I. 1975. Numerical stability in quasi-static elasto-viscoplasticity. Int. J. num. Meth. Engng. 9(1): 109-127.

Detournay, C. 1998. A simple Visco-plastic model in FLAC. FLAC version 3.4 Users' Manuel Optional Features. Itasca.

Boidy E., Pellet F., Boulon M. January 2001. (to be published). Numerical modelling of deep tunnels including time-dependent behaviour. Proc. 10th Int. Conf. IACMAG, Tucson, USA.

Nguyen-Minh, D. & Pouya, A. 1992. A framework for the analysis of underground excavations in viscoplastic medium, on account of a steady stress state [In French]. Revue Française de Geotechnique 59: 5-14.

Berest, P. 1989. Viscoplasticity in Rock Mechanics. In Geomaterials. Constitutive equations and modelling: 239-262. Elsevier Applied Science.

Laigle, F. & Kolmayer, P. 1998. Numerical modelisation for long term behaviour of underground structures [In French]. Revue Francaise de Geotechnique 85: 65-78.

Paramètres de calcul géotechnique. Magnan (ed.) 2002, Presses de l'ENPC/LCPC, Paris

IDENTIFICATION DES CARACTÉRISTIQUES VISQUEUSES D'UNE ROCHE ARGILEUSE

IDENTIFICATION OF VISCOUS PROPERTIES OF AN ARGILLACEOUS ROCK

G. Fabre et F. Pellet
Laboratoire Sols Solides Structures, Grenoble, France

RÉSUMÉ - Le comportement mécanique différé d'une marne argileuse a été mis en évidence au moyen d'essais de chargement quasi-statique, d'essais de fluage et d'essais de relaxation. Les résultats ont permis de déterminer les paramètres du modèle rhéologique de Lemaitre dans le but de prévoir les déformations viscoplastiques sur des échelles de temps plus longues.

ABSTRACT - Constant strain rate tests, creep tests and relaxation tests have shown the mechanical time-dependent behaviour of an argillaceous rock. The results permitted to determine the parameters of Lemaitre's rheological model for a long time prediction of the viscoplastic strain.

1. Introduction

L'auscultation des ouvrages souterrains profonds fait apparaître un développement parfois très important des déformations différées. Ces déformations traduisent un comportement mécanique non-linéaire de type élasto-viscoplastique endommageable. Leur origine, encore mal connue, est vraisemblablement liée à l'évolution de la microstructure du matériau, engendrée par des variations de contrainte ou des modifications de l'état hydrique et/ou thermique. Cette étude vise à améliorer la compréhension du comportement mécanique différé des roches anisotropes ; elle concerne une roche sédimentaire, une marne argileuse.

2. Étude expérimentale d'une marne argileuse

2.1. Description de la roche étudiée

La marne étudiée est considérée, de par sa formation, comme orthotrope de révolution. Les analyses minéralogiques réalisées sur plusieurs échantillons ont montré qu'elle contient une importante matrice argileuse (40 à 45%), qui cimente des cristaux de quartz et de carbonates (40 à 55%) et, dans une moindre proportion, des feldspaths et des micas. L'angle θ d'orientation des plans d'isotropie est défini par la normale v_3 et l'axe n de révolution des éprouvettes (figure 1).

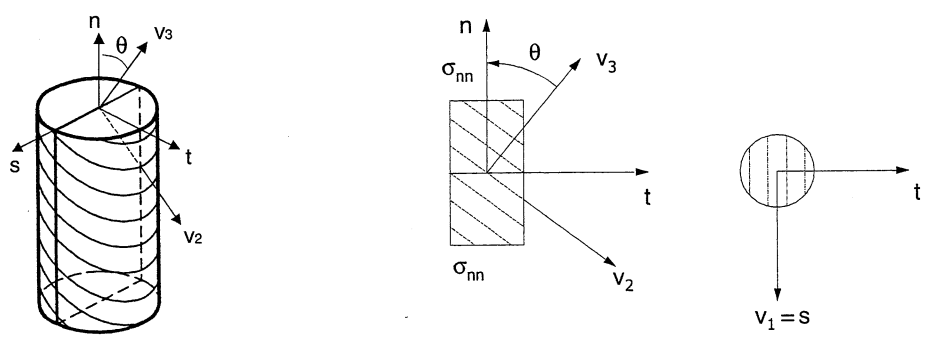

Figure 1. Définition des axes de symétrie d'une éprouvette.

2.2. Programme expérimental

Pour étudier la viscosité et l'anisotropie de cette marne, des essais de chargement quasi-statique, des essais de relaxation et des essais de fluage ont été réalisés sur des échantillons ayant des plans d'isotropie d'orientation θ différente (0 degré, 45 degrés, 90 degrés). Le programme expérimental est détaillé dans le tableau I.

Tableau I. Programme d'essais réalisés sur les échantillons de marne.

Échantillon	Orientation θ (degrés)	Type d'essai	Vitesse de déformation $\dot{\varepsilon}$ (s^{-1})
0-1	0	Chargement quasi-statique	10^{-8}
0-2	0		10^{-6}
0-3	0		10^{-4}
45-1	45	Chargement quasi-statique	10^{-6}
90-1	90		10^{-6}
0-4	0	Fluage sous 26 MPa	/
0-5	0	Relaxation	/

La réalisation d'essais de chargement quasi-statique à des vitesses de déformation décroissantes peut mettre en évidence l'existence d'une courbe limite pour laquelle la roche se déforme sans écrouissage, c'est-à-dire en temps réel, sans exhiber de déformations différées. Le seuil de contrainte σ_s atteint en fin de relaxation est, en théorie, lié à cette courbe limite puisque qu'il correspond à la contrainte atteinte pour le même taux de déformation ε_0 (figure 2).

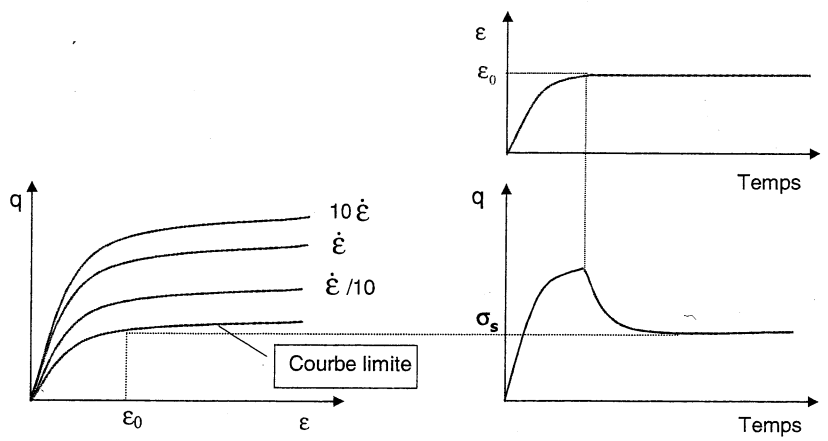

Figure 2. Correspondance entre le seuil de contrainte, σ_s, atteint en fin de relaxation et la courbe limite. (a) : Essais de chargement quasi-statique et courbe limite ; (b) : Essai de relaxation

2.3. Résultats expérimentaux

2.3.1. Essais de chargement quasi-statique

Dans la gamme de vitesse de déformation testée, entre $\dot{\varepsilon} = 10^{-8}$ et 10^{-4} s^{-1}, le comportement mécanique de la marne étudiée est peu sensible à la vitesse de chargement (figure 3b).

Les résultats des essais montrent cependant que la résistance à la rupture σ_f et la contrainte de contraction maximale σ_{cd} subissent une légère augmentation (respectivement de 7 et 12%) lorsque la vitesse de déformation passe de 10^{-8} à 10^{-4} s^{-1}. L'orientation des plans d'isotropie influence également ces contraintes caractéristiques qui semblent présenter un minimum pour θ = 45 degrés.

La déformation axiale atteinte à la rupture $(\varepsilon_{nn})_f$, qui apparaît peu sensible à la vitesse de

déformation entre $\dot{\varepsilon} = 10^{-8}$ et 10^{-4} s^{-1}, est fortement influencée par l'orientation des plans d'isotropie des échantillons. En effet, $(\varepsilon_{nn})_f$ subit une augmentation de 50% lorsque ce paramètre varie de 45 degrés (orientation pour laquelle elle est minimale) à 0 degré. De plus, la déformation volumique maximale est une fonction décroissante de l'orientation des plans d'isotropie (figure 3a).

La quasi-superposition des courbes des essais de chargement quasi-statique réalisés à 10^{-6} et 10^{-8} s^{-1} laisse penser que la courbe limite de cette marne argileuse est obtenue pour $\dot{\varepsilon} = 10^{-8}$ s^{-1} (figure 3b).

Enfin, tous ces essais de chargement quasi-statique font apparaître que, dès que la propagation des fissures devient instable ($\sigma > \sigma_{cd}$), les caractéristiques mécaniques de la marne se dégradent très rapidement, menant l'échantillon à la rupture.

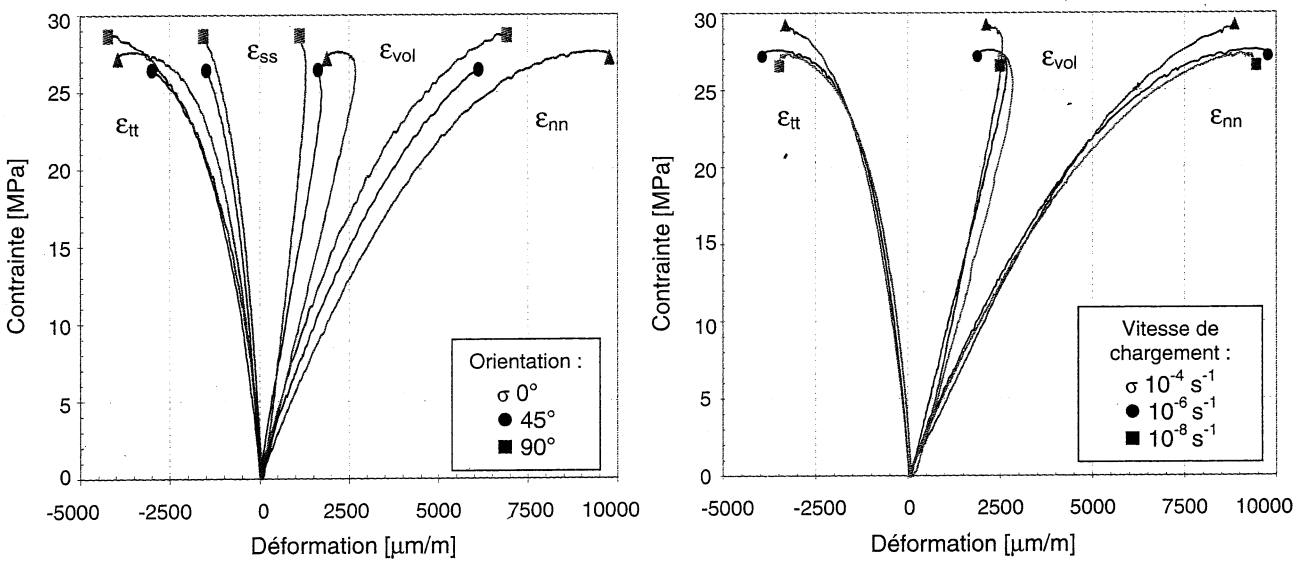

Figure 3. Courbes contraintes - déformations au cours des essais de chargement quasi-statique (a) : Essais à $\dot{\varepsilon} = 10^{-6}$ s^{-1} réalisés sur des éprouvettes ayant des plans d'isotropie d'orientation variable. (b) : Essais à vitesse variable réalisés sur des éprouvettes d'orientation 0°.

2.3.2. Essai de relaxation et de fluage

L'essai de relaxation a été réalisé à partir de $\sigma_0 = 24$ MPa. La déformation atteinte ($\varepsilon_{nn} = 3605$ µm/m) a été maintenue constante durant 42 jours et une chute de contrainte de 25 % a été enregistrée (figure 4a).

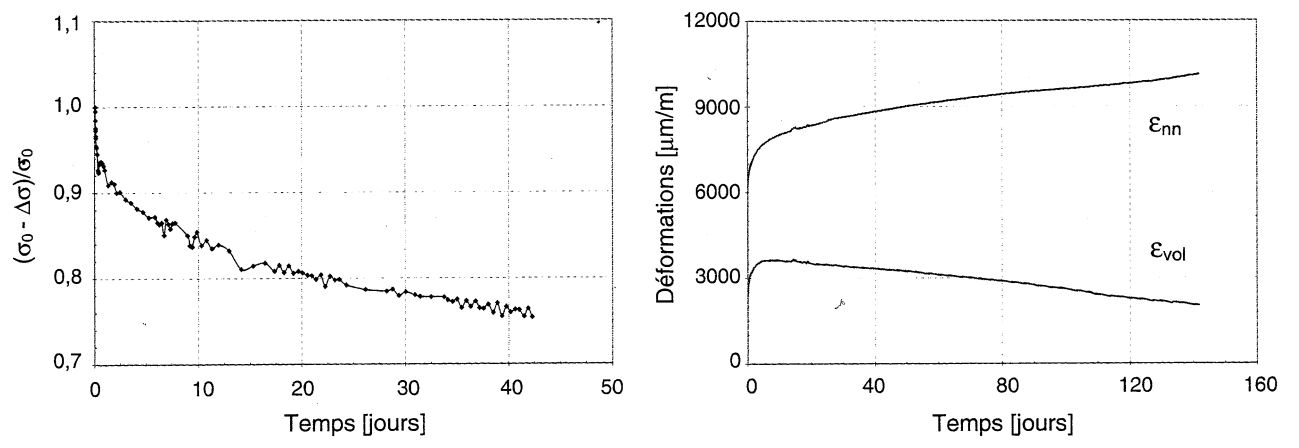

Figure 4. Essai de relaxation et essai de fluage
(a) : Relaxation des contraintes à partir de $\sigma_0 = 24$ MPa ; (b) : Fluage sous 26 MPa.

La courbe de fluage obtenue sous un déviateur de 26 MPa appliqué pendant 143 jours (figure 4b) ne présente que les phases de fluage primaire et secondaire. Le calcul de l'évolution de la vitesse de déformation en fonction du temps montre qu'au 25ème jour de l'essai cette vitesse se stabilise à $2{,}2.10^{-10}$ s^{-1}. L'évolution de la déformation volumique en fonction du temps révèle qu'après une importante contraction (ε_{vol} croissante) durant le fluage primaire, on observe une dilatance de l'échantillon qui se poursuit durant la phase de fluage secondaire à la vitesse de $8{,}6.10^{-6}$ $jour^{-1}$.

3. Modélisation du comportement mécanique différé

L'extrapolation réaliste, sur des échelles de temps séculaires, des déformations viscoplastiques mesurées en laboratoire n'est possible qu'après le calage rigoureux d'un modèle de comportement sur des résultats d'essais.

3.1. Modèle rhéologique de Lemaitre

Le modèle de Lemaitre, qui représente le comportement du solide élasto-viscoplastique à écrouissage isotrope, s'appuie sur la théorie de Perzyna (1966). Cette théorie repose sur le postulat de la partition des vitesses de déformations selon la relation :

$$\dot{\varepsilon}_{ij}^{\ tot} = \dot{\varepsilon}_{ij}^{\ el} + \dot{\varepsilon}_{ij}^{\ vp} \qquad (1)$$

où $\dot{\varepsilon}_{ij}^{\ vp}$ et $\dot{\varepsilon}_{ij}^{\ el}$ sont respectivement la partie non élastique et la partie élastique du tenseur de la vitesse de déformation. Pour exprimer cette vitesse de déformation viscoplastique, Perzyna suggère la formulation suivante :

$$\dot{\varepsilon}_{ij}^{\ vp} = \gamma\langle\Phi(F)\rangle \frac{\partial f}{\partial \sigma_{ij}} \qquad (2)$$

où : γ représente la viscosité du matériau (exprimée en s^{-1}).
$\Phi(F)$ représente la fonction d'écoulement.
$\langle . \rangle$ correspondent aux crochets de Macauly définis par :

$$\langle\Phi(F)\rangle = \frac{1}{2}(\Phi(F) + |\Phi(F)|) \qquad (3)$$

F est la surface de charge de référence :

$$F(\sigma_{ij}, \varepsilon_{ij}^{\ vp}) = \frac{f(\sigma_{ij}, \varepsilon_{kl}^{vp})}{\kappa} - 1 \qquad (4)$$

avec : f, le critère de plasticité
κ, le paramètre d'écrouissage, fonction du travail plastique.

La loi de Lemaitre (Lemaitre et Chaboche, 1996) utilise le critère de plasticité de von Mises et une loi d'écoulement de type puissance : $\Phi(F) = F^n$ ($n \geq 1$). Elle se base sur deux hypothèses fondamentales qui sont, d'une part, la partition des déformations totales en une partie élastique et une partie viscoplastique, et d'autre part, le développement des déformations viscoplastiques à volume constant ; elle s'écrit :

$$\dot{\varepsilon}^{vp} = A.(q - \sigma_S)^n .(\varepsilon^{vp})^m \qquad (5)$$

avec ε^{vp}, déformation viscoplastique,
$\dot{\varepsilon}^{vp}$, vitesse de déformation viscoplastique,
q, contrainte déviatorique,
A, n et m, paramètres caractéristiques du matériau,
σ_s, seuil de contrainte en deçà duquel aucune déformation visqueuse ne se développe.

3.2. Méthode de calage

Le calage analytique du modèle de Lemaitre sur les essais réalisés nécessite dans un premier temps d'isoler, dans la déformation axiale totale mesurée, les déformations viscoplastiques fonction du temps en retranchant les déformations élastiques instantanées. D'après l'hypothèse de la partition des déformations :

$$\varepsilon^{vp} = \varepsilon^{tot} - \varepsilon^{el} = \varepsilon^{tot} - \frac{q}{E} \qquad (6)$$

avec E, module d'élasticité, supposé connu, et q, déviateur des contraintes.

3.2.1. Calage sur les essais de chargement quasi-statique

Au cours d'un essai de chargement quasi-statique, la viscosité du matériau peut se développer en temps réel à la condition que la vitesse de déformation soit suffisamment faible et permette d'obtenir sur la courbe limite. La vitesse de déformation viscoplastique $\dot{\varepsilon}^{vp}$ tend alors vers la vitesse de déformation imposée, $\dot{\varepsilon}$. Avec l'hypothèse $\dot{\varepsilon}^{vp} = \dot{\varepsilon}$, la loi de Lemaitre s'écrit :

$$\dot{\varepsilon} = A.q^n.(\varepsilon^{vp})^m \qquad (7)$$

Soit :

$$ln\,q = \frac{1}{n}(ln\,\dot{\varepsilon} - ln\,A) - \frac{m}{n}\,ln\,\varepsilon^{vp} \qquad (8)$$

Dans un repère ($ln\,q$, $ln\,\varepsilon^{vp}$), l'équation de la droite obtenue permet de connaître (-m/n), la pente de la droite et 1/n(ln $\dot{\varepsilon}$ - $ln\,A$), son ordonnée à l'origine (figure 5). Deux degrés de liberté sont ainsi fixés.

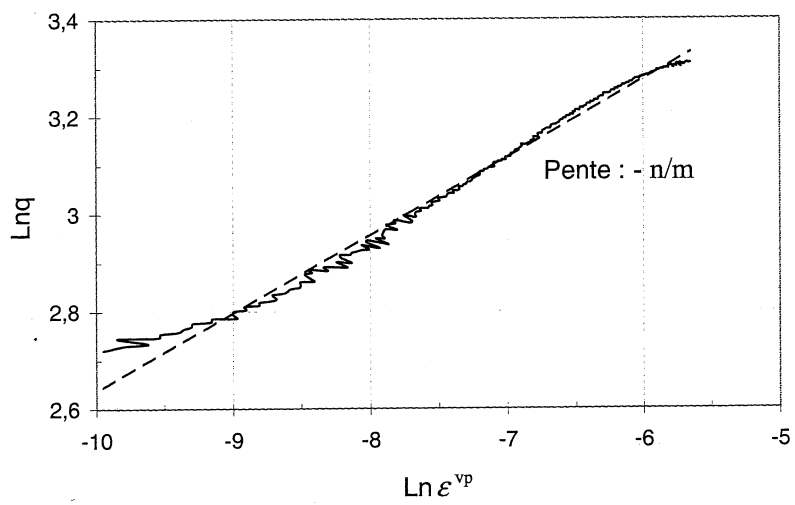

Figure 5. Evolution linéaire du logarithme du déviateur de contrainte en fonction du logarithme de la déformation viscoplastique lors de l'essai de chargement quasi-statique à $\dot{\varepsilon} = 10^{-8}\,s^{-1}$.

3.2.2. Calage sur les essais de fluage

À déviateur q constant, l'expression explicite de la loi de fluage $\varepsilon = f(t)$ s'obtient par intégration de la loi de Lemaitre en supposant $\sigma_s = 0$. Soit :

$$\varepsilon^{vp} = \left[(1-m).A.q^n.t\right]^{1/(1-m)} \qquad (9)$$

En posant $\varepsilon^{vp} = aq^{\beta}t^{\alpha}$ on obtient, par identification :

$$\alpha = \frac{1}{1-m}\ ; \qquad \beta = \frac{n}{1-m}\ ; \qquad a = [A(1-m)]^{1/(1-m)} = \left(\frac{A}{\alpha}\right)^{\alpha}. \qquad (10)$$

Avec ces paramètres et dans un repère logarithmique, la déformation viscoplastique s'écrit :

$$ln(\varepsilon^{vp}) = ln(a) + \beta\, ln(q) + \alpha\, ln(t) \qquad (11)$$

Une régression linéaire sur la droite obtenue donne α, sa pente, et $(ln(a) + \beta\, ln(q))$, son ordonnée à l'origine. Connaissant q, le déviateur de contrainte appliqué, il ne reste qu'un paramètre à caler, a ou β.

3.2.3. Exploitation des résultats d'essais de relaxation

Dans un essai de relaxation, la déformation totale est maintenue constante, donc $\dot{\varepsilon}^{tot} = 0$, et d'après la loi de Lemaitre :

$$\frac{\dot{\sigma}}{E} + A \cdot \sigma^n \cdot (\varepsilon^{vp})^m = 0 \qquad (12)$$

d'où :

$$\frac{\dot{\sigma}}{\sigma^n} = -A \cdot E \cdot (\varepsilon^{vp})^m \qquad (13)$$

Pendant l'essai de relaxation, les déformations élastiques réversibles qui diminuent sont compensées par les déformations viscoplastiques irréversibles qui se développent, de sorte que ε^{tot} = constante et $\dot{\varepsilon}^{tot} = 0$. Analytiquement, il est possible de simuler cet essai bien que l'expression littérale de la loi de relaxation en fonction du temps soit impossible à déterminer sans $\varepsilon^{vp} = f(t)$. Il suffit pour cela de fixer un pas de temps Δt et de connaître la contrainte initiale q_0 imposée à l'échantillon. L'évolution de la contrainte est alors calculée grâce à la relation de récurrence :

À t = 0 : $(\varepsilon^{vp})_0 = A.(1-m)^{1/(1-m)}.q^{n/(1-m)}.\Delta t^{1/(1-m)}$ (14a)

$q = q_0$

À t = k.Δt : $(\varepsilon^{vp})_k = (\dot{\varepsilon}^{vp})_{k-1}.\Delta t + (\varepsilon^{vp})_{k-1} = A \cdot (q_{k-1})^n.[(\varepsilon^{vp})_{k-1}]^m.\Delta t + (\varepsilon^{vp})_{k-1}$ (14b)

$q_k = q_{k-1} - E.(\dot{\varepsilon}^{vp})_{k-1}.\Delta t = q_{k-1} - E.A.(q_{k-1})^n.[(\varepsilon^{vp})_{k-1}]^m.\Delta t$

en désignant par E le module d'élasticité et (A, n, m) les paramètres de la loi de Lemaitre.

3.3. Modélisation du comportement différé

Cette méthode de calage a été appliquée, de manière très satisfaisante, aux résultats des essais de chargement quasi-statique réalisés à $\dot{\varepsilon} = 10^{-8}\ s^{-1}$ et $\dot{\varepsilon} = 10^{-6}\ s^{-1}$ et aux résultats de l'essai de fluage. Elle a permis d'obtenir par la méthode des moindres carrés une très bonne superposition des courbes expérimentale et théorique (figure 6). Les jeux de paramètres obtenus sont donnés dans le tableau II.

Tableau II. Paramètres de la loi de Lemaitre calés à partir des essais de chargement quasi-statique à $\dot{\varepsilon} = 10^{-6}\ s^{-1}$ et $10^{-8}\ s^{-1}$ et de l'essai de fluage sous 26 MPa.

	Jeu n°1	Jeu n°2	Jeu n°3
Essai	$\dot{\varepsilon} = 10^{-8}\ s^{-1}$	$\dot{\varepsilon} = 10^{-6}\ s^{-1}$	Fluage sous 26 MPa
n	8,96	7,11	21,99
m	-1,40	-1,28	- 5,66
A ($MPa.s^{-1}$)	$6,88.10^{-26}$	$6,25.10^{-23}$	$7,17.10^{-55}$

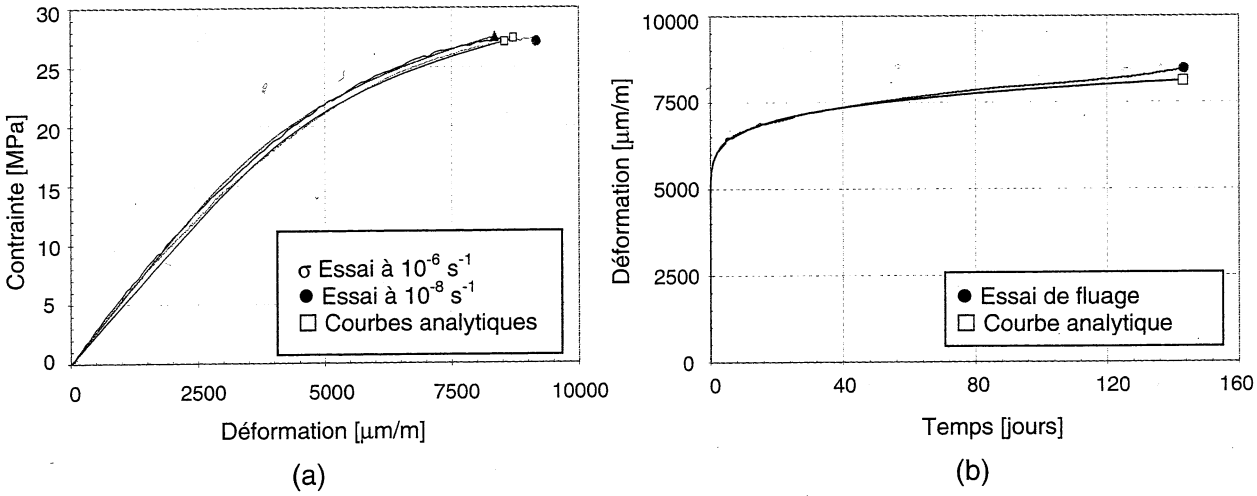

Figure 6. Calages analytiques de la loi de Lemaitre (a) : Essais de chargement quasi-statique réalisé à $\dot{\varepsilon} = 10^{-6}\,s^{-1}$ et $10^{-8}\,s^{-1}$ (b) : Essai de fluage sous 26 MPa.

3.4. Vérification analytique sur l'essai de relaxation

Les deux jeux de paramètres déterminés à partir des essais de chargement quasi-statique ont été utilisés pour simuler analytiquement un essai de relaxation à partir de 24 MPa. Les courbes obtenues sont représentées sur la figure 7 où elles sont comparées aux résultats expérimentaux.

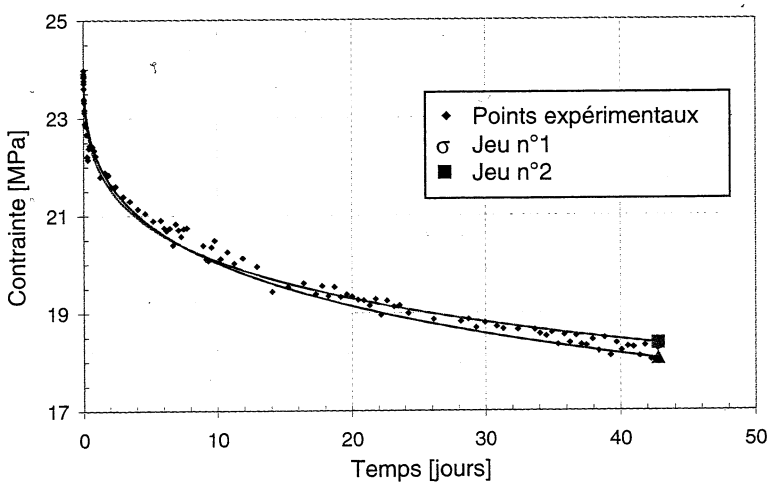

Figure 7. Modélisation analytique de l'essai de relaxation avec les jeux de paramètres de la loi de Lemaitre calés sur les résultats d'essais de chargement quasi-statique.

La courbe analytique tracée avec le jeu de paramètres déterminé à partir des résultats de l'essai de fluage faisait apparaître une importante chute de contrainte dès le premier jour de relaxation. Ce phénomène qui n'est pas observé expérimentalement, est dû à l'exposant n probablement trop élevé, que le paramètre A même très faible ne parvient pas à compenser.

3.5. Extrapolations à long terme

Le nombre d'essais réalisés étant, à l'heure actuelle, trop limité pour déduire des résultats des calages un jeu unique de paramètres avec un traitement statistique, chaque jeu a été exploité dans le but d'extrapoler les déformations à long terme lors d'un fluage sous 26 MPa. L'évolution

de la déformation viscoplastique en fonction du temps est représentée sur la figure 8.

La comparaison de ces courbes illustre les difficultés et l'importance du calage d'un modèle de comportement pour la prévision des déformations différées d'ouvrages souterrains sur des échelles de temps très longues. Les simulations analytiques d'un essai de fluage ont donné des résultats très différents : au bout de cinq ans, les déformations viscoplastiques extrapolées varient dans une plage de 1 à 40.

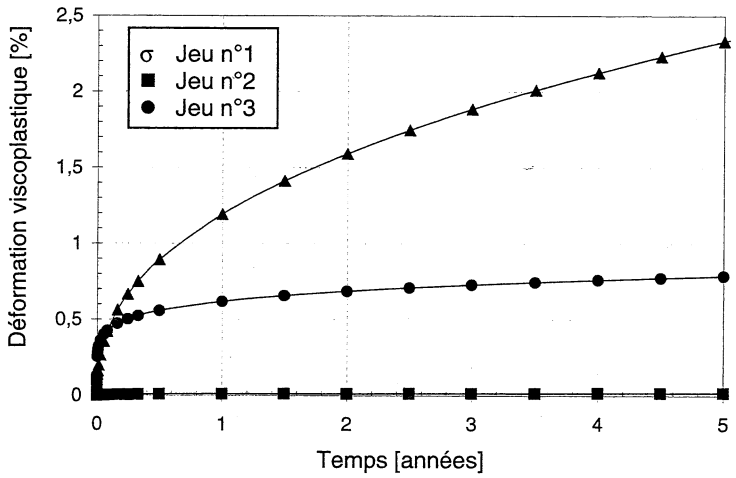

Figure 8. Prévision des déformations différées sous un déviateur de 26 MPa.

4. Conclusions

Les conclusions de cette étude sur le comportement mécanique d'une marne argileuse seront affinées grâce à des essais complémentaires réalisés dans une plage de vitesse de chargement plus large. Les résultats présentés ici ne constituent qu'une première approche. Ils ont permis néanmoins de développer une méthode de calage du modèle rhéologique de Lemaitre et de déterminer différents jeux de paramètres pour cette loi.

Cependant, l'essai de fluage ayant montré que les déformations viscoplastiques ne se développent pas rigoureusement à volume constant comme le suppose la modélisation de Lemaitre, l'introduction dans le modèle de cette dilatance liée à l'endommagement du matériau semble indispensable pour améliorer la prévision des déformations sur des échelles de temps séculaires.

5. Références bibliographiques

Boidy E., Pellet F. (2000) Identification of mechanical parameters for modelling time-dependent behaviour of shales. *Workshop ANDRA, Paris.*

Fabre G. (2001) *Étude expérimentale et théorique du comportement mécanique différé de deux roches sédimentaires.* Mémoire de DEA, Université Joseph Fourier, Grenoble.

Lemaitre J., Chaboche J.L. (1996) *Mécanique des matériaux solides.* Dunod.

Perzyna P. (1966) Fundamental problems in viscoplasticity. *Advances in Applied Mechanics, Vol 9, Academic Press, 243-377.*

Comportement mécanique de roches argileuses lors d'essais de fluage de longue durée

Frédéric Pellet et Géraldine Fabre
Université Joseph Fourier – Laboratoire 3S

Résumé

Dans cette étude du comportement mécanique différé de deux roches argileuses, trois essais de fluage multipalier de longue durée ont été réalisés. Afin de tester l'hypothèse d'une stimulation du fluage, des cycles de charge-décharge ont été mis en œuvre. L'approche expérimentale a été complétée par le calage analytique d'un modèle rhéologique utilisant la loi de Lemaitre, modifiée pour tenir compte du développement des déformations volumiques observées.

1. Introduction

Les roches argileuses ont des propriétés physiques et mécaniques qui en font des formations particulièrement intéressantes pour la construction de stockage souterrain de déchets radioactifs. Cependant, l'auscultation des ouvrages souterrains profonds fait apparaître un développement parfois très important des déformations différées qui traduisent un comportement mécanique non-linéaire de type élasto-viscoplastique endommageable. Cette étude vise, à travers des essais de fluage de longue durée, à améliorer la compréhension du comportement mécanique différé des roches argileuses dont l'origine est encore mal connue.

2. Essais de fluage de longue durée

2.1 Description des roches étudiées

Les essais mécaniques de cette étude ont été réalisés sur deux roches argileuses : l'argilite de l'Est et la marne du Mont d'Or, aux compositions minéralogiques et en particulier aux teneurs en argile, légèrement différentes (cf. tableau 1). Quelques caractéristiques physiques de ces deux roches, mesurées avant les essais, sont présentées dans le tableau 2. La résistance à la compression simple (Rc) de ces deux roches a été mesurée lors d'essais de chargement uniaxial.

Les mesures de vitesse sonique réalisées sur chaque échantillon intact ont mis en évidence l'anisotropie de structure de ces roches sédimentaires, considérées comme orthotropes de révolution. Pour l'argilite de l'Est, la vitesse mesurée parallèlement aux strates est en moyenne supérieure de 10% à la vitesse des ondes mesurée perpendiculairement au litage. Pour la marne du Mont d'Or, le contraste de vitesse est de l'ordre de 15%.

	Quartz	Carbonates	Minéraux argileux	Autres minéraux
Argilite de l'Est[1]	20 à 30 %	20 à 33 %	40 à 45 %	moins de 5 %
Marne du Mont d'Or[2]	10 %	65 %	25 %	/

Tableau 1 : Compositions minéralogiques moyennes des deux roches étudiées.

	Poids volumique ($kN.m^{-3}$)	Teneur en eau (%)	Porosité (%)	Degré de saturation (%)	Rc (MPa)
Argilite de l'Est	23,7	5,9	15,4	87,0	28
Marne du Mont d'Or	25,2	1,0	6,4	36,6	80

Tableau 2 : Caractéristiques physiques et mécaniques moyennes des deux roches étudiées.

2.2 Programme et dispositif expérimental

Le dispositif expérimental est constitué de trois bâtis de fluage dont les systèmes de chargement entièrement mécaniques sont indépendants de l'alimentation électrique.

Afin de connaître l'évolution du tenseur des déformations ε au cours des essais, les échantillons sont instrumentés avec des jauges d'extensométrie. Le nombre de jauges collées dépend, pour une roche orthotrope de révolution, de l'orientation des plans d'isotropie de l'éprouvette testée. Celle-ci est définie par l'angle θ entre $\mathbf{v_3}$ de révolution de l'orthotropie et l'axe **n** de révolution de l'éprouvette (figure 1). Pour une description complète, on se référera à Gatelier et al. (2002).

Nos échantillons ont une orientation θ = 0°. Le tenseur des déformations est donc entièrement défini en les instrumentant avec une jauge axiale et une jauge transversale dans le plan (**n**,**t**), pour mesurer respectivement les déformations ε_{nn} et $\varepsilon_{tt} = \varepsilon_{ss}$. Ces mesures permettent ensuite de calculer la déformation volumique de l'échantillon avec la relation :

$$\varepsilon_{vol} = \varepsilon_{nn} + 2\,\varepsilon_{tt}$$

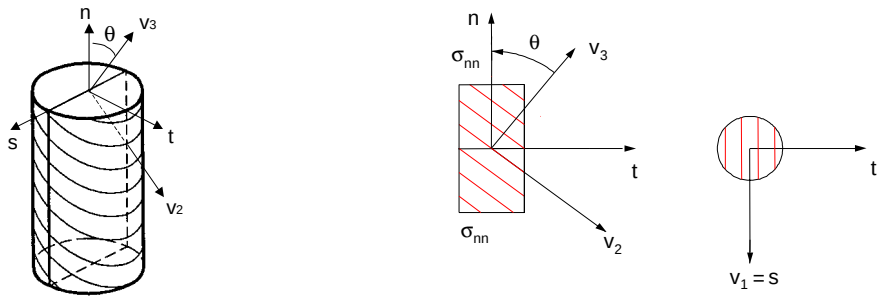

Figure 1. Définition des axes de symétrie d'une éprouvette.

Pour étudier le comportement mécanique différé de l'argilite de l'Est et de la marne du Mont d'Or, nous avons réalisé trois essais de fluage de longue durée sur des échantillons ayant des plans d'isotropie d'orientation, θ = 0°. Pour tester l'hypothèse d'une activation du fluage due à des cycles de charge-décharge, un échantillon a été soumis à plusieurs phases de charge - déchargement partiel.
Le programme expérimental est résumé dans le tableau 3.

Échantillon	Durée de l'essai	Fluage uniaxial
EST 1	321 jours	monopalier
Marne 1	230 jours	multipalier avec cycles de charge-décharge partielle
Marne 2	145 jours	multipalier

Tableau 3. Essais réalisés sur les échantillons d'argilite de l'Est et de marne du Mont d'Or.

2.3 Résultats expérimentaux

Lors de ces trois essais, malgré leur durée et les déviateurs imposés, seules les phases de fluage primaire et secondaire ont pu être observées ; l'accélération des déformations lors de la phase de fluage tertiaire n'a jamais été atteinte.

L'échantillon d'argilite de l'Est, EST 1, a été soumis à un déviateur de 26 MPa ($\approx$93 % de Rc) maintenu constant à plus ou moins 0,1 MPa près pendant 321 jours (figure 2).

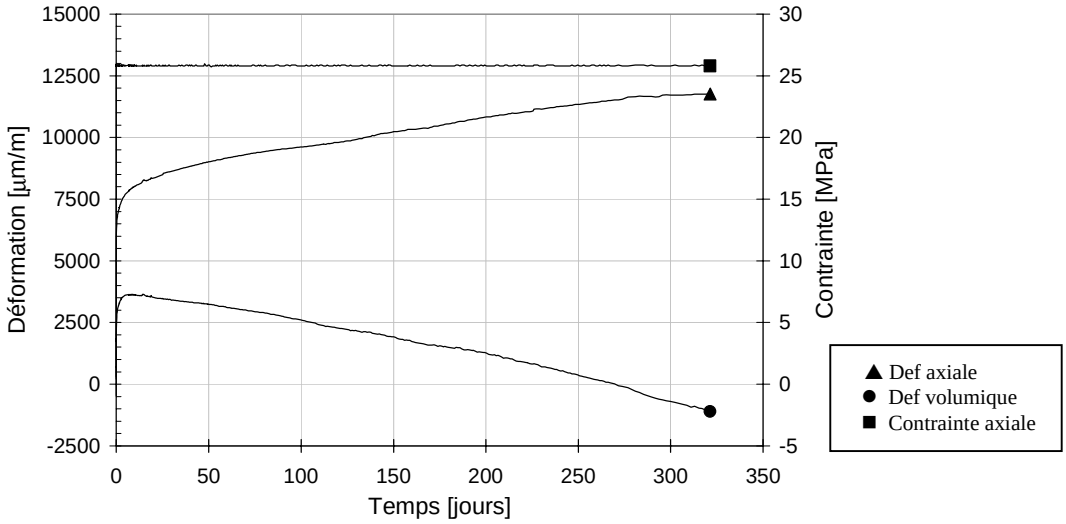

Figure 2. Courbe de fluage : Echantillon EST 1.

Le calcul de l'évolution de la vitesse de déformation en fonction du temps montre qu'au 25ème jour de l'essai cette vitesse se stabilise à $2{,}2.10^{-10}$ s^{-1}. L'évolution de la déformation volumique en fonction du temps révèle qu'après une importante contraction (ε_{vol} croissante) durant le fluage primaire, on observe une dilatance de l'échantillon qui se poursuit durant la phase de fluage secondaire à la vitesse de $1{,}0.10^{-10}$ s^{-1}.

L'échantillon de marne du Mont d'Or, Marne 1 a été soumis à cinq paliers de chargement croissants maintenus constants à plus ou moins 0,2 MPa près, et plusieurs phases de décharge jusqu'à 25 MPa maintenues 24 heures, qui ont montré une très faible amplitude de recouvrance. (figure 3). Lors du dernier palier, imposé à 51 MPa (65 % de Rc), à partir du 143ème jour de l'essai, il semble que la phase de fluage secondaire soit amorcée : la vitesse de déformation se stabilise à la valeur très faible de 3.10^{-6} $jour^{-1}$.

Pour évaluer la validité de l'hypothèse d'une activation du fluage par la mise en œuvre de cycles de décharge-recharge, la vitesse de fluage moyenne sur 24 heures a été calculée après chaque cycle. Les résultats sont représentés sur le graphe de la figure 4, chaque symbole correspondant à l'un des cinq paliers de chargement. Pendant le second palier, imposé à 38 MPa, la vitesse de fluage moyenne sur 24 heures augmente après un cycle. En revanche, lors du palier suivant imposé à 44 MPa, la tendance est inversée : les cycles semblent ralentir le fluage.

L'échantillon Marne 2 a été soumis à 4 paliers de chargement maintenus constants à plus ou moins 0,5 MPa près pendant plusieurs semaines (figure 5). Lors du dernier palier, imposé à 55 MPa (70 % de Rc), la phase de fluage secondaire n'est toujours pas amorcée : la vitesse de déformation décroît et les déformations s'amortissent.

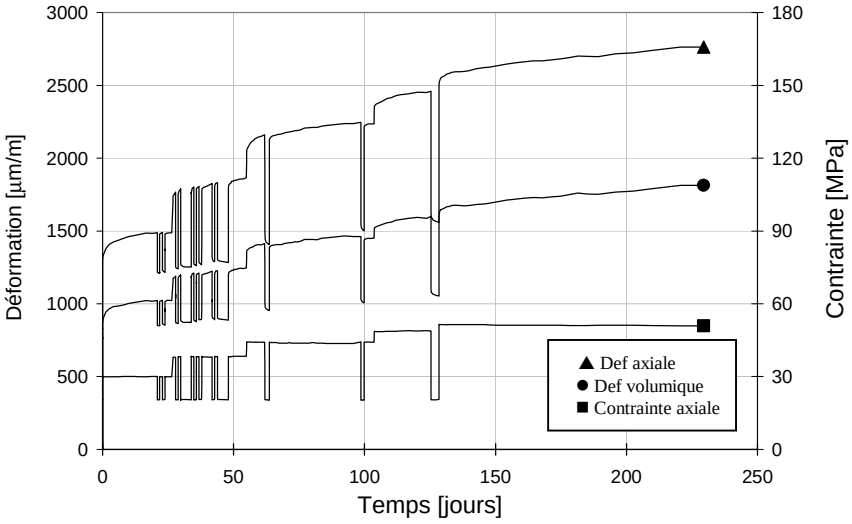

Figure 3. Essai de fluage oligocyclique réalisé sur l'échantillon de marne du mont d'or, Marne 1.

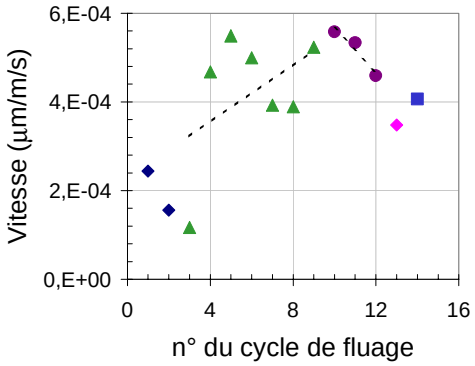

Figure 4 : Vitesses de fluage calculées sur 24 heures après un cycle de décharge-recharge.

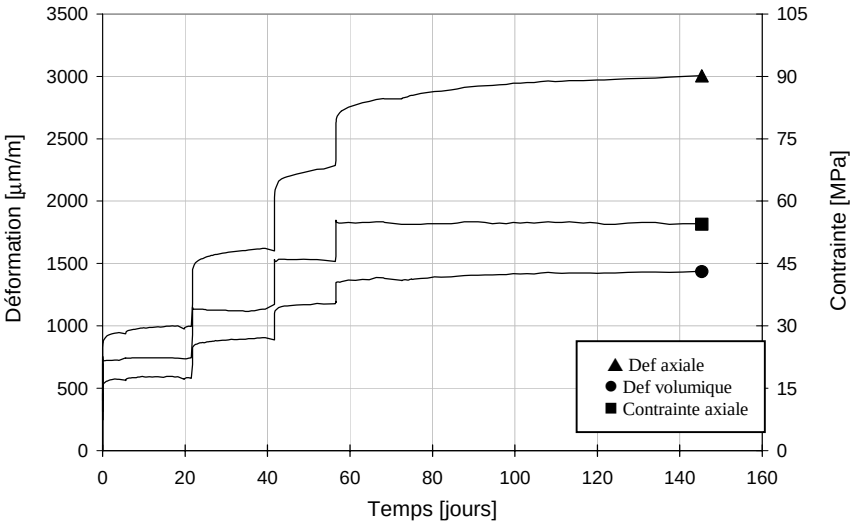

Figure 5. Essai de fluage oligocyclique réalisé sur l'échantillon de marne du mont d'or, Marne 2.

3. Modélisations des essais de fluage

3.1 Extension de la loi de comportement viscoplastique de Lemaitre : prise en compte de la déformation volumique

Le modèle de Lemaitre représente le comportement du solide élasto-viscoplastique à écrouissage isotrope ; il est décrit de manière très complète dans Boidy (2002). Sa loi se base sur l'hypothèse d'un développement des déformations viscoplastiques à volume. Expérimentalement, nous avons mis en évidence que cette deuxième hypothèse n'est pas vérifiée pour nos matériaux. Donc, pour tenir compte de la déformation volumique, dans cette loi viscoplastique, Pellet et al. (2002) a introduit un paramètre α qui traduit la contractance ou la dilatance du matériau. Cette loi de Lemaitre modifiée s'écrit :

$$\dot{\varepsilon}_{vp} = \frac{1}{\sqrt{\frac{2}{9}\alpha^2 + 1}}\,\dot{p}\left(\frac{3}{2}\frac{S}{\sigma_{eq}} + \frac{\alpha I}{3}\right)$$

où : *S*, est la partie déviatorique du tenseur des contraintes

$$\sigma_{eq} = \sqrt{\frac{3}{2}s : s}$$

Un α positif traduit un comportement contractant et un α négatif un comportement dilatant. Avec α = 0, on retrouve la loi de Lemaitre. Avec ce paramètre, les expressions explicites des déformations axiales et transversales lors d'un essai de fluage uniaxial sont finalement les suivantes :

$$\varepsilon_{nn} = \frac{q}{E} + \left(\frac{\alpha}{3} + 1\right)\left(\frac{2}{9}\alpha^2 + 1\right)^{\frac{-N}{2(N+M)}}\left[\frac{M+N}{N}\left(\frac{\left(1+\frac{\alpha}{3}\right)\sigma}{K}\right)^N t\right]^{\frac{M}{M+N}}$$

$$\varepsilon_{tt} = -\nu\frac{q}{E} + \left(-\frac{1}{2} + \frac{\alpha}{3}\right)\left(\frac{2}{9}\alpha^2 + 1\right)^{\frac{-N}{2(N+M)}}\left[\frac{M+N}{M}\left(\frac{\left(1+\frac{\alpha}{3}\right)\sigma}{K}\right)^N t\right]^{\frac{M}{M+N}}$$

Avec : *q*, le déviateur de contrainte
M, N et K, les paramètres du modèle, caractéristiques du matériau.

3.2 Modélisation des essais de fluage

Avec le modèle décrit au paragraphe précédent, en utilisant la méthode de calage explicitée par Fabre et Pellet (2002), il a été possible de modéliser analytiquement les trois essais de fluage de longue durée réalisés sur l'argilite de l'Est et la marne du Mont d'or.

Dans le cas de l'essai Marne 1, seule la courbe enveloppe, sans les cycles de décharge, ont été pris en considération. Les calages obtenus pour les essais Marne 1 et marne 2 sont très satisfaisants comme le montrent la figure 6b. Les paramètres calés sont répertoriés dans le tableau 4.

Cependant, avec ce modèle analytique simple, il est impossible de modéliser à l'aide d'un unique paramètre α les phases de contractance puis de dilatance observées durant l'essai de fluage sur l'échantillon Est 1. Seule la phase de contractance a donc été calée (figure 6a). Pour une meilleure

modélisation, il est indispensable d'introduire dans les équations de la loi utilisée l'endommagement du matériau.

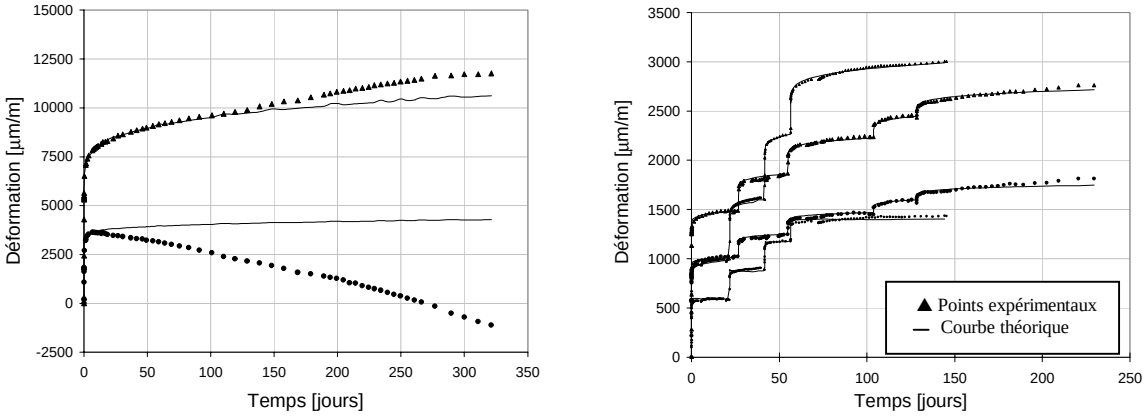

Figure 6. Calage analytique du modèle de Lemaitre modifié sur les essais de fluage de longue durée : (a) : argilite de l'Est, (b) : marne du Mont d'Or.

	E (GPa)	ν	N	M	K (MPa.s)	α
Est 1	5,0	0,2	25	6	180	0,47
Marne 1	23,0	0,15	1,07	0,31	$1{,}27.10^{15}$	0,65
Marne 2	26,8	0,13	2,85	0,79	$2{,}36.10^{6}$	0

Tableau 4. Jeux de paramètres obtenus par le calage analytique du modèle de Lemaitre modifié sur les trois essais de fluage long.

4. Conclusions

D'après les essais réalisés, il semble difficile de conclure quant à l'influence de cycles de charge-décharge sur l'activation des déformations du fluage. D'autres essais, comprenant un nombre de cycles plus importants, sont en cours et viendront compléter ces premiers résultats. Les phases de fluage tertiaire n'ont pu être observées mais ces essais de fluage ont montré que les déformations viscoplastiques se développent à volume non constant. L'approche expérimentale a donc été complétée par un premier calage analytique d'un modèle rhéologique utilisant la loi de Lemaitre, modifiée pour tenir compte de cette constatation.

Références :

Boidy E, *Comportement mécanique différé des roches tendres autour des excavations souterraines*, thèse de doctorat de l'Université Joseph Fourier, Grenoble, 2002.

Fabre G, Pellet F, *Identification des caractéristiques visqueuses d'une roche argileuse*, Int. Symp. on Identification and Determination of Soil and Rock Parameters for Geotechnical Design, Paris, 2002.

Gatelier N, Pellet F, Loret B, *Mechanical damage of an anisotropic rock under cyclic triaxial tests*, Int. J. Rock Mech. Min. Sci. & Geomech. Abstr., 39, 335-354, 2002.

Pellet F, Hajdu A, Boulon M, F. Deleruyelle & F. Besnus, *Numerical modelling of underground structures taking into account the visco-plastic behaviour and rock damage*, NUMOG VII, 2002.

Rock Mech. Rock Engng. (2004) 37 (1), 3–23
DOI 10.1007/s00603-003-0001-4

Rock Mechanics and Rock Engineering
Printed in Austria

Experimental Study of Mechanical Behaviour of Rock Joints Under Cyclic Loading

By

M. K. Jafari[1], **F. Pellet**[2], **M. Boulon**[2], and **K. Amini Hosseini**[1]

[1] International Institute of Earthquake Engineering and Seismology, Tehran, Iran
[2] Laboratory 3S, University Joseph Fourier, Grenoble, France

Received March 25, 2002; accepted February 4, 2003
Published online June 17, 2003

Summary

Evaluation of the effects of small repetitive earthquakes on the strength parameters of rock joints in active seismic zones is of interest of the designers of underground constructions. In order to evaluate these effects, it is necessary to study the behaviour of rock joints under dynamic and cyclic loadings. This paper presents the results of a systematic study on the behaviour of artificial rock joints subjected to cyclic shearing. More than 30 identical replicas have been tested using triaxial compression devices under different conditions of monotonic and cyclic loading. At the first stage a few samples have been tested in monotonic loading modes under various confining pressures and rate of displacement. In the second series of tests, small cyclic loads were applied on the samples for increasing number of cycles, frequency levels and stress amplitudes. These were then followed by monotonic loading again. The variations of maximum and residual shear strengths for each test have been studied. The results show increase of shear strength as a result of the increase in confining pressure and they display decrease of shear strength due to the increase of rate of loading, number of cycles, frequency levels and stress amplitudes.

Keywords: Roughness, second order asperities, damage, rate of loading, number of cycles, frequency level, stress amplitude.

1. Introduction

About two decades ago, there was a general believe that underground openings are not vulnerable to earthquakes and seismic loads when compared with ground surface structures. Some studies during the last years of the 70th, such as Dowding and Rozen (1978), and first years of the 80th, such as Owen and Scholl (1981), showed that underground openings are not quite safe when subjected to strong earthquakes. During the years after, Peak Particle Velocity (PPV) and Peak Particle Acceleration (PPA) of the ground motions have been used frequently by most of the designers as the key

parameter for assessing the dynamic stability of underground excavations, as mentioned by Brady and Ma (1999). Some researchers such as Dowding and Rozen (1978) and Sharma and Judd (1991) have presented experimental relations between PPV and PPA with possible damage levels of underground structures.

During each weak earthquake, some small changes occur in the rock masses along the joint surfaces and discontinuities. Accumulations of these changes during the repetitive seismic events may cause considerable displacements or even catastrophic collapses. Some of the results of the repetitive seismic loading on rock masses are accumulation of small displacements, cyclic fatigue, degradation of the asperities, etc. Considering small repetitive earthquakes, the main question is their possible effects on the properties of rock masses and if the peak parameters such as PPV or PPA are sufficient for evaluation of the stability of underground excavations. In order to find a proper answer, the behaviour of rock joint samples should be studied under cyclic loading. This could be achieved under two different conditions: the behaviour of rock joints before considerable sliding of one rock wall on the other one and the behaviour during sliding.

Most of the works carried out so far, for example Hutson and Dowding (1990), Ghosh et al. (1995) and Armand et al. (1998), have focused on the effect of cyclic loading during sliding. The methods presented in these researches can be used to evaluate the asperity degradation during the strong earthquakes that have enough energy to make considerable relative displacement between two sides of the joint surface. During the small earthquakes however, there is no large relative displacement between the joint surfaces due to the low stress applied in each event, so there would not be significant degradation of the joint surfaces. In these cases mostly accumulations of the small displacements and cyclic fatigue may occur that could decrease the joint shear strength. These conditions have been studied by Hencher (1980) and Barbero et al. (1996) that considered the behaviour of the discontinuities just prior to the occurrence of relative displacements between the contact surfaces.

In this research the effects of small cyclic loading on shear strength of rock joints using identical saw-tooth samples have been studied. In addition some experimental equations that cover the trends of the obtained results would be presented. It is recommended to complete this study with further tests on rock samples with different roughness, mineralogical composition and structure. The accuracies of the presented relations should also be improved by more tests on real samples.

2. Physical Joint Models

2.1 Experimental Constraints

In order to carry out an experimental study on rock joints, it is necessary to prepare identical samples (considering geometrical and constitutive properties) and to evaluate the relative displacements during the tests. The level of confining pressure and cyclic loading conditions should also be determined before the tests begin.

As the total relative displacements in the proposed tests are lower than 1 mm in most cases, the triaxial compression method has been selected to perform all the tests. It is possible in these tests to model jointed rock samples in a state similar to their real

underground conditions during cyclic loading. Of course this method has its own limitations. The main problem is the orientation of the joint surface inside the triaxial testing cell.

By arranging the sample inside the testing cell with a proper dip of joint plane (lower than 45 degrees with respect to the sample axis) this limitation can be overcome, as discussed by Goodman (1989). Also it is possible to determine the maximum allowable dip of the joint surface for such tests by using the Mohr-Coulomb criterion as follows, Pellet (1993):

For intact rock

$$\sigma_1 = 2c_r \tan\left(\frac{\pi}{4}+\frac{\phi_r}{2}\right) + \sigma_3\left[1 + 2\tan\phi_r \tan\left(\frac{\pi}{4}+\frac{\phi_r}{2}\right)\right] \tag{1}$$

For jointed rock

$$\sigma_1 = [c_j(1 + \tan^2\theta) + \sigma_3 \tan\theta(1 + \tan\phi_j \tan\theta)]\left(\frac{1}{\tan\theta - \tan\phi_j}\right) \tag{2}$$

where

ϕ_r is the internal friction angle of intact rock,
c_r is the cohesion of intact rock,
θ is the angle of inclination of the joint (as shown in Fig. 1),
ϕ_j is the friction angle of the joint,
c_j is the cohesion on the joint surface that is zero in the tested samples.

c_r can be evaluated from the following equation:

$$c_r = \frac{\sigma_c(1 - \sin\phi_r)}{2\cos\phi_r} \tag{3}$$

where σ_c is the uniaxial compression strength of the intact rock.

By considering different values for θ in the above equations and calculating σ_1 and σ_3 levels in different conditions, it is possible to determine the maximum possible joint surface orientation in which shearing on the joint occurs before failure in the rock.

2.2 Joint Shape

The surfaces of the tested rock joints are given regular triangular saw-tooth shapes with maximum inclination angle of (*i*-value) 15 degrees having small roughness on the surfaces of the teeth, as shown in Figs. 1 and 2. By using these shapes it is possible to observe the changes on the shear surface before and after each test. In addition the test results can be analysed easier. The joint surface area for all the samples is 30 cm^2, having 5 main asperities with wavelength 1.5 cm and amplitude 0.2 cm. It should be considered that the number and geometrical specifications of the teeth have been chosen based on practical and analytical evaluations. Other geometrical parameters of the joint surface and sample are shown in Figs. 1 and 2.

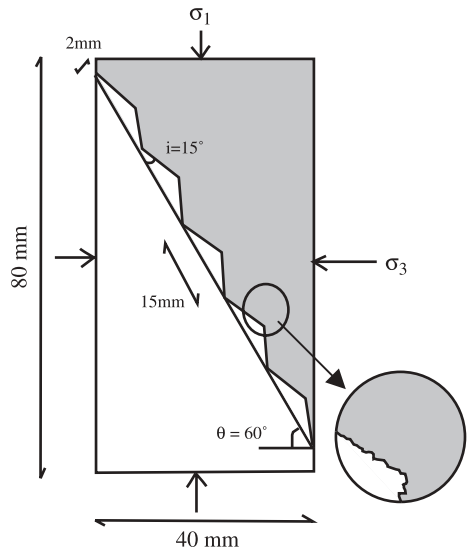

Fig. 1. Schematic section and dimensions of the prepared saw-tooth sample

2.3 Material of the Physical Model

Several studies have been carried out to develop the best possible physical models for testing intact and jointed rocks. These studies have been performed in two main

groups. In the first group Stimpson (1970), Huang and Doong (1990), Indraratna (1990), Mostyn and Bagheripour (1998), and Kusumi et al. (1998) developed their physical models using natural and artificial materials (mostly a mixture of cement or plaster with other materials such as sand). In the second group Hutson and Dowding (1990), Boulon (1995), and Armand (2000) have used rock samples with natural joint surfaces or have made artificial joints in natural rock samples using sawing machines, hydraulic or Brazilian fracturing.

Although both of the above mentioned methods have their own advantages and disadvantages, it seems that the first method would be ideal for modelling rock samples with low to medium strength (unconfined compressive strength below 60 MPa) and the second method for medium to hard rock (unconfined compressive strength above 60 MPa). Also it should be considered that the first method is easier than the second one as sawing rock materials in precise dimensions needs special devices such as CNC (Computer Numerical Control) machines, that are not easily available in rock mechanics laboratories.

In the present study the first method has been used. A special cement based mortar, called Rapidex (Lafarge Company) has been used to produce the replicas. Its uniaxial compression strength is about 55 MPa and its tensile strength (using Brazilian test) is about 8 MPa after about 24 h. For evaluation of the friction angle and cohesion, three samples have been compressed triaxially at different levels of confining pressure (2, 4 and 8 MPa) and the evaluated friction angle was about 40 degrees and cohesion was about 16.8 MPa. In order to prepare each sample, the mortar has been passed through a sieve of 0.5 mm, to remove its large particles, and then has been mixed with water in 5 to 1 weight ratio.

2.4 Sample Preparation

To produce samples as physically similar as possible, a special casting procedure has been developed. The casts consisted of PVC tubes and prismatic moulds made from silicon rubber called Silastic (Rhone-Poulene Company). The prismatic moulds of each side of the joint were put into the PVC tube and filled with the mixture of mortar and water. In each stage of sample preparation, three additional samples without joint were also prepared to determine the uniaxial compression and tensile strength of each individual sample in its same age. After 24 h the two ends of the samples were smoothed with a surface grinding machine to produce smooth and parallel surfaces perpendicular to their cylinder axis. One of the final prepared samples is shown in Fig. 2.

3. Testing Devices

The main part of experiments has been conducted using the triaxial compression machine at Laboratory 3S (Lab. 3S) of University of Joseph Fourier, in Grenoble. In addition, some of the cyclic tests were also conducted with the triaxial machine in the Rock Mechanics Laboratory (LMR) in the Swiss Institute of Technology (EPFL), in Lausanne. Photographs of these two units are shown in Fig. 3a and b.

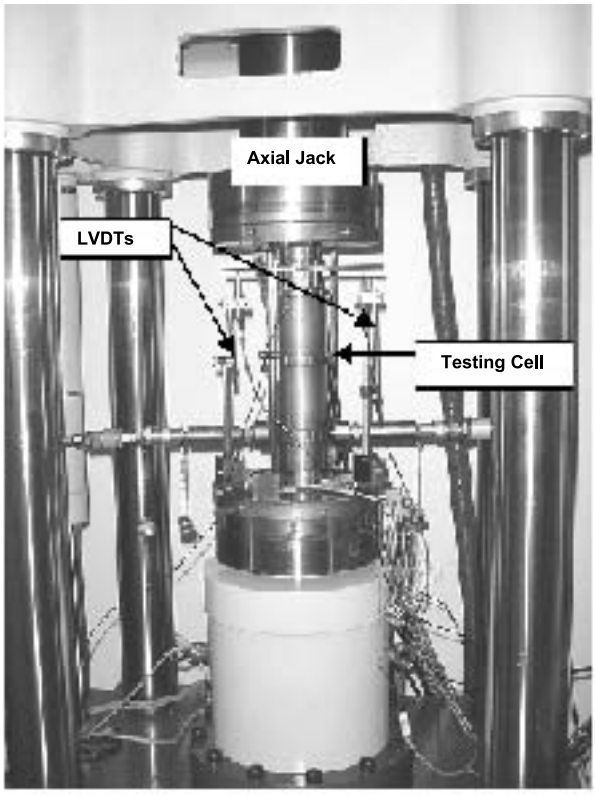

a

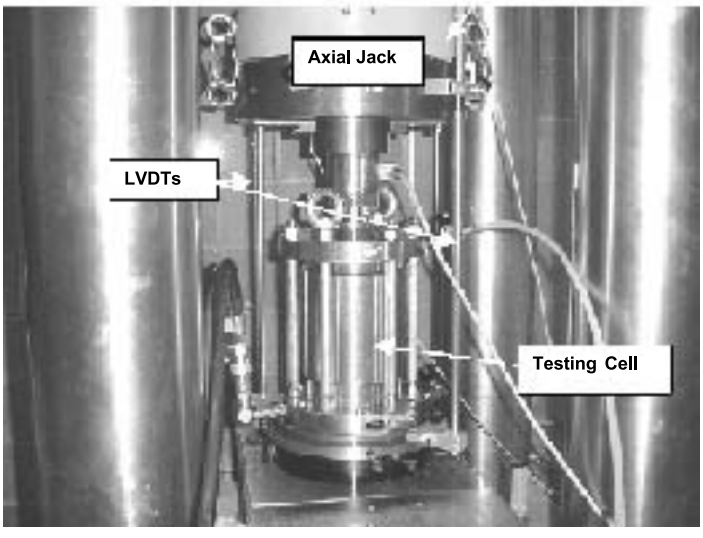

b

Fig. 3. Testing cell and axial jack; **a** laboratory 3S; **b** laboratory LMR

3.1 Testing Cells

The testing cell in Lab. 3S was a Boehler cell consisting of three parts: base, hollow cylinder and upper piston. The sample was placed on the base after greasing its two ends (to limit the effects of friction) and then covered with a membrane. After filling the cylinder with oil and being sure that there is no air inside the cylinder and its oil passages, then the upper piston was pushed on the upper side of the hollow cylinder. In LMR the testing cell had some differences and the hollow cylinder had a larger diameter. Other procedures of installing a sample into the cell were nearly the same except positioning the upper part and piston (Fig. 3).

3.2 Testing Machine

The testing machine in Lab. 3S involved two different hydraulic equipments for applying the axial load (Schenck Corporation) and the confining pressure (SBEL) and two separate control systems for axial and lateral pressures. In LMR the testing machine involved two different systems for axial loading and confining pressure (Walter + Bai). The total loading capacity of the axial hydraulic jack in Lab. 3S is 1000 kN and in LMR is 2000 kN and for confining pressure it is about 100 MPa in Lab. 3S and 20 MPa in LMR respectively. All loading systems have been equipped with a function generator to control monotonic and cyclic loads. Different modes of loading could be applied, however in the performed tests the monotonic loading and complete cyclic loading (between positive and negative values) with sinusoidal shape have been used. The maximum frequency of axial loading applied in the cyclic tests was 1 Hertz.

All measurements of displacements, force, confining pressure and time, were collected and recorded with IBM PC based systems, with the appropriate sampling rates (0.1 second for cyclic tests and 0.5 second for monotonic tests). In Lab. 3S, 4 vertical LVDTs (as shown in Fig. 3a) have been used to measure simultaneously the vertical displacements. Three of them were fixed around the testing cell, between the moving upper piston and its fixed lower part, and the last one was an individual LVDT connected to the main control machine. In LMR 3 LVDTs have been used for measuring the axial displacement (Fig. 3b). Although there were not considerable differences in the recorded values of LVDTs, their mean value has been used to analyse the data. Confining pressures were controlled with separate systems but were recorded during the tests with the same computers and data acquisition systems. All displacements have been measured between the moving piston and fixed part of the testing cells, as shown in Fig. 3.

Monotonic loading was conducted under displacement control mode and cyclic loading was performed in a combination of stress control and displacement control modes. In these tests, after each part, the system was adjusted to the other mode manually. Cyclic loads in different number, frequency, and stress amplitude were applied on each sample and then monotonic loads were applied to measure the difference of peak and residual shear strength in different testing conditions.

3.3 Evaluation of the Effects of Internal Friction of the Testing Cells and Membrane on Shear Strength

For the evaluation of the effects of piston friction with hollow cylinder, some tests have been performed without sample, with the cylinder full of oil. The results showed that the total effect due to friction is about 10% of the maximum applied load, which is removed during analysis. Also the effects of the membrane stiffness on shear strength were studied by testing the samples with one, two and three layers of membrane. The differences in the results were negligible showing the small effect of membrane stiffness on the final results.

3.4 Reproducibility of the Test Data

In order to evaluate the reproducibility of the test results, three identical samples have been tested in monotonic mode in the same conditions. The total differences between the results of these tests were approximately 1% of maximum value of shear strength. However, in order to obtain a better correlation of the testing results and to find the best relation from the trends of data (specially for the cyclic tests), additional tests in each condition were needed.

4. Testing Procedures and Results

The variation of shear strength under different conditions of monotonic and cyclic loading has been studied. The tests were performed in two main groups, monotonic and cyclic modes. In the first group the monotonic effects of the confining pressure and rate of axial displacement on shear strength have been considered, whereas in the second group the cyclic effects of the number of cycles, frequency and stress amplitude on peak and residual shear strengths have been studied.

4.1 Testing Program

A summary of the tests performed, the parameters considered in each test, and the results of some of the tests are given in Table 1. In this table the peak normal stress (σ_n) is the normal stress value corresponding with the maximum axial stress. This could be calculated by the following equation (Goodman, 1976):

$$\sigma_n = \sigma_3 + (\sigma_1 - \sigma_3)\sin^2\theta \tag{4}$$

4.2 Effect of Confining Pressure

The first series of tests explored the effect of confining pressure on the shear strength of the artificial jointed samples. Different levels of confining pressure from 0 to 6 MPa applied on different identical samples and then monotonic axial loading at controlled displacement with a rate of 0.05 mm/min were applied. The selected levels of confining pressure are similar to the levels normally encountered in underground excavations at depth lower than 300 m.

Table 1. Summary of the results of performed tests

Test no.	Type of the test	Changing parameter	Axial displacement at peak point mm	Peak shear stress MPa	Peak normal stress MPa	Residual shear stress MPa	Shear displacement at peak point mm
1	Monotonic (effect of confining pressure)	Confining pressure (1.2 MPa)	0.17	1.81	2.25	1.31	0.15
2	Monotonic (effect of confining pressure)	Confining pressure (4 MPa)	0.20	3.39	5.96	3.05	0.17
3	Monotonic (effect of confining pressure)	Confining pressure (6 MPa)	0.17	4.33	8.50	3.33	0.15
4	Monotonic (effect of rate of loading)	Rate of loading (0.05 mm/min)	0.20	3.39	5.96	3.05	0.17
5	Monotonic (effect of rate of loading)	Rate of loading (0.1 mm/min)	0.39	3.04	5.76	2.66	0.34
6	Monotonic (effect of rate of loading)	Rate of loading (0.2 mm/min)	0.34	2.66	5.53	2.51	0.30
7	Monotonic (effect of rate of loading)	Rate of loading (0.4 mm/min)	0.28	2.45	5.42	2.45	0.24
8	Cyclic – monotonic (effect of number of cycles)	Number of cycles (25 cycles)	0.09	3.30	5.91	2.94	0.08
9	Cyclic – monotonic (effect of number of cycles)	Number of cycles (50 cycles)	0.15	3.23	5.86	2.84	0.13
10	Cyclic – monotonic (effect of number of cycles)	Number of cycles (100 cycles)	0.27	3.15	5.82	2.75	0.23
11	Cyclic – monotonic (effect of number of cycles)	Number of cycles (300 cycles)	0.15	3.09	5.78	2.72	0.13
12	Cyclic – monotonic (effect of number of cycles)	Number of cycles (500 cycles)	0.11	3.04	5.75	2.68	0.09
13	Cyclic – monotonic (effect of number of cycles)	Number of cycles (1000 cycles)	0.08	3.00	5.74	2.64	0.07
14	Cyclic – monotonic (effect of number of cycles)	Number of cycles (3000 cycles)	0.11	2.99	5.73	2.63	0.10
15	Cyclic – monotonic (effect of frequency of cycles)	Frequency (1 Hz)	0.27	3.15	5.82	2.75	0.23
16	Cyclic – monotonic (effect of frequency of cycles)	Frequency (0.5 Hz)	0.50	3.26	5.88	2.88	0.43
17	Cyclic – monotonic (effect of frequency of cycles)	Frequency (0.2 Hz)	0.15	3.34	5.93	2.94	0.13
18	Cyclic – monotonic (effect of amplitude of cycles)	Amplitude of cycles (0.5 MPa)	0.42	2.93	5.69	2.93	0.36
19	Cyclic – monotonic (effect of amplitude of cycles)	Amplitude of cycles (1.6 MPa)	0.23	2.65	5.52	2.65	0.20
20	Cyclic – monotonic (effect of amplitude of cycles)	Amplitude of cycles (1.8 MPa)	0.15	2.32	4.83	2.32	0.13

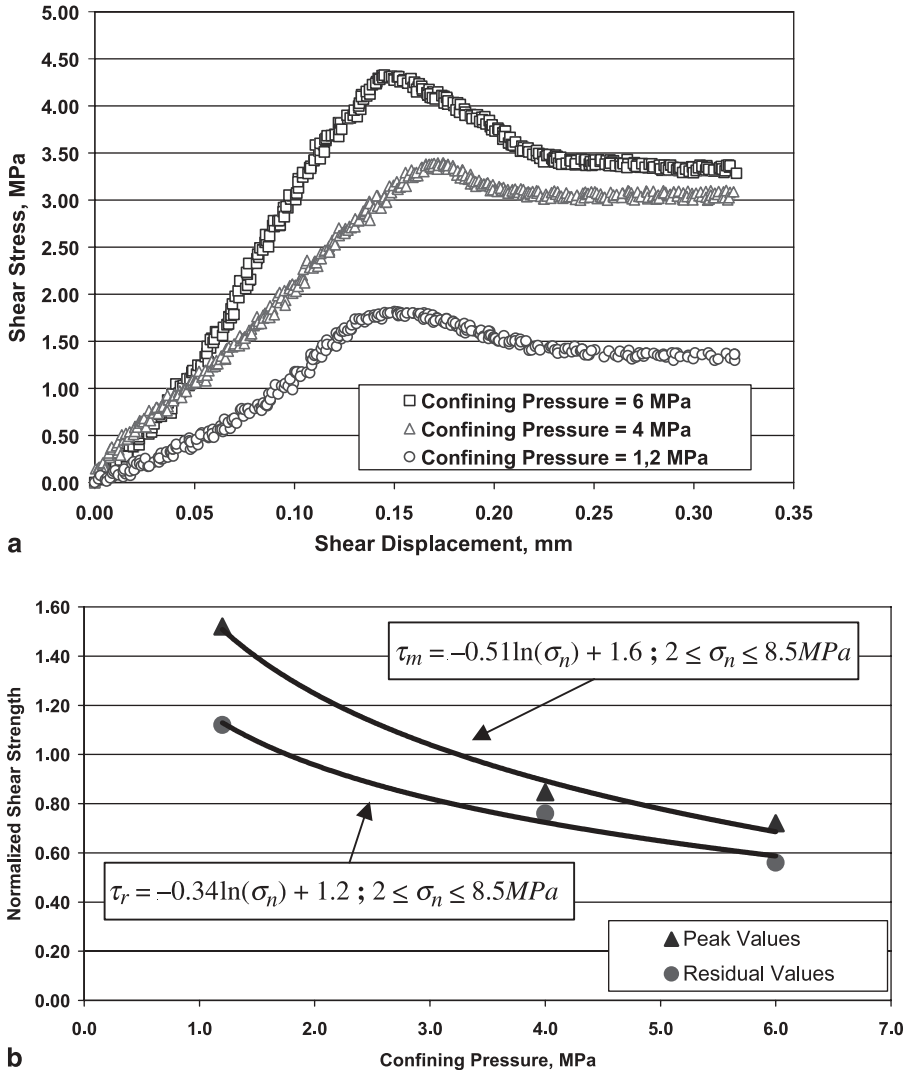

Fig. 4. **a** Shear strength versus shear displacement at different levels of confining pressure; **b** normalized peak and residual shear strength (normalized by confining pressure) versus confining pressure

The resulting shear strength versus shear displacement responses in Fig. 4a show a peak and residual value of shear strength. Goodman (1976) characterised this type of curve as representative of rough unfilled joints. There are three distinct regions for each curve in Fig. 4a, identified as elastic, peak and residual or plastic parts. In this paper, the maximum shear stress, τ_m, is called the peak shear strength and the minimum value of post peak shear stress is called the residual shear strength, τ_r. Figure 4b gives plots of normalized peak and residual shear strength (normalized by confining pressure) versus confining pressure. As shown in this figure, there are non-linear

trends for increasing shear strength with confining pressure. The best fit of the data gives the following relations:

Peak shear strength:

$$\tau_m = 1.82 \ln(\sigma_n) + 0.30 \quad \text{for} : 2 < \sigma_n < 8.5\,\text{MPa} \tag{5}$$

Residual shear strength:

$$\tau_r = 1.48 \ln(\sigma_n) + 0.34 \quad \text{for} : 2 < \sigma_n < 8.5\,\text{MPa} \tag{6}$$

where τ_m is peak shear strength, τ_r is residual shear strength and σ_n is the normal stress.

It can be concluded that the confining pressure has an important effect on the shear strength of the jointed sample, mainly for the lower range of values. By increasing the level of confining pressure, this effect decreases nearly logarithmically, which means that for very high values of confining pressure the effect of confinement on shear strength would be of a second order of importance. Hutson and Dowding (1990) and Armand et al. (1998) have reported similar results by using direct shear tests. It also should be noted that for all the samples, observations done after each test showed small changes in first order asperities over the shear surface in comparison with their initial shapes. These small changes were due to the limited applied shear displacements and relatively low level of confining pressure. There was no evidence of severe damage on the main teeth after each test, so it can be concluded that the changes occurred only on the second order asperities and roughness on the surfaces of the main teeth.

4.3 Influence of Rate of Axial Displacement

The second series of tests were performed in order to investigate the influence of the axial displacement rate on the shear strength. Four monotonic loading tests at different displacement rates equal to 0.05, 0.1, 0.2 and 0.4 mm/sec have been performed with a confining pressure of 4 MPa. The results obtained are shown in Fig. 5a. The variation of the shear strength due to the rate of axial displacement is shown in Fig. 5b, as normalized peak and residual shear strength (normalized by confining pressure) versus rate of axial displacement. The logarithmic trends between the data can be represented by the following equations:

Peak shear strength:

$$\tau_m = -0.46 \ln(\dot{w}) + 1.98 \quad \text{for} : 0.05 < \dot{w} < 0.4\,\text{mm/min} \tag{7}$$

Residual shear strength:

$$\tau_r = -0.28 \ln(\dot{w}) + 2.12 \quad \text{for} : 0.05 < \dot{w} < 0.4\,\text{mm/min} \tag{8}$$

where $\dot{w}$ is the rate of axial displacement.

Figure 5b shows that the shear strength decreases as the axial displacement rate increases. These new peak and residual values can be called fast peak and fast residual as used by Fearon (1999). Similar results have been reported by Scholtz (1990) and Boulon (1995). Another important result is the reduction of the effect of roughness for high values of shear velocity. As shown in Fig. 5a, for higher levels of displacement

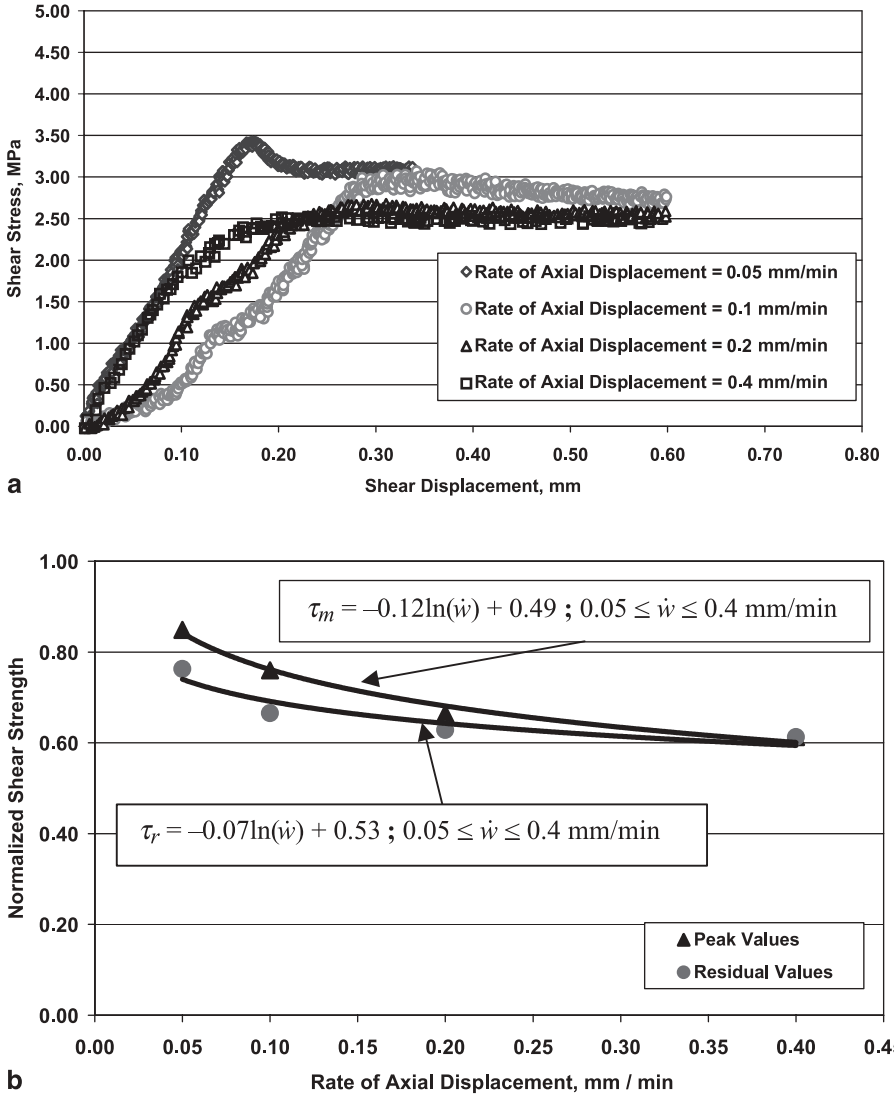

Fig. 5. **a** Variations of shear stress with rate of axial displacement under 4 MPa of confining pressure; **b** normalized peak and residual shear strength (normalized by confining pressure) versus rate of axial displacement

rates, the differences between peak and residual values become negligible. It probably means that when the rate of axial displacement and thus the shearing velocity increases, the secondary asperities do not play an important role in defining the shear strength of the jointed rocks. This remark should be taken into account for evaluating the rock mass maximum shear strength at high shear velocity (as in the case of seismic loading). The results obtained are in accordance with the previous studies reported by Crawford and Curran (1981) and Hutson and Dowding (1990). Of course, based on the presented results it seems that the importance of shear velocity is less than other

parameters such as joint roughness, confining pressure and uniaxial strength of intact rock.

The reduction of shear strength due to shearing velocity can be evaluated by considering the adhesion theory, which states that the frictional resistance is proportional to the true area of contact. As discussed by Sture et al. (1984), the true area of contact may be smaller for surfaces that are only in contact for short period of time due to a lag in elastic or plastic deformation. Thus rapidly shearing hard surfaces might exhibit lower shear strength.

4.4 Effect of Experiencing Small Cyclic Loads on Shear Strength

The effects of three different cyclic parameters including the number of cycles and their frequency and stress amplitude have been studied. For modelling of small repetitive earthquakes, small cyclic loads were applied to identical samples (stress control mode), which were then subjected to monotonic loading (displacement control mode) to evaluate the new peak and residual shear strength of the samples after experiencing small cyclic loads. Brief descriptions of the testing procedures and of the results obtained are discussed in the following.

4.4.1 Effect of the Number of Cycles

The first series of cyclic-monotonic tests focused on the effect of the number of cycles of loading (in 25, 50, 100, 300, 500, 1000 and 3000 cycles). These tests have been performed using the triaxial machine in Lab. 3S under a confining pressure of 4 MPa. The stress amplitude in all the tests was about half of the maximum value attained in monotonic tests, with a rate of 0.05 mm/min. Also the frequency of the cyclic loading in all the tests was about 1 Hz.

The method of loading was a combination of stress control and displacement control modes as already discussed. The rate of axial displacement during the displacement control tests was about 0.05 mm/min. Figures 6 to 10 show the results of these tests. The small observed variations of axial displacement corresponding with the peak values can be related to the possible experimental constraints, as taking place after the first part of the test (controlled stress) and before starting the second part (controlled displacement).

Figure 11 depicts the normalized peak and residual values of shear strength versus the number of cycles. The following equations can be used to fit the trends of behaviour:

Peak shear strength

$$\tau_m = -0.06 \ln(\mathrm{NC}) + 3.43 \quad \text{for} : 1 < \mathrm{NC} < 3000 \tag{9}$$

Residual shear strength

$$\tau_r = -0.06 \ln(\mathrm{NC}) + 3.10 \quad \text{for} : 1 < \mathrm{NC} < 3000 \tag{10}$$

where NC is Number of Cycles.

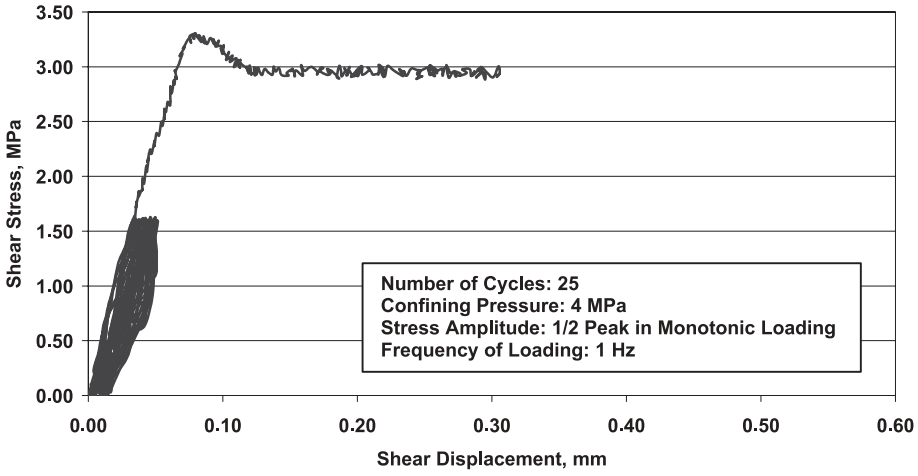

Fig. 6. Variations of shear stress with shear displacement for 25 cycles of loading

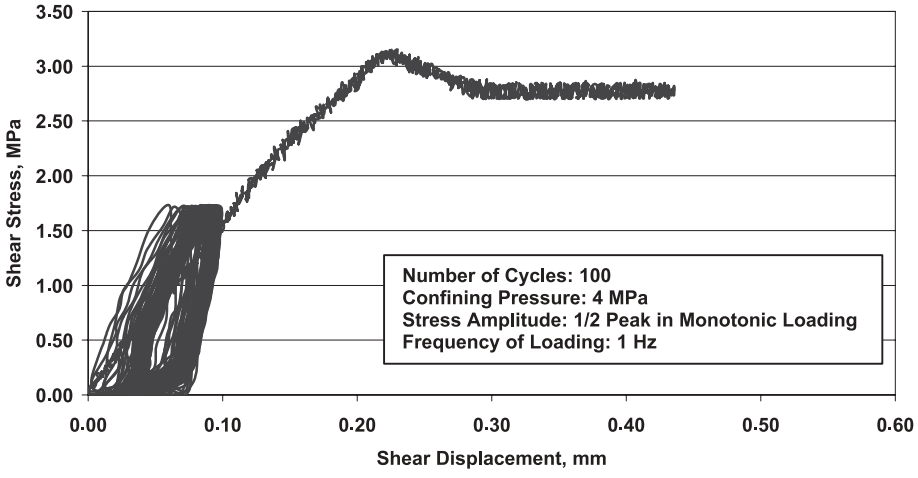

Fig. 7. Variations of shear stress with shear displacement for 100 cycles of loading

As shown in the Fig. 11, there are some differences between the levels of shear strength in the first part of the curves (lower than 300 cycles), whereas these differences become nearly negligible after 1000 cycles. It can be concluded that the shear strength of rock masses would be nearly constant after experiencing a high number of cycles, if the applied cycles have stress amplitudes lower than 50% of that at their maximum strength in monotonic loading. As discussed by Hencher (1980), dynamic loading can affect the static friction angle, so the observed reduction of shear strength can be related to reduction of friction angle.

The other important result that is apparent from Fig. 11 relates to the total effect of the number of loading cycles on shear strength. In the range of loading amplitudes

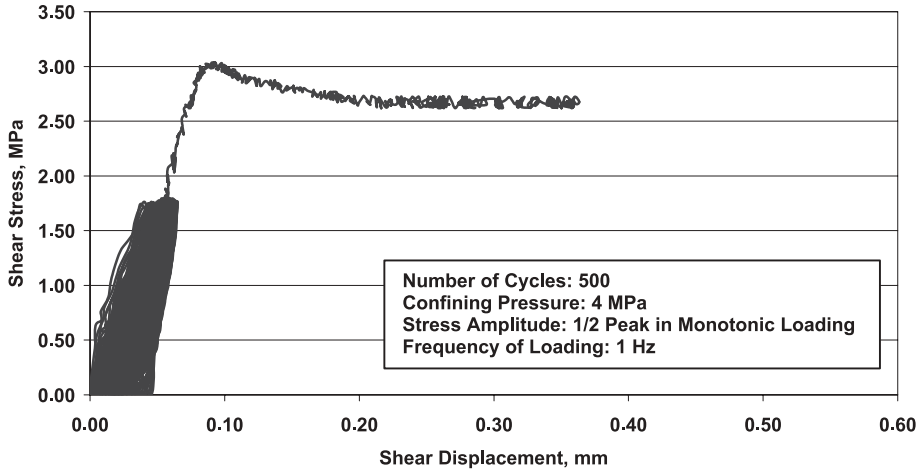

Fig. 8. Variations of shear stress with shear displacement for 500 cycles of loading

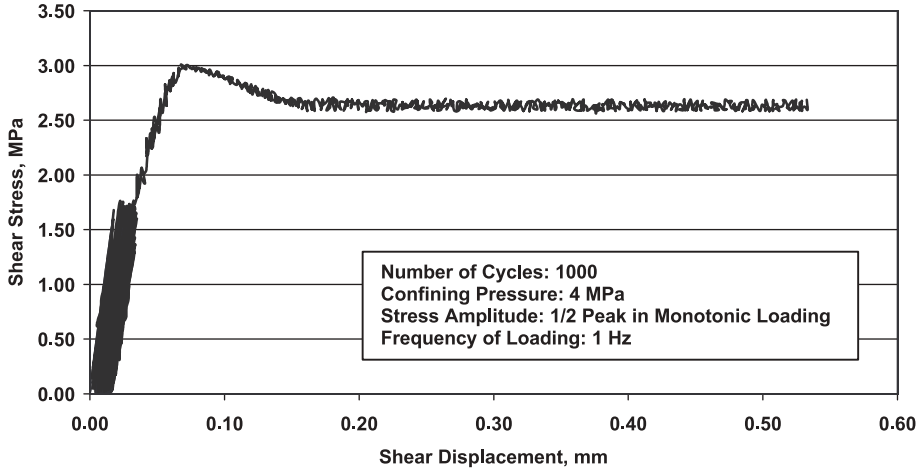

Fig. 9. Variations of shear stress with shear displacement for 1000 cycles of loading

considered, the total effect of the number of cycles on shear strength is to lower the maximum values attained in monotonic loading by no more than 20%. So it seems that by considering an appropriate factor of safety for engineering evaluations, this effect can be accounted for.

4.4.2 Effect of History of Frequency of Small Cyclic Loads

Although the frequency does not play an important role in assessing the shear strength of intact rocks, as shown by Burdine (1963), Haimson and Kim (1972) and Ray et al. (1999),

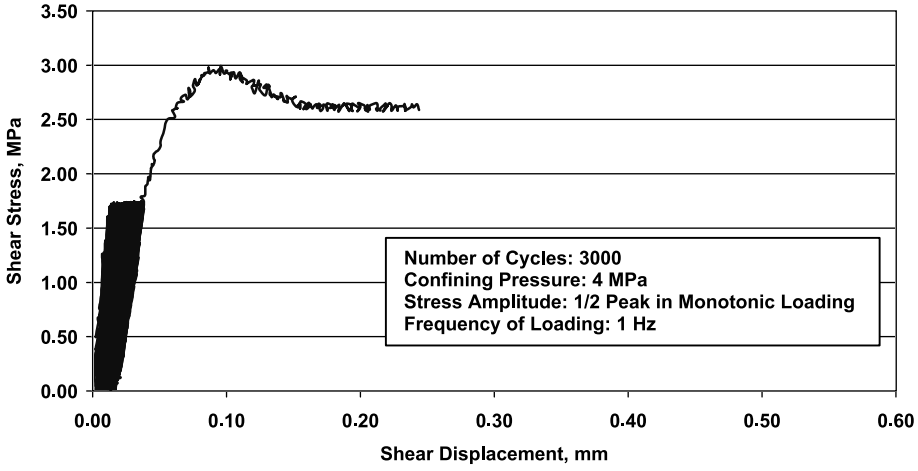

Fig. 10. Variations of shear stress with shear displacement for 3000 cycles of loading

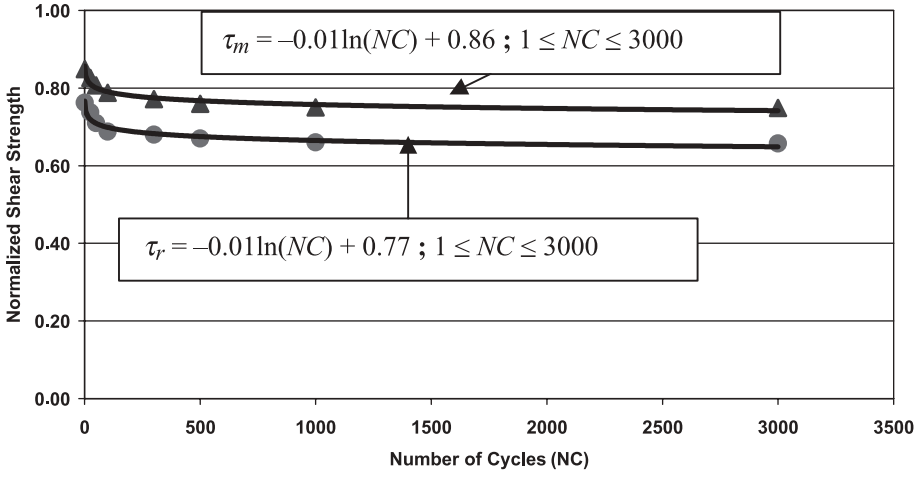

Fig. 11. Normalized peak and residual shear strength (normalized by confining pressure) versus number of cycles of loading

this could not be the case for jointed rock. This can be concluded by reviewing the reports on damaged underground structures in jointed rock during seismic events or explosions.

The effect of frequency of cyclic loading was studied with frequency between 0 to 1 Hertz for 100 cycles under 4 MPa confining pressure. Some of the results are shown in Figs. 12 and 13. Figure 14 presents the results of some of these tests as normalized peak and residual shear strength versus frequency levels. As shown in these figures, a continuous reduction of shear strength with increase of frequency has been experienced. For a better evaluation of the effects of frequency, it is necessary to perform more tests with higher levels of frequency as can be expected in near field of earthquakes or explosions.

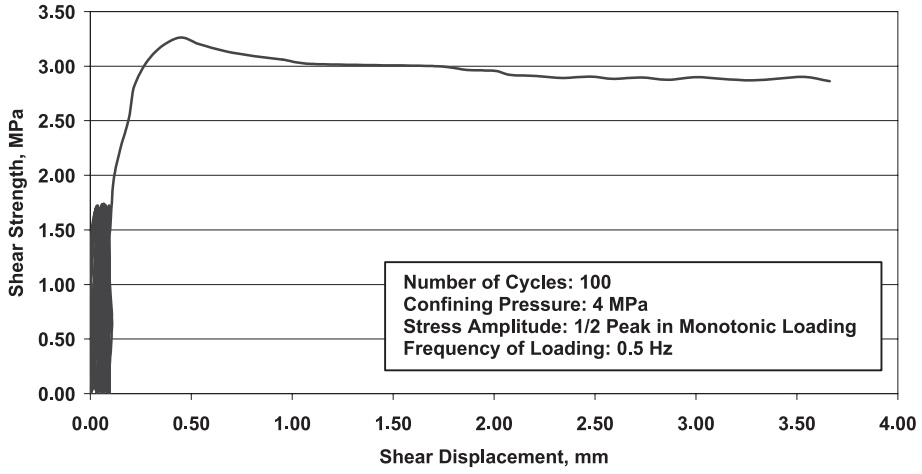

Fig. 12. Variations of shear stress with shear displacements for cyclic loading with 0.5 Hertz frequency under 4 MPa confining pressure

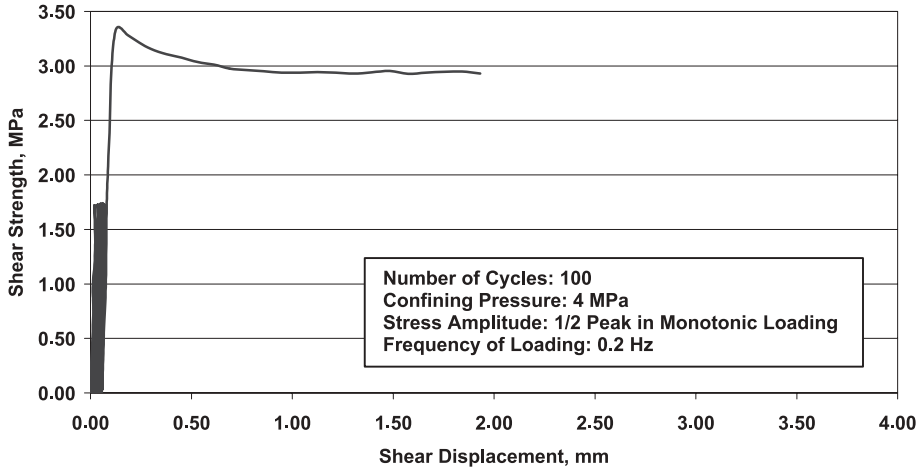

Fig. 13. Variations of shear stress with shear displacements for cyclic loading with 0.2 Hertz frequency under 4 MPa confining pressure

4.4.3 Effect of Stress Amplitude

The effect of stress amplitude was studied in LMR in Switzerland. Different levels of stress amplitude have been applied on the identical samples and shear strength have been measured after applying 100 cycles. The frequency of the cycles was 1 Hertz and the rate of axial displacement for the displacement control part of the tests was about 0.6 mm/min. All the tests have been performed under 4 MPa confining pressure. The results of some of the tests are presented in Figs. 15 and 16. A continuous trend of

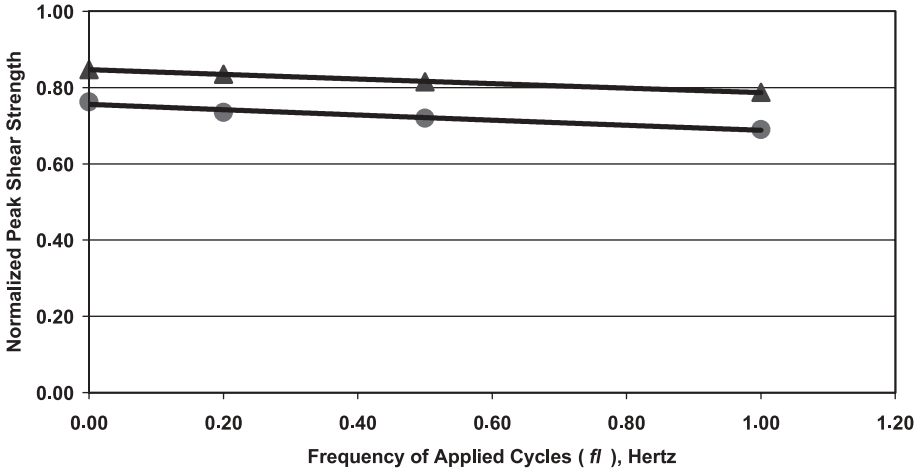

Fig. 14. Normalized peak and residual shear strength (normalized by confining pressure) versus frequency of loading

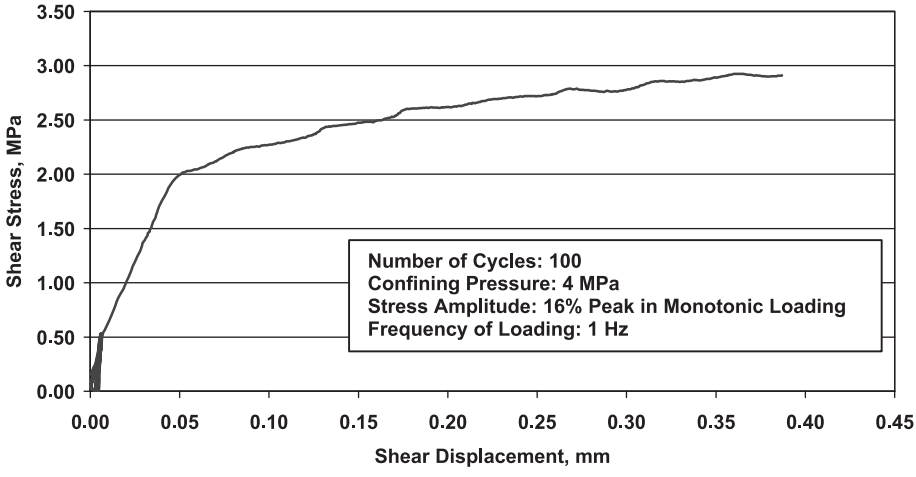

Fig. 15. Variations of shear stress with shear displacements in 0.5 MPa stress amplitude

reduction of the shear strength due to stress amplitude, as shown in these figures, is confirmed in Fig. 17. The data in Fig. 17 show an important effect of stress amplitude on shear strength of the tested samples. In fact by applying cyclic loads with amplitude more than 50% of static shear strength, shear strength decreases sharply, but below this level there is no important effect of stress amplitude on shear strength. The level of critical stress amplitude is concerned with the relative displacement and asperity condition.

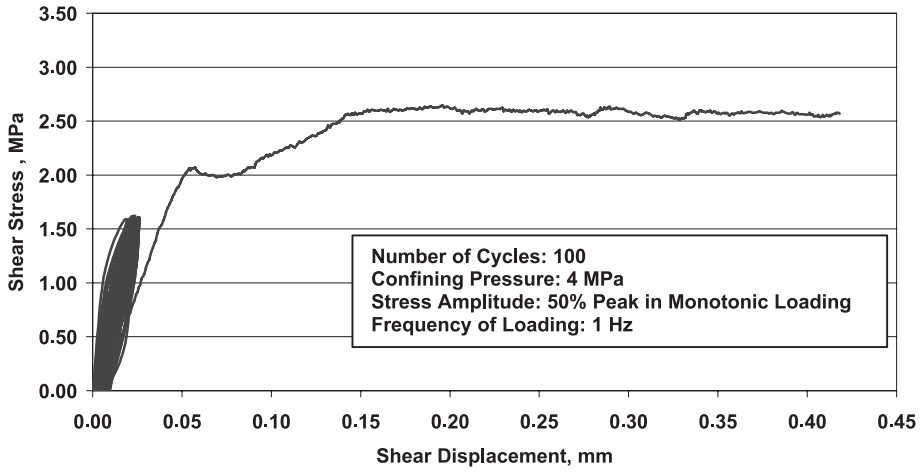

Fig. 16. Variations of shear stress with shear displacements in 1.6 MPa stress amplitude

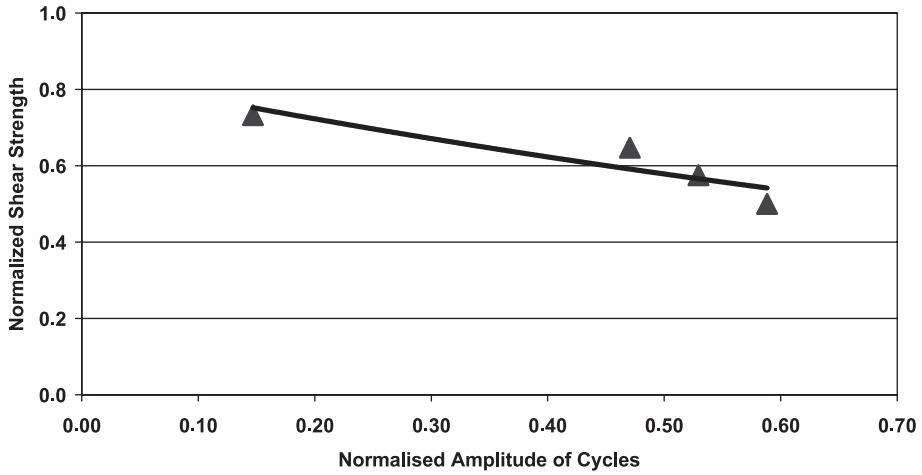

Fig. 17. Normalized mean shear strength (normalized by confining pressure) versus normalized amplitude of cyclic loading (normalized by peak value in monotonic loading condition)

The performed tests in Lab. 3S with higher levels of stress amplitude (more than 70% of static shear strength) showed that during the cyclic part the shear strength reaches its critical level and two sides of the samples start to move on each other after a few cycles. It can be concluded that during repetitive seismic loading on jointed rocks, if the stress amplitude is more than a critical value, displacement and finally instability on the under/above ground structures in rock masses may occur. This critical value can be evaluated by laboratory testing, considering several parameters such as confinement, roughness, rock type, etc.

5. Conclusions

Results of the laboratory study of the artificial rock joints presented herein show that 50's to 1000's of repetitive cyclic motions producing shear stresses of 50% of peak strength may reduce peak joint shear strength by 5 to 15%. Other main conclusions are as follows:

1. When shearing velocity along the joint surface increases from 0.04 mm/min to 0.35 mm/min in monotonic loading, the peak shear strength of artificial rock joints may reduce by 25%. In addition the effects of the second order asperities on shear strength can be eliminated when shearing velocity increases from 0.04 mm/min to 0.35 mm/min.

2. After 500 repetitive cyclic motions having shear stresses of 50% of peak strength, shear strength of artificial rock joints remains nearly constant.

3. Increasing of the frequency of cyclic motions producing shear stresses of 50% of peak strength from 0.2 to 1 Hertz in stress control stage may reduce the peak shear strength of artificial rock joints by 3 to 10% for 100 cycles.

4. If stress amplitude of the repetitive cyclic motions increases from 16% to 60% of peak strength, the shear strength of the artificial rock joints subjected to 100 stress cycles may reduce by maximum 25%.

Acknowledgement

The authors should thanks Dr. J. F. Mathier and Mr. J. Mottier, at the Laboratory LMR at the University of EPFL in Lausanne, for their kind co-operations for carrying out some parts of the tests in Switzerland.

References

Armand, G. (2000): Contribution à la caracterisation en laboratoire et à la modélisation constitutive du comportement mécanique des joints rocheux, Ph.D. Thesis, University Joseph Fourier, Grenoble.

Armand, G., Boulon, M., Papadopoulos, C., Basanou, M. E. and Vardoulakis, I. P. (1998): Mechanical behaviour of Dionysos marble smooth joints. I. Experiments. In: Rossmanith, P. (ed.), Proc., Mechanics of Jointed and Faulted Rock. 159–164.

Barbero, M., Barla, G., Zaninetti, A. (1996): Dynamic shear strength of rock joints subjected to impulse loading. Int. J. Rock Mech. Min. Sci. Geomech. Abstr. 33(2), 505–575.

Boulon, M. (1995): A 3D direct shear device for testing the mechanical behaviour and the hydraulic conductivity of rock joints. In: Rossmanith, P. (ed.), Proc. Mechanics of Jointed and Faulted Rock. 407–413.

Brady, B. H., Ma, M. (1999): Analysis of the dynamic performance of an underground excavation in jointed rock under repeated seismic loading. Geotechn. Geol. Engng. 17, 1–20.

Burdine, N. T. (1963): Rock failure under dynamic loading conditions. Soc. Pet. Eng. J. 3(1), 1–8.

Crawford, A. M., Curran, J. H. (1981): The influence of shear velocity on the frictional resistance of rock discontinuities. Int. J. Rock Mech. Min. Sci. Geomech. Abstr. 18, 505–575

Dowding, C. H., Rozen, A. (1978): Damage to rock tunnels from earthquake loading. J. Geotech. Engng Div. ASCE 104 (GT2), 175–191.

Fearon, R. (1999): Effect of displacement rate on shear strength. EPSRC, Imperial College, London.

Ghosh, A., Hsiung, S. M., Chowdhury, A. H. (1995): Seismic response of rock joints and jointed rock mass. Technical Report, NUREG/CR-6388, CNWRA 95 013.

Goodman, R. E. (1976): Methods of geological engineering. West, New York.

Goodman, R. E. (1989): Introduction to rock mechanics. John Wiley & Sons, New York.

Haimson, B. C., Kim, C. M. (1972): Mechanical behaviour of rock under cyclic loading, 13th Symp. Rock Mech. University of Illinois, 845–863.

Hencher, S. R. (1980): Friction parameters for the design of rock slopes to withstand earthquake loading. Design of dams to resist earthquake. ICE, London.

Huang, T. H., Doong, Y. S. (1990): Anisotropic shear strength of rock joints. In: Barton, N., Stephansson, O. (eds.), Proc. Rock Joints. 211–218.

Hutson, R. W., Dowding, C. H. (1990): Joint asperity degradation during cyclic shear. Int. J. Rock Mech. Min. Sci. Geomech. Abstr. 27(2), 109–119.

Indraratna, B. (1990): Development and applications of a synthetic material to simulate soft sedimentary rocks. Geotechnique 40(2), 189–200.

Kusumi, H., Nishda, K., Teraoka, K. (1998): A formulation of shear strength for rock joints included two or three different asperities. In: Rossmanith, P. (ed.), Proc. Mechanics of Jointed and Faulted Rock. 235–239.

Mostyn, G. R., Bagheripour, M. H. (1998): A new model material to simulate rock. In: Rossmanith, P. (ed.), Proc. Mechanics of Jointed and Faulted Rock. 225–230.

Owen, G. N., Scholl, R. E. (1981): Earthquake engineering of large underground structures. John A. Blume, San Francisco.

Pellet, F. (1993): Resistance et deformabilite des massifs rocheux stratifies renforces par ancrages passifs. Ph.D. Thesis, Lausanne EPEL.

Ray, S. K., Sarkar, M., Singh, T. N. (1999): Effect of cyclic loading and strain rate on the mechanical behaviour of sand stone. Int. J. Rock Mech. Min. Sci. 36, 543–549.

Scholtz, C. H. (1990): The mechanics of earthquakes and faulting. Cambridge University Press, New York.

Sharma, S., Judd, W. R. (1991): Underground opening damage from earthquake. Eng. Geol. 30, 263–267.

Stimpson, B. (1970): Modelling material for engineering rock mechanics. Int. J. Rock Mech. Min. Sci. 7, 71–121.

Sture, S., Scott, G. A., Ko, H. Y. (1984): Dynamic behaviour of jointed rock. In: Proc. of 8th World Conference on Earthquake Engineering, San Francisco.

Author's address: Dr. M. K. Jafari, International Institute of Earthquake Engineering and Seismology, P.O. Box 19395/3913, 26 Arghavan St., North Dibajee, Tehran, Iran. E-mail: jafari@dena.iiees.ac.ir

ELSEVIER

Soil Dynamics and Earthquake Engineering 23 (2003) 619–630

SOIL DYNAMICS AND EARTHQUAKE ENGINEERING

www.elsevier.com/locate/soildyn

Evaluation of shear strength of rock joints subjected to cyclic loading

M.K. Jafari[a,*], K. Amini Hosseini[a], F. Pellet[b], M. Boulon[b], O. Buzzi[b]

[a]*International Institute of Earthquake Engineering and Seismology, P.O. Box 19395/3913, Tehran, Iran*
[b]*Laboratory 3S, University Joseph Fourier, Grenoble, France*

Accepted 5 May 2003

Abstract

Variation of the shear strength of rock joints due to cyclic loadings is studied in the present paper. Identical joint surfaces were prepared using a developed moulding method with special mortar and shear tests were performed on these samples under both static and cyclic loading conditions. Different levels of shear displacement were applied on the samples to study joint behaviour before and during considerable relative shear displacement. It was found that the shear strength of joints is related to rate of displacement (shearing velocity), number of loading cycles and stress amplitude. Finally, based on the experimental results, mathematical models were developed for evaluation of shear strength in cyclic loading conditions.

Keywords: Shear strength; Roughness; Cyclic loading; Shearing velocity; Number of cycles; Stress amplitude

1. Introduction

The behaviour of rock joints under cyclic loading depends on their surface properties such as roughness, strength of asperities, separation, matedness, presence of gouge, etc. These properties may change as a result of variations in second-order asperities due to small cyclic loading, e.g. during weak earthquakes. Strong earthquakes in contrast affect mainly the first-order asperities. Previous studies have generally focused on determining the peak shear strength of rock joints under monotonic loading and their behaviour under cyclic loading conditions has been less reported. Few systematic studies are available concerning the effects of small repetitive earthquakes on the shear strength of rock joints. Hutson and Dowding [1] performed some cyclic tests on artificial sinusoidal joints and presented a wear equation for joint asperity based on the experimental results. Huang et al [2] also performed cyclic tests on saw-tooth samples to evaluate the degradation law proposed by Plesha [3]. Divoux et al [4] presented a mechanical constitutive model based on the results of cyclic shear tests. Armand et al [5] studied the frictional properties of the contacts between smooth Dionysos marble experimentally and numerically in different conditions. Kana et al [6] introduced the importance of second-order asperities in cyclic loading and suggested the interlock-friction model for dynamic shear response.

In this paper the results of an experimental investigation carried out on artificial joints will be presented. Two levels of cyclic displacement were applied on the identical prepared samples, using two types of testing machine, to simulate the effects of weak and strong earthquakes. Based on the results obtained, mathematical models were developed for evaluating the cyclic shear strength of rock joints.

2. Testing programme

Two types of joint surface have been prepared for all the tested replicas: saw-tooth and a real joint surface moulded from a fresh joint. Schematic views of these surfaces are shown in Fig. 1. The cylindrical samples (Fig. 1(a)) were prepared to evaluate the effects of small cyclic loads using a triaxial loading device, and the cubic samples (Fig. 1(b) and (c)) were designed for large displacement using a direct shear apparatus. All the samples were prepared using a special kind of mortar and a specially developed moulding method using silicone rubber. The uniaxial compression strength of the samples was more than 55 MPa and its tensile strength (determined by Brazilian tests) was about 8 MPa after 24 h. Fig. 2 shows some of the samples ready to be tested.

For the small cyclic displacement tests, two triaxial testing devices were used at the 3S Laboratory (Lab. 3S) of

* Corresponding author. Fax: +98-21-28-03-656.
E-mail address: jafari@dena.iiees.ac.ir (M.K. Jafari).

0267-7261/03/$ - see front matter © 2003 Elsevier Ltd. All rights reserved.
doi:10.1016/S0267-7261(03)00063-0

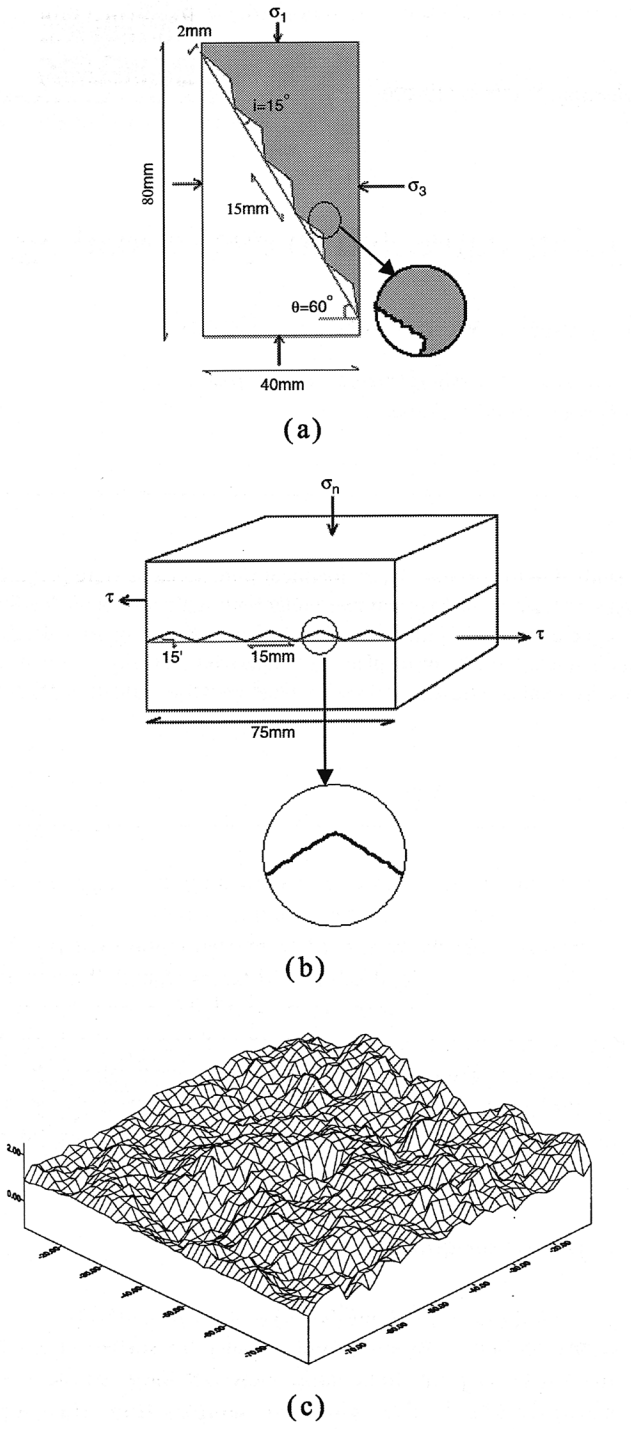

Fig. 1. (a) Saw-tooth samples for triaxial tests; (b) saw-tooth samples for direct shear tests; (c) real surface joint model for direct shear tests.

the University Joseph Fourier in Grenoble, France and at the Laboratory of Rock Mechanics (LMR) of the Swiss Institute of Technology (EPFL) in Lausanne, Switzerland. Two separate systems for applying the axial loads and confining pressure were used. All the systems were equipped with a function generator to provide different types of voltages for applying cyclic loads. All the data including displacements, forces, confining pressure and

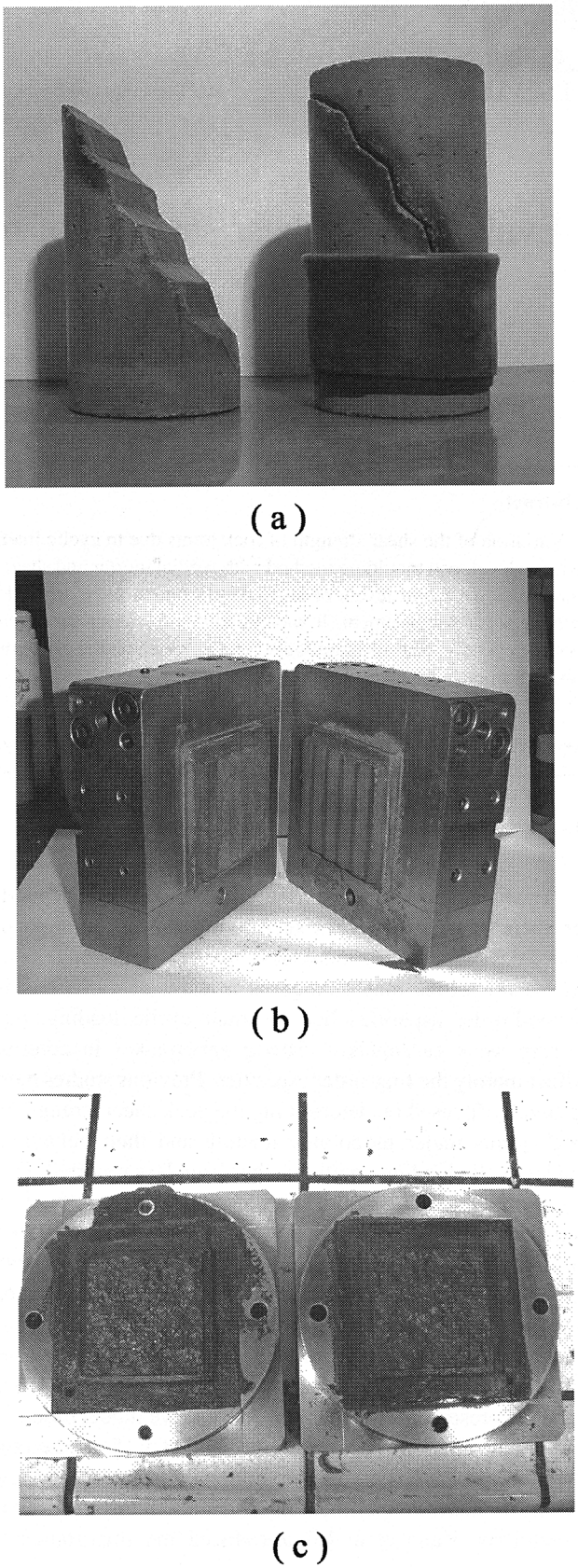

Fig. 2. Some of the prepared samples by using silicon moulds; (a) and (b) saw-tooth samples; (c) real joint surface sample.

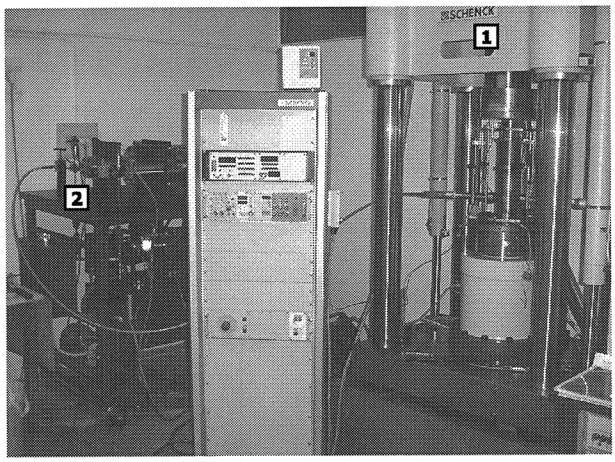

(a)

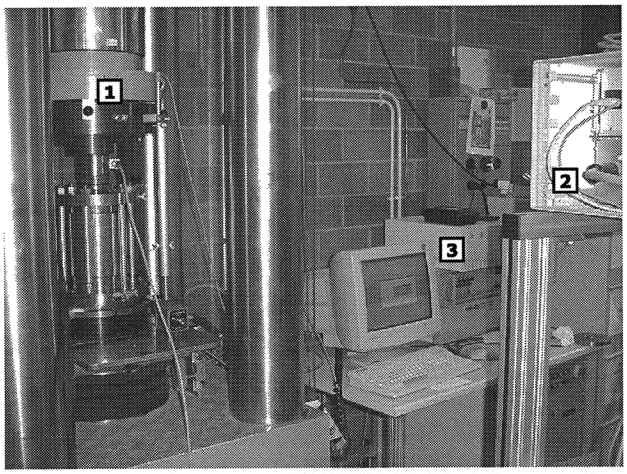

(b)

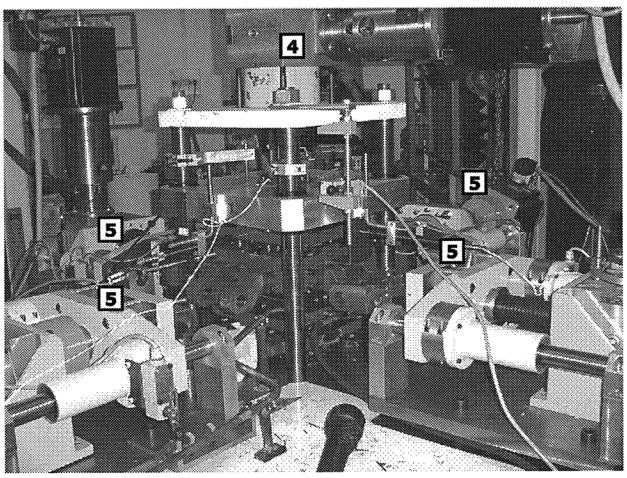

(c)

Fig. 3. Testing machines and data acquisition systems, (a) triaxial machine at Lab. 3S; (b) triaxial machine at LMR; (c) direct shear machine at Lab 3S (1—axial jack, 2—confining pressure system, 3—data acquisition system, 4—axial brushless servo-motor, 5—shearing brushless servo-motor).

time were measured and recorded by personal computer with the adjustable sampling rates. Axial displacements were measured using 4 vertical LVDTs simultaneously and their average used for analysis.

All of the large cyclic displacement tests were performed using a new direct shear testing apparatus at Lab. 3S. called BCR 3D, developed by Boulon [7]. By using two similar brushless servo-motors, the two walls of a joint can move symmetrically, so no relative rotation occurs during the shearing displacement and the normal force remains centred on the active part of the joint at any given time. Shear and normal displacements are measured by 4 LVDTs in each direction. All of the data are recorded using a standard computer and a high frequency data acquisition system. Fig. 3 shows the testing devices.

3. Effects of small cyclic displacements on shear strength

3.1. Experimental results

The triaxial tests were performed to study the behaviour of the joint samples during small cyclic displacements. Variations in shear strength in monotonic and cyclic loading conditions under different shearing velocities, numbers of cycles, and stress amplitudes were studied. The results of some of the tests performed will be presented and discussed in this paper.

3.1.1. Effects of displacement rates

In order to study the effects of displacement rates (or shearing velocity) on shear strength, some monotonic tests were performed in different ranges of axial displacement in 4 MPa confining pressure from 0.05 to 0.4 mm/s. Some of the results have been presented in Fig. 4. The differences between the curves can be related to the effects of shear velocity on second-order asperities, as the total applied displacement is limited. It is observed that shear strength reduces with increasing shear velocity, approaching the same values for the peak and residual strength at higher shearing velocities.

3.1.2. Effects of number of cycles

To study the effects of the number of stress cycles on the shear strength of rock joints two different stages were defined. In the first stage several stress cycles (between 25 and 3000 cycles) were applied on the replicas (stress control) and in the second stage the monotonic loading (displacement control) was continued to reach the ultimate shear strength.

One of the results of the tests performed is presented in Fig. 5. In the first part (Fig. 5(a)) 100 stress cycles were applied on the sample and in the second part the test was followed by monotonic loading (Fig. 5(b)). As can be observed, degradation of asperities happens mainly during the first stress cycles, being attenuated in the higher stress cycles. Due to the limited level of the shear displacement applied, asperity degradation could be related to the second-order asperities.

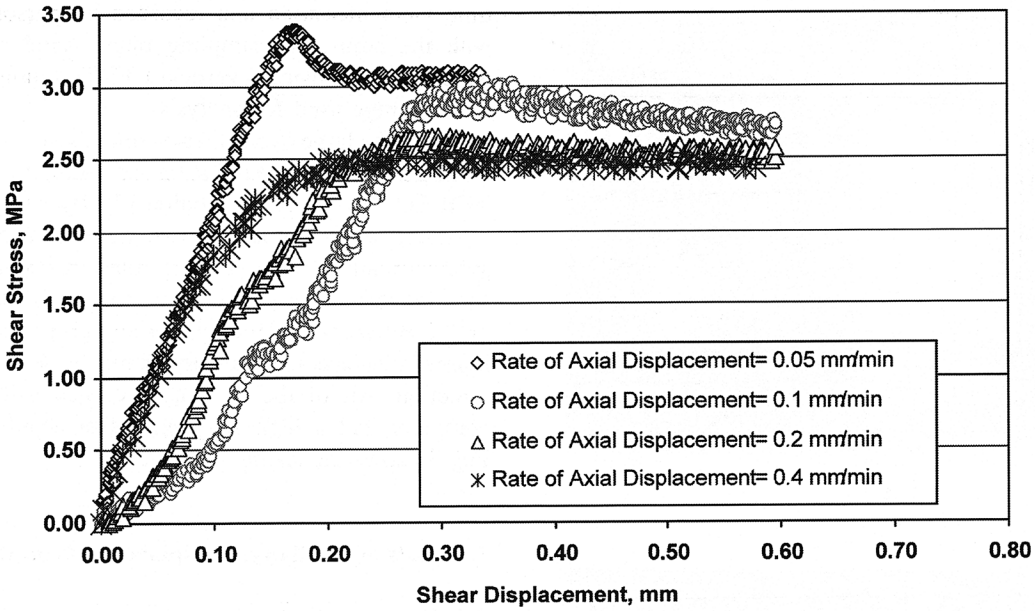

Fig. 4. Shear stress–shear displacement curve for different rates of axial displacement.

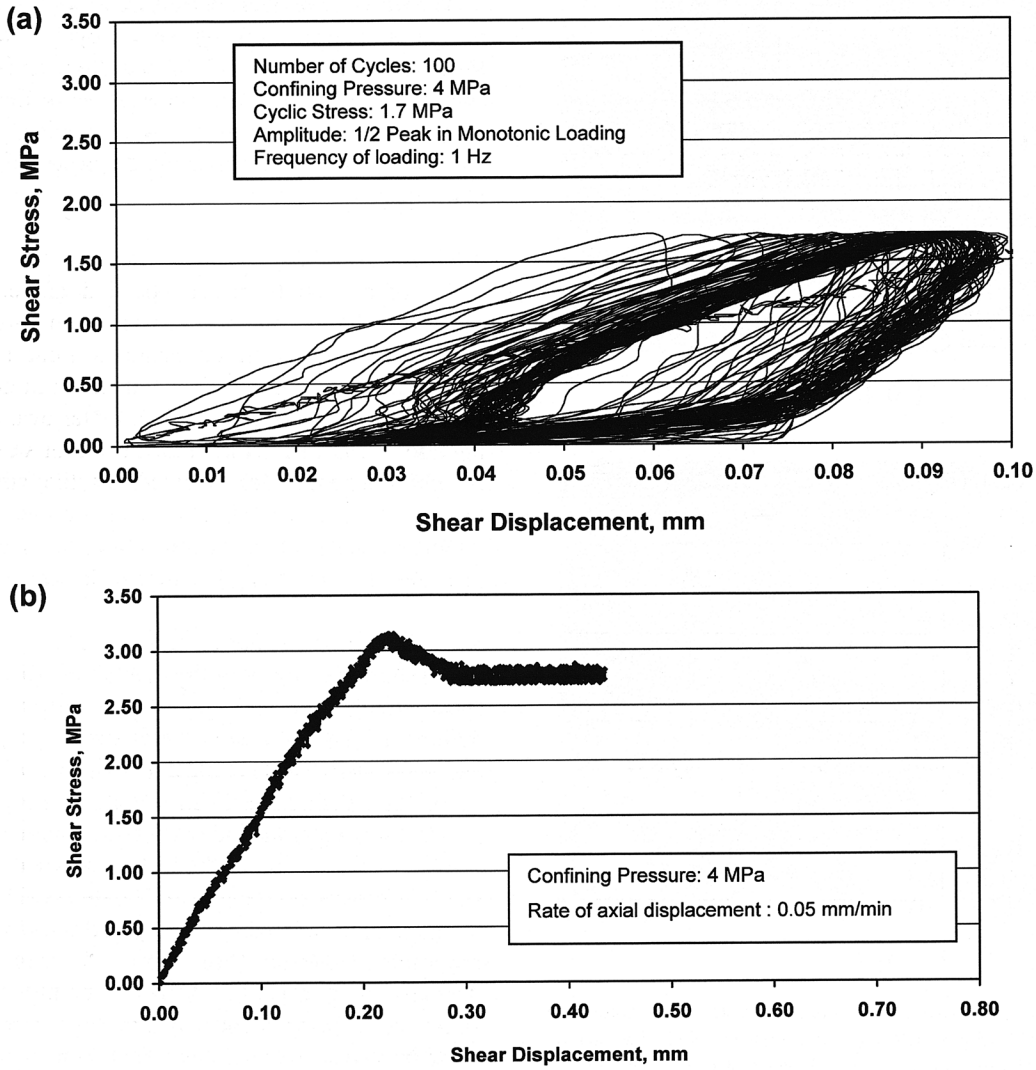

Fig. 5. The results of one of the cyclic tests on saw-tooth samples subjected to 100 loading cycles; (a) stress control part; (b) displacement control part.

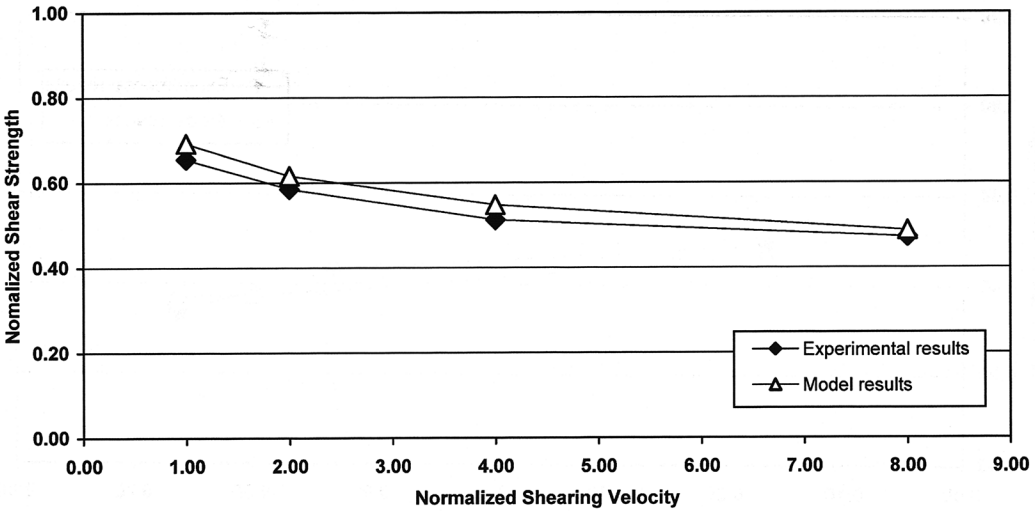

Fig. 6. Comparison of the measured and calculated shear strength at different shear velocities.

3.1.3. *Effects of stress amplitude*

The stress amplitude in the above-mentioned tests was selected as half of the maximum strength measured in monotonic loading. Some extra investigations were performed on the samples applying 100 stress cycles at different levels of stress amplitude (between 15 and 70% of maximum strength). The shear strength appears to decrease (for the same number of cycles) for higher levels of stress amplitude applied on the joint surface.

3.2. *Mathematical modelling*

Based on the test results the following relation could be proposed for evaluating shear strength under low amplitude cyclic loading

$$\frac{\tau}{\sigma_n} = \frac{a(NC_s)^m(\dot{\omega}_n A_n)^n}{1 + a(NC_s)^m(\dot{\omega}_n A_n)^n} \quad (1)$$

where τ is the shear strength, σ_n is the normal stress, NC_s is the number of stress cycles, $\dot{\omega}_n$ is the normalized shear velocity (normalized by the minimum shearing velocity during monotonic tests, in which the maximum shear strength exists), A_n is normalized stress amplitude (normalized by maximum shear strength).

Based on calibration with the results of the tests performed, the following model parameters are obtained

$$a = 0.3,\ m = -0.045,\ n = -0.17.$$

The parameter a is related to the mechanical properties of the joint sample (e.g. base friction angle, ϕ_b) and the geometrical features of joint surface. As the present investigations focused on artificial joint samples, more investigations on real rock joints with different conditions should be carried out to obtain a better evaluation of these parameters. The number of stress cycles, NC, has little effect on shear strength, represented by the small value for

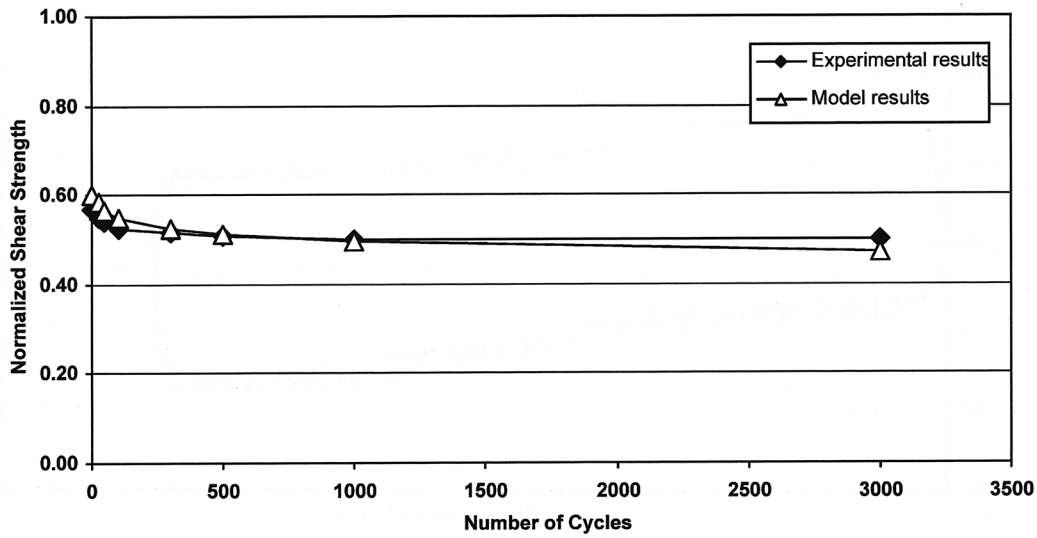

Fig. 7. Comparison of the measured and calculated shear strength for different numbers of stress cycles.

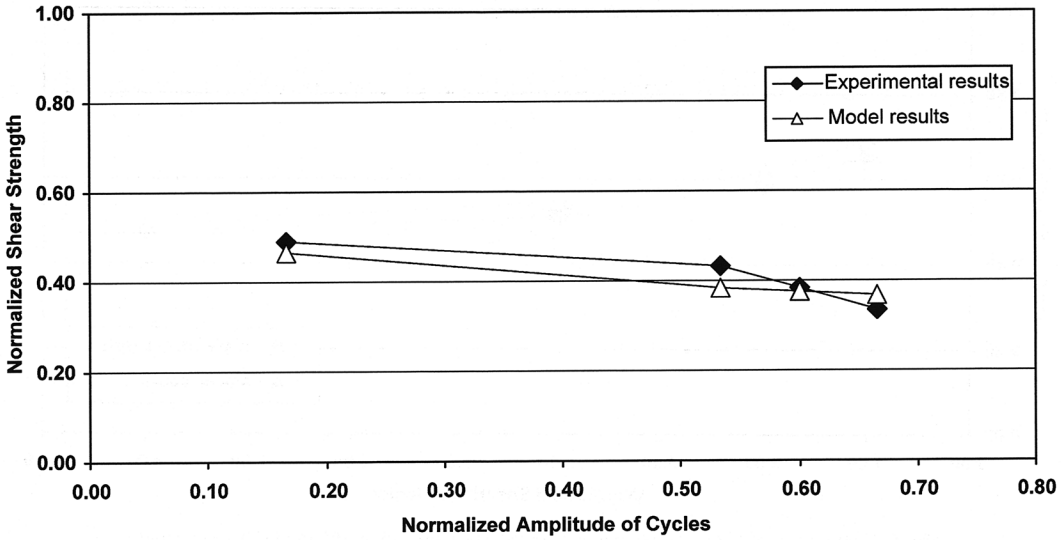

Fig. 8. Comparison of the measured and calculated results for different stress amplitudes.

the parameter m. In contrast, stress amplitude and shearing velocity have relatively large effects on shear strength due to the higher value for the parameter n. As can be observed in Figs. 6–8, the proposed model correctly simulates the experimental results with an acceptable level of precision.

4. Effects of large shear displacement on shear strength

4.1. Experimental results

In order to evaluate the shear strength of joint replicas during large cyclic displacements, direct shear tests using BCR-3D were performed on saw-tooth and real surface models of joint samples. The total relative displacement applied was 15 mm, in which each wall of the joints was moved 7.5 mm. The tests were performed at three different levels of normal stress and the variations in shear strength as well as the degradation of the asperities were studied.

4.1.1. Degradation at low levels of normal stress

At low levels of normal stress, the main shearing mechanism during cyclic displacement is sliding along the asperities. During sliding, degradation may occur in both second- and first-order asperities to smooth the shearing surface. The shear strength of the joint samples diminishes in each cycle to reach to a constant level after experiencing a few cycles (5–6 in this investigation).

In Figs. 9 and 10 the results of some of these tests performed on saw-tooth and real surface models under 1.2 MPa normal stresses are presented. Degradation of second- and mainly first-order asperities continues during

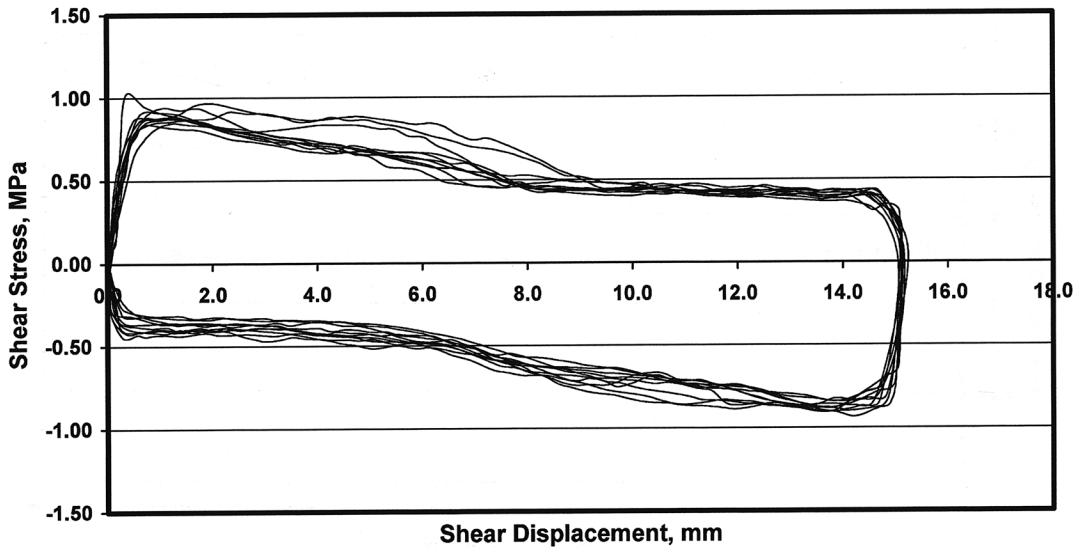

Fig. 9. Shear stress–shear displacement curve for saw-tooth samples during 10 cycles under 1.2 MPa normal stress.

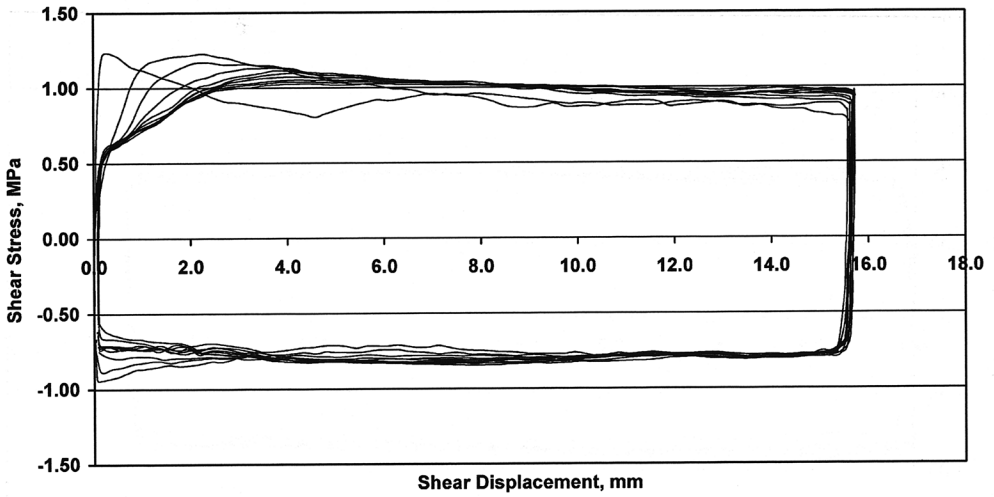

Fig. 10. Shear stress–shear displacement curve for real surface model during 10 cycles under 1.2 MPa normal stress.

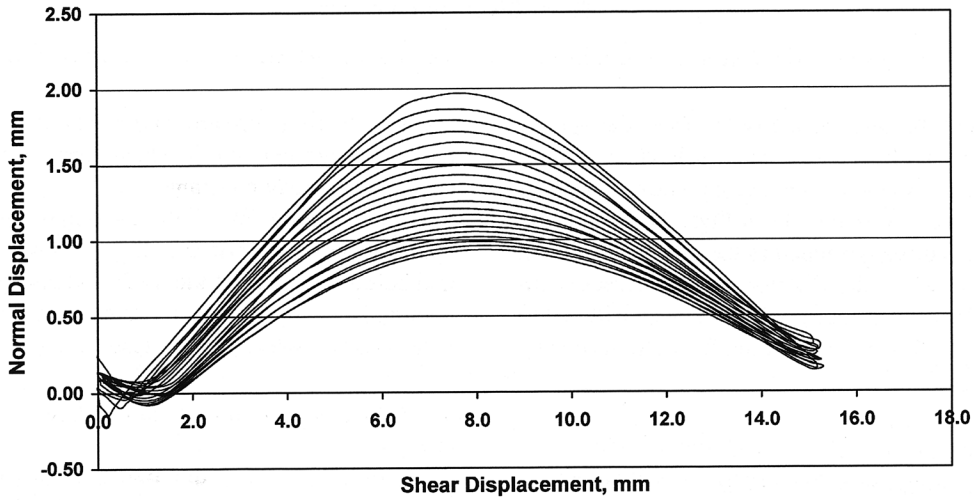

Fig. 11. Asperities degradation due to cyclic displacement at low levels of normal stress for saw-tooth samples during 10 cycles ($\sigma_n = 1.2$ MPa).

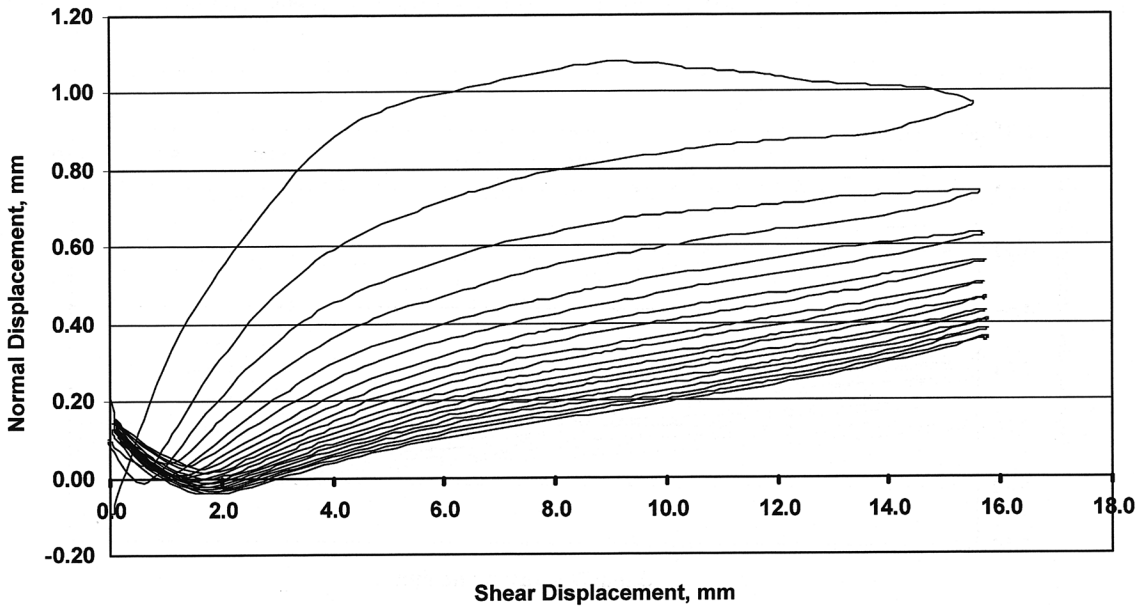

Fig. 12. Asperities degradation due to cyclic displacement at low levels of normal stress for real surface model during 10 cycles ($\sigma_n = 1.2$ MPa).

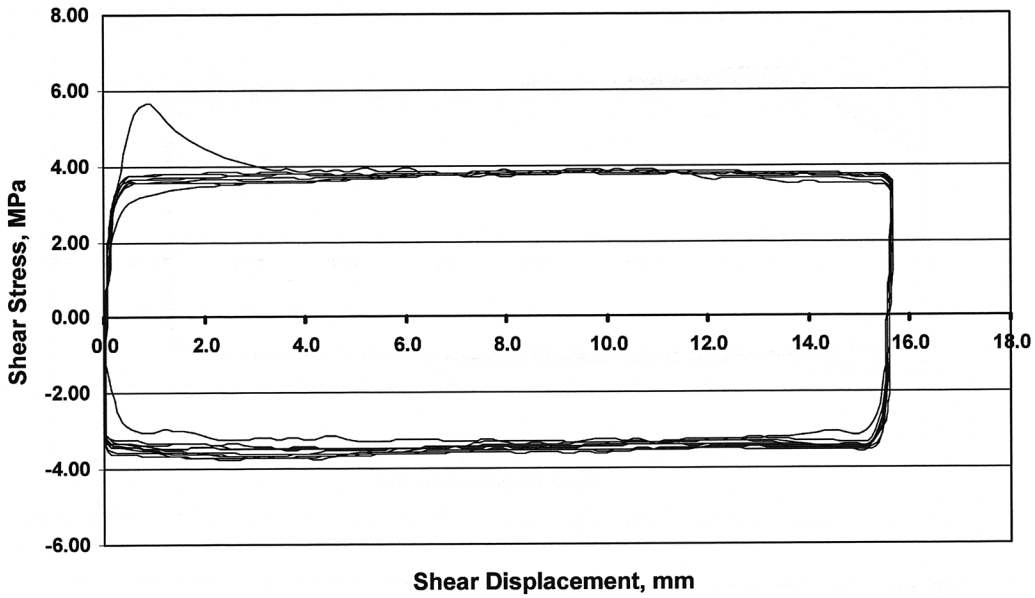

Fig. 13. Shear stress–shear displacement curve for saw-tooth samples during 10 cycles under 6.5 MPa normal stresses.

cyclic displacement, but the second-order asperities do not have any considerable effect on the shear behaviour of joint replicas as they diminish after a few cycles. The degradation trend can be observed more clearly in Figs. 11 and 12. As the shear strength is directly related to the dilation angle (i), it will be reduced when the dilation angle decreases. In addition, the effects of wearing should also be considered to obtain a better evaluation of shear strength variations during cyclic displacement.

4.1.2. Degradation under high levels of normal stress

At high levels of normal stress, asperities will be broken during shear displacement and no considerable dilation can be expected. Fig. 13 shows the results of one of the tests performed on saw-tooth replicas under 6.5 MPa normal stresses. During forward movement in the first cycle, all the teeth were cut and the shear strength for the rest of the cycles was nearly constant.

The variation in dilation–contraction curves during cyclic shearing is shown in Fig. 14. Only in the first cycle and before breaking of the teeth, some small dilation can be occurred and in the other cycles, contraction is the main mechanism observed in the tests.

4.1.3. Degradation under intermediate levels of normal stress

In order to study the transition between sliding and breaking of joint replicas during cyclic displacement, some direct shear tests were performed on saw-tooth and natural surface models of jointed samples. The results presented in

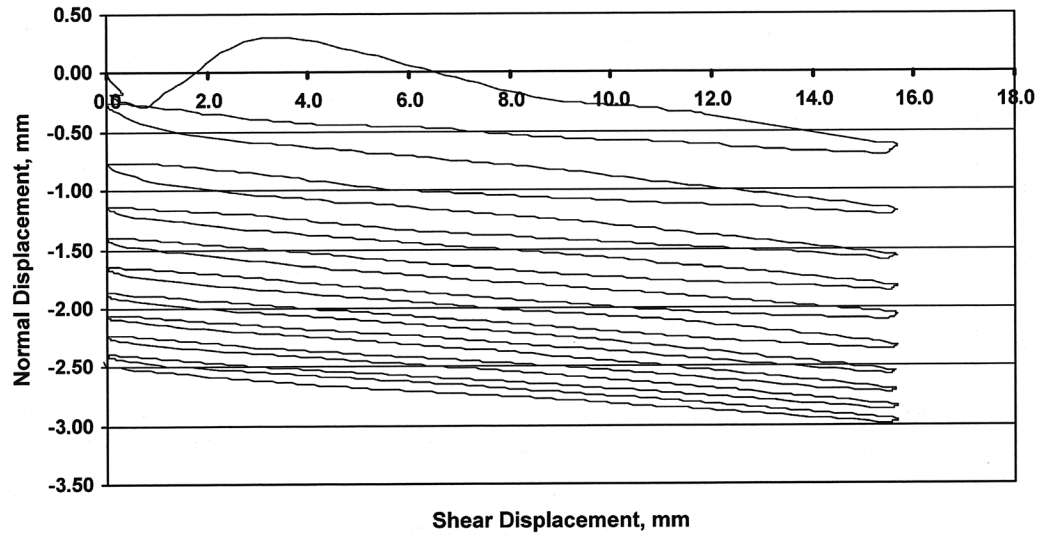

Fig. 14. Contraction due to cyclic shear displacement in high level of normal stress in saw-tooth samples ($\sigma_n = 6.5$ MPa).

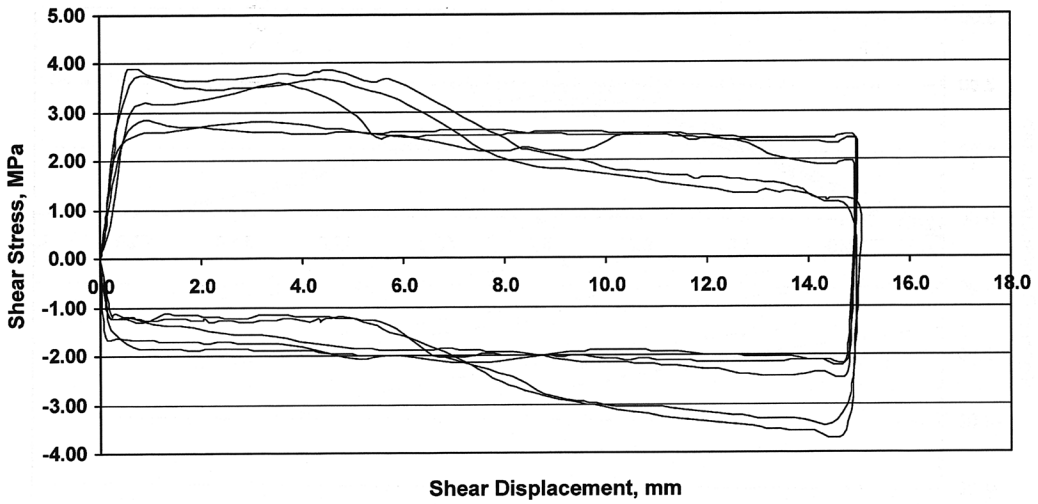

Fig. 15. Shear stress–shear displacement curve for saw-tooth sample during five cycles under 4.2 MPa normal stress.

Figs. 15 and 16 demonstrate this transitional behaviour. During the first two cycles (Fig. 15) the main controlling mechanism on the sample is sliding over the asperities, but in the third cycle teeth were broken and the behaviour has been changed. In real conditions (Fig. 16) this sharp transformation cannot be expected.

This phenomenon can be observed more clearly in dilation–contraction curves (Fig. 17). With a sliding mechanism, dilation occurs during shearing while at the breaking stage, the contraction of the sample is predominant.

4.2. Mathematical model

Based on the results of the tests performed and on the trends of the data in each group discussed, the following mathematical model was developed to evaluate the shear strength of the jointed samples during large cyclic shear displacement

$$\frac{\tau}{\sigma_n} = \frac{b(\mathrm{NC_d})^p (i_n)^q + c}{1 + b(\mathrm{NC_d})^p (D_n)^q}$$

Where τ is shear strength, σ_n is normal stress, $\mathrm{NC_d}$ is number of displacement cycles, i_n is the normalized dilation angle (normalized by the maximum angle measured before the test), D_n is normalized degradation (normalized by maximum value of asperities amplitude).

In this relation the parameters b, c, p and q can be obtained by model calibration, as follows

$$B = -0.33,\ c = 1.44,\ p = 0.12,\ q = 0.3$$

The parameters b and c are related to the mechanical properties of the sample tested, such as friction angle (ϕ) and also the geometrical features of the joint surface. Wearing and asperity degradation are functions of the number of cycles, and may have important effects on

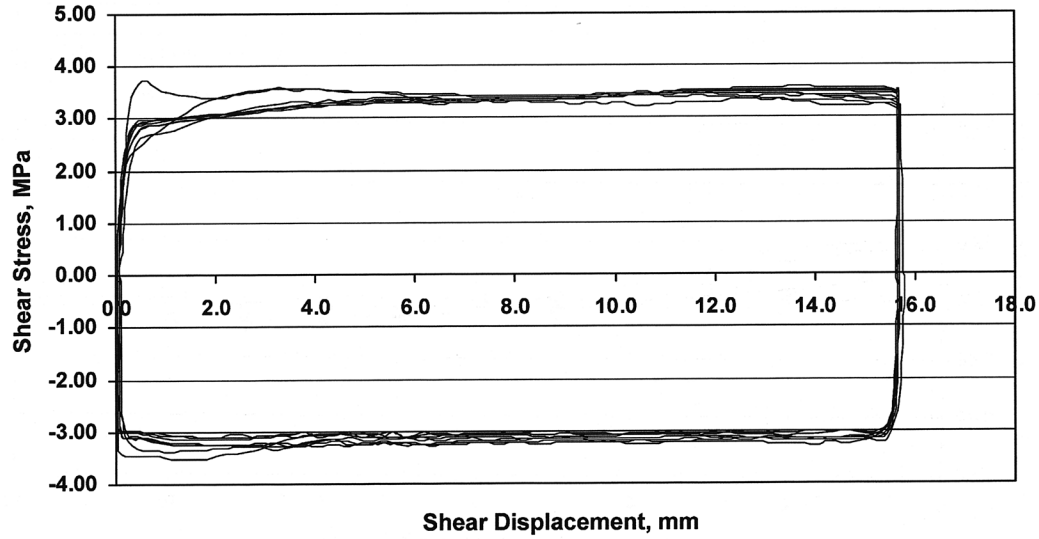

Fig. 16. Shear stress–shear displacement curve for real surface sample during 10 cycles under 4.2 MPa normal stress.

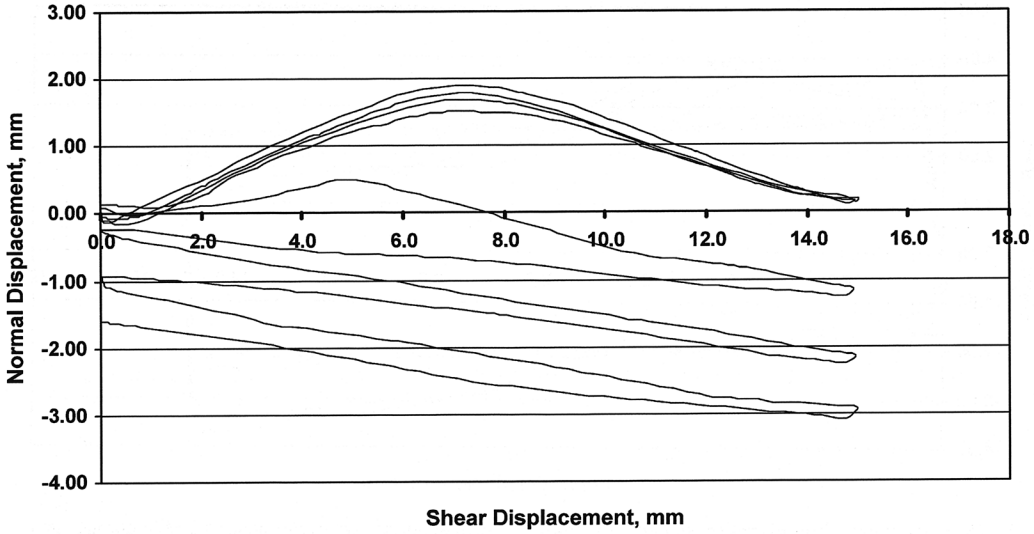

Fig. 17. Dilation–contraction behaviour of joint replicas for intermediate levels of normal stress ($\sigma_n = 4.2$ MPa).

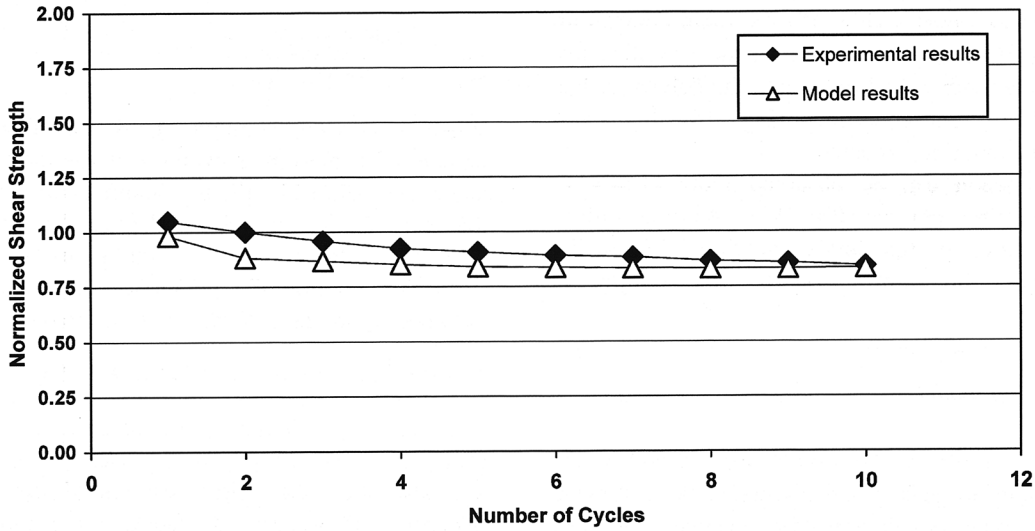

Fig. 18. Comparison of the measured and evaluated shear strength of real surface joint model at low levels of normal stress ($\sigma_n = 1.2$ MPa).

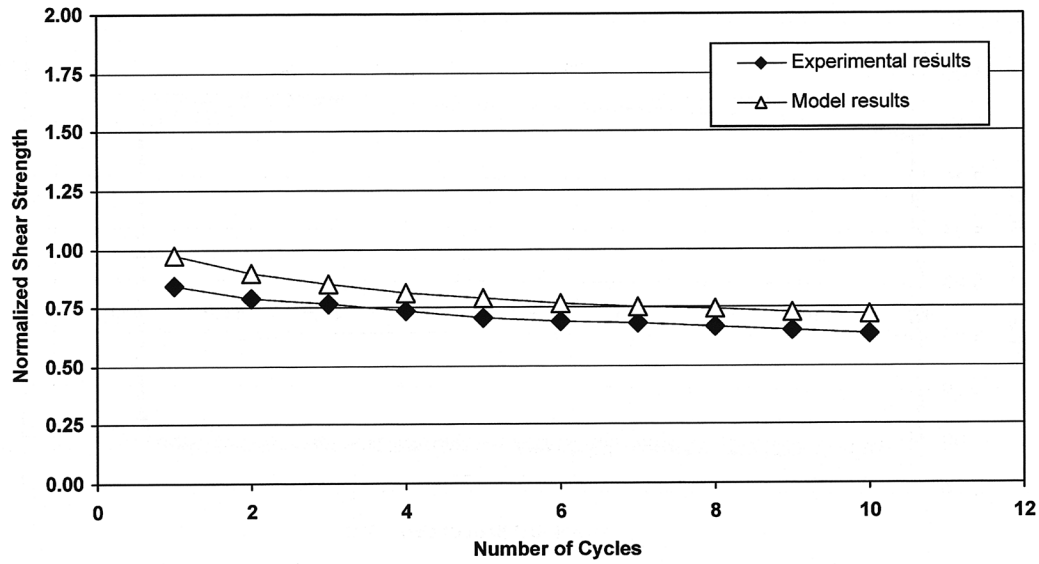

Fig. 19. Comparison of the measured and evaluated shear strength of saw-tooth joint model at low levels of normal stress ($\sigma_n = 1.2$ MPa).

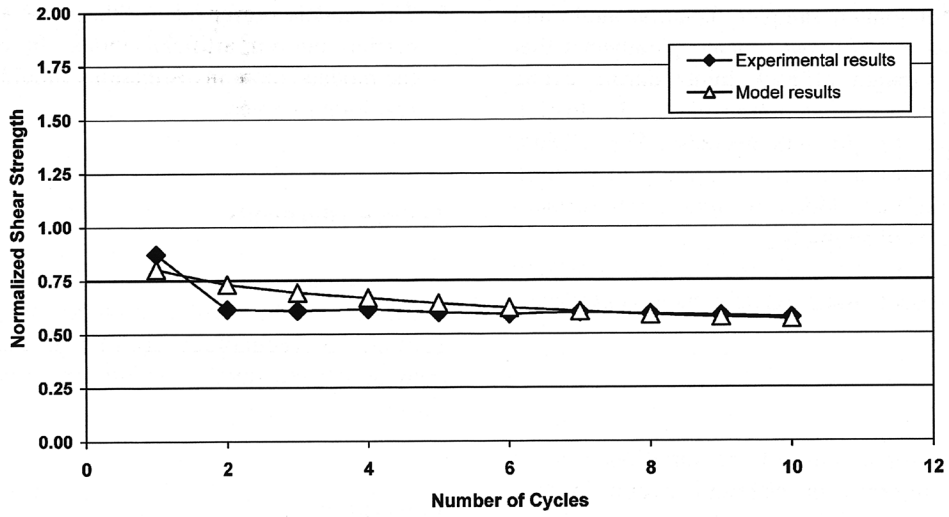

Fig. 20. Comparison of the measured and calculated shear strength of saw-tooth joint model at high levels of normal stress ($\sigma_n = 6.5$ MPa).

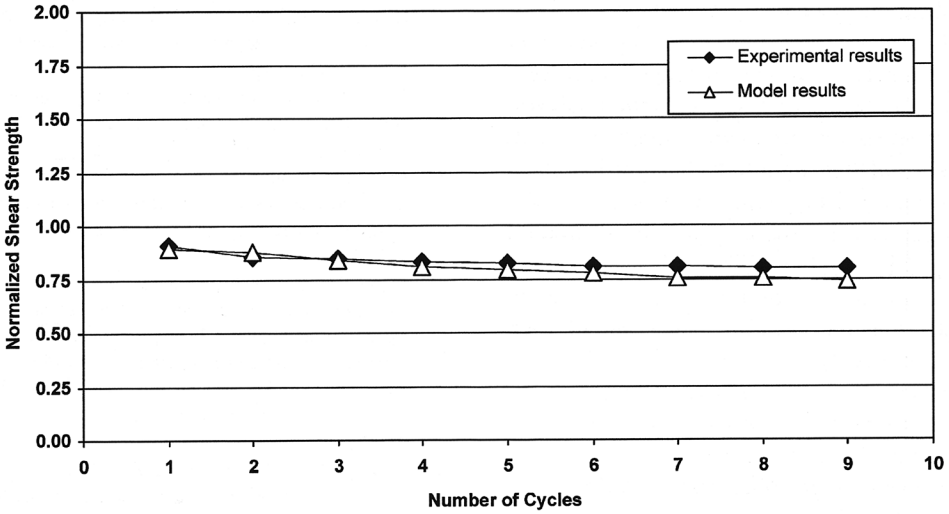

Fig. 21. Comparison of the measured and evaluated shear strength of real surface joint model at intermediate levels of normal stress ($\sigma_n = 4.2$ MPa).

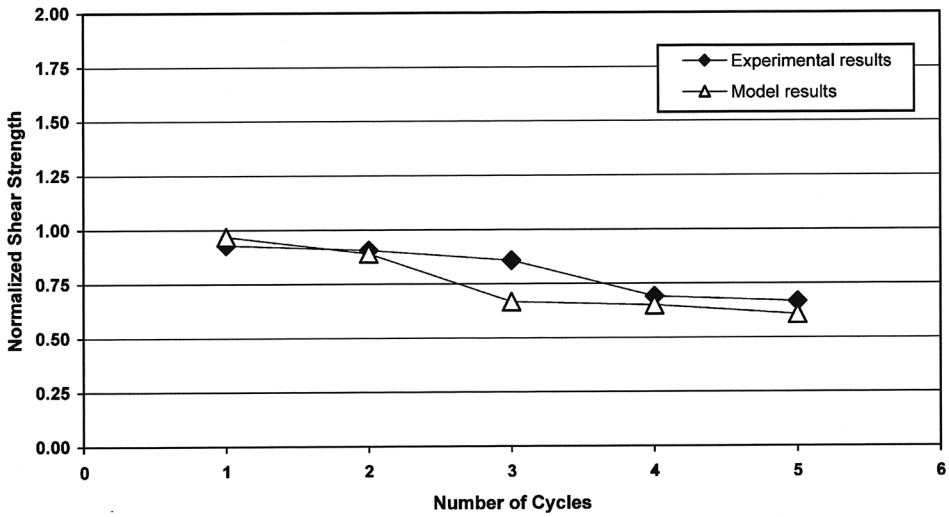

Fig. 22. Comparison of the measured and evaluated shear strength of saw-tooth joint model at intermediate levels of normal stress ($\sigma_n = 4.2$ MPa).

the shear strength of jointed samples. Dilation angle and asperity degradation are also two related parameters that control the shear strength of rock joints during cyclic displacement. If asperity degradation increases, the dilation angle and the shear strength will decrease. For a better evaluation of these parameters it is necessary to perform similar tests on different kinds of real joint surfaces (especially different wall strengths).

In Figs. 18–22 some of the test results were compared with the proposed model, and good agreement is observed.

5. Conclusion

This paper discusses a study of the variation in shear strength of joint replicas in different cyclic loading conditions. The following main conclusions may be drawn from this investigation:

1. During cyclic shear displacement, degradation of both first- and second-order asperities will occur, depending on the cyclic displacement and normal stress applied. During small earthquakes and low amplitude dynamic loadings, second-order asperities will be mainly affected, but in strong earthquakes and high amplitude dynamic loadings, both first- and second-order asperities may be damaged.
2. The shear strength of joint replicas will be decreased during small repetitive cyclic loadings. The number of loading cycles and stress amplitude are two main parameters controlling the shearing behaviour of rock joints during cyclic loading.
3. Dilation angle, degradation of asperities and wearing are three main factors which affect the shear strength of rock joints during large cyclic displacement.
4. The shear behaviour of rock joints during sliding is in direct relation with the normal stress level and may change from sliding to breaking during cyclic displacement.
5. The models presented in this paper are based on tests carried out on artificial joints. In order to improve the models, more investigations should be carried out on real joint samples.

Acknowledgements

The authors wish to thank Dr J.F. Mathier and Mr J. Mottier, at the LMR Laboratory of the Swiss Federal Institute of Technology (EPFL) in Lausanne, for their kind assistance during performing some of the triaxial tests.

References

[1] Hutson RW, Dowding CH. Joint asperity degradation during cyclic shear. Int J Rock Mech Min Sci Geomech Abstr 1990;27(2):109–19.
[2] Huang X, Haimson BC, Plesha ME, Qiu X. An investigation of the mechanics of rock joints. Int J Rock Mech Min Sci Geomech Abstr 1993;30(3):257–69.
[3] Plesha ME. Constitutive models for rock discontinuities with dilatancy and surface degradation. Int J Numer Anal Meth Geomech 1987;11: 345–62.
[4] Divoux P, Boulon M, Bourdarot E. In: Rossmanith H.-P., editor. A mechanical constitutive model for rock and concrete joints under cyclic loading. Proceedings of Damage and Failure of Interfaces; 1997. p. 443–50.
[5] Armand G, Boulon M, Papadopoulos C, Basanou ME, Vardoulakis IP. In: Rossmanith H.-P., editor. Mechanical behaviour of Dionysos marble smooth joints: I. Experiments. Proceedings of Mechanics of Jointed and Faulted Rock; 1998. p. 159–64.
[6] Kana DD, Fox DJ, Hsiung SM. Interlock/friction model for dynamic shear response in natural jointed rock. Int J Rock Mech Min Sci 1996; 33:371–86.
[7] Boulon M. In: Rossmanith H.-P., editor. A 3D direct shear device for testing the mechanical behaviour and the hydraulic conductivity of rock joints. Proceedings of Mechanics of Jointed and Faulted rock; 1995. p. 407–13.

Annexe II : Publication relative aux développements théoriques

7 - F. Pellet, A. Hajdu, F. Deleruyelle & F. Besnus, A viscoplastic constitutive model including anisotropic damage for the time dependent mechanical behaviour of rock, to be submitted.

A viscoplastic model including anisotropic damage for the time dependent mechanical behaviour of rock

F. PELLET *, A. HAJDU *, F. DELERUYELLE ** & F. BESNUS**

* University Joseph Fourier, Laboratoire Sols Solides Structures (3S), Grenoble, France

** Institute for Radiological and Nuclear Safety (IRSN), Clamart, France

Summary :

This paper presents a new model for the time dependent mechanical behaviour of rock which allows one to take into account both viscoplastic behaviour and evolution of damage with respect to time. This model is built by the association of a viscoplastic constitutive law to the damage theory. The main characteristics of this model are to take into account a viscoplastic volumic strain (i.e contractancy and dilatancy) as well as the anisotropy of damage. This latter is described by a second rank tensor. Using this model, it is possible to predict delayed rupture by determining time at failure, in creep tests for example. The identification of the model parameters is explained based on experiments such as creep tests, relaxation tests and quasi-static tests. The physical meaning of these parameters is discussed and comparisons with lab tests are presented. The ability of the model to reproduce the delayed failure observed in tertiary creep is demonstrated as well as the sensitivity of the mechanical response to the rate of loading. This model could be used to simulate the evolution of the excavated damage zone around underground openings.

Key Words :

Viscoplasticity, anisotropic damage, time dependent behaviour, dilatancy, rock, creep test, quasistatic test, time at failure.

1 Introduction

Geomaterials, and rocks in particular, have a complex mechanical behaviour which is often time-dependent. For example, following the application of a stress deviator, non-elastic deformations develop as a function of time. If the applied stress deviator is not high enough, these deformations will attenuate and stabilize; conversely, if the deviator is high, the deformation rate starts to accelerate from a certain point, leading to failure of the material.

These various phases, which have been demonstrated experimentally by several authors [1], [2], [3], [4], [5], [6], can be illustrated by the result of a compression creep test where a primary creep phase is observed during which viscous and work-hardening phenomena are evidenced, followed by a secondary creep phase during which only the viscosity phenomenon is active, and a tertiary creep phase corresponding to progressive damage of the material.

These deformations and delayed failure phenomena are of vital importance, especially for the design of such structures as underground galleries around which an area of damaged rock develops with time. This zone of damaged rock, often known as the EDZ (Excavated Damage Zone) is of the greatest importance for storage structures where the host rock is destined to play a confining role [7].

In order to model this type of behaviour, damaging viscoplastic models are used. However, most existing laws do not show the delayed irreversible volume deformations nor the anisotropy of the damage observed during laboratory tests.

This paper describes the improvements that have been made to the damaging viscoplastic law proposed by Lemaitre [8]. The procedure for identifying parameters is then described and includes a discussion of the physical implications. Finally, the model performance is compared with the results of laboratory tests.

2 Modifications of Lemaitre's model

2.1 Basic assumptions and thermodynamic framework

Lemaitre's model is a viscoplastic potential model based on the overstress concept proposed by Perzyna [9]. Before describing the changes made to the model, it is worth going over the thermodynamic formalism considered which is based on the following main hypotheses:

- Small transformation hypothesis: the total deformation can be considered as the symmetrical part of the displacement gradient operator,

- Deformation partition hypothesis: the deformation is divided into a reversible part (elastic) and an irreversible part (inelastic), as shown by the following expression:

$$\boldsymbol{\varepsilon}^{e} = \boldsymbol{\varepsilon} - \boldsymbol{\varepsilon}^{vp} \qquad [1]$$

In addition, conditions are assumed to be isothermal, thereby implying zero time-dependent temperature drift, with dissipation being purely mechanical without any thermal dissipation factor. Moreover, the geomechanical stress sign convention is applied; compressive stresses are considered positive.

This model has been drawn up by application of the mechanics of continuous media and the thermodynamics of irreversible processes. This is a phenomenological approach based on the local state method which describes the change in the physical phenomena of the medium using a certain number of state variables. Note that in order for the change process of this set of variables to be permissible from a thermodynamic standpoint, the second principle must be satisfied at each instant in terms of the Clausius-Duhem inequality. Assuming small disturbances, the general Clausius-Duhem inequality is written as follows:

$$\boldsymbol{\sigma} : \dot{\boldsymbol{\varepsilon}} - \rho(\dot{\Psi} + s\dot{T}) - \frac{1}{T}\mathbf{q} \cdot \nabla T \geq 0 \qquad [2]$$

where $\boldsymbol{\sigma}$ and $\boldsymbol{\varepsilon}$ are respectively the stress and strain tensors, ρ the density, Ψ the specific free energy, s the specific entropy, T the absolute temperature and $\mathbf{q}$ the heat flux vector. If isothermal conditions are considered, this inequality reduces to the following expression:

$$\boldsymbol{\sigma} : \dot{\boldsymbol{\varepsilon}} - \rho\dot{\Psi} \geq 0 \qquad [3]$$

The state variables define the thermodynamic potential from which the state laws are derived. In the model described here, the Helmholtz specific free energy (Ψ) was used as potential. In order to formulate the viscoplastic model with damage under isothermal conditions, the following state variables are considered:

- total deformation $\boldsymbol{\varepsilon}$,

- viscoplastic deformation $\boldsymbol{\varepsilon}^{vp}$,

- cumulative viscoplastic deformation, p, associated with the current state of work hardening of the material, and which is defined by:

$$p = \int_0^t \left(\frac{2}{3} \dot{\boldsymbol{\varepsilon}}^{vp}(t) : \dot{\boldsymbol{\varepsilon}}^{vp}(t) \right)^{1/2} dt \qquad [4]$$

- damage **D** (second-order tensor).

The free energy is then expressed as a function of the state variables by:

$$\Psi = \Psi(\boldsymbol{\varepsilon}^e, p, \mathbf{D}) \qquad [5]$$

and the Clausius-Duhem inequality is expressed in the form:

$$\boldsymbol{\sigma} : \dot{\boldsymbol{\varepsilon}} - \rho\dot{\Psi}(\boldsymbol{\varepsilon}^e, p, \mathbf{D}) \geq 0 \qquad [6a]$$

$$\boldsymbol{\sigma} : \dot{\boldsymbol{\varepsilon}}^{vp} + \left(\boldsymbol{\sigma} - \rho \frac{\partial \Psi}{\partial \boldsymbol{\varepsilon}^e} \right) : \dot{\boldsymbol{\varepsilon}}^e - \rho \frac{\partial \Psi}{\partial p} \dot{p} - \rho \frac{\partial \Psi}{\partial \mathbf{D}} : \dot{\mathbf{D}} \geq 0 \qquad [6b]$$

The variables of thermodynamic forces associated respectively with elastic deformation, with the work-hardening variable and with the damage, can then be deduced:

$$\boldsymbol{\sigma} = \rho \frac{\partial \Psi}{\partial \boldsymbol{\varepsilon}^e} \qquad [7]$$

$$R = \rho \frac{\partial \Psi}{\partial p} \qquad [8]$$

$$\mathbf{Y} = \rho \frac{\partial \Psi}{\partial \mathbf{D}} \qquad [9]$$

Given that thermal dissipation is considered to be zero, the dissipation power (Φ) is purely intrinsic (i.e., of mechanical origin) and is written as follows:

$$\Phi = \boldsymbol{\sigma} : \dot{\boldsymbol{\varepsilon}}^{vp} - R\dot{p} - \mathbf{Y} : \dot{\mathbf{D}} \geq 0 \qquad [10]$$

The change laws of the flux variables ($\dot{\boldsymbol{\varepsilon}}^{vp}, \dot{p}$ and $\dot{\mathbf{D}}$) are determined from a dissipation potential (φ):

$$\boldsymbol{\sigma} = \frac{\partial \varphi}{\partial \dot{\boldsymbol{\varepsilon}}^{vp}} \qquad [11]$$

$$R = -\frac{\partial \varphi}{\partial \dot{p}} \qquad [12]$$

$$\mathbf{Y} = -\frac{\partial \varphi}{\partial \dot{\mathbf{D}}} \qquad [13]$$

However, as a general rule, it is more practical to express the change in force variables as a function of flux variables. A Legendre-Fenchel transform is used to define a dual potential (φ^*) where the change laws are written as follows:

$$\dot{\boldsymbol{\varepsilon}}^{vp} = \frac{\partial \varphi^*}{\partial \boldsymbol{\sigma}} \qquad [14]$$

$$\dot{p} = -\frac{\partial \varphi^*}{\partial R} \qquad [15]$$

$$\dot{\mathbf{D}} = -\frac{\partial \varphi^*}{\partial \mathbf{Y}} \qquad [16]$$

The intrinsic dissipation power as a function of the dual dissipation potential is ultimately obtained by:

$$\Phi = \boldsymbol{\sigma} : \frac{\partial \varphi^*}{\partial \boldsymbol{\sigma}} + R\frac{\partial \varphi^*}{\partial R} + \mathbf{Y} : \frac{\partial \varphi^*}{\partial \mathbf{Y}} \geq 0 \qquad [17]$$

In order for the inequality to be verified, the following conditions are imposed on the dissipation potential:

- φ^* must be a convex function of the variables $\boldsymbol{\sigma}$, R and **Y,**

- φ^* must always be positive,

- φ^* must contain the origin, i.e., it must cancel out for $\sigma_{ij} = p = Y_{ij} = 0$

The second principle of thermodynamics is therefore satisfied because the intrinsic dissipation verifies:

$$\Phi \geq 0 \qquad [18]$$

For the model presented below, and in order to simplify the formulation, the dissipation potential was broken down into two parts:

$$\varphi = \Omega^{vp}(\boldsymbol{\varepsilon}^{vp}, p) + \Omega^{D}(\mathbf{D}) \qquad [19]$$

or,in terms of the dual potential :

$$\varphi^* = \Omega^{vp}(\boldsymbol{\sigma}, R) + \Omega^{D}(\mathbf{Y}) \qquad [20]$$

The first term on the right-hand side of the equation (Ω^{vp}) corresponds to the deformation and work-hardening processes, whereas the second term (Ω^{D}) corresponds to the damaging process. A specific distinction such as this is standard practice and is based on the assumption that the two dissipation processes are independent and governed by two distinct additive potentials. If the two potentials separately verify the convexity and positivity criteria, so does their sum. It therefore suffices to analyse them one by one.

2.2 Viscoplastic law with irreversible volume deformation

As a first stage, only viscous phenomena are modelled, with the delayed damage being ignored, but taking into account the volume deformation.

The classical approach in elasto-viscoplasticity consists in defining a load surface in the stress space inside which the stress states reached cause entirely reversible deformations. The framework of viscoplastic process thermodynamics, briefly summarised above, is based on the concept of equipotential surfaces. The viscoplastic law is entirely defined by the dissipation potential, thus enabling the rate of viscoplastic deformation to be calculated directly by applying the normality rule.

In its original version, Lemaitre's law makes use of the von Mises load surface which is not suited to geomaterials because it does not provide an inelastic volume deformation. Using the same procedure proposed by Lemaitre [8], but by introducing a load surface depending not only on the second deviator invariant but also on the first stress invariant, and by assuming isotropic work hardening, the following expression is obtained for dissipation potential:

$$\Omega^{vp} = \frac{K}{N+1}\left\langle \frac{f(J_2; I_1)}{K} \right\rangle^{N+1} p^{-N/M} \qquad [21]$$

where Ω^{vp} is the dissipation potential, M, N and K are viscoplastic coefficients, (< >) being Macaulay brackets. The state of work hardening is expressed by the variable p.

Note the multiplicative separation of the variables; the first part represents the perfect viscoplastic potential multiplied by the work hardening function.

Consequently, the power function form of the dissipation potential proposed by Lemaitre has been retained, replacing the von Mises criterion by a Drucker-Prager type criterion [10]. The expression of the load surface $f(J_2; I_1)$ indicates the equipotential surface function. This function is written as follows:

$$f(J_2; I_1) = \sigma_{eq} + \alpha\sigma_m - k \qquad [22]$$

with: $\sigma_{eq} = \sqrt{\frac{3}{2}\mathbf{S} : \mathbf{S}}$ [23]

$$\mathbf{S} = \boldsymbol{\sigma} - \frac{1}{3}\mathrm{tr}(\boldsymbol{\sigma}) \cdot \mathbf{I} \qquad [24]$$

$$\sigma_m = \frac{1}{3}\mathrm{tr}(\boldsymbol{\sigma}) \qquad [25]$$

$$I_1 = \mathrm{tr}(\boldsymbol{\sigma}) = 3\sigma_m \qquad [26]$$

where $\boldsymbol{\sigma}$, $\mathbf{I}$ and $\mathbf{S}$ are respectively the stress tensor, the identity tensor and the stress deviator.

The parameter α which multiplies the mean stress, is used to characterise the delayed volume deformation. It is linked to the deferred dilatancy angle, ψ, by the relation:

$$\alpha = \tan(\psi) \qquad [27]$$

The coefficient k enables the viscoplasticity threshold to be defined for cases where a specific elasticity domain is to be considered. However, this viscoplasticity threshold often proves to be very low, which is mathematically equivalent to assuming that k = 0. In that which follows, this hypothesis has been taken and the function $f(J_2; I_1)$ is written as follows:

$$f(J_2; I_1) = \sigma_{eq} + \alpha\sigma_m \qquad [28]$$

It is also worth noting that the Drucker-Prager criterion, despite being widely used in geomechanics, would merit having its field of validity more accurately defined. Among the defects that it engenders, note that it gives the same plasticity threshold under compression as under tensile stress, a fact that is not in agreement with the observations made on most geomaterials. Moreover, not all cone opening angles are physically permissible. From a certain summit angle, the cone centred on the trisecting line intersects and goes beyond the planes defined by the stress states where one of three main stresses is kept at zero value. This is equivalent to assuming tensile forces that are not physically acceptable, especially in powder media [11].

However, these defects of the Drucker-Prager criterion are considerably less penalising for a viscoplastic formulation because, in viscoplasticity, the consistency rule no longer applies [12]. The state of stresses must be located beyond the load surface in order for flow to occur. The deformation rate increases with distance from this "overstress" with respect to the load surface where the flow is infinitely slow. We therefore have a family of surfaces and, in each point on a given surface, the deformation rate modulus (or in other words the dissipation) is identical, from which the term equipotential surface is obtained. The viscoplastic dissipation potential can therefore be written as follows:

$$\Omega^{vp} = \frac{K}{N+1}\left\langle \frac{\sigma_{eq} + \alpha\sigma_m}{K} \right\rangle^{N+1} p^{-N/M} \qquad [29]$$

The viscoplastic deformation rate is then deduced from the dissipation potential simply by application of the normality rule, i.e.:

$$\dot{\boldsymbol{\varepsilon}}^{vp} = \frac{\partial \Omega^{vp}}{\partial \boldsymbol{\sigma}} \qquad [30a]$$

$$\dot{\boldsymbol{\varepsilon}}^{vp} = \frac{\partial \Omega^{vp}}{\partial \sigma_{eq}} \frac{\partial \sigma_{eq}}{\partial \boldsymbol{\sigma}} + \frac{\partial \Omega^{vp}}{\partial \sigma_{m}} \frac{\partial \sigma_{m}}{\partial \boldsymbol{\sigma}} \qquad [30b]$$

$$\dot{\boldsymbol{\varepsilon}}^{vp} = \left\langle \frac{\sigma_{eq} + \alpha \sigma_{m}}{Kp^{1/M}} \right\rangle^{N} \left(\frac{3}{2} \frac{\mathbf{S}}{\sigma_{eq}} + \frac{\alpha \mathbf{I}}{3} \right) \qquad [30c]$$

Considering isotropic work hardening of the material and assuming that there is no restoration process, the value of the variable is still increasing. The cumulative viscoplastic deformation can therefore be used as an indicator of the state of work hardening of the material. This is calculated by:

$$\dot{p} = \sqrt{\frac{2}{3} \dot{\boldsymbol{\varepsilon}}^{vp} : \dot{\boldsymbol{\varepsilon}}^{vp}} \qquad [31]$$

In this case, we obtain:

$$\dot{p} = \sqrt{\frac{2}{9}\alpha^2 + 1} \left\langle \frac{\sigma_{eq} + \alpha \sigma_{m}}{Kp^{1/M}} \right\rangle^{N} \qquad [32]$$

Because $\mathbf{I} : \mathbf{I} = 3$, $\mathbf{I} : \mathbf{S} = 0$ and $\mathbf{S} : \mathbf{S} = 2/3\sigma_{eq}^2$) and the viscoplastic deformation rate to be expressed in the following form:

$$\dot{\boldsymbol{\varepsilon}}^{vp} = \dot{p} \left(\frac{2}{9}\alpha^2 + 1 \right)^{-1/2} \left(\frac{3}{2} \frac{\mathbf{S}}{\sigma_{eq}} + \frac{\alpha \mathbf{I}}{3} \right) \qquad [33]$$

Lemaitre's model has therefore been enriched by an additional parameter α that will be called the dilatancy parameter. As far as hydrostatic loadings are concerned, it should be noted that, for a contracting material, ($\alpha > 0$), no viscoplastic flow occurs under tensile stress and, similarly, a dilatant material ($\alpha < 0$) does not flow under compressive stress, a fact that is physically acceptable.

The influence of the dilatancy parameter α on the deferred bulk behaviour for an elastically compressible material ($\nu < 0.5$) subjected to constant loading can be illustrated. Following an instantaneous elastic contractancy, viscoplastic volume deformations appear, due to material creep. For positive values of α the deferred behaviour is contracting whereas the negative values generate dilatancy. By setting $\alpha = 0$ the viscoplastic volume deformations disappear and the model reverts to Lemaitre's original form.

Note that from a thermomechanical standpoint, the expression [29] is not a standard law *stricto sensu* because the parameter, p, takes part in the dissipation potential. This is a characteristic of multiplicative work-hardening/viscosity laws which require the introduction of a further condition, in addition to the generalised normality law, in order to guarantee the Clausius-Duhem condition. One solution consists in assuming that the free energy is independent of p, in which case R (Eq 12) cancels out. It can then be said that Ω^{vp} is a convex function on condition that the parameter N is positive. For $\boldsymbol{\sigma} = \mathbf{0}$, (R = 0) we obtain $\Omega^{vp} = 0$, and the potential therefore effectively contains the origin.

The mechanical power dissipated by the viscoplastic process is then expressed by:

$$\Phi^{vp} = \boldsymbol{\sigma} : \frac{\partial \Omega^{vp}}{\partial \boldsymbol{\sigma}} - R\frac{\partial \Omega^{vp}}{\partial R} \qquad [34a]$$

$$\Phi^{vp} = \boldsymbol{\sigma} : \dot{\boldsymbol{\varepsilon}}^{vp} - R\dot{p} \qquad [34b]$$

with R = 0, the dissipation is reduced to:

$$\Phi^{vp} = \boldsymbol{\sigma} : \dot{\boldsymbol{\varepsilon}}^{vp} \qquad [34c]$$

2.3 Law of induced anisotropic damage

In this section an appropriate description is proposed for delayed damage mechanisms by introducing a tensorial damage variable and by defining a time-dependent law for this variable.

Experimental observations have highlighted anisotropic damage in rock [6]. Under a low average stress, mechanically induced microcracks are generated in extension mode (mode I), and continue to grow in the main stress direction, thereby inducing an anisotropy in the mechanical properties [5]. This induced anisotropy is therefore the result of a change in rock damage which expressed the progressive deterioration of the cohesion of the material. This causes general dilatance of the rock and subsequently leads to deferred failure.

Lemaitre's viscoplastic law is classically coupled with isotropic damage described by a scalar damage variable, D, which cannot express the anisotropy of damage. Several authors [13], [14] have shown that the geometrical properties of a given damage state can be correctly described by a second-order symmetrical tensor. The main limitation of this approach is that, in the most general case, the damage described has an orthotropic symmetry where the orthotropic axes are identified with the main directions of the damage tensor. However, this limitation is not penalising when modelling most geomaterials and a second-order symmetrical tensor, **D**, has therefore been chosen to express the damage anisotropy.

The description of material damage is based on the concept of effective stress [15], [16], [17]. Various proposals can be found in the literature regarding the formulation of a symmetrical effective stress tensor linked to a second-order damage tensor. In the model described here, the effective stress is defined as follows:

$$\tilde{\boldsymbol{\sigma}} = (\mathbf{I} - \mathbf{D})^{-1/2} \cdot \boldsymbol{\sigma} \cdot (\mathbf{I} - \mathbf{D})^{-1/2} \qquad [35]$$

where $\mathbf{I}$ and $\boldsymbol{\sigma}$ are respectively the second-order identity tensor and the stress tensor and $\tilde{\boldsymbol{\sigma}}$ the effective stress. This expression, derived from the energy equivalence principle, is that proposed by Cordebois and Sidoroff [18]. Contrary to a formulation based on the deformation equivalence principle, it has the advantage of automatically ensuring the symmetry of the effective stress tensor. Assuming that the viscoplastic and damage processes dissipate independently, the dissipation potential can be written as follows:

$$\Omega^{D} = \frac{1}{2}\mathbf{Y} : \overset{=4=}{\mathbf{S}} : \mathbf{Y} \qquad [36]$$

where $\mathbf{Y}$ is the thermodynamic force associated with the damage (second-order tensor) and $\overset{=4=}{\mathbf{S}}$ a fourth-order tensor, referred to the structure tensor.

The damage change law is then written:

$$\dot{\mathbf{D}} = \frac{\partial \Omega^{D}}{\partial \mathbf{Y}} = \overset{=4=}{\mathbf{S}} : \mathbf{Y} \qquad [37]$$

The damage effects are represented by the effective stress, $\tilde{\boldsymbol{\sigma}}$, which is substituted in the constitutive equations in place of the stress actually applied and the damage variable. Thus:

$$\dot{\boldsymbol{\varepsilon}}(\boldsymbol{\sigma}, \mathbf{D}, ...) = \dot{\boldsymbol{\varepsilon}}(\tilde{\boldsymbol{\sigma}}, ...) \qquad [38]$$

The time-dependent change in damage also depends on the state of applied stress and the present state of damage of the material. It is possible to represent them by a fictitious driving stress, $\hat{\boldsymbol{\sigma}}$, which appears in the damage change equation in place of the stress actually applied and the damage variable:

$$\dot{\mathbf{D}}(\boldsymbol{\sigma}, \mathbf{D}, ...) = \dot{\mathbf{D}}(\hat{\boldsymbol{\sigma}}, ...) \qquad [39]$$

This approach was proposed by Qi and Bertram [19]. For the drive stress, the following form has been considered:

$$\hat{\boldsymbol{\sigma}} = \left[(\mathbf{I} - \mathbf{D}) / \det(\mathbf{I} - \mathbf{D})\right]^{q/2} \cdot \boldsymbol{\sigma} \cdot \left[(\mathbf{I} - \mathbf{D}) / \det(\mathbf{I} - \mathbf{D})\right]^{q/2} \qquad [40]$$

In this expression, q is a parameter of the material enabling the damage effect on the rate of deformation to be distinguished from the effect on its change. This distinction is necessary because experimental observations show that the influence of damage is greater on the damage growth rate than on overall mechanical behaviour. Using $\hat{\boldsymbol{\sigma}}$ the thermodynamic force associated with the damage can be defined as:

$$\mathbf{Y} = \left\langle \frac{t\hat{\boldsymbol{\sigma}}}{A} \right\rangle^{r} = \sum_{i=1}^{3} \left\langle \frac{t\hat{\sigma}_i}{A} \right\rangle^{r} \vec{\hat{\mathbf{s}}}_i \otimes \vec{\hat{\mathbf{s}}}_i \qquad [41]$$

where A and r are material parameters, < > Macaulay brackets, $\hat{\sigma}_i$ and $\vec{\hat{\mathbf{s}}}_i$ the eigenvalues and the eigenvectors of $\hat{\boldsymbol{\sigma}}$ respectively, t indicates the state of triaxiality of the stresses and is expressed by:

$$t = \frac{\sigma_{eq}}{3\sigma_m} \qquad [42]$$

Note that the positivity imposed on **Y** does not exclude damage change by tensile stresses (negative stresses) because of the presence of the triaxiality term in the expression. The only non-permissible stress state is the special case where $\sigma_m = 0$ but $\sigma_{eq} \neq 0$.

The structure tensor links the damage driving forces to its structural change by taking the following form:

$$\overset{=4=}{\mathbf{S}} = (\beta - 1)\ \overset{=4=}{\mathbf{I}} + \mathbf{I} \otimes \mathbf{I} \qquad [43]$$

where $\overset{=4=}{\mathbf{I}}$ is the fourth-order unit tensor and β the anisotropy parameter of the model.

This parameter β expresses the degree of anisotropy of damage change. $\beta = 1$ corresponds to isotropic change whereas $\beta = 0$ models an anisotropic change where the damage extends only in the direction perpendicular to the driving stress. Obviously, β can take any real intermediate value. Figure 1 shows the value of the parameter β for the two extreme configurations. The damage change law is finally expressed by:

$$\dot{\mathbf{D}} = \overset{=4=}{\mathbf{S}} : \mathbf{Y} = \left((\beta - 1)\ \overset{=4=}{\mathbf{I}} + \mathbf{I} \otimes \mathbf{I} \right) : \sum_{i=1}^{3} \left\langle \frac{t\hat{\sigma}_i}{A} \right\rangle^r \vec{\hat{\mathbf{s}}}_i \otimes \vec{\hat{\mathbf{s}}}_i \qquad [44]$$

It can be shown that the form of the structure tensor implies that the eigenvectors of the damage rate tensor have the same orientation as those of the driving stress tensor. The material fails when one eigenvalue of **D** reaches a critical value $D_{crit.} = 1$.

For uniaxial stress application, with isotropic change $(\beta = 1)$ and by letting $(qr \equiv k)$, we obtain exactly the classic expression proposed by Kachanov [20] and Rabotnov [21], for describing damage growth by tertiary creep.

It is also worth noting that the unilateral effects relating to the closure and thus deactivation of microcracks have not been taken into account. In the absence of cyclic stress applications, it was considered useful to integrate the deactivation conditions in the model. Finally, the damage as defined in Equation [44] is always increasing or constant; in other words, the "healing" of the material is not authorized by the model. The damage dissipation potential is therefore defined by:

$$\Omega^D = \frac{1}{2} \mathbf{Y} : \overset{=4=}{\mathbf{S}} : \mathbf{Y} \qquad [45]$$

Ω^D is a convex function (quadratic) in **Y**. For **Y** = **0** it cancels out. In addition, the intrinsic damage dissipation is always positive or zero. It is written by:

$$\Phi^D = \mathbf{Y} : \frac{\partial \Omega^D}{\partial \mathbf{Y}} \qquad [46]$$

The fourth-order tensor $\overset{=4=}{\mathbf{S}}$ (structure tensor) is defined as being symmetrical and positive in the main reference frame of the driving forces with $0 \leq \beta \leq 1$. Given that the Macaulay brackets in **Y** guarantee the positivity of the driving tensor, the thermodynamic restrictions are therefore satisfied.

2.4 Coupling of viscoplasticity and damage

It is now possible to couple the viscoplastic law with irreversible volume deformation, and the anisotropic damage law. The advantage of coupling lies in the fact that the stress and deformation response of the material depends not only on viscous mechanisms but also, simultaneously, on the damage. Coupled calculations provide a means of obtaining the stress, deformation and damage states at any moment.

In order to describe the behaviour of a viscoplastic material capable of being work-hardened and damaged, the equivalence principle is applied simply by replacing the stress $\boldsymbol{\sigma}$ by the effective stress $\tilde{\boldsymbol{\sigma}}$ defined by Equation [35].

This modification concerns all deformations. The partition hypothesis divides the total deformation into an elastic and an inelastic part. Formulation of consistency requires replacing the stress by the effective stress in the stress vs elastic and viscoplastic deformation relations. The isotropic elastic behaviour is therefore described by Hooke's coupled law:

$$\dot{\boldsymbol{\varepsilon}}^{e} = \frac{1+\nu}{E}\dot{\tilde{\boldsymbol{\sigma}}} - \frac{\nu}{E}\mathrm{tr}(\dot{\tilde{\boldsymbol{\sigma}}})\cdot\mathbf{I} \qquad [47]$$

In the viscoplastic formalism, the only term affected by this change is the dissipation potential, the other variables of the viscoplastic model remaining unchanged. The potential is then written:

$$\Omega^{vp} = \frac{K}{N+1}\left\langle \frac{f(\tilde{J}_2;\tilde{I}_1)}{K} \right\rangle^{N+1} p^{-N/M} \qquad [48]$$

It can be seen that the potential keeps its multiplicative form and that the viscoplastic coefficients (M, N and K) remain the same. Only the equipotential surface function is subject to modifications, this being a natural consequence of applying the equivalence principle. The effective stress replaces the stress value in the calculation of the invariants and thus defines a new equipotential surface as a function of the damage state of stresses. The viscous and damage states are then coupled. This new equipotential surface is obtained by:

$$f(\tilde{J}_2;\tilde{I}_1) = \tilde{\sigma}_{eq} + \alpha\tilde{\sigma}_m \qquad [49]$$

where $\tilde{\sigma}_{eq}$ is the equivalent effective stress:

$$\tilde{\sigma}_{eq} = \sqrt{\frac{3}{2}\tilde{\mathbf{S}}:\tilde{\mathbf{S}}} \qquad [50]$$

with $\tilde{\mathbf{S}}$ the effective stress deviator:

$$\tilde{\mathbf{S}} = \tilde{\boldsymbol{\sigma}} - \frac{1}{3}\mathrm{tr}\tilde{\boldsymbol{\sigma}}\cdot\mathbf{I} \qquad [51]$$

and $\tilde{\sigma}_m$ the mean effective stress:

$$\tilde{\sigma}_m = \frac{1}{3}\mathrm{tr}\tilde{\boldsymbol{\sigma}} \qquad [52]$$

The parameter α, defined previously, expresses the dilatancy. This parameter also remains independent and is not influenced by the damage, i.e., the effects of the damage are superimposed on the viscosity effects. This separation enables more complex volume behaviours to be simulated (for example, contracting in a first stage and then dilatant).

The effective stress is calculated, as a function of the nominal stress and the damage variable, the change law of which was developed in equations [37-44].

The viscoplastic deformation rate is deduced, as seen in Equations [30 a-c], by application of the normality rule on the dissipation potential. Obviously, for the coupled model, the rate is obtained from the viscoplastic dissipation potential, modified according to Equation 48. We obtain:

$$\dot{\boldsymbol{\varepsilon}}^{\mathbf{vp}} = \frac{\partial \Omega^{vp}}{\partial \boldsymbol{\sigma}} \qquad [53a]$$

$$\dot{\boldsymbol{\varepsilon}}^{\mathbf{vp}} = \frac{\partial \Omega^{vp}}{\partial \tilde{\sigma}_{eq}} \frac{\partial \tilde{\sigma}_{eq}}{\partial \boldsymbol{\sigma}} + \frac{\partial \Omega^{vp}}{\partial \tilde{\sigma}_{m}} \frac{\partial \tilde{\sigma}_{m}}{\partial \boldsymbol{\sigma}} \quad [53b]$$

$$\dot{\boldsymbol{\varepsilon}}^{\mathbf{vp}} = \left\langle \frac{\tilde{\sigma}_{eq} + \alpha \tilde{\sigma}_{m}}{Kp^{1/M}} \right\rangle^{N} (\mathbf{I} - \mathbf{D})^{-1/2} \cdot \left(\frac{3}{2} \frac{\tilde{\mathbf{S}}}{\tilde{\sigma}_{eq}} + \frac{\alpha \mathbf{I}}{3} \right) \cdot (\mathbf{I} - \mathbf{D})^{-1/2} \qquad [53c]$$

$$\dot{\boldsymbol{\varepsilon}}^{\mathbf{vp}} = \left\langle \frac{\tilde{\sigma}_{eq} + \alpha \tilde{\sigma}_{m}}{Kp^{1/M}} \right\rangle^{N} \left(\frac{3}{2} \frac{\tilde{\tilde{\mathbf{S}}}}{\tilde{\sigma}_{eq}} + \frac{\alpha (\mathbf{I} - \mathbf{D})^{-1}}{3} \right) \qquad [53d]$$

with the notation:

$$\tilde{\tilde{\mathbf{S}}} \equiv (\mathbf{I} - \mathbf{D})^{-1/2} \cdot \tilde{\mathbf{S}} \cdot (\mathbf{I} - \mathbf{D})^{-1/2} \qquad [54]$$

The state of material work hardening, still characterised by the cumulative viscoplastic deformation, is calculated by:

$$\dot{p} = \sqrt{\frac{2}{3}} \left\langle \frac{\tilde{\sigma}_{eq} + \alpha \tilde{\sigma}_{m}}{Kp^{1/M}} \right\rangle^{N} \left\| \left(\frac{3}{2} \frac{\tilde{\tilde{\mathbf{S}}}}{\tilde{\sigma}_{eq}} + \frac{\alpha (\mathbf{I} - \mathbf{D})^{-1}}{3} \right) \right\| \qquad [55]$$

where the sign $\| \ \|$ designates the Euclidian norm. This enables the constitutive law to be cast in the following final form:

$$\dot{\boldsymbol{\varepsilon}}^{\mathbf{vp}} = \sqrt{\frac{3}{2}}\dot{p}\frac{\left(\frac{3}{2}\frac{\tilde{\tilde{\mathbf{S}}}}{\tilde{\sigma}_{eq}} + \frac{\alpha(\mathbf{I}-\mathbf{D})^{-1}}{3}\right)}{\left\|\left(\frac{3}{2}\frac{\tilde{\tilde{\mathbf{S}}}}{\tilde{\sigma}_{eq}} + \frac{\alpha(\mathbf{I}-\mathbf{D})^{-1}}{3}\right)\right\|} \qquad [56]$$

3 Identification of parameters and study of their influence based on tests results

3.1 Types of tests and definition of parameters

This section presents the method used for identifying the model parameters based on tests results. The influence of each of these parameters is then studied. To determine the mechanical properties of a damageable viscoplastic material, simple tests such as monotonous loading tests, creep tests and relaxation tests, have to be performed.

To highlight the role of each parameter, each type of test was simulated by considering a set of parameters representative of a soft rock. These simulations were carried out for a uniaxial compressive loading. The new viscoplastic model with damage previously presented in tensorial form for the general three-dimensional case is developed in Appendix for uniaxial loading. The meaning and denomination of the parameters as well as the values considered are given below :

N, is the viscosity exponent,	$2 < N < 100$
M, is the work-hardening parameter,	$2 < M < 50$
K, is the viscoplastic stiffness coefficient,	$50 < K < 10\,0000$ MPa.s
r, is the damage exponent,	$1 < r < 20$
q, is the damage progression parameter,	$0 < q < 1$
A, is the tenacity coefficient	$10 < A < 1\,000$ MPa.s

3.2 Viscoplastic and damage parameters

Consider the coupled viscoplastic model with damage. In a first stage, the value of the viscoplastic dilatancy-contractancy parameter, α, is kept equal to 0 (no viscoplastic volume deformation) and the value of the damage anisotropy parameter, β, is equal to 1 (isotropic damage). A detailed discussion, presented in the last part of the section, is devoted to a study of the influence of these two variables.

3.2.1 Viscosity exponent N

The sensitivity of the model to the viscosity exponent, N, is shown on figures 2 to 5. For each type of stress (monotonous loading test, creep test, relaxation test) two values of N were studied. Two loading rates ($\dot{\varepsilon} = \dot{\varepsilon}_0$ and $\dot{\varepsilon} = 100\dot{\varepsilon}_0$) for the monotonous loading test and three levels of initial relaxation stress (0.3 R_c, 0.6 R_c and 0.9 R_c where R_c is the uniaxial compressive strength) were simulated.

For the creep test, simulations were run with two loading levels ($\sigma = \sigma_0$ and $\sigma = 1.5\sigma_0$). It was found that, for a high value of N ($N = 5N_{ref}$), the stress has considerable influence on the axial anelastic deformation (figure 2b), whereas, conversely, when N is small ($N = N_{ref}$), the difference is less marked (figure 2a).

Under monotonous compressive loading (figure 3) a low value of the viscosity exponent leads to a significant influence of the loading rate (figure 3a). Axial deformations increase with reduction in $\dot{\varepsilon}$. On the other hand, for a high value of N (figure 3b) the influence of loading rate on the amplitude of viscoplastic deformations is much less marked. In comparison, elastic deformations are represented on the same figure by a dotted straight line.

For a high value of N, the relaxation test simulations (figure 4) give evidence of the considerable influence of initial axial stress (figure 4b). At low levels of imposed initial stress ($\sigma_0 = 0.3R_c$ or $0.6R_c$) stress relaxation is virtually non-existent. On the other hand, a low-valued viscosity exponent (figure 4a) generates much greater stress relaxation.

In summary, the main role of the viscosity exponent N is to express the sensitivity of the growth of viscous deformations to a stress variation. The experiment shows that the value of N varies between 2 and about 100: two for highly viscous materials and 100 for materials of low viscosity. A very high value of N suggests the application of an elasto-plastic law.

3.2.2 Work-hardening parameter M

The parameter, M, expresses an increase in strength as a result of work-hardening. The analysis of the work-hardening parameter, M, is presented in figures 5 to 7. Generally speaking, it is found that a low value of this variable causes viscoplastic deformations which appear rapidly, reaching higher values than those obtained with a higher work-hardening parameter. This is visible in creep conditions on figure 5. The same trend is observed under monotonous compression on figure 6 where the elastic deformation has been plotted (dotted line).

In relaxation (figure 7) a rapid fall in stress is observed for a low work-hardening parameter, whereas a higher value leads to a slower decrease in stress. After the first relaxation phase, the slope of the curve no longer appears to be sensitive to the quantity M. In practice, M varies from 2 to about 50.

3.2.3 Viscoplastic stiffness K

The influence of the viscoplastic stiffness coefficient, K, on the model response is illustrated by figures 8 to 10. In a similar manner to the observations for the work-hardening parameter, M, it is found that irreversible deformations become all the greater as K becomes smaller. This is applicable in creep (figure 8) and in monotonous compression conditions (figure 9).

The main difference between the effect of the parameter M and that of the parameter K is that the viscoplastic stiffness coefficient has no influence on the shape of the curves, but provides only a quantitative adjustment. For example, if the three creep curves (figure 8) were represented in a normalised reference frame with respect to the axial anelastic deformation on failure, like for the work-hardening parameter, M (figure 5b), three perfectly superimposed curves would be obtained. The parameter K is the only one of the viscoplastic parameters which is not adimensional. For rocks, its value ranges from 50 to 10 000 MPa·s.

3.2.4 Damage exponent r

The sensitivity of the model to variations in the damage exponent, r, is presented on figures 11 to 13. In a similar manner to the procedure followed for the analysis of the viscosity exponent, N, different values of the test parameters (imposed creep stress, σ, imposed loading rate under monotonous compression, $\dot{\varepsilon}$, and initial stress in relaxation, σ_0) were examined. Two different values of r were studied.

The creep curves (figure 11) reflect a clear dependence of imposed stress level as a function of the damage exponent. For a high value of r, failure occurs very soon after the stress application (figure 11b). The axial anelastic deformation on failure is lower for $\sigma = 1.5\sigma_0$ than that obtained for $\sigma = \sigma_0$. The smaller the damage exponent, the less sensitive the model becomes to a variation in stress level (figure 11a).

The monotonous loading tests (figure 12) show that the peak values on the axial stress-axial deformation curve are sensitive to the loading rate for a low damage exponent value. Conversely, by increasing the value of r, a less marked sensitivity to variations in $\dot{\varepsilon}$ can be modelled (figure 12a).

The simulation of a relaxation test (figure 13) indicates that a smaller damage exponent leads to greater stress relaxation (figure 13a). Conversely, with a higher value of r the relaxation is less significant, especially when a low initial stress is imposed ($\sigma_0 = 0.3\sigma_c$). It is worth noting that the difference between the two curves (figure 13a and 13b) is not viscous in origin (the viscoplastic parameters were kept constant and identical in both cases) but is rather due to deferred damage which continues to develop progressively even after axial deformation has been blocked. The damage continues to expand for as long as the stress is not zero or until failure occurs. Only the damage expansion rate reduces with decrease in stress value.

In addition, a highly accelerated rise in the damage variable was observed for a high value of r whereas a lower value generates a slower expansion. The time required to reach failure $(D = 1)$ increases when r becomes smaller. The parameter r in the model therefore reflects the dependence of the expansion of the damage variable on a stress variation. Its role is therefore similar to that of parameter N in viscoplasticity.

3.2.5 Damage progression parameter q

The analysis of the damage progression parameter, q, is shown on figures 14 to 16. The role of this parameter in the model is very clear and can be easily identified for each loading configuration. As a general rule, q can be said to be responsible for the variation in the rate of change of the damage variable, i.e., the greater the value of q the more quickly the damage expands and the more sudden failure occurs. Conversely, a lower value of q leads to a deferred, less brittle failure.

For example, in creep (figure 14) a high damage expansion parameter leads to sudden failure which is reflected in an almost total absence of the tertiary phase. As the value of q reduces, this phase becomes more distinct and a high axial anelastic deformation can be observed before failure.

The same trend is noted in monotonous compression (figure 15). As the parameter q increases, the post-peak phase becomes increasingly significant and the model describes a more ductile behaviour. Conversely, a high value of q leads to brittle failure, without strain-softening.

The simulation of relaxation tests (figure 16) shows that as the value of the damage expansion parameter increases, so the damage continues to expand in a relaxation regime. This leads to a more significant drop in stress and may possibly cause failure in relaxation conditions.

3.2.6 Tenacity coefficient A

We shall now examine the influence of the tenacity coefficient, A, on the model response to different loading configurations (figures 17 to 19). The role played by A in the damage process is comparable to that played by the coefficient K in viscoplastic conditions. The parameters K and A are used for quantitative adjustment of the values.

For example, in creep conditions (figure 17) different times to failure can be calculated by varying A, while keeping the same axial anelastic deformation expansion value. Under quasi-static compression conditions (figure 18) the tenacity coefficient affects the amplitude of the axial deformation caused by damage. It can clearly be seen that viscous axial deformation is the same (deviation of the curves with respect to the elastic line is identical) for the three values of A before the stress reaches the level where the damage effect becomes significant. On the relaxation curve (figure 19), the increase in tenacity coefficient slows down the stress reduction but the change in σ has the same general trend.

The parameter, A, thus enables the failure time to be adjusted without changing the shape of the curve $D(t)$. The higher the value of A the longer it takes for failure to occur. It can therefore be said that the parameter A reflects the damage resistance in the model. The parameter A is expressed in [MPa·s], the other damage parameters (r and q) are dimensionless.

3.2.7 Viscoplastic dilatancy parameter α and damage anisotropy parameter β

Finally, the influences of the viscoplastic dilatancy parameter, α, and damage anisotropy parameter, β are shown. These two parameters, which represent an enhancement of the classic Lemaitre model, are directly responsible for the dilatancy of irreversible volume deformations.

The general cases of anisotropy were modelled by varying the values of β between 0 and 1 in 0.5 steps. The values of α sweep a range from –0.75 to 0.75 in 0.375 steps. The results of creep test simulations are presented on figures 20 to 22. Depending on these two parameters, the delayed volume deformation can be purely contracting, purely dilatant or a combination of both, i.e., contracting first and then dilatant.

For isotropic damage (β=1), simultaneous failure is observed in the axial and lateral directions (figure 20). As the value of β decreases, damage becomes increasingly anisotropic and the tertiary creep phase in the axial direction gradually attenuates. For β=0, damage expands only in the direction perpendicular to the applied stress direction (figure 22).

Figures 23 and 24 also illustrate the influence of α and β on delayed volume behaviour. Note that after one week, the parameter α exerts a virtually exclusive influence on deferred volume deformation (figure 23). For positive values of α the behaviour is contracting (light area on figure) whereas negative values of α generate dilatancy (dark area). After four weeks of creep (figure 24), i.e., close to failure, which occurred after 31.5 days, the irreversible volume deformation is amplified. Considerable extension of the dilatant zone can also be noted for values of $\beta \neq 1$ thereby illustrating the influence of deferred anisotropic damage on volume behaviour.

The simulations of monotonous loading tests are represented on figures 25, 26 and 27. The set of parameters applied here was the same as for the creep test simulation .

It is worth noting that, for a completely anisotropic damage expansion (β=0, figure 25), the behaviour is of the brittle type. This phenomenon is due to the “latent” variation in damage in the lateral direction, leading to failure but is not reflected on the axial curves. With the progressive

reduction in anisotropy (increase in value of β) behaviour becomes ductile with an increasingly marked post-peak phase.

Note that the uniqueness of the solution is not lost because each point of a curve corresponds to a particular state of the material characterised by a time-dependent expanding damage state.

4 Comparison with test results

In this section, the performance of the damaging viscoplastic model is assessed by comparison with the results of tests carried out on a variety of rocks. However, it is rare to have access to complete experimental data bases with the results of creep, relaxation and quasi-static compressions tests on the same material. Consequently, the aim of the analysis presented in the following section is not to determine a set of unique parameters for each material studied, but rather to illustrate the capacity of the model to take into account and reproduce the various phenomena brought to light by the laboratory tests.

4.1 Creep test in uniaxial compression

4.1.1 Test on an argilite

By examining the creep behaviour of an argillite [22], the rate of change in volume was highlighted. Under a uniaxial stress of 26 MPa, the rock shows deferred volume behaviour: contracting at the start of the test but subsequently expanding (figure 28). The first phase lasts for about ten days and leads to a reduction in sample volume. There then follows a change in the volume behaviour trend; contraction of the sample is replaced by expansion (i.e dilatancy). After 270 days, the sample has the same volume as it had initially before stress application. From this time onwards, behaviour is generally dilatant. This reversal of trend could possibly be explained by a combination of contracting viscous behaviour and dilatant anisotropic damage. However, no information is available regarding the deferred failure of the rock.

In order to determine the intrinsic viscoplastic parameters of the materials, the analysis was limited to the first week of the test, i.e., the period during which deferred damage has not yet been able to exert a significant influence on the change in material deformation. For the damage parameters, the procedure followed is that proposed by Hajdu [23]. Figure 28 compares the experimental results with those obtained by the model. There is a very good approximation of the deformation induced by the uniaxial stress in the rock. The viscoplastic model, ma king allowance for deferred volume deformations, proves to be particularly well suited to modelling the complex deferred mechanical behaviour of the argilite sample.

Concerning the two new parameters introduced, namely α and β, it is worth noting that the values obtained correspond well to anisotropic damage with dilatancy.

4.1.2 Test on a marble

Another experimental result, obtained with uniaxial creep on a sample of Sicilian marble, as reported by Singh (1975), [1] was simulated by means of the model. The model parameters setting method is similar to that used for argilite. The parameters were calibrated with respect to the experimental points. Figure 29 shows the results obtained.

By examining the volume parameters obtained, a very high negative coefficient of viscoplastic expansion is noted. This result was expected, because the porosity of a rock such as marble is very low

and, as a result, it does not show a contracting phase due to micropore collapse. On the other hand, the value of the anisotropic damage parameter, β, shows the anisotropy of damage.

4.2 Quasi-static test in uniaxial compression

4.2.1 Test on an anhydrite

One result of the tests conducted at the laboratory 3S on an anhydrite is presented on Figure 30. The deferred behaviour under creep is similar to that of the argilite and shows a contracting phase followed by an expanding phase under a sufficiently high uniaxial stress. The results presented here concern only a quasi-static compression test performed at a constant rate. A negative value for α was fixed. As for the value of β, the transverse deformation is clearly greater than the axial deformation when the maximum stress is applied thus reflecting a pronounced anisotropy of damage. Figure 30 shows the model reproduction of this test.

4.2.2 Test on a granite

The last example is also taken from the literature and concerns uniaxial compression on a sample of granite taken from Lac de Bonnet [24].

Observations show that inelastic deferred deformations also appear in brittle rocks, even at stress values that may be considered low compared to the strength of the material. The deferred growth of a micro-crack can thus be considered as a viscoplastic process, thereby justifying the application of the model. Figure 31 compares the experimental results with those obtained with the model. Particularly noteworthy is the very high negative value of the parameter α. This value is very close to that obtained when making the calibration on the creep curve of the Sicilian marble.

5 Conclusion

The model presented in this paper was developed to model time dependent behaviour of rock including delayed failure. The inclusion of the Drucker Prager yield surface in the Lemaitre viscoplastic constitutive equation showed the ability of the model to exhibit dilatancy and contractancy associated with viscoplastic strain. Moreover, the introduction of a second rank tensor for damage parameters allows one to reproduce anisotropic damage observed in compression tests, either creep tests, relaxation tests or quasistatic monotonic tests.

This model requires eight parameters. The method to identify these parameters based on test results was presented and the physical signification of parameters was explained. Some comparisons with test results such as creep tests or monotonous compression tests show a good prediction of the mechanical responses, especially for time at failure.

In practice, this model can be used for the estimation of the evolution in time of the Excavated Damage Zone (EDZ) around underground openings, as for example, those planned for radioactive waste repositories. In this zone, due to the damaging process, dilatancy and porosity increase and can create possible preferential pathways for radionuclide migration. This model is capable of simulating these phenomena and it is intended to use it in the future for the modelling of underground laboratories.

6 References

[1] D. P. Singh, A study of creep of rocks, Int. J. Rock Mech. Min. Sci. & Geomech. Abstr., Vol. 12, pp. 271-276, 1975.

[2] D. A. Lockner, Room temperature creep in saturated granite, J. Geophys. Res., Vol. 98, pp. 475-487, 1993.

[3] C. H. Scholz, Mechanism of creep in brittle rock, J. Geophys. Res., Vol. 73, pp. 3295-3302, 1968.

[4] M. B. Dusseault & C. J. Fordham, Time-dependent behavior of rocks, Comprehensive rock engineering, J. A. Hudson ed., Pergamon Press, Vol. 3, pp. 119-149, 1993.

[5] P. Tapponier & W. F. Brace, Development of stress-induced microcracks in Westerly granite, Int. J. Rock Mech. Min. Sci. & Geomech. Abstr., Vol. 13, pp. 103-112, 1976.

[6] N. Gatelier, F. Pellet & B. Loret, Mechanical damage of an anisotropic rock under cyclic triaxial tests, International Journal of Rock Mechanics and Mining Sciences, Pergamon Press, vol 39, n° 3, pp 335-354, 2002.

[7] E. Boidy & F. Pellet, Identification of mechanical parameters for modeling time-dependent behavior of shale, Balkema Ed., Workshop Andra, Paris – France, pp 11-22, 2000.

[8] J. Lemaitre & J.-L. Chaboche, Aspect phénoménologique de la rupture par endommagement, J. de Mécanique Appliquée, Vol. 2, n°3, pp. 317-365, 1978.

[9] P. Perzyna, Fundamental problems in viscoplasticity, Adv. Appl. Mech, Vol. 9, pp. 247-377, 1966.

[10] D.C. Drucker & W. Prager, Soil mechanics and plastic analysis or limit design, Quarterly of Applied Mathematics, Vol. 10, pp. 157-165, 1952.

[11] J. Desrues, Limitations du choix de l'angle de frottement pour le critère de plasticité de Drucker-Prager, Revue Française de Génie Civil, Vol. 6, pp. 853-862, 2002.

[12] A. Carioso, K. Willam & G. Etse, On the consistency of viscoplastic formulations, Int. J. Solids & Structures, Vol. 37, pp. 7349-7369, 2000.

[13] J. Betten, Damage tensors in continuum mechanics, Journal de Mécanique théorique & Appliquée, Vol. 2, n°1, pp. 13-32, 1983.

[14] J. F. Shao & J. W. Rudnicki, A microcrack based continuous damage model for brittle geomaterials, Mechanics of Materials, Vol. 32, pp. 607-619, 2000.

[15] J. L. Chaboche, Le concept de contrainte effective appliqué à l'élasticité et à la viscoplasticité en présence d'un endommagement anisotrope, Colloques Internationaux du CNRS, Euromech 115, J. P. Boehler ed., pp. 737-759, 19-22 juin, Villard de Lens, France, 1979.

[16] Q.-S. Zheng & J. Betten, On damage effective stress and equivalence hypothesis, Int. J. of Damage Mechanics, Vol. 5, pp. 219-240, 1996.

[17] F. Sidoroff, Description of anisotropic damage application to elasticity, Syposium IUTAM, J. Hult & J. Lemaitre ed., pp. 237-244, May 27-30, Senlis, France, 1980.

[18] J.-P. Cordebois & F. Sidoroff, Endommagement anisotrope en élasticité et plasticité, Journal de Mécanique Théorique et Appliquée, n° spécial, pp. 45-59, 1982.

[19] W. Qi & A. Bertram, Anisotropic continuum damage modelling for F.C.C.-single crystals at high temperatures, Int. J. Plasticity,Vol. 15, n°11, pp. 1197-1215, 1999.

[20] L. M. Kachanov, Time of the rupture process under creep conditions, Izv. Adad. Nauk. USSR Otd. Tekh., Vol. 8, pp. 26-31, 1958.

[21] Y. N. Rabotnov, Creep rupture, Proc. 12th Int. Congr. Appl. Mech., Springer-Verlag, pp. 342-349, 1969.

[22] F. Pellet, E. Boidy, A. Bouvard & N. Hoteit, (2003) "Viscoplastic behavior and damage to rock related to the design of underground waste depository", proceedings of the 10th International Congress on Rock Mechanics, Sandton, South-Africa, pp 893-898.

[23] A. Hajdu, Modélisation numérique du comportement viscoplastique endommageable des roches et application aux ouvrages souterrains de stockage, Thèse de doctorat de l'Université Joseph Fourier – Grenoble I, 333pp, 2003.

[24] J. F. Shao, D. Hoxha, M. Bart, F. Homand, G. Duveau, M. Souley & N. Hoteit, Modelling of induced anisotropic damage in granites, Int. J. Rock Mech. Min. Sci.,Vol. 36, pp. 1001-1012, 1999.

[25] F. Pellet, A Hajdu, M. Boulon, F. Deleruyelle & F. Besnus, Numerical modeling of underground structures taking into account the visco-plastic behavior and damaging of rock, Proceedings of the International Conference on Numerical Models in Geomechanics - NUMOG VIII, Roma - Italy, pp 399-404, 2002.

7 Appendix

Details of the new model presented in the text are given here for the case of uniaxial loading. An axisymmetrical reference frame is considered, which allows the loading axis, noted 1, to be the axis of revolution.

The stress tensor:

$$\boldsymbol{\sigma} = \begin{bmatrix} \sigma_1 & 0 & 0 \\ 0 & 0 & 0 \\ 0 & 0 & 0 \end{bmatrix} \qquad \text{[A-1]}$$

The effective stress tensor:

$$\tilde{\boldsymbol{\sigma}} = \begin{bmatrix} \dfrac{\sigma_1}{1-D_1} & 0 & 0 \\ 0 & 0 & 0 \\ 0 & 0 & 0 \end{bmatrix} \qquad \text{[A-2]}$$

The effective deviator:

$$\tilde{\mathbf{S}} = \frac{\sigma_1}{1-D_1} \begin{bmatrix} \dfrac{2}{3} & 0 & 0 \\ 0 & -\dfrac{1}{3} & 0 \\ 0 & 0 & -\dfrac{1}{3} \end{bmatrix} \qquad \text{[A-3]}$$

and the tensor $\tilde{\tilde{\mathbf{S}}}$:

$$\tilde{\tilde{\mathbf{S}}} = \begin{bmatrix} \dfrac{2}{3}\dfrac{\sigma_1}{(1-D_1)(1-D_1)} & 0 & 0 \\ 0 & -\dfrac{1}{3}\dfrac{\sigma_1}{(1-D_1)(1-D_3)} & 0 \\ 0 & 0 & -\dfrac{1}{3}\dfrac{\sigma_1}{(1-D_1)(1-D_3)} \end{bmatrix} \qquad \text{[A-4]}$$

as well as the mean effective stress:

$$\tilde{\sigma}_m = \frac{1}{3}\frac{\sigma_1}{1-D_1} \qquad \text{[A-5]}$$

and the equivalent effective stress:

$$\tilde{\sigma}_{eq} = \frac{\sigma_1}{1-D_1} \qquad \text{[A-6]}$$

thus enabling the expression strain rate can written in the following forms. For the axial direction:

$$\dot{\varepsilon}_1^{vp} = \frac{1}{1-D_1}\left(1+\frac{\alpha}{3}\right)\left(\frac{\left(1+\frac{\alpha}{3}\right)\sigma_1}{(1-D_1)Kp^{1/M}}\right)^N \qquad \text{[A-7]}$$

and for the transversal direction:

$$\dot{\varepsilon}_3^{vp} = \frac{1}{1-D_3}\left(-\frac{1}{2}+\frac{\alpha}{3}\right)\left(\frac{\left(1+\frac{\alpha}{3}\right)\sigma_1}{(1-D_1)Kp^{1/M}}\right)^N \qquad \text{[A-8]}$$

The work-hardening scalar, p, is then calculated:

$$\left\|\left(\frac{3}{2}\frac{\tilde{\tilde{\mathbf{S}}}}{\tilde{\sigma}_{eq}}+\frac{\alpha(\mathbf{I}-\mathbf{D})^{-1}}{3}\right)\right\| = \sqrt{\left(\frac{1+\alpha/3}{1-D_1}\right)^2+2\left(\frac{-1/2+\alpha/3}{1-D_3}\right)^2} \qquad \text{[A-9]}$$

$$p = \sqrt{\frac{2}{3}}\varepsilon_1^{vp}\frac{\sqrt{\left(\frac{1+\alpha/3}{1-D_1}\right)^2 + 2\left(\frac{-1/2+\alpha/3}{1-D_3}\right)^2}}{\frac{1+\alpha/3}{1-D_1}} \qquad \text{[A-10a]}$$

and:

$$p = \sqrt{\frac{2}{3}}\varepsilon_3^{vp}\frac{\sqrt{\left(\frac{1+\alpha/3}{1-D_1}\right)^2 + 2\left(\frac{-1/2+\alpha/3}{1-D_3}\right)^2}}{\frac{-1/2+\alpha/3}{1-D_3}} \qquad \text{[A-10b]}$$

The expression of time-dependent viscoplastic deformation, under constant loading (creep test) is then obtained by integration of the expressions:

$$\varepsilon_1^{vp}(t) = \left(1+\frac{\alpha}{3}\right)\left\{\frac{M+N}{M}\left(\frac{(1+\alpha/3)\sigma_1}{K}\right)^N \int_0^t \left(\frac{1}{1-D_1}\right)^{\frac{M+N}{M}} \left(\frac{1}{1-D_1}\left[\frac{2}{3}\left(\frac{1+\alpha/3}{1-D_1}\right)+\frac{4}{3}\left(\frac{-1/2+\alpha/3}{1-D_3}\right)\right]^{-1/2M}\right)^N dt\right\}^{\frac{M}{M+N}}$$

[A-11a]

and:

$$\varepsilon_3^{vp}(t) = \left(-\frac{1}{2}+\frac{\alpha}{3}\right)\left\{\frac{M+N}{M}\left(\frac{(1+\alpha/3)\sigma_1}{K}\right)^N \int_0^t \left(\frac{1}{1-D_3}\right)^{\frac{M+N}{M}} \left(\frac{1}{1-D_1}\left[\frac{2}{3}\left(\frac{1+\alpha/3}{1-D_1}\right)+\frac{4}{3}\left(\frac{-1/2+\alpha/3}{1-D_3}\right)\right]^{-1/2M}\right)^N dt\right\}^{\frac{M}{M+N}}$$

[A11-b]

where the change in damage variables is expressed by:

$$\dot{D}_3 = \left(\frac{\sigma_1}{A(1-D_3)^{2q}}\right)^r \qquad \text{[A-12a]}$$

$$\dot{D}_1 = \beta\left(\frac{\sigma_1}{A(1-D_3)^{2q}}\right)^r \qquad \text{[A-12b]}$$

and is written in integrated form (with the conditions σ_1=constant and $D_1=D_3=0$ at t=0):

$$1-D_3=\left[1-(2qr+1)\left(\frac{\sigma_1}{A}\right)^r t\right]^{\frac{1}{2qr+1}} \qquad \text{[A-13a]}$$

$$1-D_1=\left[1-\beta(2qr+1)\left(\frac{\sigma_1}{A}\right)^r t\right]^{\frac{1}{2qr+1}} \qquad \text{[A-13b]}$$

This system of equations does not accept an analytical solution. The simulations of a creep test and a quasi-static test were programmed in Fortran language. The numerical integration method is achieved with a constant time step. However, it is possible to obtain an analytical solution in the case of a creep test with isotropic damage (β=1). The integrated form of the behaviour law is then expressed by:

$$\varepsilon_1^{vp}(t)=\left(1+\frac{\alpha}{3}\right)\left\{t_{rupt.}\frac{A}{B}\left[1-\left(1-\frac{t}{t_{rupt.}}\right)^B\right]\left[\frac{\left(1+\frac{\alpha}{3}\right)\sigma_1}{K\left(\frac{2}{9}\alpha^2+1\right)^{1/2M}}\right]^N\right\}^{1/A} \quad [$$ A-14a]

$$\varepsilon_3^{vp}(t)=\left(-\frac{1}{2}+\frac{\alpha}{3}\right)\left\{t_{rupt.}\frac{A}{B}\left[1-\left(1-\frac{t}{t_{rupt.}}\right)^B\right]\left[\frac{\left(1+\frac{\alpha}{3}\right)\sigma_1}{K\left(\frac{2}{9}\alpha^2+1\right)^{1/2M}}\right]^N\right\}^{1/A} \qquad \text{[A-14b]}$$

with:

$$A=\frac{M+N}{M} \qquad \text{[A-15]}$$

$$B=\frac{2qr-N}{2qr+1} \qquad \text{[A-16]}$$

and $t_{rupt.}$ the time to failure:

$$t_{rupt.} = \frac{1}{2qr+1}\left(\frac{\sigma_1}{A}\right)^{-r} \qquad \text{[A-17]}$$

For the monotonous loading case, the stress is expressed as a function of viscoplastic deformation for an imposed constant axial deformation rate. The elastic and viscoplastic mechanisms can no longer be separated as in the creep test because a total deformation rate is imposed and damage affects not just the viscoplastic component of deformation but also the elastic component, i.e.:

$$\dot{\varepsilon}_1^{tot} = \dot{\varepsilon}_1^{\acute{e}} + \dot{\varepsilon}_1^{vp} = cste \qquad \text{[A-18]}$$

where:

$$\dot{\varepsilon}_1^{\acute{e}} = \frac{\dot{\sigma}_1}{(1-D_1)E} \qquad \text{[A-19]}$$

Therefore we can write :

$$\dot{\varepsilon}_1^{tot} = C^{te} = \frac{\dot{\sigma}_1}{(1-D_1)E} + \frac{1}{1-D_1}\left(1+\frac{\alpha}{3}\right)\left(\frac{\left(1+\frac{\alpha}{3}\right)\sigma_1}{(1-D_1)Kp^{1/M}}\right)^N \qquad \text{[A-20]}$$

with:

$$p = \sqrt{\frac{2}{3}}\left(C^{te}t - \frac{\sigma_1}{(1-D_1)E}\right)\frac{\sqrt{\left(\frac{1+\alpha/3}{1-D_1}\right)^2 + 2\left(\frac{-1/2+\alpha/3}{1-D_3}\right)^2}}{\frac{1+\alpha/3}{1-D_1}} \; [\qquad \text{A-21]}$$

The stress increments, $d\sigma_1$, were calculated numerically for each time step, dt. The lateral deformation is then obtained for each step by substitution of the values σ_1, D_1, D_3 in:

$$d\varepsilon_3^{vp} = -\frac{\nu d\sigma_1}{(1-D_1)E} + \frac{1}{1-D_3}\left(-\frac{1}{2}+\frac{\alpha}{3}\right)\left(\frac{\left(1+\frac{\alpha}{3}\right)\sigma_1}{(1-D_1)Kp^{1/M}}\right)^N \qquad \text{[A-22]}$$

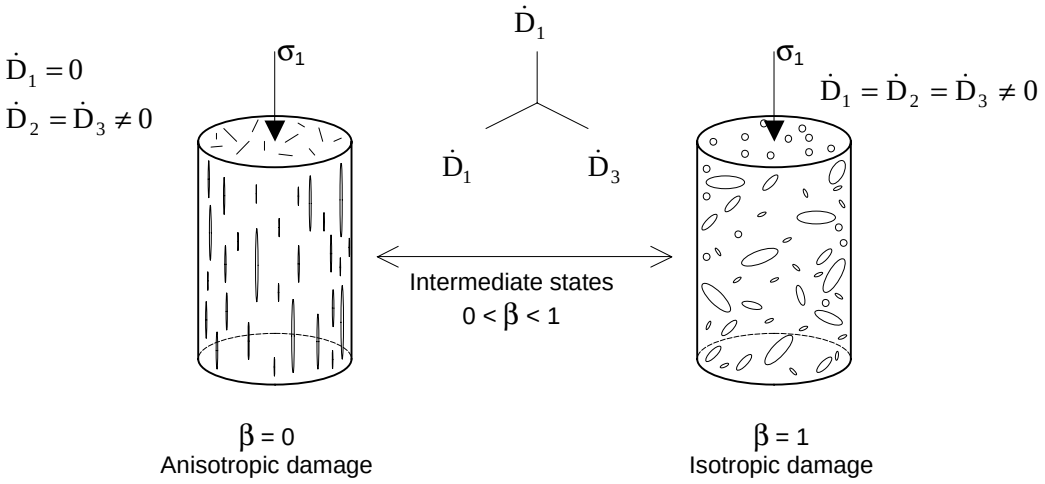

Figure 1 : Illustration of the signification of the parameter, β, for an uniaxial compressive test

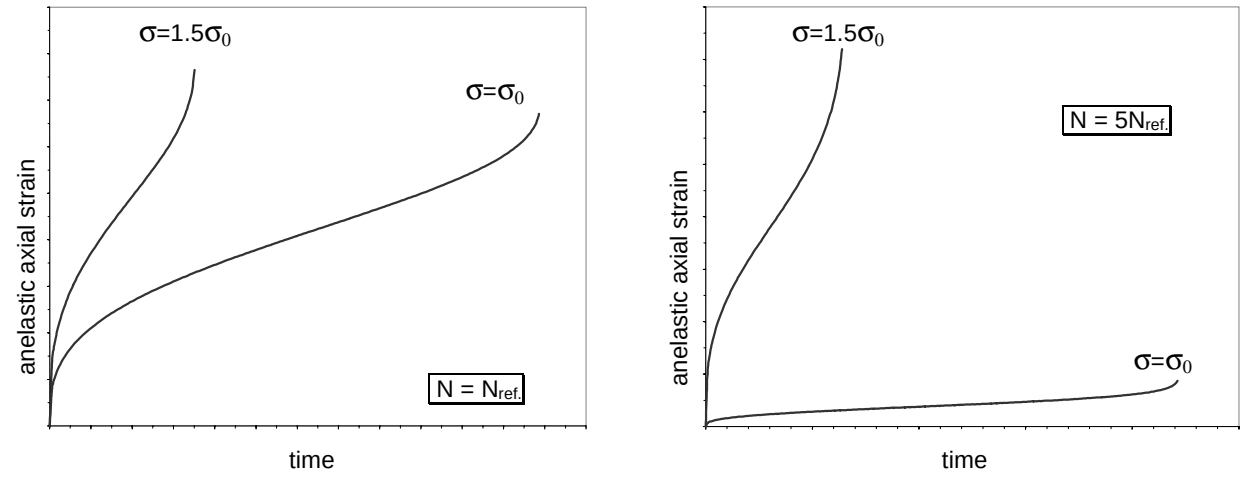

Figure 2 : Anelastic axial strain versus time for different stresses (creep tests), a- low value of viscosity exponent ($N = N_{ref.}$), b- high value of viscosity exponent ($N = 5\ N_{ref.}$)

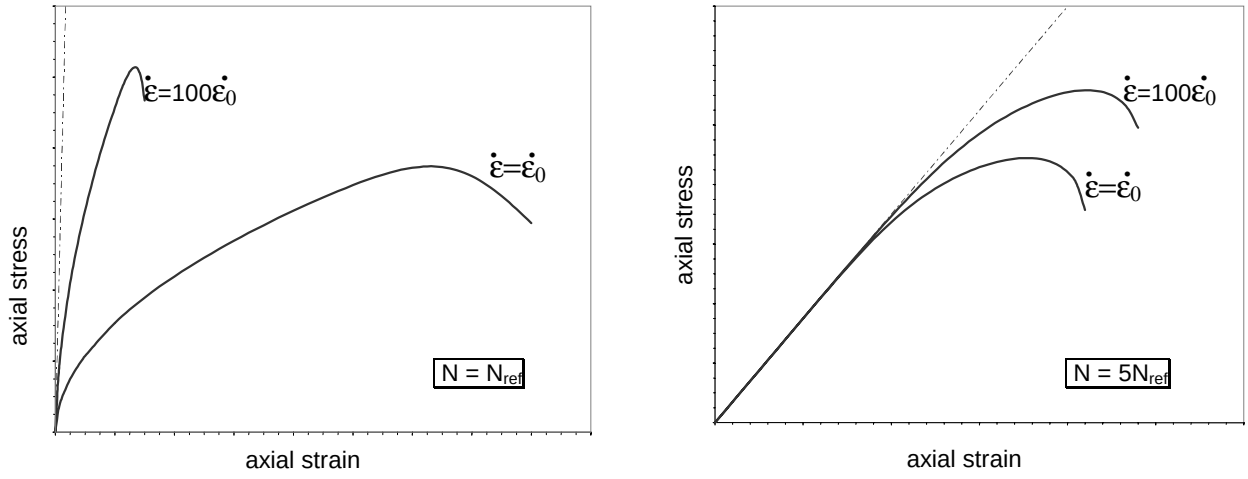

Figure 3 : Axial stress versus axial strain for different strain rates (quasistatic tests), a- low value of viscosity exponent, b- high value of viscosity exponent (N = 5 N_{ref}.)

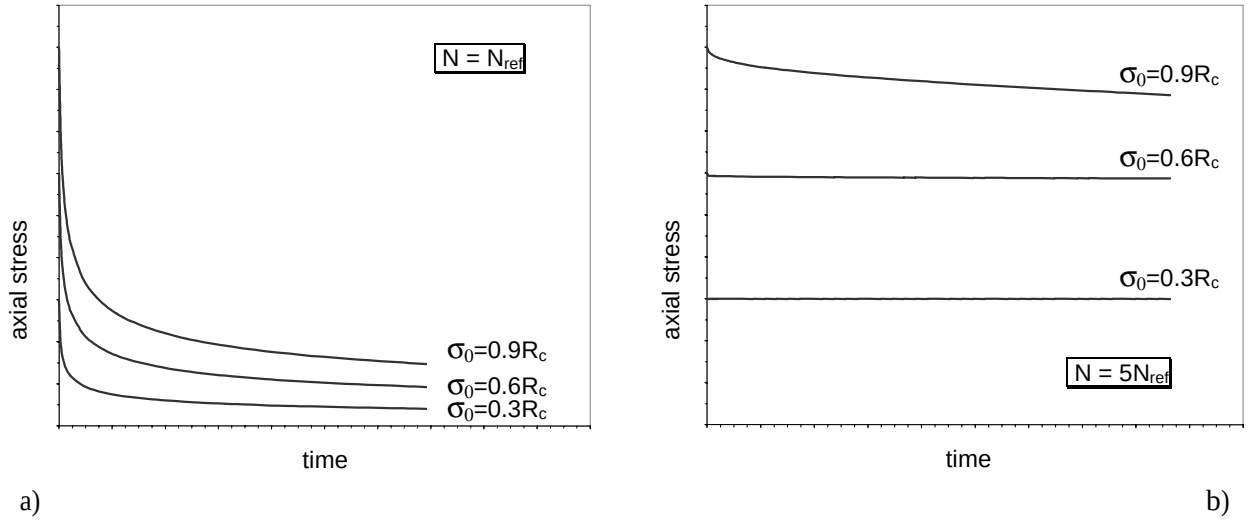

Figure 4 : Axial stress versus time for different stresses (relaxation tests), a- low value of viscosity exponent (N = N_{ref}.), b- high value of viscosity exponent (N = 5 N_{ref}.)

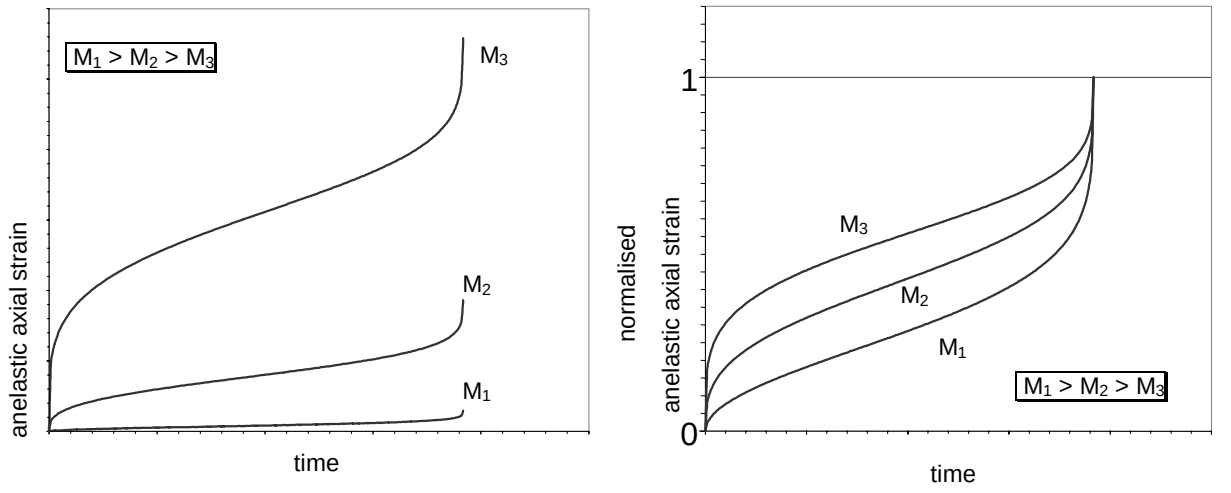

Figure 5 : Anelastic axial strain versus time for different values of the work hardening parameter, M (creep tests), a-non normalised values, b- normalised values

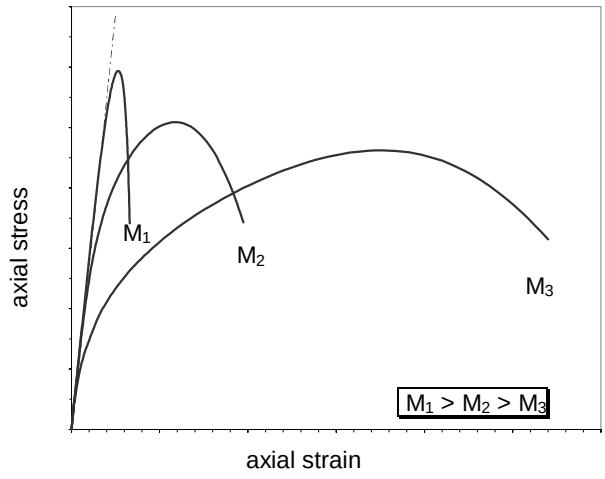

Figure 6 : Axial stress versus axial strain for different strain rates (quasistatic tests) and for different values of the work hardening parameter, M.

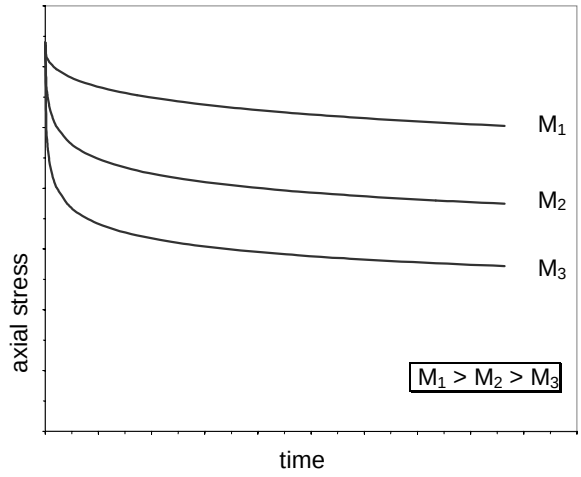

Figure 7 : Axial stress versus time for different stresses (relaxation tests) and for different values of the work hardening parameter, M.

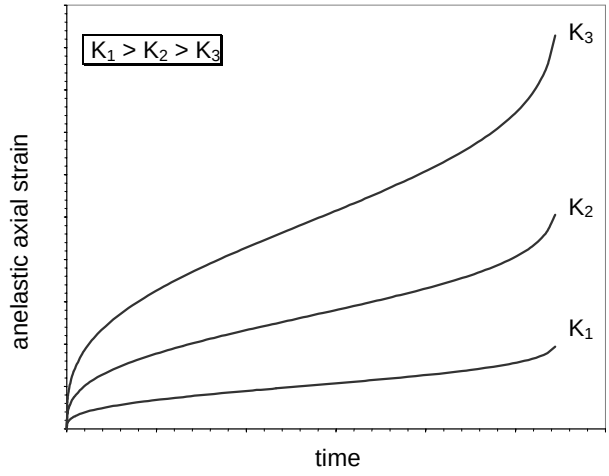

Figure 8 : Anelastic axial strain versus time (creep tests) for different values of the viscoplastic stiffness coefficient, K.

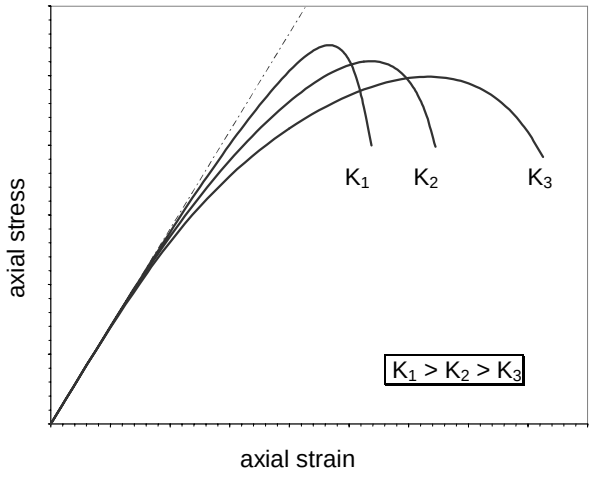

Figure 9 : Axial stress versus axial strain for different strain rates (quasistatic tests) and for different values of the viscoplastic stiffness coefficient, K.

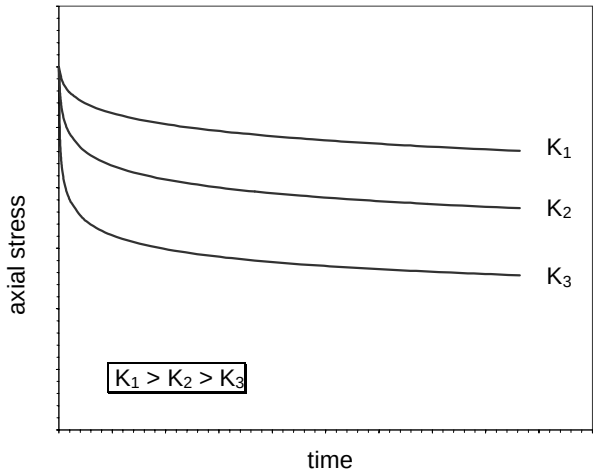

Figure 10 : Axial stress versus time for different stresses (relaxation tests) and for different values of the viscoplastic stiffness coefficient, K.

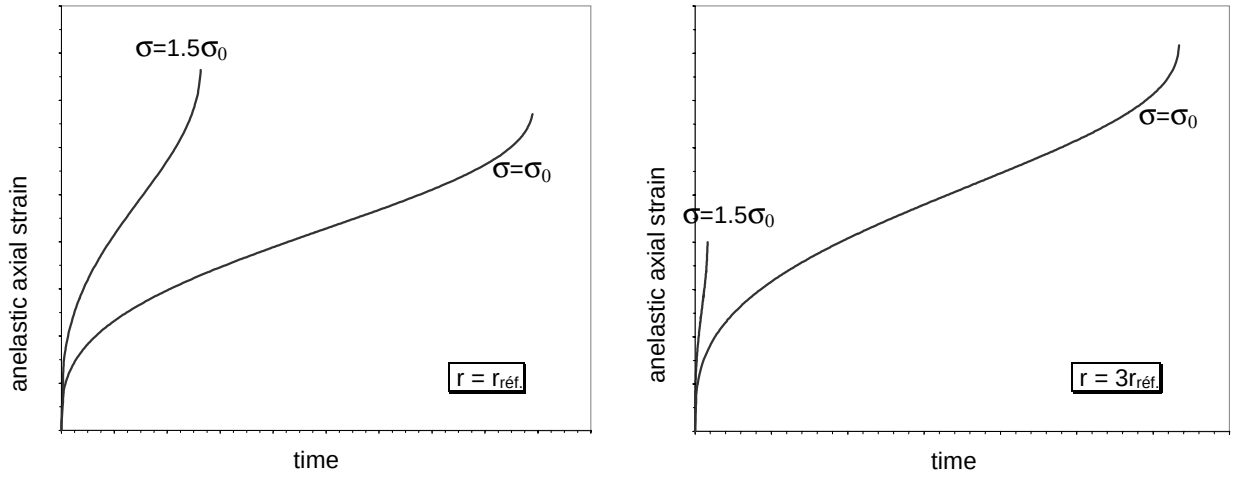

Figure 11 : Anelastic axial strain versus time for different stresses (creep tests), a- low value of damage exponent ($r = r_{ref.}$), b- high value of damage exponent ($r = 3\ r_{ref.}$)

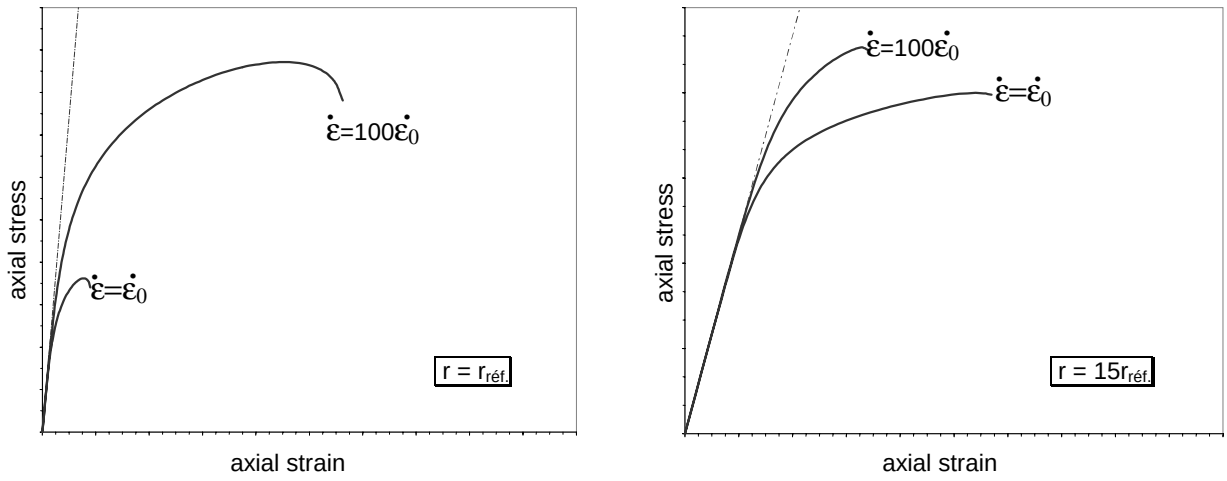

Figure12 : Axial stress versus axial strain for different strain rates (quasistatic tests), a- low value of damage exponent ($r = r_{ref.}$), b- high value of damage exponent ($r = 15\ r_{ref.}$)

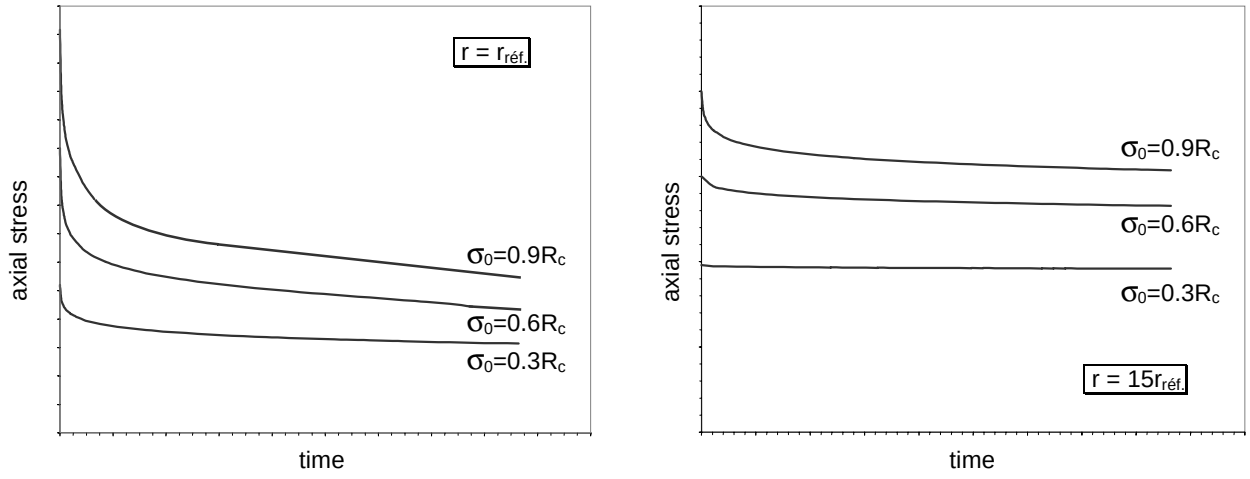

a) b)

Figure 13 : Axial stress versus time for different stresses (relaxation tests), a- low value of damage exponent ($r = r_{ref.}$), b- high value of damage exponent ($r = 15\ r_{ref.}$)

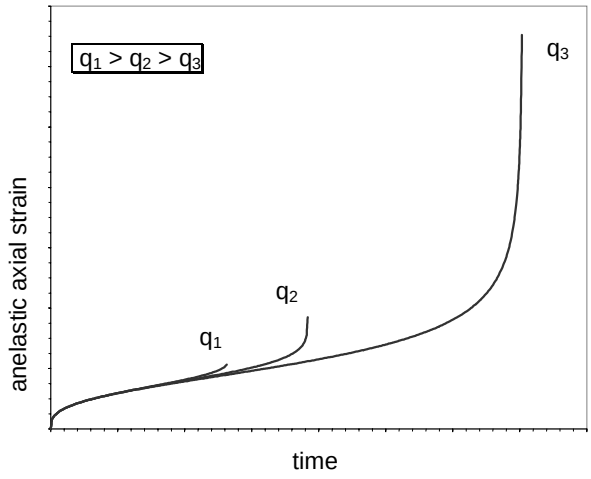

Figure 14 : Anelastic axial strain versus time (creep tests) for different values of the damage progression parameter, q.

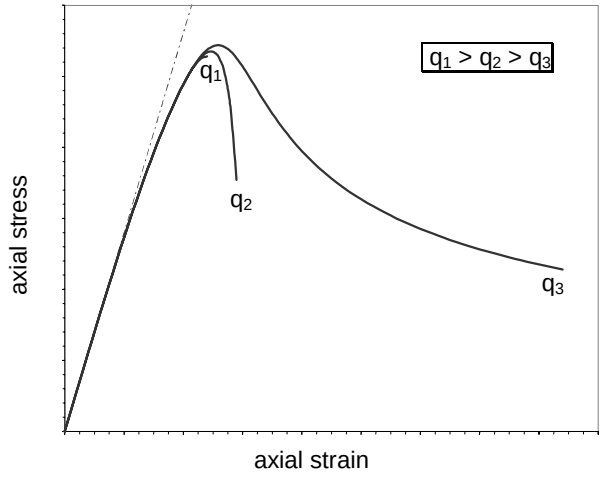

Figure15 : Axial stress versus axial strain for different strain rates (quasistatic tests) for different values of the damage progression parameter, q.

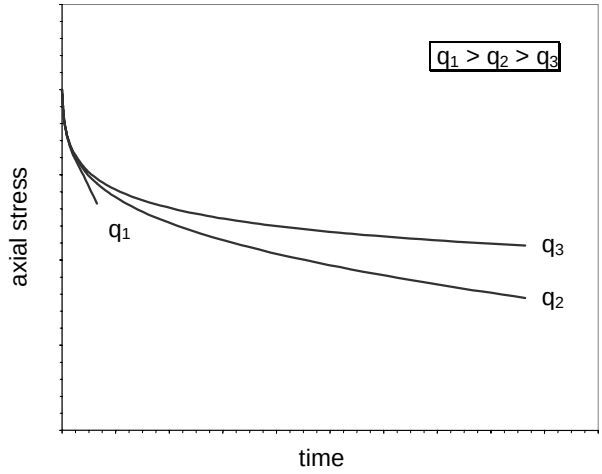

Figure 16 : Axial stress versus time for different stresses (relaxation tests) and for different values of the damage progression parameter, q.

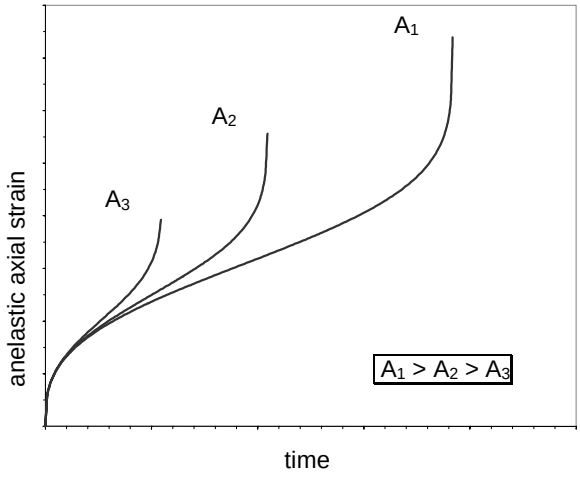

Figure 17 : Anelastic axial strain versus time (creep tests) for different values of the tenacity coefficient, A.

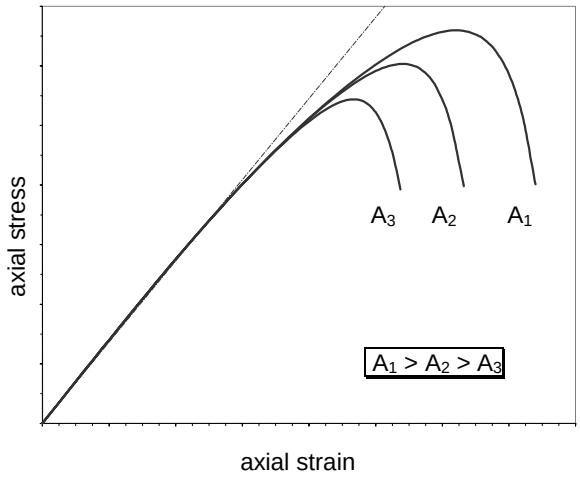

Figure 18 : Axial stress versus axial strain for different strain rates (quasistatic tests) for different values of the tenacity coefficient, A..

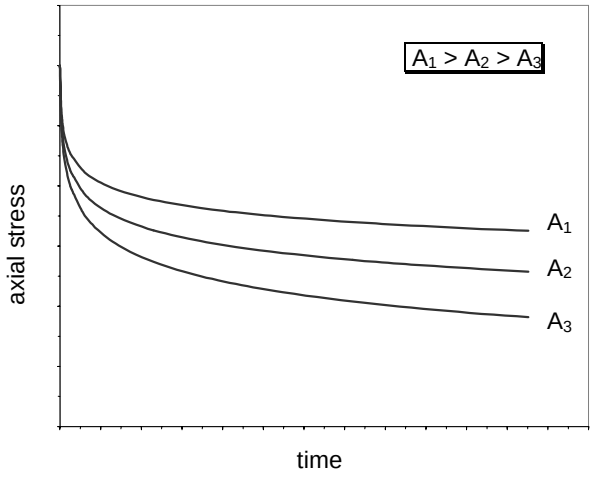

Figure 19 : Axial stress versus time for different stresses (relaxation tests) and for different values of the tenacity coefficient, A

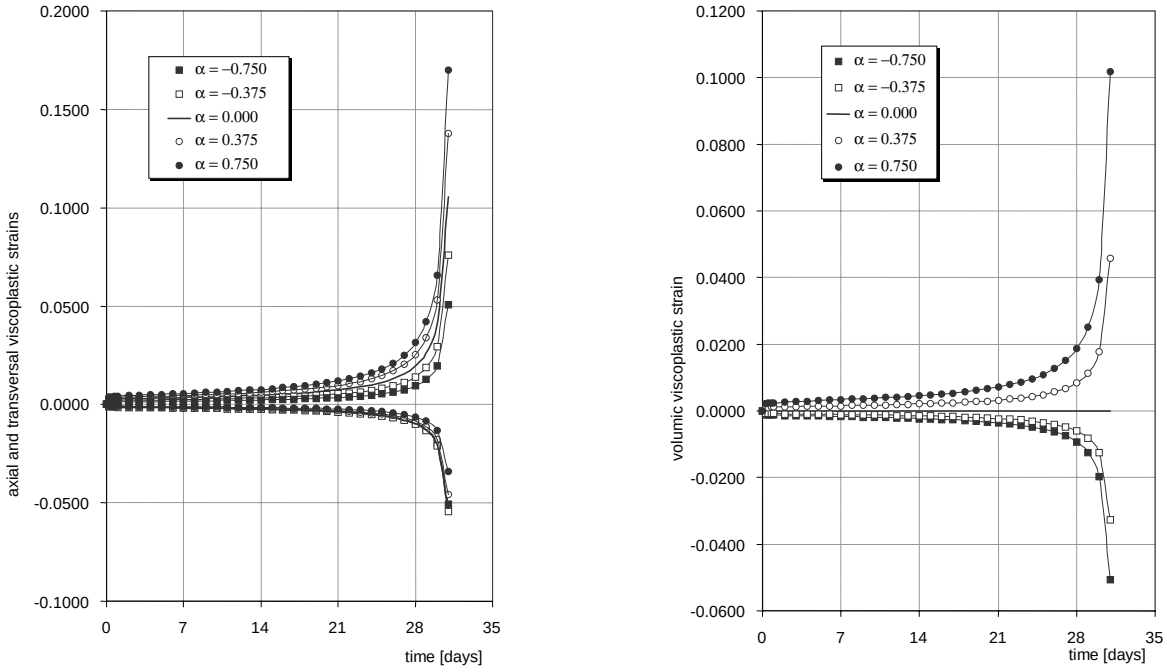

(Applied stress : 25 MPa ; M=1.5 ; N=15 ; K=5000 MPa.s; q=0.05 ; r=5 ; A=525 MPa.s)

a) b)

Figure 20 : Simulations of creep tests in uniaxial compression for anisotropic damage, $\beta=1$
a- axial and transversal strains, b- volumetric strain

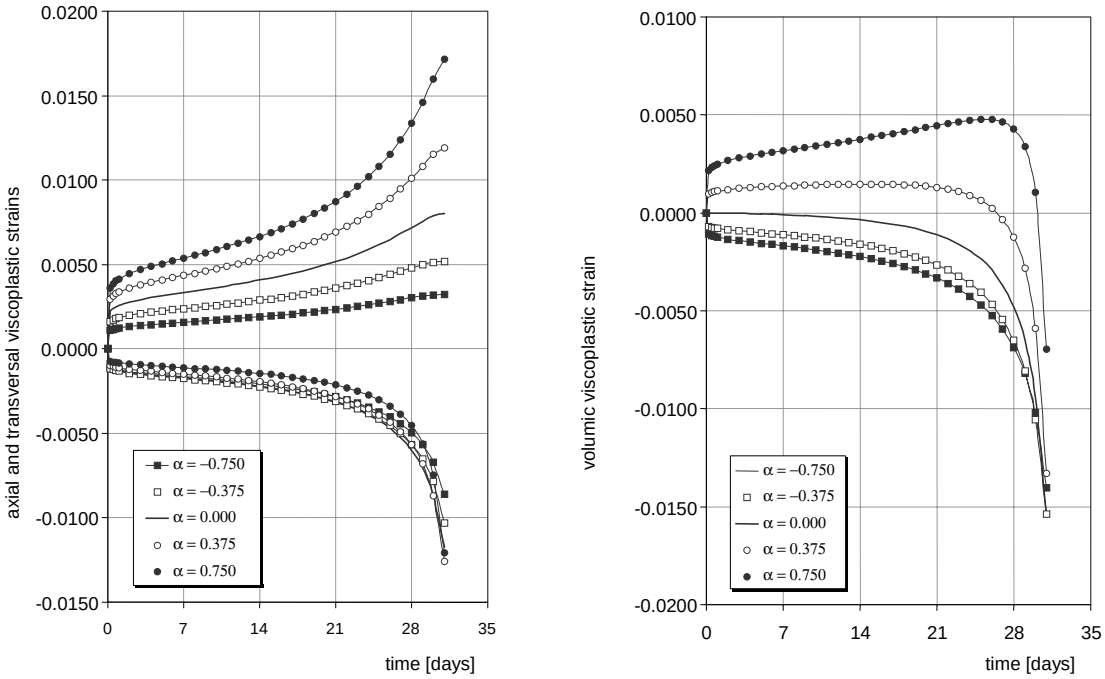

(Applied stress : 25 MPa ; M=1.5 ; N=15 ; K=5000 MPa.s; q=0.05 ; r=5 ; A=525 MPa.s)

a) b)

Figure 21 : Simulations of creep tests in uniaxial compression for anisotropic damage, β=0.5
a- axial and transversal strains, b- volumetric strain

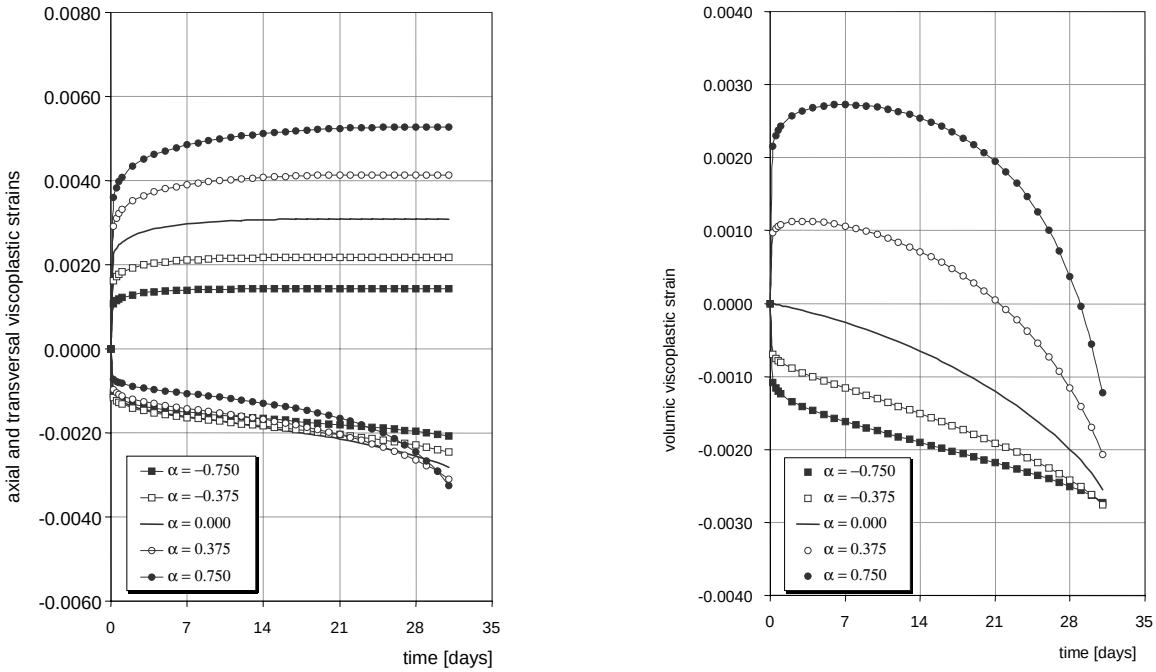

(Applied stress : 25 MPa ; M=1.5 ; N=15 ; K=5000 MPa.s; q=0.05 ; r=5 ; A=525 MPa.s)

a) b)

Figure 22 : Simulations of creep tests in uniaxial compression for isotropic damage, β=0
a- axial and transversal strains, b- volumetric strain

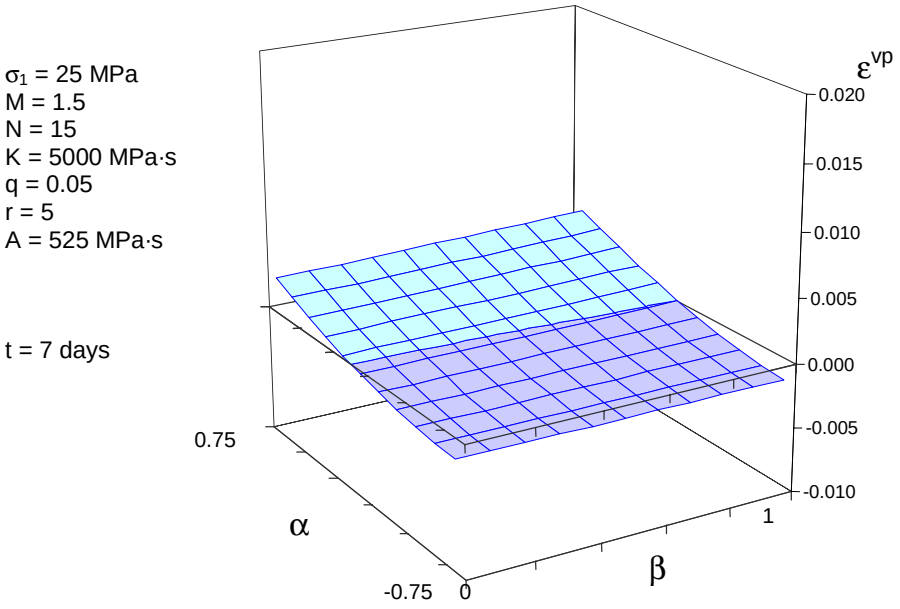

Figure 23 : Representation of viscoplastic strain as a function of dilatancy parameter (α) and damage anisotropy parameter (β) after 7 days' creep

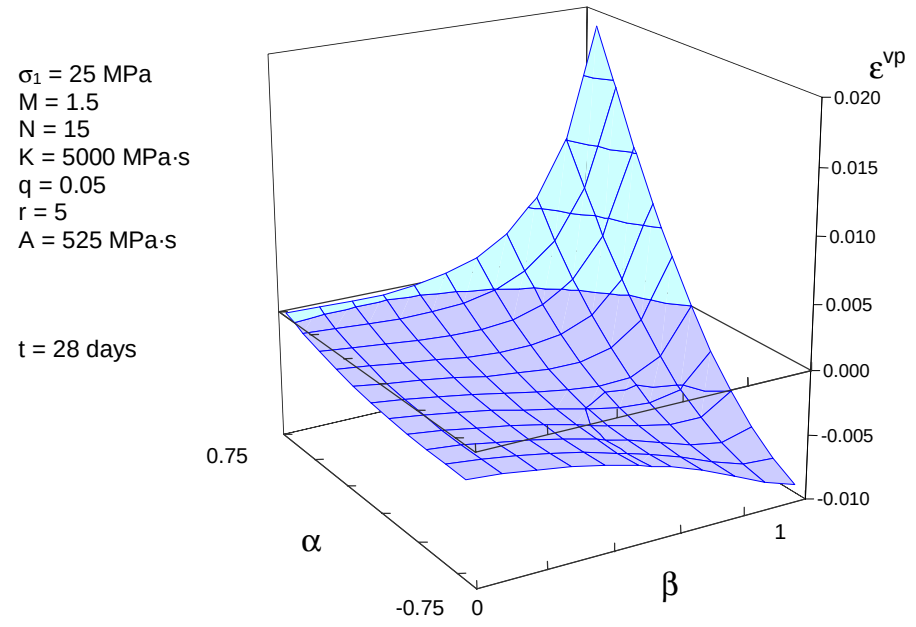

Figure 24 : Representation of viscoplastic strain as a function of dilatancy parameter (α) and damage anisotropy parameter (β) after 28 days' creep

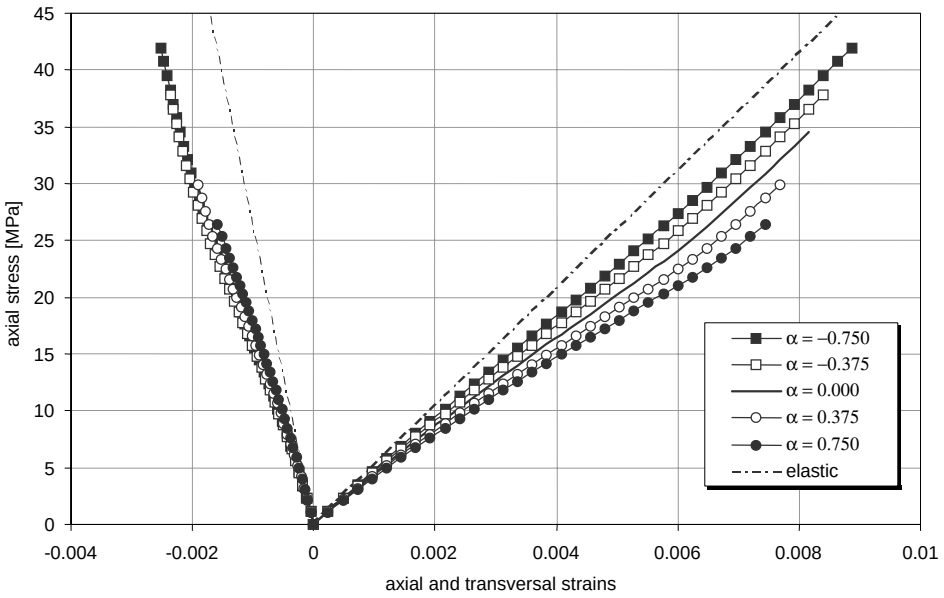

(Loading rate : 10^{-6} s^{-1} ; M=1.5 ; N=15 ; K=5000 MPa.s; q=0.05 ; r=5 ; A=525 MPa.s)

Figure 25a : Simulations of quasistatic tests in uniaxial compression for isotropic damage, β=0
Axial stress versus axial and transversal strains

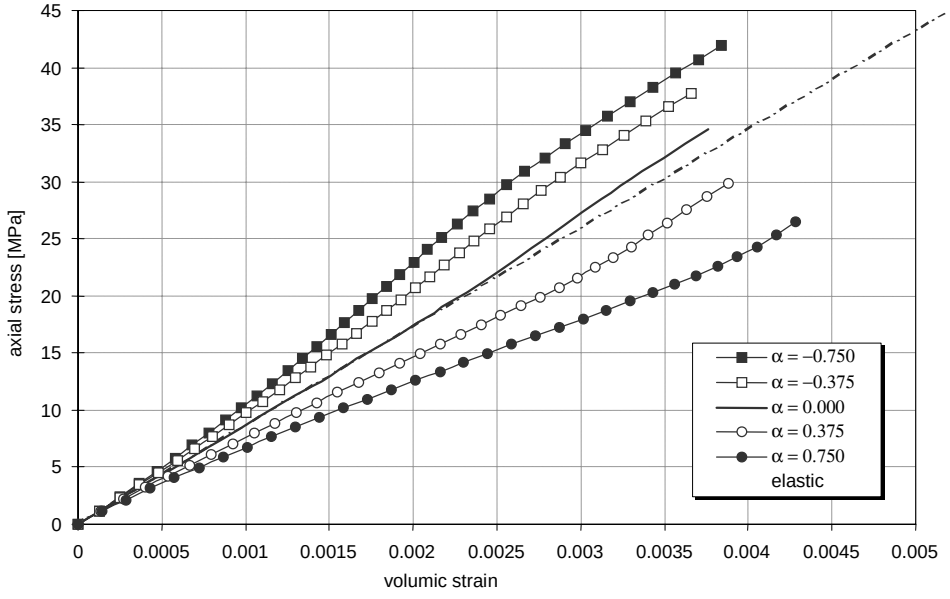

Figure 25b : Simulations of quasistatic tests in uniaxial compression for isotropic damage, β=0
Axial stress versus volumetric strains

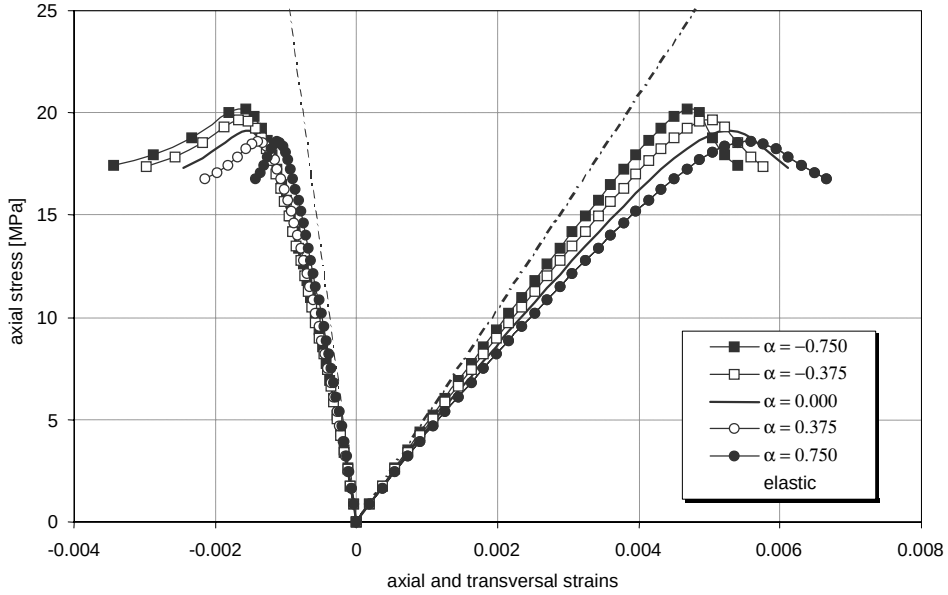

(Loading rate : 10^{-6} s^{-1} ; M=1.5 ; N=15 ; K=5000 MPa.s; q=0.05 ; r=5 ; A=525 MPa.s)

Figure 26a : Simulations of quasistatic tests in uniaxial compression for anisotropic damage, β=0.5
Axial stress versus axial and transversal strains

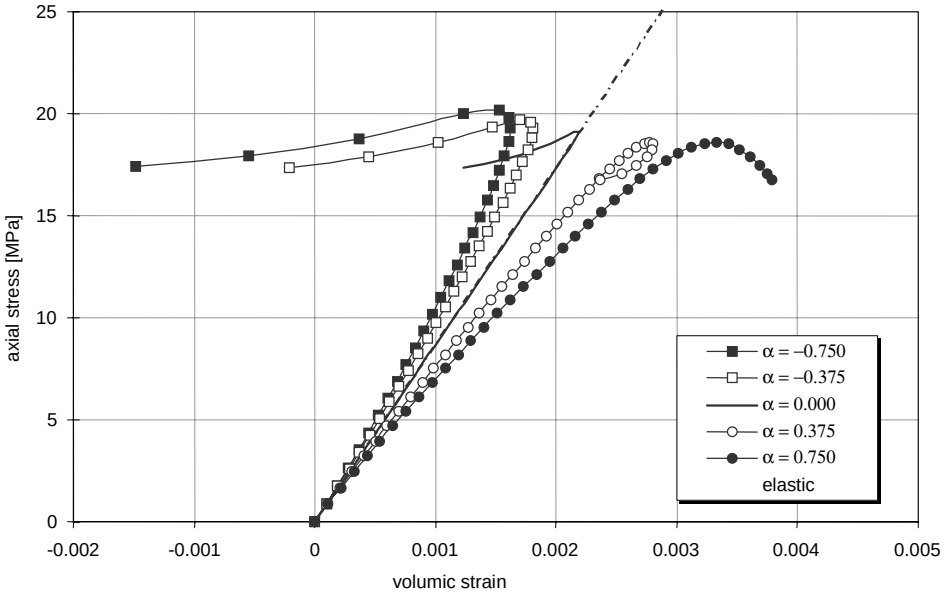

(Loading rate : 10^{-6} s^{-1} ; M=1.5 ; N=15 ; K=5000 MPa.s; q=0.05 ; r=5 ; A=525 MPa.s)

Figure 26b : Simulations of quasistatic tests in uniaxial compression for anisotropic damage, β=0.5
Axial stress versus volumetric strains

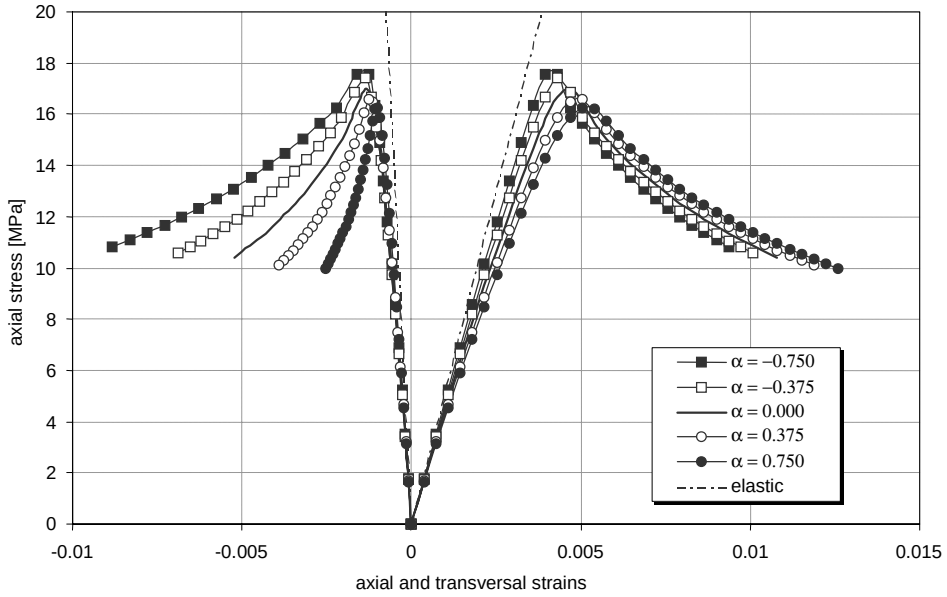

(Loading rate : 10^{-6} s^{-1} ; M=1.5 ; N=15 ; K=5000 MPa.s; q=0.05 ; r=5 ; A=525 MPa.s)

Figure 27a : Simulations of quasistatic tests in uniaxial compression for anisotropic damage, $\beta = 1$
Axial stress versus axial and transversal strains

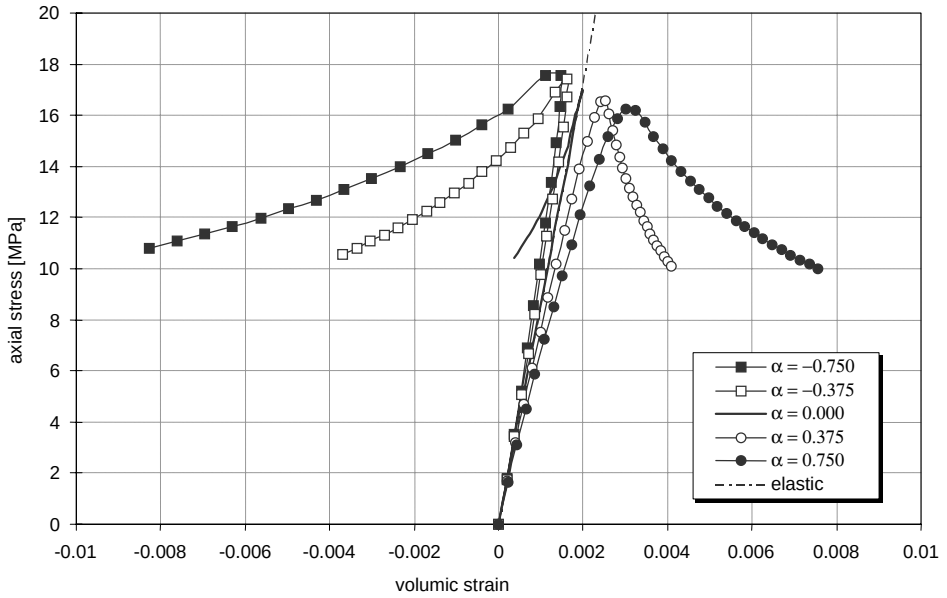

(Strain rate : 10^{-6} s^{-1} ; M=1.5 ; N=15 ; K=5000 MPa.s; q=0.05 ; r=5 ; A=525 MPa.s)

Figure 27b : Simulations of quasistatic tests in uniaxial compression for isotropic damage, $\beta = 1$
Axial stress versus volumetric strains

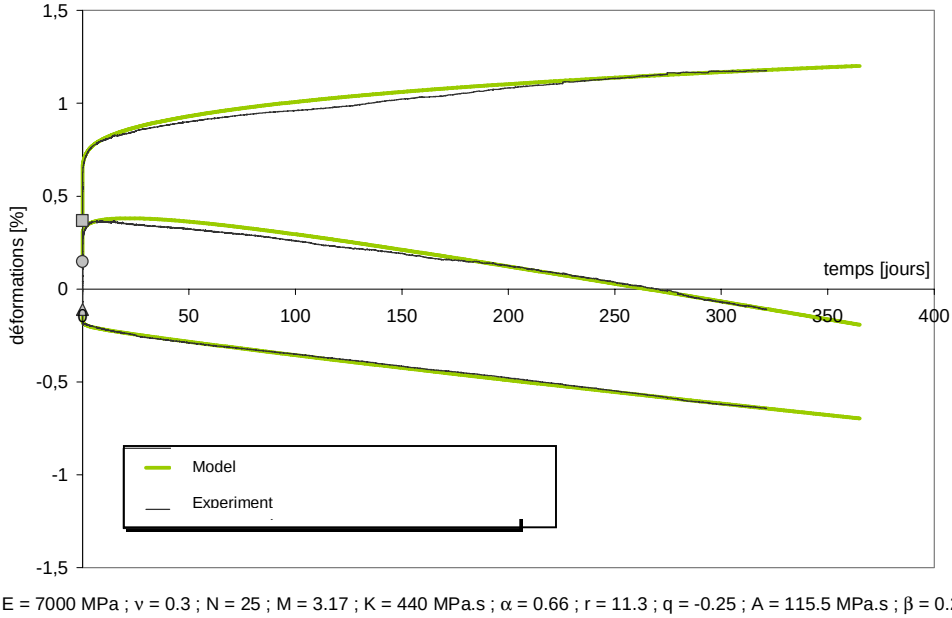

Figure 28 : Comparison between the strains-time curves obtained from the model and experimentally from a creep test performed on argillite

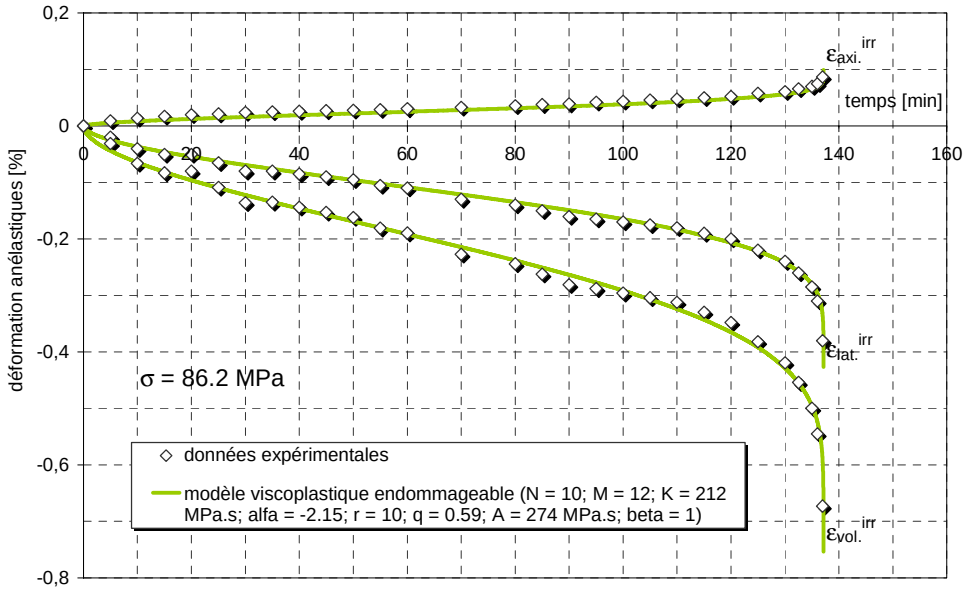

Figure 29 : Comparison between the strains-time curves obtained from the model and experimentally from a creep test performed on marble, Singh [1]

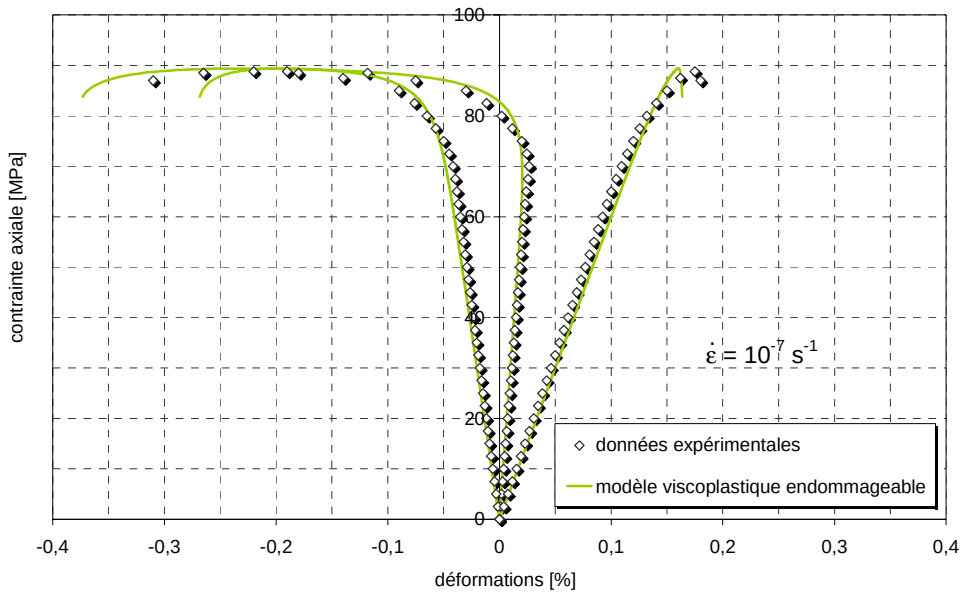

E = 60000 MPa ; ν = 0.4 ; N = 10 ; M = 75 ; K = 2100 MPa.s ; α = 0.5 ; r = 10 ; q = 0 ; A = 165 MPa.s ; β = 0.15

Figure 30 : Comparison between the stress-strains curves obtained from the model and experimentally from monotonic compression test performed on anhydrite

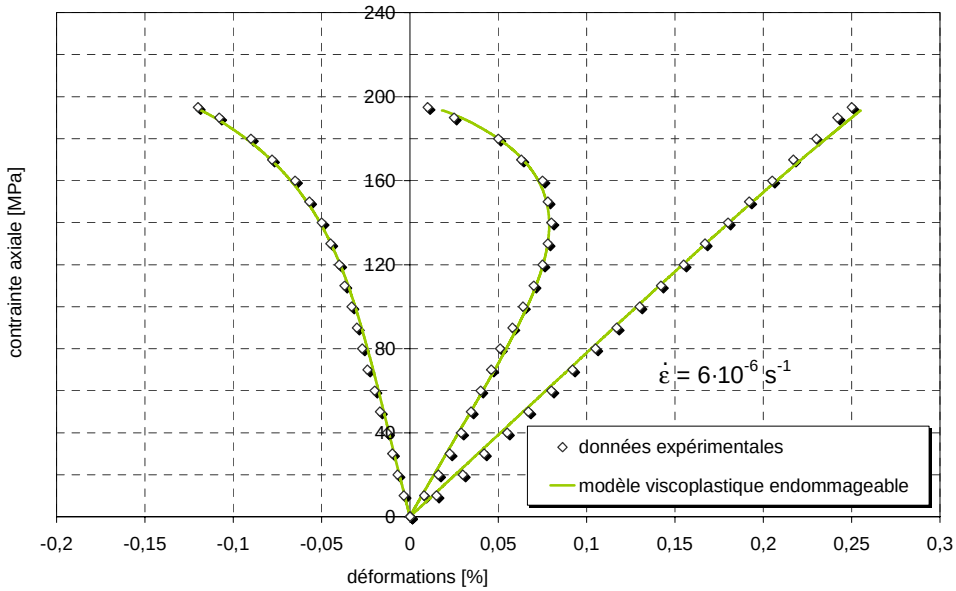

E = 78000 MPa ; ν = 0.23 ; N = 10 ; M = 10 ; K = 225 MPa.s ; α = -2.5 ; r = 10 ; q = 0.75 ; A = 370 MPa.s ; β = 0

Figure 31 : Comparison between the stress-strains curves obtained from the model and experimentally from monotonic compression test performed on granite , Shao et al. [24]

Annexe III : Publications relatives à la modélisation numérique d'ouvrages

8 - F. Pellet, F. Descoeudres & P. Egger (1993), The effect of water seepage forces on the face stability of an experimental micro tunnel, Canadian Geotechnical Journal, vol. 30, n° 2, pp 363 - 369.

9 - F. Pellet & O. Benoit (1999), Modélisation numérique 3D du comportement d'ouvrages souterrains lors de la traversée d'accidents géologiques, Proceedings of the 9th International Congress on Rock Mechanics, Paris - France, pp 213-218.

10 - E. Boidy, A. Bouvard & F. Pellet (2002), Back analysis of time-dependent behavior of a monitored tunnel, International Journal of Tunneling and Underground Space Technology, Elsevier Science, vol 17, n° 4, pp 415-424.

11 - E. Boidy, F. Pellet & M. Boulon (2001), Numerical modeling of deep tunnels including time-dependent behavior, Proceedings of the 10th International Conference on Computer Methods and Advances in Geomechanics - IACMAG, Tucson, Arizona - US, pp 1663-1668.

12 - N.P. Zokimila, E. Flavigny, F. Pellet & A. Billon (2003), Modélisation numérique du comportement à court et à long terme d'un tunnel ferroviaire, Conférence régionale africaine de Mécanique des Sols, Casablanca, Maroc, pp 233-239.

13 - F. Pellet, A Hajdu, M. Boulon, F. Deleruyelle & F. Besnus (2002), Numerical modeling of underground structures taking into account the visco-plastic behavior and rock damage, Proceedings of the International Conference on Numerical Models in Geomechanics - NUMOG VIII, Roma - Italy, pp 399-404.

National Research Council Canada
Conseil national de recherches Canada

NRC · CNRC

Reprinted from
Canadian Geotechnical Journal

Réimpression de la
Revue canadienne de géotechnique

The effect of water seepage forces on the face stability of an experimental microtunnel

FRÉDÉRIC PELLET, FRANÇOIS DESCOEUDRES, AND PETER EGGER

Volume 30 • Number 2 • 1993

Pages 363 – 369

Canada

NOTES

The effect of water seepage forces on the face stability of an experimental microtunnel

FRÉDÉRIC PELLET, FRANÇOIS DESCOEUDRES, AND PETER EGGER

Institut des Sols, Roches et Fondations, École Polytechnique Fédérale de Lausanne, 1015 Lausanne, Switzerland

Received July 15, 1992

Accepted January 15, 1993

The face heading stability of underground constructions remains quite difficult to assess, especially when groundwater is present. To investigate this, an experimental microtunnel was excavated at shallow depth in soft ground, below the water table. In agreement with field measurements of the piezometric level changes, a three-dimensional finite element analysis of groundwater flow shows that the head losses are concentrated in the close vicinity of the tunnel face. Both numerical equilibrium analysis and field measurements were used to show that the resulting seepage forces substantially increase the supporting pressure required to ensure face stability.

Key words: microtunnel, shallow depth, soft ground, seepage forces, face stability, supporting pressure.

La stabilité du front de taille des ouvrages souterrains demeure difficile à estimer, notamment en présence d'eau. Pour étudier ce cas, un micro-tunnel expérimental a été construit à faible profondeur en terrain meuble, au-dessous du niveau de la nappe phréatique. Une modélisation tridimensionnelle par éléments finis a montré, en accord avec les niveaux piezométriques mesurés sur le site, que les pertes de charges hydrauliques se concentrent dans la zone du front. Les mesures de la pression exercée au front, confirmées par une analyse numérique, ont montré que les forces de percolation résultantes augmentent substantiellement la pression de soutènement nécessaire pour assurer la stabilité du front.

Mots clés : micro-tunnel, faible profondeur, sol mou, forces de percolation, stabilité du front, pression de support.

Can. Geotech. J. **30**, 363–369 (1993)

Introduction

The underground construction of small-diameter galleries, known as microtunnels, is a technology currently employed worldwide. In contrast with traditional open-pit methods, it avoids interference with the ground surface. For this reason it is becoming popular, especially in built-up areas where space is restricted. Among current applications are the construction of sewer networks and pilot adits of larger tunnels.

In numerous cases, these microtunnels are driven in soft soil at shallow depth, below the water table. These unfavourable conditions must be controlled to ensure the stability of the construction and to avoid damage, such as the settlement of surrounding buildings. During construction, the most critical zone is located at the tunnel face, where the decompression owing to excavation and the water seepage forces generated by the water flow toward the face can lead to the collapse of the face.

To assess the supporting pressure required to ensure face stability, several methods, all based on the plasticity principle, may be used. Davis *et al.* (1980) established an analytical expression for cohesive soils in undrained conditions, and Leca and Panet (1988) have studied the more complex case of cohesive and frictional soil in drained conditions. In most cases, these methods provide good values for the required supporting pressure. However, all of these methods are only valid for tunnels driven in dry soil or saturated soil in hydrostatic conditions. No effects of water seepage forces owing to water flow toward the face are taken into account. In this case, Descoeudres and Rybisar (1987) have shown that the hydraulic gradients can reach high values in the face region and, as a consequence, must be taken into account in the stability analysis. This complex situation often leads designers to carry out numerical analyses, but unfortunately it is still quite difficult to assess the validity of the numerical results because of the lack of field measurements on full-scale constructions.

A microtunnel was excavated in an experimental site to compare numerical results and field measurements. Excavation was carried out at shallow depth just below the water table. The experimental part of this study deals with measurements of the changes of the groundwater level owing to the microtunnel excavation, as well as measurement of the pressure applied to the face. The numerical part consists of a three-dimensional finite element simulation to model the disturbance of the initial hydraulic conditions. In the last step a two-dimensional finite element equilibrium analysis taking the water seepage forces into account was performed, to find the pressure exerted at the face.

Description of the experimental microtunnel

The microtunnel was 950 mm in diameter and 3 m in length. Its axis was located 2.5 m below the ground surface (Fig. 1). The lining support consisted of three steel pipes, each 1 m in length, which were driven by jacking from a pit excavated 3 years before. The excavation of the microtunnel itself was carried out by hand. During the final stage, a circular steel plate was positioned to ensure face stability. It must be noted that this plate was perforated to allow seepage through the face section.

Printed in Canada / Imprimé au Canada

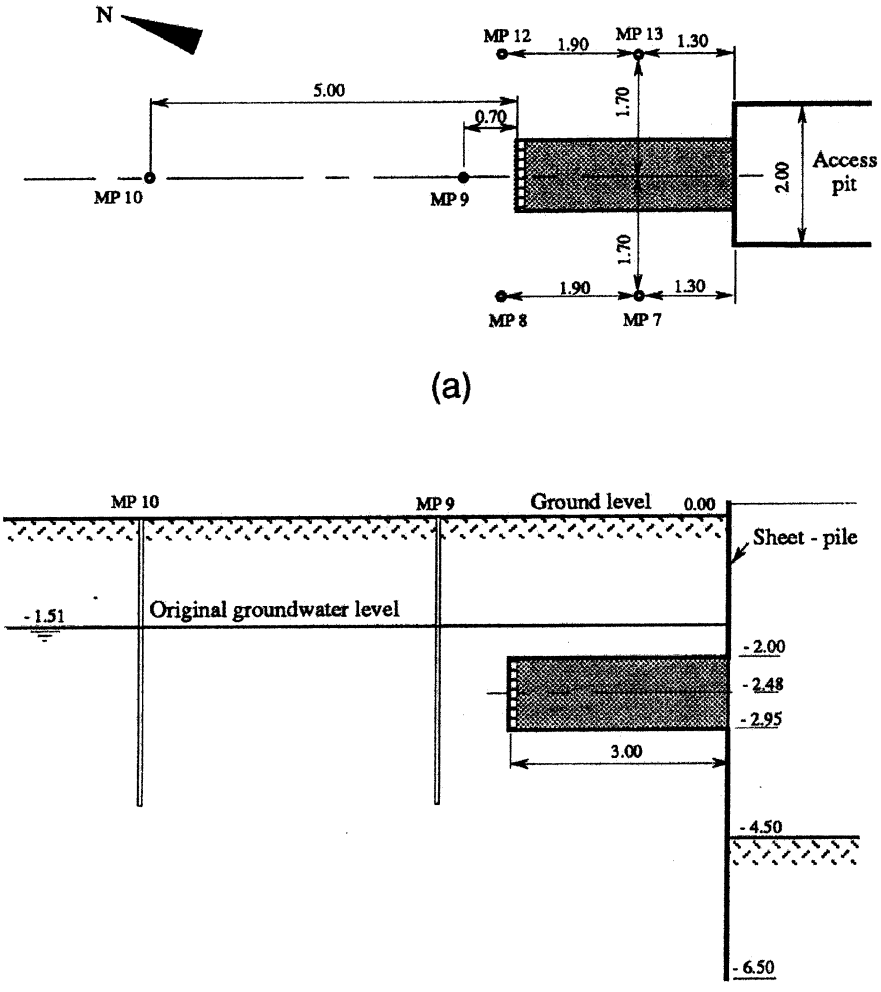

FIG. 1. Layout of the experimental microtunnel. (*a*) Plan view. (*b*) Longitudinal profile. All measurements are given in metres.

Six micropiezometers were installed to measure the hydraulic heads (Fig. 1). The supporting plate was equipped with three Glötzl pressure cells to measure the total stress exerted on the face. In addition, several settlement measuring points were placed to monitor the displacements at the ground surface.

The ground at the site consisted of glacio-lacustrine deposits, which are sandy silt or partially stratified clayey silt. Before the excavation, the water table was in a quasi-hydrostatic state with very small observed gradients (less than 1%). Numerous laboratory tests were carried out to determine the mechanical characteristics; the shear strength of the soil was assessed by direct shear tests and triaxial tests. To reproduce the stress path near the face during the excavation, triaxial tests were performed in drained conditions, both in vertical loading and in horizontal unloading. The soil internal friction angle was 27°, whereas the cohesion was in the range of 5–10 kPa because of the stratified structure of the soil. The deformational modulus was 2500 kPa. The unit weight was 15.0 kN/m^3 for dry soil and 19.5 kN/m^3 for saturated soil.

Hydraulic flow around tunnel

Field measurements of hydraulic heads

Figure 2 shows the evolution with time of the piezometric levels, measured at 4 m depth on micropiezometers MP 9 and MP 10. These are 0.7 and 5.0 m from the face of the microtunnel, respectively. The piezometric levels fluctuated depending on seasonal variations in precipitation. After each rainy period, a sudden rise of the level, occurring over a short time, is observed, followed by a slow nonlinear drop with time. Before the tunnel excavation (April–October 1990), the observed evolution was the same on MP 9 and MP 10. As expected, the piezometric level was slightly lower on MP 9. This result indicated a small flow directed towards the pit. After the excavation (from October 1990), a clear difference is observed between the piezometric levels measured by MP 9 and MP 10. This is due to the drainage of water through the face of the microtunnel. During the following 9 months (until June 1991), the groundwater level remained above the tunnel. From July 1991, because of the dry season, the water level fell progressively to reach the bottom of the face (−3.0 m) by the end of September. At this time, the face area was completely dewatered and the dif-

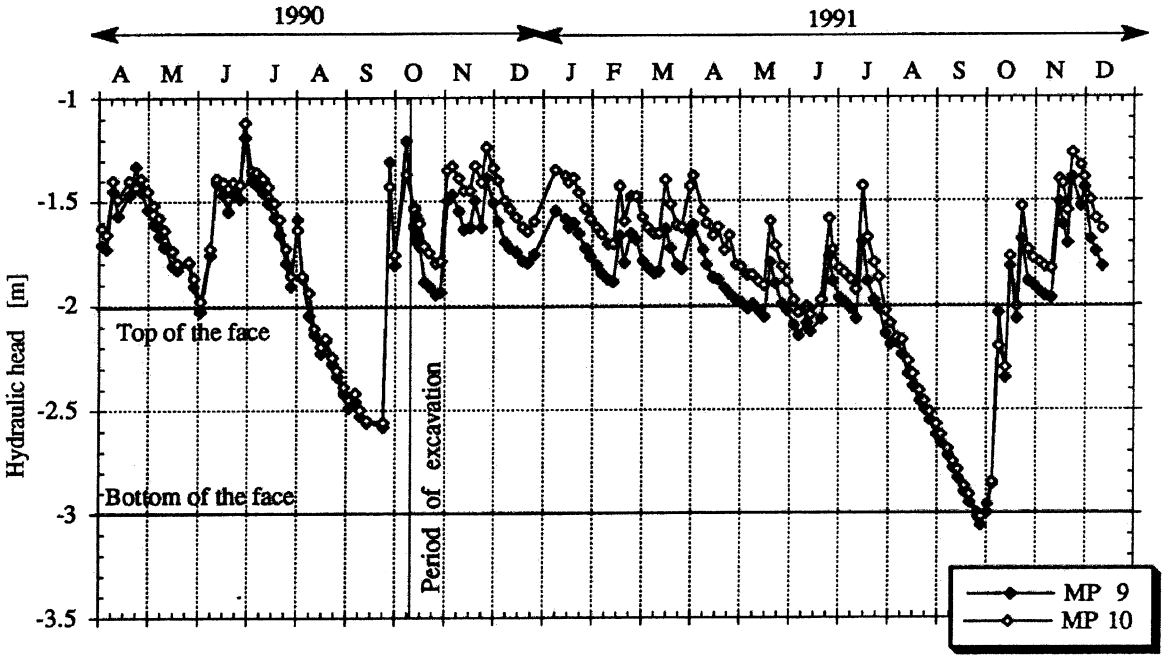

FIG. 2. Evolution of hydraulic heads with time measured at micropiezometers 9 and 10.

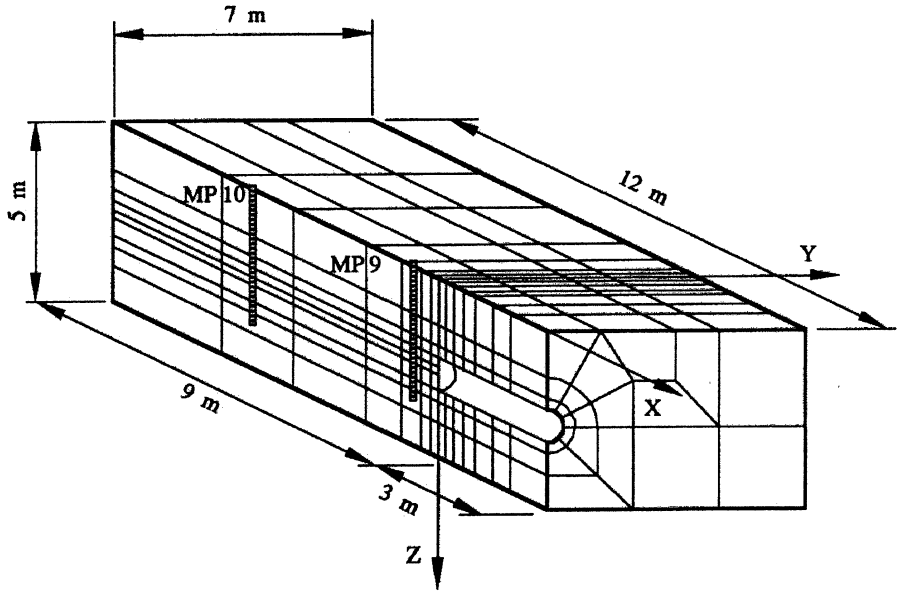

FIG. 3. Three-dimensional finite element mesh.

ference between the hydraulic heads measured on MP 9 and MP 10 vanished.

Numerical modelling of hydraulic flow

The numerical analysis was carried out by the finite element method using the program ADINAT (ADINA Engineering Incorporated 1984). This numerical code solves the governing equation of the seepage problem in porous media using Darcy's law. The element mesh (Fig. 3) is composed of 1778 nodes and 315 elements. Because of symmetry of the geometry and the boundary conditions, only one half-space of the studied domain was discretized. Twenty-node isoparametric elements with 64 Gauss points were used. The computational analysis was performed for a steady state. The program gives the hydraulic heads at each node and the flow velocities at each Gauss point.

The boundary conditions were fixed after an examination of the evolution of the hydraulic heads. The hydraulic potential was prescribed both on the right edge and on the back of the model. The front face and the plane of symmetry of the model were impermeable, as was the tunnel lining, which means that the water could only enter the tunnel by the face. Because of the quasi-hydrostatic state of the water table before the excavation of the tunnel, a constant hydraulic potential was imposed over the entire field. The input initial potential of -1.51 m corresponds to the value measured at the beginning of the excavation, after the natural subsidence of the water table.

TABLE 1. Comparison of the computed and measured hydraulic heads (m)

		Measured			Computed		
Piezometer	Z_o	Z_f	ΔZ	ΔZ_{10}	Z_f	ΔZ	ΔZ_{10}
MP 7-13	−1.51	−1.74	0.23	0.20	−1.75	0.24	0.15
MP 8-12	−1.51	−1.73	0.22	0.19	−1.75	0.24	0.15
MP 9	−1.51	−1.73	0.22	0.19	−1.78	0.27	0.18
MP 10	−1.51	−1.54	0.03		−1.60	0.09	

NOTE: Z_o, original hydraulic head; Z_f, lowered hydraulic head; $\Delta Z = Z_o - Z_f$, difference between original and lowered head; $\Delta Z_{10} = \Delta Z - \Delta Z_{(MP10)}$, difference between the lowered head and MP 10.

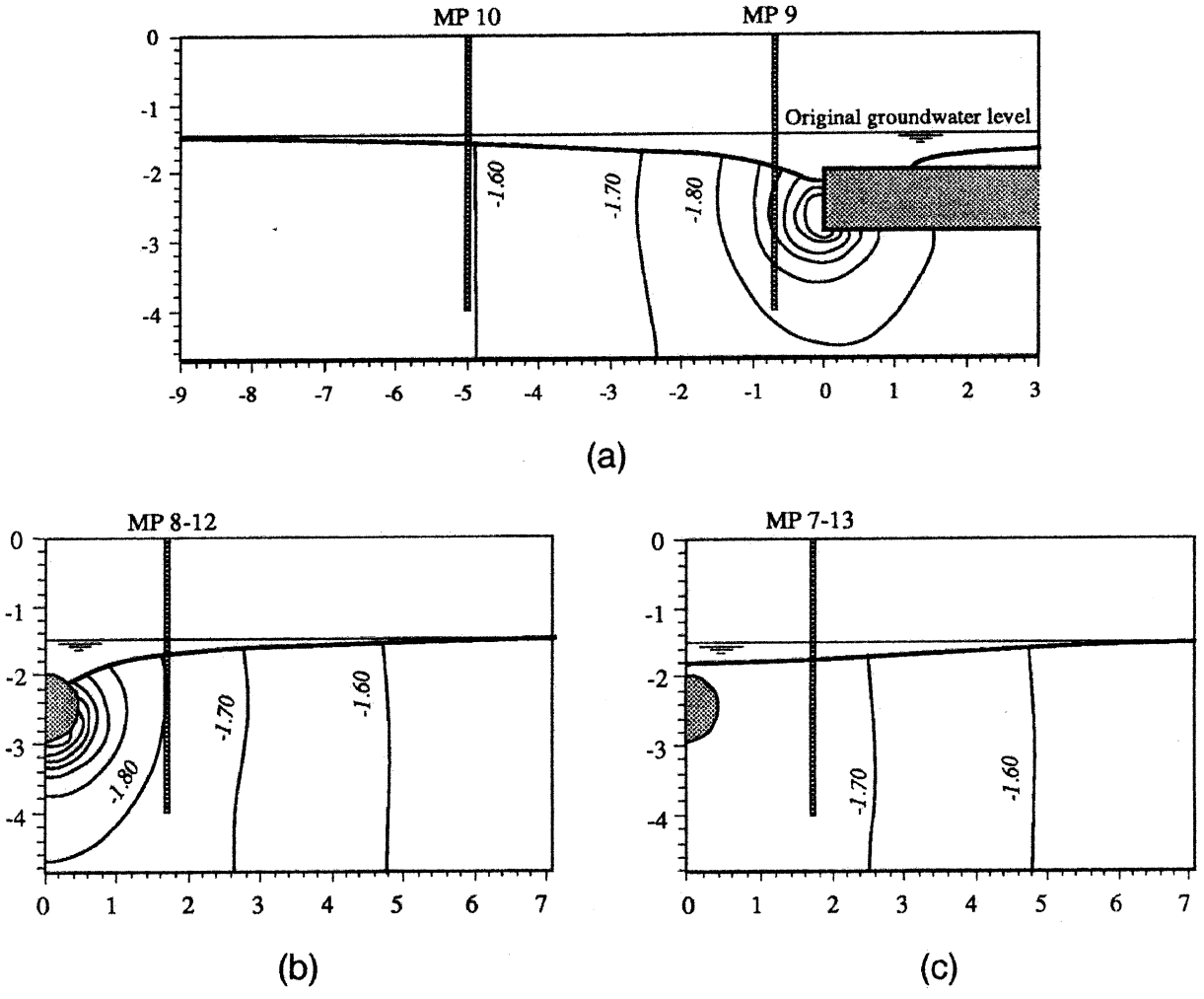

FIG. 4. Hydraulic isopotential network (Δh = 1 m). (*a*) Longitudinal profile. (*b*) Cross section at the face. (*c*) Cross section 1.5 m ahead of the face.

Discussion of numerical results

The comparison of the computed and measured hydraulic heads required special care. As already stated, the water level reduction is partly due to the natural subsidence after each rainy period and partly to the seepage through the face of the tunnel. In such a situation, the comparison should extend for a long period during which the average groundwater level in the surrounding area is kept approximately constant. The hydraulic heads reported in Table 1 (reference is the ground surface) are average values computed from October 1990 to April 1991. A close agreement was observed between computed and measured hydraulic heads, even if these latter are slightly higher (lowering is more important in the computed case).

To assess the drainage effect through the tunnel face, neglecting the vertical infiltration owing to rainfall, it is more convenient to compare the differences between two points. Micropiezometers MP 10 and MP 9, the most distant and the nearest to the face, respectively, were chosen. The average measured difference, which was 4 cm during the

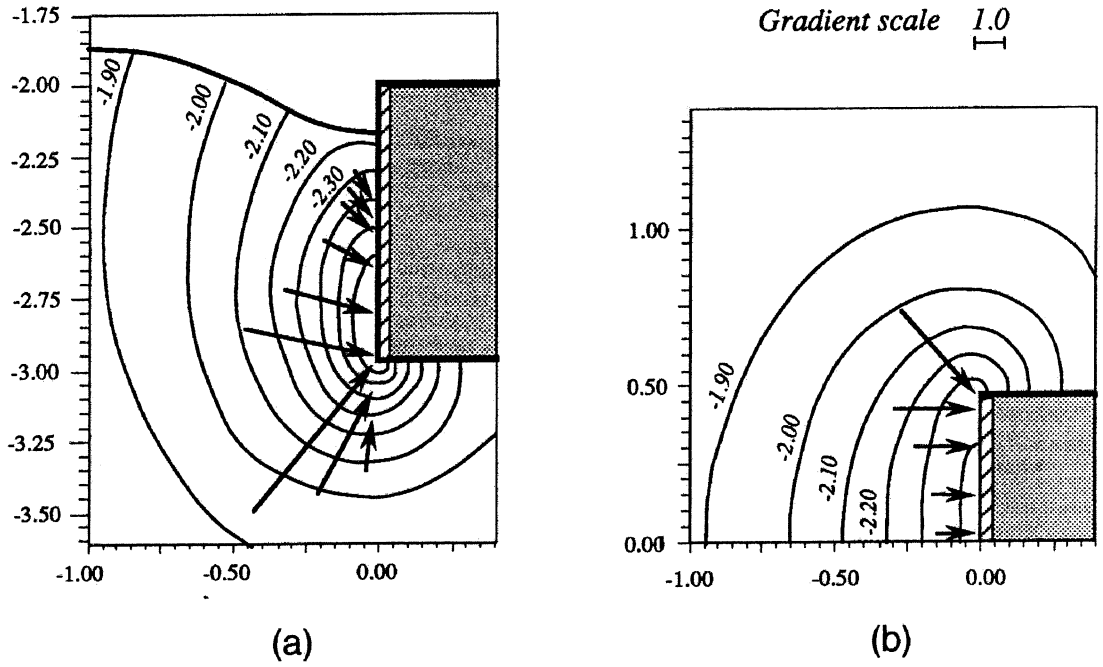

FIG. 5. Hydraulic gradients in the vicinity of the face. (*a*) Longitudinal profile. (*b*) Plan view.

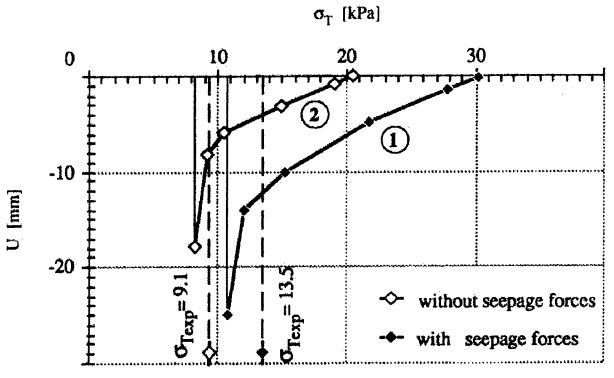

FIG. 6. Supporting pressure σ_T versus face displacement U (finite element method results).

6 months preceding the tunnel excavation, increased to 19 cm for the following 6 months (Fig. 2). The measured hydraulic head loss of 15 cm leads to a 17% deviation from the computed value reported in Table 1 (18 cm). The free surface of the water table and the isopotential-lines network are represented both on the longitudinal section (Fig. 4*a*) and on two typical cross sections (Figs. 4*b*, 4*c*). The hydraulic head losses are concentrated in the close vicinity of the face where the tunnel is partially dewatered.

The resulting hydraulic gradients reach very high values whose maxima are located at the perimeter of the face section. The gradient distributions are represented in an enlarged longitudinal section (Fig. 5*a*) and in a plan view (Fig. 5*b*). The maximum value, which is 6.1, acts at the bottom of the face with an important vertical component. It must be pointed out that their intensities decrease rapidly with distance from the face.

The water discharge entering into the tunnel through the face is directly proportional to the permeability parameter, which is difficult to determine accurately. In situ tests (Lefranc tests) and laboratory tests led to a value of 10^{-4} m/s. For this value, the computed water discharge was 0.43 L/min, more than the average measured value of 0.30 L/min. This discrepancy is probably due to some leakage observed at the face of the access pit.

Stability of the tunnel face

Observations and field measurements

It must be pointed out that the short-term stability (undrained conditions) of the face was ensured during the excavation of the microtunnel. During the period when the tunnel face was partially below the water table, from October 1990 to April 1991, the pressure exerted at the face was measured by the Glötzl cells. The average value was 13.5 kPa. As the face moved a few millimeters before encountering the supporting plate, it was considered that this pressure should correspond to the active failure pressure of the soil. A simple check indicates that at the centre of the plate, the earth pressure at rest (k_o) is 24 kPa (computed using $K_o = 1 - \sin \phi'$), whereas the active pressure (computed with no cohesion) should be 18 kPa. During the period when the tunnel face was completely dewatered (from August to September 1991), the pressure measured at the face decreased significantly to an average value of 9.1 kPa.

It must be noted that no significant displacements of the ground surface were measured. This was expected because the lining support was placed before the excavation. For such a case, Egger (1985) showed that ground displacements are negligible. At the end of the observation period, the supporting plate was removed and collapse of the face occurred. The failure surface did not reach the ground surface.

Numerical modelling of the mechanical behaviour

For the stability problem, the numerical analysis was carried out with the finite element program EFEMER (Dudt and Pellet 1989). The problem was studied in plane strain conditions, using an elastoplastic constitutive equation taking

TABLE 2. Numerical and measured values of supporting pressure exerted on the face support

	Supporting pressure σ_T (kPa)		
	Without water seepage forces	With water seepage forces	Increase (%)
Measured	9.1	13.5	48
Numerical results	8.3	10.9	31
Deviation (%)	9	19	

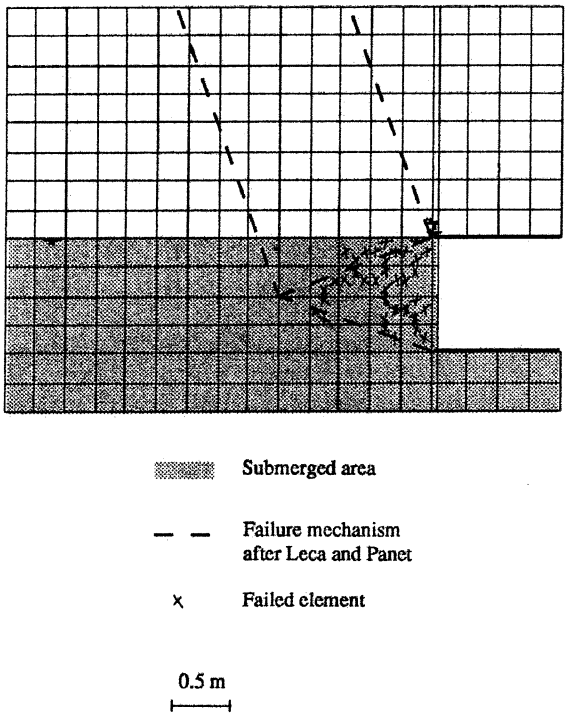

FIG. 7. Failure mechanism for the two-dimensional finite element equilibrium analysis.

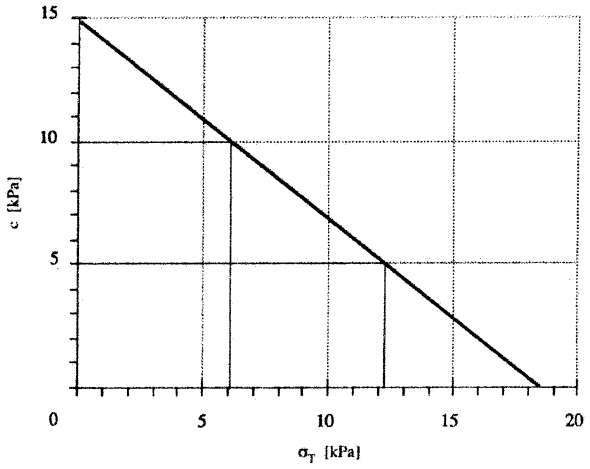

FIG. 8. Supporting pressure versus cohesion (after Leca and Panet 1988).

softening into account. The peak cohesion was 10 kPa and the residual cohesion was zero. The initial state of stresses was applied, and the soil elements located below the water table were loaded both by uplift and by seepage forces. The latter are volumetric forces that were computed and introduced at each relevant node. As mentioned above, the hydraulic gradients decreased rapidly behind the face. Thus, seepage forces acting more than 1.5 m behind the face were neglected. To simulate the progressive mobilization of the stresses acting on the face support, without generating tensile stress in the soil mass, a thin layer of fictitious elements was set up at the soil–support interface. By decreasing the stiffness of these elements at each computational step, soil strength was progressively mobilized. After complete mobilization, the pressure acting on the face tended toward a minimum value.

The supporting pressure versus displacement relation is represented in Fig. 6. The supporting pressure tends to 8.3 kPa for the dewatering period (curve 2) and 10.9 kPa for the period of partial submersion (curve 1). The measured and computed values are summarized in Table 2. The associated displacement of 25 mm corresponds to the initial gap between the face and the supporting plate. The extension of the failure area is drawn in Fig. 7.

By comparison, the supporting pressure for the completely dewatered case may be assessed using the two-dimensional lower bound solution proposed by Leca and Panet (1988):

$$[1] \quad \sigma_T = \frac{1}{K_p}\left[\gamma D\left(\frac{C}{D} + \frac{1}{2}\right) - \sigma_c\right]$$

where σ_T is the supporting pressure, γ is the unit weight of dry soil, σ_c is the unconfined compressive strength, K_p is the coefficient of passive earth pressure, C is the overburden thickness, and D is the diameter of tunnel.

In the laboratory tests the cohesion varied between 5 and 10 kPa. The corresponding calculated values of supporting pressure are 12.2 and 6.1 kPa, respectively. They encompass, therefore, both numerical and experimental results. The supporting pressure versus cohesion relationship is represented in Fig. 8.

Discussion

Good agreement was observed between the numerical and the measured values of supporting pressure exerted on the face support (Table 2). The deviations are 9 and 19%, respectively for the dewatered and the submerged cases. Despite some dispersion, this leads to the conclusion that the supporting pressure required to ensure stability of the tunnel face for a partially submerged tunnel, compared with the dewatered case, is increased by approximately 30–50%. This variation of the supporting pressure is due to the disappearance of the water seepage forces, as well as the development of suction. These negative interstitial water pressures

would lead to an increase in the apparent cohesion in the soil mass. However, this observation cannot be directly extrapolated to larger tunnels because of scale effects. In fact, as the dimensions increase, the volumetric forces such as seepage forces increase more quickly than the surface forces, such as the cohesion.

Conclusion

This study has led to a precise description of the impact of an experimental microtunnel on the surrounding hydraulic conditions and has also provided valuable information on the stability of the construction.

The three-dimensional finite element analysis shows that the hydraulic head losses are concentrated close to the tunnel face and are in agreement with field measurements of the piezometric levels. As a consequence, the generated water seepage forces increase the supporting pressure required to ensure face stability. This was shown both by the two-dimensional numerical equilibrium analvsis and by the experimental measurements.

These results, which cannot be directly extended to a larger tunnel because of the scale effect, show that it is possible to quantify the effect of water seepage forces on the tunnel face stability. The future development of numerical methods should encourage designers to use them for better prediction of the required supporting pressure, leading to safer design of underground constructions.

Acknowledgement

This study is part of a project on behaviour and transport in unsaturated media. It was entirely supported by the Swiss National Fund for Scientific Research.

ADINA Engineering Inc. 1984. ADINAT. A finite element program for automatic dynamic incremental non-linear analysis of temperatures. ADINA Engineering Incorporated, Watertown, N.Y.

Davis, H.E., Gunn, M.J., Mair, R.J., and Seneviratne, H.N. 1980. The stability of shallow tunnels and underground openings in cohesive material. Géotechnique, **30**: 397–416.

Descoeudres, F., and Rybisar, J. 1987. Écoulement d'une nappe livre vers un tunnel. Publication de la Société Suisse de Mécanique des Sols et des Roches, **115**: 3–7.

Dudt, J.P., and Pellet, F. 1989. EFEMER, un programme de calcul par éléments finis en élasto-plasticité, présentation générale. Institut des Sols, Roches et Fondations, École Polytechnique Fédérale de Lausanne, Lausanne, Switzerland.

Egger, P. 1985. Stabilité des tunnels à faible profondeur et tassements en surface. Rapport 108 de l'Office Fédéral de Routes, Bern, Switzerland.

Leca, E., and Panet, M. 1988. Application du calcul à la rupture à la stabilité du front de taille d'un tunnel. Revue Française de Géotechnique, **43**: 5–19.

Modélisation numérique 3-D du comportement d'ouvrages souterrains lors de la traversée d'accidents géologiques

3-D numerical simulation of the behaviour of underground structures crossing faulted zone

Dreidimensionale numerische Modellierung des Verhaltens unterirdischer Bauwerke während der Durchquerung geologisch kritischer Zonen

F. PELLET & O. BENOIT, Laboratoire 3S, Université Joseph Fourier, Grenoble, France

ABSTRACT : In this paper, the results of a 3D numerical simulation of underground excavation through faulted zone are presented. This study is focused on the determination of the influence of the most relevant parameters based on some cases histories reported on the litterature. The numerical results show the influence of the length of the zones, length of the excavation steps, initial conditions and geomechanical properties of squeezing rocks.

RÉSUMÉ: Dans cet article, on présente les résultats d'une modélisation numérique tridimensionnelle du creusement d'un tunnel au travers d'un accident géologique représenté par une couche de moindre résistance. Cette étude qui est destinée à mesurer le poids des principaux paramètres a été réalisée à la suite de l'analyse de cas de rupture de fronts d'ouvrages publiés dans la littérature. Les résultats numériques montrent l'importance des principaux facteurs affectant la stabilité de l'ouvrage que sont, outre les caractéristiques mécaniques des matériaux, la longueur de la zone de roches broyées, la longueur des étapes d'excavation ainsi que les conditions de contraintes initiales.

ZUSAMMENFASSUNG: In diesem Artikel werden die Ergebnisse einer dreidimensionalen numerischen Modellierung eines Tunnelvortriebes, der eine geologisch kritische Zone durchquert, die durch eine weniger widerstandsfähige Schicht dargestellt wird, vorgestellt. Diese Studie ist dazu bestimmt die Bedeutung der wichtigsten Parameter zu bestimmen, welche im Anschluß einer Untersuchung im Fall eines Bruches der Stirnflächen der Bauwerke verwirklicht worden sind. Dieser Fall ist in der Literarur veröffentlicht.Infolgedessen zeigen die numerischen Ergebnisse die Bedeutung der wichtigsten Faktoren, welche die Standsicherheit des Bauwerkes beeinflussen. Unter diesen Faktoren sind die mechanischen Eigenschaften der Werkstoffe, die Länge der Zone des gebrochenen Gesteins, die Länge der Stufen der Ausschachtung, sowie die Zustände der Anfangsspannungen zu nennen.

1 EXTENDED ABSTRACT

Underground works being constructed in rock formations may encounter crushed and decompressed rock resulting from serious tectonic movements. These formations, which in addition often contain captive aquifers under high pressure, represent one of the major difficulties in excavating underground works, and numerical models are usually needed to forecast their behaviour. Indeed, the behaviour of crushed rock has a direct effect on the method used and the time taken to complete a structure, as well as on the safety of workers and equipment, and the long-term behaviour of the structure. Furthermore, environmental impact and hydrogeological conditions (such as water resources, etc.) are other factors that need to be controlled.

This article presents the results and conclusions obtained by finite-difference 3D numerical simulation (Figure 1). The aim of the study was to measure the relative importance of the main parameters involved, and was performed after analysing cases of excavation front failures described in the literature. Subsequently, the numerical results showed the importance of the main factors affecting the stability of the structure. In addition to the mechanical characteristics of the material, these include the length of the crushed rock zone, the length of the various stages of excavation, and the initial mechanical and hydraulic stress conditions.

The phenomena of stress redistribution, arch effects and vault development (Figure 3) all contribute to wall convergence in underground excavations, as illustrated at various stages of work in Figure 2a, 2b and 2c. The influence of the loading path on the location and development of failure during progressive unconfinement of the sample as a result of excavation work can be clearly seen in Figure 4a, 4b, 4d and 5.

Despite the fact that current numerical computation codes cannot claim to simulate all the thermal, hydraulic and mechanical mechanisms involved, these results nevertheless show the importance of detailed modelling in determining the main parameters that affect the behaviour of underground structures in extreme conditions. Future developments in modelling techniques (including numerical procedures and computer facilities) should enable a more systematic reverse analysis of the behaviour of monitored structures.

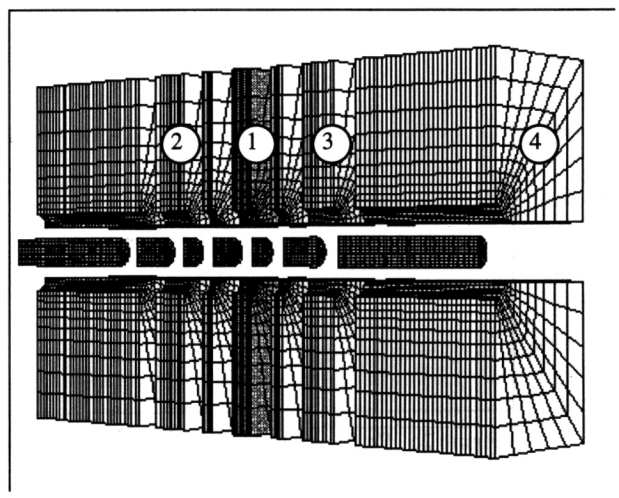

Figure 1 : Vue tridimensionelle du modèle étudié

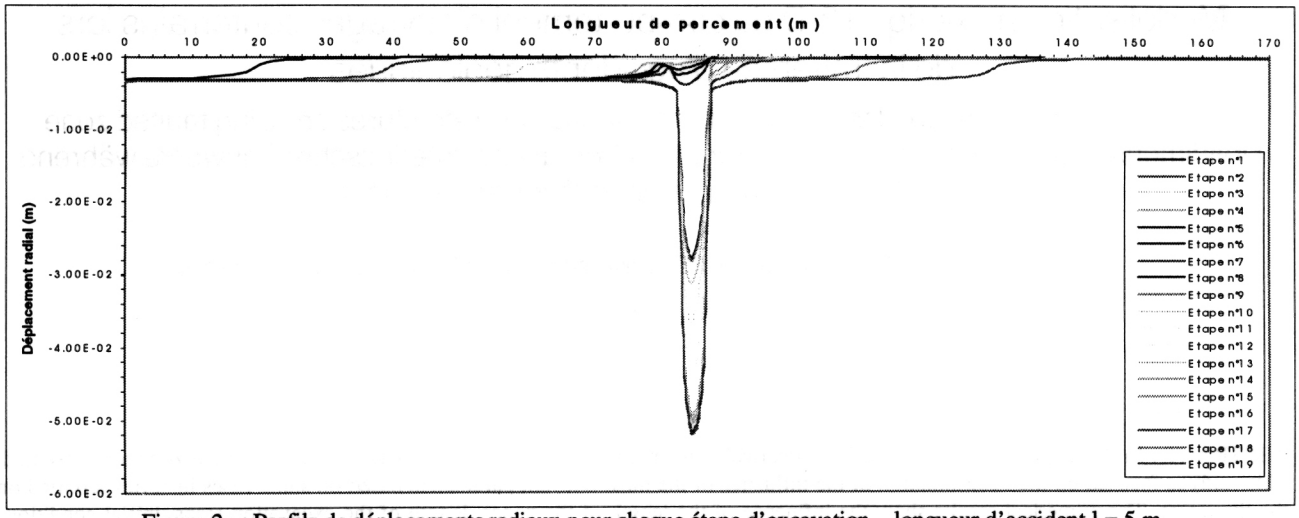

Figure 2a : Profils de déplacements radiaux pour chaque étape d'excavation – longueur d'accident l = 5 m

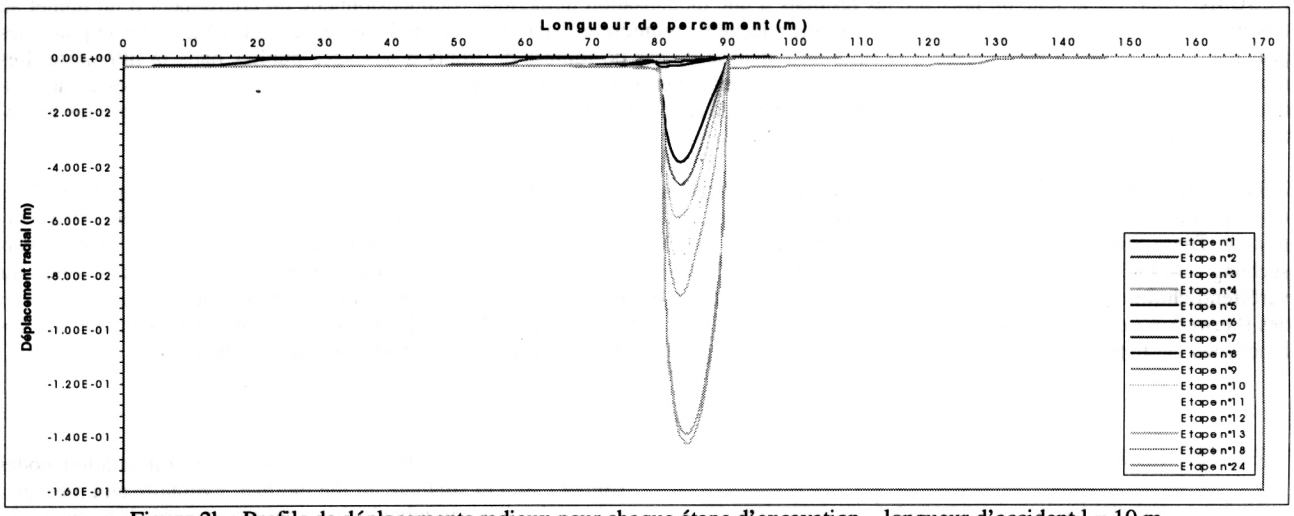

Figure 2b : Profils de déplacements radiaux pour chaque étape d'excavation – longueur d'accident l = 10 m

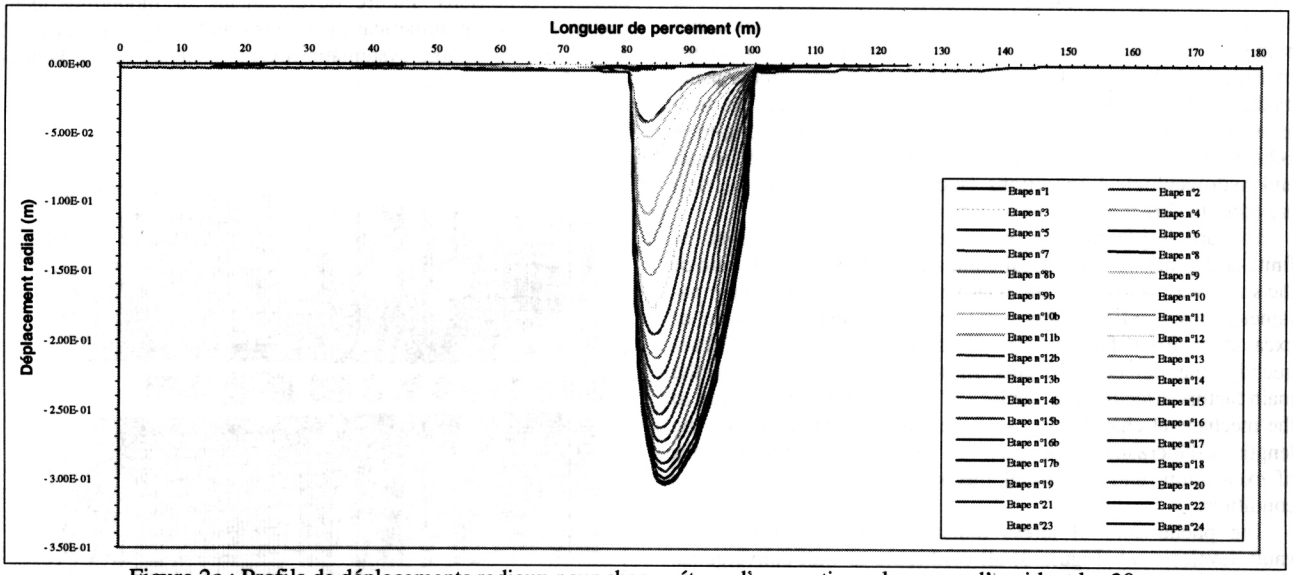

Figure 2c : Profils de déplacements radiaux pour chaque étape d'excavation – longueur d'accident l = 20 m

2 INTRODUCTION

La construction d'ouvrages souterrains en massifs rocheux peut recouper des zones fortement tectonisées constituées de roches broyées et décomprimées qui sont bien souvent de surcroît, le siège d'aquifères sous hautes pressions.

La traversée de ces zones constitue l'une des difficultés majeures dans le creusement d'ouvrages souterrains profonds pour laquelle la prévision du comportement mécanique de l'ouvrage est nécessaire. Il s'agit en effet de choisir le mode d'exécution de l'ouvrage, d'estimer la durée de réalisation et de s'assurer que la sécurité du chantier sera suffisante. Enfin, on cherche à prévoir le comportement de l'ouvrage à long terme.

Bien que la définition du modèle géologique reste souvent difficile à établir et que le comportement mécanique de ces roches broyées soit mal connu, le recours aux modèles numériques est de plus en plus fréquent, ne serait ce dans un premier temps, que pour estimer qualitativement le comportement de l'ouvrage et fixer l'ordre de grandeur des déplacements à attendre (Gioda et Cividini 1996, Kropik et Mang 1996, Mémier et al. 1995)

Dans cet article, on présente les résultats d'une modélisation numérique réalisée par différences finies pour une géométrie tridimensionnelle.

Cette étude, destinée à mesurer le poids des principaux paramètres, a été réalisée à la suite de l'analyse de cas de rupture de fronts d'ouvrages publiés dans la littérature (Aydan et al. 1996, Panet 1996, Steiner 1996). Une journée d'étude de la Société Suisse des Ingénieurs et Architectes fût récemment consacrée à la maîtrise d'accidents géologiques dans la construction de tunnels (SIA, 1998). Parmi les plus importants, on peut citer celui survenu lors du percement du tunnel autoroutier du Gran Sasso en Italie qui fût causé par la traversée d'une faille non reconnue constituée de mylonite et de cataclasites (Lunardi, SIA 1998). Plus récemment, l'effondrement du tunnel des Hurtières (Falconnat et Hingant, SIA 1998) causé par le recoupement d'un ancien sillon glaciaire de géométrie complexe, a illustré les difficultés engendrées par ce type d'accidents.

Les résultats numériques de cette étude montrent l'importance des principaux facteurs influençant la stabilité de l'ouvrage que sont, outre les caractéristiques mécaniques des matériaux, la longueur de la zone de roches broyées, la longueur des étapes d'excavation ainsi que les conditions de contraintes initiales.

3 MODELE ET PARAMETRES

L'analyse numérique a été menée avec le logiciel FLAC3D, (Billaux et Cundall 1993) en utilisant un modèle de comportement élasto-plastique avec le critère de Mohr-Coulomb.

Les dimensions du modèle étudié (Figure 1) ont été fixées pour un tunnel standard de 10 mètres de diamètre. La longueur totale du domaine étudié est de 160 m pour une largeur de 55 m et une hauteur de 110, ce qui est suffisant pour limiter les effets de bord. Seule la demi-section de l'ouvrage est étudiée.

L'épaisseur de l'accident géologique varie de 0.5 à 2 fois le diamètre, soit de 5 à 20 m. Le modèle est divisé en quatre zones : La zone 1 représente l'accident géologique à l'intérieur duquel, la longueur des mailles correspondant aux tranches d'excavation est de 1 m. Les zones 2 et 3 (mailles de longueur variant entre 1 est 3 m) font la transition avec la zone 4 qui représente le massif rocheux sain situé de part et d'autre de l'accident. La longueur des mailles est de 5 m.

Les conditions aux limites sont classiques, déplacements bloqués sur 3 faces dont le plan de symétrie et forces nodales imposées sur les 3 faces opposées. Les contraintes initiales sont isotropes (K_0 égal à 1).

Afin de modéliser au mieux la réalité, le calcul de l'excavation du tunnel est fait par étapes. Le percement du tunnel s'effectue en pleine section et se décompose en 24 étapes ou plus durant lesquelles une tranche de terrain de 1 à 20 m est retirée. La roche saine est excavée par tranches un peu plus importantes. En s'approchant de l'accident, l'épaisseur de terrain excavé diminue passant à 5 puis 2 et 1 m à 3 m de l'accident. Cette réduction a deux justifications. Premièrement, lorsqu'un tunnel s'approche d'une zone difficile, la cadence est réduite (sauf si les ingénieurs n'ont pas reconnu l'accident). Deuxièmement, du point de vue numérique, il est important d'excaver progressivement pour que le calcul se stabilise plus rapidement. A l'intérieur de l'accident, l'excavation est menée mètre par mètre.
Au-delà de cette zone, la longueur des tranches s'allonge. L'excavation est arrêtée lorsque le front de taille arrive à 40 m de la fin du modèle. Cette marge de 8 rayons a été adoptée afin de limiter les effets de bords et de bien apprécier l'influence du front de taille.

4 ANALYSE DES RESULTATS

Plusieurs séries de calculs ont été réalisés en faisant varier les caractéristiques géomécaniques et surtout la longueur de l'accident traversé. Les caractéristiques géomécaniques de base pour les matériaux constituant le modèle sont reprises ci-dessous. Elles correspondent à un granite de bonne qualité pour le massif sain et à des roches broyées (mylonites) de faibles caractéristiques pour l'accident :

Granite	E = 30 GPa
	ν = 0.25
Roches broyées	E = 1 GPa
	ν = 0.4
	ϕ = 25 degrés
	c = 0.3 MPa

Les calculs qui sont réalisés pour les longueurs d'accident de 5, 10 et 20 m portent respectivement les noms de CL5, CL10, CL20.

4.1 *Analyse des déplacements de convergence*

Le champ de contraintes initial étant isotrope, les déplacements consécutifs à l'excavation sont uniformes sur le périmètre du tunnel. Les profils des déplacements radiaux en fonction de la longueur de percement sont donc identiques en voûte et en piédroit.

4.1.1 *Accident de 5 mètres de longueur*

Les déplacements radiaux dits de convergence dans l'accident géologique augmentent au fur et à mesure de l'avancement de l'excavation. On observe sur la figure 2a une augmentation substantielle lorsque le front traverse l'accident. De l'étape 8 à l'étape 13, l'évolution des déplacements dans la zone élastoplastique atteint un maximum de 53 mm correspondant à la sortie du front de taille de la zone de l'accident.

Dans le massif sain la convergence élastique calculée par le modèle numérique 3D correspond à la valeur issue d'un calcul analytique 2D. Par contre, dans la zone de l'accident, la différence entre les déplacements radiaux donnés par le calcul numérique 3D et ceux fournis par la méthode analytique 2D, en introduisant les caractéristiques de la roche broyée, est très im portante.

La modélisation numérique montre un déplacement 72 fois plus petit. Cela illustre bien l'effet voûte qui se développe dans cette zone de moindre résistance par le report d'une partie des contraintes sur la partie saine du massif.

4.1.2 *Accident de 10 mètres de longueur*

De l'étape 1 à l'étape 8, le profil des déplacements élastiques radiaux est identique à celui calculé par la méthode analytique 2D (Figure 2b). De l'étape 9 à l'étape 18, les déplacements radiaux dans l'accident géologique augmentent au fur et à mesure de l'excavation, c'est à dire de l'éloignement du front. Ils atteignent la valeur de 142 mm à la sortie du front de taille de l'accident.

Pour ce cas, l'écart entre les déplacements radiaux obtenus numériquement et ceux calculés analytiquement est toujours très important (rapport de 27). Cependant, l'augmentation de l'épaisseur de l'accident tend à réduire cet écart.

4.1.3 *Accidents de 20 mètres de longueur*

Dans la première partie (étape 1 à 8) le profil des déplacements radiaux correspond toujours au profil élastique analytique. De l'étape 9 à l'étape 18, les déplacements radiaux dans l'accident géologique augmentent pour atteindre 320 mm (Figure 2c). Le rapport entre les déplacements radiaux numériques et analytiques tombe à 10.

4.2 *Redistribution des contraintes*

L'examen des profils des déplacements montre que l'effet voûte contribue à réduire considérablement les convergences dans l'accident. Cet effet qui provoque des contraintes de cisaillement au contact accident massif sain se matérialise par la réorientation des contraintes principales comme l'illustre la figure 3 pour une longueur d'accident de 20 m.

Dans le massif sain, loin de l'accident, la valeur de σ_1 correspond à valeur attendue par la méthode analytique 2D tandis que près de l'accident, elle augmente du fait des reports de charge de l'effet de voûte. Au milieu de l'accident, elle est plus faible bien que supérieure à celle calculée analytiquement avec les caractéristiques de la roche broyée.

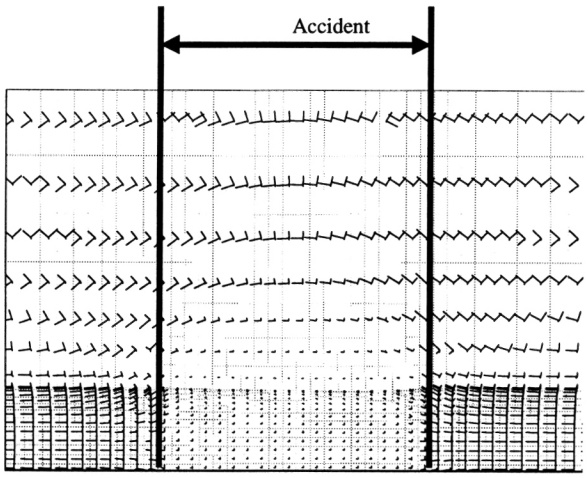

Figure 3 : Redistribution des contraintes dans la zone de l'accident

4.3 *Chemin de contraintes et développement de la rupture*

Afin de suivre l'évolution des contraintes dans le modèle au cours de l'excavation, les chemins de contrainte en certains points ont été tracés pour le cas d'un accident de 20 m de longueur (Figures 4). Initialement, la contrainte moyenne, p, est égale à la contrainte initiale, σ_0, alors que la contrainte déviatoire, q, est nulle.

Dans le massif sain, loin de l'accident et en clé de voûte (Figure 4a), la contrainte p reste constante et égale à la contrainte initiale tout au long de l'excavation. La contrainte q augmente progressivement avec l'arrivée du front pour atteindre 10 MPa après son passage (étapes 3 à 4). La variation de la contrainte principale majeure (σ_1 tangente à la section du tunnel) est donc égale à la variation de la contrainte principale mineure (σ_3 radiale dans la section du tunnel) mais de signe opposé. Dans la même section mais à l'axe du tunnel (Figure 4b), la roche subit dans un premier temps une augmentation du déviateur associé à une diminution de la contrainte moyenne puis, dans un second temps, une réduction simultanée des deux. Cela correspond à un chemin en extension consécutif au déconfinement lié à l'excavation.

Au milieu de l'accident (Figures 4c et 4d), l'allure du chemin de contraintes en clé de voûte correspond à une extension latérale (augmentation du déviateur et diminution de la contrainte moyenne). La rupture est atteinte bien avant le passage du front. A l'axe de l'ouvrage, l'arrivée du front de taille provoque une extension latérale du massif (p diminue et q augmente), puis lorsque le front s'approche, la contrainte q diminue de manière drastique.

L'apparition de la rupture se manifeste par la mise en plasticité de la zone du front. La figure 5 donne un exemple des zones rompues au moment où le front est au milieu de l'accident de 20 m. L'extension de la rupture est plus importante au centre qu'au contact accident massif sain.

Après le percement complet du tunnel, le calcul signale une extension de la zone rompue au centre de l'accident de l'ordre de 3 fois le diamètre initial de l'ouvrage. Le calcul analytique2D donne dans la même situation un rapport de 6. Cette observation confirme le rôle positif de l'effet de voûte.

5 INFLUENCE DES PARAMETRES

L'influence de l'épaisseur de l'accident géologique et des caractéristiques mécaniques du matériau le constituant est déterminante sur les déplacements radiaux, les cisaillements au contact de l'accident, les contraintes principales et les zones plastiques.

5.1 *Longueur de l'accident*

Pour ce jeu de caractéristiques mécaniques, la méthode analytique 2D donne une convergence finale de 0.53 % de convergence normalisée. Cette convergence est largement surestimée car l'effet voûte qui n'est pris en compte réduit considérablement les déplacements radiaux. La Figure 6 montre l'évolution de la convergence en fonction de l'épaisseur de l'accident.

En première approximation on obtient en extrapolant sur la base d'une régression en fonction de puissance, que l'effet voûte ne se fait plus sentir (c'est à dire que la valeur de la convergence calculée numériquement en 3D correspond à celle calculé analytiquement en 2D) pour une longueur d'accident de l'ordre de 11 fois le diamètre. Des calculs complémentaires sont évidemment à effectuer avec d'autres jeux de caractéristiques afin de valider ces estimations.

Il faut noter aussi que pour de grandes convergences l'hypothèse de base de la méthode analytique supposant de petites déformations mérite d'être discutée. Des mécanismes de rupture localisée se développent probablement bien avant.

5.2 *Distribution des contraintes*

Les phénomènes de redistribution de contraintes, effet d'arche et développement de voûte, jouent un rôle favorable sur l'évolution de la convergence des parois de l'excavation souterraine qui est illustrée pour les différentes phases aux Figures 2a, 2b, 2c. L'influence du chemin de chargement que subit l'échantillon lors du déconfinement progressif consécutif à l'excavation de l'ouvrage sur la localisation et le développement de la rupture est clairement mis en évidence aux figures 4a, 4b, 4c, 4d.

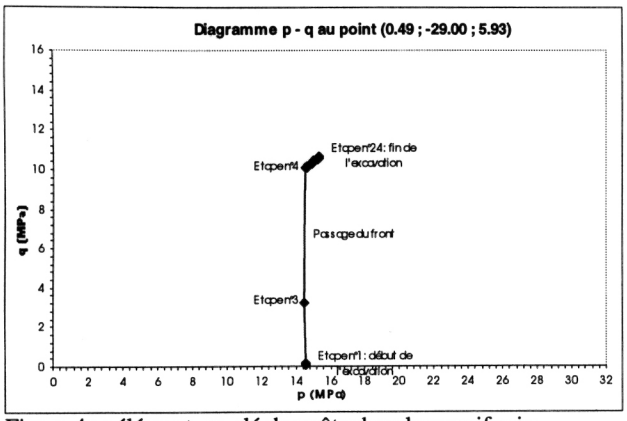

Figure 4a : élément en clé de voûte dans le massif sain

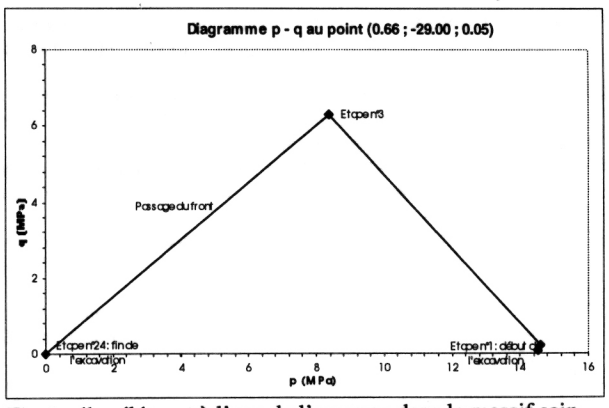

Figure 4b : élément à l'axe de l'ouvrage dans le massif sain

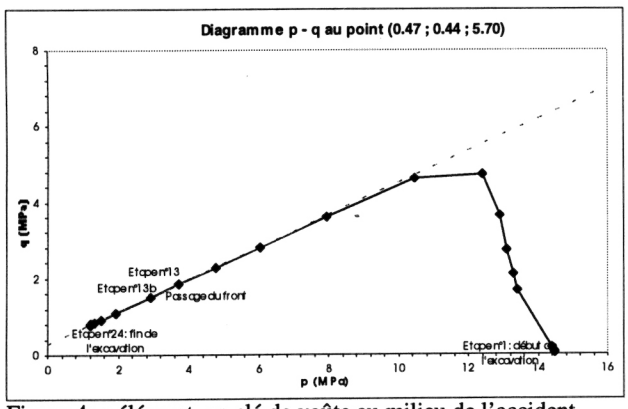

Figure 4c : élément en clé de voûte au milieu de l'accident

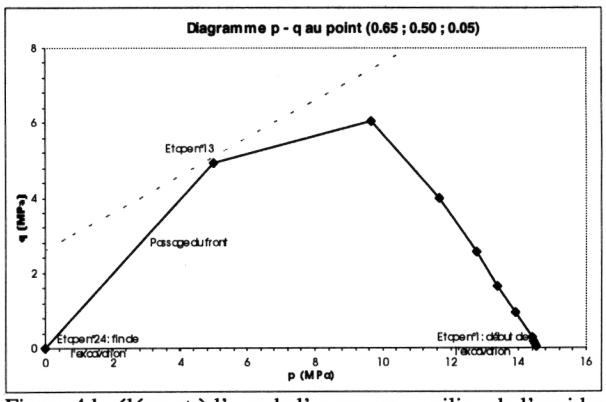

Figure 4d : élément à l'axe de l'ouvrage au milieu de l'accident

Figure 4 : Chemins de contraintes consécutifs à l'excavation pour une longueur d'accident de 20 m

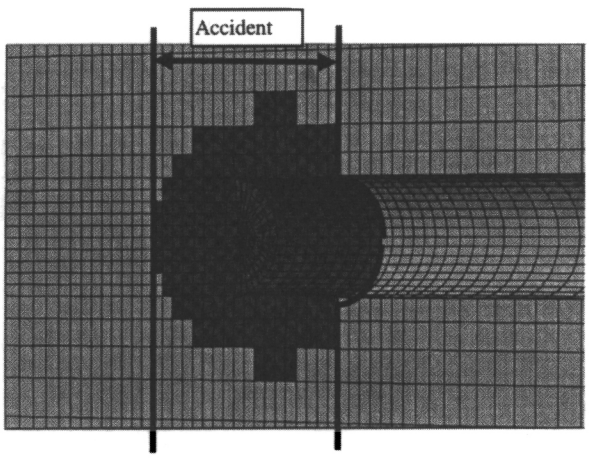

Figure 5 : Zones plastiques (front de taille au milieu de l'accident)

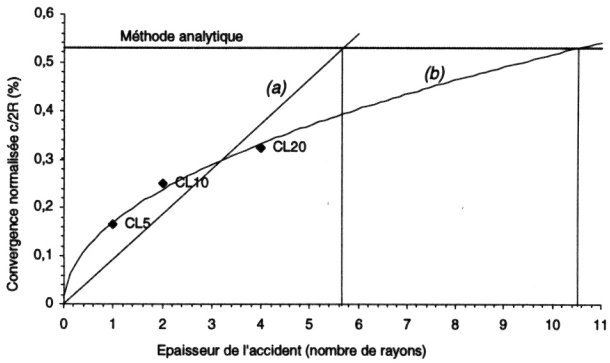

Figure 6 : Convergences au centre de l'accident en fonction de la longueur de l'accident

6 CONCLUSION

Cette étude a montré l'importance capitale de la prise en compte d'une géométrie tridimensionnelle pour l'étude du comportement de tunnels creusés en terrains hétérogènes.

L'estimation des convergences, le développement des zones plastiques et finalement l'estimation des efforts que devront supporter les soutènements sont grandement influencés par l'effet voûte qui dépend des caractéristiques mécaniques et surtout de la longueur de l'accident traversé.

Bien qu'à l'heure actuelle les codes de calcul numériques ne puissent pas prétendre modéliser l'ensemble des mécanismes thermo-hydro-mécanique mis en jeu dans les géomatériaux (notamment, la présence d'eau sous fortes pressions), ces résultats montrent l'importance d'une modélisation fine sur l'évolution des principaux paramètres affectant le comportement des ouvrages souterrains dans des conditions extrêmes. Dans le futur, le développement des moyens informatiques devrait permettre une meilleure compréhension des phénomènes mécaniques développés lors du percement de tunnels

7 REFERENCES

AYDAN O., AKAGI T., KAWAMOTO T. (1996), *The squeezing potential of rock around tunnels: theory and prediction with examples taken from Japan,* Rock Mechanics and Rock Engineering, vol 29, n°3, pp 125-143.

BILLAUX D., CUNDALL P. (1993), *Simulation des géomatériaux par la méthode des éléments Lagrangiens*, Revue Française de Géotechnique, n°63, pp 9-21.

GIODA G., CIVIDINI A. (1996), *Numerical methods for the analysis of tunnel performance in squeezing rocks,* Rock Mechanics and Rock Engineering, vol 29, n°4, pp 171-193.

KOVARI K., ANAGNOSTOU G.(1996), *The ground response curve in tunnelling through short fault zones* , Proc. 8th ISRM Congress, Tokiyo, pp 611-614, 1995.

KROPIK C., MANG H.A. (1996), *Computational mechanics of the excavation of tunnels*, Engineering Computations, vol. 13, n°7, pp 49-69.

MEMIER B., MADIER C., PERRODO M. (1995), *Modélisation 3D du creusement d'un tunnel*, Tunnels et Ouvrages Souterrains, n°129, pages 160-164

PANET M. (1996), *Two case histories of tunnels through squeezing rocks*, Rock Mechanics and Rock Engineering, vol 29, n°3, pp 155-164, 1996.

SOCIETE SUISSE DES INGENIEURS ET ARCHITECTES (SIA 1998), Groupe Spécialisé pour les Travaux Souterrains, La Maîtrise d'accidents géologiques dans la construction de tunnels, Documentation , D 0149, 1998.

STEINER W. (1996), *Tunneling in squeezing rocks: case histories,* Rock Mechanics and Rock Engineering, vol 29, n°4, pp 211-246.

PERGAMON

Tunnelling and Underground Space Technology 17 (2002) 415–424

Tunnelling and Underground Space Technology
incorporating Trenchless Technology Research

www.elsevier.com/locate/tust

Back analysis of time-dependent behaviour of a test gallery in claystone

E. Boidy[a,*], A. Bouvard[a], F. Pellet[b]

[a]*Coyne et Bellier, 9 Allée des Barbanniers, 92632 Gennevilliers Cedex, France*
[b]*University Joseph Fourier, Laboratory 3S, BP 53, 38041 Grenoble Cedex 9, France*

Received 20 June 2002; received in revised form 29 August 2002; accepted 3 September 2002

Abstract

This paper presents a back analysis of the time-dependent behaviour of a monitored tunnel in Switzerland. It concerns a specific section of the Mont Terri reconnaissance gallery which was excavated in creeping rock. From a theoretical point of view, Lemaitre's viscoplastic model was implemented in the FLAC 2D finite-difference numerical code. Particular attention was paid to the stability of the numerical solution for such an explicit mode of resolution. Lemaitre model parameters were successfully fitted on creep tests and then on in situ convergence measurements after a complete numerical simulation. Based on the comparison of strain and stress measured in the lining with the calculated values, time-dependent behaviour can finally be extrapolated over a period of approximately 10 years. Scale effects between results of in situ and laboratory fittings are also discussed. The aim of these investigations is to justify the interest of Lemaitre's model for the analysis of time-dependent behaviour of underground structures over a long period of time.

Keywords: Rheology; Creep; Claystones; Lemaitre's model; Numerical modelling; Tunnel; Mont Terri; Scale effects

1. Introduction

Predicting the long-term behaviour of underground structures is not an easy task, because it needs a reliable constitutive model which can interpret measurements of viscous phenomena (Boidy and Pellet, 2000). It is also well known that rock properties measured on samples in the laboratory cannot be extrapolated directly to field scale without due precaution.

For this reason, it is necessary to compare numerical simulations with measurements obtained on monitored tunnels over long periods. Unfortunately these kinds of data are very scarce. This paper presents the back analysis of the time-dependent behaviour of the Mont Terri reconnaissance gallery which was instrumented over a period of 8 years. The study concerns a specific section which was excavated and left without any support system for approximately 3 months, after which a stiff lining consisting of a concrete ring was installed. This ring also has restrained time-dependent convergence. Kohler (1995) reported all construction stages.

*Corresponding author. Fax: +33-1-4185-0374.
E-mail address: eric.boidy@coyne-et-bellier.fr (E. Boidy).

2. Presentation of the case studied

2.1. Location and geological context

The Mont Terri tunnel is one of several structures on the A16 'Transjurane' motorway which links the Swiss plateau (Bern) to France (Belfort). The tunnel consists of a single two-lane tube for traffic in both directions. The Mont Terri reconnaissance gallery was excavated (by drilling and blasting) in 1989 in order to investigate the geological conditions and mechanical properties of the rock (Fig. 1).

Since the opening of the motorway at the end of 1998, the reconnaissance gallery has served as an escape way. In the winter of 1997/1998, a new gallery with a total length of approximately 230 m and several lateral niches were excavated to host an underground research laboratory. An extended European research programme was performed to study the feasibility of nuclear waste disposal in claystones (Thury and Bossart, 1999). The location of the different underground structures is given in Fig. 1.

0886-7798/02/$ - see front matter
PII: S0886-7798(02)00066-4

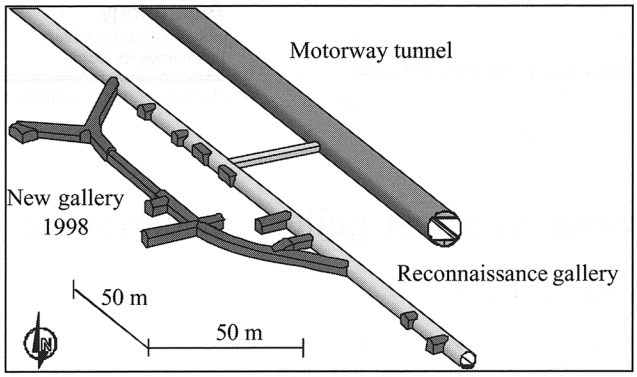

Fig. 1. Relative location of the different underground structures at the Mont Terri site, after Thury and Bossart (1999), © Geotech Institute, Bern.

The reconnaissance gallery crosses sedimentary clay formations, including Dogger shales (Oxfordian and Aalenian stages), Lias marls and Triassic anhydrite marls (Keuper stage). Schaeren and Norbert (1989) have given a simplified longitudinal geological section along the motorway tunnel (Fig. 2). The maximum overburden is approximately 370 m. The cross-section is almost perfectly circular and the average radius of the lined gallery is approximately 2.35 m.

The longitudinal section studied in this paper is in the Opalinus claystones formation from the Aalenian stage. Theses stiff clays have a bad reputation because of their swelling and creeping characteristics. The overburden of approximately 250 m consists mainly of silty and sandy layers, with 40–80% clay minerals, 10–40% quartz and 5–40% calcite (Thury and Bossart, 1999). The longitudinal section studied here is shown in Fig. 3.

This zone presents three lithostratigraphic sub-units:

- Sub-unit 1: 55 m of marly shales with lenses of grey and sandy limestone between tunnel metres TM 780 and TM 835;
- Sub-unit 2 (shaly facies): 30 m of argillaceous shales with millimetric thick layers of sandstone between TM 840 and TM 870;
- Sub-unit 3 (sandy facies): 15 m of shales with many layers of sandstone at TM 875 to TM 890.

In the shaly facies, the gallery was excavated without any support system. The concrete invert was cast when the gallery face reached tunnel metre TM 874.6, where

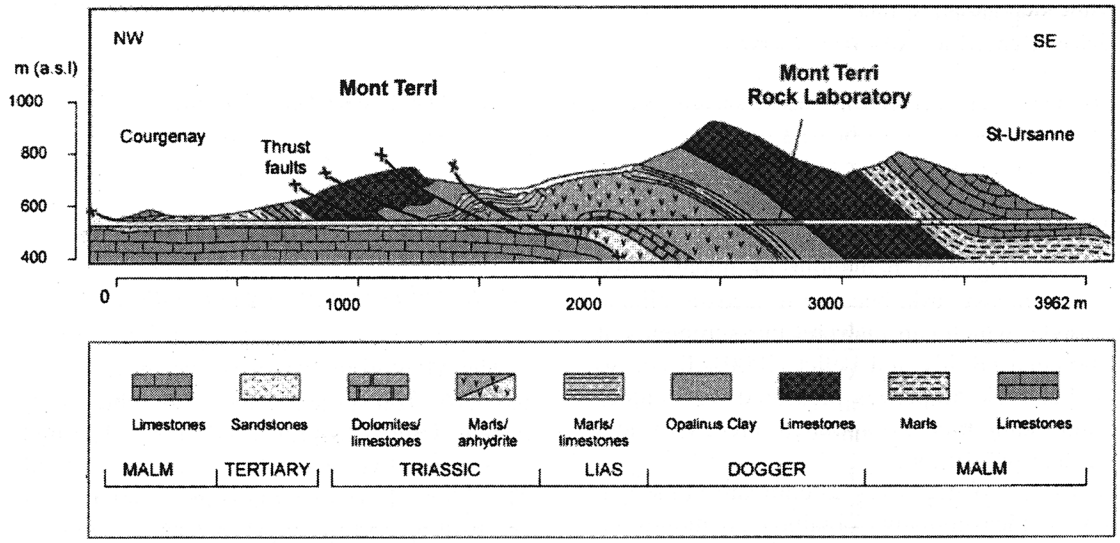

Fig. 2. Longitudinal geological section through the Rangiers massif along the motorway tunnel, after Schaeren and Norbert (1989).

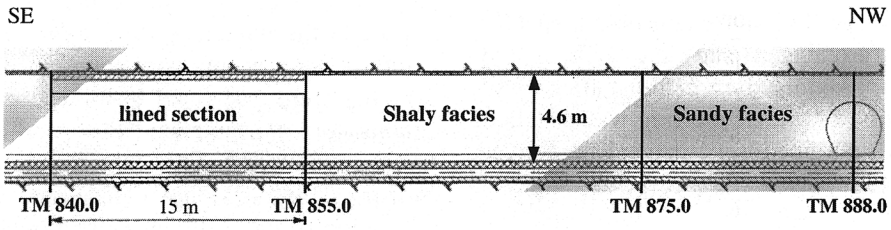

Fig. 3. Simplified longitudinal geological section along the reconnaissance gallery, after Kohler (1995).

excavation was stopped for one month. Three months after excavation, a stiff lining consisting of a 30-cm thick concrete ring was installed between tunnel metres TM 840 and TM 855.

2.2. Instrumentation

Along the lined longitudinal section of the gallery (TM 840 to 855), several cross-sections were instrumented during the excavation phase, as well as after lining (see Table 1 and Fig. 4). Two standard profiles of convergence measurements are located at TM 850.5 and TM 852.5. At TM 850.5, four borehole extensometers were also installed 11 days after excavation. After lining, a third profile was monitored at TM 847.5 (Fig. 3), where pressures were measured in the concrete ring. Kohler (1995) has reported the location of measurement apparatus (Fig. 4). The description of these devices is given in Table 1. Instrumentation measurements were recorded after each stage of excavation.

3. Time-dependent numerical modelling

3.1. Lemaitre's viscoplastic model

The viscoplastic constitutive equations adopted for modelling time-dependent behaviour of the gallery are related to Lemaitre's model (Lemaitre and Chaboche, 1996). This model is based on the overstress theory formulated by Perzyna (1966) for rate-sensitive plastic materials. The equations describe the transient creep phase, which is defined by a decrease of the viscoplastic strain rate vs. time under a constant stress level. Swelling phenomena and the effect of pore pressure and seepage are completely neglected.

Basically the total strain rate, $\dot{\varepsilon}_{ij}$, can be divided into an instantaneous reversible (elastic) part, $\dot{\varepsilon}^{e}_{ij}$, and an irreversible (viscoplastic) part, $\dot{\varepsilon}^{vp}_{ij}$:

$$\dot{\varepsilon}_{ij} = \dot{\varepsilon}^{e}_{ij} + \dot{\varepsilon}^{vp}_{ij} \tag{1}$$

where the irreversible strain rate includes both viscous and plastic effects and is given by the following relationship:

$$\dot{\varepsilon}^{vp}_{ij} = \gamma \langle \Phi(F) \rangle \frac{\partial G}{\partial \sigma_{ij}} \tag{2}$$

In this expression, γ is the viscosity coefficient, G is the viscoplastic potential, F corresponds to the static yield function, and Φ is the flow rule. The brackets defined by Macauly, $\langle\rangle$, control the latter function in the following way:

$$\begin{aligned} &\langle \Phi(F) \rangle = 0 \qquad \text{if: } \Phi(F) < 0 \\ &\langle \Phi(F) \rangle = \Phi(F) \qquad \text{if: } \Phi(F) > 0 \end{aligned} \tag{3}$$

Function F depends on the second invariant of the stress tensor q, by assuming a von Mises loading surface, and on the strain-hardening parameter κ. The strain-hardening parameter is a function of accumulated viscoplastic strains (second invariant of the stress tensor) which can be expressed by:

$$\varepsilon_{vp} = \int_0^t \left(\frac{2}{3} \dot{\varepsilon}^{vp}_{ij} \cdot \dot{\varepsilon}^{vp}_{ij} \right)^{1/2} d\tau \tag{4}$$

Tab. 1. Monitoring programme and devices for the three profiles studied, at tunnel metres TM 850.5, TM 852.5, and TM 847.5

Monitoring programme – Step 1 : Excavation			Measurement period
① to ⑧	8 convergence references on studs cemented into the unlined walls of the tunnel	TM 852.5 TM 850.5	3 months
Ⓐ Ⓑ Ⓒ Ⓓ	4 borehole extensometers: measurements at: 0.5 – 1 – 2 – 4 – 9 m depth	TM 850.5	3 to 12 months
G5 to G9	Invert: 5 Glötzl flat stress cells at rock interface	TM 847.5	8 years
C5 to C7	Invert: 3 vibrating-wire strainmeters	TM 847.5	15 months
Monitoring programme – Step 2 : Lining			
G1 to G4	Sidewalls and crown: 4 Glötzl flat stress cells at rock interface	TM 847.5	8 years
GI to GV	Sidewalls and crown: 5 Glötzl flat stress cells in concrete	TM 847.5	15 months
C1 to C4	Sidewalls and crown: 4 vibrating-wire strainmeters	TM 847.5	15 months

The assumption of isotropic hardening is also involved. In practical terms, the law is simplified by considering two further assumptions. Firstly, the constitutive law can be defined as being associated, for which the viscoplastic potential, G, corresponds to the second invariant of the stress tensor q. This assumption considers that viscoplastic strains are developed without any volume changes. Secondly, in order to get a representative model, power laws have been introduced for the flow rule, Φ, and for the strain-hardening parameter, κ, as proposed by Lemaitre. Eqs. (5) and (6) sum up the relationships considered.

$$\Phi(F)=(F+1)^n \tag{5}$$

$$\kappa(\varepsilon_{vp})=(\varepsilon_{vp})^{-m/n} \tag{6}$$

Thus, Boidy (2002) gives the following expression for the viscoplastic strain rate:

$$\dot{\varepsilon}_{ij}^{vp}=\frac{3}{2}A\cdot q^{n-1}\cdot(\varepsilon_{vp})^m s_{ij} \tag{7}$$

where:

- s_{ij} is the deviatoric part of the stress tensor,
- q is the second invariant of the stress tensor.

This law requires the following three parameters to be identified:

- A, the viscosity coefficient of the rock ($A>0$),
- n, the stress exponent ($n\geq 1$),
- m^*, the strain-hardening exponent ($m^*=-m/n\geq 0$) with the following restriction:

$$0\leq m^*\leq 1-1/n \tag{8}$$

3.2. Study of critical time-stepping

3.2.1. Numerical explicit stability criterion

The Lemaitre constitutive equations were developed and implemented in the FLAC 3.4 two-dimensional explicit finite-difference programme (Itasca, 2000). For such a simulation, special analysis of the time step is necessary in order to ensure the stability of the time-dependent numerical solution (Billaux and Cundall, 1993). As the system is required to always be in mechanical equilibrium, the time-dependent stress increment must not be large compared to the strain-dependent stress increment; otherwise, out-of-balance forces will rapidly become large, and inertial effects may affect the solution. Cormeau (1975) has given the expression of the critical time step for such an explicit mode of resolution in the general case. For Lemaitre's constitutive equations, the critical time step becomes:

$$\Delta t_{crit}=\frac{4(1+\nu)}{3E\alpha\beta a\cdot q^{\beta-1}\cdot t^{\alpha-1}} \tag{9}$$

where E is the elastic loading modulus; ν is the Poisson's ratio; α and β are exponents; and a represents the viscosity parameter. The last three of these constants are functions of the previous parameters m, n and A, with the following relationships:

$$\alpha=\frac{1}{1-m};\ \beta=\alpha\cdot n=\frac{n}{1-m};\ a=\left(\frac{1}{\alpha}A\right)^{\alpha} \tag{10}$$

Thus, for the creep path, the simplified equations can be formulated as follows:

$$\varepsilon_{vp}=a\cdot q^{\beta}\cdot t^{\alpha} \tag{11}$$

3.2.2. Definition of an admissible time step

The safety factor to be applied to the critical time step of Cormeau has been determined by Boidy (2002) and Boidy et al. (2001). The conclusions of this study match the observations of Detournay (1998) who recommends, for practical purposes, to take a safety factor between 100 and 1000 for the estimation of the admissible time. In this case, by analyzing the evolution of numerical unbalanced forces after each time step, Boidy (2002) shows that stability of the numerical solution is ensured. In practical terms, for an engineering simulation, it is advisable to choose an admissible time step in order to satisfy requirements of accuracy and computation time. Thus, the choice of a suitable safety factor allows engineers to optimize the performance of numerical modelling.

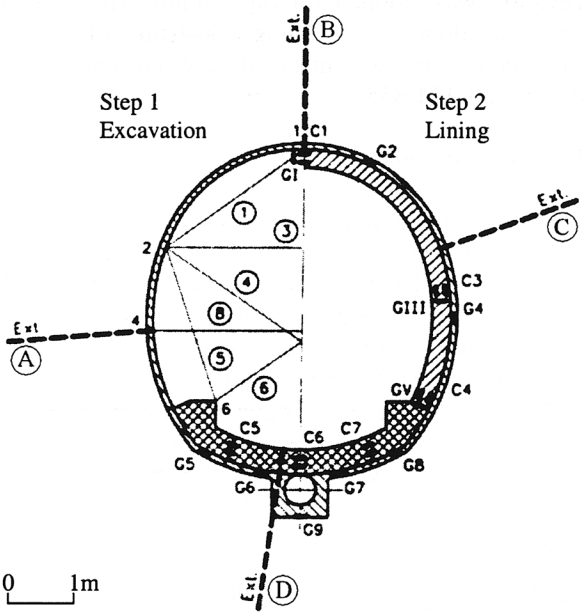

Fig. 4. Cross-section of the reconnaissance gallery and location of measurement apparatus, after Kohler (1995).

4. Comparison of experimental data with numerical results

4.1. Identification of Lemaitre model parameters on the base of creep tests

First of all, Lemaitre model parameters were determined on triaxial creep tests under confining pressure.

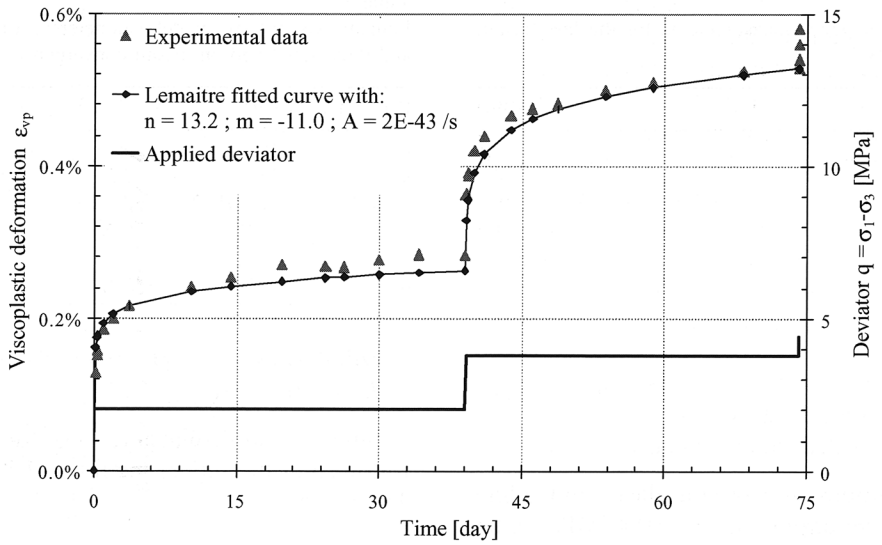

Fig. 5. Lemaitre's model fitted on triaxial creep tests from Kharchafi and Descoeudres (1995)—isotropic confining pressure equal to 0.6 MPa.

The samples tested by the École Polytechnique Fédérale de Lausanne (EPFL) were taken from the shaly facies in the motorway tunnel. The water content of these samples was quite high, near 8%, but the degree of saturation was less than 95%. Kharchafi and Descoeudres (1995) report the results of creep tests. They retain the test presented on Fig. 5. It is representative of the time-dependent behaviour of all the samples.

This test was performed in three steps:

- first the consolidation stage under 0.6 MPa of isotropic confining pressure maintained during 24 h;
- then an axial compression stage with a constant stress rate of 0.25 MPa·min^{-1} until 2 MPa deviatoric stress is reached;
- finally, two creep stages at, respectively, 2 and 3.8 MPa of deviatoric stress.

The complete test was performed over 75 days. The viscoplastic strains are related to transient creep as shown on Fig. 5. The two deviatoric stress levels for creep give the Lemaitre model parameters, which are reported in Table 3 in the next paragraph. Parameter β is a little bit lower than 1, according to the observations made by Kharchafi and Descoeudres (1995).

4.2. Identification of Lemaitre model parameters from in situ measurements

For modelling the time-dependent behaviour of Mont Terri gallery, it is first necessary to determine the elastic properties of the rock.

4.2.1. Gallery convergence interpretation

In order to obtain a modulus of elasticity which may be representative of decompression of the host rock, the analysis takes into account the interpretation of gallery convergence with the law proposed by Sulem et al. (1987a). Delayed displacements are due to face advancement effect and to time-dependent behaviour of the rock. Based on the separation of these two phenomena, Sulem et al. (1987b) proposed the following expression for gallery convergence, $C_{(x,t)}$, which is a function of both time, t, and distance from the working face, x. The total convergence is given by the following relation:

$$C_{(x,t)} = C_{\infty,0}\left(1-\left(\frac{X}{X+x}\right)^2\right)\left[1+m\left(1-\left(\frac{T}{T+t}\right)^n\right)\right] \quad (12)$$

where:

- X is the characteristic distance of the excavation; $4X$ corresponds to the distance over which the working face effect is felt,
- T is the characteristic time of the ground,
- $C_{\alpha,0}$ corresponds to the instantaneous convergence obtained in the case of an infinite rate of face advancement,
- the time, t, and the distance from the working face, x, are related to the speed of face advancement, v, by the expression: $x = v \cdot t$.

The final gallery convergence can also be expressed by the expression:

$$C_{\infty,\infty} = C_{\infty,0}[1+m] \quad (13)$$

The fitting of Sulem's law on gallery convergence measurements recorded at TM 852.5 (Fig. 7) gives the parameters listed in Table 2.

Thus, the in situ rock modulus, E_r, can be appraised by:

$$E_r = \frac{2(1+\nu_r)}{C_{\infty,0}} r \cdot \sigma_0 \quad (14)$$

Table 2
Parameters fitted on convergence measurements for the law formulated by Sulem et al. (1987b)

Parameter	Value
$C_{\infty,0}$ [mm]	5.5
X [m]	4
T [day]	16
α	1.2
n	1/3

with:

- σ_0: the initial stress, assumed to be isotropic
- ν_r: the Poisson's ratio, equal to 0.4
- r: the average excavated radius, equal to 2.5 m

Under these conditions, the in situ elastic unloading modulus is found to be approximately 8000 MPa. After identification of short-term behaviour properties, a parametric study was made on Lemaitre model constants, and especially on the viscosity factor, A. For the modelling of time-dependent gallery convergence, three sets of parameters were tested. They are reported in Table 3.

According to the Coulomb criterion, the short-term strength parameters given by Kohler (1995, 1997) are the following. They are not considered in the viscoplastic modelling:

- cohesion: $c=0.5$ to 2.6 MPa
- friction angle: $\varphi=28°$

The other assumptions for these computations are that:

- the lining is assumed to be in perfect contact with the ground,
- the behaviour of the concrete ring is elastic.

The characteristics of the concrete are the following:
- modulus of elasticity, $E_c=20\,000$ MPa
- Poisson's ratio, $\nu_c=0.2$

4.2.2. Axisymmetrical mesh

The modelling of the Mont Terri gallery convergence is performed for an axisymmetrical configuration for which no effects of stratification and thick layers of sandstone can be considered. This configuration induces assumptions of characteristic homogeneity and initial isotropic state of stress. The initial stress, σ_o, is equal to 6.35 MPa (250 m overburden). Fig. 6 shows the axisymmetrical numerical model.

The mesh built with the FLAC 2D numerical code complies with the following boundary conditions:

- longitudinal displacements are blocked on both opposite cross-sections,
- radial displacements are blocked along the symmetrical axis,

Table 3
Lemaitre viscoplastic model parameters: set EPFL fitted on creep tests and three sets fitted on in situ convergence measurements

Parameter	No. 1	No. 2	No. 3	EPFL
n	15.7	15.7	15.7	13.2
m	−13.3	−13.3	−13.3	−11.0
A [s^{-1}]	$\mathbf{3\times10^{-63}}$	$\mathbf{3\times10^{-62}}$	$\mathbf{3\times10^{-61}}$	2×10^{-43}
α	0.07	0.07	0.07	0.083
β	1.1	1.1	1.1	1.1
a	5×10^{-5}	6×10^{-5}	7×10^{-5}	3.4×10^{-4}

- radial stress is uniform on the external radius (i.e. $Ko=1.0$).

Stresses and displacements of the mesh are especially followed at the tunnel metres TM 852.5, TM 850.5 and TM 847.5.

4.2.3. Principle of time-dependent modelling

In order to constitute an axisymmetrical model, the successive construction stages of the gallery have been simplified. The working face advancement retained is shown on Fig. 7 and explained below:

- excavation until TM 853. No support installed; the 2-cm thick shotcrete of the Fig. 4 is not taken into account;
- working face stopped at TM 853 between 27th February and 13th March 1989; the installation of the invert on 2nd March is not taken into account;
- new stage of excavation, reaching TM 874.6 on 16th March; the blasting rounds increase from 1.20 m (four steps), to 2.25 m (two steps) and finally to 4.10 m (three steps);
- second stop of the excavation at TM 874.6 until 17th April;
- installation of the lining from TM 840 to TM 855 on 26th May.

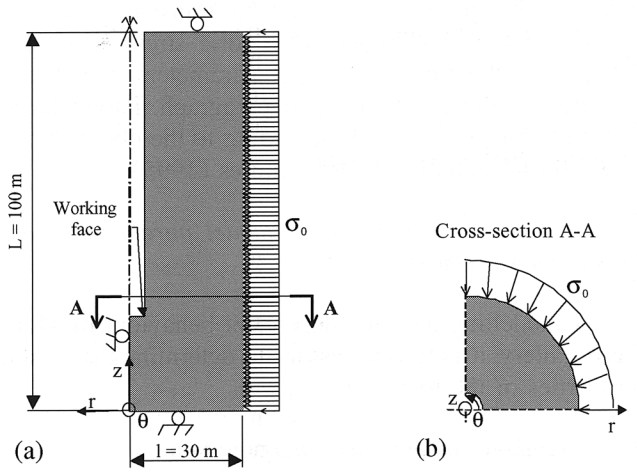

Fig. 6. Geometry of the model mesh: (a) longitudinal section, (b) typical cross-section.

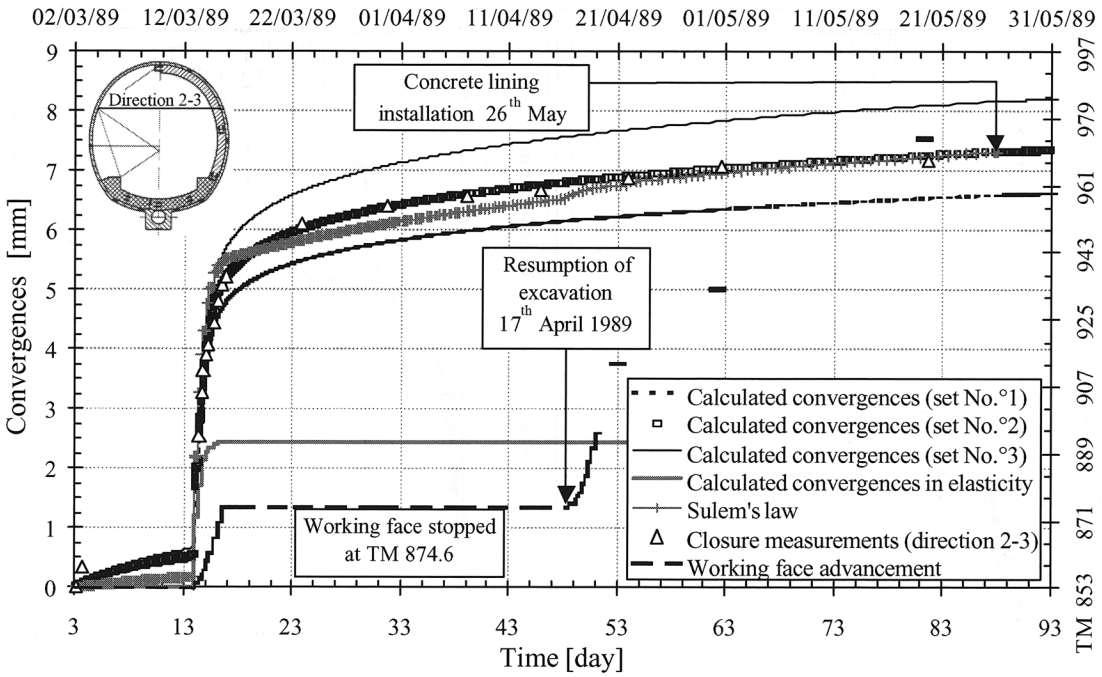

Fig. 7. Measured and computed convergences for different sets of parameters at TM 852.5. Comparison with the tendency given by Sulem's law—Origin of the measurements: 2nd March ($t=3$ days), after Kohler (1995, 1997).

After each excavation stage, gallery convergence and displacements within the rock are measured and recorded. The first measurements were taken on 2nd March at TM 852.5 and on 10th March at TM 850.5. Between March 3rd and 14th, the gallery face was stopped but, unfortunately, no measurements were recorded. After installation of the lining, the measurements of strains and stresses in the concrete and at the rock interface started. The measurements of gallery convergence were also stopped. Displacement measurements within the rock continued for a period of one year.

4.2.4. Results of the parametric study

The time stepping of the numerical modelling was defined on the basis of the results from Section 3.2.2. After each excavation stage the initial time-step is very small. It was fixed at 10^{-4} s and a geometrical time-step progression was chosen:

$$\Delta t_{n+1}^{[t+\Delta t_n]} = p^g \, \Delta t_n^{[t]} \tag{15}$$

where p^g is the parameter of the geometrical progression fixed at 1.0005.

The aim of the parametric study, which takes the three sets of parameters listed in Table 3 into account, is to fit the Lemaitre's viscoplastic model on convergence data at TM 852.5. Before interpreting convergence measurements, it is important to note that measurements do not cover displacements developed ahead of the working face, because the monitoring profile could not be equipped closer than 0.5 m from face.

Calculated convergences are two times the radial displacement at the gallery wall. The origin of measurements is set at 2nd March. Fig. 7 shows the results obtained for elastic and viscoplastic simulations. They are compared with recorded data and with the curve corresponding to Sulem's law (Kohler, 1995, 1997).

Set of parameters No. 2 leads to a very close match with recorded data for time-dependent evolution. Fig. 7 also shows that time-dependent convergences are quite important in comparison with results obtained in the elastic case. This is clear from the first excavation stages. In addition, the distance over which the effect of the working face is felt seems to be less than 20 m, because the resumption of excavation on 17th April did not induce an acceleration of gallery convergence. This is well reproduced by Lemaitre's model but is less obvious with Sulem's law.

4.3. Comparison of extensometric measurements with numerical results

Displacement measurements within the rock have been recorded in borehole extensometers installed in four directions distributed over the periphery of the gallery. They are 9 m long and are cemented to the tunnel wall. They give the displacements inside the rock, at 0.5 m, 1 m, 2 m and 4 m from the wall. Fig. 8a shows the measured and computed displacement (extensometer A) vs. time up until the installation of the lining. The Lemaitre model parameters are those of the

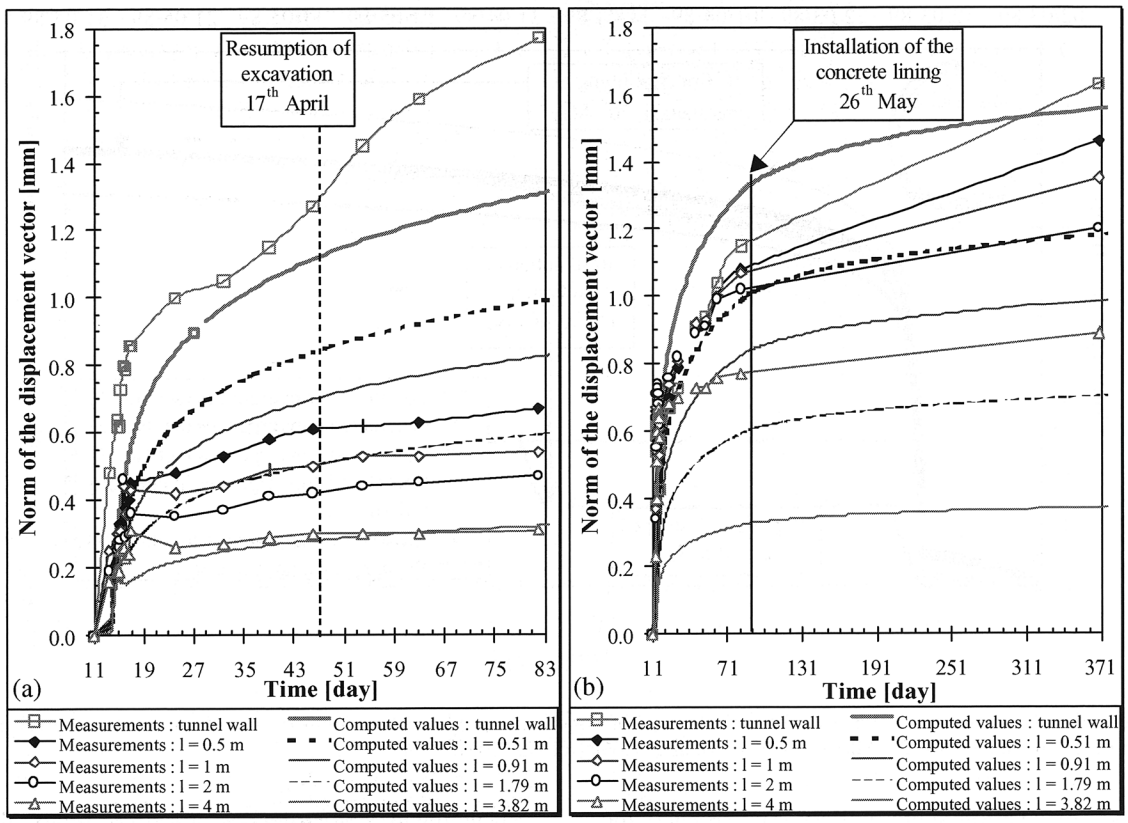

Fig. 8. Displacements and computed values vs. time within the rock in: (a) borehole extensometer A until lining installation, (b) borehole extensometer B over one year—Origin of the measurements: 10th March ($t=11$ days), after Kohler (1995, 1997).

fitted set No. 2. Fig. 8b gives the same results for extensometer B, but over a 1-year period. Both extensometers give the same order of magnitude for displacement data as the numerical modelling. The tendency evolution is quite similar with a small acceleration of in situ displacements after the resumption of excavation of the working face. The difference between displacement data and calculated values at the tunnel wall is certainly the consequence of damage, which is not taken into account in the modelling. In addition to that, Fig. 8b also shows a small decrease of computed displacement rates after the installation of the lining. This decrease is less obvious on instrumental data.

4.4. Extrapolation of long-term behaviour

The concrete ring was installed on 26th May, i.e. 3 months after the end of the first excavation stage. The strains and stresses of the lining were measured in the monitored profile at TM 847.5, which has been presented in Table 1. The origin of all measurements is 31st May. Fig. 9a,b show the higher normal stress and the contact pressure between the rock and the lining measured in the crown vs. time. On these figures have also been shown the results of numerical modelling with set No. 2. It appears clearly that computed stresses and contact pressures are greater than recorded data. This is probably the consequence of:

- temperature rise of the concrete for some hours after its installation;
- shrinkage of concrete during its curing time (a few months).

Although the monitoring of stress is prone to inaccuracy, measured and calculated stresses have much the same evolution over approximately 9 years.

It is very interesting to complete this analysis by comparing the measured strains in the lining with the numerical results. Fig. 10 gives the maximal orthoradial strains which were measured on the internal and external radii. These measurements are located in the crown. There is also good agreement in spite of concrete shrinkage.

4.5. Scale effects

As shown by Chin and Rogers (1987), the viscosity is found to be much lower in in situ measurements than in laboratory tests performed on small intact samples. Several orders of magnitude divide the different values of viscosity. This is clearly in agreement with the results of the parametric study made for the identification of

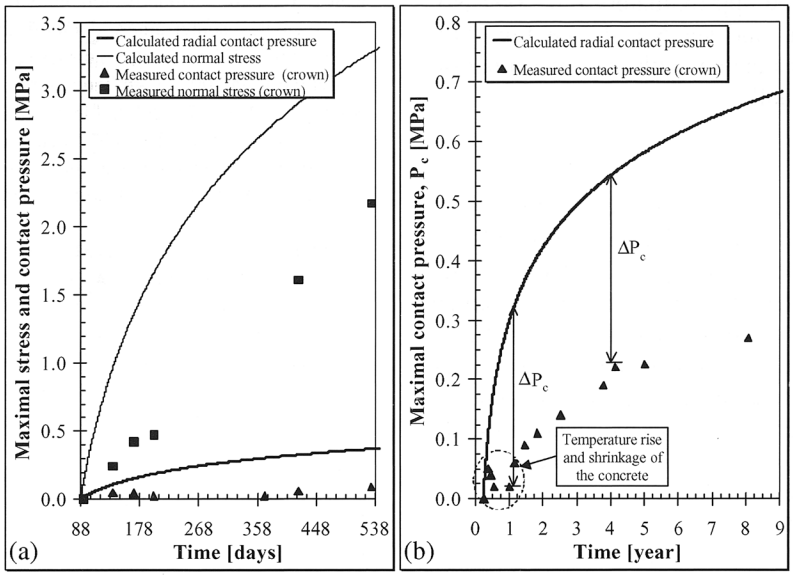

Fig. 9. Comparison of measured and computed stresses in the lining at TM 847.5 vs. time (a) over 15 months, (b) over 9 years—Origin of the measurements: 31st May ($t=93$ days), after Kohler (1995, 1997).

Lemaitre model parameters. The viscosity coefficient, A, is far more important in laboratory tests (set EPFL) than in situ measurements (set No. 2).

This scale effect is illustrated on Fig. 11, which represents a creep test simulation under 10 MPa of deviatoric stress for 20 days. The viscoplastic strains are reported after normalization to instantaneous elastic strains, by considering an average deformation modulus of 7000 MPa. Also shown is the curve corresponding to the set of parameters which was obtained for the sandy facies in the Opalinus clays (after Boidy, 2002).

The time-dependent behaviour of this formation is in the middle of the space demarcated by the other two curves corresponding to set EPFL and to set No. 2. This discrepancy is probably due to variations of water content between the different facies. The unique parameter, which presents very small variations, is the param-

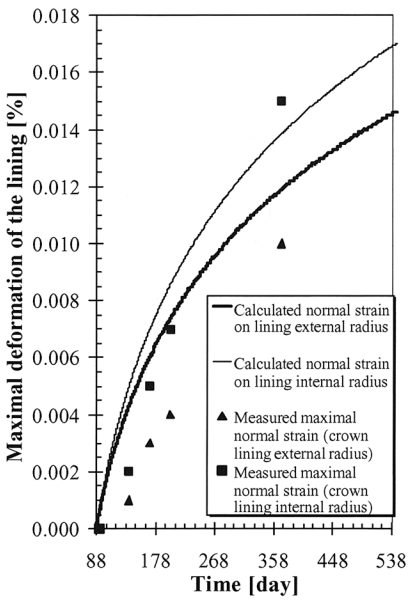

Fig. 10. Comparison of measured and computed strains of the lining at TM 847.5 vs. time over 15 months—Origin of the measurements: 31st May ($t=93$ days), after Kohler (1995, 1997).

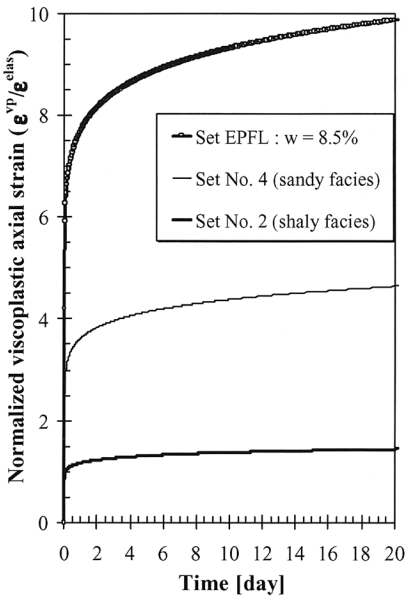

Fig. 11. Creep test simulation under 10 MPa deviatoric stress. Comparison of Lemaitre sets of parameters obtained in situ and in the laboratory—initial elastic strain fixed at $\varepsilon^{elas}=1.43\times10^{-3}$—set of parameters No. 4: $n=13.2$; $m=-11.0$; $A=2\times10^{-47}$ s^{-1}.

eter α. It was found to be approximately 0.07 (set No. 2) and 0.083 (set EPFL and set No. 4, see Fig. 11). Thus, the inaccuracy associated with its determination can be assumed to be small.

5. Conclusion

Numerical simulation of time-dependent behaviour of Mont Terri gallery shows that the Lemaitre viscoplastic model is relevant on an engineering scale. The parameters of this model were determined on the basis of creep tests and then compared to those identified from measurement data. The study shows some discrepancies between creep of small samples and time-dependent behaviour of monitored cross-sections excavated in shaly marls. Although there is a real scale effect on the viscosity parameter, the comparison reveals that the long-term tendency of time-dependent behaviour does not change much. Thus, the prediction capability of the model seems to be reliable over a period of approximately 10 years.

This research was performed in the spirit of the 'MODel Accompanying a Project' (MODAP), which was defined by Tardieu and Ozanam (1997). A MODAP model has to take the entire history of a project into account. As shown by the Mont Terri gallery study, the quality of time-dependent prediction can only get better via monitoring and observation. Given the complexity of the phenomena, the MODAP must be built up gradually, and can also be improved. Thus, observation and analysis of reality in light of the model are the main aspects for understanding the phenomena at play around underground structures.

Acknowledgments

The authors wish to thank Bonnard et Gardel S.A., Consulting Engineers, and the rock mechanics laboratory of the École Polytechnique Fédérale de Lausanne, Switzerland (EPFL), for having provided much useful information on the Mont Terri monitored gallery and on the time-dependent mechanical properties of Opalinus clays.

References

Billaux, D., Cundall, P.A., 1993. Simulation des géomatériaux par la méthode des éléments Lagrangiens. Revue Française de Géotechnique 63, 9–21.

Boidy, E., 2002. Modélisation numérique du comportement différé des cavités souterraines, doctoral thesis, Grenoble 1 University, 317 pp, [Online]. http://theses-en-ligne.ccsd.cnrs.fr/documents/archives0/00/00/15/46/index.html (Available: 21-8-2002).

Boidy, E., Pellet, F., 2000. Identification of mechanical parameters for modeling time-dependent behaviour of shales, ANDRA Workshop, Behaviour of deep argillaceous rocks: theory and experiment; Proc. Int. Workshop on Geomech., Paris, October 11–12, 2000, 13 p.

Boidy, E., Pellet, F., Boulon, M., 2001. Numerical modeling of deep tunnels including time-dependent behaviour. In: Desai et al. (Eds.), Computer Methods and Advances in Geomechanics, Balkema, Rotterdam, pp. 1663–1668.

Chin, H.-P., Rogers, J.D., 1987. Creep parameters of rocks on an engineering scale. Rock Mech. Rock Eng. 20, 137–146.

Cormeau, I., 1975. Numerical stability in quasi-static elasto/viscoplasticity. Int. J. Num. Methods Eng. 9, 109–127.

Detournay, C., 1998. A Simple Viscoplastic Model in FLAC, FLAC 2D Version 3.4 User Guidelines, Itasca, 7 pp.

Itasca, 2000. FLAC 2D Version 4.0, Online Manual.

Kharchafi, M., Descoeudres, F., 1995. Comportement différé des roches marneuses encaissant les tunnels, Colloque Mandanum Craies et Schistes GBMR, Brussels, 10 pp.

Kohler, P., 1997. Instrumentation and monitoring of a highway tunnel in swelling rock-case study: Mont Terri Tunnel, short course. Rock Mechanics Issues of Highly Stressed Rock for Deep Tunneling. EPFL, Lausanne 29 pp.

Kohler, P., 1995. Dimensionnement d'un tunnel basé sur l'auscultation de la galerie de reconnaissance. Journées d'étude de la SIA, Formation Continue Universitaire D0701, 57–67.

Lemaitre, J., Chaboche, J.-L., 1996. Mécanique des matériaux solides, Dunod, pp. 253–341.

Perzyna, P., 1966. Fundamental problems in viscoplasticity.Advances in Applied Mechanics, Vol. 9. Academic Press, New York, pp. 243–377.

Schaeren, G., Norbert, J., 1989. Tunnels du Mont Terri et du Mont Russelin. La traversée des 'roches à risques': marnes et marnes à anhydrite. Journées d'étude de la SIA, Formation Continue Universitaire D037, 19–24.

Sulem, J., Panet, M., Guenot, A., 1987. Closure analysis in deep tunnels, Abstract. Int. J. of Rock Mech. & Min. Sci. & Geomech. 24, 145–154.

Sulem, J., Panet, M., Guenot, A., 1987. An analytical solution for time-dependent displacements in a circular tunnel, Abstract. Int. J. of Rock Mech. & Min. Sci. & Geomech. 24, 155–164.

Tardieu, B., Ozanam, O., 1997. Le modèle accompagnateur de projet, conception et suivi des grandes infrastructures, Revue Française de Génie Civil, Vol. 1, special issue, 159 pp.

Thury, M., Bossart, P., 1999. Mont Terri Rock Laboratory, Results of the Hydrogeological, Geochemical and Geotechnical Experiments Performed in 1996 and 1997, Geological Reports 23, National Hydrological and Geological Service, Bern, 191 pp.

Computer Methods and Advances in Geomechanics, Desai et al. (eds) © 2001 Balkema, Rotterdam, ISBN 90 5809 183 X

Numerical modeling of deep tunnels including time-dependent behavior

E. Boidy
Coyne et Bellier, Consulting Engineers, France
F. Pellet & M. Boulon
Laboratory 3S, University Joseph Fourier, Grenoble, France

Time-dependent behavior of geomaterials, for instance creep, is of a great importance for the design of deep underground structures such as that for waste disposals. Indeed, in order to ensure safety for several centuries, a good prediction of deformations and damage is needed. For this purpose, a new visco-plastic law has been implemented in a two-dimensional explicit finite-difference program. For such a long time prediction, a special analysis of the time step is required to define an allowable discretisation of the time period of study. This approach is based on experience and theoretical analysis. All these considerations are very important for engineers because for such cases, no back experience is available to modify the models afterwards.

1 INTRODUCTION

The design of underground structures, excavated in rate sensitive materials, like shales, requires the determination of a time-dependent constitutive law able to predict the long term behavior. This study analyses the stability of the numerical solution. The approach connects the modelisation of relaxation test and deep circular tunnel in order to manage an allowable time step discretisation. The time-dependent constitutive law which has been implemented in the finite-difference program FLAC 3.4, corresponds to the model proposed by Lemaitre (1996).

2 LEMAITRE'S VISCO-PLASTIC POWER LAW

This law is based on the overstress visco-plasticity theory formulated by Perzyna's (1966) for rate-sensitive plastic materials and gives incremental constitutive equations for the transient creep phase. The basic assumption is that the strain rate can be decomposed into an instantaneous reversible (elastic) part and irreversible part :

$$\dot{\varepsilon}_{ij} = \dot{\varepsilon}^{e}_{ij} + \dot{\varepsilon}^{vp}_{ij} \tag{1}$$

where irreversible strain rate combines viscous and plastic effects and is given by the following relationship :

$$\dot{\varepsilon}^{vp}_{ij} = \gamma \langle \Phi(F) \rangle \frac{\partial G}{\partial \sigma_{ij}} \tag{2}$$

with the next notations :

γ = viscosity coefficient of the material; G = visco-plastic potential; F = static yield function; Φ = flow rule, controlled by the brackets defined by Macauly : $< \Phi(F) > = ½ [\Phi(F) + |\Phi(F)|]$, where $|\Phi(F)|$ is the classical absolute value.

The function F includes the overstress concept through the classical plastic function f and the strain hardening parameter κ, which depends only on the update accumulated visco-plastic strains (second invariant of the stress tensor). The assumption of isotropic hardening is also involved. This function F has the following form :

$$F(\sigma_{ij}, \varepsilon^{vp}_{kl}) = \frac{f(\sigma_{ij}, \varepsilon^{vp}_{kl})}{\kappa(\varepsilon_{vp})} - 1 \tag{3}$$

with:

$$\mathcal{E}_{vp} = \int_0^t \left(\frac{2}{3} \dot{\varepsilon}^{vp}_{ij} \otimes \dot{\varepsilon}^{vp}_{ij} \right)^{\frac{1}{2}} d\tau \tag{4}$$

Practically, all theses expressions are simplified by considering two other assumptions. First, the constitutive law can be defined as associated, for which f correspond to G and can be linked directly to the second invariant of the stress tensor q by assuming a Von Mises model :

$$f = G = q \tag{5}$$

This assumption takes into account that visco-plastic deformations develop without any volume changes, which has been verified experimentally for shales. On the other hand, in order to come out onto a practical and representative tool, power laws for

the flow rule Φ and for the strain hardening parameter κ have been introduced like that proposed by Lemaitre. The relationships are summed up below by the equations (6a) and (6b).

$$\Phi(F) = (F+1)^n \tag{6a}$$

$$\kappa(\varepsilon_{vp}) = (\varepsilon_{vp})^{-m/n} \tag{6b}$$

Thus, the irreversible strain rate which combines viscous and plastic effects is given by the following relation :

$$\dot{\varepsilon}_{ij}^{vp} = \frac{3}{2} A.q^{n-1}.(\varepsilon_{vp})^m \mathbf{s}_{ij} \tag{7}$$

where $\mathbf{s}_{ij}$ is the deviatoric part of the stress tensor; q is the second invariant of the stress tensor. This law needs the identification of the three following parameters :

- A, the viscosity coefficient of the material ($A > 0$),
- n, the stress exponent ($n \geq 1$),
- m^*, the strain hardening exponent ($m^* = -m/n \geq 0$) checking the following restriction : $m^* \leq 1-1/n$.

In order to match to relaxation tests, a strain rate threshold has been introduced into our model. This improvement induces a steady-state behavior as soon as the visco-plastic strain rate goes below a specific threshold detected in laboratory. This law has been developed and implemented in the two-dimensional explicit finite-difference program (FLAC 3.4) with the Fish language. The time stepping is also submitted to stability conditions, especially analyzed and discussed in the following paragraph.

3 STUDY OF CRITICAL TIME STEPPING

3.1 *Numerical explicit stability criterion*

For such a long term prediction, a special analysis of the time step is necessary in order to define the critical discretisation of the time period of study. As the system is required to be always in mechanical equilibrium, the time-dependent stress increment must not be large compared to the strain-dependent stress increment; otherwise, out-of-balance forces will rapidly become large, and inertial effects (which are theoretically absent) may affect the solution. Cormeau (1975) has given the expression of the critical time step for such an explicit mode of resolution in the general case. The stability limit, in the case of Lemaitre's visco-plastic law, becomes :

$$\Delta t_{crit} = \frac{4(1+\nu)}{3E\alpha\beta a.q^{\beta-1}.t^{\alpha-1}} \tag{8}$$

where E is the loading modulus; ν is the Poisson's ratio; α and β are exponents; a represents the viscosity parameter. This three constants are function of the previous parameters m, n and A.

They verify the three next relationships listed in equation (9).

$$\alpha = \frac{1}{1-m};\ \beta = \alpha.n = \frac{n}{1-m};\ a = \left(\frac{1}{\alpha}A\right)^{\alpha} \tag{9}$$

3.2 *Definition of an allowable time step*

For a good evaluation of the time step influence, a theoretical reference must be verified with numerical results. The relaxation test has been chosen (after a quasi-static loading) to avoid the perturbation related to initial conditions. Indeed, the sample represented by an axisymmetric mesh is just jammed between the plates of the frame after loading (at constant strain rate, about 10^{-6} s^{-1}, until 26 MPa of axial compression).

Long term mechanical characteristics for this relaxation modelisation are the following ones :

$$\begin{cases} E = 3620 \text{ MPa} \\ \nu = 0.3 \\ n = 9.25 \\ m = -1.77 \\ A = 10^{-25} \text{ (MPa, s}^{-1}\text{)} \end{cases}$$

with a minimal threshold of steady creep motion state close to 10^{-9} s^{-1}.

Various initial time steps have been tested in order to study how rapidly the initial perturbation is calmed. For this calculation, an allowable time step value would be around 0.1 s. Close to 10 s, it engenders a very net imbalance (Fig. 1a), but not necessarily irreversible at long-term because depending also on the geometrical time progression, defined by the expression :

$$\Delta t_{n+1}[t + \Delta t_n(t)] = p\Delta t_n(t) \tag{10}$$

where p is the geometrical pace of this progression.

According to Cormeau, the initial critical time step would be around 30 s and also 300 times superior to the allowable value. The safety factor (S.F.) to apply to the critical time step of Cormeau can also be determined. This approach joins Detournay's observations (1998), who recommends practically to take a safety factor between 100 to 1000 on the estimation of the critical time step proposed by Itasca.

At long term, it is the geometrical pace p which is major on the stability of the solution (Fig. 1b). Indeed, regardless of the value of the initial time step, there is stability of the computation, with some reversible oscillations around the analytical solution for a pace equal to p = 1.001. On the other hand, for a not adapted geometrical pace, it is possible to be in conditions of instability or at least with an inadmissible precision of the solution. But even if there is a substantial margin of error for a time period tested, the whole stability is not necessarily challenged in the long term.

The two following figures display successively the influence of the initial time step t_o (Fig. 1a) and the geometrical pace p (Fig. 1b).

Through these different numerical responses, it becomes possible to give the safety factor on the cri-tical time step defined by Cormeau to comply with a good accuracy. This factor reaches 500 to 1000.

In this case, the allowable solution kept here (with t_o = 0.1 s and p = 1.001) induces a factor around 750, as presented on the Figures 2a, b.

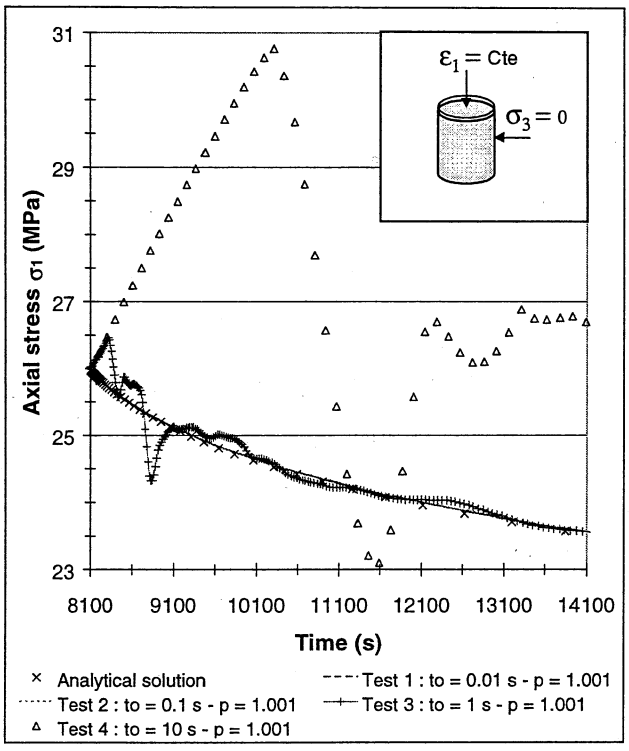

Figure 1a. Influence of the initial time step (t_o) on the numerical stability. Zoom at short term.

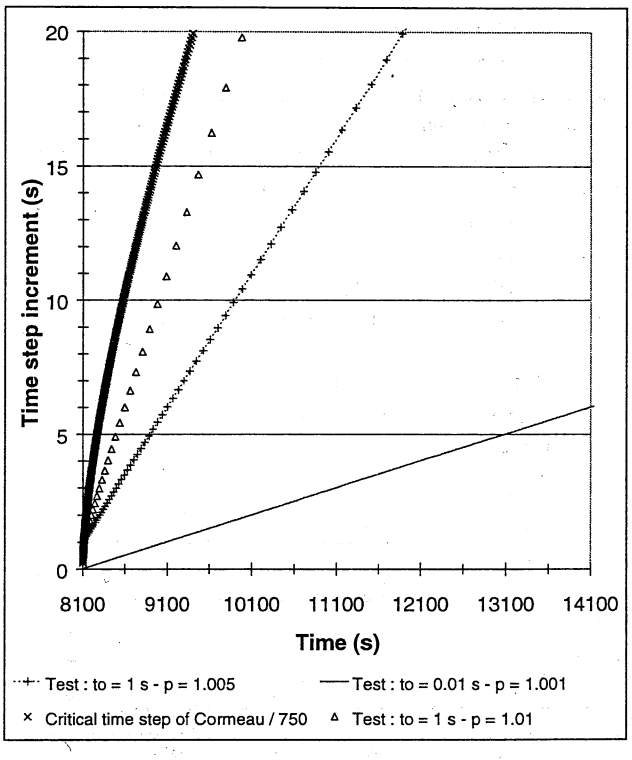

Figure 2a. Definition of an allowable zone of time progression. Zoom at the beginning of the relaxation.

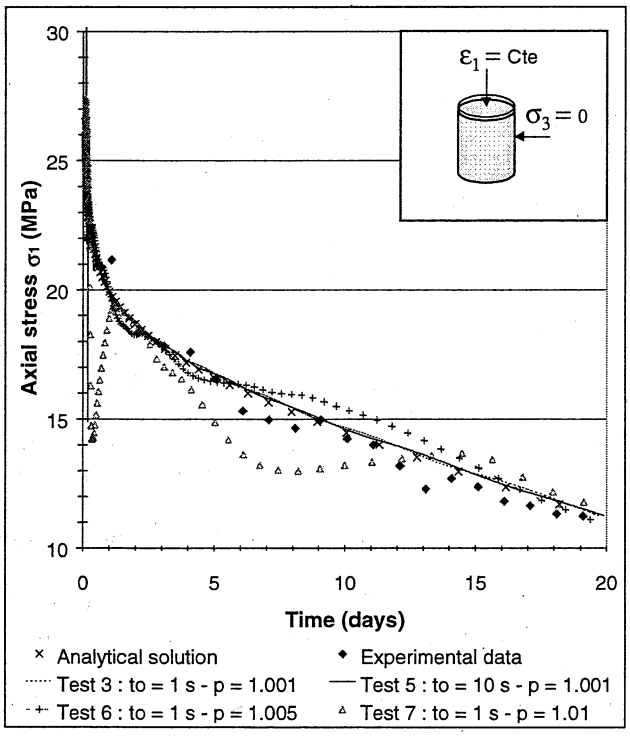

Figure 1b. Influence of the initial time step on the numerical stability. Long term behavior compared to experimental data on shales.

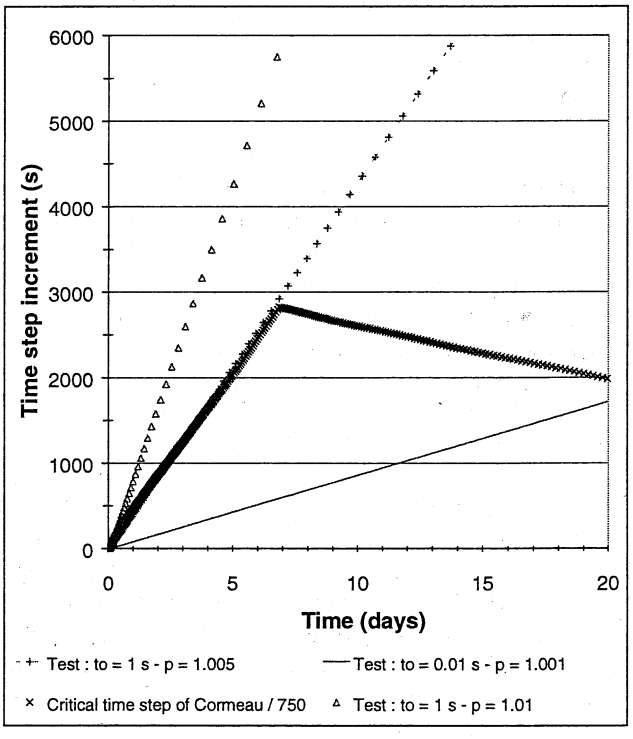

Figure 2b. Long term progression of the allowable time step.

3.3 *Implications for deep circular tunneling*

Practically, for an engineering calculation, it is advisable to choose an allowable time stepping in order to satisfy requirements of precision and computation time. Indeed, the design of a complex underground structure like deep excavations or tunnels can require till 48 hours of calculation time for behavior extrapolation over data for several centuries. Also, precision has a cost and a good management of time stepping allows engineers to optimize the performance of numeral modelisation. Thus, an adequate safety factor on time stepping is very interesting.

To illustrate this aim, we propose to display the behavior of the rock face around a deep circular tunnel. Assumption of stress isotropy is made here with $\sigma_v = \sigma_h = 12$ MPa, and time-dependent phenomena start after a decompression related to the excavation and supposed elastic. Figure 3 shows the 2D-mesh and the initial conditions of the model.

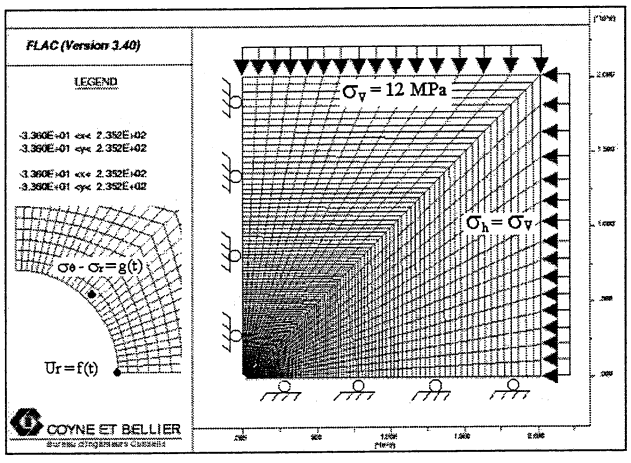

Figure 3. Flac zone geometry and model boundary conditions

The Lemaitre's law uses the same time-dependent proprieties like for the modelisation of the relaxation test but any strain rate threshold hasn't been introduced. The aim of this calculation was to qualify time-dependent displacements and relaxation of the rock face all around the tunnel over a period of time of two centuries.

Thus, the initial time step has been fixed to 10 s in order to reach a good accuracy as soon as one month. Then, the important result demonstrated by Nguyen-Minh and Pouya (1992), concerning the existence of a stationary stress state, can be used for a long time prediction such as this. Considering a safety factor S.F = 750 on the critical time step defined by Cormeau (and justified before on relaxation test modelisation), it is also possible to succeed rapidly in the determination of an allowable geometrical progress for a specific duration of the envisaged study (here 200 years). By introducing this safety factor, the geometric pace p was found around 1.0005.

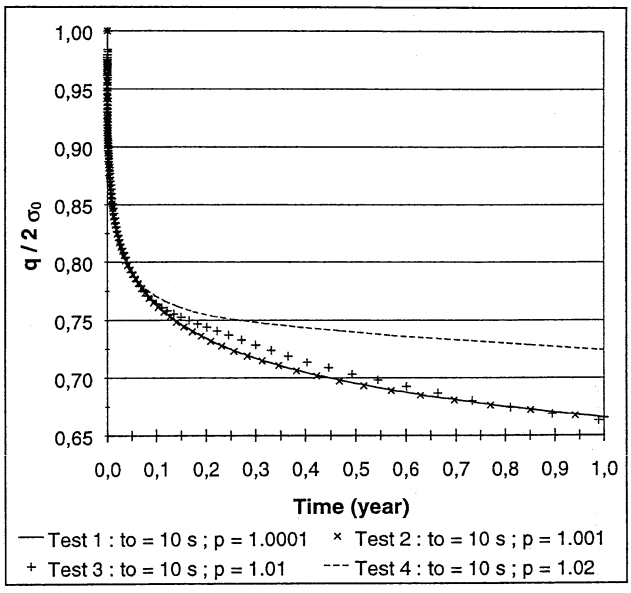

Figure 4a. Deviator variations at the tunnel wall (one year)

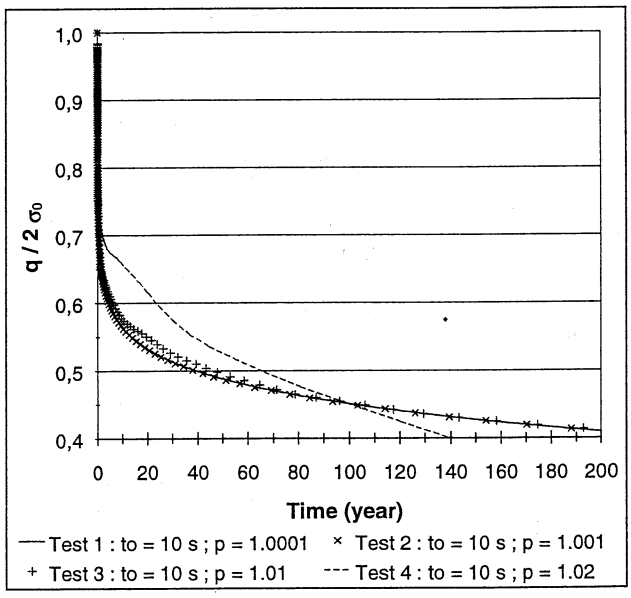

Figure 4b. Deviator variations at the tunnel wall (200 years)

For this example, the reduced deviator near the tunnel wall, $q / 2\sigma_0 = (\sigma_\theta - \sigma_r)_t / (\sigma_\theta - \sigma_r)_{to}$ (Figs 4a, b), and the radial strain at the tunnel wall, U_r / r (Figs 5a, b) can also be indexed dependent on time. The different numerical tests show that the solution is stable with an acceptable precision as soon as the pace p is lower than 1.001. For a pace p higher, there is a real risk of overvaluation of the galleries' closure.

This simple approach is a real investment for engineers because this classic modelisation requires ¼ hour CPU time for a pace p = 1.02, but it rises to more than 2 days with p = 1.0001. Thus with an allowable geometrical progress (p = 1.001), the saving of CPU time is important, about 90% in relation to the smaller progression tested. It is also possible to optimize this computation in 4 hours.

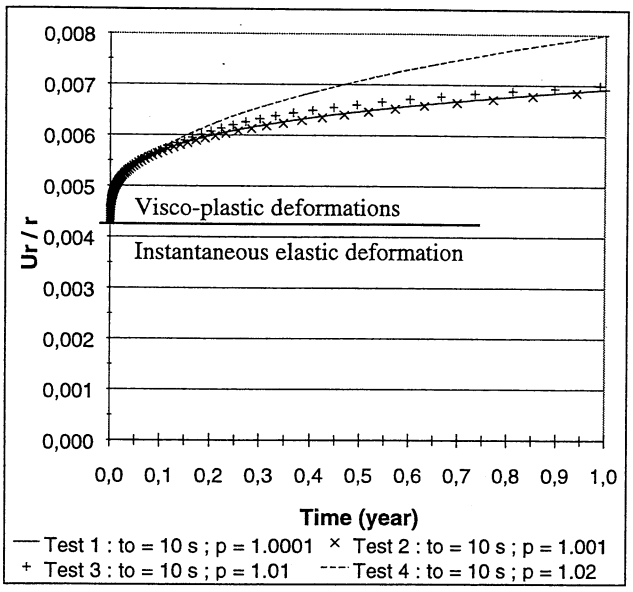

Figure 5a. Gallery's closure variations (one years)

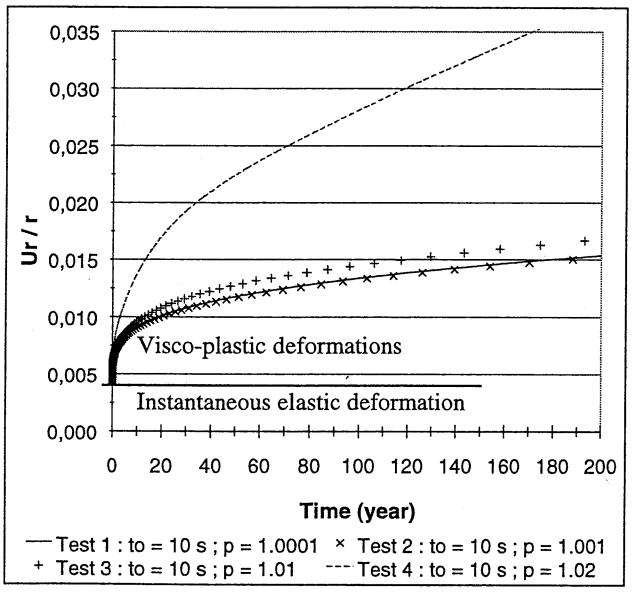

Figure 5b. Gallery's closure variations (200 years)

3.4 *Analysis of unbalanced forces*

In order to challenge the previous results, unbalanced forces variations have been followed during creep, and reported on Figure 7.

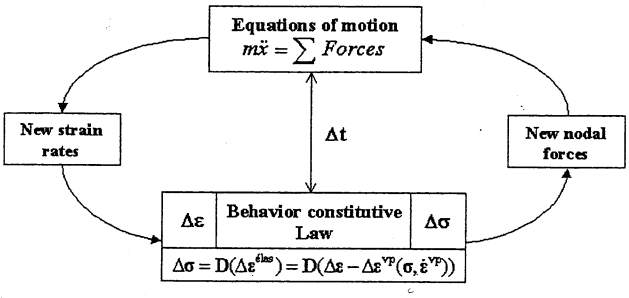

Figure 6. Explicit scheme of resolution during a time step Δt

The equations of motion, which govern the explicit resolution scheme (Fig. 6), must be damped to provide quasi-static solutions (without inertial effects). An alternative damping algorithm is available in FLAC for this kind of situations like creep in which a significant uniform motion drives the model. This damping is called "combined damping" and is more efficient at removing kinetic energy compared to local damping for this special case. The scheme of the algorithm consists of a damping force composed of equal contributions from expressions based on velocity and on unbalanced forces rate. Combined damping scheme was used for the modelisation of relaxation tests where time-dependent motion appeared generalized in the whole model. But for the application on the circular tunnel, local or combined damping induce the same imbalance inasmuch as the damping force is enough strong which is always verified for an allowable time progress.

It is also very interesting to analyze the variations of the maximum unbalanced force during creep and this for each previous geometrical progress. The Figure 6 shows clearly that a pace p = 1.001 is allowable but a pace p = 1.01 becomes critical for this problem.

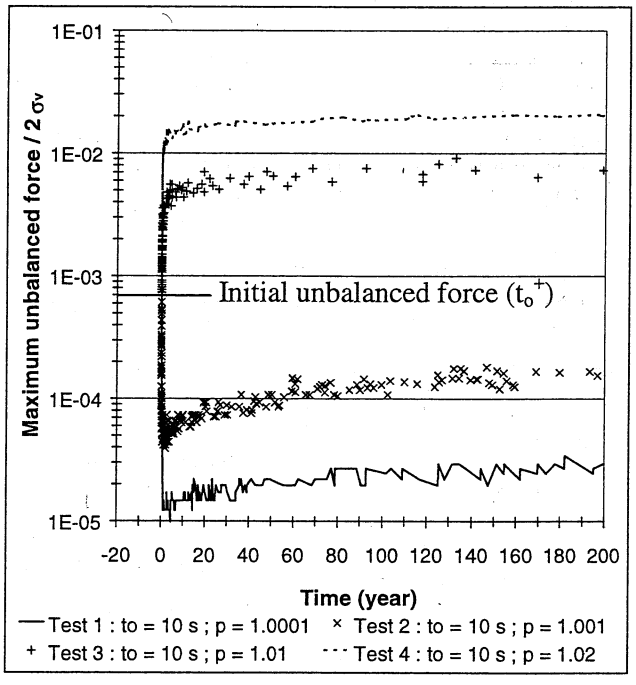

Figure 7. Variations of maximal unbalanced force during creep

4 CONCLUSIONS

The study of time-dependent behavior of geomaterials, requires a specific analyze of the time stepping and a justification for the allowable time step progression chosen. In this way, a special attention has been directed towards the Lemaitre's visco-plastic law which has been implemented in the explicit fi-

nite-difference program FLAC 3.4. The theoretical critical time step defined by Cormeau can also constitute a reference on which a safety factor around 100 to 1000 must be apply in order to define an allowable time stepping. For the example presented in this article, unbalanced forces variations during creep confirm that stability was insured in this case.

In the future, we expect to define more precisely some numerical general rules, which could be followed for such time-dependent modelisation. On the other hand, we hope to validate this approach with in-situ measurements to extrapolate this behavior for a very long period of time (several centuries).

5 REFERENCES

Berest, P. 1989. Viscoplasticity in Rock Mechanics. In *Geomaterials. Constitutive equations and modelling*: 239-262. Elsevier Applied Science.

Boidy, E. & Pellet, F. 2000 [to be published]. Identification of mechanical parameters for modeling time-dependent behavior of shales. In ANDRA Workshop, *Behavior of deep argillaceous rocks: Theory and experiment; Proc. Int. Workshop on Geomech., Paris, 11-12 October 2000.*

Billaux, D. & Cundall, P. 1993. Modeling of Geomaterials using the Lagrangian Element method [In French]. *Revue Francaise de Geotechnique* 63: 9-21.

Cormeau, I. 1975. Numerical stability in quasi-static elasto-viscoplasticity. *Int. J. num. Meth. Engng.* 9(1): 109-127.

Detournay, C. 1998. A simple Visco-plastic model in FLAC. *FLAC version 3.4 Users' Manuel Optional Features.* Itasca.

Laigle, F. & Kolmayer, P. 1998. Numerical modelisation for long term behaviour of underground structures [In French]. *Revue Francaise de Geotechnique* 85: 65-78.

Lemaitre, J. & Chaboche, J.L. 1996. *Mecanique des materiaux solides*: Dunod.

Nawrocki, P.A. & Mroz, Z. 1999. A constitutive model for rock accounting for viscosity and yield stress degradation. *Computers and Geotechnics* 25(4): 247-280.

Nguyen-Minh, D. & Pouya, A. 1992. A framework for the analysis of underground excavations in viscoplastic medium, on account of a steady stress state [In French]. *Revue Française de Geotechnique* 59: 5-14.

Malan, D.F. 1999. Time-dependent Behaviour of deep level tabular excavations in hard rock. *Rock Mech. Rock Engng.* 32: 123-155.

Perzyna, P. 1966. Fundamental Problems in Viscoplasticity. In Academic Press (ed.), *Advances in Applied Mechanics* 9: 243-377.

L'implication de la géotechnique dans le développement des infrastructures en Afrique; Sahli, Bahi & Khalid (ed.)©, ISBN 9954-8407-0-2

Modélisation numérique du comportement à court et long terme d'un tunnel ferroviaire

Zokimila N.P., Flavigny E. & Pellet F.
Laboratoire 3S – Sols, Solides Structures, Grenoble, France

Billon A.
S.N.C.F, Direction de l'Ingénierie, Paris, France

RESUME : Certains tunnels ferroviaires sont anciens et présentent des désordres nécessitant des travaux de reprise ou de confortement. Ces désordres peuvent être dus à un effet du temps. Cet article présente une modélisation d'un tunnel ferroviaire construit il y a plus de 150 ans. Une modélisation doit reprendre l'historique de l'ouvrage pour en suivre son évolution temporelle. La modélisation présentée ci dessous comporte alors les différentes phases suivantes : initialisation des contraintes, creusement et on peut ensuite décrire l'évolution en utilisant une loi de comportement viscoplastique. L'évolution des déplacements sur plus de 200 ans peut alors être simulée.

1 INTRODUCTION

1.1 Objet de l'étude

La présente recherche s'inscrit dans le cadre d'un projet d'étude de la stabilité mécanique des tunnels ferroviaires de la SNCF. Elle comprend des essais mécaniques, de laboratoire, faits sur des échantillons de matériaux prélevés sur les sites en questions, et surtout à la simulation numérique du comportement mécanique des ouvrages, à court et à long terme.
Cet article consiste, essentiellement, en la présentation et analyses des résultats de la modélisation numérique du comportement du tunnel de La Nerthe. L'accent est mis sur les effets des travaux de construction (creusement, soutènement) et d'entretien (renforcement par boulonnage) ainsi que l'effet différé (fluage ou mécanisme de rupture de la roche) sur la stabilité de l'ouvrage.

1.2 Descriptions géométrique et matérielle de l'ouvrage et de la roche hôte

Le tunnel ferroviaire de la Nerthe, construit vers 1843 à 1848, se situe sur la ligne de chemin de fer de Paris à Marseille. Elle traverse la chaîne de l'étoile de Marseille, avec une couverture maximale de 180 m. La figure 1 , (Nasri, V. et al. 1998) montre une coupe transversale théorique précisant la géométrie et les dimensions de l'ouvrage. Sa section, à rayons multiples, dégage une hauteur sous clé d'environ 7,50 m par rapport au plan de roulement et une largeur de 8 m. Le revêtement est constitué de moellons, aux piédroits, et de briques, à la voûte, d'une épaisseur moyenne d'environ 0,70 m. Le radier, en moellons, a une épaisseur d'environ 0,35 mètres.

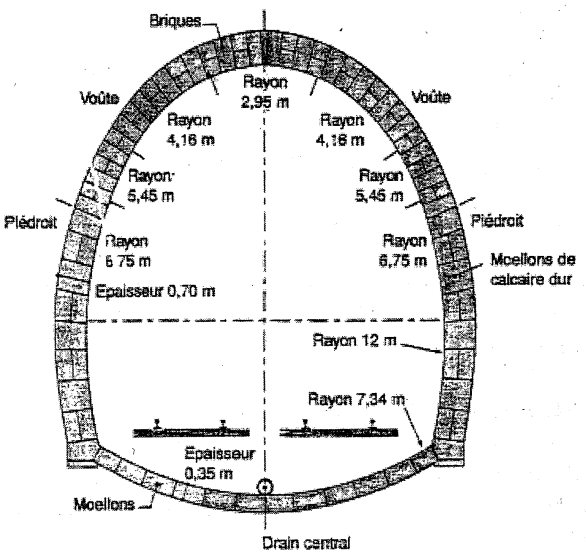

Figure 1. Section type du tunnel de la Nerthe

Les formations géologiques, traversées par ce tunnel, appartiennent à l'étage Bégudien du crétacé supérieur qui sont constituées d'alternances marno-calcaires avec intercalations de niveaux conglomératiques et ligniteux (Nasri, V. et al. 1998).

Des essais de fracturation, réalisés en 1994 (Nasri, V. et al. 1998) ont permis de mettre en évidence

des contraintes résiduelles d'origine tectonique orientation vraisemblable N-S.
Les tableaux suivants indiquent respectivement les propriétés mécaniques du massif autour du tunnel de la Nerthe et celles des matériaux constituants le revêtement.

Tableau 1. Propriétés mécaniques du massif autour du tunnel de la Nerthe (Nasri, V. et al. 1998)

Paramètre	Valeur
Module de Young, E [MPa]	3175
Coefficient de poisson, ν	0,3
Poids volumique, γ [kN/m^3]	23
Cohésion, C [kPa]	250
Angle de frottement interne, φ [°]	30
Résistance à la compression R_c [kPa]	900

Tableau 2. Propriétés mécaniques des matériaux constituants le revêtement (Nasri, V. et al. 1998)

Paramètre	Briques	Moellons
Module de Young, E [MPa]	6 200	25 000
Coefficient de poisson, ν	0,2	0,2
Résistance à la compression, R_c[MPa]	10	20
Résistance à la traction, R_t [MPa]	1	2
Poids volumique, γ [kN/m^3]	22	25

2 MODELISATION NUMERIQUE

L'objectif de la modélisation est d'étudier la stabilité élastoplastique et viscoplastique de l'ouvrage. Dans cette optique, la simulation du comportement du massif est effectuée, dans un premier temps, avec une loi de comportement élastoplastique parfait, utilisant le critère de Mohr-Coulomb. Les résultats obtenus pourraient être comparés à ceux obtenus par Nasri V. et al (1998). Ensuite, on distinguera une modélisation prémisse du comportement à long terme de l'ouvrage, réalisée avec la loi de comportement viscoplastique de Lemaitre. Le calcul est effectué avec le code FLAC 4.0, logiciel bidimensionnel développé par la société Itasca.
Caractéristiques de FLAC
FLAC est un programme de différences finies explicite. Il permet de tenir compte des phases de construction des objets à modéliser et de lois de comportement, élastoplastique et viscoplastique. Avec le langage FISH du code, l'utilisateur peut aussi implémenter sa propre loi de comportement.
En faisant une comparaison entre FLAC et la méthode des éléments finis, on peut noter que les deux méthodes transforment un ensemble ou système d'équations en équations de matrice pour chaque élément, reliant des forces aux nœuds aux déplacements aux nœuds. Bien que des équations de FLAC soient dérivées de la méthode des différences finies, les matrices résultantes d'élément, pour un matériau élastique, sont identiques à ceux de la méthode d'éléments finis.

Cependant, les principaux points qui différencient FLAC de la méthode classique des éléments finis sont l'utilisation d'un schéma par discrétisation mixte (Marti et Cundall 1982). Les équations dynamiques du mouvement sont employées pour résoudre le système. Contrairement aux méthodes implicites plus habituelles, FLAC met en ouvre la méthode explicite.
Ces différences présentent des avantages, mais il y a deux inconvénients : la simulation de comportements linéaires est plus lente avec FLAC qu'avec des programmes d'éléments finis et le temps de résolution est déterminé par le rapport entre la plus longue période réelle et la plus courte période réelle dans le système modélisé. En effet, un pas de temps unité uniforme $\Delta t = 1$ est adopté pour le système entier.

2.1 Présentations des différentes phases de la modélisation

Pour la modélisation en élastoplasticité parfaite de type Mohr-Coulomb, la simulation du comportement mécanique du tunnel de la Nerthe comprend trois phases successives, correspondantes aux étapes de sa construction en partant de l'état naturel du massif. En viscoplasticité, elle comprend une phase supplémentaire simulant le comportement différé de l'ouvrage. Les différentes étapes sont développées ci-dessous.

2.1.1 Etablissement des contraintes initiales

Cette phase consiste à établir l'état de contraintes initiales en appliquant les conditions aux limites et initiales. Cette étape permet d'établir l'équilibre du modèle, avant toutes altérations (excavation, etc.).

2.1.1.1 Dimensionnement et discrétisation du modèle

Pour des raisons de symétrie de la géométrie et du chargement, on modélise seulement la moitié du modèle et pour qu'il ne prenne pas de proportion importante.

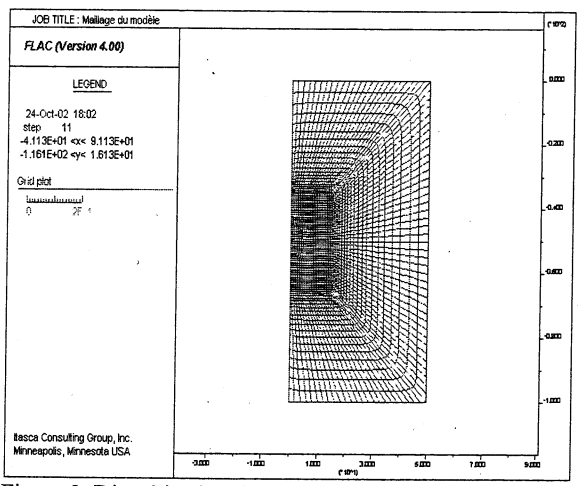

Figure 2. Discrétisation du modèle réalisés avec FLAC

Afin de réduire l'effet de bord (influence des conditions aux limites), on a adopté une distance égale à 5 fois la largeur du tunnel dans la direction horizontale et 6 fois sa hauteur sous le radier ainsi qu'au-dessus de la voûte. Un maillage progressif est appliqué au modèle (plus fin à proximité du tunnel) pour une meilleure précision des résultats et pour ne pas trop pénaliser le temps de calcul. La figure 2 montre la discrétisation du modèle.

2.1.1.2 Conditions aux limites

La contrainte verticale correspondant à la moyenne des poids de terre couvrant le tunnel (agissante au-dessus du modèle) est :

$$\sigma_v = \gamma.h = 2{,}99 \text{ MPa}$$

où : γ est le poids volumique de la roche
h est la hauteur moyenne de couverture
Le coefficient d'anisotropie des contraintes, en section transversale, K_0 a été fixé égal à 2. Ce qui permet de déduire la valeur de la contrainte horizontale à appliquer au modèle :

$$\sigma_h = K_0.\sigma_v = 5{,}98 \text{ MPa}.$$

L'effet de la pesanteur est négligé puisque sa variation suivant la hauteur du modèle est faible par rapport à la valeur des contraintes agissantes dans son volume.
Le déplacement horizontal, *u*, suivant l'axe de symétrie (*u=0* pour *x=0*) est bloqué ainsi que le déplacement vertical, *v*, à la base du modèle (*v=0* pour *y=0*) (figure 3).
La loi de comportement du massif (marnes) est élastoplastique parfait, de type Mohr-Coulomb (Nasri, V. et al. 1998).
L'équilibre est établi après un certain nombre de pas de temps de calcul (11 pas de temps).
La figures 4 montre l'établissement des contraintes initiales.

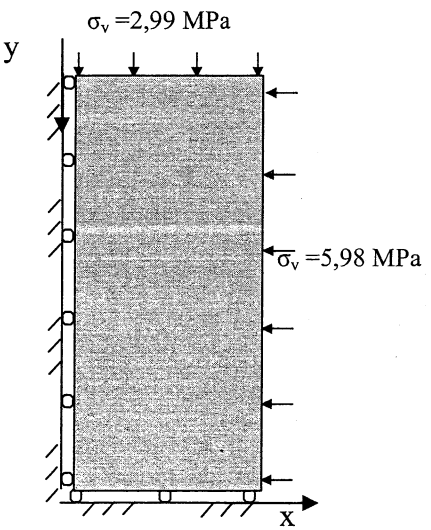

Figure 3. Etablissement des contraintes initiales - Champ des contraintes verticales en Pa

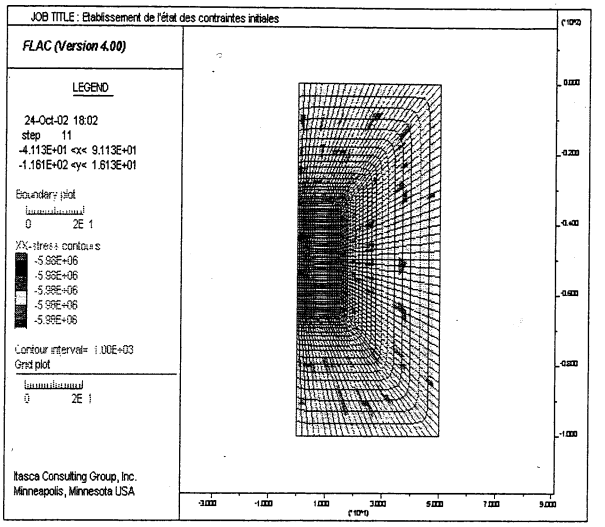

Figure 4 : Etablissement des contraintes initiales - Champ des contraintes horizontales en Pa

Une fois que les contraintes initiales sont établies,, on peut procéder aux étapes suivantes.

2.1.2 Excavation du tunnel et pose du revêtement

La méthode creusement utilisée, lors de la construction de ce tunnel, était *la méthode anglaise*, (Nasri, V. et al. 1998). Cette méthode suppose, à priori, que la pose du revêtement s'effectue pendant le creusement du tunnel. Cependant, l'effet du revêtement sur le comportement du massif rocheux va être mis en évidence en comparant les réponses du modèle, quand l'excavation s'effectue sans ou avec revêtement.

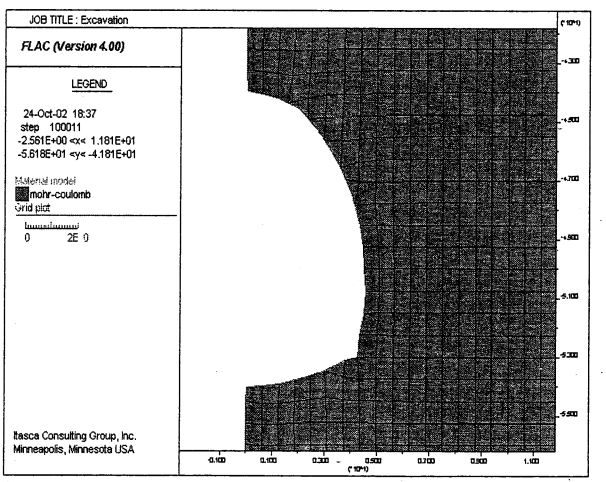

Figure 5. Géométrie du tunnel excavé

2.1.2.1 Excavation du tunnel

Cette phase est le creusement du tunnel. Dans ce calcul, cette opération est effectuée instantanément

quitte à négliger le taux de confinement dont l'implication dans la simulation ne permet forcement pas d'aboutir à de résultat idéal, surtout dans le cas où chargement serait anisotrope. L'excavation du tunnel est réalisée en annulant les éléments concernés. Les déplacements dans le modèle sont initialisés à zéro puisqu'on ne tient compte que les déplacements du à l'excavation du tunnel. La figure 5 montre la géométrie du tunnel, après excavation. Le comportement du massif est élastoplastique parfait avec le critère de Mohr-Coulomb.

2.1.2.2 Pose du revêtement

Le revêtement, constitué de moellons aux piédroits, de briques en voûte et de moellons en radier (figure 1), est modélisé par un ensemble d'éléments de poutre bidimensionnels standards à trois degrés de liberté (deux déplacements u, v et une rotation M) à chaque extrémité (*extrémités a* et *b*) (figure 6).

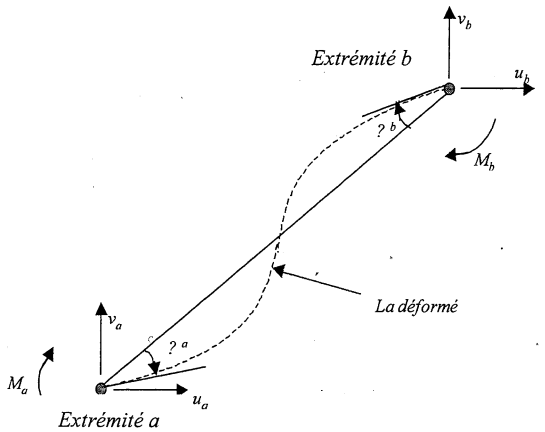

Figure 6. Elément constitutif du revêtement

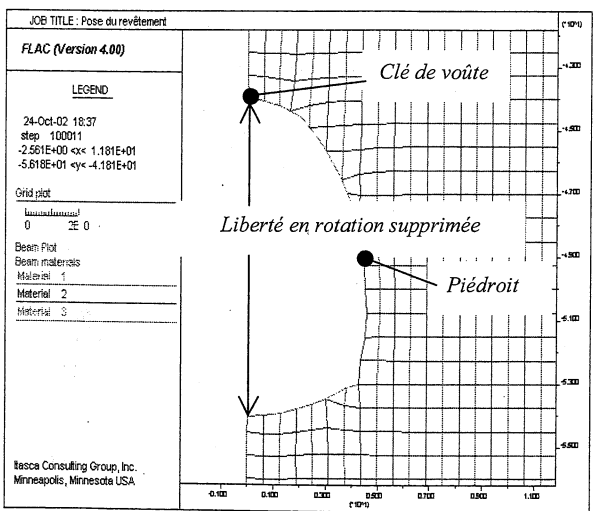

Figure 7. Les différents matériaux constituants le revêtement

Son comportement est élastique linéaire, sans limite de rupture. Les propriétés d'un revêtement sont son module d'élasticité E, son épaisseur e et son moment d'inertie I.
En déformation plane, une rectification doit être effectuée sur le module de Young de chaque élément constitutif du revêtement, en le multipliant par un facteur $1/(1-\nu^2)$.
Pour de raison de symétrie, les rotations des deux extrémités du revêtement sont bloquées.
La figure 7 montre les différents matériaux constituants le revêtement (moellons en radier et piédroit et briques en voûte).

Les figures 8 et 9 comparent les déviateurs des contraintes ($q=\sigma_3-\sigma_1$), respectivement à la clé de voûte et au piédroit, avec et sans revêtements, en fonction du nombre de pas de temps de calcul.

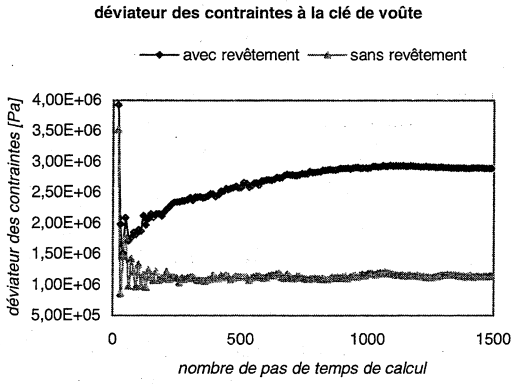

Figure 8. Comparaison des déviateurs à la clé de voûte, sans et avec revêtement, en fonction du nombre de pas de temps de calcul

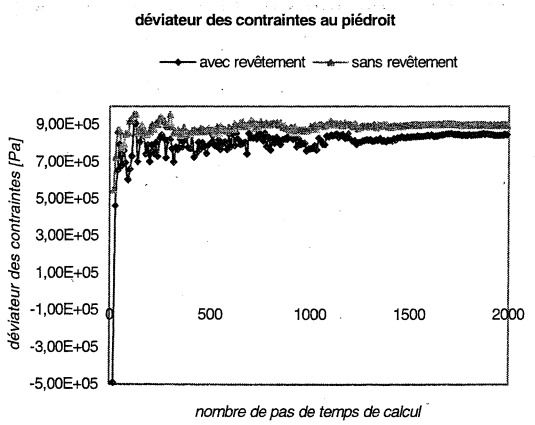

Figure 9. Comparaison des déviateurs au piédroit, sans et avec revêtement, en fonction du nombre de pas de temps de calcul

La figure 8 laisse apparaître que les déviateurs ont diminué à l'issue de l'excavation du tunnel à proximité de la clé de voûte tandis qu'ils enregistrent une petite augmentation à proximité du piédroit. Cette diminution est très prononcée sans revêtement du fait du relâchement de contrainte à l'issue de l'exca-

vation. Cependant, on constate que la pose du revêtement à permis de stabiliser la baisse du déviateur en confinant la paroi du tunnel.

La figure 10 présente le champ des contraintes déviatoires à proximité de l'ouvrage et le diagramme des forces axiales dans le revêtement. Elle montre qu'en confinant la paroi du tunnel, le revêtement encaisse des charges. Le diagramme des efforts axiaux dans le revêtement indique qu'ils sont plus élevées au radier.

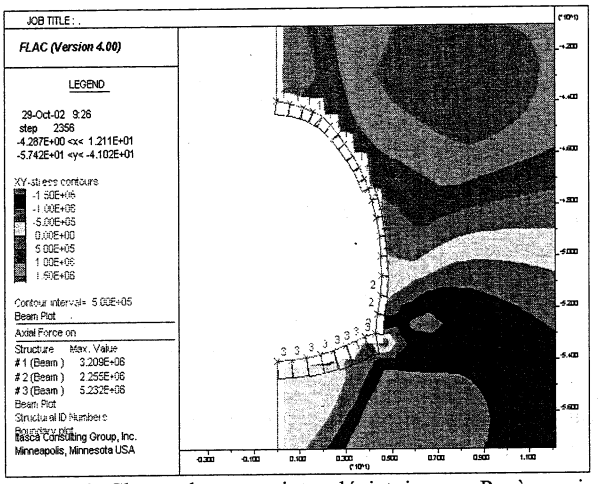

Figure 10. Champ des contraintes déviatoires, en Pa, à proximité de l'ouvrage et le diagramme des forces axiales dans le revêtement, en N

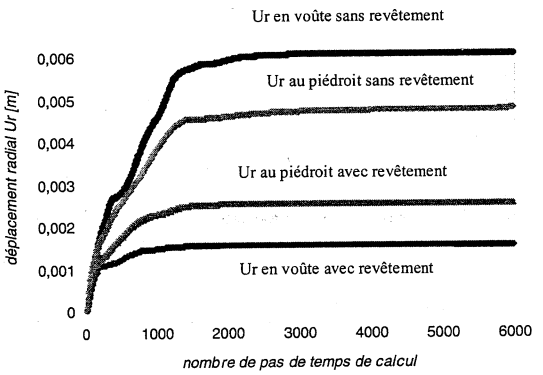

Figure 11. Comparaison des déplacements radiaux en voûte et au piédroit, sans et avec revêtement, en fonction du nombre de pas de temps de calcul

Une comparaison des déplacements radiaux en voûte et au piédroit, avec et sans revêtement, est donnée par la figure 11. Elle laisse apparaître que la convergence est maximale sans revêtement et minimale avec revêtement en voûte. L'action du revêtement se traduit par l'amortissement considérable de la convergence du tunnel, allant jusqu'à 70 % de la convergence totale (sans revêtement).

2.1.3 Comportement à long terme du massif

La loi de comportement viscoplastique sans endommagement de Lemaitre est retenue pour la simulation du comportement différé du massif autour du tunnel.

2.1.3.1 Loi viscoplastique de Lemaitre

Cette loi est basée sur la théorie de la viscoplasticité formulée par Perzyna (1966) pour des matériaux sensibles à la vitesse de déformation. Elle s'appuie sur deux hypothèses fondamentales.
La première estime que la déformation totale peut être décomposée en une partie élastique réversible est une partie viscoplastique irréversible. Ce principe s'exprime par l'équation suivante :

$$\varepsilon_{ij} = \varepsilon_{ij}^{e} + \varepsilon_{ij}^{vp} \qquad (1)$$

où ε_{ij} constitue le terme des déformations totales, ε_{ij}^{e} la partie élastique réversible et ε_{ij}^{vp} la partie viscoplastique irréversible.

La seconde hypothèse suppose que les déformations viscoplastiques se développent à volume constant.
La loi de Lemaitre propose une expression du tenseur des vitesses de déformation viscoplastique sous la forme:

$$\dot{\varepsilon}^{vp} = A\left(\frac{q-\sigma_s}{F_o}\right)^{n}(\varepsilon_{vp})^{m} \qquad (2)$$

où $\dot{\varepsilon}^{vp}$ est la vitesse de déformation viscoplastique, A le coefficient de viscosité du matériau, q le second invariant du tenseur des contraintes, σ_s le seuil de contrainte de déclenchement du comportement différé, n l'exposant de la contrainte ($n \geq 1$), F_o correspond à l'unité de contrainte de référence, fixée à 1 MPa (Boidy E., 2002) et m*, l'exposant de l'écrouissage du matériau $m^{*} = -m/n \geq 0$.

Cette loi a donc été implémentée dans le code FLAC en utilisant le langage FISH (Boidy E., 2002.

2.1.3.2 Critère de stabilité et gestion du pas de temps de calcul

Dans les méthodes explicites, une analyse particulière sur le choix du pas de temps est indispensable pour les calculs en fluage afin d'assurer la stabilité et la précision des calculs. Dans le cas de la loi de Lemaitre, Cormeau (1975) a donné l'expression du seuil de stabilité en fonction des paramètres d'élasticité et des paramètres de la loi viscoplastique de Lemaitre :

$$\Delta t_{crit} = \frac{2}{3\beta} \frac{2(1+\nu) q^{1-\beta}}{E \alpha a t^{\alpha-1}} \quad (3)$$

avec $\alpha = \frac{1}{1-m}$, $\beta = \frac{n}{1-m}$, $a = \left(\frac{A}{\alpha}\right)^{\alpha}$, E le module de Young et ν le coefficient de poisson.

Toutefois, l'application directe de ce seuil ne garantit pas une précision satisfaisante. Afin d'obtenir une solution avec une bonne précision, un pas de temps adéquat doit être choisi. Cela implique l'application d'un facteur d'une valeur de 100 à 1000 (Detournay 1998).
En dehors de la détermination délicate du pas de temps initial, il faut aussi tenir compte de la progression géométrique des incréments définie par :

$$\Delta t_{n+1}[t + \Delta t_n(t)] = p \Delta t_n(t) \quad (4)$$

où p est un multiplicateur de progression.

2.1.3.3 Simulation numérique

Les propriétés mécaniques du massif autour du tunnel de la Nerthe n'ont pas été encore calées avec la loi de Lemaitre. On a alors utiliser un autre type de matériau dont on dispose les paramètres issus de calage avec la loi de Lemaitre (Sahli, M. et al. 2001). Ces paramètres sont présentés dans les tableaux 3 et 4.

Tableau 3. Propriétés mécaniques estimées [4]

Paramètre	Valeur
Module de Young, *E [MPa]*	6000
Coefficient de poisson, *v*	0,44
Poids volumique, *γ [kN/m³]*	22

Tableau 4. Paramètres de Lemaitre [4]

Paramètre	Valeur
A [s]	2,39E-51
n	14,8
m	-9

A part les propriétés précitées, deux paramètres supplémentaires sont nécessaires pour la simulation avec la loi de Lemaitre. Il s'agit des paramètres numériques : le temps de calcul de la vitesse de déformation initiale, ***ttini*** (qui doit être inférieur au pas de temps critique (ou minimal), ***min***, déterminée par la relation (3) et le seuil de déclenchement du fluage, ***seuil*** calculé par la formule (5)

$$seuil = \sigma_{vo}(K_o - 1)/3 \quad (5)$$

Dans ce calcul les valeurs attribuées à ces deux paramètres sont les suivantes :

- *ttini* = 1^{E}-21
- *seuil* = 0,996 MPa

Un choix judicieux des paramètres numériques tels que le pas de temps initial, ***min*** et maximal, ***max*** ainsi que du paramètre de progression spatiale, ***lmul*** est nécessaire pour assurer la stabilité et la bonne convergence du calcul.
Dans ce calcul ses valeurs sont les suivantes :

- *min* = 1^{E}-20
- *lmul* = *1.002*
- *max* = 10^{9}

Le calcul est piloté par les fonctions FISH nommés ***Fluage*** et ***Increment*** qui assurent conjugalement la prise des histoires (déformations, contraintes…), la commande et le contrôle automatique du calcul de fluage de 200 ans. Elles déclenchent aussi l'arrêt automatique du calcul une fois que cette durée serait écoulée.
La figure 12 présente l'évolution des déviateurs en voûte et en piédroit, pendant 200 ans après son excavation, avec et sans revêtement. On constate en voûte qu'avec ou sans revêtement, les déviateurs diminuent avant de stabiliser définitivement. Tandis qu'ils sont faibles et stable en piédroit.

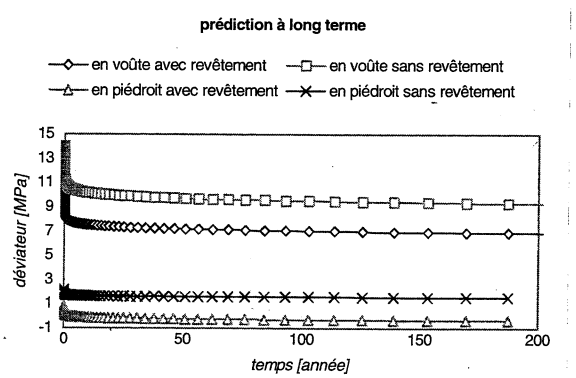

Figure 12. Evolution des déviateurs en voûte et en piédroit sur une période de 200 ans, avec et sans revêtement

La comparaison des déplacements radiaux qui se sont développés en voûte et au piédroit, sur une période de 200 ans après l'excavation du tunnel, avec et sans revêtement est donnée par la figure 13. La convergence de la paroi du tunnel est maximale en piédroit sans revêtement et est minimale en voûte avec revêtement.

Les figures 14 et 15 montrent respectivement le diagramme des déformations axiales qui se sont développées dans le revêtement et le champ des déformations plastiques à proximité de la paroi du tunnel sur une période de 200 ans.

Dans le revêtement, la valeur des déformations est maximale en voûte (notamment la zone comprise entre la clé de voûte et le rein). Ce qui est en cohérence avec le champ des déformations à proximité de la paroi du tunnel. Celui-ci laisse apparaître des déformations importantes en voûte, à l'extrados du revêtement.

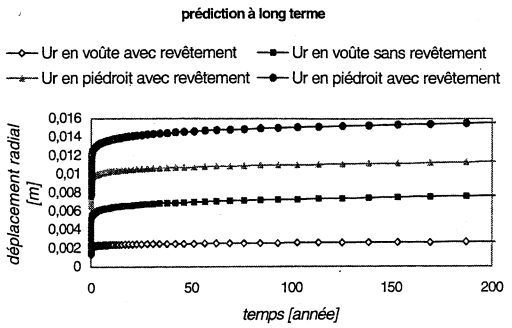

Figure 13. Comparaison des déplacements radiaux en voûte et au piédroit, avec et sans revêtement, sur une période de 200 ans

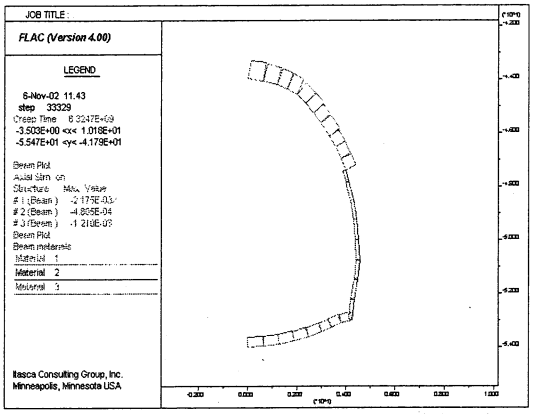

Figure 14. Diagramme des déformations axiales du revêtement sur une période de 200 ans

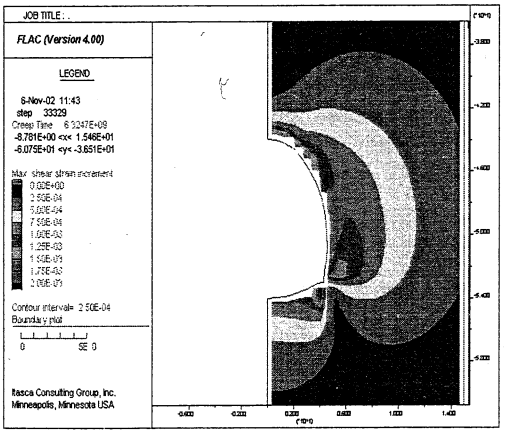

Figure 15. Champ des déformations plastiques à proximité du tunnel sur une période de 200 ans

3 CONCLUSION

Dans l'ensemble, les calculs laissent apparaître des résultats satisfaisants, notamment pour la modélisation élastoplastique parfaite (Mohr-Coulomb). Ils sont en accord avec les résultats des calculs faits par Nasri V. et al.. La modélisation du comportement à long terme, présentée dans ce rapport, est une illustration de l'utilisation de la loi de comportement viscoplastique de Lemaitre. En effet, les calculs ont été faits avec des propriétés estimées, à défauts d'essais de laboratoires faits sur échantillons représentatifs du site. Néanmoins, cette étude montre la portée de la méthode de calcul utilisée et de la loi de Lemaitre pour l'étude de la stabilité mécanique à court et surtout à long terme des tunnels ferroviaires afin de pouvoir prédire rationnellement leur comportement

REFERENCES

Cormeau, I. 1975. Numerical stability in quasi-static elasto-viscoplasticity. *Int. J. num. Meth Engng.*, 9(1) : 109-127.

Detournay, C. 1998. A simple Visco-plastic model in FLAC. *FLAC version 3.4 Users' Manuel Optional Features, Itasca.*

Nasri, V., Ramondec, P. & Magnan J.P. 1998. Conception d'un système de renforcement pour le tunnel ferroviaire de la Nerthe. *Bulletin des laboratoires des Ponts et Chaussées,* PP 53-59.

Boidy, E.& Pellet, F. 2000. Identification of mechanical parameters for modeling time-dependent behavior of shales. In ANDRA Workshop, Behavior of deep argillaceous rocks : Theory and experiment ; *Proc. Int. Workshop on Geomech., Paris, 11-12 October.*

Pellet, F., Sahli, M., Boidy, E. & Boulon, M. 2000. Modeling of time-dependent behaviour of sandstone for deep underground openings. *Proc. int. Conf. On Engng. And Tech. Science (ICETS), Beijing, China.vol 1, pp 431-438*

Boidy, E., Pellet, F. & Boulon, M. 2001. Numerical modelling of deep tunnels including time-dependent behaviour. *Proc. 10th Int. Conf. IACMAG, Tucson, USA, January.*pp 1663-1668

Sahli, M., Pellet, F., Boidy, E. & Fabre, G. 2001. Modeling of vicous behaviour of rocks for deep tunnels. *Proc. Of ISRM Regional Symposium, Eurock, Espoo, Finland, pp541-546.*

Boidy, E. 2002. Modélisation numérique du comportement différé des cavités souterraines, *Thèse de Doctorat UJF, Grenoble 1.*

Numerical Models in Geomechanics – NUMOG VIII, Pande & Pietruszczak (eds)
© 2002 Swets & Zeitlinger, Lisse, ISBN 90 5809 359 X

Numerical modelling of underground structures taking into account the viscoplastic behaviour and rock damage

F. Pellet, A. Hajdu, M. Boulon
Laboratory 3S, University Joseph Fourier, Grenoble, France

F. Besnus & F. Deleruyelle
Institute for Protection and Nuclear Safety, Paris, France

ABSTRACT: This paper deals with the prediction of the time-dependent development of the Excavation Damage Zone (EDZ) surrounding tunnels and galleries. Prediction of the damaged zone is of the greatest importance especially for the design of underground storage facilities for which a change in porosity may lead to leakage through the rock mass. The constitutive model used for the time-dependent behaviour of rock was first proposed by Lemaitre. It is a viscoplastic model, which includes the damage effect for simulating tertiary creep (i.e., failure). In order to validate the choice of this model, finite element computations were performed. In the last part of this study, the constitutive model is applied to vertical shafts to estimate the extent of the EDZ. Computation sequences include simulation of the behaviour over a period of 500 years. This point is of particular interest for the design of underground nuclear waste disposal facilities.

1 INTRODUCTION

It is well known that excavation of underground openings leads to a stress redistribution, which may provoke the development of a plastified zone surrounding the cavity. For common civil engineering works, numerical computations are conducted to verify that rock strength is not exceeded so far as stability of openings is concerned. However, in the case of caverns built for storing gas, oil or nuclear waste, this verification is not sufficient. It is required to check that pre-peak damage of material do not produce a substantial increase of porosity. In such a case undesirable leakage through the host rock would produce contamination.

It is also well known that development of strains is, for the most part, time-dependent. In such conditions, the prediction of the expansion of the excavation damage zone (EDZ) becomes more difficult. In the following sections, an attempt to simulate this process is explained. Numerical simulation of time-dependent behaviour requires the use of viscoplastic constitutive equations for computing both creep deformation and stress relaxation.

It is commonly assumed that creep occurs without volumetric strain. All these considerations lead us to use a viscoplastic constitutive model known as the Lemaitre model with a damage function.

2 BASIC HYPOTHESES

The geomechanical context allows some preliminary simplifications within continuum mechanics:

Hypothesis 1; the following developments are limited to the case of small transformations (total strain is the linearized symmetric part of the displacement gradient).

Hypothesis 2; the evolutions of the continuum are supposed to take place under isothermal conditions (at constant temperature in a closed system, without heat exchange). Since its derivative is zero, the temperature will not appear as a thermodynamic variable in the expression of the specific free energy and the dissipation potential will be purely intrinsic without a thermal component.

Hypothesis 3; the strain partition hypothesis is retained. The total strain is divided into elastic (reversible) and inelastic (irreversible) parts. In order to model the long-term behaviour of openings, the viscosity of the rock has to be taken into account. Supposing that the viscous phenomenon is manifest simultaneously with plastification, in other words it is supposed to be absent in the elastic domain, the irreversible strain component corresponds to the coupled viscoplastic effects and the hypothesis of partition can be written:

$$\dot{\boldsymbol{\varepsilon}} = \dot{\boldsymbol{\varepsilon}}^{\mathrm{e}} + \dot{\boldsymbol{\varepsilon}}^{\mathrm{vp}} \qquad (1)$$

where $\dot{\boldsymbol{\varepsilon}}$ = total strain rate, $\dot{\boldsymbol{\varepsilon}}^{\mathbf{e}}$ = elastic strain rate, and $\dot{\boldsymbol{\varepsilon}}^{\mathbf{vp}}$ = viscoplastic strain rate. Boldface denotes tensors, i.e., $\mathbf{a} = a_{ij}$.

Hypothesis 4; the elastic behaviour is linearly isotropic and the elastic strain rate is defined classically as:

$$\dot{\boldsymbol{\varepsilon}}^{\mathbf{e}} = \frac{1+\nu}{E}\dot{\boldsymbol{\sigma}} - \frac{\nu}{E}tr(\dot{\boldsymbol{\sigma}})\mathbf{I} \tag{2}$$

where E = Young's modulus, ν = Poisson's ratio, $\dot{\boldsymbol{\sigma}}$ = stress rate tensor and $\mathbf{I}$ = the second-order identity tensor.

3 THERMODYNAMIC APPROACH

The local state method assumes that a certain number of variables defines completely the thermodynamic state of the material at a given point and time. For a viscoplastic solid these are the two observable variables: the total strain $\boldsymbol{\varepsilon}$ and the temperature T, and the two internal variables: the viscoplastic strain $\boldsymbol{\varepsilon}^{\mathbf{vp}}$ and a strain hardening parameter. The classical Lemaitre model considers isotropic hardening, thus the hardening variable is a scalar. Usually, because of its simplicity and for its correct representation in the case where the initial stress orientation does not change considerably within the mass (i.e., no cyclic load), the cumulated deviatoric viscoplastic strain, p, is used. By definition p can be obtained as:

$$\dot{v}^{vp} = tr(\dot{\boldsymbol{\varepsilon}}^{\mathbf{vp}}) \tag{3a}$$

$$\dot{\mathbf{e}}^{\mathbf{vp}} = \dot{\boldsymbol{\varepsilon}}^{\mathbf{vp}} - (\dot{v}^{vp}/3)\mathbf{I} \tag{3b}$$

$$\dot{e}^{vp} = \sqrt{\frac{2}{3}}\,\|\dot{\mathbf{e}}^{\mathbf{vp}}\| \tag{3c}$$

$$p = \int_0^t \dot{e}^{vp}\,dt \tag{3d}$$

where the notation $\|a\|$ denotes the Euclidean norm of the second-order tensor defined as: $\|a\| = (a_{ij}a_{ij})^{1/2}$ (Einstein's summation convention is retained). The specific free energy function depends on the thermodynamic state variables. Considering an isothermal system (Hypothesis 2) and applying the strain partition postulate (Hypothesis 3):

$$\boldsymbol{\varepsilon}^{\mathbf{e}} = \boldsymbol{\varepsilon} - \boldsymbol{\varepsilon}^{\mathbf{vp}} \tag{4}$$

the free energy function can simply be written as:

$$\Psi = \Psi(\boldsymbol{\varepsilon}^{\mathbf{e}}, p) \tag{5}$$

The associated thermodynamic variables are the stress tensor $\boldsymbol{\sigma}$ and the thermodynamic force R that is related to hardening:

$$\sigma = \rho\frac{\partial\Psi}{\partial\boldsymbol{\varepsilon}^{\mathbf{e}}} \tag{6}$$

$$R = \rho\frac{\partial\Psi}{\partial p} \tag{7}$$

where ρ is the density of the material.

The formulation of the constitutive law deduces directly from the dissipation potential function $\Omega = \Omega(\boldsymbol{\sigma}, R, p)$. Among the numerous possible expressions for the dissipation function the Lemaitre model works with a power function of the form:

$$\Omega = \frac{K}{N+1}\left\langle\frac{J_2(\boldsymbol{\sigma}) - k - h'(p)}{K}\right\rangle^{N+1} p^{\gamma} \tag{8}$$

where K, N and γ are material parameters, $h'(p)$ is the hardening modulus and k the elastic threshold. Macauly's brackets designate the value $\langle a\rangle = (a+|a|)/2$ and $J_2(\boldsymbol{\sigma})$ refers to the second stress invariant. In practice the second stress invariant is frequently replaced by Von Mises' equivalent stress, defined as:

$$\sigma_{eq} = \sqrt{3J_2(\boldsymbol{\sigma})} = \sqrt{\frac{3}{2}}\|\mathbf{s}\| \tag{9}$$

where $\mathbf{s}$ is the deviatoric part of the stress tensor. Note that it is possible to make the hardening modulus correspond to the thermodynamic force since hardening is supposed to be positive and of an isotropic nature. Thus:

$$h'(p) = \rho\frac{\partial\Psi}{\partial p} = R \tag{10}$$

Moreover the elastic-viscoplastic strain partition permits the omission of the elastic threshold in the viscoplastic domain, which involves $k = 0$, and means that creep occurs at any stress level on top of the respective elastic deformation. Thus the potential dissipation function takes the form:

$$\Omega = \frac{K}{N+1}\left\langle\frac{\sigma_{eq} - R}{K}\right\rangle^{N+1} p^{\gamma} \tag{11}$$

In the derivative:

$$\dot{p} = -\frac{\partial\Omega}{\partial R} = \left\langle\frac{\sigma_{eq}}{K}\right\rangle^{N} p^{\gamma} \tag{12}$$

the exponent γ must be negative as the flow rate always decreases during hardening. Considering $\gamma = -N/M$, the evolution equation for p becomes:

$$\dot{p} = \left(\frac{\sigma_{eq}}{Kp^{1/M}}\right)^{N} \tag{13}$$

Finally the viscoplastic strain rate can be written as:

$$\dot{\boldsymbol{\varepsilon}}^{\mathbf{vp}} = \dot{p}\frac{\partial\sigma_{eq}}{\partial\boldsymbol{\sigma}} = \frac{3}{2}\left(\frac{\sigma_{eq}}{Kp^{1/M}}\right)^{N}\frac{\mathbf{s}}{\sigma_{eq}} \tag{14}$$

4 DAMAGE COUPLED TO VISCOPLASTICITY

The appearance of damage and its progressive development may lead to rupture of the rock. In order to take into account this phenomenon, the notion of effective stress is applied:

$$\tilde{\sigma} = \frac{\sigma}{1 - D_n} \tag{15}$$

which means that stress is calculated on the section that effectively resists those forces. Index n refers to the section's directional normal. Considering an initially isotropic material and supposing that the damaging process does not induce anisotropy, the damage variable D_n can be represented by a scalar with the following properties:

$$D_n = D \quad \forall \vec{n} \in [0, 1] \tag{16}$$

D varies from 0 to 1. $D = 0$ corresponds to the intact state and $D = 1$ to failure. The adopted evolution law is defined as:

$$\dot{D} = \left(\frac{\sigma}{A}\right)^r (1 - D)^{-k} \tag{17}$$

Damage coupled strain rate can be expressed now. Its elastic component is:

$$\dot{\varepsilon}^e = \frac{1 + \nu}{E} \frac{\dot{\sigma}}{1 - D} - \frac{\nu}{E} \frac{tr(\dot{\sigma})}{1 - D} \mathbf{I} \tag{18}$$

and its viscoplastic component is:

$$\dot{\varepsilon}^{vp} = \frac{3}{2(1 - D)} \left[\frac{\sigma_{eq}}{(1 - D) K p^{1/M}}\right]^N \frac{\mathbf{s}}{\sigma_{eq}} \tag{19}$$

5 DETERMINATION OF PARAMETERS

A complete test campaign was carried out on shale samples including constant strain rate compression tests, relaxation tests and creep tests. The Lemaitre viscoplastic damage model requires six independent parameters. They can be divided into two groups. M, N and K are related to the rate-dependent behaviour of the solid while A, r and k are related to the damaging process. The identification of the rate-dependent material constants on various compression and relaxation tests constitutes the subject of former works (Boidy & Pellet 2000, Boidy et al. 2001, Fabre & Pellet 2002) and therefore is not detailed in this paper. The final set of values is presented in Table 1.

Damage parameters govern the progressive material deterioration terminated by macroscopic failure through the internal damage variable D (Equation 17).

Table 1. Material parameters for shale.

Elastic constants	Viscoplastic constants	Damage constants
$E = 5.9$ GPa	$M = 3.9$	$k = 22.4$
$\nu = 0.3$	$N = 22.0$	r = 13.3
	$K = 289.9$ MPa·s	$A = 114.5$ MPa·s

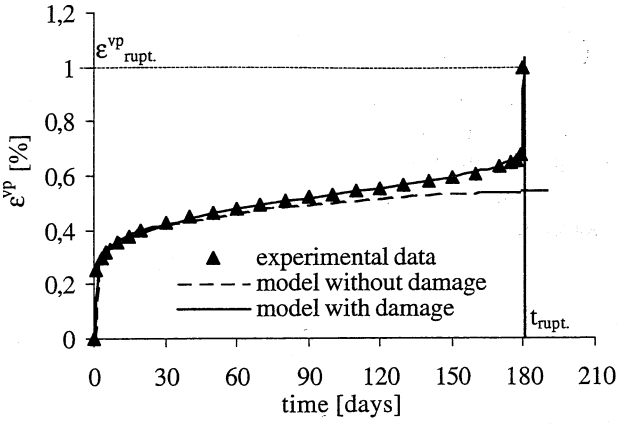

Figure 1. Analytical viscoplastic strain with and without damaging.

In order to determine the three damage parameters a monoaxial constant load creep test was analyzed. Experimental points for a constant 26 MPa compressive stress are represented in Figure 1.

In the first step damaging phenomena were not considered. Under classical monoaxial initial conditions (i.e., $\sigma = \sigma_1, \sigma_2 = \sigma_3 = 0$ and $\dot{\sigma} = 0$) Equation 14 can be particularly easily integrated and allows one to express an $\varepsilon^{vp} = f(t)$ function of the form:

$$\varepsilon^{vp} = \left[\frac{M + N}{M} \left(\frac{\sigma}{K}\right)^N t\right]^{\frac{M}{M+N}} \tag{20}$$

With the help of previously identified material constants, purely viscoplastic strain evolution has been computed analytically. Results are shown on Figure 1 by a dotted line. It can be seen that this model reproduces properly the primary creep but differs considerably from experimental observations as soon as damage becomes significant (steady-state creep and tertiary creep). For an appropriate model of the entire strain path, the damaging process has to be taken into account. Rupture time ($t_{rupt.}$) and strain ($\varepsilon^{vp}_{rupt.}$) can be drawn from experimental data (Figure 1). Integrating Equation 17 and Equation 19 and still considering a monoaxial case they can be calculated as:

$$t_{rupt.} = \frac{1}{k + 1} \left(\frac{\sigma}{A}\right)^{-r} \tag{21}$$

$$\varepsilon_{rupt.}^{vp} = \left[\frac{M+N}{M(k-N)}\left(\frac{\sigma}{A}\right)^{-r}\left(\frac{\sigma}{K}\right)^{N}\right]^{\frac{M}{M+N}} \quad (22)$$

and the integrated form of the strain evolution function as:

$$\varepsilon^{vp} = \varepsilon_{rupt.}^{vp}\left[1-\left(1-\frac{t}{t_{rupt.}}\right)^{\frac{k-N}{k+1}}\right]^{\frac{M}{M+N}} \quad (23)$$

On the basis of these relations the damage constants can be determined (see Table 1).

Comparison between the analytical solution, presented by a continuous line on Figure 1, and the experimental result shows satisfactory correlation from the primary stage of creep until the complete failure of the specimen.

6 NUMERICAL EXAMPLE

Numerical simulations were performed with the finite element program Cast3m. A simple 2D plane strain problem is presented to demonstrate the model's ability to predict long-term behaviour of the rock mass around deep underground openings. The horizontal section of a 6 m diameter vertical shaft was considered. Only a quarter of the opening was modeled due to its axial symmetry. Standard linear quadrilateral elements with 2×2 numerical integration points were used to discretize the structure. The stress field is supposed to be isotropic with $\sigma_0 = 10$ MPa. The gravity load was neglected because the gravity gradient is perpendicular to the model's plane. Mesh dimensions and boundary conditions of the problem are designated in Figure 2.

Temporal evolution of the excavation damage zone (EDZ) and wall convergence were analyzed over a period of 500 years. The numerical iteration process was automatically managed by Cast3m. The code adopts an adaptive algorithm and determines the suitable time step as a function of the convergence difficulty of the previous iteration. The calculations took about 1/4 hour with the 800 element mesh for a 500-year-long study time.

The numerically calculated radial time-dependent wall displacements are illustrated in Figure 3.

It can be seen that the cavity's closure shows approximately the same tendency up to 100 years, then the model without damage becomes stable while the model with damage continues increasing and reaches 40% higher values after 500 years in the u_r/R ratio. For a 6 m diameter shaft this result corresponds to a convergence of ~25 mm and ~35 mm respectively. These displacements are from purely viscoplastic nature and were calculated after reinitialization following load application and excavation simulation.

In Figure 4 are presented some results in terms of orthoradial stress redistribution near the opening.

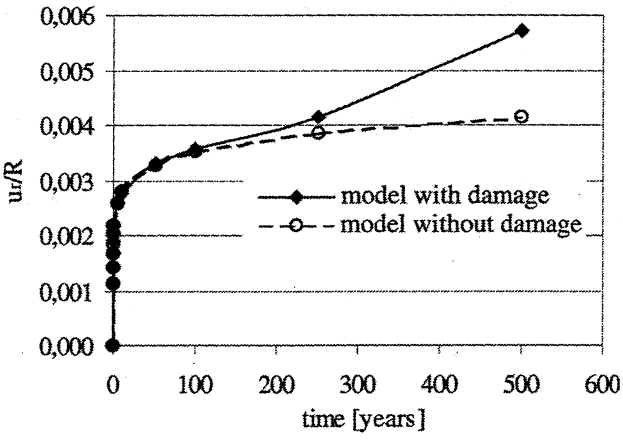

Figure 3. Cavity's closure versus time. Comparison between models including and not including damage.

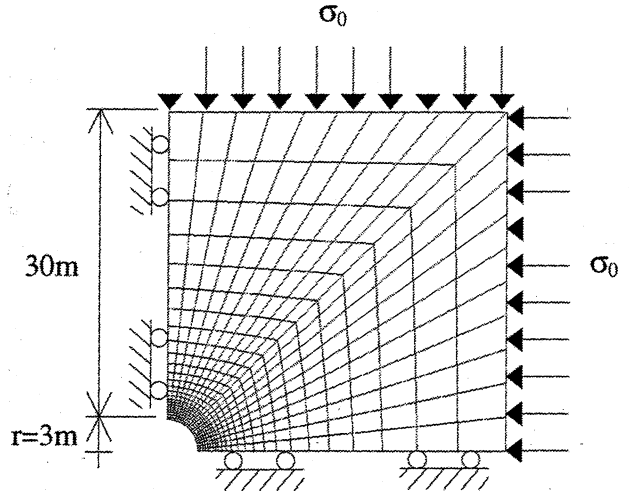

Figure 2. Model geometry and boundary conditions.

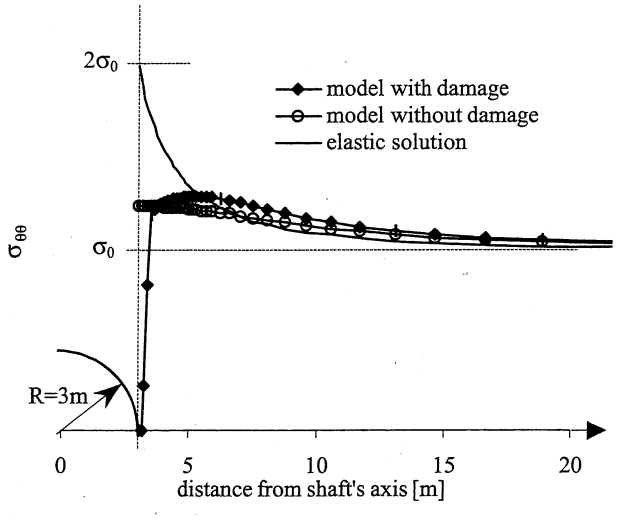

Figure 4. Orthoradial stress redistribution in the mass after 500 years.

Compared with the elastic solution important stress relaxation can be observed around the opening with the viscoplastic models. The most significant difference between models with and without damage consists in the appearance of a failed zone at the cavity wall where the material resistance falls to zero. This phenomenon influences visibly the stress redistribution around the shaft.

Excavation damaged and ruptured zones are visualized in Figures 5 and 6. A damage criterion has been formulated on the basis of the hardening parameter in order to highlight objectively the influence of damage phenomena on the extension of the damaged zone. As seen above (Equations 3a–d) this internal variable measures the cumulated deviatoric viscoplastic strain and is thus related directly to progression of damage. Material is considered damaged if $p \geq 3.75 \times 10^{-3}$ for both models. In Figure 5 results for a study time of 100 years are presented. Obtained damaged zones are shown simultaneously with the model including damage on the left-hand side (Figure 5a) and with the classical viscoplastic model on the right-hand side (Figure 5b). No significant difference can be noticed.

In Figure 6 computation time has been pushed to 500 years. The EDZ surrounding the shaft is now much more developed in both cases. Note the appearance of the darker ring around the cavity, which corresponds to the failed zone. This zone is obviously nonexistent for the classical model.

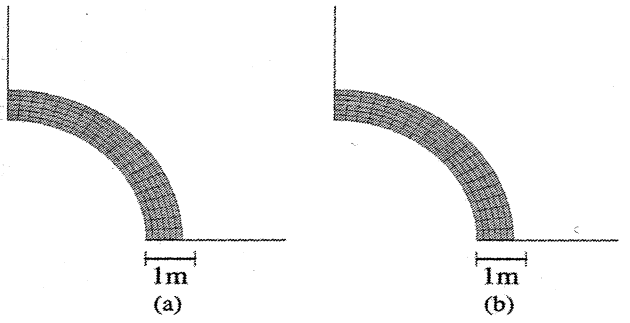

Figure 5. Excavation damage zone around the opening after 100 years.

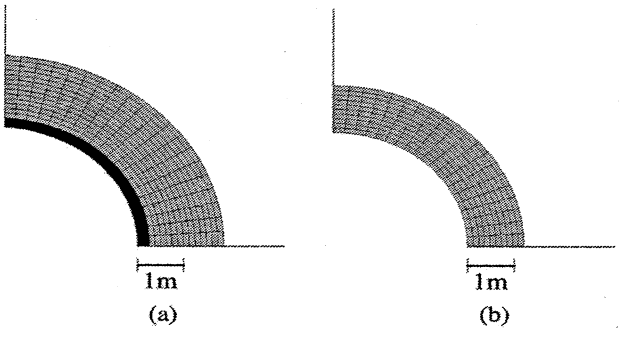

Figure 6. Excavation damage zone around the opening after 500 years.

An evolution of the extension of the damaged zone from 0.75 m to 1.25 m for the classical model (Figure 6b) and up to 1.85 m for the Lemaitre model with damage (Figure 6a) can be observed. The ruptured zone reaches a depth of about 0.25 m and its propagation seems unstable at the end of the studied time period.

7 CONCLUSIONS

A rate-dependent, strain-hardening, damage-coupled viscoplastic model, known as the Lemaitre model, and its formulation have been presented. After evaluating the material parameters for shale samples, a simple numerical application has been investigated within the framework of plane strain finite element analysis of deep underground storage facilities. Comparisons between classical non-damaging and damage-coupled viscoplasticity underlined the importance of taking into account the damaging phenomena.

The Lemaitre model assumes that creep occurs without volumetric strain. However recent experiments show that for most shales progressive damage and failure are associated with an increase of volumetric strain, in other words, with dilatancy. The phenomenological model presented in this paper can be improved by replacing Von Mises' yield criterion with a different criterion more suitable for geomaterials.

Future works includes applying the enhanced model for more complex three-dimensional cases simulating different construction stages (i.e., step-by-step excavation, support installation, etc.).

REFERENCES

Boidy E. & Pellet F. Identification of mechanical parameters for modelling time-dependent behaviour of shales, *ANDRA Workshop on Geomechanics, Paris 11–12 October 2000.*

Boidy E., Pellet F. & Boulon M. Numerical modeling of deep tunnels including time-dependent behavior, *Proc. 10th IACMAG Conf., Tucson, Arizona, 7–12 January 2001.*

Chaboche J.L. & Rousselier G. On the plastic and viscoplastic constitutive equations - Parts I and II, *J. Pressure Vessel Tech., ASME, Vol. 105 (1983) pp. 153–164.*

Charlez A. Rock mechanics – theoretical fundamentals, *Vol. I Technip, Paris, 1991.*

Cristescu N.D. & Hunsche U. Time effects in rock mechanics, *John Wiley & Sons, England, 1998.*

Fabre G. & Pellet F. Identification of viscous properties of an argillaceous rock, *Int. Symp. PARAM 2002, Paris, to be published.*

Jaeger J.C. & Cook N.G.W. Fundamentals of rock mechanics, *Chapman and Hall, London, 1979 (3rd edition).*

Ladanyi B. Time-dependent response of rock around tunnels, *Comprehensive Rock Engineering, Pergamon Press, Vol. 2, pp. 77–111.*

Lama R.D. & Vutukuri V.S. Handbook on Mechanical Properties of Rocks, *Vol. III, Trans Tech Publications, 1978.*

Lemaitre J. & Chaboche J.-L. Mécanique des matériaux solides, *Dunod, Paris, 1985.*

Perzyna P. Fundamental problems in viscoplasticity, *Adv. Appl. Mech., Vol. 9 (1966) pp. 243–377, Academic Press, New York.*

Perzyna, P. Thermodynamic theory of viscoplasticity, *Adv. Appl. Mech., Vol. 11 (1971) pp. 313–354, Academic Press, New York.*

Annexe IV : Publication de synthèse de ma thèse de Doctorat

14 - F. Pellet & P. Egger (1996), Analytical model for the mechanical behavior of bolted rock joints subjected to shearing, Rock Mechanics and Rock Engineering, Springer Verlag, Ed. H.H Einstein & K. Kovari, vol. 29, no 2, pp 73-97.

Rock Mech. Rock Engng. (1996) 29 (2), 73–97

Rock Mechanics and Rock Engineering

Analytical Model for the Mechanical Behaviour of Bolted Rock Joints Subjected to Shearing

By

F. Pellet[1] and **P. Egger**[2]

[1]Bonnard & Gardel, Consulting Engineers, Lausanne, Switzerland
[2]Swiss Federal Institute of Technology, Lausanne, Switzerland

Summary

This study proposes a new analytical model for the prediction of the contribution of bolts to the shear strength of a rock joint. The main characteristics of this model are the accounts for the interaction of the axial and the shear forces mobilised in the bolt, as well as the large plastic displacements of the bolt occurring during the loading process. The complete curve of the bolt contribution as a function of the displacement along the joint can be computed, and the maximum bolt contribution is obtained by dissociating the bolt cohesion and the confinement effects. The comparison of the performances of this analytical model with test results shows its capacity to describe the observed phenomena. The effects of the most important parameters such as bolt inclination, mechanical properties of bolt material, rock strength and joint friction angle are clearly established and discussed.

1. Introduction

The reinforcement of rock masses by untensioned rock bolts is widely used to ensure stability and to restrain deformation of rock engineering structures, such as rock slopes or underground cavities (Fig. 1). The mechanical action of the bolt is, however, still difficult to assess, especially for bolts installed in fractured rock masses. As a matter of fact, there is no unanimously approved method for the dimensioning of the reinforcement system.

The effectiveness of rock bolts depends on numerous parameters which must be considered for the stability analysis of reinforced rock structures. The most important are the nature and the conditions of the rock mass, as well as the bonding conditions and the type of the reinforcement element.

The present study proposes a new analytical model for the mechanical behaviour of bolted rock joints subjected to shearing. It allows the computation of both the strength and the deformability properties of a bolted rock joint, when the failure mechanism involves sliding displacements along the rock joints. Only untensioned fully grouted rock bolts are investigated.

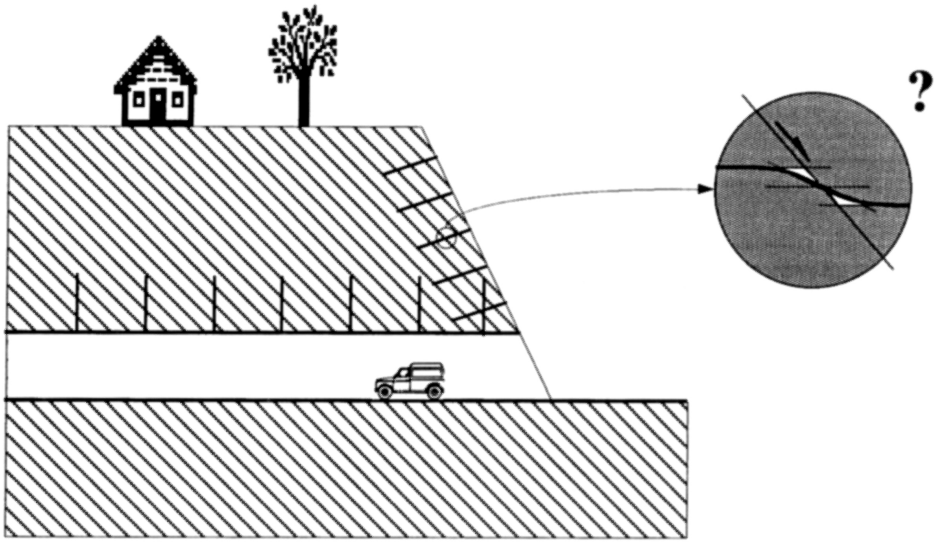

Fig. 1. Stability problem in a stratified rock mass reinforced by untensioned bolts

2. Outline of previous studies

Conceptual Model for Bolted Rock Joints

When a bolted rock joint is subjected to shearing, the bolt is deformed as the displacement increases (Fig. 2). At the intersection between the bolt and the jo force R_O, is mobilised in the bolt. This force results from the axial force N the shear force Q_O, acting in the bolt.

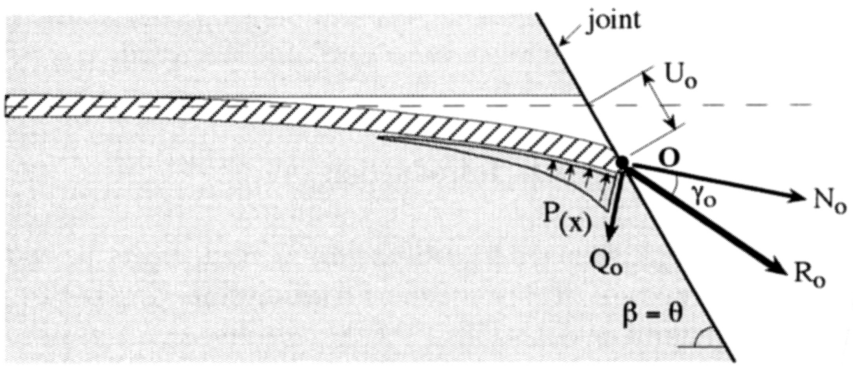

Fig. 2. A bolted rock joint subjected to shearing

The strengthening effect of the bolt can be divided in two ter Pellet, 1991). The first one, which is related to the parallel compon to the joint, can be treated as an additional cohesion. The secon connected with the normal component of the force in the bolt, can an increase of the confining stress. Thus, using the Mohr-Coulo strength of the bolted joint can be expressed by adding the reinfo bolt to the intrinsic strength of the joint. It leads to:

$$\tau = (c_j + \Delta c_b) + (\sigma_{no} + \Delta\sigma_{nb}) \tan \phi_j$$

where cj : joint cohesion
ϕ_j : joint friction angle
σ_{no} : initial confining stress
$\Delta\sigma_{nb}$: increase of confining stress provided by the bolt
Δc_b : additional cohesion provided by the bolt.

The difficulty lies in the determination of the intensities and the directions of the forces mobilised in the bolt during the shearing process.

Experimental Studies

A lot of experimental programs were performed in order to describe in a qualitative manner the behaviour of bolted rock joint. One of the first was reported by Bjurström (1974). He carried out direct shear tests on blocks of granite reinforced by fully grouted bolts. Then, Azuar (1977), Haas (1981), Dight (1983), Schubert (1984), Spang (1988), Egger and Zabuski (1991) and Ferrero (1993) continued experimental studies on different types of rock material reinforced by various elements. All these studies enable one to draw the following conclusions:

- When the angle between the joint plane and the bolt axis is small (i.e., steeply inclined bolt), the displacement on the joint at the bolt failure is insignificant. On the other hand, for a bolt placed perpendicular to the joint, the failure of the bolt occurs at a large joint displacement.
- When the strength of the host rock is high, the joint displacement at failure becomes smaller and the maximum bolt contribution decreases slightly.
- When the joint friction angle increases, the maximum bolt contribution is improved, depending on the bolt orientation with respect to the joint.
- The tensioning of the bolt has a favourable effect both on the stiffness and on the strength of the bolted rock joint.

Analytical Approaches

Several equations have been developed to predict the behaviour of a bolted rock joint. The simplest of them considers only the axial force acting in the bolt (Bjurström, 1974). By taking the components of this force on the joint plane, it is then possible to compute the reinforcement effect of the bolt. This approach does not take into account the shear force mobilised in the bolt nor the deformation of the bolt (i.e., bolt rotation) across the joint. As a result, the direction of the force acting in the bolt is not accurately described.

More elaborated expressions were developed to take into account the deformation of the bolt during the loading process. Most of them were based on the first order theory of the beams on elastic supports formulated using the small displacements theory. As a consequence, these formulations are valid only for the early stages of the loading process. Dight (1983) proposed an expression to predict the maximum force mobilised in the bolt as well as the associated displacement on the joint. The failure of the bolt is determined by the combination

of axial and shear forces, whereas the displacement is computed taking into account the yields of the grout. Based on Dight's work, Holmberg (1991) proposed a method which gives a good prediction on the maximum bolt contribution when the bolt is inclined to the joint.

Furthermore, Spang and Egger (1990) proposed empirical expressions to compute the maximum bolt contribution and the associated joint displacement.

Numerical Modelling

Although numerical modelling is not the centre of this study, it seems useful to remind the principal possible approaches. The first one considers an equivalent material which behaves in effectively the same way as the reinforced rock mass. Such an approach, which was illustrated by Gerrard and Pande (1985) for simple loading conditions, does not take into account the effective action of the bolt. In most cases, only the axial effect of the bolt is taken into account. Another approach has been proposed by Aydan (1989). He developed a special bolt joint element with special consideration for both the axial and the shear stiffness provided by the bolt. The shear stiffness, however, is taken into account by simply considering the shear modulus of the bolt material and of the grout material. The numerical modelling of a bolted joint taking into account the effective behaviour of each component is probably the most accurate approach. Swoboda and Marenče (1992) developed a special substructuring calculation where the bolt is analysed with the help of large displacements theory. This bolt element is coupled with a joint element for the joint behaviour.

Conclusions

Whatever the chosen analytical approach, it is necessary to properly model the behaviour of the bolt itself. Therefore, it is required to develop an accurate solution to compute both the strengthening and the stiffening effect of the bolts. This theory must take into account yielding and plastic strain of the bolt and must be formulated with the help of the large displacement theory. Moreover, the shear force mobilised in the bolt as well as the stiffness the bolt provides must be considered.

3. Analytical Formulation for the Behaviour of a Bolted Rock Joint

The analytical description of the behaviour of a bolted rock joint must take into account the multiple interaction phenomena occurring between the bolt, the grout and the surrounding medium. As previously stated, the objective is to establish the relation between the force, R_O acting in the bolt at the joint level and the corresponding displacement, U_O, on the joint (Fig. 2). Ultimately, the prediction of both the maximum bolt contribution to the joint shear strength as well as the maximum displacement are required.

Description of the Deformational Process of the Bolt

When a bolted rock joint is subjected to a shear displacement, the bolt deflects, and at the same time, the host material (i.e., grout or rock) provides a reaction. The bolt is thus axially and transversally loaded by a set of forces composed of an axial force, N, a shear force, Q, and a bending moment, M.

Based on experimental studies (e.g. Spang and Egger, 1990), the deformed shape of the bolts exhibits two singular points. The first one is the intersection between the joint and the bolt (point O) where the curvature of the deformed shape of the bolt is zero. According to the beam theory, at this point the bending moment is zero. Therefore, only axial and shear forces act in the bolt. The second one is the point of the maximum curvature (point A) where the bending moment is maximum and the shear force is zero.

Experimental studies also show that the yield limit of the bolt corresponds to the appearance of two plastic hinges located in the point of maximum bending moment. Thus the bolt yields by the combination of a bending moment and an axial force in point A. Beyond the yield limit, the bolt behaves plastically until it breaks down in point O under the action of the axial and shear forces.

From the beginning of the loading process, the host material supplies a reaction on a bolt's length which increases until the bolt yields. Even though at the early stage of the loading process the host material may behave elastically, a rigid perfectly plastic behaviour is assumed. This assumption is justified because the elastic portion of the material behaviour is extremely small in comparison with the plastic portion.

Mechanical System and Basic Hypotheses

For purpose of equilibrium analysis, the bolt can be considered as a semi-infinite beam loaded at one end by both an axial force N_O, and a shear force Q_O, which are dependent on each other (Fig. 3).

The description of the bolt behaviour must be divided in two sections. The first one concerns the elastic range (i.e. from the beginning of the loading process to the yield of the bolt), and the second one deals with the plastic range (i.e. from the yield to the failure of the bolt). It is then necessary to determine the yield and failure limits of the bolt.

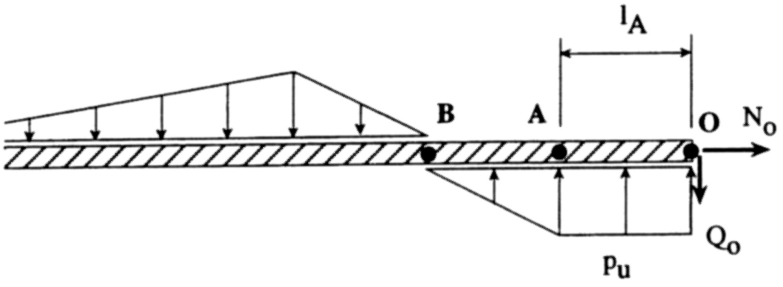

Fig. 3. Mechanical system

Yield Limit of the Bolt

As it was previously stated, point A is the location of the maximum bending moment (i.e., shear force is zero). The length, l_A, on which the reaction acts, can be simply computed by establishing the following equilibrium equation:

$$l_A = \frac{Q_O}{p_u} \tag{1}$$

where p_u : maximum bearing pressure per unit of length (yielding pressure of the grout)
l_A : distance from point O and point A

From the moment equilibrium equation, the maximum bending moment acting at point A can be expressed as a function of the shear force acting at point O:

$$M_A = \frac{Q_O^2}{2p_u} \tag{2}$$

where M_A : bending moment acting in the bolt at point A.

Based on the theory of beams loaded simultaneously by a bending moment an axial force, the expression of the normal stress, σ, in a bolt section is expressed by:

$$\sigma = \frac{M_A}{W} \pm \frac{N_O}{A} \tag{2a}$$

where $A = \pi D^2/4$
$W = \pi D^3/32$.

When A, W and M_A are substituted by their expressions in Eq. 2a, the shear force acting in point O and leading to the yield limit in point A (i.e., upper fibber of the bolt section reach yield stress of the bolt material) is obtained:

$$Q_{oe} = \frac{1}{2}\sqrt{p_u D_b \left(\frac{\pi D_b^2 \sigma_{el}}{4} - N_{oe}\right)}, \tag{3}$$

where Q_{oe} : shear force acting at point O at the yield stress of the bolt material
N_{oe} : axial force acting at point O at the yield stress of the bolt material
D_b : bolt diameter
σ_{el} : yield stress of the bolt material.

Failure Criterion of the Bolt

For the failure of the bolt material in point O, the Tresca criterion is used. The maximum force acting in the bolt at point O is expressed as a combination of the shear force and of the axial force. This interaction formula, first established by Dight (1983), is expressed here as a function of the shear force:

$$Q_{of} = \frac{\pi D_b^2}{8}\sigma_{ec}\sqrt{1 - 16\left(\frac{N_{of}}{\pi D_b^2 \sigma_{ec}}\right)^2}, \tag{4}$$

where Q_{of} : shear force acting at point O at the failure of the bolt material
N_{of} : axial force acting at point O at the failure of the bolt material
σ_{ec} : failure stress of the bolt material.

These two relations are represented in Fig. 4. The elastic limit (Eq. 3) is parabolic, whereas the failure criterion is elliptical (Eq. 4).

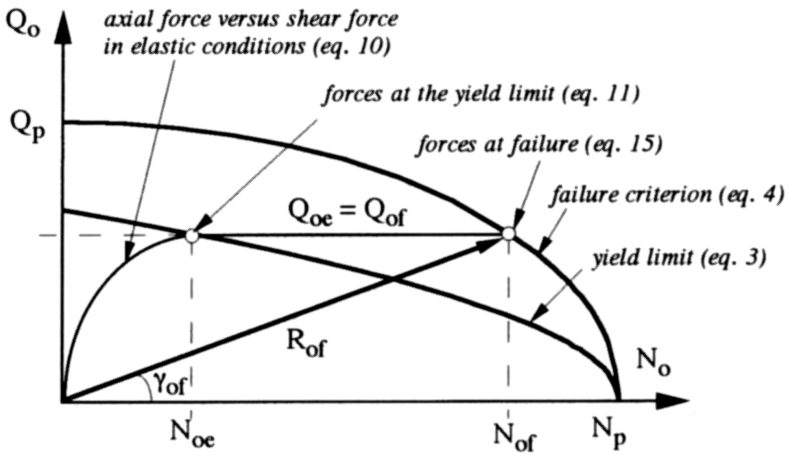

Fig. 4. Shear force versus axial force in the bolt

Behaviour of the Bolt in the Elastic Stage

When a beam is loaded simultaneously by a shear force and an axial force which are dependent on one another, the differential equation governing its deflection has no simple solution. Therefore, it is proposed to use a variational approach, based on an energetic concept. First, the deformed shape of the beam must be assumed. The quality of the solution depends on the capability of the chosen function to describe the deformed shape of the bolt. In addition it must satisfy the boundary conditions (maximum curvature in point A and zero curvature in point O).

For the transversal displacement of the beam, the chosen function is the solution of the differential equation governing the deflection of a beam on elastic support (Hetenyi, 1946). Di Prisco (1989) shows that this function fits very well with experimental results. The transversal displacements are expressed by:

$$v_{(x)} = v_o \, e^{-x/l_o} \cos\left(\frac{x}{l_o}\right). \tag{5}$$

The axial displacement was assumed to vary linearly along the deformed part of the beam. Thus:

$$u_{(x)} = -u_o\left(1 - \frac{2x}{3\pi l_o}\right). \tag{6}$$

In these expressions, l_o, is a reference length which will be expressed as a function of l_A

$$l_o = \frac{\pi}{4} l_A.$$

The expression of the total complementary energy is obtained from the calculation of the internal strain energy and the work of the external forces (see Appendix I). When the total complementary energy is minimized with respect to the displacements, u_o and v_o, the relations between forces and displacements become:

$$u_o = \frac{24\, N_o\, Q_o}{E\; p_u\; \pi\, D_b^2} \tag{7}$$

$$v_o = \frac{8192\, Q_o^4\, b}{E\, \pi^4\, p_u^3\; D_b^4} \tag{8}$$

where E : elastic modulus of the bolt material
b : constant term defined in Appendix I.

When the angle, β, between the bolt axis and the joint, is considered, the following kinematic condition must be added:

$$\mathrm{tg}\beta = \frac{v_o}{u_o} \tag{9}$$

Thus, Eqs. 7 and 8 combined give the relation between the shear force and the axial force acting in the bolt:

$$Q_o = \sqrt[3]{\frac{3\; N_o\; p_u^2\; \pi^3\; \mathrm{tg}\beta\; D_b^2}{1024\; b}} \tag{10}$$

This relation is drawn in Fig. 4. The determination of the forces at the yield limit leads to the following third order equation, which is the combination of Eqs. 3 and 10:

$$Q_{oe}^3 + Q_{oe}^2 \left(\frac{3\; p_u\; \pi^3\; D_b\; \mathrm{tg}\beta}{256\; b} \right) - \left(\frac{3\; p_u^2\; \pi^4\; D_b^4\; \mathrm{tg}\beta\; \sigma_{el}}{4096\, b} \right) = 0 \tag{11}$$

The solution of this equation furnishes the shear force and the axial force in the bolt. Then, if the forces which act in the bolt are known, it is possible to compute the displacement, U_{oe}, and the rotation, ω_{oe}, of the bolt, which are represented in Fig. 5.

$$U_{oe} = \frac{8192\; Q_{oe}^4\; b}{E\; \pi^4\; D_b^4\; p_u^3\; \sin\beta} \tag{12}$$

$$\omega_{oe} = -\frac{2048\; Q_{oe}^3\; b}{E\; p_u^2\; \pi^3\; D_b^4} \tag{13}$$

Behaviour of the Bolt in the Plastic Stage

In the plastic stage, the bending stiffness of the bolt drops due to the appearance of the plastic hinges. Therefore the part $O - A$ of the bolt behaves as a truss, and only the axial force grows. The shear force in the bolt remains constant ($Q = Q_{oe}$ at

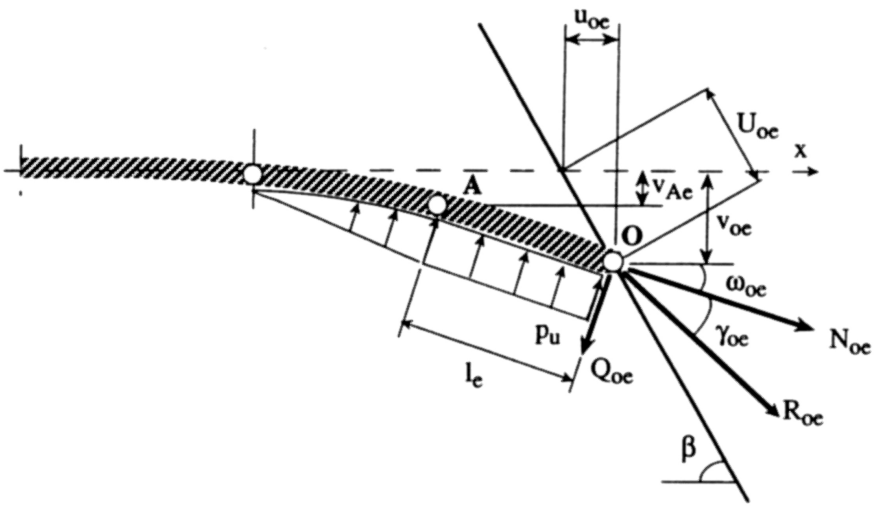

Fig. 5. Displacements and rotations of the bolt for elastic conditions

point O), and the shape of the bolt between the hinges can be considered to be linear. This simplification was found by Di Prisco (1989) as a reasonable assumption.

The determination of the forces acting in the bolt at failure is simply achieved by solving the following equations, which are drawn in Fig. 4:

$$Q_{of} = Q_{oe} \tag{14}$$

$$N_{of} = \frac{\pi\ D_b^2}{4}\sigma_{ec}\sqrt{1 - 64\left(\frac{Q_{oe}}{\pi\ D_b^2\ \sigma_{ec}}\right)^2}. \tag{15}$$

As the deformed shape of the bolt between points A and O is linear (Fig. 6), the computation of the displacement and the rotation at the end of the bolt can be done by the use of the large displacements formulation. It is shown by simple geometrical consideration that the following expression gives a good approximation of the increment of plastic rotation, $\Delta\omega_{op}$:

$$\Delta\omega_{op} = \arccos\left[\frac{l_e}{l_f}\sin^2\beta \pm \sqrt{\cos^2\beta\left(1 - \left(\frac{l_e}{l_f}\right)^2\sin^2\beta\right)}\right] \tag{16}$$

where l_e : distance between bolt extremity (point O) and the location of the maximum bending moment (point A) when the yield limit is reached
l_f : length of the part $O - A$ at failure
ϵ_f : bolt strain at failure.

with:

$$l_f = l_e(1 + \epsilon_f). \tag{17}$$

The solution of Eq. 16 gives the increment of plastic rotation and then allows for the calculation of the plastic displacement, ΔU_{op}:

$$\Delta U_{op} = \frac{Q_{oe}\ \sin\ \Delta\omega_{op}}{p_u\ \sin(\beta - \Delta\omega_{op})}. \tag{18}$$

As the bolt strain at failure is equal to the sum of the elastic and the plastic strains, the total rotation, ω_{of}, and the total displacement, U_{of}, of the end of the bolt at failure are respectively computed by the following formulas:

$$\omega_{of} = \omega_{oe} + \Delta\omega_{op} \tag{19}$$

$$U_{of} = U_{oe} + \Delta U_{op}. \tag{20}$$

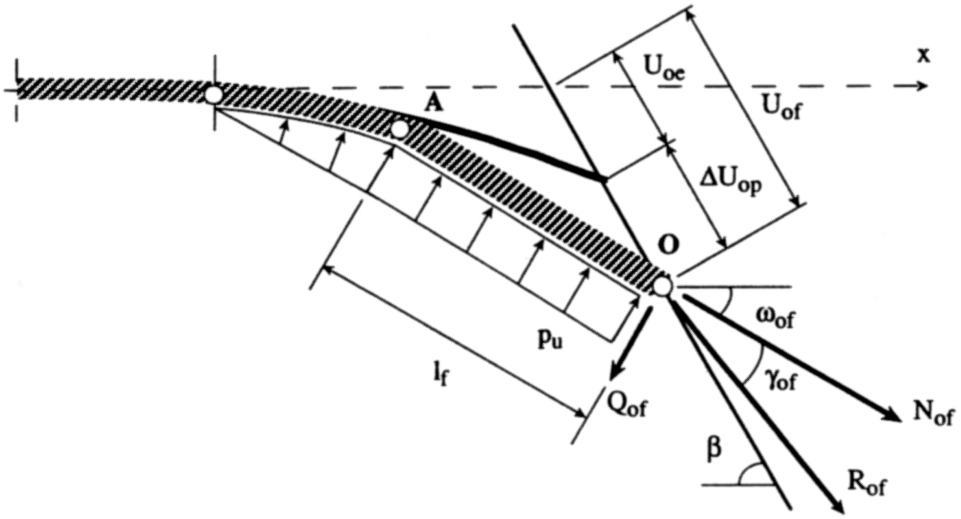

Fig. 6. Displacements and rotations of the bolt for plastic conditions

Between the yield limit and the failure point the axial stiffness of the bolt drops. This decrease may be expressed as an inverse function of the axial force. The increment of the axial force, ΔN_o, grows proportionally to the plastic lengthening of the bolt, Δl_p:

$$\Delta N_o = K^* \, \Delta l_p. \tag{21}$$

K^* is the secant axial stiffness, which can be computed by the following formula:

$$K_i^* = \frac{K_{i-1}^*}{(K_e/K_f)^{(1/n)}} \tag{22}$$

where K_e : axial stiffness in elastic conditions
K_f : secant axial stiffness at failure
K_i^* : axial stiffness at the considered step
n : chosen number of steps between the elastic limit and the failure.

Strength and Associated Displacement of the Bolted Joint

At each step of the loading process, both the axial and shear forces acting at the end of the bolt as well as the rotation and the displacement, are known. With the combination of forces and the use of the Mohr-Coulomb criterion for joint strength, it is possible to compute the contribution of the bolt to the total reinforced rock joint strength (Fig. 7):

$$T_b = R_{ot} + R_{on} \text{ tg } \phi_j \tag{23}$$

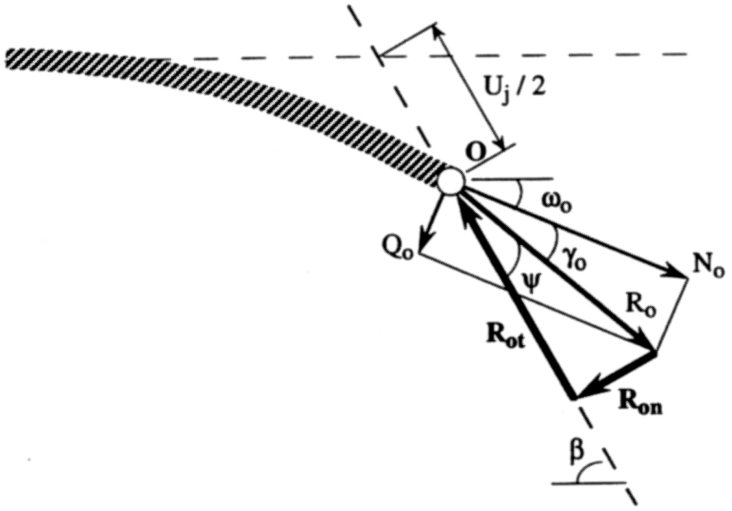

Fig. 7. Decomposition on the joint of forces acting in the bolt

The additional cohesion, Δc_b, related to the tangential force, and the confining effect, $\Delta\sigma_{nb}$, can be computed as follows:

$$\Delta c_b = \frac{R_{ot}}{A_j} \tag{24}$$

$$\Delta\sigma_{nb} = \frac{R_{on}}{A_j} \tag{25}$$

where R_{on} : component normal to the joint of the force in the bolt
R_{ot} : component parallel to the joint of the force in the bolt
A_j : surface area of joint

Estimating the Rock Reaction

The last point is the determination of the bearing capacity, p_u, that the host rock or the grout can provide. Due to the gap left by the bolt displacement in the vicinity of the joint, the grout material becomes unconfined. Therefore, the bearing capacity can be expressed by the following formula:

$$p_u = K\ \sigma_c\ D_b \tag{26}$$

where K : load factor ($K \geq 1$)
σ_c : unconfined compressive strength of the host material (grout or rock)
D_b : bolt diameter

4. Evaluation of the Theory

In order to evaluate the influence of the most important parameters, a parametric study was carried out. Furthermore, the performances of the analytical model are compared with both experimental results and other analytical predictions. Finally, a numerical example of the computation of the bolt contribution and the associated joint displacement is given in Pellet (1994).

Parametric Study

The parametric study was carried out by varying the main characteristics with the following ranges:

- angle between the joint and the bolt axis $0 < \beta < 90°$
- strength of the rock $10 < \sigma_c < 200$ MPa
- joint friction angle $15 < \phi_j < 45°$
- load factor $K = 1$

Bolt is made in a standard steel with the following mechanical characteristics:

- stress at yield $\sigma_{el} = 600$ MPa
- stress at failure $\sigma_{ec} = 600$ MPa
- strain at failure $\epsilon_f = 20\%$

To make the comparison easier, the results are presented in normalised parameters. Each force is divided by the maximum tensile force of the bolt, N_p, and each displacement is divided by the bolt diameter, D_b.

Bolt Contribution to the Shear Strength of the Rock Joint

First, the mobilisation of the axial force versus the shear force in the bolt during the loading process is examined. If it is intuitively obvious that the more inclined the bolt is, the larger the axial force acting in the bolt will be, the influence of the strength of the host material is less evident. As shown in Fig. 8, the lower the strength is, the larger the axial force acting in the bolt will be. As a consequence, the bolt contribution should be significantly better.

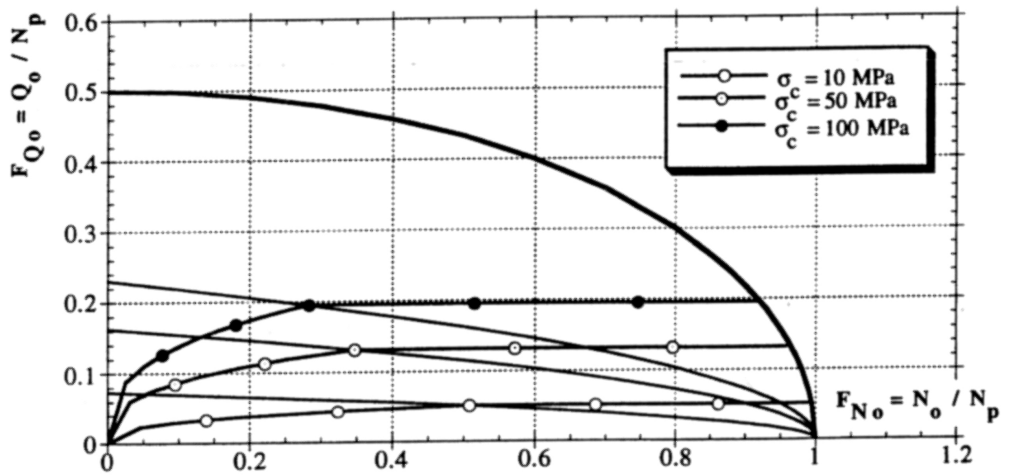

Fig. 8. Shear force versus axial force in the bolt for $\beta = 60°$ and different values of σ_c

As previously mentioned, the bolt contribution on the joint shear strength can be decomposed into a cohesion term related to the component acting parallel to the joint and into a confining term due to the component acting perpendicularly to the joint. It is shown in Fig. 9 that when the bolt is inclined on the joint (i.e., small angle between the bolt and the joint), the cohesion term is high and the confining effect is low. As the

angle between the bolt and the joint increases, the cohesion term decreases while the confining term increases. When the bolt is perpendicular to the joint and for $\phi_j = 30°$, the cohesion and the confining terms have approximately the same magnitude.

As shown in Fig. 10, the bolt contribution on the shear strength depends on the bolt inclination. Moreover, the shapes of the curves vary depending on the joint friction angle. For a low value of the joint friction angle, the optimum contribution of the bolt is obtained when the bolt is steeply inclined. On the other hand, for a large value of the joint friction angle, the optimum contribution occurs when the bolt is hardly inclined. As previously stated, this is due to the effect of the confining term, which is maximum when the bolt is perpendicular to the joint.

Maximum Joint Displacement

The inclination of the bolt has a great influence on the maximum joint displacement (Fig. 11). The greatest displacement is reached when the bolt is normal to the joint. As the angle between the bolt and the joint decreases, the displacement drops rapidly. The rock strength also has a great influence on the displacement. As shown in Fig. 12, the displacement is large when the rock is weak, and it decreases as the rock's strength increases, whatever the bolt position is.

Comparisons with Test Results

The analytical predictions are compared with the test results presented by Pellet et al. (1995a). Tests were carried out with a high capacity press on large models

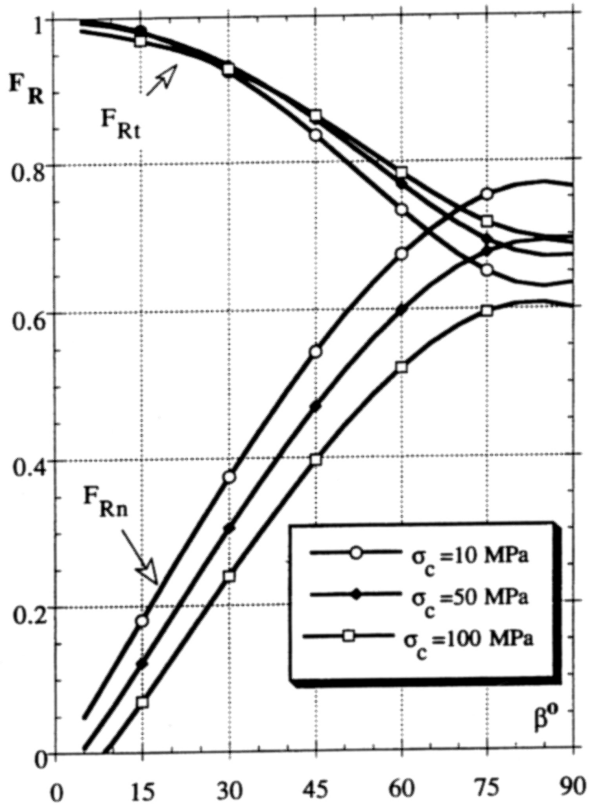

Fig. 9. Additional cohesion R_t and confining effect R_n versus bolt inclination for different values of σ_c

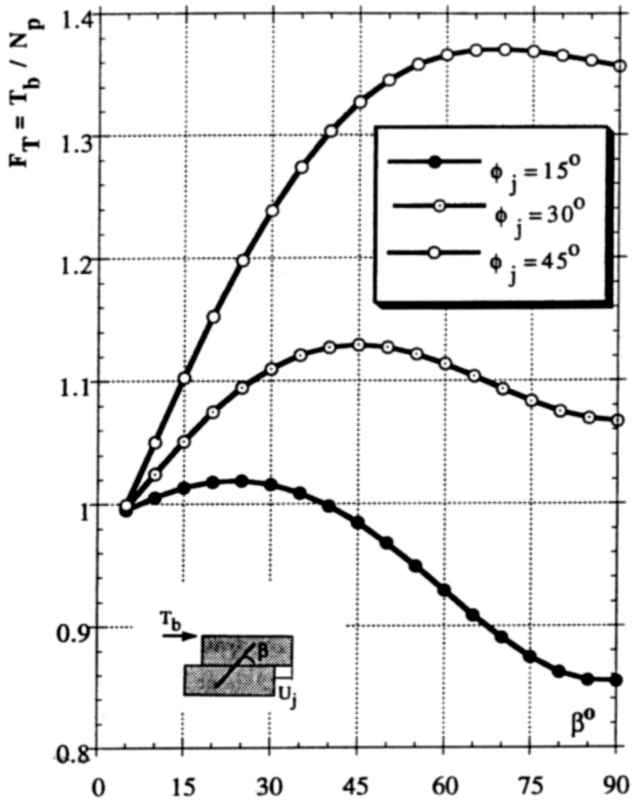

Fig. 10. Bolt contribution versus bolt inclination for different values of ϕ_j

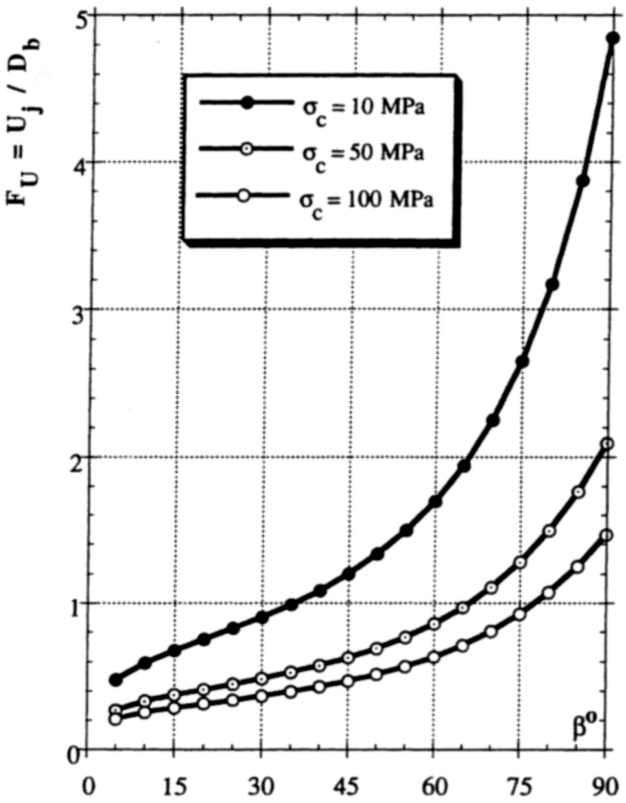

Fig. 11. Maximum joint displacement versus bolt inclination for different values of σ_c

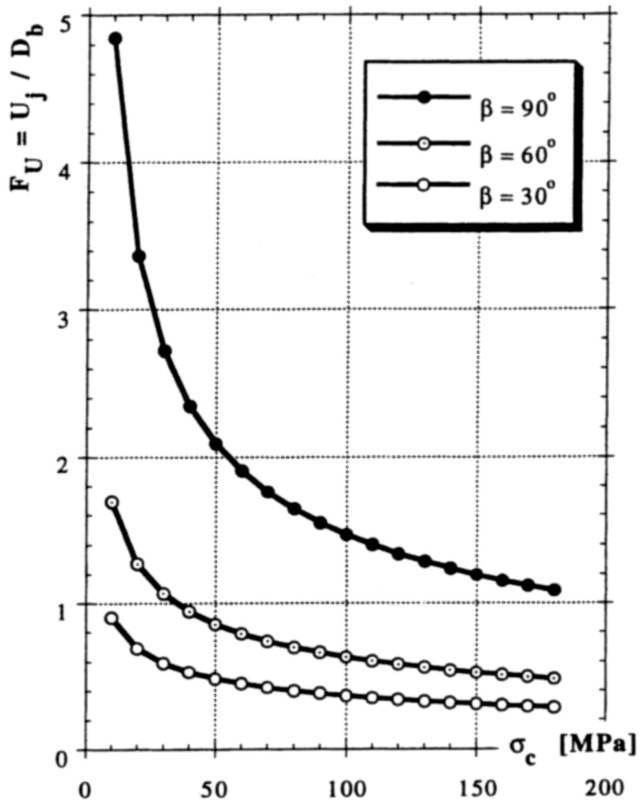

Fig. 12. Maximum joint displacement versus strength of the host material for different values of β

built in limestone. The models were reinforced by steel bars grouted with an epoxy resin. The mechanical properties of the material were the following.

- unconfined compressive strength of the rock $\sigma_c = 150\,\text{MPa}$
- unconfined compressive strength of the grout $\sigma_c = 60\,\text{MPa}$
- bolt diameter $D_b = 3\,\text{mm}$
- yield limit of steel $\sigma_{ec} = 600\,\text{MPa}$
- strain at failure $\epsilon_f = 20\%$
- joint friction angle $\phi_j = 25^\circ$

The experimental curves are plotted in terms of bolt contribution, T_b, versus joint displacement, U_j, for two bolt orientations. A good agreement between experimental and analytical results can be observed in Figs. 13 and 14. For the bolt contribution, the deviation is less than 5%. For the prediction of the joint displacement at failure the agreement is less evident because the bolts did not fail at the same time. The maximum deviation is 29%.

In order to extend the comparison, the performances of the analytical model are compared with the results of the direct shear tests reported by Spang (1988). Tests were performed on samples of concrete and sandstone having the following mechanical characteristics.

- unconfined compressive strength of the sandstone $\sigma_c = 10\,\text{MPa}$
- unconfined compressive strength of the concrete $\sigma_c = 40\,\text{MPa}$
- unconfined compressive strength of the grout $\sigma_c = 36\,\text{MPa}$

- bolt diameter $D_b = 8\,\text{mm}$
- yield limit of steel $\sigma_{ec} = 670\,\text{MPa}$
- strain at failure $\epsilon_f = 13.5\%$
- joint friction angle $\phi_j = 32^\circ$

In the case of small differences between rock and grout strength, the analytical results are close to experimental datas (Fig. 15). When the host rock is weaker than the grout material, the experimental results lie between the analytical curves computed with rock and grout strength (Fig. 16).

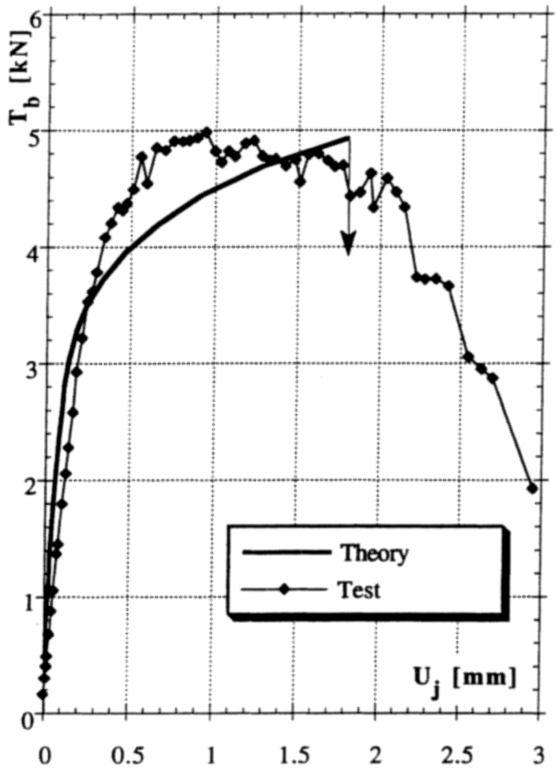

Fig. 13. Bolt contribution versus joint displacement for limestone model with $\beta = 45^\circ$

Comparisons with Existing Analytical Predictions

The expression proposed by Bjurström (1974) and the relation established by Spang (1988) are plotted against test results in Figs. 17 and 18. Because of its semi-empirical nature, Spang's formula is valid for bolts placed between 60 and 90 degrees.

It can be observed (Fig. 17) that when the angle between the bolt and the joint is small, the proposed theory and Bjurström's expression are close. On the other hand, when the bolt is perpendicular to the joint, Bjurström's expression underestimates the bolt contribution. For such a case, Spang's formula and the proposed theory fit very well.

For the estimation of the maximum joint displacement Spang's formula and the proposed theory exhibit the same tendency (Fig. 18).

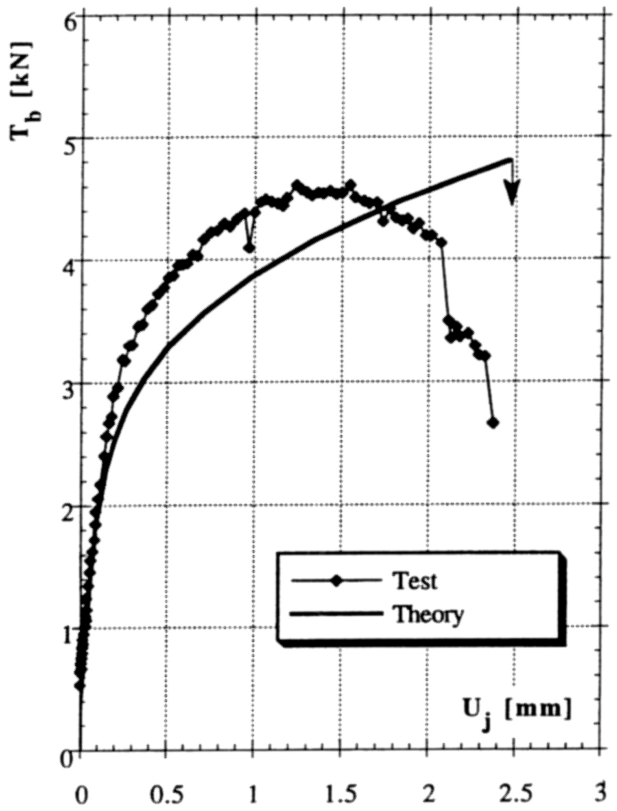

Fig. 14. Bolt contribution versus joint displacement for limestone model with $\beta = 60°$

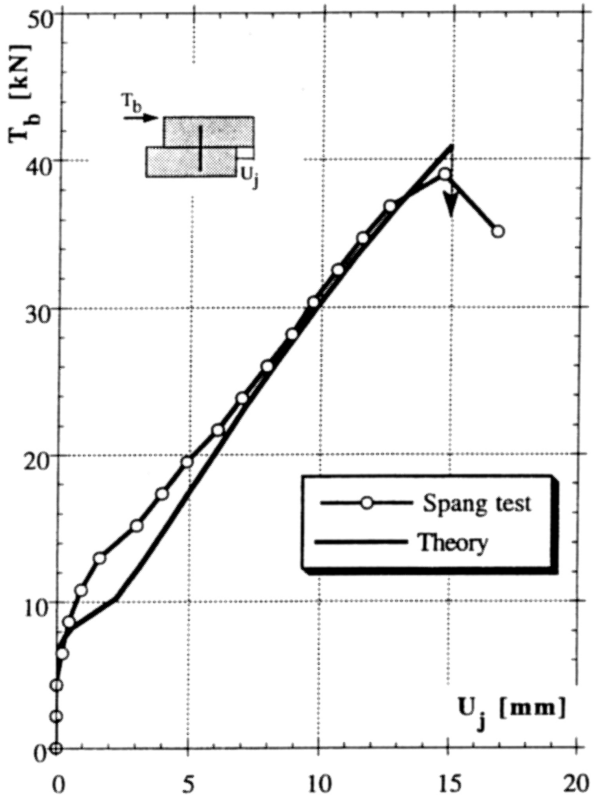

Fig. 15. Bolt contribution versus joint displacement for concrete sample, $\beta = 90°$

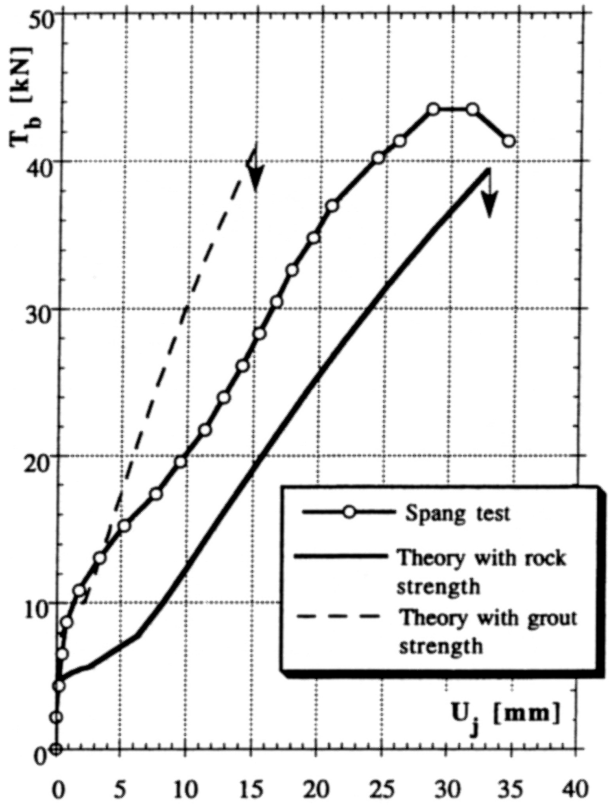

Fig. 16. Bolt contribution versus joint displacement for sandstone sample, $\beta = 90°$

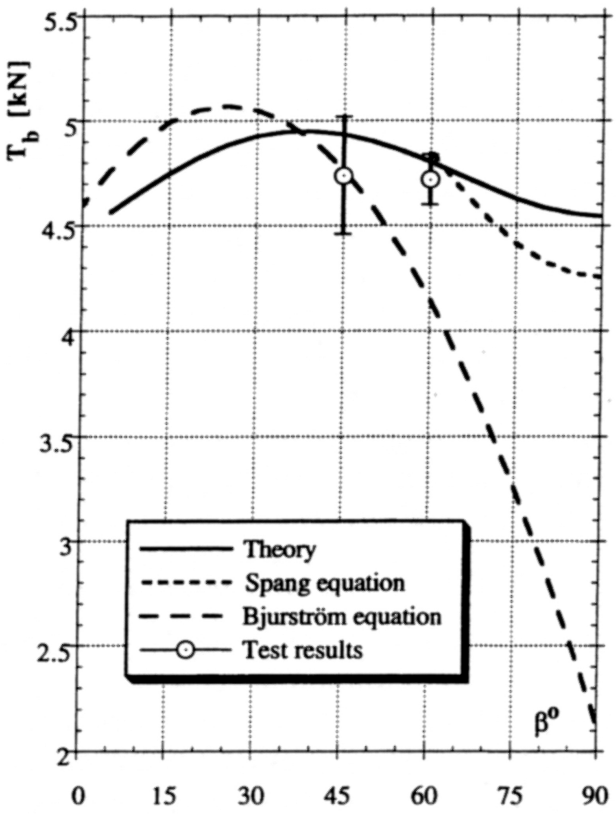

Fig. 17. Bolt contribution versus bolt inclination

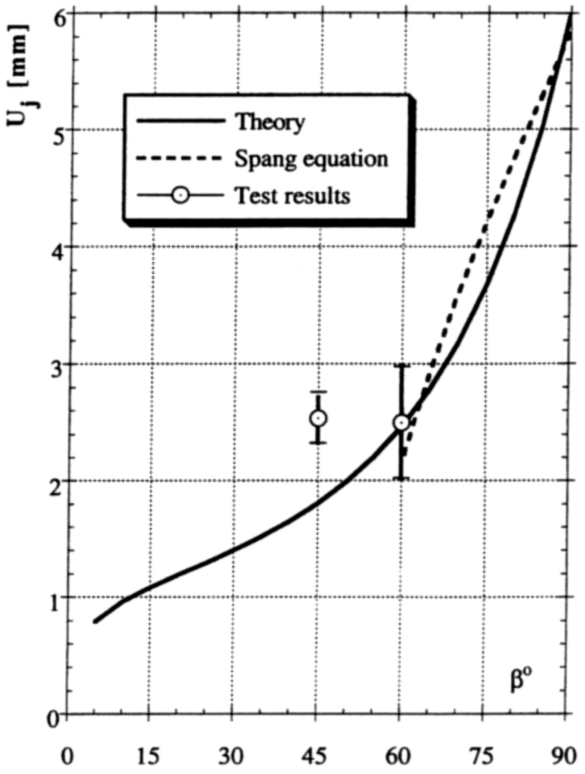

Fig. 18. Maximum joint displacement versus bolt inclination

5. Conclusion

The analytical model developed for this work allows the prediction of the complete load-displacement curve for a bolted rock joint subjected to shearing. The maximum bolt contribution to the shear strength of the bolted rock joint, as well as the maximum displacement on the joint can be obtained. The additional cohesion as well as the confining effect can be computed separately and the influence of the most important geometrical and mechanical parameters are highlighted.

The comparison of the analytical predictions with the tests results obtained on large scale models or by direct shear tests gives good results. It is shown that the proposed model improves the prediction of a bolted rock joint, especially when the bolt is nearly normal to the joint.

Based on this analytical development, it is possible to perform the dimensioning of the reinforcement system for practical application of rock structures such as rock slopes and underground cavities.

Appendix: Solution of the Bolt Equilibrium by a Variational Approach

The method consists in the selection of functions, which describes the deflection of the bolt and satisfies the boundary conditions. The total complementary energy of the system is calculated, and the unknown parameters u_o and v_o which correspond to the sought displacements are obtained by minimization of the

function. The bolt geometry and the loading forces are shown in Fig. 19. For simplification as well as to avoid any confusions, the characteristic length l_o of the bar is denoted l and the maximum pressure exerted by the host material p_u is p. The axis X is inverted in order to simplify the integration computation.

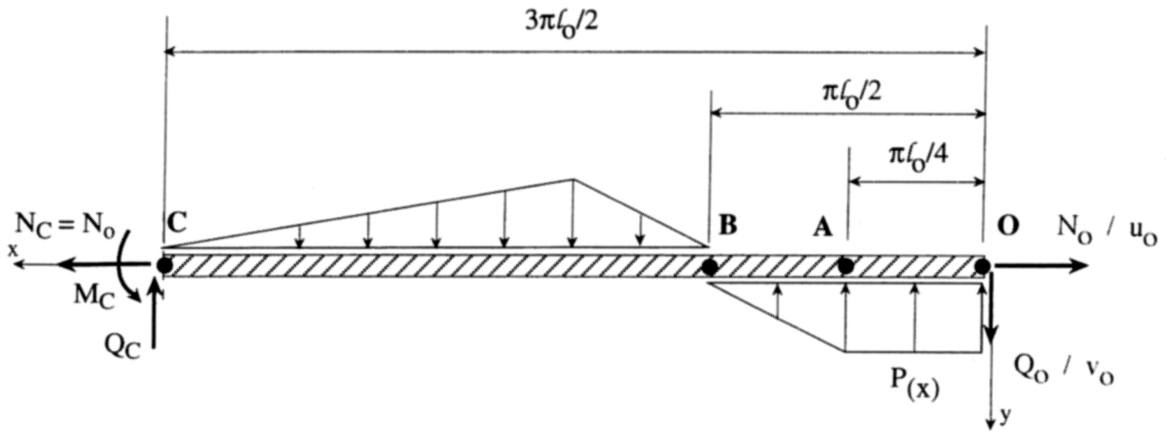

Fig. 19. Bolt geometry and system of loading

Displacements Functions

The chosen function describing transversal displacements is the solution of the differential equation governing the deflection of semi-infinite beam on elastic supports, simply loaded by transversal force (no axial force). The equation and its first and second derivatives are:

$$v_{(x)} = v_o \, e^{-x/l} \cos\left(\frac{x}{l}\right)$$

$$v'_{(x)} = -\frac{v_o}{l} \, e^{-x/l}\left[\cos\left(\frac{x}{l}\right) + \sin\left(\frac{x}{l}\right)\right]$$

$$v''_{(x)} = \frac{2\,v_o}{l^2} \, e^{-x/l} \sin\left(\frac{x}{l}\right)$$

Axial displacements are expressed by the following function. The equation and its first and second derivatives are:

$$u_{(x)} = -u_o\left(1 - \frac{2\,x}{3\,\pi\,l}\right)$$

$$u'_{(x)} = \frac{2\,u_o}{3\,\pi\,l}$$

$$u''_{(x)} = 0$$

Boundary Conditions

at $x = 0$:

$$v_{(x)} = v_o$$

$$v'_{(x)} = -\frac{v_o}{l}$$

$$v''_{(x)} = 0$$

$$u_{(x)} = -u_o$$

at $x = 3\pi l/2$:

$$v_{(x)} = 0$$

$$v'_{(x)} = \frac{v_o}{l} e^{-3\pi/2} \approx 0$$

$$v''_{(x)} = -\frac{2v_o}{l^2} e^{-3\pi/2} \approx 0$$

$$u_{(x)} = 0$$

Deformation Energy U

The deformation energy U is expressed as follows:

$$U = \frac{1}{2}\int_0^{3\pi l/2} \left[E\ A_b\ u'^{\,2}_{(x)} + E\ I\ v''^{2}_{(x)}\right] dx$$

$$U = \frac{1}{2}\int_0^{3\pi l/2} E\ A_b\ \frac{4\ u_o^2}{9\pi^2 l^2}\ dx + \frac{1}{2}\int_0^{3\pi l/2} E\ I\ \frac{4\ v_o^2}{l^4}\ e^{-2x/l} \sin^2\left(\frac{x}{l}\right) dx$$

The integration gives:

$$U = \frac{E\ A_b\ u_o^2}{3\ \pi\ l} + \frac{E\ I\ v_o^2}{4\ l^3}$$

where E : elasticity modulus of bolt,
A_b : cross-section of bolt,
I : moment of inertia of bolt.

Work of External Forces W

The calculation proves, that it is sufficient to integrate the work of the rock reaction pressure over the length from 0 to $\pi l/2$. On the other hand, the forces acting at the left end of the bar (point C) do not produce any work, as the displacements and the rotation in this point are equal to zero.

$$W = N_o u_o + Q_o v_o - \int_0^{\pi l/2} p_{(x)}\ v_{(x)}\ dx$$

The reaction pressure is constant from 0 to $\pi l/4$, and linearly decreases from $\pi l/4$

to $\pi l/2$, as the following function:

$$p_{(x)} = p\left(2 - \frac{4x}{\pi l}\right)$$

Then:

$$W = N_o u_o + Q_o v_o - p\ v_o \int_0^{\pi l/4} e^{-x/l} \cos\left(\frac{x}{l}\right) dx$$

$$- p\ v_o \int_{\pi l/4}^{\pi l/2} \left(2 - \frac{4x}{\pi l}\right) e^{-x/l} \cos\left(\frac{x}{l}\right) dx$$

and after integration:

$$W = N_o u_o + Q_o v_o - p\ v_o l\left(\frac{1}{2} + \frac{\sqrt{2}\, e^{-\pi/4} - 2e^{-\pi/2}}{\pi}\right)$$

Complementary Total Energy

The complementary total energy Π of the system is expressed as the difference between the energy of deformation U and the work W of external forces.

$$\Pi = U - W$$

$$\Pi = \frac{E\ A\ u_o^2}{3\ \pi\ l} + \frac{E\ I\ v_o^2}{4\ l^3} - N_o u_o - Q_o v_0 + p\ v_o\, l\left(\frac{1}{2} + \frac{\sqrt{2}\, e^{-\pi/4} - 2e^{-\pi/2}}{\pi}\right)$$

Calculation of Displacements at O

Minimization of the energy function for v_o gives:

$$\frac{\partial \Pi}{\partial v_o} = \frac{E\ I\ v_o}{2\ l^3} - Q_o + pl\left(\frac{1}{2} + \frac{\sqrt{2}\, e^{-\pi/4} - 2e^{-\pi/2}}{\pi}\right) = 0$$

$$v_o = \frac{2\ l^3}{E\ I}\left[Q_o - pl\left(\frac{1}{2} + \frac{\sqrt{2}\, e^{-\pi/4} - 2e^{-\pi/2}}{\pi}\right)\right]$$

Introducing $l = 4\,Q_o/\pi p$ one obtains:

$$v_o = \frac{128\, Q_o^4}{E\ I\ \pi^3\ p^3}\left[1 - \frac{4}{\pi}\left(\frac{1}{2} + \frac{\sqrt{2}\, e^{-\pi/4} - 2e^{-\pi/2}}{\pi}\right)\right]$$

$$v_o = b\ \frac{128\, Q_o^4}{E\ I\ \pi^3\ p^3}$$

where $b = 0.27$

For displacement u_o:

$$\frac{\partial \Pi}{\partial u_o} = \frac{2\ E\ A\ u_o}{3\ \pi\ l} - N_o = 0$$

$$u_o = \frac{3\ \pi\ l\ N_o}{2\ E\ A}$$

Substitution $l = 4\,Q_o/\pi p$ gives:

$$u_o = \frac{6\ N_o\ Q_o}{E\ A\ p}$$

List of Symbols

Mechanical Properties

σ_c	unconfined strength of the host material
p_u	maximum bearing pressure applied on the bolt by the host material
ϕ_j	joint friction angle
σ_{el}	yield limit of the bolt material
σ_{ec}	failure limit of the bolt material
Δc_b	cohesion due to bolt contribution
$\Delta\sigma_{nb}$	confining stress due to bolt contribution

Geometrical Characateristics

D_b	bolt diameter
l_A	distance between bolt extremity (point O) and the location of the maximum bending moment (point A)
l_e	distance between bolt extremity (point O) and the location of the maximum bending moment (point A) when the yield limit is reached
l_f	length of the part $O - A$ at failure
Δl_p	plastic lengthening of the bolt
A_j	surface of joint

Angles and Displacements

θ	dip angle of the joint
β	angle between the joint and the bolt axis
ω_o	rotation of the bolt extremity (point O)
ω_{oe}	rotation of the bolt extremity when yield limit is reached
ω_{of}	rotation of the bolt extremity when failure is reached
$\Delta\omega_{op}$	plastic rotation of the bolt extremity
γ_o	angle between axial and shear force acting at the bolt extremity (point O)
u_o	axial displacement of the bolt extremity
v_o	transversal displacement of the bolt extremity

U_o displacement of the bolt extremity in the joint direction
ΔU_{op} plastic displacement of the bolt extremity in the joint direction
U_j displacement on the joint

Forces and Moments

N_o axial force in the bolt extremity
N_{oe} axial force in the bolt extremity at yield limit
N_{of} axial force in the bolt extremity at failure
Q_o shear force in the bolt extremity
Q_{oe} shear force in the bolt extremity at yield limit
Q_{of} shear force in the bolt extremity at failure
M_A bending moment at point A
R_o total force in the bolt
R_{oe} total force in the bolt at yield limit
R_{of} total force in the bolt at failure
R_{on} component of the total force in the bolt perpendicular to the joint
R_{ot} component of the total force in the bolt parallel to the joint
T_b bolt contribution to the joint shear strength
T_{be} bolt contribution to the joint shear strength at yield limit
T_{bf} bolt contribution to the joint shear strength at failure

Normalised Parameters

F_T ratio of the bolt contribution to the maximum tensile force of the bolt
F_R ratio of the total force in the bolt to the maximum tensile force of the bolt
F_{Rn} ratio of the perpendicular component of the total force in the bolt to the maximum tensile force of the bolt
F_{Rt} ratio of the parallel component of the total force in the bolt to the maximum tensile force of the bolt
F_N ratio of the axial force in the bolt to the maximum tensile force of the bolt
F_Q ratio of the shear force in the bolt to the maximum tensile force of the bolt
F_U ratio of the displacement on the joint to the bolt diameter

References

Aydan, Ö. (1989): The stabilisation of rock engineering structures by rockbolts. Ph.D. Thesis, Nagoya University, Japan.

Azuar, J. J. (1977): Stabilisation de massifs rocheux fissurés par barres d'acier scellées. Rapport de recherche No 73, Laboratoire Central des Ponts et Chaussées, Paris, France.

Bjurström, S. (1974): Shear strength of hard rock jointed reinforced by grouted untensioned bolts. In: Proc., 3rd ISRM Congress, Denver, USA, 1194–1199.

Di Prisco, M. (1989): Sul comportamento a taglio delle barre d'armatura nel calcestruzzo. L'azione di spinotto: Risultati sperimentali e modellazione matematica. Doctorate Thesis, Politecnico di Milano, Italia.

Dight, P. M. (1983): Improvements to the stability of rock walls in open pit mines. Ph.D. Thesis, Monash University, Australia.

Egger, P., Pellet, F. (1991): Strength and deformation properties of reinforced jointed media under true triaxial conditions. In: Proc., 7th ISRM Congress, Aachen, Germany, 215–220.

Egger, P., Zabuski, L. (1991): Behaviour of rough bolted joints in direct shear tests. In: Proc., 7th ISRM Congress, Aachen, Germany, 1285–1288.

Ferrero, A. M. (1993): Resistenza al taglio di discontinuita' rinforzate. Doctoral Thesis, Technical University of Torino, Italy.

Gerrard, C. M., Pande, G. N. (1985): Numerical modelling of reinforced rock masses – I. Theory, computers and geotechnics, Vol. 1, 293–318.

Haas, C. J. (1981): Analysis of rock bolting to prevent shear movement in fracturated ground. Mining Engng. 33 (6), 698–704.

Hetényi, N. (1946): Beam on elastic foundation – Theory with applications in the fields of civil and mechanical engineering. The University of Michigan Press.

Holmberg, M. (1991): The mechanical behaviour of untensionned grouted rock bolts. Ph. D. Thesis, Royal Institute of Technology, Stockholm, Sweden.

Pellet, F. (1994): Strength and deformability of jointed rock masses reinforced by rockbolts. English Translation of the Doctoral Thesis 1169, Swiss Federal Institute of Technology, Lausanne, Switzerland.

Pellet, F., Egger, P., Ferrero, A. M. (1995a): Contribution of fully bonded rock bolts to the shear strength of joints: Analytical and experimental evaluation. In: Proc. 2nd Int. Conference on Mechanics of Jointed and Faulted Rock, MJFR-2, Vienna.

Pellet, F., Egger, P., Descoeudres, F. (1995b): A method for the design of a bolting system for rock slopes. In: Proc., 8th ISRM Congress, Tokyo.

Schubert, P. (1984): Das Tragvermögen des Mörtelversetzten Ankers unter aufgezwungener Kluftverschiebung. Doctoral Thesis, Montanuniversität, Leoben, Austria.

Spang, K. (1988): Beitrag zur rechnerischen Berücksichtung vollvermörtelter Anker bei der Sicherung von Felsbauwerken in geschichtetem oder geklüftetem Gebirge. Thèse de doctorat No 740, Ecole Polytechnique Fédérale de Lausanne, Switzerland.

Spang, K., Egger, P. (1990): Action of fully-grouted bolts in jointed rock and factors of influence, Rock Mech. Rock Engng. 23, 201–229.

Swoboda, G., Marenče, M. (1992): Numerical modelling of rock bolts in intersection with fault system. Proc. Numerical models in Geomechanics, NUMOG IV, Swansea, U.K., 729–738.

Authors' address: Dr. F. Pellet, 11 route de Livron, F-74100 Annemasse, France.

Activités de recherche et d'enseignement

Position actuelle

Maître de conférence à l'Université Joseph Fourier - Grenoble I - France, depuis septembre 1996:

- Enseignant au Département de Géotechnique de l'Ecole Polytechnique de l'Université de Grenoble I (Polytech'Grenoble), http://polytech.ujf-grenoble.fr
- Chercheur au Laboratoire Sols Solides Structures (3S-UMR 5521), Grenoble, http://www.3s.hmg.inpg.fr
- Adresse professionnelle :

Université Joseph Fourier - Laboratoire Sols Solides Structures (3S)
Domaine Universitaire - BP 53, 38041 Grenoble Cedex 09 - France
tél. : 04 76 82 70 23
fax: 04 76 82 70 00
email1 : frederic.pellet@inpg.fr
email2 : frpellet@wanadoo.fr

Activités de recherche

Principales activités de recherches contractuelles

- Institut de Radioprotection et de Sûreté Nucléaire (IRSN) : Recherches sur le comportement mécanique à long terme des roches en vue du stockage en souterrain de déchets radioactifs, depuis 1999.
- Coyne et Bellier, Ingénieurs consultants : Modélisation numérique du comportement différé de cavités souterraines, 1999-2001.
- Société Nationale des Chemins de Fer : Etude du vieillissement de tunnels anciens, 2001.

Principales collaborations internationales

- Massachusetts Institute of Technology (MIT), Cambridge, MA : Time dependent behavior of rock, collaboration avec le Prof. H.H. Einstein, depuis 2001.
- International Institute of Earthquake Engineering and Seismology, Tehran - Iran: Dynamic behavior of rock joints, collaboration avec le Prof. M.K. Jafari, depuis 2001.
- Tsinghua University, Beijing - China: Mechanics of anisotropic materials, collaboration avec le Prof. Z.Q. Zheng, programme (4B3/003) financé par le Ministère des Affaires Etrangères Français, 1998-2001.
- Ecole Hassania des Travaux Publics de l'Etat, Casablanca - Maroc : Tunnels à faible profondeur en sites urbains, collaboration avec le Prof. M. Sahli dans le cadre d'un programme TEMPRA financé par la Région Rhônes-Alpes, 1999.
- Ecole Polytechnique Fédérale de Lausanne (EPFL), Suisse : Etude de faisabilité de stockages de déchets radioactifs en souterrains profonds, collaboration avec le Prof. P. Egger, 1999.

Directions de thèses

Achevées :

- Nicolas Gatelier, "Etude expérimentale et numérique de l'endommagement des roches anisotropes", thèse de doctorat présentée en janvier 2001, co-dirigée avec le Professeur Benjamin Loret.
- Eric Boidy, "Modélisation numérique du comportement différé des cavités souterraines", thèse de doctorat financée en convention CIFRE par Coyne et Bellier, présentée en avril 2002, dirigée seul avec agrément.
- Attila Hajdu, "Comportement viscoplastique endommageable des roches et application aux grandes cavités souterraines de stockage", thèse de doctorat financée par l'Institut de Radioprotection et de Sûreté Nucléaire (IRSN), soutenance prévue en décembre 2003, co-dirigée avec le Professeur Marc Boulon.

En cours :

- Géraldine Fabre, "Analyse micro-mécanique de l'endommagement viscoplastique des roches anisotropes", soutenance en octobre 2004.
- Pierre Zokimila, "Modélisation numérique par homogénéisation du comportement des ouvrages de stockage à grande échelle", soutenance en octobre 2004.

Directions de DEA

- Farouk Fourar-Laidi, "Modélisation numérique par analyse inverse du comportement à long terme d'ouvrages souterrains" Diplôme d'Etude Approfondie (DEA) en Mécanique des Milieux Géophysiques et Environnement, 2003.

- Géraldine Fabre, "Comportement différé et endommagement des roches argilo-marneuses en relation avec la réalisation d'ouvrages de stockages souterrains profonds", Diplôme d'Etude Approfondie (DEA) en Mécanique des Milieux Géophysiques et Environnement, 2001.

- Pierre Zokimila, "Modélisation numérique des ouvrages de serrement pour les cavités souterraines de stockage", Diplôme d'Etude Approfondie (DEA) en Mécanique des Milieux Géophysiques et Environnement, 2001.

- Mahmaoud Ait Yaha, "Etude expérimentale du fluage des roches", Diplôme d'Etude Approfondie (DEA) en Mécanique des Milieux Géophysiques et Environnement, 1999.

- Olivier Benoit, "Modélisation numérique de tunnels profonds traversant un accident géologique", Diplôme d'Etude Approfondie (DEA) en Mécanique des Milieux Géophysiques et Environnement, 1998.

Directions de Post-Doc et de doctorants étrangers

- Zohra Zerfa "Modélisation à grande échelle du comportement différé et de l'endommagement d'ouvrages souterrains de stockage" études pour l'Institut de Radioprotection et de Sûreté Nucléaire, de Septembre 2003 à Septembre 2004

- Kambod Amini Hosseini "Behaviour of Jointed Rocks Subjected to Cyclic Loading", d'avril 2001 à février 2002.

- Rabah Arab "Etude du comportement mécanique d'un stockage en formation géologique profonde : synthèse des connaissances sur les techniques de réalisation des ouvrages souterrains dans les domaines du génie minier et du génie civil" études pour l'Institut de Radioprotection et de Sûreté Nucléaire, de Octobre 1999 à Mars 2000.

Liste de Publications

Chapitre d'ouvrage

1- F. Pellet, M. Boulon, M. Souley et F. Homand (2000), "Comportement mécanique des discontinuités", Chapitre 5, Manuel de mécanique des roches, Tome 1: Fondements, Comité Français de Mécanique des Roches, Presses de l'Ecole des Mines, Paris, pp 105-127.

Revues internationales

2- F. Pellet, A. Hajdu, F. Deleruyelle & F. Besnus (2004), A viscoplastic constitutive model including anisotropic damage for the time dependent mechanical behaviour of rock, submitted.

3- M.K. Jafari, F. Pellet, M. Boulon & K. Amini Hosseini (2004), "Experimental study of mechanical behaviour of rock joints under cyclic loading", Rock Mechanics and Rock Engineering, Springer Verlag, Ed. G. Barla, vol 37, n° 1, pp 3-23.

4- M. K Jafari , K Amini Hosseini, F. Pellet, M. Boulon & O. Buzzi (2003), "Evaluation of Shear Strength of Rock Joints Subjected to Cyclic Loading", Soil Dynamics and Earthquake Engineering, Elsevier Science, vol 23, no 7, pp 619-630.

5- E. Boidy, A. Bouvard & F. Pellet (2002), "Back analysis of time-dependent behavior of a monitored tunnel", International Journal of Tunneling and Underground Space Technology, Elsevier Science, vol 17, n° 4, pp 415-424.

6- M.K. Jafari, K. Amini Hosseini, M. Boulon, F. Pellet, H. Jalaly, A. Uromeihy & O. Buzzy (2002), "Laboratory investigation on shear strength variation of joint replicas due to low and high amplitude cyclic displacements", Journal of Seismology and Earhquake Engineering, vol 4, no 2, pp 37-49.

7- N. Gatelier, F. Pellet & B. Loret (2002), "Mechanical damage of an anisotropic rock under cyclic triaxial tests", International Journal of Rock Mechanics and Mining Sciences, Pergamon Press, vol 39, n° 3, pp 335-354.

8- F. Pellet & P. Egger (1996), "Analytical model for the mechanical behavior of bolted rock joints subjected to shearing", Rock Mechanics and Rock Engineering, Springer Verlag, Ed. H.H Einstein & K. Kovari, vol. 29, no 2, pp 73-97.

9- F. Pellet, F. Descoeudres & P. Egger (1993), "The effect of water seepage forces on the face stability of an experimental micro tunnel" Canadian Geotechnical Journal, vol. 30, n° 2, pp 363 - 369.

Revues nationales

10- F. Pellet (1995), "Résistance et déformabilité des massifs rocheux stratifiés renforcés par ancrages passifs - Application au calcul d'ouvrages souterrains", Tunnels et Ouvrages Souterrains, n° 129, pp 190-196.

11- F. Pellet, P. Egger & F. Descoeudres (1995), "Comportement mécanique d'une paroi expérimentale renforcée par clouage", Revue Française de Géotechnique, n° 71, pp 49-60.

12- F. Descoeudres & F. Pellet (1991), "Comportement mécanique de l'écran de soutènement d'une tranchée expérimentale étroite", Revue Française de Géotechnique, n° 55, pp 5 - 15.

Compte-rendus de congrès internationaux

13- F. Pellet, F. Z. Zerfa, A. Hajdu, F. Deleruyelle & F. Besnus (2004), "Numerical modelling of the Excavated Damaged Zone around underground openings", Proc 3rd Asian Rock Mechanics Symposium, Kyoto, Japan, accepted for publication.

14- K. Amini Hosseini, F. Pellet, M.K. Jafari (2004), "Shear strength reduction of rock joints due to cyclic loading" Proc 13th World Conference on Earthquake EngineeringVancouver, B.C., Canada, accepted for publication

15- N.P. Zokimila, E. Flavigny, F. Pellet & A. Billon (2003), Modélisation numérique du comportement à court et à long terme d'un tunnel ferroviaire, Conférence régionale africaine de Mécanique des Sols, Casablanca, Maroc, pp 233-239.

16- F. Pellet & G. Fabre (2003), "Comportement mécanique de roches argileuses lors d'essais de fluage de longue durée", Colloque du GdR Forpro - CNRS, La Grande Motte – France, septembre 2003.

17- F. Pellet, E. Boidy, A. Bouvard & N. Hoteit, (2003) "Viscoplastic behavior and damage to rock related to the design of underground waste depository", proceedings of the 10th International Congress on Rock Mechanics, Sandton, South-Africa, pp 893-898.

18- F. Pellet, K. Amini Hosseini, M.K. Jafari, M. Boulon (2003), "Evaluation of the behaviour of jointed rocks due to small repetitive seismic loading", 4th International Conference on Seismology and Earthquake Engineering, CD Rom SEE4, Tehran, Iran.

19- K. Amini Hosseini, M. Boulon, M.K. Jafari, F. Pellet and O. Buzzy (2003) ", "The effects of high amplitude cyclic shear displacements on the shear strength of jointed rocks, 4th

International Conference on Seismology and Earthquake Engineering, CD Rom SEE4, Tehran, Iran.

20- G. Fabre & F. Pellet (2002), "Identification des caractéristiques visqueuses d'une roche argileuse", Proceedings of the International Symposium on Identification and Determination of Soil and Rock Parameters for Geotechnical Design, PARAM, Paris - France, pp 33-40.

21- F. Pellet, A Hajdu, M. Boulon, F. Deleruyelle & F. Besnus (2002), "Numerical modeling of underground structures taking into account the visco-plastic behavior and damaging of rock", Proceedings of the International Conference on Numerical Models in Geomechanics - NUMOG VIII, Roma - Italy, pp 399-404.

22- M. Sahli, F. Pellet, E. Boidy & G. Fabre (2001), "Modeling of viscous behavior of rocks for deep tunnels", Proceedings of the International Eurock Symposium, 2001, Espoo - Finland, pp 541-546.

23- E. Boidy, F. Pellet & M. Boulon (2001), "Numerical modeling of deep tunnels including time-dependent behavior", Proceedings of the 10th International Conference on Computer Methods and Advances in Geomechanics - IACMAG, Tucson, Arizona - US, pp 1663-1668.

24- F. Pellet, N. Gatelier & B. Loret (2000), "Experimental study of damage of an anisotropic rock using cyclic triaxial test", Proceedings of the International Eurock Symposium, 2000, Aachen - Germany, pp 687-692.

25- F. Pellet, M. Sahli, E. Boidy & M. Boulon (2000), "Modeling of time-dependent behavior of sandstones for deep underground openings", Proceedings of the International Conference on Engineering and Technological Sciences - ICETS 2000, Session 5, Science Press, Beijing - China, pp 431-438.

26- G Armand, M. Boulon & F. Pellet (2000), "Direct shearing of rock joints: relations between mechanical mesoscopic evolution and microscopic fractal description", Proceedings of the International Conference on Engineering and Technological Sciences - ICETS 2000, Session 5, Science Press, Beijing - China, pp 339-346.

27- E. Boidy & F. Pellet (2000), "Identification of mechanical parameters for modeling time-dependent behavior of shale", Workshop Andra, Paris – France, pp 11-22.

28- F. Pellet & O. Benoit (1999), "Modélisation numérique 3D du comportement d'ouvrages souterrains lors de la traversée d'accidents géologiques", Proceedings of the 9th International Congress on Rock Mechanics, Paris - France, pp 213-218.

29- F. Pellet & M. Boulon (1998), "A constitutive model for the mechanical behavior of bolted rock joint", Proceedings of the 3rd International Conference on the Mechanics of Jointed and Faulted Rock, MJFR-3, Wien - Austria, pp 179-183.

30- F. Pellet & P. Egger (1995), "Analytical model for the behavior of bolted rock joints and practical applications", Proceedings of the International Symposium on Anchors in Theory and Practice, Salzburg - Austria, pp 93 – 100.

31- F. Pellet, P. Egger & A.M. Ferrero (1995), "Contribution of fully bonded rock bolts to the shear strength of joints: Analytical and experimental application", Proceedings of the 2nd International Conference on the Mechanics of Jointed and Faulted Rock, MJFR-2, Wien - Austria, pp 873 – 878.

32- F. Pellet, P. Egger & F. Descoeudres (1995), "A method for the design of a bolting system for rock slopes", Proceedings of the 8th International Congress on Rock Mechanics, Tokyo - Japan, pp 409 – 412.

33- F. Pellet, F. Descoeudres & P. Egger (1992), "Water seepage forces and stability of a micro tunnel in porous media". Proceedings of the International Symposium on Porous and Fractured Unsaturated Media - Transport and Behavior, Ascona - Switzerland, pp 323 – 332.

34- P. Egger & F. Pellet (1992), "Numerical and experimental investigation of the behavior of reinforced jointed medias", Proceedings of the International Conference on Fractured and Jointed Rock Masses, Lake Tahoe, California - US, vol. 2, pp 277 – 282.

35- F. Pellet (1991), "Experimental study of reinforced jointed models under true triaxial conditions", Proceedings of the 5th Young Geotechnical Engineers Conference, Grenoble - France.

36- P. Egger & F. Pellet (1991), "Strength and deformation properties of reinforced jointed medias under true triaxial conditions", Proceedings of the 7th International Congress on Rock Mechanics, Aachen - Germany, pp 215 – 220.

37- P. Egger & F. Pellet (1990), "Behavior of reinforced jointed medias under multiaxial loadings", Proceedings of the International Conference on Rock Joints, Loen - Norway, pp 191 – 194.

Présentations orales lors de congrès scientifiques

38- "Viscoplastic behavior and damage to rock related to the design of underground waste depository", 10th International Congress on Rock Mechanics, Sandton - South Africa, Septembre 2003.

39- "Evaluation of the behaviour of jointed rocks due to small repetitive seismic loading", 4th International Conference on Seismology and Earthquake Engineering, SEE4, Tehran, Iran, Mai 2003.

40- "Numerical modeling of deep tunnels including time-dependent behavior", Conference on Computer Methods and Advances in Geomechanics - IACMAG, Tucson, Arizona - US, Janvier 2001.

41- "Modeling of time-dependent behavior of sandstones for deep underground openings", International Conference on Engineering and Technological Sciences - ICETS 2000, Session 5, Beijing - China, Octobre 2000.

42- "Modeling of time-dependent behavior of shale for deep underground openings", Alert Conference, Aussois - France, Octobre 2000.

43- "Analytical model for the behavior of bolted rock joints and practical applications", International Symposium on Anchors in Theory and Practice, Salzburg - Austria, Octobre 1995.

44- "Water seepage forces and stability of a micro-tunnel in porous media", International Symposium on Porous and Fractured Unsaturated Medias - Transport and Behavior, Ascona - Switzerland, Septembre 1992.

45- "Numerical and experimental investigation of the behavior of reinforced jointed media", International Conference on Fractured and Jointed Rock Masses, Lake Tahoe, California - US, Juin 1992.

46- "Behavior of reinforced jointed medias under multiaxial loadings", International Conference on Rock Joints, Loen - Norway, Juin 1990.

Présentations orales données à l'invitation de personnalités scientifiques

47- "Endommagement des roches et comportement à long terme des ouvrages souterrains " , Seminar Tunnelling and site remediation, Ecole Polytechnique Fédérale de Lausanne, Suisse, à l'invitation du Professeur L. Vulliet, février 2003.

48- "Modeling of time dependent behavior of rock related to the design of underground openings", séminaire donné au Massachusetts Institute of Technology, Cambridge, MA - US, à l'invitation du Professeur H.H. Einstein, juin 2002.

49- "Experimental investigations and numerical modeling of viscoplastic behavior of rock including damage effect" séminaire donné à Harvard University, Cambridge, à l'invitation du Professeur J.R. Rice, mai 2002.

50- "Modeling of time-dependent behavior of shale for deep underground openings", séminaire donné au Academy of Sciences Institute, Wuhan - China, à l'invitation du Professeur L. Tingjie, octobre 2000.

51- "Modeling of time dependent behavior of claystones for deep underground openings" séminaire donné à la Chinese Water Resources Commission (CWRC), Wuhan - China, à l'invitation du Professeur C. Zhengquan, octobre 2000.

52- "Analytical model for the behavior of bolted rock joint and practical applications" séminaire donné à l'University of Tsinghua, Beijing - China, à l'invitation du Professeur Z.Q. Zheng, juin 1999.

53- "Quelques aspects théoriques et expérimentaux du comportement mécanique des massifs rocheux renforcés", séminaire donné au Laboratoire 3S, Grenoble - France, à l'invitation du Professeur M. Boulon, février 1996.

54- "Résistance et déformabilité des massifs rocheux stratifiés renforcés par ancrages passifs - Application au calcul d'ouvrages souterrains", exposé donné lors de l'assemblée générale de l'Association Française des Travaux en Souterrains pour la réception du prix de l'AFTES, Paris - France, décembre 1994.

55- "Résistance et déformabilité des massifs rocheux stratifiés renforcés par ancrages passifs", séminaire donné au Comité Français de Mécanique des Roches, Paris - France, octobre 1993.

56- "Présentation d'une presse véritablement triaxiale pour l'étude du comportement des massifs renforcés", séminaire donné à l'Ecole Polytechnique, Palaiseau - France, à l'invitation du Professeur P. Berest, octobre 1990.

57- "Etude du comportement de l'écran de soutènement d'une tranchée expérimentale", séminaire donné pour les journées d'études du Fonds National Suisse de la Recherche Scientifique, Lausanne - Switzerland, juin1989.

Principaux rapports scientifiques récents

58- "Etude de la rupture différée autour des cavités souterraines : Application au tunnel de Tournemire", rapport rédigé pour l'Institut de Radioprotection et de Sûreté Nucléaire (IRSN), avril 2004.

59- "Modélisation numérique par homogénéisation du comportement des ouvrages de stockage à grande échelle", rapport rédigé pour l'Institut de Radioprotection et de Sûreté Nucléaire (IRSN), janvier 2003.

60- "Formulation d'un modèle élasto-viscoplastique endommageable avec prise en compte de la déformation volumique irréversible" rapport rédigé pour l'Institut de Radioprotection et de Sûreté Nucléaire (IRSN), mai 2002

61- "Modélisation numérique des comportements élastique anisotrope et viscoplastique", rapport rédigé pour l'Institut de Radioprotection et de Sûreté Nucléaire (IRSN), janvier 2001.

62- “Modélisation numérique 3D de l’intersection d'un puits et d'une galerie horizontale”, Rapport rédigé pour l'Institut de Radioprotection et de Sûreté Nucléaire (IRSN), juillet 2000.

63- “Synthèse des connaissances sur les techniques de réalisation des ouvrages souterrains dans les domaines du génie minier et du génie civil”, Rapport rédigé pour l'Institut de Radioprotection et de Sûreté Nucléaire (IRSN), mars 2000.

Thèse de doctorat

64- “Résistance et déformabilité des massifs rocheux stratifiés renforcés par ancrages passifs”, Thèse n° 1169, Ecole Polytechnique Fédérale de Lausanne, 201p, Octobre 1993, (Prix de l’Association Française des Travaux en Souterrains 1994).

Activités d'Enseignement

Principaux cours et travaux dirigés enseignés

- Ingéniorat 1ère année : Identification physique des géomatériaux : 36 h/an depuis 1996.
- Ingéniorat 2ème année : Mécanique des roches : 28 h/an depuis 1998.

  Modélisation des massifs rocheux par éléments distincts : 16 h/an depuis 99.

  Eléments finis pour la géotechnique : 16 h/an depuis 1996.

  Stabilité des pentes : 16 h/an depuis 1996.
- Ingéniorat 3ème année : Ouvrages souterrains en site urbain : 20 h/an depuis 1997.
- 3ème cycle (Master) : Mécanique des roches et des massifs rocheux 24 h/an.

Cours enseignés lors de cycles de formation continue

- Session de formation sur la Méthode des Eléments Finis en Géotechnique (PLAXIS), Grenoble - France, Mai 1999.
- Programme "Tunnels en Sites Urbains", Ecole Hassania des Travaux Publics de l'Etat (EHTPE), Casablanca - Maroc, avril 1999.
- Journées d'études des Architectes en chef des monuments historiques sur les moyens actuels de modélisation et de calcul applicables aux monuments anciens, "Modélisation des ouvrages historiques par la méthode des éléments distincts", Paris -France, Septembre 1998.
- Cours Post-grade en génie urbain, Ecole Polytechnique Fédérale de Lausanne (EPFL), Lausanne - Suisse, février 1995.

Annexe : Contenu des principaux cours enseignés à l'Ecole Polytechnique de l'Université de Grenoble I

Identification physique des géomatériaux

Durée : 12 h cours, 12 h TD et 16 h TP

Prérequis : aucun

Enseignants : Frédéric Pellet et Géraldine Fabre

Descriptif et objectifs : caractérisation physique et chimique des sols et des roches en vue de la description de leur comportement hydro-mécanique.

Plan de cours :

- Présentation du milieu naturel : L'écorce terrestre, altération des roches et formation des sols, particularités du comportement mécanique des géomatériaux, schématisation du milieu naturel.
- Le modèle polyphasique : Poids spécifique et densité, indice des vides et porosité, teneur en eau et degré de saturation.
- Les roches : Les types de roches, le massif rocheux et ses discontinuités, la matrice rocheuse, structure et texture, composition minéralogique, comportement mécanique, vitesse des ondes sonores et index de qualité.
- Les sols grenus ou pulvérulent : Analyse de la granulométrie, morphologie des grains, densité relative, compacité, teneur en éléments fins, propriétés mécaniques, problèmes géotechniques propres aux sols grenus, liquéfaction des sables etc.
- Les sols fins : Définition, nature et structure des argiles, principaux minéraux argileux, sédimentométrie, surface spécifique, consistance et limites d'Atterberg, teneur en matière organique, activité et sensibilité des argiles, propriétés mécaniques, problèmes géotechniques propres aux sols fins, gonflement, gélivité, dispersivité.
- Utilisation des géomatériaux dans le génie civil : Essais sur les granulats, dureté, attrition, abrasivité, fragmentation dynamique, teneur en éléments fins et état de propreté, contrôle et mise en œuvre, portance, densité, critère de filtre et drainage, nomenclature et

classifications des sols, corrélations entre paramètres physiques et caractéristiques mécaniques, cohésion et angle de frottement interne.

Mécanique des roches

Durée : 12 h cours, 8 h TD et 8 h de TP

Prérequis : Géologie générale, mécanique des milieux déformables

Enseignants : Frédéric Pellet et Yves Orengo

Descriptif et objectifs : Comprendre et décrire le comportement mécanique des roches et des massifs rocheux dans le but de dimensionner les ouvrages réalisés au rocher,

Plan de cours :

- Nature et structure des formations rocheuses : différentes formations rocheuses (ignées, sédimentaires, métamorphiques), caractérisation et classification empirique des massifs rocheux (RMR), structure crystalline et texture de la matrice rocheuse,
- Observation expérimentale du comportement mécanique des roches : essais de compression simple et essai triaxial, traction directe et indirecte, propagation des ondes, émission acoustique,
- Rupture de la matrice rocheuse : rupture fragile et ductile, mécanique de la rupture, bifurcation et localisation des déformations, plasticité et critères de rupture, comportement post-rupture,
- Déformabilité de la matrice rocheuse : lois de comportement, élasticité linéaire isotrope et anisotrope, endommagement, visco-élasticité et visco-plasticité, fluage et gonflement,
- Comportement thermo hydro mécanique : Conductivités hydraulique et thermique, couplage thermo-hydro-mécanique, théorie de Biot,
- Comportement mécanique des discontinuités : Caractérisation morphologique, essai de cisaillement, déformabilité des joints, critères de rupture et endommagement, modèle hydraulique,
- Modélisation numérique du comportement des massifs rocheux : Approche continue et homogénéisation (MEF), Approche discontinue et Méthode des Eléments Distincts,
- Travaux dirigés de modélisation : Application de la méthode des éléments distincts à la stabitité de versants rocheux, de cavités souterraines et de fondations de barrage (code Udec).

Application de la méthode des éléments finis à la Géotechnique

Durée : 6 h cours et 16 h TD

Prérequis : Méthode des éléments finis

Enseignants : Marc Boulon, Etienne Flavigny, Frédéric Pellet

Descriptif et objectifs : Comprendre la logique de fonctionnement d'un logiciel éléments finis adapté à la géotechnique.Utiliser la méthode des éléments finis dans le cadre d'un mini-projet pour le calcul d'ouvrages géotechniques. Mettre en œuvre les données et analyser de manière critique les résultats de calcul.

Plan de cours :

- Rappels généraux sur la méthode des éléments finis : Equations ponctuelles d'un problème de physique (écoulement en milieu poreux), Formulation variationnelle, Formulation discrétisée, Résolution numérique
- Principales phases de calcul par éléments finis : Problème linéaires, Problèmes non linéaires, Notion d'étape de chargement
- Présentation d'un logiciel éléments finis développé pour les applications géotechniques : Environnement Windows, Pré et post traitement, Spécificité relative à la géotechniques
- Etude de cas : Fondation superficielle (étude académique guidée), Soutènement d'une fouille (mini-projet), Remblai de préchargement, avec consolidation du sol, Ouvrages souterrains

Ouvrages souterrains en site urbain

Durée : 12 h cours et 12 h visites de chantier

Prérequis : Mécanique des sols et des roches

Enseignant : Frédéric Pellet

Descriptif et objectifs : Comprendre la spécificité des ouvrages souterrains en site urbain et acquérir les méthodes de calcul adaptées.

Plan de cours :

- Spécificité des constructions souterraines en site urbain

- Méthode de construction dans les sols et les roches tendres
- Excavations au tunnelier
- Stabilité de la section courante et du front de taille
- Tassements en surface
- Impact sur l'environnement